

The Handbook of Environmental Chemistry 40
Series Editors: Damià Barceló · Andrey G. Kostianoy

Andrea Scozzari
Elissavet Dotsika *Editors*

Threats to the Quality of Groundwater Resources

Prevention and Control

 Springer

The Handbook of Environmental Chemistry

Founded by Otto Hutzinger

Editors-in-Chief: Damià Barceló • Andrey G. Kostianoy

Volume 40

Advisory Board:

**Jacob de Boer, Philippe Garrigues, Ji-Dong Gu,
Kevin C. Jones, Thomas P. Knepper, Alice Newton,
Donald L. Sparks**

More information about this series at <http://www.springer.com/series/698>

Threats to the Quality of Groundwater Resources

Prevention and Control

Volume Editors: Andrea Scozzari · Elissavet Dotsika

With contributions by

I. Adurno · M. Bavusi · R. Bernini · E. Bessonova ·
R. Biddau · S. Bortnikova · I. Catapano · J. Chao · R. Cidu ·
G. De Martino · C. Di Natale · F. Dini · E. Dotsika ·
M. Doveri · B. El Mansouri · A. Fekri · A. Filippidis ·
P. Gamaletsos · A. Godelitsas · J. Göttlicher · E. Gueguen ·
Y. Karin · M. Kili · V. Lapenna · A. Loperte · Y. Manstein ·
M. Menichini · A. Mridekh · B. Nisi · G. Persichetti ·
B. Raco · E. Rizzo · O. Saeva · M. Schneider · A. Scozzari ·
F. Soldovieri · S. Straface · G. Testa · L. Thomas ·
E. Tzamos · A. Winkler · N. Yurkevich



Springer

Editors

Andrea Scozzari
CNR Institute of Information Science and
Technologies (CNR-ISTI)
Pisa
Italy

Elissavet Dotsika
Institute of Material Science
NCRS “Demokritos”
Aghia Paraskevi
Attiki
Greece

ISSN 1867-979X ISSN 1616-864X (electronic)
The Handbook of Environmental Chemistry
ISBN 978-3-662-48594-1 ISBN 978-3-662-48596-5 (eBook)
DOI 10.1007/978-3-662-48596-5

Library of Congress Control Number: 2015958018

Springer Heidelberg New York Dordrecht London
© Springer-Verlag Berlin Heidelberg 2016

This work is subject to copyright. All rights are reserved by the Publisher, whether the whole or part of the material is concerned, specifically the rights of translation, reprinting, reuse of illustrations, recitation, broadcasting, reproduction on microfilms or in any other physical way, and transmission or information storage and retrieval, electronic adaptation, computer software, or by similar or dissimilar methodology now known or hereafter developed.

The use of general descriptive names, registered names, trademarks, service marks, etc. in this publication does not imply, even in the absence of a specific statement, that such names are exempt from the relevant protective laws and regulations and therefore free for general use.

The publisher, the authors and the editors are safe to assume that the advice and information in this book are believed to be true and accurate at the date of publication. Neither the publisher nor the authors or the editors give a warranty, express or implied, with respect to the material contained herein or for any errors or omissions that may have been made.

Printed on acid-free paper

Springer-Verlag GmbH Berlin Heidelberg is part of Springer Science+Business Media
(www.springer.com)

Editors-in-Chief

Prof. Dr. Damià Barceló

Department of Environmental Chemistry
IDAEA-CSIC
C/Jordi Girona 18–26
08034 Barcelona, Spain
and
Catalan Institute for Water Research (ICRA)
H20 Building
Scientific and Technological Park of the
University of Girona
Emili Grahit, 101
17003 Girona, Spain
dbcqam@cid.csic.es

Prof. Dr. Andrey G. Kostianoy

P.P. Shirshov Institute of Oceanology
Russian Academy of Sciences
36, Nakhimovsky Pr.
117997 Moscow, Russia
kostianoy@gmail.com

Advisory Board

Prof. Dr. Jacob de Boer

IVM, Vrije Universiteit Amsterdam, The Netherlands

Prof. Dr. Philippe Garrigues

University of Bordeaux, France

Prof. Dr. Ji-Dong Gu

The University of Hong Kong, China

Prof. Dr. Kevin C. Jones

University of Lancaster, United Kingdom

Prof. Dr. Thomas P. Knepper

University of Applied Science, Fresenius, Idstein, Germany

Prof. Dr. Alice Newton

University of Algarve, Faro, Portugal

Prof. Dr. Donald L. Sparks

Plant and Soil Sciences, University of Delaware, USA

The Handbook of Environmental Chemistry

Also Available Electronically

The Handbook of Environmental Chemistry is included in Springer's eBook package *Earth and Environmental Science*. If a library does not opt for the whole package, the book series may be bought on a subscription basis.

For all customers who have a standing order to the print version of *The Handbook of Environmental Chemistry*, we offer free access to the electronic volumes of the Series published in the current year via SpringerLink. If you do not have access, you can still view the table of contents of each volume and the abstract of each article on SpringerLink (www.springerlink.com/content/110354/).

You will find information about the

- Editorial Board
- Aims and Scope
- Instructions for Authors
- Sample Contribution

at springer.com (www.springer.com/series/698).

All figures submitted in color are published in full color in the electronic version on SpringerLink.

Aims and Scope

Since 1980, *The Handbook of Environmental Chemistry* has provided sound and solid knowledge about environmental topics from a chemical perspective. Presenting a wide spectrum of viewpoints and approaches, the series now covers topics such as local and global changes of natural environment and climate; anthropogenic impact on the environment; water, air and soil pollution; remediation and waste characterization; environmental contaminants; biogeochemistry; geoecology; chemical reactions and processes; chemical and biological transformations as well as physical transport of chemicals in the environment; or environmental modeling. A particular focus of the series lies on methodological advances in environmental analytical chemistry.

Series Preface

With remarkable vision, Prof. Otto Hutzinger initiated *The Handbook of Environmental Chemistry* in 1980 and became the founding Editor-in-Chief. At that time, environmental chemistry was an emerging field, aiming at a complete description of the Earth's environment, encompassing the physical, chemical, biological, and geological transformations of chemical substances occurring on a local as well as a global scale. Environmental chemistry was intended to provide an account of the impact of man's activities on the natural environment by describing observed changes.

While a considerable amount of knowledge has been accumulated over the last three decades, as reflected in the more than 70 volumes of *The Handbook of Environmental Chemistry*, there are still many scientific and policy challenges ahead due to the complexity and interdisciplinary nature of the field. The series will therefore continue to provide compilations of current knowledge. Contributions are written by leading experts with practical experience in their fields. *The Handbook of Environmental Chemistry* grows with the increases in our scientific understanding, and provides a valuable source not only for scientists but also for environmental managers and decision-makers. Today, the series covers a broad range of environmental topics from a chemical perspective, including methodological advances in environmental analytical chemistry.

In recent years, there has been a growing tendency to include subject matter of societal relevance in the broad view of environmental chemistry. Topics include life cycle analysis, environmental management, sustainable development, and socio-economic, legal and even political problems, among others. While these topics are of great importance for the development and acceptance of *The Handbook of Environmental Chemistry*, the publisher and Editors-in-Chief have decided to keep the handbook essentially a source of information on "hard sciences" with a particular emphasis on chemistry, but also covering biology, geology, hydrology and engineering as applied to environmental sciences.

The volumes of the series are written at an advanced level, addressing the needs of both researchers and graduate students, as well as of people outside the field of

“pure” chemistry, including those in industry, business, government, research establishments, and public interest groups. It would be very satisfying to see these volumes used as a basis for graduate courses in environmental chemistry. With its high standards of scientific quality and clarity, *The Handbook of Environmental Chemistry* provides a solid basis from which scientists can share their knowledge on the different aspects of environmental problems, presenting a wide spectrum of viewpoints and approaches.

The Handbook of Environmental Chemistry is available both in print and online via www.springerlink.com/content/110354/. Articles are published online as soon as they have been approved for publication. Authors, Volume Editors and Editors-in-Chief are rewarded by the broad acceptance of *The Handbook of Environmental Chemistry* by the scientific community, from whom suggestions for new topics to the Editors-in-Chief are always very welcome.

Damià Barceló
Andrey G. Kostianoy
Editors-in-Chief

Editorial Note and Acknowledgements

We intend this book for a wide audience of readers, such as students, researchers, policy-makers, and stakeholders at various levels. In particular, it is intended for those experts who want to widen their vision to contiguous fields of expertise. This approach can also be useful in order to enhance the mutual understanding between researchers having different backgrounds. Without the aim to be exhaustive, this book is intended as a stimulus for a multidisciplinary vision of the many interconnected aspects of groundwater protection, exploitation, monitoring, and the risks associated with the management of groundwater resources.

Chapters of this book have been peer-reviewed by two reviewers per each chapter. In some cases, more than one review round was needed. Reviewers have been selected partly internal and partly external to the book project. Some of the reviewers chose to remain anonymous. The editors are very indebted to the reviewers for their great contribution to the overall quality of the book.

Those who agreed to be acknowledged are listed here:

Dr. Matteo Lelli, National Research Council (CNR-IGG), Italy
Dr. Gianfranco Morelli, Geostudi Astier, Italy
Prof. Rosa Cidu, University of Cagliari, Italy
Prof. Orlando Vaselli, University of Florence, Italy
Prof. Salvatore Straface, University of Calabria, Italy
Dr. Francesco Soldovieri, National Research Council (CNR-IREA), Italy
Dr. Giulio Giovannetti, National Research Council (CNR-IFC), Italy
Dr. Massimo Guidi, National Research Council (CNR-IGG), Italy
Prof. Bouabid El Mansouri, Ibn Tofail University, Morocco
Dr. Marco Doveri, National Research Council (CNR-IGG), Italy
Dr. Brunella Raco, National Research Council (CNR-IGG), Italy

The editors of this book must also acknowledge Emanuela Ferro and Cristina Rosamilia for their invaluable technical aid in the revision process.

Also, we are grateful to the Editors-in-Chief of this book series for the opportunity given, and in particular to Prof. Andrey Kostianoy for having stimulated the build-up phase of this project.

Finally, our sincere thanks go to the contributors of this volume, which have always shown a great availability and engagement, since the beginning of the book project.

Andrea Scozzari and Elissavet Dotsika

Contents

Introduction	1
Andrea Scozzari and Elissavet Dotsika	
Protection of Groundwater Resources: Worldwide Regulations and Scientific Approaches	13
Marco Doveri, Matia Menichini, and Andrea Scozzari	
Threats to the Quality of Water Resources by Geological CO₂ Storage: Hydrogeochemical and Other Methods of Investigation: A Review	31
L. Thomas, M. Schneider, and A. Winkler	
Groundwater Contamination: Environmental Issues and Case Studies in Sardinia (Italy)	53
Riccardo Biddau and Rosa Cidu	
Geological Sources of As in the Environment of Greece: A Review	77
Platon Gamaletsos, Athanasios Godelitsas, Elissavet Dotsika, Evangelos Tzamos, Jörg Göttlicher, and Anestis Filippidis	
Groundwater Contamination Studies by Environmental Isotopes: A review	115
Barbara Nisi, Brunella Raco, and Elissavet Dotsika	
The Importance of Reduced-Scale Experiments for the Characterization of Porous Media	151
S. Straface and E. Rizzo	
Mathematical Models as Tools for Prevention and Risk Estimates of Groundwater Pollution: Contributions and Challenges	175
Bouabid El Mansouri, Malika Kili, Jamal Chao, Ahmed Fekri, and Abdelaziz Mridekh	

Groundwater Monitoring and Control by Using Electromagnetic Sensing Techniques 193
M. Bavusi, V. Lapenna, A. Loperte, E. Gueguen, G. De Martino, I. Adurno, I. Catapano, and F. Soldovieri

Pollution Detection by Electromagnetic Induction and Electrical Resistivity Methods: An Introductory Note with Case Studies 225
Yuri Manstein and Andrea Scozzari

The Combination of Geoelectrical Measurements and Hydro-Geochemical Studies for the Evaluation of Groundwater Pollution in Mining Tailings Areas..... 239
Svetlana Bortnikova, Nataliya Yurkevich, Elisaveta Bessonova, Yury Karin, and Olga Saeva

Microfluidic Optical Methods: A Review..... 257
Genni Testa, Gianluca Persichetti, and Romeo Bernini

Non-conventional Electrochemical and Optical Sensor Systems..... 279
Corrado Di Natale, Francesca Dini, and Andrea Scozzari

Index 313

Introduction

Andrea Scozzari and Elissavet Dotsika

Abstract Groundwater is the only source of water supply for some countries in the world and the main source for many other countries. Especially in the European Union and in the United States of America, the role of high-quality groundwater is fundamental for the drinking water supply, and this is true also for some countries in Asia, Africa and Australia. Thus, in a growing number of contexts, safeguarding drinking water supplies is strictly linked with the protection of local groundwater resources. The usage of groundwater for irrigation has also a relevant share in many countries, sometimes contributing to stress the resource. The assessment of groundwater vulnerability and the individuation of potential hazards are thus becoming common and often compelling issues. Given this particular background, this introductory chapter illustrates the motivational framework of this book and outlines its contents.

Keywords Freshwater pollution, Groundwater management, Water quality, Water resources protection

Content

References 10

A. Scozzari (✉)
CNR Institute of Information Science and Technologies (CNR-ISTI), Via Moruzzi 1, 56124
Pisa, Italy
e-mail: a.scozzari@isti.cnr.it

E. Dotsika
Institute of Material Science, NCSR “Demokritos”, 153 10 Aghia Paraskevi, Attiki, Greece

There are known scenarios of incrementing attention and general concerns about worldwide freshwater resources. The trend of global water usage and withdrawal, the impact of climate change on the availability and on the exploitation possibilities of water resources and the impact of men activities on freshwater supplies are among the various aspects that people involved in the water sector have to deal with, systematically. The many challenges regarding this complicated context involve a diversified array of communities, which include stakeholders at various levels, scientists, technologists, industrial companies, water managers and policy-makers, encouraging the idea that a wide multidisciplinary framework can actively enhance communication, assist decision-making and mitigate the consequences of anthropic pressure on water resources, which are often combined with climate effects. Indeed, decision-makers who understand the scientific aspects of emerging water risks and the existing countermeasures are in a better position to determine policy and legal frameworks, in order to promote sound environmental management and protection. This is also in accordance with the demand for a global water governance [1], due to the general acknowledgment that technology and infrastructures alone are not enough to deal with the complexity of water management practices.

Despite the increasing general awareness about the arising issues, there are different degrees of perception towards water problems in the involved communities, which are also variable on a regional basis. Notwithstanding the wide literature produced, there's still some underestimation of the potential environmental security risks (and their implications) for the near and the middle-term future at regional levels, while local issues are typically more tangible. Nevertheless, there is an already well-established literature about a variety of risks, such as the eventuality of conflicts involving shared water bodies, the increased hazards for the health of populations, possible migratory movements and more general trans-boundary issues, which are often discussed in the frame of the prospected climate change scenarios [2–5]. The interested reader can expand the research much beyond the cited literature, which is just proposed as a possible starting point, given the wide availability of books, journal articles, reports and project deliverables focused on the various aspects of securing water supplies.

According to the “World Water Development Report 4” by UNESCO [6], “Water quality is inextricably linked with water quantity as both are key determinants of supply. Compared to water quality, water quantity has received far more investment, scientific support and public attention in recent decades. However, water quality is just as important as water quantity for satisfying basic human and environmental needs”. The consciousness of the threats to the quality of water resources, the assessment of regulatory frameworks and the development of techniques to monitor and mitigate such threats play a key role for the preservation and the future availability of the resources under exploitation. This aspect is an essential component in the frame of minimising the environmental stress and its consequent security issues [7]. The issue of managing and securing water supplies represents a general challenge involving a large part of the world, and it's not limited to the areas which are considered more exposed to problems of scarcity. According to the

data acquired by the Eurobarometer (European Commission) in 2006, “when asked to list the five main environmental issues that Europeans are worried about, averaged results for the EU25 show that nearly half of the respondents are worried about ‘water pollution’ (47%), with figures for individual countries going up as far as 71%” [8]. Even if Europeans are beginning to perceive the risks concerning the water supply for human consumption, in most of the developed and industrialised countries, the majority of people take safe drinking water for granted. As yet, about 800 million people in the world are lacking safe drinking water from improved sources, according to the latest UN-Water Annual Assessments [9–11] and the relating Thematic Factsheets. The deficit of improved sources of drinking water is not necessarily related with scarcity; it’s instead commonly due to the lack of infrastructures and, in many cases, to various forms of pollution threatening the existing resources, in a context where the risk posed by climate change represents an additional threat [10]. The general mismatch between pro capita renewable freshwater and percentage of population accessing to safe water can be observed in several maps, which are currently available online [12–14]. Both geogenic and anthropogenic contamination sources participate in this complex scenario, where agricultural activities, industrial sites and human settlements represent the major anthropogenic threats to the quality of water. Also, the major problems of pollution are not necessarily individuated in the most industrialised countries (e.g. 80% of sewage in developing countries is discharged untreated into water bodies, according to the UN-Water Thematic Factsheet “Water Quality” [15]).

It is well known that about 96.5% of the water on the Earth is ocean water, while the total amount of freshwater storage is about 2.5%, being the remaining classified as other saline water. According to Shiklomanov [16, 17], 68.7% of the existing freshwater lies in the icecaps, in the glaciers or permanent snow cover, while about 30.1% of the total freshwater is groundwater. Inland water (including rivers, lakes, soil moisture, swamps) is representing only about 0.3% of the existing freshwater, keeping ground ice and permafrost out of the calculated budget. Despite its proportionally small amount, the surface water storage represents a strategic resource, which historically had a major impact over civilisation and still plays a fundamental role in many countries, besides being easily in the focus of trans-boundary water problems. Still, the above figures say that groundwater represents about 99% of the freshwater available for use, justifying its enormous importance, and it’s characterised by an uneven global distribution and a very diversified role on a geographical basis [18]. Despite the heterogeneous patterns in terms of availability, usage, qualitative and quantitative characteristics, the exploitation of groundwater aquifers presents common issues regarding their susceptibility to degradation. Potential vulnerabilities of groundwater reservoirs actually depend on various factors, e.g. the hydrogeological and geochemical contexts, the abstraction rates, the policy of usage and the surrounding human activities, which are among the most influencing variables. In particular, the policy of exploitation and the distribution among the various categories of users (i.e. agricultural, domestic, industrial) is very specific to each country [19, 20], and also the environmental stressors potentially affecting the availability and quality of groundwater are often peculiar to each

territory. For this reason, all the aspects linked with the exploitation and protection of the resource should ideally be managed at different scales, from regional to local, aiming at a truly sustainable use, which takes into account the environmental factors characterising each analysed scenario and the connected aspects of vulnerability.

At a global level, surface water is still largely prevailing over groundwater in terms of withdrawn quantities (source: FAO AQUASTAT [19]), but high figures of abstracted groundwater (including non-renewable one) are widespread in countries which are prone to problems of scarcity, especially for what regards the agricultural use. The balance between exploitation of surface water and groundwater reservoirs is very variable on a geographical basis, and it is not necessarily driven by the local abundance of surface water. Various additional factors, including the degree of economic development in the region and the state of degradation of surface water bodies, contribute to determine such balance. In the future, this heterogeneity in the distribution, exploitation and usage of freshwater storage will still be present and probably exacerbated by the demographic trends, the industrial development and climate change scenarios [17].

According to UNESCO [21], “groundwater is the only source of water supply for some countries in the world (e.g., Denmark, Malta, Saudi Arabia). Groundwater in Tunisia is 95% of the total water resources withdrawn, in Belgium it is 83%, in the Netherlands, Germany and Morocco it is 75%”. Also, “in most European countries (Austria, Belgium, Denmark, Hungary, Romania and Switzerland) groundwater use exceeds 70% of the total water consumption”.

The role of high-quality groundwater is fundamental for the drinking water supply and for domestic uses in general [22]. According to the Statistical Office of the European Union (Eurostat), groundwater is the main source of municipal water supplies in most European countries [20]. Latest cumulated values of water abstraction by source and by sector of use, referred to EU28 plus Switzerland, indicate that groundwater abstraction for the public water supply is about 60% of the total. In particular, the report by UNESCO [21] specifies that “water supply of such European cities as Budapest, Copenhagen, Hamburg, Munich, Rome and Vienna is completely or almost completely based on groundwater, and for Amsterdam, Brussels and other cities it provides for more than half of the total water demand”.

It is thus clear how crucial is the protection of groundwater against misuse and degradation and its future role in this framework, being largely the main freshwater resource for vital needs at a global level. To reinforce this concept, it is important to note what Shiklomanov [17] says, “all water resources estimates are optimistic because no account is taken of the qualitative depletion of water resources through the ever increasing pollution of natural waters. This problem is very acute in the industrially developed and densely populated regions where no efficient waste water purification takes place. The major sources of intensive pollution of waterways and water bodies are contaminated industrial and municipal waste water as well as water returning from irrigated areas”. And also, “Every cubic metre of contaminated waste water discharged into water bodies and water courses spoils up

to 8–10 m³ of pure water”. This means that the reliable availability of water does not depend only on climate-induced or men-induced scarcity, but it’s also deeply influenced by the hazards to the quality of water, which potentially reduce the portion of the safely usable resource. The combination of the factors stated above stresses the importance of safeguarding water resources as a whole, implying that the particular role and the peculiarities of groundwater deserve a special attention.

Safeguarding groundwater necessarily includes the analysis and proactive prevention of the threats to the quality and availability of the resource. In fact, the characterisation of aquifer systems shall comprise the assessment of its quantitative characteristics, its eventual trends of depletion and the risks of deterioration in its quality (e.g. salinisation, industrial pollution, chemicals from agricultural activities, intrusion of urban wastewater, etc.). The assessment of such vulnerabilities is a key point in the frame of a strategic management of groundwater reservoirs, and it represents also a highly multidisciplinary exercise.

There are known threats of overexploitation and pollution of groundwater resources, particularly dealing with their very valuable renewable portion, in addition to the exploitation of non-renewable and even fossil water (as defined in [23]). As a consequence, there is evidence of the extreme importance to monitor, protect against pollution and manage the underground water storage in an optimal way. It is thus clear how effective inputs to decision-making come from the availability of data, assessment methods, monitoring technologies, models and the entire scientific and technological framework contributing to mitigate the exposure of groundwater resources to the known risks, in terms of quality and quantity. In addition, the assessment of a complete scenario involves the proper evaluation of the water footprints associated with the involved stakeholders [24], as it comes to an effective decision-making. Under this point of view, the wide interdisciplinary approach that is required to deal with the assessment and protection of the aquifer systems can also contribute to reduce the conflicts within stakeholders.

Prevention starts by knowing the main threats to the resource and its whole surrounding ecosystem; in particular, the protection of groundwater resources is connected with the action of controlling the entire encompassing environment, including the direct monitoring of the aquifer system, but not limited to it. In fact, there is a widespread consciousness nowadays that the scope of investigations and monitoring activities cannot be limited to the mere performing of direct measurements of the quality of water. The potential of new technological possibilities for investigating and modelling the whole environmental context and its background conditions is nowadays well perceived. In addition to that, only an overall vision that goes further merely technological viewpoints can potentially allow scientists, stakeholders and decision-makers to individuate and address the most relevant risks in an efficient way and determine effective countermeasures.

Chapters of this book focus on the scientific and technological aspects regarding the assessment and surveillance of groundwater resources, with the idea of providing a description of relevant issues and the possibilities to investigate them. Readers coming from diverse backgrounds can read across the contribution of multiple

disciplines with the option of going deeper through the suggested specialised literature. For this reason, the book is organised in order to bring the reader through various viewpoints, according to the diverse disciplines involved, without certainly being exhaustive, but with the aim of picking up emblematic topics for the relevance of their subjects in the context of groundwater protection and control.

The first chapter (by Doveri et al. [25]) introduces the concept of protection area of a groundwater source for human consumption, focusing on the regulations and the related scientific-technical approaches. This is a fundamental aspect to be brought to the readers' attention, before investigating pollution mechanisms and analysing possible sources of contamination. The concept of vulnerability, the assessment of the risks associated with local activities and the study of the hydrogeological background represent a common framework to all the possible kinds of contamination. In particular, the definition of protection zones is essential for safeguarding groundwater withdrawals for human consumption.

The following chapter (by Thomas et al. [26]) investigates the potential impact on groundwater quality resulting from geologic carbon sequestration, which is a practice introduced in the last decades in order to reduce the emissions of greenhouse gases to the atmosphere. Risks for freshwater resources can arise from low pH values and the subsequent dissolution of minerals, which may cause high concentrations in trace elements that are potentially dangerous for the human health. This aspect makes the threats to the quality of groundwater associated with the sequestration of geologic carbon clearly compelling. Ascending saline intrusion into shallower freshwater aquifers is an additional important risk discussed by the authors, which is also illustrated and discussed in the chapter.

Contamination sources can be either of natural origin or connected with human activities. The chapter by Biddau and Cidu [27] presents exemplary situations in which the geogenic degradation and the anthropogenic contamination mechanisms can be discriminated, in terms of natural water/rock interactions or as a consequence of mining activities. The chapter is focused on the assessment of contamination by heavy metals in the groundwater of Sardinia Island and has a general applicability in terms of understanding the background processes and the role played by the natural baseline of contaminants in such discriminations.

In particular, for what regards water pollution by arsenic (As), the variety of sources and the relevant concentrations found in Greece make this country a peculiar territory in order to generalise and better understand the methodology for the assessment of contamination from As. The review work by Gamaletsos et al. [28] analyses the geological sources of arsenic in the environment of Greece, which are demonstrated to affect underground, surface, and marine aquatic environments. Anthropogenic and natural sources are discussed also in this chapter, and the different degrees of exposure of the populations are considered, as a function of the geographic location, of the kind of source and of the transport mechanisms of As.

A complete assessment of groundwater quality implies the quantification of the total recharge and the identification of the various sources involved, in order to keep track of the origin and fate of chemical compounds, including eventual pollutants.

Methods based on stable isotope signatures represent a powerful toolset for the separation of groundwater flow in its components and reveal the association between specific polluting sources and their respective portion of the total pollutants in the groundwater flow. The review work by Nisi et al. [29] gives a view on the importance of environmental isotopes in the context of groundwater quality assessments. The chapter deals with well-established isotopic systematics as well as nontraditional isotopes, in order to give an overview of the analytical possibilities, their implications and the potential usage of this class of methods.

In order to build a complete scenario of possible pollution mechanisms, it is fundamental to include the physical modelling of the groundwater flow and the connected modelling of the solute transport phenomena. In this framework, a basic step for a proper representation of the natural conditions is the collection of information about potential contamination sources, the hydrological context and the hydrogeological layers of the investigated volumes. Mapping the layers representing the studied aquifers and aquitards implies to establish the magnitudes and spatial distributions of the hydrodynamic and hydrodispersive parameters of the porous media. The chapter by Straface and Rizzo [30] describes the development of a completely artificial experimental site, which enables to determine the scale effect of hydraulic conductivity in a homogeneous porous medium. A frequent practical situation consists in the need to characterise a large site with few direct borehole data available. According to the experiments discussed in the chapter, the trend of the hydraulic conductivity appears to behave regardless of the heterogeneity of the porous medium, as it's also supported by former literature [31, 32]. The inherent complexity and heterogeneity of the subsoil and the general scarcity of data for a precise description of the whole hydrogeological system suggest the use of stochastic approaches [31] for the estimation of the parameters pertaining to the involved media, based on the observation of macroscopic properties. This latter aspect stresses very much the importance of this kind of reduced scale experiments and the high degree of generalisation that they make possible.

The collection of physical observations and the knowledge of possible chemical interactions lead to the development of numerical models of flow and transport phenomena in saturated porous media. Such models represent a primary source of information for simulating possible scenarios and evaluating potential risks of pollution. Moreover, the numerical modelling of groundwater flow and solute transport permits a better understanding of the mechanisms of contamination, in particular when combined with other available techniques of investigation (e.g. physico-chemical measurements, isotope methods, geophysical surveys, etc.). In fact, due to the wide range of techniques that are available nowadays, the most comprehensive characterisation of an exploited aquifer and its neighbouring environment involves a large variety of disciplines. It must also be noted, as remarked in the chapter by Doveri et al. [25], the high importance of the geological and hydrogeological foundations, which are the basis of the conceptual model of an aquifer system. The chapter by El Mansouri et al. [33] addresses mathematical modelling techniques for groundwater studies according to a deterministic approach. After a brief introduction of the symbolic math for the implementation

of hydrodynamic and transport laws, the chapter shows some practical impacts of the numerical models derived from the symbolic formulations. The numerical modelling of groundwater flow and solute transport, in the wider context that is today called “hydroinformatics”, covers a fundamental part of the technical support to the management, protection and exploitation of groundwater resources. In this broad framework, the chapter by El Mansouri et al. [33] poses the attention on the assessment of potential groundwater pollution from a landfill for municipal solid wastes, finalised to the delimitation of the protection zone of catchments destined to the drinking water network.

In addition to the capability of simulating scenarios by using modelling techniques (e.g. for the evaluation of protection zones), nowadays technologies offer a wide range of possibilities for the control and surveillance of groundwater pollution from human activities. One important aspect is the capability to detect and keep under control eventual contamination processes by using nonintrusive geophysical methods, which, in combination with the direct measurements of the quality of the abstracted water, contribute to build a nowadays classical technological platform for in situ assessments. The chapter by Bavusi et al. [34] gives an overview of electromagnetic techniques, proposed as a suite of fast, non-invasive and low-cost monitoring methods for subsoil investigations. The chapter focuses on sensing techniques able to support pollution surveys in groundwater bodies: electrical resistivity tomography (ERT), ground-penetrating radar (GPR), time-domain-induced polarisation (time-domain IP), and self-potential (SP). The chapter also illustrates the importance of combining the results of different techniques, with the aim of reducing the intrinsic ambiguities of the electromagnetic methods. Undoubtedly, the cooperative use of different measurement approaches, the conceptual knowledge of the domain under observation and the capability to make models of the observed processes contribute to the creation of a robust assessment framework.

Following this concept, the synergic usage of ERT and electromagnetic induction (EMI) is reported in the chapter by Manstein et al. [35], where the capability to investigate the contamination status and possible threats to the quality of groundwater is evaluated in three selected case studies. All the analysed situations regard anthropogenic pollution sources, chosen in order to cover a variety of distinct environmental problems. The chapter shows results obtained by field surveys regarding the remediation of an abandoned zinc factory, the monitoring of a pipeline for oil transportation and the assessment of a disposal of buried expired pesticides.

A further proof of the highly multidisciplinary context dealing with the threats to the quality of groundwater is given in the chapter by Bortnikova et al. [36], which illustrates a combination of electromagnetic measurements and hydro-geochemical studies for the assessment of groundwater pollution in mining areas. Sulphide-rich solutions with high concentrations of metals are the resulting wastes of mining activities in the studied location and contaminate both surface water and groundwater bodies. The research presented by the authors has the purpose to assess the penetration of toxicants into the groundwater horizon and estimate the amount of accumulated tailings, in order to predict future trends of the concentrations of

contaminants in the groundwater samples. This study represents a classical example of a threat to the quality and availability of water resources originated by human activities. In fact, the leaching of metals from the tailings stockpiled in the plant and the consequent migration of drainage solutions led to a significant pollution of groundwater, involving the local drinking water supply.

At this stage, the role played by direct measurement techniques of the quality of water is clear to the reader and deserves some dedicated analysis. Analytical laboratory techniques are well covered by an abundant literature, which is also partly mentioned in the chapters of this book dealing with hydro-geochemical aspects and isotope methods. The two final chapters of this book are intended to introduce promising technologies for the continuous monitoring of the quality of water, which are outside the classical toolset of analytical techniques. The review work by Testa et al. [37] offers a relevant survey of the state-of-the-art microfluidic optical methods for water monitoring and analysis, which have a big potential in terms of analytical possibilities and industrial implementation. The development of the so-called labs-on-chip offers the opportunity to design future highly portable and low-cost analytical systems, having the intrinsic capability to work with very small sample quantities and very fast analytical times. This review chapter explores the various working principles that lie behind these devices, such as absorption, refractive index variations, fluorescence, Raman scattering and phosphorescence. A section about biosensors is also included, briefly introducing this wide and rapidly growing family of sensing devices, with quite a number of literature references allowing the reader to probe further into the subject.

Last, the chapter by Di Natale et al. [38] illustrates electroanalytical and optical methods that are alternative to standard laboratory practices and are offering an interesting perspective for applications requiring a fast characterisation of liquids as well as for change detection purposes. Electronic tongues (or e-tongues) based on electrochemical principles are discussed in the chapter, as an example of sensor techniques capable to provide overall water quality indicators. Such nonconventional approaches are not meant as an alternative to the standard methods, but they are seen as methods for extracting some aggregate chemical information from a signal pattern (often consisting in a large dataset) useful for continuous monitoring applications. In particular, the surveillance of the quality of water destined to the human consumption can take benefit from low-cost distributed devices suitable for change detection applications, which are sensitive to a broad range of parameters and of possible pollutants. In this context, there is nowadays a strong pressure towards the development of smart sensors to be displaced in a water distribution infrastructure, with the perspective to reach such a high degree of pervasivity to be even installed on single water taps.

In conclusion, the aim of this introductory chapter was to provide motivation for this editorial work and outline its contents, which want to target a wide and much diversified audience, covering different sectors of expertise. Also, a broader discussion of the various topics addressed in this book can be done by accessing the ample literature cited by our chapters' authors.

References

1. Gleick PH (ed) (2014) The world's water volume 8: the biennial report on freshwater resources. Island Press, Washington, DC. doi:[10.5822/978-1-61091-483-3_5](https://doi.org/10.5822/978-1-61091-483-3_5)
2. Quevauviller P (2011) Adapting to climate change: reducing water-related risks in Europe – EU policy and research considerations. *Environ Sci Pol* 14(7):722–729. doi:[10.1016/j.envsci.2011.02.008](https://doi.org/10.1016/j.envsci.2011.02.008), Elsevier B.V
3. Allouche J (2011) The sustainability and resilience of global water and food systems: political analysis of the interplay between security, resource scarcity, political systems and global trade. *Food Policy* 36(Suppl 1):S3–S8. doi:[10.1016/j.foodpol.2010.11.013](https://doi.org/10.1016/j.foodpol.2010.11.013), Elsevier B.V
4. Ludwig R, Roson R, Zografos C, Kallis G (2011) Towards an inter-disciplinary research agenda on climate change, water and security in Southern Europe and neighboring countries. *Environ Sci Pol* 14(7):794–803. doi:[10.1016/j.envsci.2011.04.003](https://doi.org/10.1016/j.envsci.2011.04.003), Elsevier B.V
5. Scheffran J, Battaglini A (2011) Climate and conflicts: the security risks of global warming. *Reg Environ Chang* 11(Suppl 1):S27–S39. doi:[10.1007/s10113-010-0175-8](https://doi.org/10.1007/s10113-010-0175-8), Springer-Verlag
6. WWAP (World Water Assessment Programme) (2012) The United Nations world water development report 4: managing water under uncertainty and risk. UNESCO, Paris
7. Scozzari A, El Mansouri B (eds) (2011) Water security in the Mediterranean region, NATO science for peace and security series C: environmental security. Springer, Dordrecht, pp v–viii. doi:[10.1007/978-94-007-1623-0](https://doi.org/10.1007/978-94-007-1623-0)
8. European Commission (2015) Introduction to the new EU Water Framework Directive. http://ec.europa.eu/environment/water/water-framework/info/intro_en.htm. Accessed 11 June 2015
9. World Health Organization (2010) UN-Water global annual assessment of sanitation and drinking-water (GLAAS) 2010. World Health Organization (WHO), Switzerland
10. World Health Organization (2012) UN-Water global annual assessment of sanitation and drinking-water (GLAAS) 2012. World Health Organization (WHO), Switzerland
11. World Health Organization (2014) UN-Water global annual assessment of sanitation and drinking-water (GLAAS) 2014. World Health Organization (WHO), Switzerland
12. Nature.com (2015) Nature water map – total renewable freshwater. http://www.nature.com/nature/focus/water/renewable_map.html. Accessed 11 June 2015
13. Nature.com (2015) Nature water map – access to safe drinking water. <http://www.nature.com/nature/focus/water/map.html>. Accessed 11 June 2015
14. Gamapservr.who.int (2015) http://gamapservr.who.int/mapLibrary/Files/Maps/Global_water_2012.png. Accessed 11 June 2015
15. UN-Water World Water Day 2013, thematic factsheet: “Water quality”. http://www.unwater.org/fileadmin/user_upload/watercooperation2013/doc/Factsheets/water_quality.pdf. Accessed 11 June 2015
16. Howard Perlman U (2015) Where is Earth's water? USGS Water-Science School. <http://ga.water.usgs.gov/edu/waterdistribution.html>. Accessed 11 June 2015
17. Shiklomanov IA (1998) World water resources: a new appraisal and assessment for the 21st century. UNESCO, Paris
18. Margat J, van der Gun J (2013) Groundwater around the world: a geographic synopsis. CRC/Balkema, Boca Raton, pp 376. ISBN 9781138000346
19. Fao.org (2015) AQUASTAT – FAO's information system on water and agriculture. <http://www.fao.org/nr/water/aquastat/main/index.stm>. Accessed 11 June 2015
20. European Union Statistical Office (Eurostat) (2015) Water – eurostat. <http://ec.europa.eu/eurostat/web/environment/water>. Accessed 11 June 2015
21. Zektser IS, Everett LG (2004) Groundwater resources of the world and their use, vol 6, IHP-VI, series on groundwater. UNESCO, Paris
22. Quevavillier P (2005) Groundwater monitoring in the context of EU legislation: reality and integration needs. *J Environ Monit* 7:89–102, The Royal Society of Chemistry

23. Foster S, Loucks DP (eds) (2006) Non-renewable groundwater resources: a guidebook on socially-sustainable management for water-policy makers, vol 10, IHP-VI, series on groundwater. UNESCO, Paris
24. Hoekstra AY, Chapagain AK (2008) Globalization of water: sharing the planet's freshwater resources. Wiley-Blackwell, Malden. ISBN 978-1-4051-6335-4
25. Doveri M, Menichini M, Scozzari A (2015) Protection of groundwater resources: worldwide regulations and scientific approaches. *Hdb Env Chem*. doi:[10.1007/698_2015_421](https://doi.org/10.1007/698_2015_421)
26. Thomas L, Schneider M, Winkler A (2015) Threats to the quality of water resources by geological CO₂ storage: hydrogeochemical and other methods of investigation: a review. *Hdb Env Chem*. doi:[10.1007/698_2013_232](https://doi.org/10.1007/698_2013_232)
27. Biddau R, Cidu R (2015) Groundwater contamination: environmental issues and case studies in Sardinia (Italy). *Hdb Env Chem*. doi:[10.1007/698_2013_242](https://doi.org/10.1007/698_2013_242)
28. Gamaletsos P, Godelitsas A, Dotsika E, Tzamos E, Göttlicher J, Filippidis A (2013) Geological sources of as in the environment of Greece: a review. *Hdb Env Chem*. doi:[10.1007/698_2013_230](https://doi.org/10.1007/698_2013_230)
29. Nisi B, Raco B, Dotsika E (2014) Environmental isotopes in groundwater studies: a review. *Hdb Env Chem*. doi:[10.1007/698_2014_281](https://doi.org/10.1007/698_2014_281)
30. Straface S, Rizzo E (2013) The importance of reduced-scale experiments for the characterization of porous media. *Hdb Env Chem*. doi:[10.1007/698_2013_231](https://doi.org/10.1007/698_2013_231)
31. Renard P, de Marsily G (1997) Calculating equivalent permeability: a review. *Adv Water Resour* 20(5–6):253–278
32. Sanchez-Vila X, Guadagnini A, Carrera J (2006) Representative hydraulic conductivities in saturated groundwater flow. *Rev Geophys* 44, RG3002. doi:[10.1029/2005RG000169](https://doi.org/10.1029/2005RG000169)
33. El Mansouri B, Kili M, Chao J, Fekri A, Mridekh A (2013) Mathematical models as tools for prevention and risk estimates of groundwater pollution: contributions and challenges. *Hdb Env Chem*. doi:[10.1007/698_2013_240](https://doi.org/10.1007/698_2013_240)
34. Bavusi V, Lapenna V, Loperte A, Gueguen E, De Martino G, Adurno I, Catapano I, Soldovieri F (2013) Groundwater monitoring and control by using electromagnetic sensing techniques. *Hdb Env Chem*. doi:[10.1007/698_2013_243](https://doi.org/10.1007/698_2013_243)
35. Manstein Y, Scozzari A (2014) Pollution detection by electromagnetic induction and electrical resistivity methods: an introductory note with case studies. *Hdb Env Chem*. doi:[10.1007/698_2014_277](https://doi.org/10.1007/698_2014_277)
36. Bortnikova S, Yurkevich N, Bessonova E, Karin Y, Saeva O (2013) The combination of geoelectrical measurements and hydro-geochemical studies for the evaluation of groundwater pollution in mining tailings areas. *Hdb Env Chem*. doi:[10.1007/698_2013_234](https://doi.org/10.1007/698_2013_234)
37. Testa G, Persichetti G, Bernini R (2013) Microfluidic optical methods: a review. *Hdb Env Chem*. doi:[10.1007/698_2013_253](https://doi.org/10.1007/698_2013_253)
38. Di Natale C, Dini F, Scozzari A (2013) Non-conventional electrochemical and optical sensor systems. *Hdb Env Chem*. doi:[10.1007/698_2013_254](https://doi.org/10.1007/698_2013_254)

Protection of Groundwater Resources: Worldwide Regulations and Scientific Approaches

Marco Doveri, Matia Menichini, and Andrea Scozzari

Abstract The increasing role of groundwater in municipal water networks in many countries of the world makes the protection of groundwater resources an essential practice for safeguarding drinking water supplies. Several scientific-technical approaches are adopted worldwide to face this issue. In addition, some countries mainly depend on groundwater also for non-domestic use, making this topic even more critical. This chapter provides an overview of the main directives and their related technical aspects, concerning the protection zones of groundwater sources for human consumption. The main results of a multidisciplinary study are also presented, highlighting how the knowledge of physical and chemical aspects of groundwater bodies is a fundamental tool for protecting this vital resource and assuring its availability for the future generations.

Keywords Groundwater protection directives, Multidisciplinary approach, Protection areas

M. Doveri (✉) and M. Menichini
Istituto di Geoscienze e Georisorse-Consiglio Nazionale delle Ricerche (IGG-CNR), Via
Moruzzi 1, 56124 Pisa, Italy
e-mail: doveri@igg.cnr.it

A. Scozzari
Istituto di Scienza e Tecnologie dell'Informazione-Consiglio Nazionale delle Ricerche (ISTI-
CNR), Via Moruzzi 1, 56124 Pisa, Italy

Contents

1	Introduction	14
2	Protection Areas of Groundwater Sources for Human Consumption	15
2.1	Directives and Technical Aspects	15
2.2	Scientific-Technical Approaches	20
2.3	Case of Study: A Hydrogeological Approach Tested on Groundwater Sources of Tuscany (Italy)	23
3	Conclusions	26
	References	27

1 Introduction

Most of the available freshwater on Earth is stored in the underground [1]; consequently groundwater represents the main resource in terms of available quantities for water supply. Worldwide, more than two billion people depend on groundwater for their daily water use [2].

In many areas of the world, groundwater bodies represent the most important and safest source of drinking water [3, 4]. In the European countries, for example, the groundwater exploitation provides water for human consumption for 70% of the population on average [5].

According to the World Business Council for Sustainable Development, groundwater withdrawals supply 40% of industrial water [6] and groundwater use for irrigation is also significant and increasing. Siebert et al. [7] estimated that, globally, 38% of the areas with irrigation infrastructures are irrigated by groundwater.

Moreover, the exploitation of groundwater bodies will likely increase in order to face the climate change and the significant increasing of the global water demand, which has been predicted as a consequence of the economic expansion, population growth, and urbanization [8].

The general human pressure on groundwater becomes stronger if we consider those areas in which urban, industrial, and agricultural settlements are particularly developed, such as the alluvial and coastal plains. Globally, more than 150 million of people live below the altitude of 1 m a.s.l. and 250 million live below the altitude of 5 m a.s.l. [9]. Also, the touristic attitude that often characterizes the coastal areas causes a significant seasonal increase of the population. As a consequence, these areas are frequently interested by the deterioration of the environmental system and in particular of their water resources. Pollution phenomena as well as the overexploitation of groundwater cause a progressive qualitative and quantitative worsening of the stored water. One of the most recurring effects is the variation of the natural equilibrium between fresh and sea waters, with consequent advancing of the seawater intrusion in the coastal aquifers [10].

In this framework, the protection of groundwater is a must. Looking ahead, optimal management and preservation of this vital resource are required in order to assure its availability for the future generations. Taking into account the existent

water directives, a correct and strategic planning of the groundwater management should be based on specific studies aimed at characterizing the groundwater bodies in terms of quality and quantity, defining the thresholds values of pollutants in water, and delimiting the protection areas for drinkable water sources. These issues are often faced once a specific critical situation occurs and consequently for aquifer systems already intensely exploited and sometimes polluted, e.g., plain and coastal aquifers. Nevertheless, since groundwater is difficult and expensive to restore once polluted and/or overexploited, such kinds of studies and preventive actions are strongly recommended also on aquifers moderately exploited hitherto (e.g., fractured and karst aquifers), in order to protect their strategic groundwater resources.

In this chapter we focus on the issue of the protection areas of groundwater resources for human consumption, firstly performing an overview on the scientific-technical approaches and the directive tools adopted by different countries worldwide and then introducing the main results achieved in recent studies.

2 Protection Areas of Groundwater Sources for Human Consumption

2.1 Directives and Technical Aspects

In the most developed countries, specific directives have been elaborated and adopted in order to drive actions aimed at protecting water bodies exploited for drinking water supply. Pioneering actions on this matter were performed by the USA and Germany, whose guidelines [11–13] are fundamental references to face the protection of groundwater abstractions. Even though different approaches are adopted by each country, as a general outline we observe a delineation of zones surrounding the sources of drinking water, in which several activities are prohibited or restricted.

Some countries are in an initial stage in terms of protection areas of groundwater sources or they have not yet started these practices because more stringent problems, such as the scarcity of water resources, take the priority.

The next sections provide a brief overview of the approaches that have been introduced worldwide, described on a regional basis.

2.1.1 Europe

With the Directive 2000/60/EC, the European Parliament and the Council [14] established a framework for a community action in the field of water policy, in which water protection is a primary objective. According to this directive, protected areas have to be defined for water bodies having particular interest (Annex IV of the Directive), including those exploited for drinking water supply (Drinking Water

Protected Areas – DWPAs). For the latter, member states shall ensure the necessary protection and may provide to establish safeguard zones (SGZs). Guidance documents were also produced [15] in order to clarify the relationship between DWPAs and SGZs.

Member states have approached this issue by domestic legislation, in which, although with some technical differences, three main zones are mentioned [5, 16], in order to define the SGZs (or source protection zones – SPZs):

- Z1 An inner zone, which is the area immediately surrounding the abstraction point and is geometrically defined by a specific distance from the exploitation point
- Z2 An intermediate zone, which corresponds to the area surrounding the previous one and is generally delineated on the base of a reference travel time
- Z3 An outer zone, which is the area around a source, within which all groundwater recharge is presumed to be discharged by such source (catchment zone)

In some cases a subdivision of these main zones can be provided. In Germany, the Z3 can be optionally subdivided into two zones if its longitudinal extent exceeds 2 km [3], whereas in Belgium [17] and Italy (D. Lgs. 152/2006; Italian State-Regions agreement signed on 12th of December 2002), the Z2 can be further subdivided into two zones, whose boundaries are representative of different travel times. On the other hand, in some countries, e.g., France and the United Kingdom [16], a fourth zone can also be added in agreement with specific hydrogeological features or vulnerability conditions. Figure 1 shows a general scheme of the SGZs subdivision.

2.1.2 USA

The federal law “Safe Drinking Water Act” (SDWA) requires many actions in order to protect drinking water and its sources. Accordingly, each state shall provide to determine the Wellhead Protection Areas (WHPAs), which is defined as “the surface and subsurface area surrounding a water well or a field of water wells, supplying a public water system, through which contaminants are reasonably likely to move toward and reach such water well or well-field.” After the Amendments of 1986 to the SDWA, the US Environmental Protection Agency faced hydrogeological aspects of groundwater protection, providing a “Guideline for Delineation of Wellhead Protection Areas (WHPAs)” [11]. Hypothetical situations in different hydrogeological settings are described, as well as a basis for several delineation methods, highlighting subzones (Fig. 2) of WHPA named ZOI (area overlying the cone of depression), ZOC (the whole catchment), and ZOT (zone of transport for specific travel times). Criteria on which WPHA delineation may be based include distance, drawdown, travel time, flow system boundaries, and the capacity of the aquifer to assimilate contaminants. Such document describes criteria and methods that can be adopted for WHPAs delineation; however states

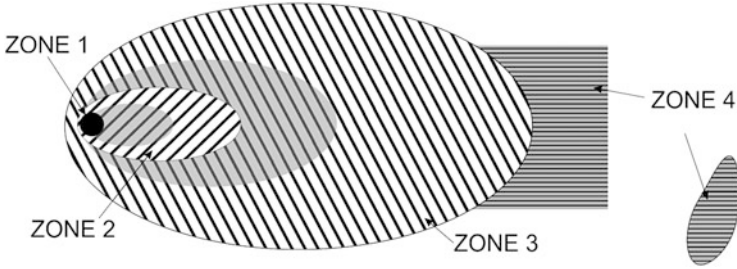


Fig. 1 General scheme of SGZs subdivision in European countries. In gray, optional subzones (see text)

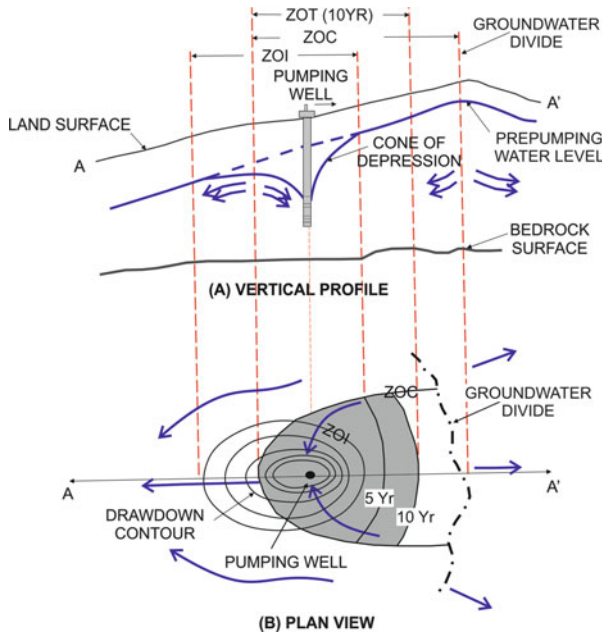


Fig. 2 Example of subzones of the WHPA according US EPA (after [11])

have flexibility in developing their WHPA programs as a function of their specific hydrogeological and environmental contexts.

2.1.3 Australia

The Australian National Water Quality Management Strategy is a joint national approach for improving water quality in Australia and New Zealand. In this framework national documents specifically covering groundwater protection have been produced, such as the ones by the Agriculture and Resources Management

Council of Australia and New Zealand [18, 19], in which wellhead protection plans are considered as one of the main tools for the protection of groundwater resources. Before the release of these documents, a small number of protection plans had been developed. One of these examples is described by ARMCANZ [18], in which a simplified approach based on concentric protection zones around the wellhead defines three zones with different prohibitions or restrictions in terms of land use and human activities. The nearest zone (Zone I) consists of a circular shape of radius 50 m and encompasses the water authority compound around the wellhead, including adjacent private areas where necessary. The second zone (Zone II) is arbitrarily delineated basing on a travel time of 10 years, and the third zone (Zone III) corresponds with the catchment area where greater than 10 years residence time is available.

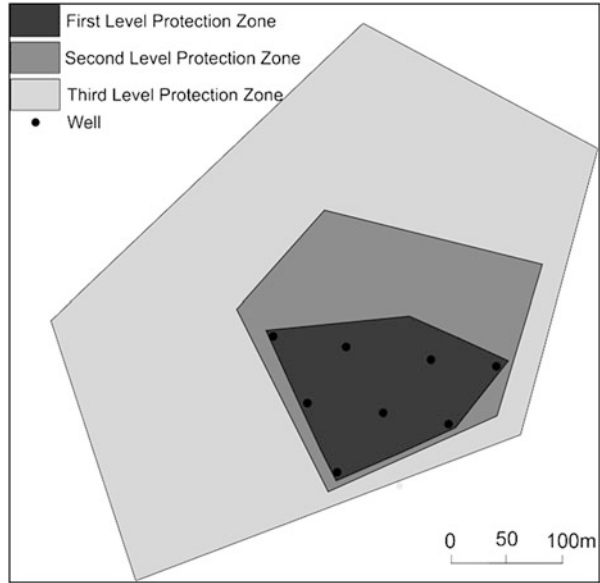
More recently, explicit planning has been developed, by providing actions of protection within specific catchments, termed Public Drinking Water Source Areas (PDWSAs). The policy for the protection of PDWSAs includes three priority classification areas (P1, P2, P3) based on the management of risk and two types of protection zones distinguished in wellhead protection zones (WHPZs) and reservoir protection zones (RPZs) [20]. P1 and P2 areas are managed to ensure that there are no risk and no increased risk of water source pollution, respectively. Most land uses produce some risk to the quality of water and are therefore defined as “incompatible” in P1 areas, whereas some activity is allowed within P2 areas for land uses that are defined as either “compatible with conditions” or “acceptable.” P3 areas are defined to manage the risk of pollution to the water source from catchment activities and are declared over areas where water supply sources coexist with other land uses such as residential, commercial, and light industrial development. WHPZs encompass the drinking water sources and are generally circular with a radius of 500 m or 300 m, for sources that are in P1 or P2 areas. RPZs consist of a statutory 2 km wide buffer area around the top water level of storage reservoirs.

2.1.4 China

China is the world’s most populous country, with a consequent high request of water for human consumption. On the other hand, the distribution of water resources in China is highly diverse, thus negatively affecting social and economic growth in some regions [21]. Estimations by the Ministry of Water Resources [22] highlighted as in 2005 about 300 million people in China were unable to access safe drinking water, both in terms of quality and quantity. In spite of that, and although the law tools invite to establish a protection system for zones of drinking water sources [23–25], delineation of protection zones for groundwater sources is still at the initial stage [4], and in the locations where it has been performed, there is a lack of practical protective measures [26].

According to legislation [27], drinking water source reserves are classified into Grade I and Grade II. It is moreover possible to delimit a certain area at the periphery of a drinking water source reserve as a quasi-reserve. In the Grade-I

Fig. 3 Polygonal partitioning of protection zones for the well field in Dawukou District of Shizuishan City, China (after Wenjuan et al. [28]).



zone, any buildings or activities are not permitted, excluding those linked to water supply facilities and their management and protection. Within the Grade-II and quasi-reserve zones, it is prohibited to build, renovate, or enlarge any construction project discharging pollutants and seriously polluting waters. No technical criteria are given by the regulation. In fact, different case studies dealing with groundwater sources for human consumption in China report different ways to define the boundaries of the three zones. For the Grade-I and Grade-II zones, a benchmark travel time is generally taken into account. Wenjuan et al. [28] and Baoxiang and Fanhai [4] refer to 100 days and 60 days for the Grade-I protection and to 1,000 days and 10 years for the Grade-II protection, respectively. The quasi-reserve zone is chiefly referred to the whole catchment; nevertheless a residence time of groundwater is sometimes considered (e.g., 25 years in Baoxiang and Fanhai [4]). The shapes of the protection zones can be circular, elliptical, irregular, and even polygonal (Fig. 3) as a function of delineation methodologies (e.g., analytical rather than empirical) and of the source arrangement (e.g., single source rather than multipoint sources).

2.1.5 Africa

Many African countries have problems both with water scarcity and with pollution. For what regards the MENA region (Middle-East North Africa), large territories are characterized by arid and semiarid conditions where groundwater constitutes the main source of water supply, thus making the protection of this resource indispensable [29]. In this context, there is some degree of cooperation between the involved

countries and foreign states having a significant experience about the protection of groundwater resources, on the basis of cooperation agreements.

In Sub-Saharan Africa, US EPA promotes the development and implementation of Water Safety Plans (WSPs) to improve the capacity of urban providers to deliver safe drinking water in a sustainable way [30]. WSPs consist in a “catchment to consumer” approach, which uses a health-based risk assessment methodology for identifying the greatest vulnerabilities to contamination within a drinking water supply system.

In North Africa, projects have been developed by means of the cooperation among Arab countries and Germany [31, 32], facing the issue of the management, protection, and sustainable use of groundwater. A proposal of guideline for the delineation of groundwater protection zones was also produced [32], in which a typical scheme with three zones of protection (reflecting different levels of risk) surrounding the abstraction point is presented. Different criteria for the delimitation of zones are suggested as a function of two main aquifer system types, based on a near homogeneous (e.g., unconsolidated aquifer) or heterogeneous (e.g., karst aquifer) distribution of groundwater flow velocities, respectively. The travel time is the most prominent factor for the delineation of groundwater protection zones for the first category of aquifers, whereas an approach based on the vulnerability is preferred for the second category of aquifers.

2.2 Scientific-Technical Approaches

As previously described, the protection of drinking water sources is generally approached by means of the delineation of zones surrounding the abstraction points (hereafter safeguard zones, SGZs) and by defining prohibitions and restrictions within such areas in term of land use and activities. Within a SGZ three or more subzones are generally distinguished as a consequence of the different degree of protection that is needed. Several methods for delineating such zones have been developed worldwide and are described in guideline documents or proposed in scientific papers. In general, the choice of the methodology is linked with the availability and the kind of hydrogeological data available, in addition to the aquifer typology. In the following subsections, the main approaches that are used worldwide are listed and briefly described.

2.2.1 Geometric Methods

These methods consist in drawing a shape (Fig. 4), which is either determined by purely geometric criteria or by considering both geometric aspects and hydrodynamic features. The geometric approach is generally used where other and more sophisticated methods cannot be applied. The simplest method consists in drawing a circle of an arbitrary fixed radius around each abstraction (Fig. 4a). The radius can

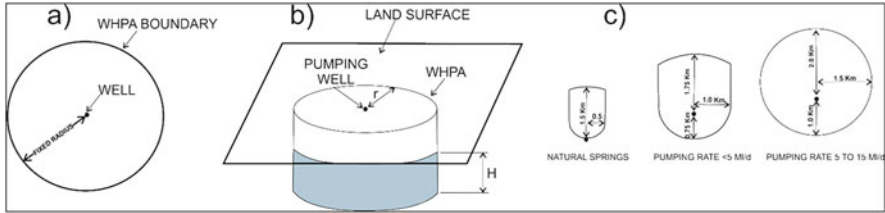


Fig. 4 Geometric methods for delineating SGZs. (a) Arbitrary fixed radius. (b) Calculated radius: the radius (r) determines a volume of water that is pumped from the well in a specified time period. (c) Simplified variable shapes: various standardized forms are generated by analytical equations and provided to calculate the upgradient extent on the base of times of travel (after US [11])

also be defined by taking into account the average distance corresponding to a given time of travel, averaged as a function of the different hydrogeological contexts insisting in the studied region. A similar method provides circular or semicircular protection areas using radii that are calculated by using volumetric equations. These latter consider hydrogeological parameters (e.g., porosity) and the volume of water drawn in a specified time interval from the well (Fig. 4b; Eqs. 1 and 2).

$$r = \sqrt{\frac{Q t}{\pi n H}}, \tag{1}$$

$$r = \sqrt{\frac{2 Q t}{\pi n H}}, \tag{2}$$

where Q is the pumping rate (m^3/s), n is the aquifer porosity, H is the length of well screen (m), and t is the travel time (s).

Equation (2) refers to the half-circle method, which takes into account the flow direction by replacing the circular shape used for the simplest SGZ with a half circle having the same area. Such new asymmetrical shape is oriented to the upgradient direction [33], to encompass the effect of the flow. The travel time used as a reference is chosen in order to allow the occurrence of processes that adequately decrease the concentration of contaminants before they reach the well (i.e., dilution, dispersion, cleanup).

Another approach is the generation of various standardized and representative shapes (Fig. 4c) by using analytical equations (Sect. 2.2.2). Standardized shapes are calculated for different sets of hydrogeological conditions (essentially different values of T and hydraulic gradient) and well-pumping rates; then the more appropriate shape is applied to the wellhead zone and oriented according to the flow patterns. The down-gradient and lateral limits of the standardized shapes are defined by the uniform flow equation (Fig. 5) [34, 35], whereas the upgradient extent is estimated by considering a specific time of travel. By applying different times of travel, it is possible to identify several subzones forming the entire SGZ.

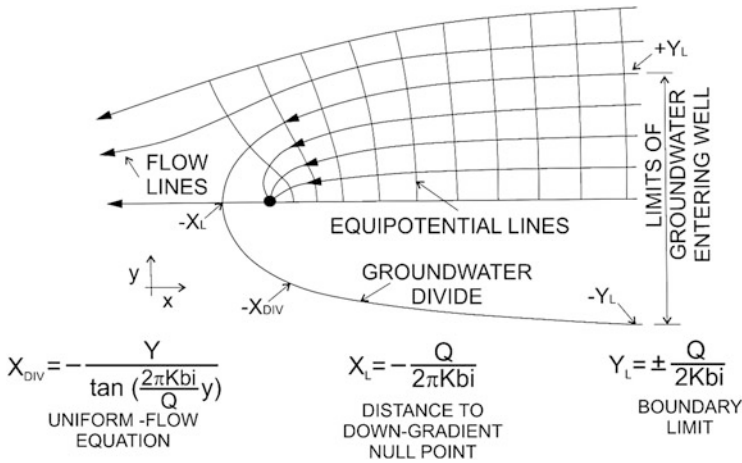


Fig. 5 SGZs delineation using the analytical method for a confined aquifer. Q well pumping rate, K hydraulic conductivity, b saturated thickness, i hydraulic gradient, π : 3.1416 (modified, after [34])

2.2.2 Analytical Methods

According to this class of methods, the delineation of SGZs is based on a set of equations, which assume two-dimensional horizontal flow and are applied to each abstraction or group of abstractions, accordingly to site-specific hydrogeological parameters. The latter can include hydraulic gradient, hydraulic conductivity, transmissivity, porosity, and saturated thickness of the aquifer. The assumption of uniform flow (and its relating equations) is often used for the definition of the downgradient and of the lateral limits (Fig. 5). The extent of the upgradient can then be evaluated basing either on specific travel times or on hydrogeological boundaries.

Analytical approaches were used by several authors for the definition of the capture zones of wells, considering both aquifers of infinite extent (e.g., [36]) and in the presence of boundaries (e.g., [37, 38]).

It must finally be noted that there are literature examples and relating software showing how this type of delineation can be automated by using analytical element models running on a computer, e.g., WhAEM and GFLOW [33].

2.2.3 Hydrogeological Mapping

This methodology provides the delineation of the protection areas by summarizing within hydrogeological maps the information derived from geological, geophysical, hydrogeological, and hydro-geochemical surveys. Starting from geological observations, changes of lithology corresponding to contrasts of permeability can be individuated and correlated with the boundaries of the protection areas. Surface

geophysical data coupled with the geological interpretation may provide the spatial arrangement of buried structures, thus indicating possible groundwater divides linked to structural conditions. Hydrogeological mapping may also encompass groundwater-level contour lines, which can contribute to the identification of groundwater divides. Moreover, results of dye tracing tests can be included, as a tool to verify the recharge area and the flow systems. Also the vulnerability-based methodology (e.g., [39–41]) can be classified as a hydrogeological mapping approach, given the overlapped and integrated elaboration among several thematic layers (e.g., topography, permeability, fractures' density, etc.).

2.2.4 Numerical Models

Flow and transport numerical modeling represents a good practice for SGZs accomplishment (e.g., [17, 42–45]), as it's also discussed in the chapter by El Mansouri et al. inside this book. A wide variety of software (calculation modules, user interfaces, and complete suites for flow and transport models) are available to perform numerical modeling (e.g., Groundwater Vistas, Visual Modflow, GMS, Feflow, etc.). The input data consist of hydrodynamic and hydrodispersive parameters, aquifer geometries, recharge rates, and the location of some boundaries in which flow conditions and solute concentrations have to be defined. This approach is particularly useful for delineating SGZs where the hydrogeological framework is complex. Nevertheless, a large amount of data is required in order to develop a proper numerical model.

One critical aspect is that the predictions generated by these models are often considered as the portrait of exact scenarios by public policy decision-makers. Hence, and because “more than one model construction can produce the same output” [46], it is not sufficient to calibrate the models by using experimental data, but it is also mandatory to perform a background work, which consists in building a reliable conceptual framework that takes into account the modeling hypothesis and their associated uncertainties.

2.3 *Case of Study: A Hydrogeological Approach Tested on Groundwater Sources of Tuscany (Italy)*

This section refers to a particular case study, in which the hydrogeological approach was used.

According to the Italian law (D.Lgs. 152/2006; Italian State-Regions agreement signed on 12 of December 2002), the three subzones of a SGZ are named *absolute safety zone*, *respect zone* and *protection zone*, respectively. The first zone is simply defined by geometric criteria (minimum radius 10 m); the second one is delimited on the base of a travel time (60, 180, or 365 days), when the available data and the

hydrodynamic context are favorable, otherwise by means of the so-defined “hydrogeological approach,” which should encompass geological, hydrogeological, and geochemical data. The assessment of the protection zone (the third subzone of the SGZ) always follows the hydrogeological approach.

Due to their major importance in terms of safeguard, the respect zones in Italy have been delimited for several abstractions according to the said guidelines. Instead, for the delineation of protection zones (PZs), there are no official documents nor a significant number of case studies.

In the framework of a project funded by the administration of the Tuscany region, several studies were carried out in the areas surrounding several abstraction points of drinking water located in different parts of the regional territory. Fifteen PZs were delimited [47] by means of an integrated multidisciplinary approach thanks to cooperation between CNR-IGG, the Water Authorities (WAs), and the Integrated Urban Water Management Companies (IUWM-Cs). In the following of this section, the general approach adopted for delineating PZs is briefly discussed and some main results of its application are presented.

After a preliminary examination and elaboration of the existing/available data, a survey program was developed in collaboration with the WAs and the IUWM-Cs. The new surveys covered the following activities: (1) hydrogeological measurements (water head, flow rates) and hydraulic tests, (2) on-site measurements of chemical-physical parameters of the water and collection of water samples for the laboratory analyses of chemical and isotopic parameters, and (3) geological surveys and/or drilling of new boreholes to acquire new stratigraphic information.

A general scheme describing the integrated approach and the data used for its elaboration is reported in Fig. 6. The diagram shows how the geochemical, hydrodynamic, structural, and meteorological information converge into the process for the assessment of a protection zone.

The example discussed in this work regards a well field located next to the southern border of the Apuan Alps (NW Tuscany-Italy; Fig. 7). The well field is situated in the “Camaiole Basin” and it is made up by 32 wells; it drains about 300 L/s from an alluvial aquifer (gravel/pebbles, unconfined or semi-confined) whose substratum consists of permeable carbonate rocks, which widely outcrops on the nearby reliefs (Fig. 7).

Based on the scheme of Fig. 6, the study aimed at individuating the catchment basin for the well field and the main results achieved can be summarized as follows:

- The analysis of geological structures pointed out that in the area a general North-South groundwater flow is favored by a combination of bedding and/or foliation attitude and fold axis plunges. The main fault system leads to the partitioning of groundwater flow into different sub-basins. In addition, the study of the hydrostructures highlighted some possible hydrogeological divides and a presumable loss of groundwater from the “Camaiole Basin” toward the catchment at SE;
- A piezometric map was achieved for the alluvial aquifer that is exploited by the well field. The contours of the hydraulic head show a feeding from the carbonate complexes, which outcrop in the surrounding area. Three major streamlines exist

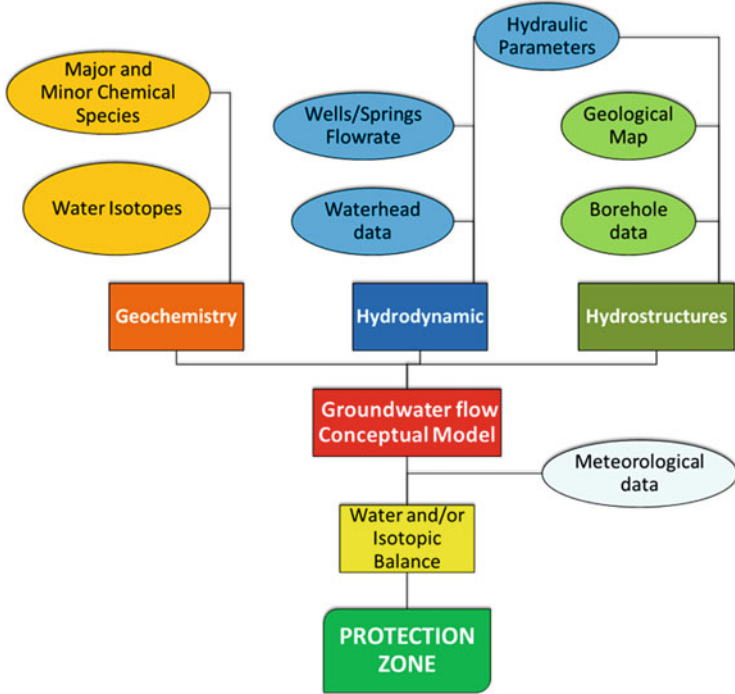


Fig. 6 Schematic diagram describing the integrated approach. Data provided as input are shown in *elliptical boxes*

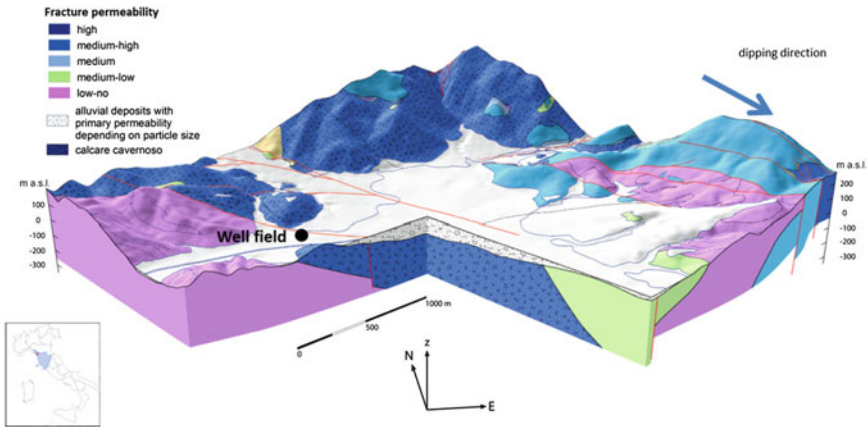


Fig. 7 3D representation of the hydrogeological structures (after [47]). The fractured hydrogeological units with permeability medium to high are made up by carbonate lithologies

and they converge toward the well field. After dividing the piezometric map into stream tubes, Darcy and Kamenskij equations were applied using the transmissivity values estimated by means of several pumping tests. In this way major and minor inputs at the system were identified:

- Chemical and water-isotope analyses have been performed twice, both for the abstractions under study and for a number of water points (about 15 springs, wells, and stream waters) in their surroundings. Among these, six springs were opportunely selected in order to assess the relationship “altitude/ $\delta^{18}\text{O}\%$,” which is useful to achieve the average altitudes of the recharge of water abstractions [48, 49]. By combination of chemical and isotopic data, the presence of some inputs and of their mixing products was verified. Chemical features suggested what kind of lithology is involved in the water-rock interaction processes (e.g., Calcare Cavernoso for the SO_4 values or sandstone for the SiO_2 values), whereas isotopes indicated the average altitudes of infiltration for the different inputs. Taking into account these aspects and the mixing processes, it’s been possible to achieve indications both on the areas involved in feeding the abstractions and on their importance in terms of quantity.

Based on all the above mentioned information, the catchment area was delineated for the well field. This polygon was additionally validated by means of the water and isotopic budget: for each zone in which the same hydrogeological complex outcrops, both infiltration rate (<http://www.sir.toscana.it/>, for meteorological data; [50] for the infiltration coefficients) and the average values of $\delta^{18}\text{O}\%$ (comparing the average altitudes and the relationship “altitude/ $\delta^{18}\text{O}\%$ ”) were estimated. Furthermore, these isotopic signatures were weighted by using the infiltration rates, thus obtaining the weighted mean of $\delta^{18}\text{O}\%$ concerning the entire feeding area. The evaluated value (-6.41%) resulted congruent with analyses’ results for the water samples collected at the well field (-6.48%).

After this validation, the final PZ was delimited, also allowing the distinction of two subzones, A and B, which, respectively, correspond to the chief zone and the secondary zone in terms of feeding (Fig. 8).

3 Conclusions

Groundwater bodies represent the safest source for satisfying water demand. Moreover, based on the expected scenarios of global climate change and degradation of surface water bodies, it is predictable that the claim for this resource will increase in the future. In this framework, the protection of groundwater is unavoidable, in order to guarantee safe water supplying for the next generations.

Hence, the appropriate knowledge of physical and chemical aspects of the aquifer systems becomes more and more a necessary prerequisite in order to face the several issues involved with the protection of groundwater, implying the necessity to develop robust conceptual hydrogeological models. Despite the

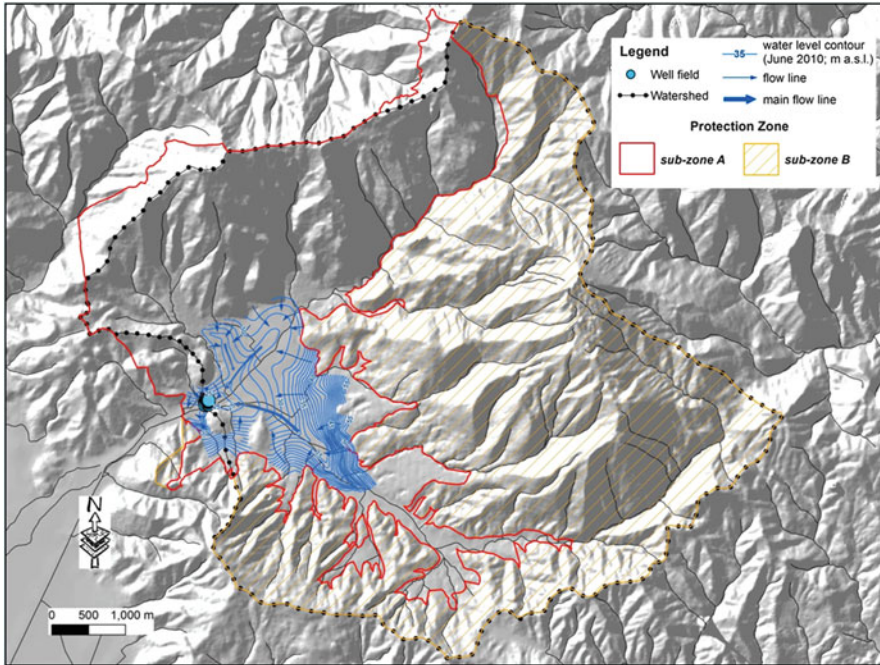


Fig. 8 Well-field protection zone. Water-level contour lines refer to the unconfined aquifer system that exists in the plain surrounding the well field and it is made up by alluvial sediments in the shallower part and mainly by carbonate rocks at depth. Subzone A is the main feeding area of the groundwater system exploited by the well field. Subzone B is the area from which a minor feeding occurs

relevant investment of resources necessary for the production and interpretation of multidisciplinary experimental data, a well-grounded conceptual framework should not be overcome with the direct use of specific and more straightforward tools (e.g., numerical modeling without sufficient experimental data, empirical methods based on few parameters and/or limited datasets, etc.). In particular, a comprehensive approach, following the guidelines and the examples discussed in this chapter, gives the perspective of an improved planning of the groundwater management, with a high chance of long-term benefits.

References

1. Shiklomanov IA (1998) World water resources: a new appraisal and assessment for the 21st century. A summary of the monograph: World Water Resources, International Hydrological Programme, UNESCO, Paris
2. Hiscock KM (2011) Groundwater in the 21st century – meeting the challenges. In: Anthony J, Jones A (eds) Sustaining groundwater resources: a critical element in the global water crisis, in International Year of Planet Earth, pp 207–225

3. Zhu Y, Balke KD (2008) Groundwater protection: what can we learn from Germany? *J Zhejiang Univ Sci B* 9(3):227–231
4. Baoxiang Z, Fanhai M (2011) Delineation methods and application of groundwater source protection zone. *Water Resource and Environmental Protection (ISWREP)*, 2011 International Symposium on Volume: 1 doi:10.1109/ISWREP.2011.5892945. (IEEE Conference Publications): pp 66–69
5. Martínez Navarrete C, Grima Olmedo J, Durán Valsero JJ, Gómez Gómez JD, Luque Espinar JA, de la Orden GJA (2008) Groundwater protection in Mediterranean countries after the European water framework directive. *Environ Geol* 54:537–549
6. WBCSD (2009) Facts and trends – water. World Business Council for Sustainable Development. <http://www.wbcsd.org/Pages/EDocument/EDocumentDetails.aspx?ID=137>. Accessed 10 Sept 2014
7. Siebert S, Burke J, Faures JM, Frenken K, Hoogeveen J, Döll P, Portmann FT (2010) Groundwater use for irrigation – a global inventory. *Hydrol Earth Syst Sci* 14:1863–1880
8. Rosegrant MW, Cai X, Cline SA (2002) *World Water and Food to 2025: dealing with scarcity*. International Food Policy Research Institute, Washington, 322 pp
9. UNESCO (2007) *Global sea-level: past, present and future*. Reprint from IOC Annual Report 2006: pp 8
10. Custodio E (2002) Coastal aquifers as important natural hydrogeological structures. In: Bocanegra E, Martínez D, Massone H (eds) “Groundwater and Human Development”: 1905–1918. Bremerhaven, Germany
11. U.S. EPA (1987) Guidelines for delineation of wellhead protection areas. Office of Groundwater Protection, EPA-Washington, Reprinted in 1993 as EPA 440/5-93-001, 212 pp
12. DVGW (1995) Guidelines on drinking water protection areas – part 1: groundwater protection areas. Code of practice W 101, 23 pp. (in German)
13. USGS (1998) Estimating areas contributing recharge to wells. US Geological Survey Circular 1174, Denver, 14 pp. <http://water.usgs.gov/ogw/pubs/Circ1174/>. Accessed 6 Feb 2015
14. European Communities (2000) Directive 2000/60/CE of the European Parliament and of the council of 23 October 2000 establishing a framework for community action in the field of water policy. *Off J Eur Communities*, Luxembourg, L 327
15. European Communities (2007) Guidance Document No. 16. Guidance on Groundwater in Drinking Water Protected Areas. Common Implementation Strategy for the Water Framework Directive (2000/60/EC), Luxembourg, p 34
16. García García A, Martínez Navarrete C (2005) Protection of groundwater intended for human consumption in the water framework directive: strategies and regulations applied in some European countries. *Pol Geol Inst Spec Pap* 18:28–32
17. Derouane J, Dassargues A (1998) Delineation of groundwater protection zones based on tracer tests and transport modeling in alluvial sediments. *Env Geol* 36(1-2):27–36
18. ARMCANZ (1995) Guidelines for groundwater protection in Australia. Publication of the Agriculture and Resource Management Council of Australia and New Zealand (ISBN 0 642 19558 7), 83 pp
19. ARMCANZ (1996) Allocation and use of groundwater: a national framework for improved groundwater management in Australia. Occasional Paper Number 2 (ISBN 0 642 27117 81), Agriculture and Resource Management Council of Australia and New Zealand, 16 pp
20. DoE (2004) Land use compatibility in public drinking water source areas. Water Quality Protection Note, July 2004, Government of Western Australia-Department of Environment, www.environment.wa.gov.au
21. Nitikin D, Shen C, Wang Q J, Zou H (2012) Water service delivery reform in China: safeguarding the interests of the Poor. *Ann Econ Finance* (13-2):463–487
22. MWRC (2014) Safe drinking water webpage of the Ministry of Water Resources of China. <http://www.mwr.gov.cn/english/sdw.html>. Accessed 10 Sept 2014

23. D74/2002 (2002) Water Law of the People's Republic of China. Decree No. 74 of the President of the People's Republic of China. <http://www.mwr.gov.cn/english/laws.html> Accessed 10 Sept 2014
24. DL 382/99 (1999) Decreto-Lei of the Ministerio do Ambiente of Portugal. Diário da República I Série-A, No. 222-22/9/1999
25. L1984/11/01. Law of the People's Republic of China on the Prevention and Control of Water Pollution. <http://www.mwr.gov.cn/english/laws.html>. Accessed 10 Sept 2014
26. Wang H, Yu X (2014) A review of the protection of sources of drinking water in China. *Nat Res Forum* 38:99–108
27. L2008/06/01 (2008) Law of the People's Republic of China on the prevention and control of water pollution as revised on June 1st, 2008. www.fao.org/docstore/2008/chn23549.doc Accessed 10 Sept 2014
28. Wenjuan X, Jing J, Jinling Z (2011) Preliminary partition of groundwater protection zones by empirical formula method. *Int J Geomatics Geosci* 2:589–594
29. Scozzari A, El Mansouri B (eds) (2011) Water security in the Mediterranean region: an international evaluation of management, control, and governance approaches, NATO Science for Peace and Security Series C: Environmental Security, Springer. doi:10.1007/978-94-007-1623-0_1
30. U.S. EPA (2014) EPA efforts in Sub-Saharan Africa. <http://www2.epa.gov/international-cooperation/epa-efforts-sub-saharan-africa#water> Accessed 10 Sept 2014
31. Schelkes K, Hobler M, Schmidt G, Steinbach V (2004) Management, protection and sustainable use of groundwater – results of long-term technical cooperation in the Middle East. In: Fathi Z, Wolfgang J (eds) *Water in the Middle East and in North Africa*. Springer-Verlag, Berlin/Heidelberg/New York, pp 129–143. ISBN 3-540-20771-6
32. Margane A (2003) Guideline for delineation of groundwater protection zones. *Management, Protection and Sustainable Use of Groundwater and Soil Resources in the Arab Region*, vol 5, p 329
33. OhioEPA (2009) Drinking water source protection area: delineation guidelines and process manual, environmental protection agency of Ohio. http://www.epa.ohio.gov/portals/28/documents/swap/swap_delin_guidance.pdf. Accessed 10 Sept 2014
34. Todd DK (1980) *Groundwater hydrology*. Wiley, New York, 535 pp
35. Grubb S (1993) Analytical model for estimation of steady-state capture zones of pumping wells in confined and unconfined aquifers. *Ground Water* 31–1:27–32
36. Shan C (1999) An analytical solution for the capture zone of two arbitrarily located wells. *J Hydrol* 222(1):123–128
37. Intaraprasong T, Zhan H (2007) Capture zone between two streams. *J Hydrol* 338:297–307
38. Samani N, Zarei-Doudeji S (2012) Capture zone of a multi-well system in confined and unconfined wedge-shaped aquifers. *Adv Water Resour* 39:71–84
39. Pochon A, Tripet JP, Kozel R, Meylan B, Sinreich M, Zwahlen F (2008) Groundwater protection in fractured media: a vulnerability-based approach for delineating protection zones in Switzerland. *Hydr J* 16:1267–1281
40. Elewa HH, Shohaib RE, Qaddah AA, Noursir AM (2013) Determining groundwater protection zones for the Quaternary aquifer of northeastern Nile Delta using GIS-based vulnerability mapping. *Environ Earth Sci* 68:313–331
41. Lo Russo S, Taddia G (2012) Aquifer Vulnerability Assessment and Wellhead Protection Areas to Prevent Groundwater Contamination in Agricultural Areas: An Integrated Approach. *J Water Resour Prot* 4:674–685
42. Kinzelbach W (1986) *Groundwater Modelling. An Introduction with sample Programs in Basic*. Elsevier, Oxford, p 328
43. Rayne TW, Bradbury KR, Muldoon MA (2002) Delineation of capture zones for municipal wells in fractured dolomite, Sturgeon Bay, Wisconsin, USA. *Hydrogeol J* 9:432–450
44. Rock G, Kupfersberger H (2002) Numerical delineation of transient capture zones. *J Hydrol* 269:134–149

45. Saravanan R, Balamurugan R, Karthikeyan MS, Rajkumar R, Anuthaman NG, Navaneetha Gopalakrishnan A (2011) Groundwater modeling and demarcation of groundwater protection zones for Tirupur Basin – a case study. *J Hydro Environ Res* 5:197–212
46. Oreskes N, Shrader-Frechette K, Belitz K (1994) Verification, validation, and confirmation of numerical models in the Earth sciences. *Science New Series* 263(5147):641–646
47. Menichini M, Da Prato S, Doveri M, Ellero A, Lelli M, Masetti G, Nisi B, Raco B (2015) An integrated methodology to define Protection Zones for groundwater-based drinking water sources: an example from the Tuscany Region, Italy. *Italian J Groundw* 139:21–27
48. Doveri M, Mussi M (2014) Water isotopes as environmental tracers for conceptual understanding of groundwater flow: An application for fractured aquifer systems in the “Scansano-Magliano in Toscana” area (Southern Tuscany, Italy). *Water* 6:2255–2277
49. Doveri M, Menichini M, Cerrina Feroni A (2013) Stable water isotopes as fundamental tool in karst aquifer studies: some results from isotopic applications in the Apuan Alps carbonatic complexes (NW Tuscany). *IJECE* 1:33–50
50. Piccini L, Pranzini G, Tedici L, Forti P (1999) Le risorse idriche degli acquiferi carbonatici del comprensorio apuo-versiliense. *Quad Geol Appl* 6(1):61–78

Threats to the Quality of Water Resources by Geological CO₂ Storage: Hydrogeochemical and Other Methods of Investigation: A Review

L. Thomas, M. Schneider, and A. Winkler

Abstract In the last decades, geological storage of CO₂ is under discussion, in order to reduce emissions of greenhouse gases to the atmosphere, as a contribution to the mitigation of climate change. Deep saline aquifers in sedimentary basins are being considered as the most prominent locations for CO₂ storage and sequestration. This chapter provides an overview of recent research regarding CO₂ storage with focus on hydrogeochemical methods of investigation, gas–water–rock interactions and monitoring methods as well as potential risks to freshwater resources. The main trapping mechanisms for CO₂ in deep geological formations are: (1) hydrodynamic trapping as a supercritical fluid below the caprock, (2) residual trapping within the pores of reservoir rocks, (3) solution trapping as aqueous species dissolved in formation water, and (4) mineral trapping by precipitation of carbonate minerals. However, risks for freshwater resources can arise due to low pH values. As a consequence, the dissolution of minerals is causing high concentrations in trace elements that are potentially dangerous for human health. Another aspect is ascendant saline water which could intrude into shallower fresh water aquifers due to the displacement caused by injection pressure. Hydrogeochemical monitoring methods are recommended to detect possible CO₂ leakage.

Keywords CCS, CO₂-sequestration, Gas–water–rock interaction, Geological carbon dioxide storage, Groundwater monitoring, Hydrogeochemical modeling, Hydrogeochemistry, Saltwater intrusion

L. Thomas (✉), M. Schneider and A. Winkler
Institute of Geological Sciences, Hydrogeology Group, Freie Universität Berlin,
Malteserstr. 74-100, Haus B, 12249 Berlin, Germany
e-mail: L.Thomas@fu-berlin.de

Contents

1	Introduction	32
2	Hydrogeochemical Methods of Investigation	34
2.1	Water Analysis and Plausibility Checks	34
2.2	Hydrochemical Characterization and Statistics	34
2.3	Stability Field- and Activity- or Phase-Diagrams	36
3	CO ₂ -Sequestration and Other Subsurface Activities	38
3.1	Pressure Distribution and Saltwater Migration	38
3.2	Hydrogeochemical Reactions and (Gas)–Water–Rock Interactions	40
3.3	Monitoring Methods	43
3.4	Prevention and Control	44
4	Concluding Remarks	45
	References	47

Abbreviations

BTEX	Benzene, toluene, ethylbenzene, and xylenes
CCS	Carbon dioxide capture and storage
DIC, DOC	Dissolved inorganic and organic carbon
EC	Electrical conductivity
EOR	Enhanced oil recovery
GWB	The geochemist's workbench
PFT	Perfluorocarbon tracer gases
TDS	Total dissolved solids
U.S. EPA	U.S. environmental protection agency
WHO	World health organization

1 Introduction

Due to climate change and the necessity for reducing greenhouse gases within the atmosphere the possibility of geological CO₂ storage or carbon dioxide capture and storage (CCS), also known as sequestration, is under worldwide investigation, especially in the last decade.

CCS and other subsurface activities like hydro-fracking, unconventional gas exploitation as well as geothermal energy production or enhanced oil recovery (EOR) have an impact on the geological underground and the groundwater within the aquifers. It is therefore essential to prevent negative effects on freshwater aquifers, which are often used as drinking water resources.

The main concern about CO₂ capture and storage is the potential risks due to:

- Displacement of saltwater or high mineralized brines and upconing of these waters into freshwater aquifers caused by pressure increase.
- Discharge of saltwater or CO₂ at the surface.

- Leakage due to faults, fractures, or weakness zones within the caprock as well as abandoned wells and boreholes.
- Solution, mobilization, and transport of contaminants and toxic elements like heavy metals, trace elements and organic compounds due to gas–water–rock interactions. Moreover supercritical CO₂ acts as a highly efficient solvent for hydrocarbons.

In recent years numerous publications dealt with the impacts of geological CO₂ storage on groundwater resources [1–26].

A review of recently published results regarding the potential impact of underground geological storage of carbon dioxide in deep saline aquifers on shallow groundwater resources is given by Lemieux [27]. He distinguished the near field impact due to upward vertical migration of free-phase CO₂ to surficial aquifers within a distance of a few hundreds of meters around the injection zone and the far field impacts which can possibly occur many kilometers away from the injection zone and are caused by the large-scale migration of displaced brines or elevated pressures [27].

According to IPCC [28], three different storage mechanisms for CO₂ in geological formations can be distinguished:

- Stratigraphic and structural trapping (physical trapping)
Here it means physical trapping of CO₂ below low-permeability seals (caprocks). Sedimentary basins have such closed, physically bound traps or structures, which are occupied mainly by saline water, oil, and gas. Structural traps include those formed by folded or fractured rocks.
- Hydrodynamic trapping (physical trapping)
Hydrodynamic trapping can occur in saline formations where fluids migrate very slowly over long distances. When CO₂ is injected into a formation, it displaces saline formation water and then migrates buoyantly upwards, because it is less dense than the water. When it reaches the top of the formation, it continues to migrate as a separate phase until it is trapped as residual CO₂ saturation (residual CO₂ trapping) or in local structural or stratigraphic traps within the sealing formation. In the longer term, significant quantities of CO₂ dissolve in the formation water (solubility trapping) and then migrate with the groundwater [28].
- Geochemical trapping
This means the trapping of CO₂ due to geochemical interactions with the rock and formation water also referred to as mineral trapping.

This chapter gives an overview of hydrogeochemical and other methods of investigation to assess potential risks arising from the geological storage of CO₂. The focus lies on hydrogeochemical reactions, especially the gas–water–rock interactions, such as mineral dissolution and precipitation, adsorption/desorption, and the potential buffering capacities of different mineral phases.

2 Hydrogeochemical Methods of Investigation

2.1 Water Analysis and Plausibility Checks

Hydrogeochemical characterization of groundwater of different origin and the evaluation of their mixing ratios require an accurate analysis of their hydrochemical and physicochemical composition.

Therefore, the sensitive parameters such as temperature, pH, redox potential (Eh or pe), dissolved O₂-content, HCO₃⁻ (alkalinity), and electrical conductivity (EC) as well as NH₄⁺, NO₂⁻, H₂S, HS⁻ and Si-species must be determined on site.

An overview of sampling and analytical techniques with emphasis on geothermal fluids is given by Arnórsson et al. [29].

Plausibility checks should be carried out to evaluate the quality and reliability of hydrochemical analyses. For this purpose it is useful to compare the measured values of electrical conductivity and the analyzed amount of total dissolved solids (TDS) as a sum of dissolved cations and anions. Furthermore, the ionic balance is used to assess the quality of hydrochemical analyses. Here, the sum of cations and anions should be nearly identical, with an allowed analytical error of approximately ±5%, depending on the salinity of the water.

The pH value can be checked up with the dissolved carbonate equilibria and the measured Eh value with the equilibria of redox sensitive parameters.

2.2 Hydrochemical Characterization and Statistics

To judge the salinity of water samples, the classification by Davis and de Wiest [30] can be used, which is based on the total concentration of dissolved constituents:

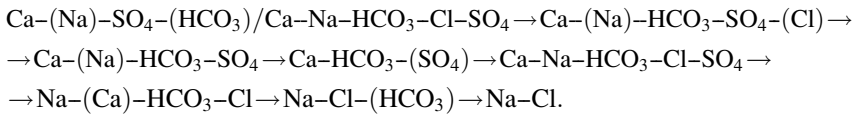
• Fresh water (mg/L)	0–1,000
• Brackish water (mg/L)	1,000–10,000
• Saltwater (mg/L)	10,000–100,000
• Brine (mg/L)	>100,000

This classification is especially useful to distinguish waters of different origin and hydrogeochemical genesis in the aquifers of deep sedimentary basins.

Another classification considers all ions with 20 mmol(eq)% as a minimum of the sum of the cations and the anions (each with 100% as a total). The ions are specified in the order cations–anions with decreasing frequency.

Hydrogeological investigations in the southern districts of Berlin, a region typical for the North-eastern German Basin, showed different types of groundwater in the Cenozoic aquifers, which could be distinguished by Wurl [31] on the basis of statistical methods and the classification mentioned above. He described the

following groundwater types as well as their mixing types from the first aquifer with anthropogenic influence to the deepest aquifer with geogenic salinization as follows:



This shows the increasing salinization with depth connected with the prominence of sodium and chloride as prevailing ions.

As this is a good example for the hydrogeological situation in the North German Basin, these investigations can be useful to assess the risks for groundwater resources due to geological CO₂ storage.

With sufficient data, a classification using multivariate statistical analyses should be carried out. In addition to a correlation analysis, mainly the factor analysis, the discriminant analysis and the cluster analysis are useful [31, 32].

To visualize the ion ratios of different waters, graphical representations such as Piper- or Durov-diagrams are helpful [33, 34].

The calculation of the various ion ratios can be used for the evaluation of dilution or mixing effects and possible water-rock interactions or ion exchange processes.

The representation of ion ratios is well suited to draw conclusions about the origin and genesis of deep waters in sedimentary basins. Particularly suitable are the ratios of the ion concentrations versus chloride and bromide, as these are regarded as conservative, nonreactive ions [35].

Especially the bromide/chloride ratios are valuable to assess the origin and genesis of deep saline waters in sedimentary basins. This method was developed by Rittenhouse [36] and is also used for assessing the genesis of oilfield waters.

Isotope studies are another method to investigate the origin and genesis as well as the movement and distribution processes of groundwater within the aquifer. Especially the heavy stable isotopes of the water molecule, deuterium and oxygen-18 and the radioactive isotopes tritium (esp. ³H/³He) and carbon-14 can be used as indicators of the circulation of groundwater and its residence times. Detailed descriptions of investigation methods of isotopes in the environment and their interpretation are given, e.g., by Fritz and Fontes [37, 38]; Hoefs [39] and Pearson et al. [40].

Thermodynamic computer programs like PHREEQC [41], WATEQ [42], WATEQ4F [43], EQ3/6 [44], SOLMINEQ [45], NETPATH [46], GWB – The Geochemist's Workbench et al. [47, 48] are valuable tools to describe a solution with respect to its saturation state regarding different mineral phases and to determine the distribution of various aqueous species within the solution. Furthermore, they can be used to calculate the hydrochemical composition of mixed solutions and the potential for mineral precipitation and dissolution respectively, the redox equilibria within a solution, as well as the prediction and quantification of scaling or corrosion in the sense of a worst case scenario in production processes [35].

However, thermodynamic equilibrium models do not take into account reaction kinetics and often there are no sufficient thermodynamic data for solid solutions.

2.3 Stability Field- and Activity- or Phase-Diagrams

Injection of supercritical CO₂ causes a sharp drop of the pH value of the fluid in contact with CO₂ phases as reported, e.g., by Kharaka et al. [12] or Pham et al. [49].

Low pH values cause increasing solubility of compounds which are otherwise in a solid state. The pH dependence of the solubility of potential hazardous compounds can be represented in activity or stability diagrams.

Potential risks for freshwater resources can arise due to the dissolution of galena (PbS) or arsenopyrite (FeAsS) and accordingly realgar (As₄S₄) or orpiment (As₂S₃) as a by-product of the decay of arsenic minerals. These minerals are often found in sedimentary rocks under reducing conditions. Even low levels of arsenic can be toxic to humans and so it is a highly undesirable impurity of potable water resources. According to the drinking water standards of the U.S. Environmental Protection Agency (U.S. EPA) and the WHO guidelines for drinking water, the upper limit for arsenic has been set to 10 µg/L.

According to Apps et al. [2], CO₂ leakage into a shallow aquifer can lead to long-lasting mobilization of hazardous trace elements, in particular arsenic and lead, near the intrusion location and farther downstream. Their thermodynamic equilibrium calculations identified As and Pb as trace elements with the highest potential for exceeding regulatory water quality limits at elevated CO₂ concentrations.

Figure 1 shows the aqueous arsenic species and their phase boundaries according to the Eh/pH conditions of a solution. In aqueous solutions HAsO₄²⁻ is the dominant species above a pH of 7.2. Between pH 2.5 and pH 7.2, H₂AsO₄²⁻ is the dominant species. Under reducing conditions, As(OH)_{3(aq)} is the dominant species up to pH 9.2.

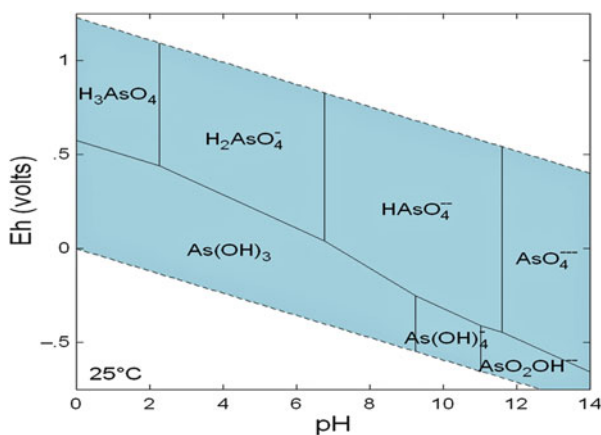


Fig. 1 Eh/pH – diagram of the system As–O–H showing arsenic species in aqueous solutions. Activity of As = 10⁻⁴ (mol/kg), T = 25°C, p = 1.013 bar. Phase boundaries constructed with GWB

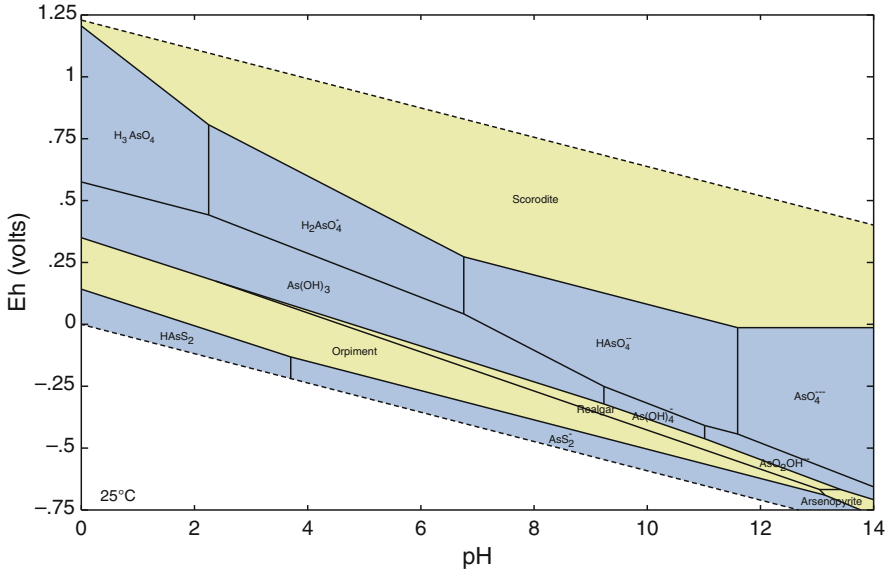


Fig. 2 Eh/pH – diagram of the system As–S–Fe–C–O–H showing arsenic species in aqueous solutions and stability fields of mineral phases. The assumed activities (mol/kg) for dissolved species are: $\text{SO}_4^{2-} = 10^{-4}$, $\text{HCO}_3^- = 10^{-3}$, $\text{Fe}^{2+} = 10^{-3}$, $\text{As} = 10^{-4}$, $T = 25^\circ\text{C}$, $p = 1.013 \text{ bar}$. Phase boundaries constructed with *GWB*

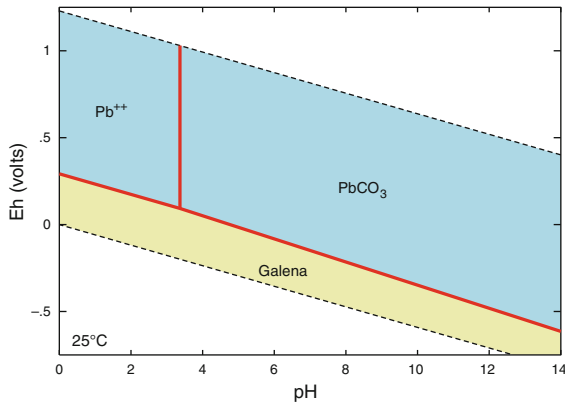


Fig. 3 Eh/pH – diagram of the system Pb–S–C–O–H showing lead species in aqueous solutions and stability fields of mineral phases. The assumed activities (mol/kg) for dissolved species are: $\text{SO}_4^{2-} = 10^{-3}$, $\text{HCO}_3^- = 10^{-3}$, $\text{Pb}^{2+} = 10^{-6}$. Phase boundaries constructed with *GWB*

The stability fields of the various arsenic mineral phases together with the aqueous species are shown in Fig. 2.

As an example for the dissolution of heavy metals under acid conditions, Fig. 3 shows the aqueous lead species and their phase boundaries as well as the stability field for galena as mineral phase according to the Eh/pH conditions of a solution. In aqueous solutions $\text{PbCO}_3(\text{aq})$ is the dominant species above a pH of 3.2. At a lower

pH, Pb^{2+} is the dominant species. Under reducing conditions, PbS (galena) is the stable mineral phase.

Wang and Jaffe [50] pointed out that the dissolved Pb concentration due to the dissolution of galena increases as the partial pressure of CO_2 in equilibrium with the solution increases. This is due to decreasing pH values. However, their model simulations showed that the detrimental effect of CO_2 intrusion would significantly decrease in aquifers with high alkalinity and pH buffering capacity such as calcite bearing aquifers [50].

3 CO_2 -Sequestration and Other Subsurface Activities

3.1 Pressure Distribution and Saltwater Migration

In its supercritical state of aggregation the properties of carbon dioxide are between those of a gas and those of a liquid. Its density is like those of a liquid but its viscosity is like a gas. Supercritical CO_2 occurs at pressure and temperature conditions above the critical point for carbon dioxide, i.e. at temperatures above 304.13 K (30.98°C) and pressures above 7.375 MPa (73.75 bar). The pressure/temperature phase diagram of carbon dioxide is shown in Fig. 4.

Supercritical carbon dioxide is also used for the exploitation of oil reservoirs by means of EOR.

Because of the lower density of supercritical CO_2 compared to the density of a brine in the deep saline aquifer, the injected CO_2 will flow along the surface of the target formation below the caprock due to buoyancy. The flow path as well as the pressure distribution within the aquifer depends on porosity and permeability of the target formation.

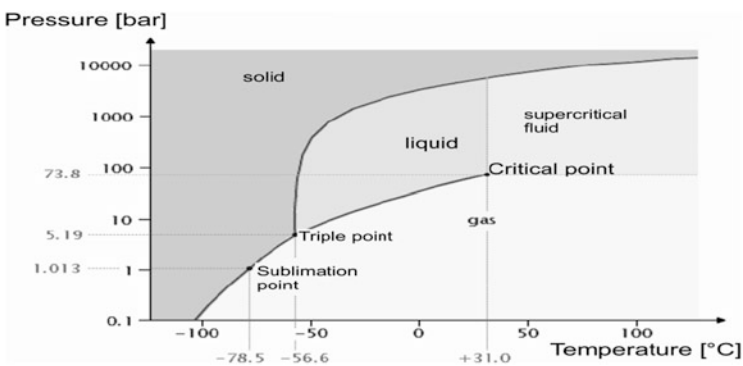


Fig. 4 Pressure/Temperature phase diagram of CO_2 . Under normal pressure and temperatures CO_2 is in the gas phase. The triple point is at 5.19 bar and -56.6°C . This is the lowest pressure at which liquid CO_2 exists. Liquid carbon dioxide at 20°C requires a pressure of 30 bar. At 73.8 bar and 31.0°C is the critical point at which CO_2 is in a supercritical fluid phase. The sublimation point is the point at which under normal pressure (1.013 bar) CO_2 goes directly from the solid phase into the gas phase (at -78.5°C)

If the injection rates and therefore the pressures are too high, they can cause fractures in the caprock or damages and failures in the casing of a borehole even in the wider surrounding of the injection site.

Moreover, injected supercritical CO₂ is “dry” relative to groundwater and water will be dissolved in dry CO₂. Experimental determinations of the solubility of water in supercritical carbon dioxide were carried out by King et al. [51].

As a consequence water might be extracted from the clays within the caprock at the contact with dry CO₂. This might induce shrinkage and increasing permeabilities within the caprock, as described by Gaus [52].

On the other hand, “dry” supercritical CO₂ could cause an “evaporation effect” on the formation water, leading to a precipitation of supersaturated mineral phases. Here, due to their fast reaction kinetics the most important minerals are the carbonates, the sulfates and other evaporites. All of these reaction processes in the context of CO₂ storage are poorly understood and so far no substantial research has been carried out to assess their relevance with respect to carbon capture and sequestration. Further laboratory work on core samples regarding clay dehydration and desiccation is necessary to evaluate these important issues.

Continued injection can displace the formation water and increase its flow velocity which could lead to a discharge along different flow paths. Hydraulic modeling of the target formation and their surrounding as well as pressure monitoring of the injection site is therefore essential to avoid leakages due to excessive pressure conditions. Modeling of the geological and structural conditions should also consider reactive transport modeling.

Birkholzer et al. [53] developed a numerical model to investigate the multiphase flow and multicomponent transport of CO₂ and brine in response to CO₂ injection into an idealized multilayer formation. They used the TOUGH2/ECO2N simulator [54, 55] to simulate the transient pressure buildup, spatial CO₂ plume evolution as well as brine flow and transport. Their results show that the permeability of the sealing layers has a strong effect on the vertical and the lateral pressure propagation as well as brine displacement behavior within the storage formation. Considerable pressure buildup in the storage formation is predicted more than 100 km away from the injection zone, while the lateral brine transport velocity and migration distance are less significant [53]. However, these simulations were carried out assuming an ideal aquifer/aquitard system with homogeneous layers without any leakage along faults and fractures or abandoned wells.

The environmental impact of large-scale pressure buildup and related brine displacement depends mainly on the hydraulic connectivity between deep saline aquifers and the overlying freshwater aquifers. A hydraulic communication between the deep storage formation and freshwater aquifers enables an upward migration of brine due to pressure buildup at depth. Possible impacts are a change of the discharge and recharge areas, a rising water table and changes in water quality [53].

So far, hydrogeochemical reactions in most of the simulations were not sufficiently taken into account. Furthermore, no studies of the mineral reactions exist with respect to changes in the porosities and permeabilities within the aquifer.

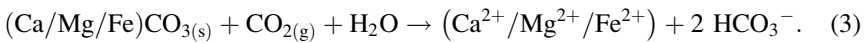
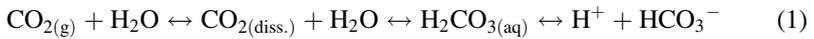
The following section describes the main gas–water–rock interactions, which must be considered regarding underground CO₂ storage.

3.2 *Hydrogeochemical Reactions and (Gas)–Water–Rock Interactions*

In the course of underground storage of CO₂ in the Frio-I Brine Pilot test, Texas, USA, Kharaka et al. [12] reported a sharp drop of pH values in the Frio Formation water from 6.3 at subsurface conditions (modeled) prior to injection to a pH value of about 3 at subsurface conditions of the water in contact with supercritical CO₂. Thus, the brine becomes highly undersaturated with respect to various minerals in the host rock. Because of high mineral dissolution rates at such low pH values, the fluid will be enriched in its ion content. On the longer term, the pH value of the fluid increases due to mineral dissolution. The brine should gradually evolve towards its pre-injection composition, but this could take thousands of years [12].

Carbonates are ubiquitous minerals within the aquifer and because of their relatively fast reaction kinetics the first ones which will dissolve due to solutions that are highly enriched in carbonic acid.

The chemical reactions of CO_{2(g)}-intrusion into an aquifer, the formation and dissociation of carbonic acid and the subsequent dissolution of carbonates, notably calcite, magnesite, dolomite, siderite, can be described as follows:



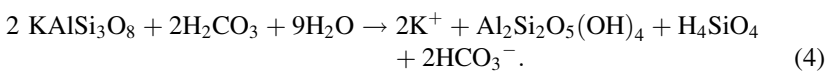
Another effect causing high alkalinity in a solution is the increasing solubility of carbonates with the increasing salinity of a solution [35].

Due to reaction kinetics, aluminosilicate minerals dissolve much slower and their dissolution is generally not congruent but follows incongruent reactions as described for feldspars in reactions 4–8.

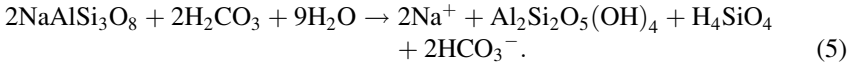
The dissolution of feldspars leads to an enrichment of silica, potassium, sodium, calcium, magnesium, iron (ferric or ferrous), and aluminum in the fluid. These dissolved substances are available for the formation of authigenic mineral phases. Some important authigenic mineral formations after previous feldspar dissolution are kaolinite, chlorite, and quartz.

The solution reactions of feldspars can be described as follows:

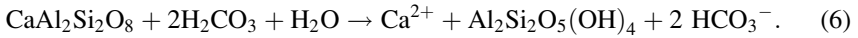
- Dissolution of orthoclase and formation of kaolinite and silica:



- Dissolution of albite and formation of kaolinite and silica:



- Dissolution of anorthite and formation of kaolinite:

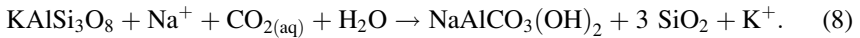


Similar hydrogeochemical processes were described by Thomas [35] regarding formation waters within deep aquifers in the North German basin.

If there is sufficient supply of dissolved CO₂ within the fluid, albite can be altered into dawsonite:



In deep saline waters with high ambient Na⁺ concentrations and acid-induced K-feldspar dissolution, the formation of dawsonite and associated mineral trapping of CO₂ can be described as follows [56]:



Another possibility of CO₂ mineral trapping is the conversion of kaolinite, an alteration product of feldspar dissolution (reactions 4–6), in dawsonite (reaction 9):

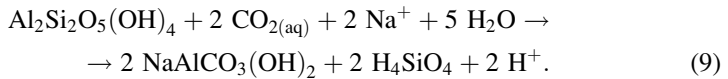
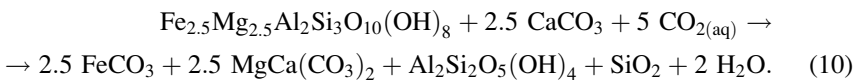


Figure 5 shows an example of the equilibrium activity fields of the aluminum silicates under hypothetical reservoir conditions.

In the course of CO₂ injection, aluminum silicates will be transformed to dawsonite as a stable mineral phase (Fig. 6).

Finally, other clay minerals like chlorite can induce mineral trapping of CO₂ by precipitation of siderite and dolomite as secondary carbonates [52]:



Another important CO₂ trapping mineral is ankerite with the chemical formula Ca(Fe,Mg,Mn)(CO₃)₂. Precipitation of siderite and ankerite requires Fe²⁺ supplied

Fig. 5 Equilibrium activity diagram of aluminum silicates at $T = 75^\circ$, $p = 170$ bar. The assumed activities (mol/kg) for dissolved species are: $\text{Ca} = 0.01$, $\text{Cl} = 1$, $T = 75^\circ$, $p = 170$ bar. Phase boundaries constructed with GWB

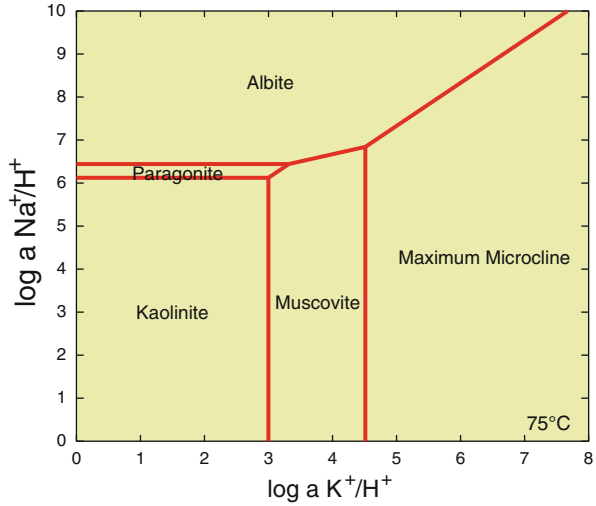
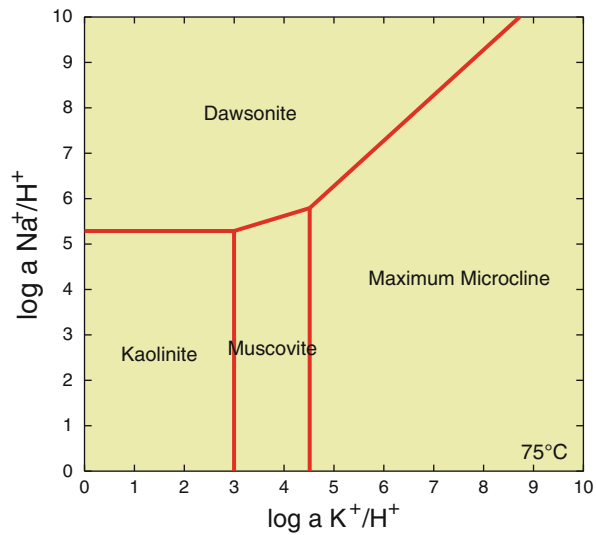


Fig. 6 Equilibrium activity diagram of aluminum silicates at $T = 75^\circ$, $p = 170$ bar, fugacity of $\text{CO}_2(\text{g}) = 5$. The assumed activities (mol/kg) for dissolved species are: $\text{Ca} = 0.01$, $\text{Cl} = 1$. Phase boundaries constructed with GWB



mainly by chlorite and by some hematite dissolution [57]. The precipitation of secondary carbonates results in decreased porosities.

Clearly, the CO_2 mineral-trapping capacities depend on the primary mineral composition of the host rocks and therefore they are very site specific.

The acid-induced reactions due to the injection of large quantities of CO_2 could buffer the pH significantly on the longer term, depending on reaction kinetics.

If CO_2 injection rates are faster than the fluid-rock reaction kinetics, lower pH values will persist for some time after injection but will ultimately return to some equilibrium leading to an increase in pH [56].

Another aspect of a low pH-value of a fluid in contact with the injected supercritical CO₂ as described above is its corrosion potential with respect to well pipes, casings, and cements. This could create pathways in former impermeable sealings and allow leakage of CO₂ and possibly contaminated fluids and therefore could have a severe environmental impact on freshwater resources. The main concern is the enrichment of heavy metals or arsenic due to mineral dissolution as well as organic compounds due to supercritical CO₂ as an effective solvent for organic substances.

Zheng et al. [25] carried out reactive transport simulations focused on the mobilization of lead and arsenic as a result of the dissolution of galena (PbS) and arsenopyrite (FeAsS). They concluded that adsorption/desorption is the most important process controlling the fate of hazardous constituents mobilized by CO₂ leakage.

Adsorption via surface complexation is an important process with respect to transport and mobilization of heavy metals or arsenic. The most common adsorbents in sedimentary rocks are goethite, kaolinite, illite, and smectite with high adsorption capacities. However, desorption/adsorption and dissolution/precipitation of heavy metals interact with each other. These processes depend on mineral surfaces and their complexation capacities as well as reaction kinetics and so they are extremely site specific. Desorption of trace metals due to decreasing pH values may be of more importance on water quality than dissolution of minerals.

3.3 *Monitoring Methods*

Monitoring methods of dissolved CO₂ including reactive transport modeling has been tested in various pilot sites of CO₂ injection [12, 13, 26, 58–73].

The simplest method to monitor the effects of CO₂ injection is the measurement of the pressure distribution within the aquifers. Pressure monitoring should be carried out downhole in situ because measurements at the surface can be inaccurate due to wellbore storage effects. Pressure monitoring methods at the CO₂ storage site at Ketzin (Germany) are described by Henniges et al. [74]. CO₂ plumes can also be monitored using temperature signals [75] or geoelectrical methods [76].

White et al. [77] described methods of geophysical monitoring. Amplitude and travel times of reflected seismic waves change in an aquifer containing injected CO₂ due to the alteration of the bulk density. 3-D seismic surveys before, during, and after CO₂-injection can deliver a time-lapse picture of the movement of fluids in the subsurface, known as 4-D seismic with the time as 4th dimension. This technique is used to map the movement of CO₂ in the formation and to locate the moving CO₂ front [77]. Another geophysical monitoring method is the electrical resistance tomography, because CO₂ alters the electrical resistivity in a geological formation [78].

However, Kharaka et al. [12] pointed out that geophysical investigations are not able to detect dissolved CO₂ as this is possible only if CO₂ is present in significant amounts, of ~5% of pore space, as a separate phase.

Therefore, hydrogeochemical monitoring methods are a valuable tool to detect increased CO₂ concentrations in the fluid or as a gas phase.

As described in Sect. 3.2, CO₂–water–rock interactions lead to increasing concentrations especially not only of Ca²⁺, Mg²⁺, HCO₃⁻, Fe²⁺, and Mn²⁺ but also of K⁺ and Na⁺, connected with a decrease of the pH value in the solution. These reactions are the reason of an increased electrical conductivity of the fluid.

Furthermore, increased bromide contents can be an indicator of an ascendancy of deep saline waters as bromide is enriched in most brines in deep sedimentary basins.

Temperature measurements of the fluids can give a hint to an influx of deep saline waters or changed discharge conditions.

For the on-site monitoring it is therefore useful to measure electrical conductivity, pH, temperature, and pressure directly in the observation wells as well as the bicarbonate content on site. These analyses should be supplemented by laboratory measurements of major cations, especially dissolved Fe²⁺, Ca²⁺, Mg²⁺, Mn²⁺, Na⁺, and anions (Cl⁻, SO₄²⁻) as well as bromide, dissolved inorganic and organic carbon (DIC, DOC), gas composition and the isotopes ¹⁸O of the fluids and the CO₂. Further investigations should include the isotopes ¹³C of DIC and CO₂, trace metals, arsenic and the total amount of BTEX (benzene, toluene, ethylbenzene, and xylenes) because supercritical CO₂ is an excellent solvent for organic compounds.

Stable carbon isotopes are used as tracers to monitor the fate and migration of injected CO_{2(g)} in the subsurface at the Ketzin pilot site, Germany [79].

To detect a leakage of the injected CO₂, it is possible to add perfluorocarbon tracer gases (PFT) to the injected CO₂ because they migrate with a potential CO₂ breakthrough and so they can be used to monitor migration of supercritical CO₂ as described by Kharaka et al. [12].

Groundwater monitoring wells in the near field should be installed above the confining layer to identify potential CO₂ leakage at the injection site.

Deep monitoring wells should be used for pressure monitoring of the injection zone for detecting changes within the injection reservoir. Pressure monitoring should be carried out in the injection zone, in the confining layer and above the confining layer to recognize any possible anomalies immediately.

Observation wells must be installed at various distances from the injection well for monitoring of pressure and water properties as well as the gas content. A pressure increase can possibly be detected over 100 km away from the injection site in the so-called far-field and could have an effect on the saltwater/freshwater interface, causing a rise of the groundwater table. This is to be considered when planning a monitoring network around an injection site.

3.4 Prevention and Control

The most promising geologic reservoirs for carbon dioxide storage seem to be the exploited gas reservoirs, because it is assumed that they are impermeable to any possible escape of gases.

Assuming a geothermal gradient of 3°C/100 m and a hydrostatic pressure increase of 10 bar/100 m, the depth of an injection well must be at least 800 m, to keep the supercritical state of injected CO₂ (see Fig. 4).

However, the effects of injection pressures can extend for kilometers, depending on porosities and permeabilities of the host rock and the confining layer and the salinities of the fluids.

Therefore, a comprehensive knowledge of the hydrogeologic and particularly hydraulic conditions within the aquifers, the hydrogeochemical composition of the deep groundwater and the mineralogical constituents of the reservoir rocks as well as the confining layers is essential. This includes aquifer properties such as thickness, areal extent and structure, mineral composition, porosity and permeability as well as hydrophysical parameters such as pressure, temperature, elasticity, compressibility, fluid saturation, and storage coefficient. Furthermore, hydrochemical and physico-chemical parameters of the formation water as described above must be known.

Hydraulic and hydrogeochemical modeling including reactive transport modeling are valuable tools to simulate the impacts of CO₂ injection, considering that hydrogeological conditions as mentioned above are extremely site-specific.

Another aspect is the assessment of the existence of abandoned or other wells or boreholes in the affected region, which can extend to over 10,000 km² depending on the geological conditions and the injection rate and pressure. It is therefore important to inspect the plugging of those wells, whether they provide a sufficient seal and do not communicate between different aquifers. Hydraulic modeling, carried out by Birkholzer et al. [53], showed that a pressure buildup of 0.7 bar (≈ 7 m hydrostatic head of freshwater) in the storage formation could be predicted 100 km away from the injection zone.

Evaluation of appropriate injection pressures is also essential to prevent fracturing of the confining layer due to excessive pressures.

Long-term monitoring as described in Sect. 3.3 is necessary to prevent or to detect environmental impacts due to geological CO₂ storage.

4 Concluding Remarks

Due to climate change and the necessity to reduce greenhouse gases in the atmosphere, geological CO₂ storage and sequestration is considered to be one option for mitigating the negative environmental impacts of these gases.

Sandstone aquifers containing saline waters in deep sedimentary basins are considered as potential locations for CO₂ injection provided that they are sealed with thick impermeable layers.

However, the main concern over geological CO₂ storage is a possible release of CO₂ due to leakage and adjacent leaching of trace metal bearing minerals or the displacement of saltwater, respectively, brines, into freshwater aquifers. Further risks could arise from dissolved organic compounds because supercritical carbon dioxide is an excellent solvent for those constituents. Increased BTEX concentrations therefore can occur, especially in the vicinity of petroleum, natural gas, or coal deposits.

To maintain CO₂ in a dense, supercritical fluid phase, under normal geological conditions with a geothermal gradient of 3°C/100 m and normal hydrostatic pressure, the minimum depth for CO₂ storage is 800 m below surface.

Trapping mechanisms for CO₂ in deep geological formations are:

- Hydrodynamic trapping as a supercritical fluid below the caprock
- Residual trapping within the pores of reservoir rocks
- Solution trapping as aqueous species dissolved in formation water
- Mineral trapping by precipitation of carbonate minerals

Mineral trapping occurs on the longer term due to the slower reaction kinetics of the involved aluminum silicates, but as a result CO₂ is trapped for a long time, incorporated in carbonate minerals. In sandstone aquifers, major CO₂ trapping minerals are dawsonite and ankerite. The precipitation of siderite and ankerite requires aqueous Fe²⁺-species, mainly supplied by chlorite and/or hematite dissolution and reduction. Dissolved Na⁺-species, provided by the dissolution of Na-feldspars, convey the precipitation of dawsonite.

These (gas)–water–rock interactions change the porosities and permeabilities of the aquifers. Thus, mineral dissolution and precipitation can modify the fluid flow.

Precipitation of mineral phases can cause a plugging (clogging) of pore spaces. This leads to a reduction of both the storativity of the target formation and the injection capacity.

Monitoring methods should include the physicochemical parameters pressure, temperature, electrical conductivity, pH and redox potential of the fluids as well as TDS, alkalinity, major cations and anions, trace elements, and BTEX.

Hydrochemical monitoring can detect dissolved CO₂ in smaller amounts whereas geophysical methods can be used to trace the plume of supercritical CO₂.

To monitor possible effects of dissolved CO₂ on groundwater resources, hydrochemical monitoring should be favored.

Long-term monitoring is essential to detect impacts of CO₂ injection on groundwater both in the near field and in the far field of the injection site.

Until now, there are only a few laboratory investigations [15, 20, 80–82] carried out on core material regarding the rock composition, the mineral content of the host rock and the caprock as well as their porosities and permeabilities and their changes due to gas–water–rock interactions. Therefore, further studies are necessary regarding gas–water–rock interactions and their influence upon porosities and permeabilities of the aquifers. They should also include the reaction kinetics and the thermodynamic properties of the relevant mineral phases under high temperatures and pressures. The determination of reliable reaction rates of minerals regarding dissolution and precipitation is necessary to calculate the long-term trapping capacities of minerals. Also, investigations regarding sorption and ion exchange are important for the evaluation of possible impacts of CO₂ leakage on shallow groundwater. Moreover, the role of organic compounds in gas–water–rock interactions needs further study [83].

However, laboratory experiments have the disadvantage that reaction kinetics are often too slow to be determined within the appropriate time periods. Nevertheless, long-term reactions can be predicted by equilibrium modeling using thermodynamic computer programs such as PhreeqC, GWB, or others.

Hydrogeochemical modeling and reactive transport modeling are therefore valuable tools to assess gas–water–rock interactions and to predict hydrogeochemical reactions in the course of carbon dioxide storage.

Seepage of CO₂ can occur due to faulty well casing or cementing or poorly sealed abandoned wells. Investigation of all the wells and boreholes within the area influenced by CO₂ storage activities is therefore essential.

Intrusion of the injected CO₂ into groundwater causes a sharp drop of pH and enhanced mineral dissolution, leading to increasing contents of trace metals. Aquifers with a considerable amount of carbonates and high alkalinity are able to diminish this detrimental effect of CO₂ injection because of their high pH buffering capacities.

Therefore, the selection of a potential storage site for CO₂ sequestration requires detailed investigations of the mineralogical composition, porosities, and permeabilities of the storage formation, the caprock and the overlying aquifers as well as the hydrochemical conditions of the fluids within the aquifers. All these parameters are also needed for reactive transport modeling and the evaluation of storage capacities, pressure distribution, and risk assessment.

However, the hydrogeological, hydrogeochemical, and hydraulic conditions are very site-specific and quantitative predictions, required for an integrated risk assessment, should be supported by site-specific modeling as well as laboratory experiments and field tests.

Moreover, a detailed long-term monitoring program must be established to avoid possible negative impacts on freshwater resources due to geological CO₂ storage.

References

1. Apps JA, Zhang Y, Zheng L, Xu T, Birkholzer JT (2009) Identification of thermodynamic controls defining the concentrations of hazardous elements in potable ground waters and the potential impact of increasing carbon dioxide partial pressure. *Energy Procedia* 1:1917–1924
2. Apps JA, Zheng L, Zhang Y, Xu T, Birkholzer JT (2010) Evaluation of potential changes in groundwater quality in response to CO₂ leakage from deep geologic storage. *Trans Porous Media* 82(1):215–246
3. Audigane P, Chiaberge C, Lions J, Humez P (2009) Modeling of CO₂ leakage through an abandoned well from a deep saline aquifer to fresh groundwater. In: *Proceedings of TOUGH symposium 2009*, Lawrence Berkeley National Laboratory, Berkeley, p 8
4. Bachu S, Celia MA (2009) Assessing the potential for CO₂ leakage, particularly through wells, from geological storage sites. In: McPherson BJ, Sundquist ET (eds) *Carbon sequestration and its role in the global carbon cycle*. AGU Monograph. AGU, Washington, pp 203–216
5. Bachu S, Gunter WD, Perkins EH (1994) Aquifer disposal of CO₂: hydrodynamic and mineral trapping. *Energy Convers Manage* 35(4):269–279
6. Birkholzer JT, Apps J, Zheng L, Zhang Y, Xu T, Tsang C-F (2008) Research project on CO₂ geological storage and groundwater resources, quality effects caused by CO₂ intrusion into Shallow Groundwater. Technical Report. Earth Sciences Division, Lawrence Berkeley National Laboratory, Berkeley, p 352
7. Birkholzer JT, Zhou Q, Zhang K, Jordan P, Rutqvist J, Tsang C-F (2008) Research project on CO₂ geological storage and groundwater resources: large-scale hydrogeological evaluation and impact on groundwater systems, Annual report October 1, 2007 to September 30, 2008. Lawrence Berkeley National Laboratory, Berkeley
8. Birkholzer JT, Zheng L, Spycher N, Varadharajan C, Nico PS (2010) Groundwater quality changes in response to CO₂ leakage from deep geological storage. *Geol Soc Am Abstr* 42(5):45
9. Holloway S, Savage D (1993) The potential for aquifer disposal of carbon dioxide in the UK. *Energy Convers Manage* 34(9–11):925–932

10. Jaffé PR, Wang S (2003): Potential effect of CO₂ releases from deep reservoirs on the quality of fresh-water aquifers. In: Gale J, Kaya Y (eds) Proceedings of the 6th international conference on Greenhouse Gas Control Technologies, vol. 2, 1–4 October 2002, Kyoto, Japan. Greenhouse Gas Control Technologies, pp 1657–1660
11. Keating EH, Fessenden J, Kanjorski N, Koning DJ, Pawar R (2010) The impact of CO₂ on shallow groundwater chemistry: observations at a natural analog site and implications for carbon sequestration. *Environ Earth Sci* 60(3):521–536
12. Kharaka YK, Thordsen JJ, Hovorka SD, Nance HS, Cole DR, Phelps TJ, Knauss KG (2009) Potential environmental issues of CO₂ storage in deep saline aquifers: geochemical results from the Frio-I brine pilot test, Texas, USA. *Appl Geochem* 24:1106–1112
13. Kharaka YK, Thordsen JJ, Kakouros E, Ambats G, Herkelrath WN, Beers SR, Birkholzer JT, Apps JA, Spycher NF, Zheng L, Trautz RC, Rauch HW, Gullickson KS (2010) Changes in the chemistry of shallow groundwater related to the 2008 injection of CO₂ at the ZERT field site, Bozeman, Montana. *Environ Earth Sci* 60:273–284
14. Kolak JJ, Burruss RC (2006) Geochemical investigation of the potential for mobilizing non-methane hydrocarbons during carbon dioxide storage in deep coal beds. *Energy Fuel* 20:566–574
15. Labus K, Bujok P (2011) CO₂ Mineral sequestration mechanisms and capacity of saline aquifers of the upper Silesian coal basin (Central Europe) – modeling and experimental verification. *Energy* 36:4974–4982
16. Lewicki JL, Birkholzer JT, Tsang C-F (2007) Natural and industrial analogues for leakage of CO₂ from storage reservoirs: identification of features, events, and processes and lessons learned. *Environ Geol* 52:457–467
17. Nicot J-P, Hovorka SD, Choi J-W (2009) Investigation of water displacement following large CO₂ sequestration operations. *Energy Procedia* 1:4411–4418
18. Person M, Banerjee A, Rupp J, Medina C, Lichtner P, Gable C, Pawar R, Celia M, McIntosh J, Bense V (2010) Assessment of basin-scale hydrologic impacts of CO₂ sequestration, Illinois basin. *Int J Greenhouse Gas Control* 4:840–854
19. Pruess K (2008) On CO₂ fluid flow and heat transfer behavior in the subsurface, following leakage from a geologic storage reservoir. *Environ Geol* 54:1677–1686
20. Smyth RC, Hovorka SD, Lu J, Romanak KD, Partin JW, Wong C, Yang C (2009) Assessing risk to fresh water resources from long term CO₂ injection: laboratory and field studies. *Energy Procedia* 1:1957–1964
21. Van der Meer LGH (1992) Investigations regarding the storage of carbon dioxide in aquifers in the Netherlands. *Energy Convers Manage* 33(5–8):611–618
22. Würdemann H, Möller F, Kühn M, Heidug W, Christensen NP, Borm G, Schilling FR, CO₂SINK Group (2010) CO₂SINK – From site characterisation and risk assessment to monitoring and verification: One year of operational experience with the field laboratory for CO₂ storage at Ketzin, Germany. *Int J Greenhouse Gas Control* 4:938–951
23. Yamamoto H, Zhang K, Karasaki K, Marui A, Uehara H, Nishikawa N (2009) Numerical investigation concerning the impact of CO₂ geologic storage on regional groundwater flow. *Int J Greenhouse Gas Control* 3:586–599
24. Zheng L, Apps JA, Zhang Y, Xu T, Birkholzer JT (2009) On mobilization of lead and arsenic in groundwater in response to CO₂ leakage from deep geological storage. *Chem Geol* 268:281–297
25. Zheng L, Apps JA, Zhang Y, Xu T, Birkholzer JT (2009) Reactive transport simulations to study groundwater quality changes in response to CO₂ leakage from deep geological storage. *Energy Procedia* 1:1887–1894
26. Zheng L, Apps JA, Spycher N, Birkholzer JT, Kharaka Y, Thordsen J, Kakouros E, Trautz R (2009) Geochemical modeling of changes in shallow groundwater chemistry observed during the MSU-ZERT CO₂ injection experiment. In: Proceeding of the TOUGH Symposium, Lawrence Berkeley National Laboratory, Berkeley, p 10

27. Lemieux J-M (2011) Review: the potential impact of underground geological storage of carbon dioxide in deep saline aquifers on shallow groundwater resources. *Hydrogeol J* 19:757–778
28. IPCC (2005): IPCC special report on carbon dioxide capture and storage. In: Metz B, Davidson O, de Coninck H, Loos M, Meyer L (eds) Prepared by Working Group III of the Intergovernmental Panel on Climate Change. Cambridge University Press, Cambridge, p 442
29. Arnórsson S, Bjarnason JÓ, Giroud N, Gunnarsson I, Stefánsson A (2006) Sampling and analysis of geothermal fluids. *Geofluids* 6:203–216
30. Davis SN, de Wiest RJM (1967) *Hydrogeology*. Wiley, New York, p 463
31. Wurl J (1995) Die geologischen, hydraulischen und hydrochemischen Verhältnisse in den südwestlichen Stadtbezirken von Berlin. *Berliner Geowiss Abh, A* 172:164S
32. Tabachnick BG, Fidell LS (2006) *Using multivariate statistics*, 5th edn. Addison-Wesley, New York
33. Piper AM (1944) A graphic procedure in the geochemical interpretation of water analyses. *Trans Am Geophys Union* 25(6):914–928
34. Durov SA (1948) Natural waters and graphic representation of their composition. *Dokl Akad Nauk SSSR* 59:87–90
35. Thomas L (1994) Hydrogeochemische Untersuchungen an Ölfeldwässern aus NW-Deutschland und dem Oberrheingraben und ihre Modellierung unter dem Aspekt der Entwicklung eines Expertensystems für Fluid-Rock-Interactions (XPS FROCKI). Diss. FU Berlin, 166 S. (1993); *Berliner Geowiss Abh, A*, 165 (1994): 167 S
36. Rittenhouse G (1967) Bromine in oilfield waters and its use in determining possibilities of origin of these waters. *Am Assoc Petrol Geol Bull* 51(12):2430–2440, Houston, Texas
37. Fritz P, Fontes JC (1980) *Handbook of environmental isotope geochemistry*, vol 1. Elsevier, Amsterdam, p 545
38. Fritz P, Fontes JC (1986) *Handbook of environmental isotope geochemistry*, vol 2. Elsevier, Amsterdam
39. Hoefs J (2009) *Stable isotope geochemistry*, 6th edn. Springer, Berlin, p 285
40. Pearson FJ, Balderer W, Loosli HH, Lehmann BE, Matter A, Peters TJ, Schmassmann H, Gautschi A (1991) *Applied isotope hydrogeology – a case study in Northern Switzerland*. Technical Report 88-01, Nagra, p 439, Baden/Switzerland
41. Parkhurst DL, Appelo CAJ (1999) User's guide to PhreeqC (version 2) – a computer program for speciation, batch-reaction, one-dimensional transport, and inverse geochemical calculations. *Water Res Invest Rep* 99(4259):4312
42. Truesdell AH, Jones BF (1974) WATEQ, a computer program for calculating chemical equilibria of natural waters. *J Res USGS* 2:233–248
43. Ball JW, Nordstrom DK (2001) User's manual for WATEQ4F, with revised thermodynamic data base and test cases for calculating speciation of major, trace, and redox elements in natural waters. USGS, open-File Report 91-183 (1991, revised 2001), p 188
44. Wolery TJ (1992) EQ3/6, a software package for geochemical modeling of aqueous systems: Package overview and installation guide (Version 7.0). UCRL-MA-110662 PT I, Lawrence Livermore National Laboratory, p 66
45. Kharaka YK, Gunter WD, Aggarwal PK, Perkins EH, DeBraal JD (1988) SOLMINEQ.88: a computer program for geochemical modeling of water-rock interactions. U.S. Geological Survey, Water-Resources Investigations Report, 88-4227, p 420
46. Plummer LN, Prestemon EC, Parkhurst DL (1994) An interactive code (NETPATH) for modeling NET geochemical reactions along a flow PATH Version 2.0.- U.S. Geol. Survey, Water Resources Investigations Report 94-4169, p 130
47. Bethke CM (2010) *Geochemical and biogeochemical reaction modeling*, 2nd edn. Cambridge University Press, Cambridge, p 564
48. Bethke CM, Yeakel S (2012) *The geochemist's workbench – release 9.0. Reference manual – aqueous solutions*. LLC, Champaign, p 409

49. Pham VTH, Lu P, Aagaard P, Zhu C, Hellevang H (2011) On the potential of CO₂-water-rock-interactions for CO₂ storage using a modified kinetic model. *Int J Greenhouse Gas Control* 5:1002–1015
50. Wang S, Jaffe PR (2004) Dissolution of a mineral phase in potable aquifers due to CO₂ releases from deep formations; effect of dissolution kinetics. *Energ Convers Manage* 45:2833–2848
51. King MB, Mubarak A, Kim JD, Bott TR (1992) The mutual solubilities of water with supercritical and liquid carbon dioxide. *J Supercritical Fluid* 5:296–302
52. Gaus I (2010) Role and impact of CO₂-rock interactions during CO₂ storage in sedimentary rocks. *Int J Greenhouse Gas Control* 4:73–89
53. Birkholzer JT, Zhou Q, Tsang C-F (2009) Large-scale impact of CO₂ storage in deep saline aquifers: a sensitivity study on pressure response in stratified systems. *Int J Greenhouse Gas Control* 3:181–194
54. Pruess K, Oldenburg CM, Moridis G (1999) TOUGH2 user's guide, version 2.0.-Report LBNL-43134, Lawrence Berkeley National Laboratory, Berkeley
55. Pruess K (2005) ECO2N: a TOUGH2 fluid property module for mixtures of water, NaCl, and CO₂. Technical report. LBNL-57952, Lawrence Berkeley National Laboratory, Berkeley, p 76
56. Benezeth P, Palmer DA, Anovitz LM, Horita J (2007) Dawsonite synthesis and reevaluation of its thermodynamic properties from solubility measurements: implications for mineral trapping of CO₂. *Geochim Cosmochim Acta* 71:4438–4455
57. Xu T, Apps JA, Pruess K (2005) Mineral sequestration of carbon dioxide in a sandstone-shale system. *Chem Geol* 217:295–318
58. Audigane P, Gaus I, Czernichowski-Lauriol I, Pruess K, Xu T (2007) Two-dimensional reactive transport modeling of CO₂ injection in a saline aquifer at the Sleipner site, North Sea. *Am J Sci* 307(7):974–1008
59. Baines SJ, Worden RH (eds) (2004) Geological storage of carbon dioxide. *Geol Soc London, Special Publications* 233:1–6
60. Bergmann P, Yang C, Lüth S, Juhlin C, Cosma C (2011) Time-lapse processing of 2D seismic profiles with testing of static correction methods at the CO₂ injection site Ketzin (Germany). *J Appl Geophys* 75:124–139
61. Cantucci B, Montegrossi G, Vaselli O, Tassi F, Quattrocchi F, Perkins EH (2009) Geochemical modeling of CO₂ storage in deep reservoirs: the Weyburn project (Canada) case study. *Chem Geol* 265:181–197
62. Carroll S, Hao Y, Aines R (2009) Transport and detection of carbon dioxide in dilute aquifers. *Energy Procedia* 1:2111–2118
63. Dong Y, Li G, Li M, Wu R (2009) Impact of large-scale CO₂ geologic storage in deep saline aquifers: an example from the Songliao Basin, China. In: *Proceeding of the TOUGH symposium 2009*. Lawrence Berkeley National Laboratory, Berkeley, p 6
64. Gasda SE, Bachu S, Celia MA (2004) Spatial characterization of the location of potentially leaky wells penetrating a deep saline aquifer in a mature sedimentary basin. *Environ Geol* 46:707–720
65. Ivandic M, Yang C, Lüth S, Cosma C, Julin C (2012) Time-lapse analysis of sparse 3D seismic data from the CO₂ storage pilot site at ketzin, Germany. *J Appl Geophys* 84:14–28
66. Johnson JW, Nitao JJ (2003) Reactive transport modeling of geologic CO₂ sequestration at Sleipner. In: Gale J, Kaya Y (eds) *Proceedings of the 6th international conference on Greenhouse Gas Control Technologies*, vol. 1, 1–4 October 2002, Kyoto, Japan. *Greenhouse Gas Control Technologies*, pp 327–332
67. Kharaka YK, Cole DR, Hovorka SD, Gunter WD, Knauss KG, Freifeld BM (2006) Gas-water-rock interactions in Frio formation following CO₂ injection: implications for the storage of greenhouse gases in sedimentary basins. *Geology* 34(7):577–580
68. Michael K, Golab A, Shulakova V, Ennis-King J, Allinson G, Sharma S, Aiken T (2010) Geological storage of CO₂ in saline aquifers – a review of the experience from existing storage operations. *Int J Greenhouse Gas Control* 4:659–667

69. Nicot J-P (2008) Evaluation of large-scale CO₂ storage on freshwater sections of aquifers: an example from the Texas gulf coast basin. *Int J Greenhouse Gas Contrl* 2:582–593
70. Schilling F, Borm G, Würdemann H, Möller F, Kühn M, CO₂SINK Group (2009) Status report on the first European on-shore CO₂ storage site at Ketzin (Germany). *Energy Procedia* 1:2029–2035
71. Spangler LH, Dobeck LM, Repasky KS, Nehrir AR, Humphries SD, Barr JL, Keith CJ, Shaw JA, Rouse JH, Cunningham AB, Benson SM, Oldenburg CM, Lewicki JL, Wells AW, Diehl JR, Strazisar BR, Fessenden JE, Rahn TA, Amonette JE, Barr JL, Pickles WL, Jacobson JD, Silver EA, Male EJ, Rauch HW, Gullickson KS, Trautz R, Kharaka Y, Birkholzer J, Wielopolski L (2009) A shallow subsurface controlled release facility in Bozeman, Montana, USA, for testing near surface CO₂ detection techniques and transport models. *Environ Earth Sci* 60:227–239
72. Vong CQ, Jacquemet N, Picot-Colbeaux G, Lions J, Rohmer J, Bouc O (2011) Reactive transport modeling for impact assessment of a CO₂ intrusion on trace elements mobility within fresh groundwater and its natural attenuation for potential remediation. *Energy Procedia* 4:3171–3178
73. Xu T, Kharaka YK, Doughty C, Freifeld BM, Daley TM (2010) Reactive transport modeling to study changes in water chemistry induced by CO₂ injection at the Frio-I brine pilot. *Chem Geol* 271:153–164
74. Hennings J, Liebscher A, Bannach A, Brandt W, Hurter S, Köhler S, Möller F, CO₂SINK Group (2011) P-T- ρ and two-phase fluid conditions with inverted density profile in observation wells at the CO₂ storage site at Ketzin (Germany). *Energy Procedia* 4:6085–6090
75. Bielinski A, Kopp A, Schütt H, Class H (2008) Monitoring of CO₂ plumes during storage in geological formations using temperature signals: numerical investigation. *Int J Greenhouse Gas Contrl* 2:319–328
76. Kiessling D, Schmidt-Hattenberger C, Schuett H, Schilling F, Krueger K, Schoebel B, Danckwardt E, Kummerow J, CO₂SINK Group (2010) Geoelectrical methods for monitoring geological CO₂ storage: first results from cross-hole and surface-downhole measurements from the CO₂SINK test site at Ketzin (Germany). *Int J Greenhouse Gas Contrl* 4:816–826
77. White CM, Strazisar BR, Granite EJ, Hoffman JS, Pennline HW (2003) Separation and capture of CO₂ from large stationary sources and sequestration in geological formations—coalbeds and deep saline aquifers. *J Air Waste Manag Assoc* 53(6):645–715
78. Newmark RL, Ramirez AL, Daily WD (2001) Monitoring carbon dioxide sequestration using electrical resistance tomography (ERT): sensitivity studies. *Natl Energy Technol Lab, Pittsburgh, PA*, pp 1–18
79. Myrntinen A, Becker V, van Geldern R, Würdemann H, Morozova D, Zimmer M, Taubald H, Blum P, Barth JAC (2010) Carbon and oxygen isotope indications for CO₂ behaviour after injection: first results from the Ketzin site (Germany). *Int J Greenhouse Gas Contrl* 4:1000–1006
80. Sass BM, Gupta N, Chattopadhyay S, Ickes J, Byrer CW (2003) Evaluation of CO₂ sequestration in saline formations based on geochemical experiments and modeling. In: Gale J, Kaya Y (eds) *Proceedings of the 6th international conference on Greenhouse Gas Control Technologies*, vol. 2, 1–4 October 2002, Kyoto, Japan. *Greenhouse Gas Control Technologies*, pp 1641–1644
81. Lu J, Partin JW, Hovorka SD, Wong C (2010) Potential risks to freshwater resources as a result of leakage from CO₂ geological storage: a batch-reaction experiment. *Environ Earth Sci* 60:335–348
82. Fischer S, Liebscher A, Wandrey M, CO₂SINK Group (2010) CO₂-Brine-rock interaction – first results of long-term exposure experiments at in situ P-T conditions of the Ketzin CO₂ reservoir. *Chem Erde-Geochem* 70(3):155–164
83. Xu T, Zheng L, Tian H (2011) Reactive transport modeling for CO₂ geological sequestration. *J Petrol Sci and Eng* 78:765–777

Groundwater Contamination: Environmental Issues and Case Studies in Sardinia (Italy)

Riccardo Biddau and Rosa Cidu

Abstract In this study, the arsenic (As), cadmium (Cd), lead (Pb), and zinc (Zn) contamination has been evaluated in the groundwater of Sardinia (Italy). Contamination by such chemical species is among the most relevant risks for many populations, thus giving general interest to the case studies presented in this chapter. A brief introduction about the European legislative framework is given, followed by a description of the analytical methods used and a discussion of the results. Two areas were selected as case studies: the Osilo area, devoted to geogenic degradation, and the Iglesiasiente–Fluminese mining district mainly affected by anthropogenic contamination. The geochemical controls on the natural baselines of As, Cd, Pb, and Zn are generally related to natural sources, mostly derived from water–rock interaction processes in areas of known mineral occurrences. In fact, median concentrations of the investigated elements in the mineralized areas are much higher than those of the corresponding median regional values and sometimes exceed the Italian limits for drinking water. In the Iglesiasiente–Fluminese mining district very high concentrations of Cd, Pb, and Zn were measured in groundwater that circulates in areas affected by past mining activities.

The results of this study clearly show that the understanding of the trace metal pollution trends, and the distinction of the anthropogenic impacts on the aquifer systems, is essential for evaluating the natural baseline of contaminants as well as for distinguishing the relevant processes that influence their chemical characteristics. Such information, together with the geological features of a region and/or subregion, should be taken into account prior to defining regulatory limits of contaminants in groundwater.

Keywords Arsenic, Cadmium, Groundwater quality, Lead, Sardinia, Zinc

R. Biddau and R. Cidu (✉)

Dipartimento di Scienze Chimiche e Geologiche, Università di Cagliari, via Trentino 51, 09127 Cagliari, Italy

e-mail: r.biddau@gmail.com; cidur@unica.it

Contents

1	Introduction	54
2	Sampling and Analytical Methods	57
3	Geology and Groundwater Quality in Sardinia	58
4	Groundwater Quality in the Osilo Area	60
5	Groundwater Quality in the Iglesiente–Fluminese Area	63
6	Conclusions	73
	References	74

Abbreviations

EC	European community
EU	European union
GURI	Gazzetta ufficiale della Repubblica Italiana
ICP-MS	Inductively coupled plasma mass spectrometry
ICP-OES	Inductively coupled plasma optical emission spectrometry
RAS	Regione autonoma della Sardegna
TDS	Total dissolved solids
WHO	World Health Organization

1 Introduction

The chemistry of groundwater widely depends on complex geological, geochemical, hydrogeological, and climatic factors, which control the chemical evolution and give rise to large spatial variations at a range of scales. Temporal variations in groundwater chemistry are also to be expected in response to varying atmospheric inputs, changes in aquifer mineralogy, and solubility and kinetic controls related to varying residence times [1]. In addition, human activities may have an important effect on the chemistry of groundwater due to pollution from agricultural, industrial, and mining activities. The knowledge of physical and chemical processes that control the quantity and quality of groundwater is therefore essential for the effective management of this valuable resource and its sustainable use.

The knowledge of the groundwater quality becomes mandatory for achieving the purposes of the European Community (EC) Water Framework Directive [2]. This Directive aims at maintaining and improving the aquatic environment in the Community and establishes a framework for Community action in the field of water policy. In particular, Member States shall protect, enhance, and restore all bodies of groundwater, ensuring a balance between abstraction and recharge of groundwater, with the aim of achieving good groundwater status at the latest 15 years after the date of entry into force of the Directive (i.e., in the year of 2015). For groundwater the need for better understanding of their intrinsic quality, and how their characteristics are acquired, is strongly required. Any significant and sustained upward trend in the concentration of any pollutant should be identified and

reversed. In order to establish effective actions for reversing pollution trends, it is fundamental to define the natural (baseline) levels for each pollutant. This will allow distinguishing high concentrations derived by natural sources (i.e., water–rock interaction processes) from those related to anthropogenic activities.

Some chemical constituents have been shown to cause widespread health effects in humans as a consequence of exposure through drinking water (e.g., [3]). On this basis, the World Health Organization (WHO) established guideline values for several elements [4]. According to the International Agency for Research on Cancer, arsenic (As) and cadmium (Cd) belong to Group 1 that includes constituents with sufficient evidence of carcinogenicity in humans [5]. In the EC, Cd, Cd compounds, Pb and Pb compounds have been identified as priority hazardous substances [2]. In contrast with As, Cd, and Pb, zinc (Zn) is an essential element for plant and animal metabolism and is not considered of health concern at levels normally observed in drinking water [4]. However, it should be noted that Zn is a regulated element in groundwater in the Italian legislation [6].

Metals and metalloids occur as natural constituents usually dispersed in the earth crust. In areas hosting ore deposits, several toxic or harmful elements may occur in groundwater at natural concentrations that exceed the standards established by national and international authorities for drinking water and the protection of aquatic life (e.g., [7, 8]). The potential for contamination is increased when mining operations expose metal-bearing deposits to erosion as well as when mining-related wastes are dumped on the earth surface thus enhancing weathering processes. In some cases, the contamination continues persisting in the environment many years after the cessation of mining operations (e.g., [9] and reference therein).

Statistical methods are widely used to assess baseline concentrations of solutes in aquifers [10]. Statistics should not be used in isolation, but in association with a basic understanding and investigation of the underlying processes controlling groundwater chemistry [1]. Such approach has been used in this study focused on the investigation of groundwater contamination by As, Cd, Pb, and Zn. Two case studies were selected: the Osilo one is an example of geogenic degradation of the water quality, while in the Iglesias–Fluminese one both geogenic and anthropogenic contamination of water occur.

The study areas are located in Sardinia (Italy), an island of the western Mediterranean Sea (Fig. 1). Sardinia represents an ideal site to investigate the influence of natural (geological) and mining activities on the quality of groundwater because, in spite of its relatively small surface (24,000 km² approximately), Sardinia was a prominent mining region for base metals in Italy and a relevant one in Europe. In addition, with a population of approximately 1.6 million people mostly concentrated in large towns, and industrial activities mainly located nearby the coast (Fig. 1), many areas are unaffected by diffuse anthropogenic pollution, so that pristine conditions of water quality can be evaluated.

River waters collected in artificial basins constitute about 70% of the water supplied for domestic, agricultural, and industrial uses in Sardinia. However, due to the climatic peculiarity of the region, characterized by long periods of heat and drought interrupted by relatively short rainy periods with occasional heavy rain

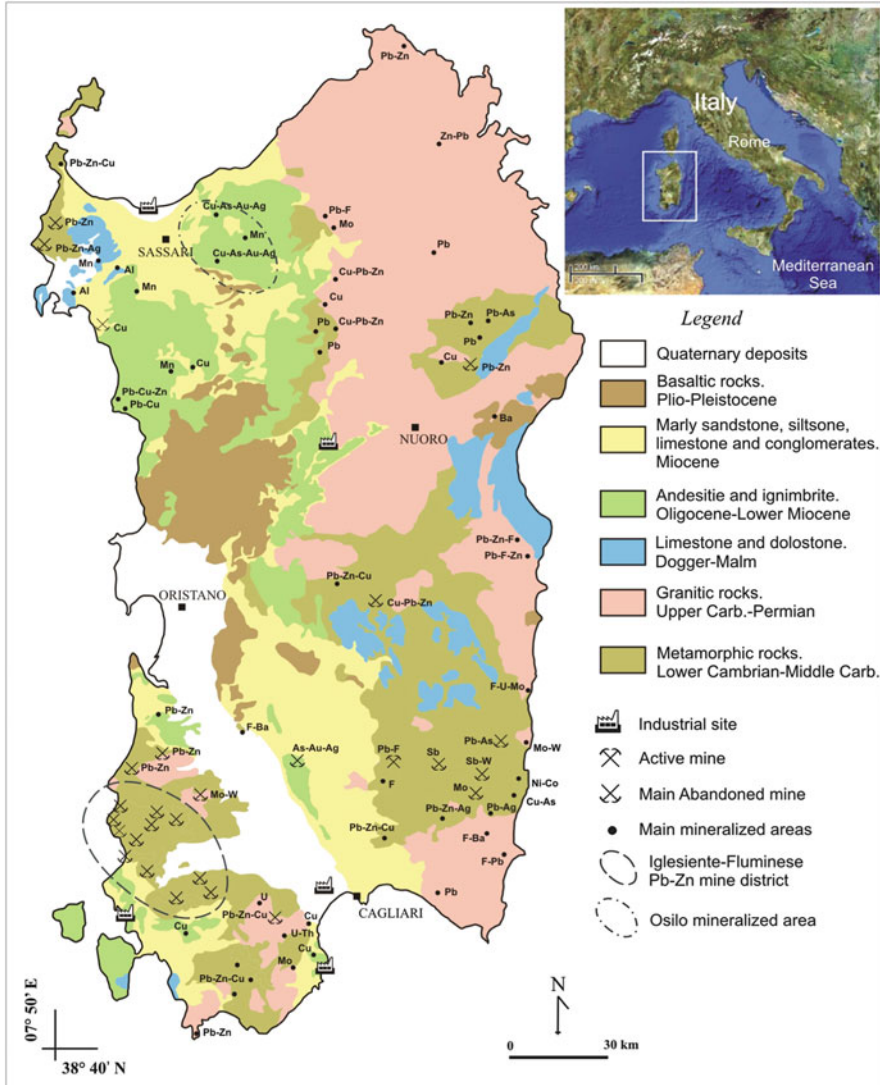


Fig. 1 Geological sketch map of Sardinian island ([51], modified) showing the locations of the most important mines and the mineralized areas ([27], modified), and the industrial sites

events, the flow of rivers and streams strongly depends on rainfall and may vary by few orders of magnitude in a year as well as from one year to another. Consecutive years of drought have been common in the past, resulting in restrictions in water supply for domestic use in several town and villages of the island. Accordingly, groundwater is an important resource when droughts occur, as well as in areas where the reservoirs lack [11, 12].

2 Sampling and Analytical Methods

The dataset used for assessing the groundwater quality in Sardinia includes 454 water analyses. Data on 211 groundwater samples derive from several surveys carried out at the University of Cagliari between 2001 and 2012 [13–23], including data on 50 water samples that are yet unpublished. The samples comprise spring waters mostly located away from major towns, villages, and industrial areas; they were selected for the purpose of minimizing potential anthropogenic impacts on the water quality. Waters affected by mining activities were not considered in the calculation of baseline values for the considered elements. Additional data on 193 groundwater samples derived from the groundwater-monitoring program established by the Sardinian Regional Government [24] were considered in the calculation of the regional baseline values for the considered elements.

In the study area of Osilo, 43 spring and borehole samples were collected from 2000 to 2003, with surveys repeated under different seasonal conditions. The complete dataset and analytical details are reported elsewhere [18].

In the study area of Iglesias–Fluminese, hydrogeochemical surveys have been carried out from 1996 to 2008, with the aim of investigating the impact of past mining on the quality of groundwater. Data considered in this study refer to sampling campaigns undertaken in 2005 and 2006 ([20] and references therein) and in 2008 [9]. The selected data include high-flow springs used as drinking-water supplies as well as low-flow springs and a few shallow wells, in which water is considered not to be directly affected by the local mining activities, though located in mineralized areas. The samples indicated as mine waters include water collected at shafts and flooded adits following rebound.

The analytical procedure used at the University of Cagliari can be summarized as follows. At the sampling site, the physical–chemical parameters and alkalinity (titration with HCl 0.01 N and methyl orange indicator) were measured; the water was filtered (0.4 μm pore size, Nuclepore polycarbonate) into pre-cleaned high-density PE bottles and acidified with supra-pure HNO_3 (1%, v/v) for element analyses by either quadrupole ICP-MS using Rh as internal standard or ICP-OES [25]. In order to check potential contamination during sampling and analysis, blanks were prepared in the field with ultrapure water (MILLI-Q, 0.06 $\mu\text{S}/\text{cm}$) and processed using the same procedures used for the water samples. Detection limits were determined as follows: the mean value and standard deviation of a significant number of blanks analyzed within an analytical sequence were calculated; the value corresponding to 5σ was taken as the detection limit. The value equal to the detection limit was assumed in the case of undetected concentration. Both precision and accuracy were evaluated using standard reference solutions. Estimated analytical errors were less than 10%.

3 Geology and Groundwater Quality in Sardinia

A simplified geological map of Sardinia with the location of relevant mines, mineralized areas, and industrial sites is presented in Fig. 1. Widespread Paleozoic formations, mainly consisting of granitic and metamorphic rocks, extend nearly continuously from north to south in the eastern part of the island. Second in abundance are Tertiary and Quaternary volcanic and sedimentary rocks. Mesozoic carbonate rocks occur less frequently and lay on the Paleozoic basement.

Stratabound deposits are the more economic ores in Sardinia. They are mainly hosted in the Lower Paleozoic rocks. In southwest Sardinia sphalerite–galena–barite deposits mostly occur as massive sulfides and partly as Mississippi Valley type. In central and southeast Sardinia, stratabound mineralization consists of scheelite, arsenopyrite, antimonite, and chalcopyrite–sphalerite–galena massive sulfides. Some skarn deposits are connected to the granite intrusion [26, 27]. Exploitation was carried out intensively from 1880 to 1980.

The abandoned mines are nowadays a remarkable heritage included in the Environmental and Historical Geomining Park of Sardinia, sponsored by the UNESCO. However, these sites also represent potential environmental risks, particularly due to the weathering of mining-related wastes still left nearby the mines and the occurrence of highly contaminated water flowing out of adits. Following the assessment of contamination status with respect to baseline conditions at abandoned mines, remediation actions will be planned by the Sardinian Regional Government.

More recently, auriferous epithermal deposits have been discovered in Tertiary volcanic rocks [28]. An epithermal, high-sulfidation gold deposit was exploited at Furtei in central Sardinia, from 1997 to 2003 [29, 30].

The natural baselines of several elements in groundwater of Sardinia were recently evaluated [31]. Figures 2a–d show the geographical distributions of As, Cd, Pb, and Zn concentrations, basic statistics (Fig. 2e), and the cumulative frequency plot (Fig. 2f). The Italian limits (dashed lines in Fig. 2f) of As (10 µg/L), Cd (5 µg/L), and Pb (10 µg/L) in drinking water and the Zn limit (3,000 µg/L) in groundwater are also reported [32].

Taking into account that groundwater samples circulating in contaminated sites were excluded in the selection of the database, the distribution ranges of contaminants shown in Fig. 2e are likely to be close to the baseline values. The median concentrations of As, Cd, and Pb were below 1 µg/L, whereas the median concentration of Zn was less than 10 µg/L in the Sardinian groundwater. However, up to 4% of the samples considered contain As, Cd, and Pb in excess of the respective limit in drinking water. Also, the maps in Fig. 2a–d pinpoint the areas of relatively high values due to the widespread presence of mineralization in the island. High As concentrations in groundwater samples are related to arsenopyrite and enargite in Tertiary volcanic rocks, respectively, in the north and central Sardinia and to arsenopyrite in metamorphic rocks in southeast Sardinia (Fig. 2a). Elevated Cd concentrations in groundwater samples occur in south Sardinia

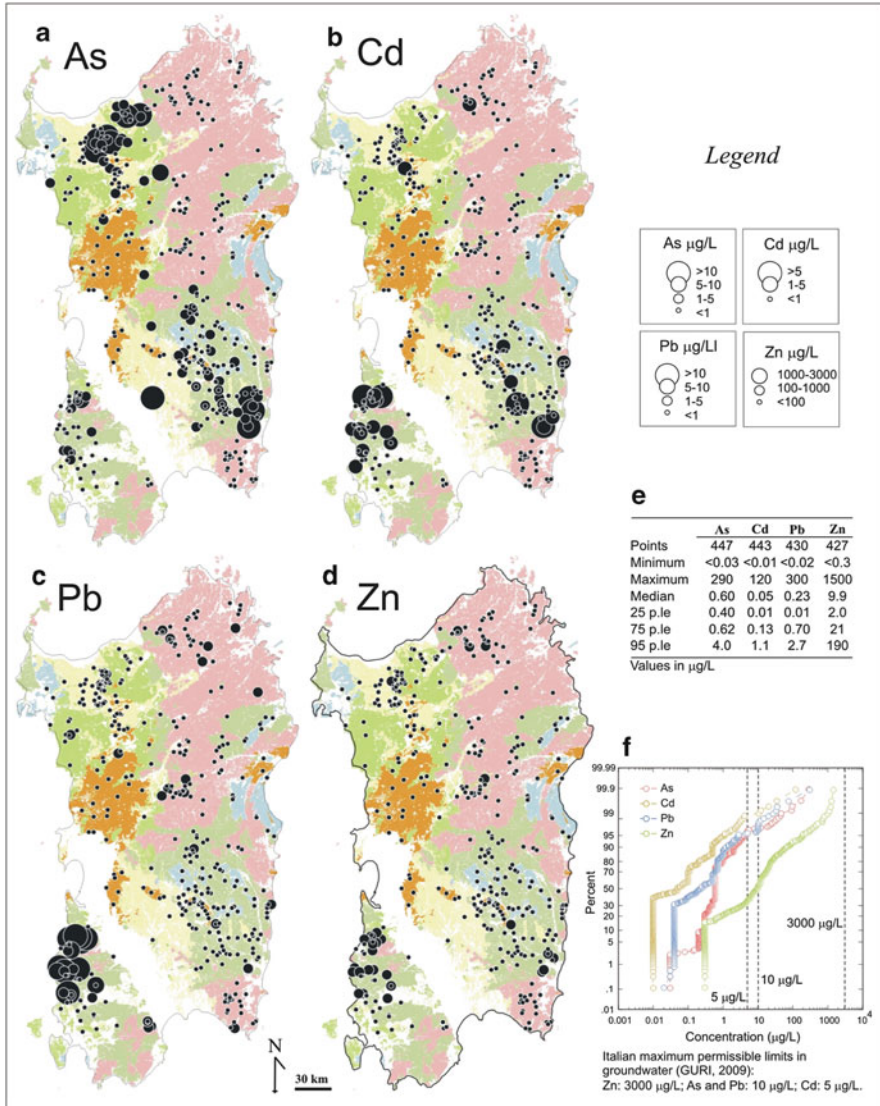


Fig. 2 Maps showing the occurrence of As (a), Cd (b), Pb (c), and Zn (d) concentrations in Sardinian groundwater samples; (e) basic statistical data; (f) cumulative-frequency diagrams

(Fig. 2b) and are mostly related to sphalerite. Geochemical maps for Pb (Fig. 2c) and Zn (Fig. 2d) also show relatively high concentrations in groundwater of southwest Sardinia, an area with prominent Pb–Zn sulfide mineralization (Sulcis–Iglesiente–Fluminese mining districts); in this area, relatively high values (>10 $\mu\text{g/L}$, i.e., above drinking-water standards) of Pb occur, whereas Zn concentration is less than 3,000 $\mu\text{g/L}$.

Following the Sardinian context described above, two study areas will be investigated in more detail: the Osilo area in north Sardinia and the Iglesias–Fluminese in southwest Sardinia.

4 Groundwater Quality in the Osilo Area

It is useful to recall that the Osilo area was selected for representing a case study where water contamination was unrelated to anthropogenic activities, but was associated with the occurrence of an epithermal Au–Ag deposit.

A geological sketch map of the Osilo area is reported in Fig. 3. It is characterized by Tertiary volcanic rocks, mainly composed of andesite that underwent widespread alteration (potassic, propylitic, or argillic) and subordinate ignimbrite. Marine and lacustrine sediments (Lower to Middle Miocene) and Quaternary basalts outcrop above the Tertiary volcanic rocks in the southern part of the area [33]. Metal mineralization at Osilo occurs in a number of low-sulfidation, epithermal quartz veins related to fracture systems trending about E–W. The veins are hosted in the andesitic rocks, are generally 1–10 m wide and up to 3 km long, crop out discontinuously along their length, and are usually brecciated and re-cemented by saccharoidal quartz. The silicified materials underwent a pyritization process, resulting in a fine dissemination of iron sulfide. The mineral assemblage consists of abundant pyrite (FeS_2), arsenopyrite (FeAsS , with traces of Ni, Co, Cu, and Sb), Ag-tetrahedrite ($(\text{Cu,Fe})_{12}\text{Sb}_4\text{S}_{13}$)–freibergite ($(\text{Ag,Cu,Fe})_{12}(\text{Sb,As})_4\text{S}_{13}$) (with traces of Zn, Cu, Ag, Pb, Bi, and Hg) and tennantite ($\text{Cu}_{12}\text{As}_4\text{S}_{13}$), and subordinate stibnite (Sb_2S_3), marcasite (FeS_2), galena (PbS , Ag-rich with trace of Bi), and sphalerite (ZnS). Electrum (AuAg , 20–50 wt% Ag) and argentite (Ag_2S) are hosted in pyrite and are the main Au- and Ag-bearing minerals. Economic mineralization was known to occur over a 250–300 m vertical range, and the resources were estimated at 12 tons of Au and 50 tons of Ag, with average grade of 7.1 g/t Au and 30 g/t Ag [28, 34]. The gold deposit was expected to be exploited, but it remained unmined up to the present (i.e., 2013).

In the Osilo area the rolling topography ranges from 766 m above sea level (a.s.l.), in the northern part of the area, to 200 m a.s.l. in the southern part. Vegetation cover is irregularly distributed, and soils are poorly developed in most parts of the area. The mean rainfall is 760 mm/year, with 72 rainy days/year, and dry periods usually extending from May to October [11]. Mean annual temperature is 16.5°C with high evapotranspiration (>60%). Surface drainage consists of intermittent streams following lines of structural weakness. The hydrogeology is dominated by the presence of aquifers in volcanic rocks. Piezometric surfaces generally follow the surface morphology with preferential discharges to thalweg, where the topographic surface cuts through the water table. The local groundwater flow is roughly from north to south, except in the northernmost catchments where east to west trending flow prevails. In the Osilo area there are a number of springs characterized by low average flow rates (<0.1 L/s); most of the springs originate

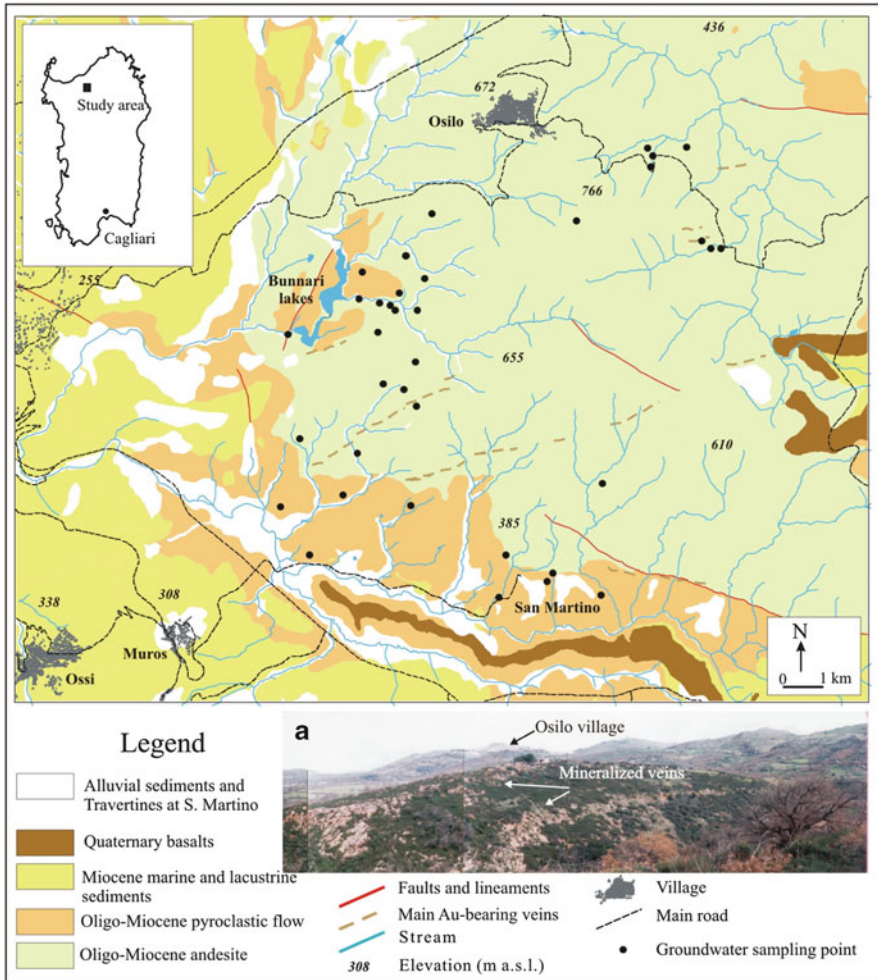


Fig. 3 Geological sketch map of the Osilo area ([51], modified) with locations of groundwater samples. (a) The landscape of the Osilo area: foreground a silicified body south of the Bunnari Lake, background the Osilo village

from andesitic aquifers, having shallow circulation and relatively short residence times with recharge to the aquifers directly from rainfall. In the southern part of the area there are some warm springs (San Martino) showing nearly constant temperature (19–21°C) at different seasons, high pCO₂ values, and a flow rate of about 1 L/s. These waters are considered to be representative of a regional and prolonged circulation in the andesitic rocks with tritium unit values close to zero (TU = 0.6 in 1982; [35]), thus suggesting relative long residence times. An inflow of CO₂ gas from deep origin is supposed to occur in their aquifer [36]. At the emergence of the San Martino springs as well as at emergence of other springs

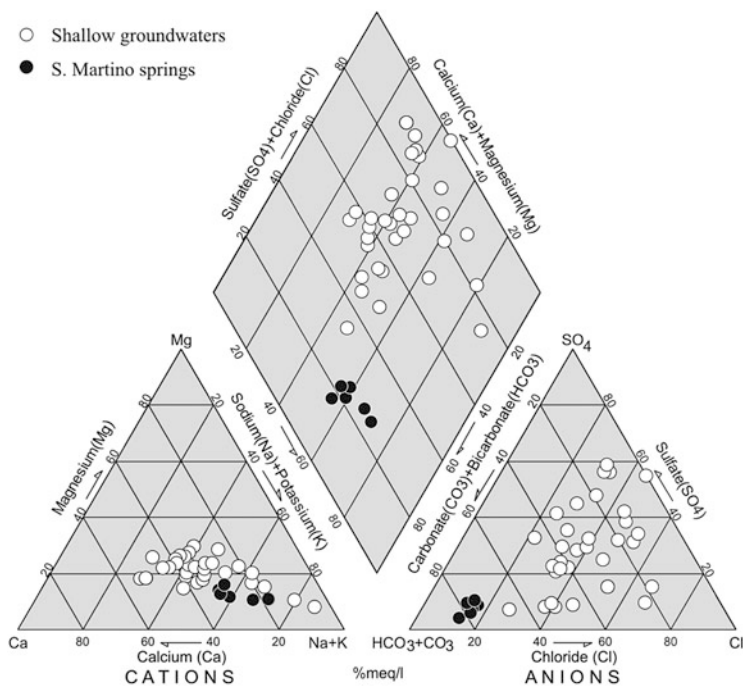


Fig. 4 Piper diagram showing major components in the Osilo waters (sampling date, October 2001)

related to mineralized veins, abundant precipitation of brownish deposits of Fe-oxy-hydroxides occurs. These ferruginous waters are sometimes found in the immediate vicinity of non-ferruginous springs unrelated to mineralized veins.

Hydrogeochemical surveys were aimed to evaluate the baseline conditions for assessing the potential impact of eventual mining on the quality of waters. In this paper a summary of chemical characteristics will be reported while focusing on the arsenic occurrence in groundwater at Osilo.

The pH values range from acidic to alkaline (4.0–8.0). The lowest pH values were measured in groundwater samples interacting with the mineralized bodies. Values of the redox potential are usually in the range of 0.3–0.5 V, although some boreholes and the San Martino waters show slightly reducing conditions. The shallow groundwater samples exhibit considerable variation in salinity (total dissolved solids, TDS, in the range of 0.3–2.8 g/L), whereas the San Martino waters have the highest salinity (TDS up to 4.6 g/L). The San Martino springs were the only samples clearly distinguished from the others as a marked NaHCO₃ composition (Fig. 4), owing to the high pCO₂. These waters reach oversaturation with respect to calcite, and travertine deposits occur close to their emergence; historical data on the San Martino waters show a nearly constant temperature, pH, TDS, and chemical composition [37]. At sites other than San Martino, groundwater samples show a general trend with

increasing TDS values, from Ca(Mg)-HCO₃ to Na(Ca)-Cl-SO₄ composition; the dissolved sulfate increases in correspondence of mineralized areas, likely due to pyrite oxidation. Seasonal variability in TDS and concentrations of chemical components occur, with dilution processes observed in correspondence of rainy periods.

Figure 5 shows the map of As concentration in groundwater samples at Osilo. The concentration of dissolved As varies from <1 up to 290 µg/L. Speciation calculations indicate that As occurs mostly in its (V) valence state, with the H₂AsO₄⁻ species dominant at pH < 6.5 and HAsO₄²⁻ prevalent at pH > 6.5 (Fig. 5a). The effect of water-rock interaction is well marked at sites where the groundwater comes into contact with the mineralized bodies. Here, As concentrations in the range of 10–290 µg/L are observed as result of the weathering of pyrite and arsenopyrite [18]. Arsenic concentrations are not correlated with pH, Eh, and TDS values, but the high-Fe waters contain the highest As concentrations. Shallow groundwater located close to the ore veins and the San Martino waters showed Fe concentrations in the range of 1–80 mg/L. At the Eh–pH conditions observed, iron in the waters was probably present in particles <0.4 µm (the pore size through which the water was filtered) or in colloidal forms. Given the high Fe content, these waters deposit reddish-orange precipitates upon discharge; according to XRD analyses, the precipitated material is mainly composed of two-line ferrihydrite. Transmission electron microscope observations showed that the ferrihydrite is mainly amorphous, although areas of nanocrystals were also identified. On the basis of the electronic patterns, the nanocrystals are composed of goethite [18], likely derived from the transformation of two-line ferrihydrite [38]. Analytical results of some elements contained in the ferrihydrite show small variations in composition, with As being the most abundant element among minor components (Table 1), confirming the strong ability of Fe-oxy-hydroxides to trap this element (see, e.g., [39]).

The high-As concentrations measured in the Fe-rich groundwater samples at Osilo are likely associated with small ferrihydrite particles, which are not retained by filtering through 0.4 µm in size. Relatively high concentrations of As in the S. Martino waters may be related either to weathering of the ore deposit or to the long residence time. Due to the widespread presence of mineralization, the baseline for arsenic in groundwater at Osilo is estimated to be higher than the regional value (Fig. 5b).

5 Groundwater Quality in the Iglesiasente–Fluminese Area

The Iglesiasente–Fluminese mining districts, located in SW Sardinia (Fig. 6), have been a prominent area for the exploitation of Pb and Zn in Italy. The Pb–Zn deposits in the Iglesiasente–Fluminese mining districts were exploited since the pre-Roman times. The recent industrial exploitation started in the mid-1800, reaching a peak (more than 40 mines in operation) in the 1950s. In the 1960–1970 mining became

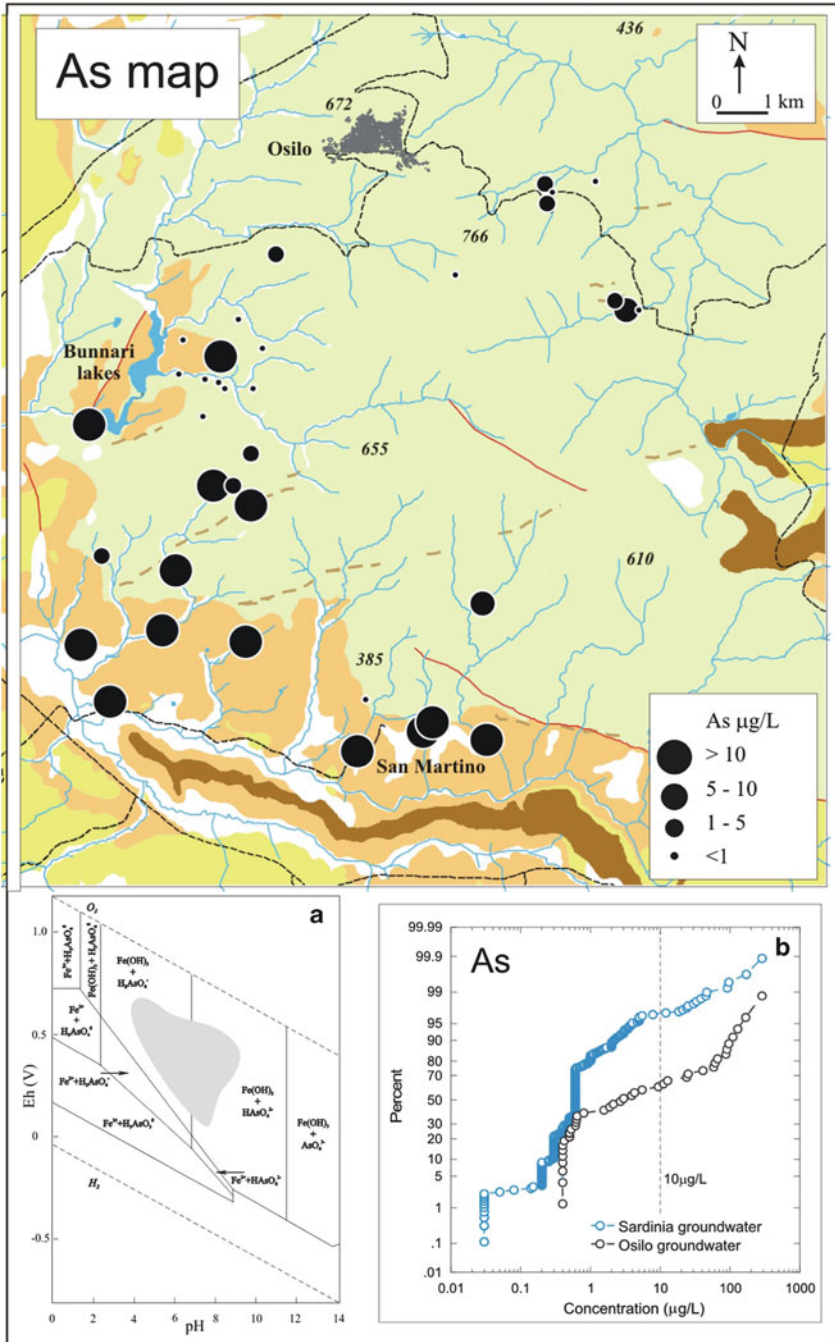


Fig. 5 Map showing the concentrations of arsenic in groundwater samples in the Osilo area (data refer to sampling in 2001). (a) Eh–pH diagram of the system As–Fe–H–O, at 25°C and 1 bar

Table 1 Concentrations of minor components in the ferrihydrite materials collected at the emergence of some Fe-rich springs, which drain the gold deposit in the Osilo area

Element (mg/kg)	Sample			
	185	194	317	402 (S. Martino)
As	1,700	2,400	5,600	7,500
Cd	31	29	32	34
Co	<0.3	2.2	5.3	11
Cu	<0.02	<0.02	<0.05	<0.3
Mn	nd	195	nd	145
Ni	<0.8	<0.8	<1.9	<1.6
Pb	27	29	31	33
Tl	<0.2	<0.2	<1.7	nd
Zn	57	341	550	550

nd not determined

uneconomic due to exhaustion of the high-value resources and the extreme competition of foreign mining districts. Such decline has resulted in the decreasing of mining activities, until complete closure of mines in 1998. A description of host rocks, dominant ores, and period of exploitation in the most important mines is reported in Table 2.

The geological setting in SW Sardinia is schematized in Fig. 6. It is characterized by Paleozoic formations that underwent several complex phases of deformation [40]. The Lower Cambrian formations are comprised of the basal Nebida Group, consisting of about 500 m of siliciclastic, shallow water sediments, with carbonate and marl intercalations, and the overlying Gonnesa Group made up of 300 to 600 m of shallow water platform carbonates [41]. Middle Cambrian–Lower Ordovician sediments are comprised of nodular limestone (Campo Pisano Formation, Iglesias Group, 50–80 m) and slates (Cabitzza Formation, Iglesias Group, 400 m); Upper Ordovician sediments in angular unconformity on the Gonnesa and Iglesias Groups consist of continental conglomerates and sandstone, followed by marine slates that formed until late Ordovician–Silurian [42]. Ore bodies consist of massive sulfides (sedimentary exhalative) located in the lower part of the Cambrian sequences and lower-grade sulfides (Mississippi Valley type) located at the top of the carbonate sequences. The most abundant ore minerals are sphalerite (ZnS) and galena (PbS), with variable pyrite (FeS₂) contents; barite (BaSO₄) and fluorite (CaF₂) are abundant at some locations. Near the surface, ore bodies are generally oxidized and consist mostly of smithsonite (ZnCO₃), hydrozincite (Zn₅(CO₃)₂(OH)₆), and cerussite (PbCO₃) [43].



Fig. 5 (continued) (modified after [50]); the shaded area represents the Eh–pH value of the groundwater samples collected at Osilo from 2000 to 2003. **(b)** Cumulative distribution plot comparing arsenic concentrations in Sardinia and Osilo groundwater samples

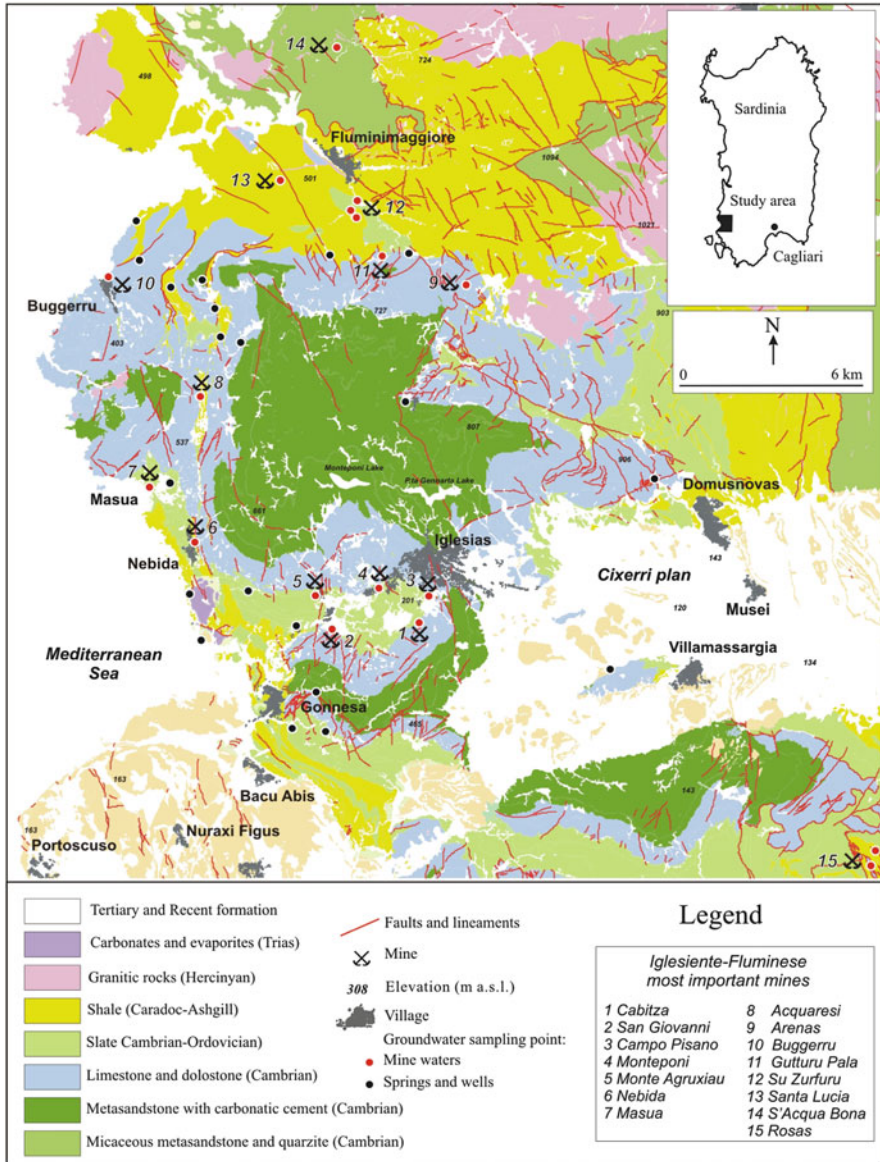


Fig. 6 Geological sketch map of the Iglesiasiente–Fluminese mining district ([51], modified) showing the locations of relevant abandoned mines and groundwater samples

In this area the availability of water from reservoirs (i.e., Monteponi lake and Punta Gennarta lake) is low, but groundwater represents a valuable resource that supplies water to a local population of approximately 60,000 inhabitants. The high-flow ($\gg 10$ L/s) springs occur in the Cambrian carbonate formations, which host

Table 2 Description of relevant abandoned mines in the Iglesias–Fluminese mining district

Mine name	Host rock	Dominant ore	Exploitation period
S'Aquabona	Siliciclastic sediments	(Ag)Pb–Zn	1900–1975
Santa Lucia	Slate–conglomerate–limestone	OxZn	1880–1942
		Pb	1880–1942
		Ba–F	1945–1968
Su Zurfuru	Slate–conglomerate–limestone	F–(Ag)Pb–Ba	1890–1968
		Py–Zn–Pb	
Gutturu Pala	Dolostone–limestone–breccia	Py–Zn >> Pb	1880–1992
Arenas	Limestone–quartzite	Ba–Ce–Pb(+Py)	1870–1982
Masua	Limestone–breccia	Zn > Pb	1960–1998
Nebida	Limestone–breccia	Zn > Pb	1883–1981
Monte Agruxiau	Limestone–dolostone–breccia	OxZn–Zn > Pb	1880–1978
Monteponi	Limestone–dolostone–breccia	(Ag)Pb	1640–1800
		Zn > Pb(+Py)	1860–1996
		Zn > OxZn > Pb(+Py)	1860–1998
Campo Pisano	Dolostone in paleokarst	Zn > OxZn > Pb(+Py)	1860–1998
		Pb > Ba	
San Giovanni	Limestone–dolostone	Zn > Pb	1860–1998
Rosas	Limestone–dolostone	Zn–Pb	1850–1960

Ba barite, *Ce* cerussite, *F* fluorite, *OxZn* oxidized, *Zn* minerals, *Py* pyrite and pyrrhotite, *Pb* galena, (*Ag*)*Pb* Ag-rich galena, *Zn* sphalerite

the most important aquifers due to intense fracturing and karst processes. Several springs with low flow (usually <1 L/s) also occur in the sandstone and siliciclastic formations.

Large parts of the Cambrian aquifers have been affected by the dewatering required at most mines for allowing exploitation at depth. The main drainage system running under exploitation was located in the Monteponi mine. Pumping stations were successively installed at increasing depths to decrease the water table from ~80 m above sea level to 160 m below sea level. The groundwater pumped out of Monteponi was highly saline, with dissolved chloride and sodium (11 and 6 g/L, respectively, in 1996), attributed to the seawater contamination; concentrations of metals, particularly Pb, Cd, and Hg, were also relatively high [44]. The pumping rate was gradually reduced from 1,500 L/s in January 1997 to 100 L/s in June 1997, and the system was shut down in August 1997. As flooding progressed at Monteponi, the water table level rose at nearby mines too; this effect extended eastwards to the Campo Pisano mine and westwards to the San Giovanni, Nebida, and Masua mines. Following rebound, the water table at Monteponi and nearby mines reached 45 m above sea level in 2005. In the Fluminese, soon after closure of the mines, groundwater flowed out from several adits, such as at S'Acquabona, Su Zurfuru, Santa Lucia, Gutturu Pala, and Buggerru mines [45].

The location of the Iglesias–Fluminese groundwater samples considered in this study is shown in Fig. 6. The chemical composition of water shows near neutral to slightly alkaline pH (7.1–8.2), reflecting dominant circulation in carbonate rocks. Most waters show Eh values above 0.4 V, indicating oxidizing conditions, likely due to the relatively fast groundwater circulation through karst features and fractures.

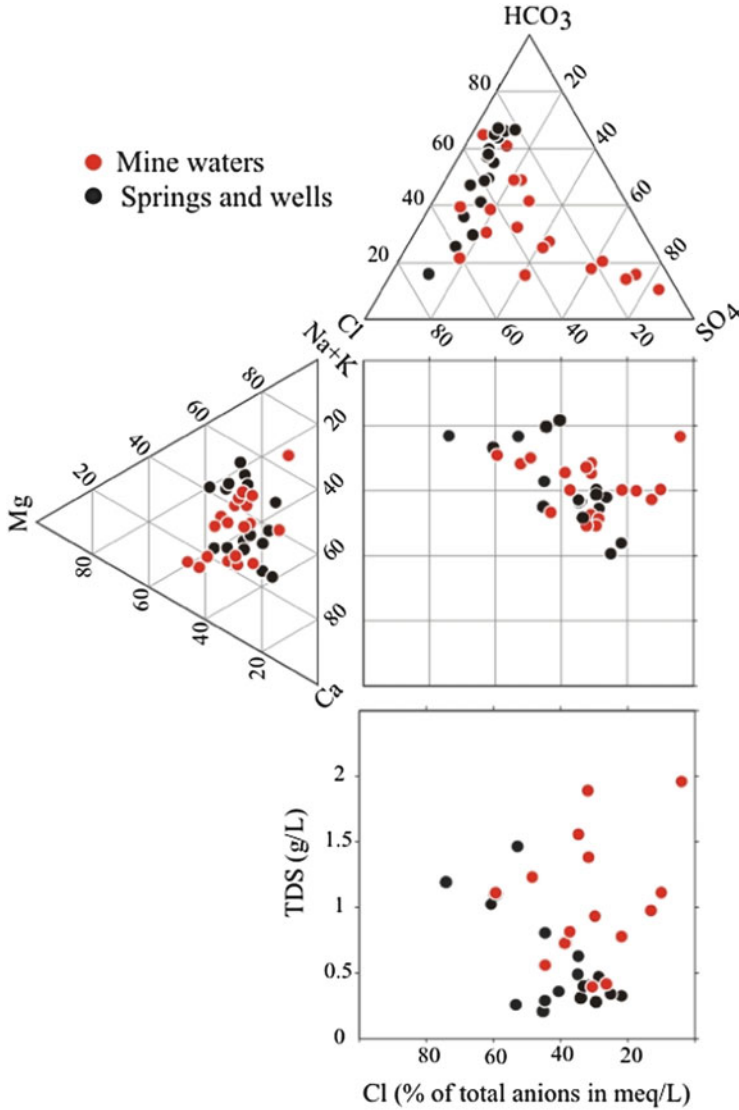


Fig. 7 Durov plot showing major ions dissolved in the Fluminese–Iglesiente groundwater. *Triangular plots on the left and top* show the relative abundance of each cation and anion, respectively (i.e., the percentage of each ion to the cation or anion sum, with values expressed in meq/L). The TDS values are shown in the *lower graph*

Figure 7 shows the Durov plot for the studied waters from the Iglesias–Fluminese. Water from springs and wells outside of the mines is dominantly Ca–Mg bicarbonate with relatively low salinity, generally in the range of 0.3–0.6 g/L TDS. The chemical composition of these water samples is not

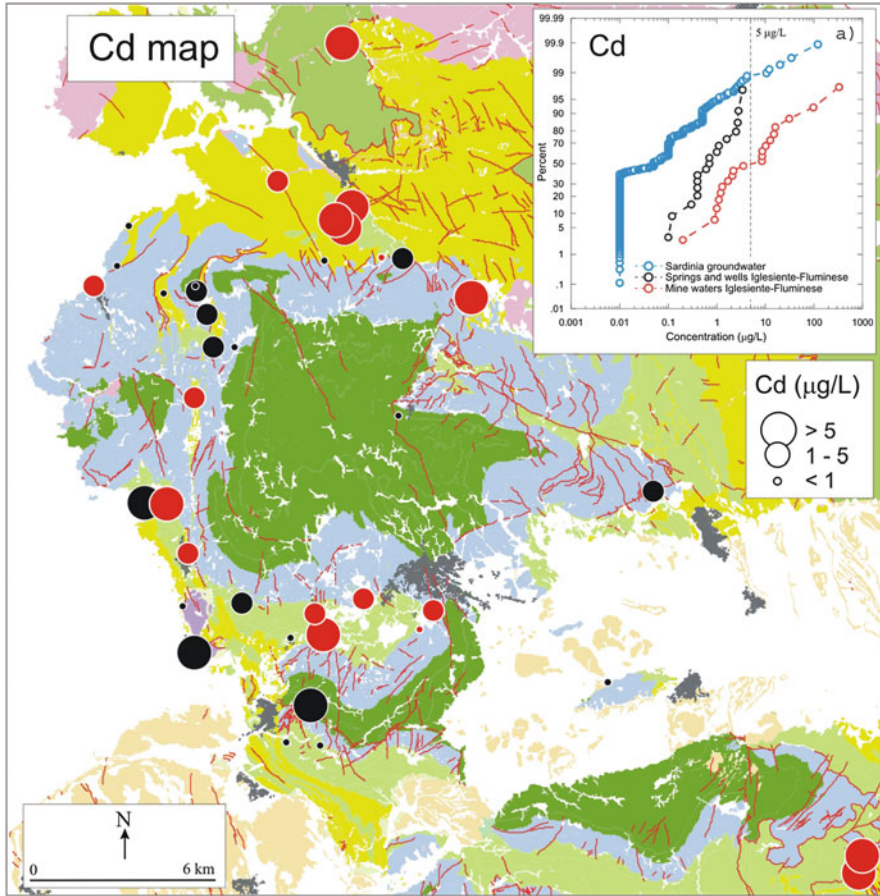


Fig. 8 Map showing the concentrations of cadmium in the Ilesiente–Fluminese area; (a) cumulative distribution plot comparing cadmium concentrations in Sardinia and Ilesiente–Fluminese groundwater samples

influenced by past pumping at Monteponi and clearly reflects the interaction of water with carbonate formations. The mine waters are distinguished by higher salinity, in the range of 0.9–6 g/L TDS, with dominant chloride and sulfate anions (Fig. 7). The chloride enrichment was related to seawater contamination due to the intensive pumping at Monteponi [44]. The sulfate enrichment observed in most mine waters derives from the oxidation of sulfide minerals.

Figures 8, 9, and 10, respectively, show the maps of Cd, Pb, and Zn concentrations in the Ilesiente–Fluminese groundwater. A wide range of metal concentrations is observed: 1–330 µg/L Cd, 1–80 µg/L Pb, and 13–55,000 µg/L Zn. The extreme concentrations of metals observed in the mine waters are not surprising given the diffused Pb–Zn mineralization in this area. Moreover, the local baseline values for Cd, Pb, and Zn are expected to be higher than the regional

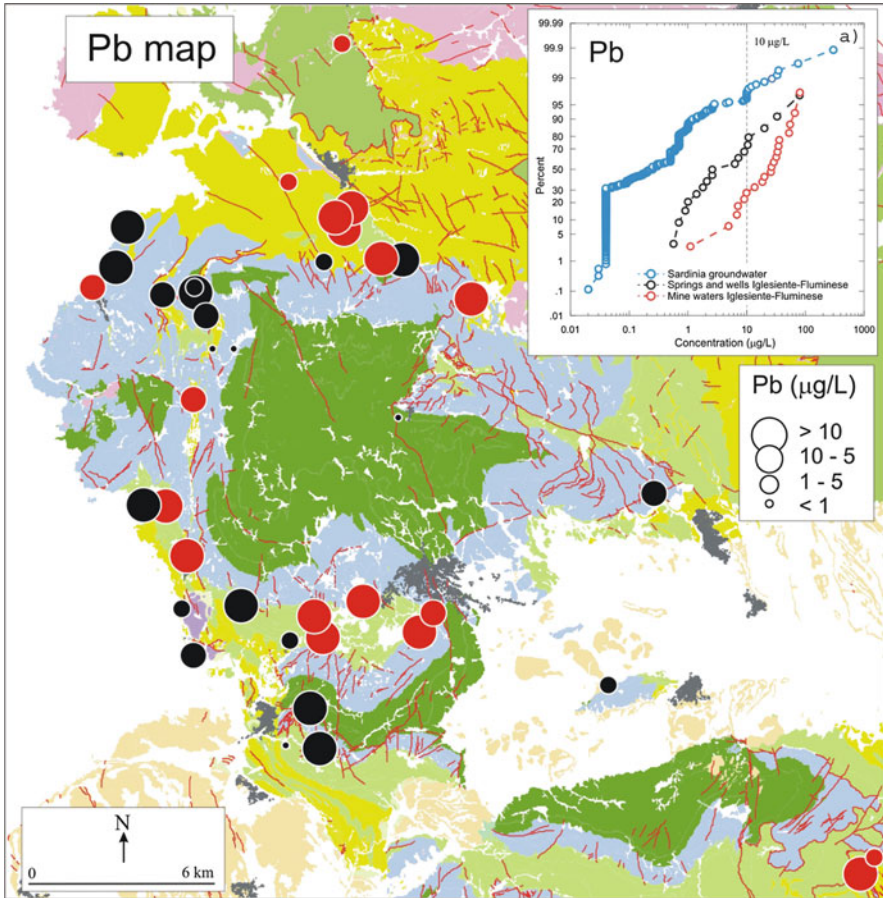


Fig. 9 Map showing the concentrations of lead in the Iglesiasite–Fluminese area; (a) cumulative distribution plot comparing lead concentrations in Sardinia and Iglesiasite–Fluminese groundwater samples

values. In fact, dissolved Pb exceeds the limit ($10 \mu\text{g/L}$, Fig. 9a) in some springs and wells, which also include waters considered not to be directly affected by past mining activity. It should be pointed out that many of these springs are used for supplying drinking water in the area. The concentrations of Cd and Zn are below the limits of 5 and $3,000 \mu\text{g/L}$, respectively (Figs. 8a and 10a).

The oxidation–dissolution of galena and sphalerite is presumably the main source of Pb, Zn, and Cd. The mobility of Pb is often limited owing to sorption onto clay minerals, organic matter, and/or Fe-oxy-hydroxide minerals [46]. In comparison with Pb, the solubility of Zn carbonate and hydroxides is moderately high; accordingly, Zn is expected to occur in groundwater at concentrations higher than Pb. It is likely that one of the limiting factors to Zn mobility is the presence of Fe-oxy-hydroxide and clay minerals [46]. Thermodynamic equilibria were

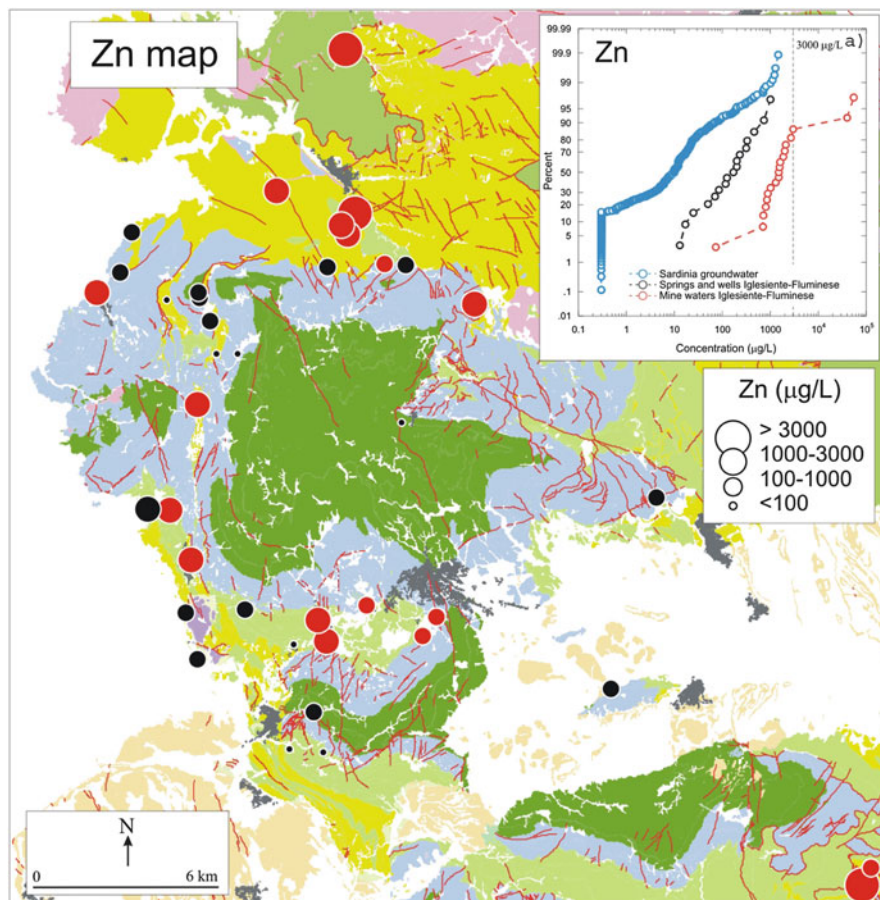


Fig. 10 Map showing the concentrations of zinc in the Iglesias–Fluminese; (a) cumulative distribution plot comparing zinc concentrations in Sardinia and Iglesias–Fluminese groundwater samples

calculated for smithsonite and cerussite. In Fig. 11a it can be observed that most of the mine water samples reach the equilibrium with smithsonite, while few samples approach the equilibrium with cerussite, though most mine waters are not far from it, as it is shown in Fig. 11b. The undersaturation of all waters with respect to cerussite might be explained taking into account the Pb speciation in solution. The most abundant Pb species in waters circulating in the Cambrian carbonate formations is PbCO_3^0 ; this aqueous species is stable under the observed pH conditions [47, 48] and may persist at long distance from Pb sources, though a portion of aqueous Pb might be sorbed on Fe- and Mn-bearing solid phases. All samples are largely undersaturated with respect to anglesite (PbSO_4). Cadmium displays a geochemical behavior similar to that of Zn, because Cd can substitute Zn in sphalerite. It is observed that any increase of Zn content in water is accompanied by an increase in Cd

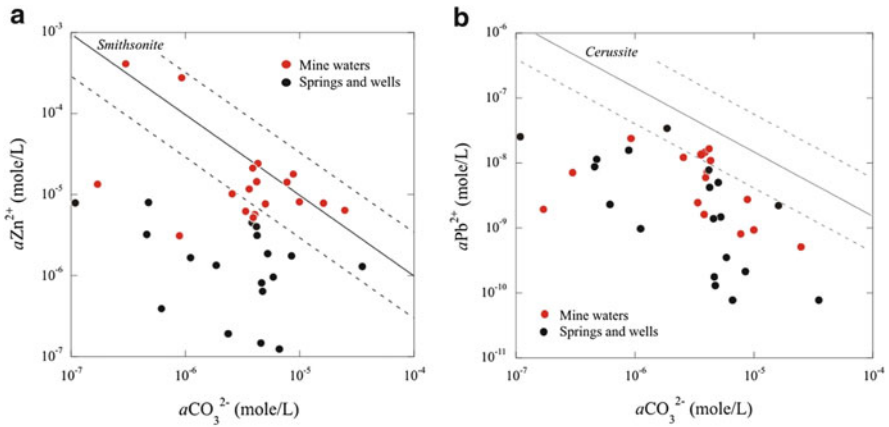


Fig. 11 Activities of Zn²⁺ (a) and Pb²⁺ (b) versus CO₃²⁻ in the Iglesiasite–Fluminese groundwater; the area within *dashed lines* indicates equilibrium with respect to smithsonite and cerussite, respectively

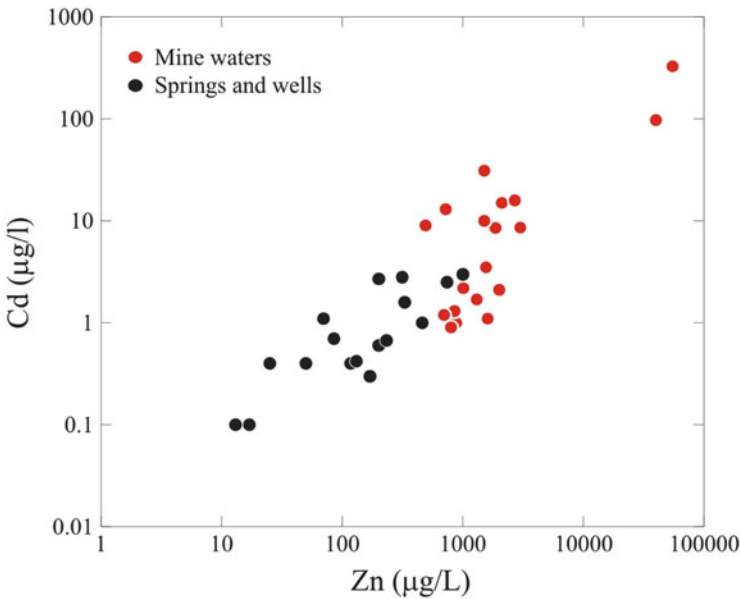


Fig. 12 Dissolved Cd versus Zn concentrations in the Iglesiasite–Fluminese groundwater samples

(Fig. 12), with a Zn/Cd ratio of about 200, a value close to that frequently observed in sphalerite (e.g., [49]). Cadmium was mostly present as Cd²⁺ species, with CdCO₃⁰ species only prevailing at pH > 8.

The available data on groundwater in the Iglesias–Fluminese show that the carbonate rocks hosting the aquifers in the area largely neutralize water acidification brought about by the oxidation of sulfide minerals. However, some spring waters, very important for the supply of drinking water to nearby towns and villages, exceed the required standard for Pb and therefore need to be blended with uncontaminated water.

6 Conclusions

Groundwater is a valuable natural resource that needs to be protected from contamination. For preserving the groundwater quality and achieving an efficient groundwater management, it is required to improve the understanding of the water–rock interaction processes, in particular with reference to the natural, geologically controlled baseline chemistry.

The geochemical controls on the occurrence of arsenic, cadmium, lead, and zinc in groundwater are discussed in two case studies located in the island of Sardinia (Italy): the Osilo area, devoted to illustrate a geogenic degradation of groundwater, and the Iglesias–Fluminese mining district aimed to highlight both geogenic and anthropogenic contamination.

The widespread presence of mineralization in Sardinia has a strong effect on the chemical quality of natural waters, major risks being associated with the flow of contaminated water from mine adits and the weathering of mining-related wastes.

Referring to the chemical elements considered in this study, higher concentrations of As, Cd, Pb, and Zn in groundwater, exceeding the Italian standards for drinking water and the protection of aquatic life, are generally related to natural sources, i.e., derived from water–rock interaction processes in areas of known mineral occurrences. Median concentrations for As, Cd, Pb, and Zn in groundwater from the case study areas are higher than the corresponding median values estimated on the whole Sardinian island (regional variations).

In Sardinia, groundwater constitutes about 30% of the water supplied for domestic and agricultural uses, but this percentage increases in some areas of the island, including the Iglesias–Fluminese. Therefore, a sustainable economic development, as well as environmental protection, requires adequate management and monitoring programs aimed to preserve the groundwater quantity and quality.

Acknowledgements This work was supported by the Italian MIUR (PRIN 2002 responsible L. Fanfani; PRIN 2004 and 2009 responsible R. Cidu), the Regione Autonoma della Sardegna (project KNOW L.R.7/2010 R. Cidu and L.R.7/2007 R. Biddau), and the Fondazione Banco di Sardegna.

References

1. Edmunds WM, Shand P, Hart P, Ward RS (2003) The natural (baseline) quality of groundwater: a UK pilot study. *Sci Total Environ* 310:25–35
2. European Communities (EU) (2000) Directive 2000/60/EC of the European Parliament and of the Council of 23 October 2000 establishing a framework for Community action in the field of water policy. Official Journal of European Communities, Luxembourg
3. Watts RJ, Teel AL (2003) Groundwater and air contamination: risk, toxicity, exposure assessment, policy, and regulation. In: Holland HD, Turekian KK (eds) *Treatise on geochemistry*, vol 9.01. Elsevier–Pergamon, Oxford, pp 1–16
4. World Health Organization (WHO) (2006) *Guidelines for drinking-water quality*, 4th edn. World Health Organization, Geneva, ISBN: 92 4 154696 4 (Annex 4)
5. World Health Organization (WHO) (2012) Agents classified by the IARC monographs. World Health Organization, International Agency for Research on Cancer. <http://monographs.iarc.fr/ENG/Classification/> Accessed 6 March 2013
6. Gazzetta Ufficiale della Repubblica Italiana (GURI) (2009) Decreto legislativo 16 marzo 2009. n. 30: Attuazione della direttiva 2006/118/CE, relativa alla protezione delle acque sotterranee dall'inquinamento e dal deterioramento. Gazzetta Ufficiale della Repubblica Italiana n. 79 del 4-4-2009, Roma (in Italian)
7. Plumlee GS, Logsdon MJ (1998a) Reviews in economic geology. In: Plumlee GS, Logsdon MJ (eds) *The environmental geochemistry of mineral deposits. Part A: processes, techniques and health issues*. Society of Economic Geologist, Inc, pp 29–64
8. Plumlee GS, Logsdon MJ (1998b) Reviews in economic geology. In: Plumlee GS, Logsdon MJ (eds) *The environmental geochemistry of mineral deposits. Part B: case studies and research topics*. Society of Economic Geologist, Inc, pp 373–581
9. Cidu R, Dadea C, Desogus P, Fanfani L, Manca PP, Orrù G (2012) Assessment of environmental hazards at abandoned mining sites: a case study in Sardinia, Italy. *Appl Geochem* 27:1795–1806. doi:10.1016/j.apgeochem.2012.02.014
10. Reimann C, Filzmoser P, Garrett RG (2005) Background and threshold: critical comparison of methods of determination. *Sci Total Environ* 346:1–16
11. Regione Autonoma della Sardegna (RAS) (1998) Nuovo studio dell'idrologia superficiale della Sardegna. Regione Autonoma della Sardegna, Ente Autonomo del Flumendosa (Scientific Responsible: Carlo Cao Pinna), Cagliari (in Italian)
12. Regione Autonoma della Sardegna (RAS) (2003) Piano di Tutela Acque (Regional plan for water protection). Regione Autonoma della Sardegna, Cagliari (in Italian)
13. Caboi et al (2001) Hydrogeochemistry in the Flumendosa river basin (Sardinia, Italy). In: Cidu R (ed) *Proceeding of the 10th international symposium on water rock interaction – WRI-10, Villasimius, Italy*, vol 1. 10–15 June 2001, A.A. Balkema, Rotterdam, pp 465–468
14. Biddau R, Dadea C, Fanfani L, Lorrà M, Rundeddu L (2002) Caratterizzazione delle acque nell'areale del cervo sardo di Montevecchio-Ingurtosu-Piscinas (Sardegna sud-occidentale). *Dipartimenti di Scienze della Terra dell'Università degli Studi di Cagliari*. Internal Report, p 55
15. Biddau R, Cidu R, Frau F (2002) Rare earth elements in waters from the albitite-bearing granodiorites of central Sardinia, Italy. *Chem Geol* 182:1–14
16. Cidu R, Mulas AD (2003) Geochemical features of thermal waters at Benetutti (Sardinia). *Rend Sem Fac Scienze Università di Cagliari* 73(1):39–53
17. Lorrà M (2004) *Geochemica dell'uranio nelle acque sotterranee della zona di Sarrala (Sardegna)*. Tesi di Dottorato inedita, Università degli Studi di Cagliari, Dipartimento di Scienze della Terra (in Italian)
18. Biddau R, Cidu R (2005) Hydrogeochemical baseline studies prior to gold mining: a case study in Sardinia (Italy). *J Geoch Explor* 86:61–85
19. Cidu R, Caboi R, Biddau R, Petrini R, Slejko F, Flora O, Stenni B, Aiuppa A, Parello F, Valenza M (2008) Caratterizzazione idrogeochimica ed isotopica e valutazione della qualità delle acque superficiali e sotterranee campionate nel foglio 549 Muravera. In: Ottonello G (ed) *GEOBASI – Il foglio IGMI No. 549 Muravera*. Pacini Ricerca Editore, pp 149–183 (in Italian)

20. Cidu R, Biddau R, Fanfani L (2009) Impact of past mining activity on the quality of groundwater in SW Sardinia (Italy). *J Geochem Explor* 100:125–132
21. Pichiri F (2007) Valutazione della qualità delle acque nell'area di Nurri-Orroli. Unpublished Master Thesis, Università degli Studi di Cagliari, Dipartimento di Scienze della Terra, AA 2006–2007 (in Italian)
22. Melis F (2010) Valutazione della qualità di acque di sorgente in Gallura. Unpublished Master Thesis, Università degli Studi di Cagliari, Dipartimento di Scienze della Terra, AA 2009–2010 (in Italian)
23. Iba MF (2011) Studio per la valutazione del potenziale geotermico dell' Anglona (Sardegna Settentrionale). Unpublished Master Thesis, Università degli Studi di Cagliari, Dipartimento di Scienze della Terra, AA 2010–2011 (in Italian)
24. Regione Autonoma della Sardegna (RAS) (2010) Caratterizzazione, obiettivi e monitoraggio dei corpi idrici sotterranei della Sardegna, p 133 (in Italian)
25. Cidu R (1996) Comparison of ICP-MS and ICP-OES in the determination of trace elements in water. *Atom Spectrosc* 17:155–162
26. De Vivo B, Boni M, Marcello A, Di Bonito M, Russo A (1997) Baseline geochemical mapping of Sardinia, Italy. *J Geochem Explor* 60:77–90
27. De Vivo B, Boni M, Costabile S (1998) Formational anomalies versus mining pollution: geochemical risk maps of Sardinia, Italy. *J Geochem Explor* 64:321–337
28. Rayner J, Manis D (2001) Gold in Sardinia: recent developments in exploration and exploitation. In: Cidu J (ed) Proceedings of the 10th international symposium on water–rock interaction. Villasimius, Italy, pp 741–744
29. Cidu R, Da Pelo S, Frau F (2011) Impact of gold mining on the aquatic system: a case study at Furtei (Sardinia, Italy). In: Proceedings of the IMWA congress, 4–11 September 2011, Aachen, pp 575–579
30. Cidu R, Da Pelo S, Frau F (2013) Legacy of cyanide and ARD at a low-scale gold mine (Furtei, Italy). *Mine Water Environ* 32:74–83
31. Biddau R (2012) Approccio geochimico-statistico per la valutazione del background geochimico nelle acque sotterranee. Applicazioni agli acquiferi della Sardegna. FSE 2007–2013, L.R.7/2007, p 123 (in Italian). Regione Autonoma della Sardegna, Cagliari (in Italian)
32. GURI, Gazzetta Ufficiale della Repubblica Italiana (2006) Decreto legislativo 3 aprile 2006. n. 152 Norme in materia ambientale. Gazzetta Ufficiale della Repubblica Italiana n. 88 del 14-4-2006, suppl. ord. n. 96, Roma (in Italian)
33. Soriga A (1993) Aspetti minerogenetici del sistema idrotermale di Osilo-S. Martino. Università' degli Studi di Cagliari, corso di laurea in scienze geologiche. Unpublished Thesis, Department of Earth Sciences University of Cagliari, Italy (in Italian)
34. Simeone R, Simmons SF (1999) Mineralogical and fluid inclusion studies of low-sulfidation epithermal veins at Osilo (Sardinia). *Italy Miner Depos* 34:705–717
35. Dettori B, Zanzari AR, Zuddas P (1982) Le acque termali della Sardegna. Ricerche Geotermiche in Sardegna, CNR-PFE-RF 10 Pisa, pp 56–86 (in Italian)
36. Caboi R, Cidu R, Fanfani L, Zuddas P, Zanzari AR (1993) Geochemistry of the high-pCO₂ waters in Logudoro, Sardinia. *Italy Appl Geochem* 8:153–160
37. Cidu R, Fanfani L, Shand P, Edmunds WM, Van't Dack E, Gijbels R (1995) Hydrogeochemical exploration for gold in the Osilo area, Sardinia. *Italy Appl Geochem* 10:517–530
38. Drits VA, Sakharov BA, Al S, Manceau A (1993) Structural model for ferrihydrite. *Clay Miner* 28:185–207
39. Sparks DL (2000) New frontiers in elucidating the kinetics and mechanisms of metal and oxyanion sorption at the soil mineral/water interface. *J Plant Nutr Soil Sci* 163:563–570
40. Carmignani L, Oggiano G, Barca S, Conti P, Eltrudis A, Funedda A, Pasci S, Salvatori I (1997) Memorie descrittive della Carta Geologica D'Italia. Geologia della Sardegna (Note illustrative della Carta Geologica della Sardegna a scala 1:200.000). Istituto Poligrafico e Zecca dello Stato, Roma, p 272 (in Italian)

41. Pillola GL, Leone F, Loi A (1998) The Cambrian and Early Ordovician of SW Sardinia. *Giornale Geologia* 60:25–38
42. Boni M, Costabile S, De Vivo B, Gasparri M (1999) Potential environmental hazard in the mining district of southern Iglesias (SW Sardinia, Italy). *J Geochem Explor* 67:417–430
43. Boni M (1994) Ores in southwestern Sardinia. In: Bechstädt T, Boni M (eds) *Sedimentological, stratigraphical and ore deposits field guide of the autochthonous Cambro–Ordovician of southwestern Sardinia*. Mem Descr Carta Geol Ital Serv Geol Naz 48:155–184
44. Cidu R, Biagini C, Fanfani L, La Ruffa G, Marras I (2001) Mine closure at Monteponi (Italy): effects of the cessation of dewatering on the quality of shallow groundwater. *Appl Geochem* 16:489–502
45. Cidu R, Di Palma M, Medas D (2007) The Fluminese mining district (SW Sardinia): impact of the past lead–zinc exploitation on aquatic environment. In: Cidu R, Frau F (eds) *Proceedings of IMWA symposium 2007: water in mining environments, 27–31 May 2007*, Mako Edizioni, Cagliari, pp 47–51
46. Kabata-Pendias A, Pendias H (2000) *Trace elements in soils and plant*, 3rd edn. CRC, London
47. Stumm W, Morgan JJ (1996) *Aquatic chemistry*, 3rd edn. Wiley, New York
48. Cidu R (2011) Mobility of aqueous contaminants at abandoned mining sites: insights from case studies in Sardinia with implications for remediation. *Environ Earth Sci* 64:503–512. doi:10.1007/s12665-010-0874
49. Monteiro LVS, Bettencourt JS, Bello RMS, Juliani C, Tassinari CCG, Oliveira TF, Pérez-Aguillar A (2003) Sulfur, carbon, oxygen and strontium isotopic evidences for the genesis of the hydrothermal zinc non-sulfide and sulfide mineralizations in the Vazante, Ambrosia and Fagundes deposits, MG, Brazil. *Short Papers IV South American symposium on isotope geology*, 24–27 August 2003, Salvador, pp 748–751
50. Brookins DG (1988) *Eh–pH diagrams for geochemistry*. Springer, Berlin
51. Regione Autonoma della Sardegna (RAS) (2013) *Carta geologica di base della Sardegna in scala 1:25000*. <http://www.sardegnaeoportale.it/argomenti/cartageologica.html>

Geological Sources of As in the Environment of Greece: A Review

Platon Gamaletsos, Athanasios Godelitsas, Elissavet Dotsika,
Evangelos Tzamos, Jörg Göttlicher, and Anestis Filippidis

Abstract This review summarizes the existing data about the geological sources of As in Greece; their variety and the relevant concentrations make Greece a peculiar territory to generalize and better understand the methodology for their assessment. These sources concern As-containing ores in active and abandoned mining areas, geothermal/hydrothermal waters, lignites in exploited and unexploited deposits, As-minerals in various rock types such as metamorphic rocks, and mineral dust originating in Sahara desert. It is considered that As release from the above sources, in conjunction with various anthropogenic As fluxes, occasionally creates distinct areas with contaminated groundwater, soils, marine and atmospheric environment.

To the memory of Constantine Zenghelis (1870–1957, Professor of Chemistry and Metallurgy in Technical University of Athens, Professor of Chemistry and Rector in University of Athens) and Constantine Ktenas (1884–1935, Professor of Mineralogy in University of Athens) who first studied As minerals in Greece at the beginning of the twentieth century.

P. Gamaletsos (✉)

Faculty of Geology & Geoenvironment, University of Athens, Panepistimioupolis,
15784 Zographou, Greece

Karlsruhe Institute of Technology, ANKA Synchrotron Radiation Facility,
Hermann-von-Helmholtz-Platz 1, 76344 Eggenstein-Leopoldshafen, Germany
e-mail: platon_gk@geol.uoa.gr; platon.gamaletsos@kit.edu

A. Godelitsas

Faculty of Geology & Geoenvironment, University of Athens, Panepistimioupolis,
15784 Zographou, Greece

E. Dotsika

Institute of Material Science, NCRS “Demokritos”, 153 10 Aghia Paraskevi, Attiki, Greece

E. Tzamos and A. Filippidis

Department of Geology, Aristotle University, 54124 Thessaloniki, Greece

J. Göttlicher

Karlsruhe Institute of Technology, ANKA Synchrotron Radiation Facility,
Hermann-von-Helmholtz-Platz 1, 76344 Eggenstein-Leopoldshafen, Germany

In general, Greece has been reported as a global As “hot spot” and it is argued that a significant amount of the Hellenic population might be affected by As pollution. The most important and permanent As source seems to be geothermal/hydrothermal fluids, due to faults and volcanic activity, affecting the underground, surface, and marine aquatic environment.

Keywords Arsenic, Geothermal, Greece, Minerals, Ores, Volcanoes

Contents

1	Introduction	78
2	Geological Sources of As in Mining Areas	81
2.1	Arsenic in Kassandra Active Mines (Chalkidiki)	81
2.2	Arsenic in Lavrion Pb–Zn–Ag Abandoned Mine (Attica)	87
2.3	Arsenic in Kirki Pb–Zn Abandoned Mines (Thrace)	89
2.4	Arsenic in the Perama Hill Au–Ag Active Mine (Thrace)	90
2.5	Arsenic in Ni-Laterite Active Mines (Central and Northwestern Greece)	91
2.6	Arsenic in Lachanas Sb–W Abandoned Mine (Thessaloniki)	92
2.7	Arsenic in Bauxite Active Mines (Central Greece)	92
3	Other Occurrences of As Ore Minerals in Greece	93
4	Arsenic in Areas with Geothermal Fluids and Volcanic Activity	97
5	Arsenic in Coals	100
6	Potential Arsenic Sources in Metamorphic Rocks	103
7	Arsenic in Phosphate Deposits	104
8	Arsenic in Desert (Saharan) Dust and “Red Rain”	105
9	Conclusion	105
	References	106

Abbreviations

BAB	Back-arc basin
MLC	Megalopolis lignite center
MOR	Mid-ocean ridge
P-ALC	Ptolemais-amymteon lignite center
SAAVA	South aegean active volcanic arc
SWAT	Soil and water assessment tool
UCC	Upper continental crust

1 Introduction

Greece is considered to face significant environmental problems related to elevated As concentrations in groundwater, soils, and the marine environment [1, 2]. In fact, Greece is included among the As-polluted “hot spots” of the entire world [3]. According to the Geochemical Atlas of Europe [4], the As-polluted soils are mainly located in northern Greece (Macedonia), as well as in Attica including the Cycladic Islands. On the other

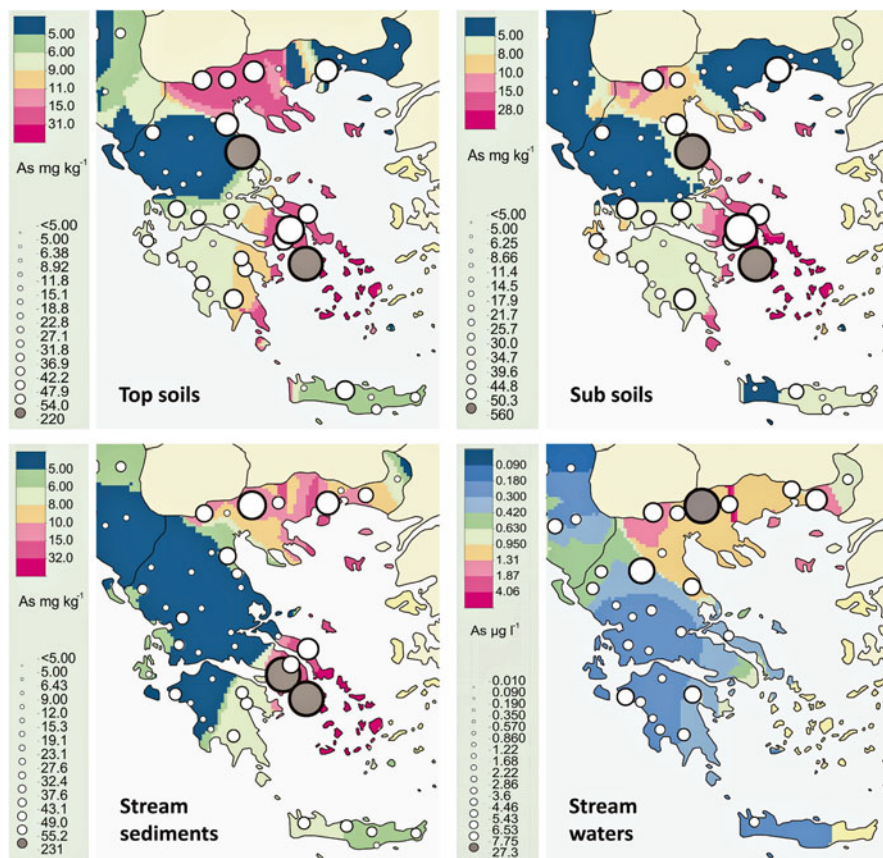


Fig. 1 Part of the Geochemical Map of Europe (modified after the EuroGeoSurveys – FOREGS Geochemical Baseline Database [4]) showing the distribution of As in top and sub-soils (*upper left map*: top layer soils; *upper right map*: sub layer soils) as well as in stream sediments (*lower left map*) and in stream waters (*lower right map*) in Greece. The lowest As concentrations are represented by the *smallest-open-circle* symbol, contracting to the highest As concentrations that are shown by the *biggest-gray-circle* symbol (dot size scale size). The multiple-grade color scale is based on the measured As concentration levels. All the values of As concentrations, in soils and sediments, below 9.60 ppm are called “background” [137]

hand, the highest concentrations of As in stream waters are observed in northern Greece (Fig. 1). The population in Greece exposed to As pollution is estimated to be 150,000 people [5]. The sources of As are both anthropogenic and natural. Of note, thermal springs (geothermal waters) and mining areas are of great significance [5]. The data, in the literature, about anthropogenic sources of As in Greece are still not extended. These sources are presumably related to fertilizers, pesticides, municipal wastes, and coal combustion in thermal power plants. Also, there are facts indicating that serious contamination of the environment in Greece, with regard to As, is attributed to combustion of fossil fuels [e.g., 6]. However, it is believed that the natural

(geological) sources of As are equally significant and mainly concern As-containing ores in active and abandoned mining areas, geothermal/hydrothermal waters due to faults (northern Greece) and volcanic activity (southern Greece), coals (mainly lignites in exploited and unexploited deposits), As-minerals in various rock types such as metamorphic rocks, and, certainly, the mineral dust flux derived from Sahara desert (Fig. 3). Consequently, the scope of this review is to summarize all of the existing data about geological sources of As in Greece and to serve as the basis of future scientific research on this issue.

Arsenic, as a chemical element, has been known in Greece since Prehistoric times. In particular, most of the Early Bronze Age in Greece (4000–2500 BC) was actually an age of arsenical copper. Arsenical copper was an advantageous Cu–As alloy, with nominally 1–6 wt% As, which allowed the manufacturing of harder tools in the prehistoric world. Relevant artifacts have been found all over the Aegean, and particularly in Crete, as well as in Evia (3.12 wt% As) dated 4000 BC and Thessaly (average 2.9 wt% As) dated 3700–3300 BC. The geological source of As in Prehistoric Greece might be in Cyclades, perhaps in Kythnos island, but this hypothesis is still questionable [7–9]. Another hypothesis is that the prehistoric sources of As could be related to primitive mining in Anatolia (Asia Minor). Later, the historical Lavrion (or Laurium) mines, located at Attica peninsula, were used in Classical Greece as the principal source of Ag and wealth for the Athenian State. In Lavrion mines there are many As minerals but perhaps they were not given appropriate attention by the ancient Greek philosophers and scientists inasmuch Theophrastus (known as the Father of Mineralogy, 371–287 BC) mentioned only native As and realgar (As_2S_3), of unknown origin, in his treatise “*On Stones*” (*Περὶ Λίθων*) (Caley and Richards [10] and Eichholz [11] referring to Latin translation – 1495–1498 AC in Venice and 1578 AC in Paris – and first English translation – 1746 in London – of Vaticanus 1302 and 1305 Codices). The Lavrion mines were also operated during the nineteenth century and Zenghelis [12] reported analyses for As in minerals from this area, as well as from Greek islands. In the same report [12] there is also a map indicating As in eastern Thessaly. Moreover, Ktenas [13] approved the occurrence of realgar (As_2S_3) in the same area (see Fig. 2). On the basis of the data of the Ministry of Economy of Greece, 659 and 14 t of As-oxide (As_2O_3 : 99.40 wt %) were produced on 1931 and 1947, respectively, in Lavrion mines [14, 15]. It seems that after the 1950s there was no further production of As from Greek mines. Nowadays, the Lavrion mines are abandoned and mainly secondary As minerals can be found (e.g., annabergite, adamite, see Fig. 2 and Table 1), but important As ores (Au-containing arsenopyrite/As-pyrite, see Fig. 2 and Table 1) are exploited in Kassandra Pb–Zn–Ag–Au active mines in eastern Chalkidiki (Macedonia, northern Greece). Finally, it should be emphasized that the magnitude of Greek geological sources of As is evident from a variety of As minerals discovered in the country for the first time in the world (Table 2). Very recently, peculiar As-sulfides of possible biogenic origin were also discovered in the floor of the submarine crater of Kolumbo volcano located north of Santorini at the Hellenic Volcanic Arc [16–18].

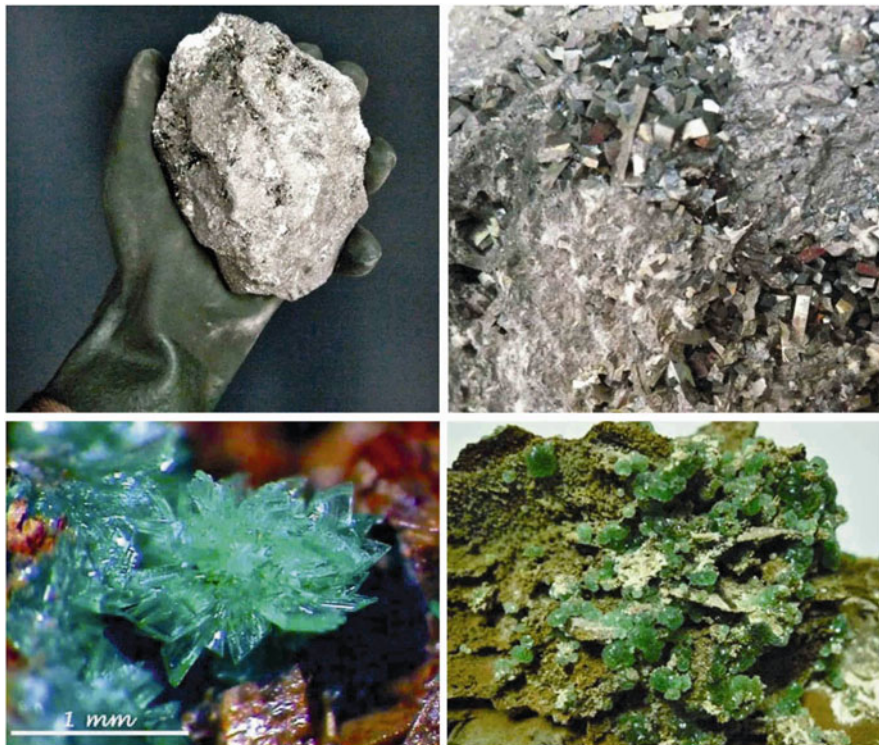


Fig. 2 Representative As minerals from Greece. *Upper photos:* Typical mm-sized arsenopyrite (FeAsS) crystals in massive As-ore from Kassandra Mines (Olympias), eastern Chalkidiki; *lower left photo:* annabergite ($\text{Ni}_3(\text{AsO}_4)_2 \cdot 8\text{H}_2\text{O}$) from Lavrion mines, Attica [<http://www.mindat.org/photo-15308.html>]; *lower right photo:* adamite ($\text{Zn}_2(\text{AsO}_4)\text{OH}$) mm-sized crystal aggregates from Lavrion mines, Attica

2 Geological Sources of As in Mining Areas

2.1 Arsenic in Kassandra Active Mines (Chalkidiki)

The Kassandra mines (Olympias, Madem Lakkos/Mavres Petres) massive sulfide –Pb–Zn–Ag–Au– ore deposits, in eastern Chalkidiki peninsula (Macedonia, Greece; see Fig. 3 and Table 1), are developed as strata bound and/or fracture controlled and in places stratiform within the calcitic-rhodochrositic marbles, biotite-hornblende gneisses, and amphibolites that have been regionally deformed and metamorphosed [19, 20]. The Madem Lakkos ores can be divided into three different types: a massive sulfide ore, a disseminated sulfide ore as well as a skarn ore, due to geochemical and mineralogical characteristics [20]. Massive sulfide ore deposits, exploited at Kassandra mines, accommodate arsenopyrite (As: 29–33 wt% [21]; see Fig. 2 and Table 3) together with pyrite (and/or As-pyrite), sphalerite,

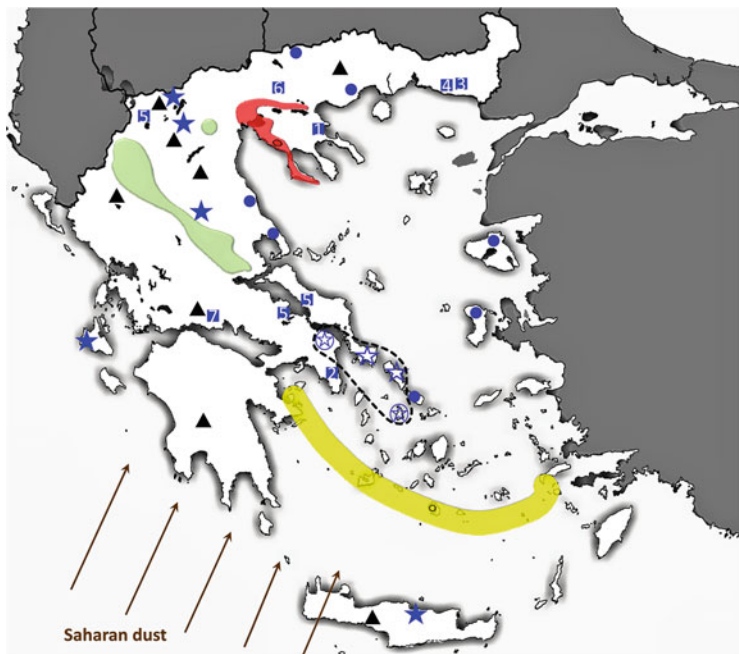


Fig. 3 Geological sources of As in Greece (see also Tables 1, 2, and 4) concerning mining areas, ore occurrences (in non-Ophiolitic rocks), coals, As-containing rock-forming minerals in metamorphic rocks of the Attico-Cycladic Crystalline Complex (included into “*dashed-line*”), and Neogene phosphate deposits. Areas in northern Greece where sediments, soils, cave deposits, and underground waters contain As due to geothermal fluids circulating through deep faults, are marked with a “*red transparent curve*” (the spot of highest As release – western Chalkidiki – is also mentioned). The South Aegean Active Volcanic Arc (SAAVA), known also as Hellenic Volcanic Arc, where high amounts of As are released due to hydrothermal fluids originating in intense volcanic activity, is designated by a “*yellow transparent curve*” (the spot of highest As release – Santorini – is also mentioned). The Ophiolitic rocks of Greece, hosting occasionally As-bearing minerals associated with massive sulfide ores, are marked with “*transparent green curves.*” The Saharan dust supply, mainly in southwestern and south Greece, is also indicated by *brown arrows*

chalcopyrite, galena, and various Sb-minerals (e.g., boulangerite) [19, 20]. Arsenopyrite and pyrite occur mainly as coarse, idiomorphic grains. As-pyrite grains were measured by Nebel et al. [20] to contain 2,600–4,900 ppm (massive sulfide ore samples), 1,400–5,000 ppm (disseminated sulfide ore samples) and 810 ppm (skarn ore samples) of As, respectively. Cabri and Chryssoulis [22] gave more details about Au in pyrite (As-poor pyrite), As-pyrite and arsenopyrite from Olympias mine [22]. Recently, Hahn et al. [23] performed geochronology in Olympias arsenopyrite and concluded an age of 26.1 ± 5.3 Ma related to metamorphic core complex exhumation [23]. Additionally, the trace elements analysis [20] revealed that also sphalerite derived from Madem Lakkos massive sulfide ore contains elevated As amount (55–1,700 ppm), while sphalerite from the disseminated sulfide

Table 1 Location of geological sources of As in Greece and their relevant symbols shown in Fig. 3

Symbols of geological sources	Location of geological sources
<i>Blue solid squares</i> : mining areas	(1) Kassandra Pb–Zn–Ag–Au active mines, at Olympias and Stratonis (eastern Chalkidiki, Macedonia, northern Greece); (2) Lavrion abandoned Pb–Zn–Ag mines, Lavrion (Attica, Greece); (3) Kirki Pb–Zn abandoned mines, including (a) the hydrothermal Pb–Zn Aghios Philippos deposit, north of Kirki flotation plant, and (b) the Pagoni Rachi polymetallic deposit, south of the Pb–Zn Aghios Philippos deposit, both hosted at the abandoned Kirki mining area, between Sappes and Esmi (Thrace, northeastern Greece); (4) Perama Ag–Au active mines, Perama Hill, northeastern of Petrota graben (Thrace, Greece); (5) Ni-laterite active mines that are mainly situated (a) at Agios Ioannis mines at Kokkino area, Larymna (Fthiotida, central Greece) (b) at Agios Ioannis area (central Evia) and (c) Kastoria (western Macedonia, Greece); (6) Lachanas Sb–W abandoned mine (NNE of Thessaloniki city, Macedonia, Greece); (7) Bauxite active mines at Parnassos–Ghiona Mts. (central Greece)
<i>Blue solid circles</i> : ore occurrences in non-Ophiolitic rocks	Asimotrypes area (Pangeon Mt. Serres-Kavala, Macedonia); Agistro area (Serres, Macedonia); Agria area (Volos/Pelion Mt, Thessaly); Agia area (Ossa/Kissavos Mt, Thessaly); Tinos Island at Panormos and Apigania Bay; Chios Island at Keramos area; Lesvos Island at Kalloni gulf
<i>Black solid triangles</i> : coals	Megalopolis lignite-bearing basin (Peloponnese), Florina-Ptolemais-Servia lignite-bearing basin (western Macedonia), Drama lignite-bearing basin (eastern Macedonia), Domeniko lignite deposit (Elassona, Thessaly), Ioannina lignite basin (Epirus), Plakia lignite deposit (Crete Island), and Pera-Lakkos mine at Parnassos-Ghiona bauxite mines (central Greece)
<i>Blue open and circled stars</i> : metamorphic rocks of Attico-Cycladic Crystalline complex	<i>Blue open stars</i> represent southern Evia and at Andros Island occurrences, while blue circled stars represent occurrences at Syros Island (Cyclades) and Varnavas area (Attica)
<i>Blue solid stars</i> : Neogene phosphate deposits	Palliki peninsula (Kefalonia Island), Heraklion area (Crete Island), Komnina area and Vegora lignite quarry (Florina-Ptolemais lignite basin, western Macedonia), Drymos area (Sarantaporo-Elassona basin, Thessaly)

Table 2 As-minerals that have been found in Greece for the first time in the literature; source: Commission on New Minerals, Nomenclature and Classification (CNMNC) of the International Mineralogical Association (IMA) (International Mineralogical Association (IMA), personal communication)

As-mineral ^a	CNMNC approved formula	Year/IMA No.	Locality
Agardite-(Nd)	$\text{Nd}(\text{Cu}^{2+})_6(\text{AsO}_4)_3(\text{OH})_6 \cdot 3\text{H}_2\text{O}$	2010-056	Lavriion
Attikaite	$\text{Ca}_3\text{Cu}_2\text{Al}_2(\text{AsO}_4)_4(\text{OH})_4 \cdot 2\text{H}_2\text{O}$	2006-017	Lavriion
Georgiadesite	$\text{Pb}_4(\text{As}^{3+}\text{O}_3)\text{Cl}_4(\text{OH})$	1907	Lavriion
Hilarionite	$\text{Fe}_3^{+2}(\text{SO}_4)(\text{AsO}_4)(\text{OH}) \cdot 6\text{H}_2\text{O}$	2011-089	Lavriion
Kamarizaite	$\text{Fe}_3^{+3}(\text{AsO}_4)_2(\text{OH})_3 \cdot 3\text{H}_2\text{O}$	2008-017	Lavriion
Kirkiite	$\text{Pb}_{10}\text{Bi}_3\text{As}_3\text{S}_{19}$	1984-030	Kirki
Nealite	$\text{Pb}_4\text{Fe}(\text{AsO}_3)_2\text{Cl}_4 \cdot 2\text{H}_2\text{O}$	1979-050	Lavriion
Zincolivenite	$\text{CuZn}(\text{AsO}_4)(\text{OH})$	2006-047	Lavriion

^aAccording to Dunn and Rouse [134] thorikosite from Lavriion mines has chemical formula of $(\text{Pb}_3\text{Sb}_{0.6}\text{As}_{0.4})(\text{O}_3\text{OH})\text{Cl}_3$ and seems to accommodate low As amount. On the other hand, IMA/CNMNC (International Mineralogical Association (IMA), personal communication) does not accept the argument that thorikosite is an As-containing mineral. Thus, IMA has decided to include thorikosite, with the given chemical formula of $\text{Pb}_3\text{O}_3\text{Sb}^{3+}(\text{OH})\text{Cl}_2$, in the official IMA/CNMNC list of minerals as a non-As-containing mineral

ore accommodates As content between 76 and 400 ppm as well. Moreover, high concentrations of As also were measured [20] in galena either from the massive or from the disseminated Madem Lakkos sulfide ore (3.6–510 ppm), respectively. Furthermore, As-sulfominerals (Table 3) are represented by tennantite [19, 20] and colusite (in selected disseminated sulfide ore samples from Madem Lakkos; [20]). It is noteworthy that for the first time in Greek territory seligmannite was reported to be hosted in these sulfide ores and especially to coexist with enargite in Madem Lakkos orebody by Nicolaou [24]. The presence of seligmannite was also reported by Nebel et al. [20].

Except Olympias and Madem Lakkos/Mavres Petres Pb–Zn–Ag–Au mines, Skouries Cu–Au porphyry [25, 26] is also located in Kassandra mining area, containing very low As amounts (1–6 ppm). However, a similar porphyry-Cu system exists in Fissoka area [26] possessing high As concentration (up to 21,000 ppm) in contrast to other sampling sites of the porphyry-Cu systems.

Due to mining activity in Kassandra mines region, As can be detected in surface waters of three local separated sub-basins (i.e., Kokkinolakkas, Kerasia, and Piavitsa sub-basins) [27]. The results showed that the enriched As concentration in stream waters is mainly influenced by the sulfide mineralization on the hydrogeochemistry of the corresponding streams (As content in Kerasia stream waters: 7–42 ppb and in Piavitsa stream waters: 4–141 ppb) and secondarily is affected by the mining activity (As content in Kokkinolakkas stream waters: 8–45 ppb). On the other hand, As in soils of Stratoni village [28] seems to be immobilized in insoluble secondary phases probably preventing its migration to underground waters. Up to now, there are no references in the literature about elevated As concentrations in potable water of the area. Nevertheless, the As distribution in waters and soils of Kassandra mines region is not extended, despite the huge As

Table 3 As-minerals involved in ores from Greek mining areas [with ideal chemical formulas based on: IMA Database of Mineral Properties, created and maintained by the RRUFF Project [135] in partnership with the IMA/CNMNC List of Mineral Names [136] compiled by Ernest H. Nickel and Monte C. Nichols, March 2007, supplied through the courtesy of Material Data, Inc. and based on the database MINERAL, which MDI makes available as a free download to the mineralogical community (http://rruff.info/about/about_IMA_list.php)]

Mine/ore	As-bearing minerals (in alphabetical order)
Kassandra Mines (Olympias and Stratoni), eastern Chalkidiki, Macedonia, northern Greece (active)/Pb–Zn–Ag–Au sulfides	Arsenopyrite; As-pyrite; Colusite; Enargite; Tennantite; Seligmannite
Lavrion, Attica, central Greece (abandoned)/Pb–Zn–Ag sulfides	Adamite; Agardite-(Nd); Annabergite; Arsenic (native arsenic); Arsenosiderite; Arsenocrandallite; Arsenopyrazite; Arsenopyrite; Arsenopolybasite; Antikaite; Austinite; Beudantite; Conicalcite; Duftite; Enargite; Georgiadesite; Gersdorffite; Hilarionite; Löllingite; Luzonite; Nealite; Pearceite; Proustite; Rammelsbergite; Realgar; Scorodite; Tennantite; Zincolivenite
Kirki mining area, Thrace, northeastern Greece (abandoned)/Pb–Zn-sulfides	Arsenopyrite; Beudantite; Bukovskiyite; Enargite; Jordanite; Kirkiite; Luzonite; Pearceite; Selligmanite; Scorodite; Tennantite; As-bearing Tetrahedrite ^a ; Zincian tennantite/tetrahedrite
Perama Hill, Thrace, northeastern Greece (active)/Au–Ag	Enargite; Luzonite; Tennantite
Aghios Ioannis, Larymna and Aghios Ioannis, Evia, central Greece; Kastoria, western Macedonia, Greece (active)/Ni-laterite	As in goethite ^b

(continued)

Table 3 (continued)

Mine/ore	As-bearing minerals (in alphabetical order)
Lachanas area, Thessaloniki, Macedonia, northern Greece (abandoned)/Sb-W	Arsenopyrite
Parnassos-Ghiona Mts., Central Greece (active)/bauxite	As in Al-oxyhydroxides ^c ; As in Fe–Cr–Ti-bearing phases ^d
Ideal chemical formulas of As-bearing ore minerals: Adamite: $Zn_2(AsO_4)OH$; Agardite-(Nd): $Cu^{2+}_6Nd(AsO_4)_3(OH)_6 \cdot 3H_2O$; Annabergite: $Ni_3(AsO_4)_2 \cdot 8H_2O$; Arsenic (native arsenic): As; Arseniosiderite: $Ca_2Fe^{3+}_3O_2(AsO_4)_3 \cdot 3H_2O$; Arsenocrandallite: $CaAl_3(AsO_4)(AsO_3OH)(OH)_6$; Arsenogoyazite: $SrAl_3(AsO_4)(AsO_3OH)(OH)_6$; Arsenopyrite: FeAsS; Arsenopolybasite: $[Ag_9CuS_4](Ag,Cu)_6(As,Sb)_2S_7$; Attikaite: $Ca_3Cu_2Al_2(AsO_4)_4(OH)_4 \cdot 2H_2O$; Ausnitrite: $CaZnAsO_4(OH)$; Beudantite: $PbFe^{3+}_3(AsO_4)(SO_4)(OH)_6$; Bukovskiyite: $Fe^{3+}_2(AsO_4)(SO_4)(OH) \cdot 7H_2O$; Colusite: $Cu_{13}VA_{5,3}S_{16}$; Conichalcite: $CaCuAsO_4(OH)$; duftite $PbCuAsO_4(OH)$; Enargite: Cu_3AsS_4 ; Georgiadessite: $Pb_4(As^{3+}O_3Cl_4)(OH)$; Gersdorffite: NiAsS; Hilarionite: $Fe^{3+}_2(SO_4)(AsO_4)(OH) \cdot 6H_2O$; Jordanite: $CuPbAsS_3$; Kirkiite: $Pb_{10}Bi_3As_3S_{19}$; Löllingite: FeAs ₂ ; Luzonite: Cu_3AsS_4 ; Nealite: $Pb_4Fe(AsO_3)_2Cl_4 \cdot 2H_2O$; Pearceite: $Cu(Ag,Cu)_6Ag_9As_2S_{11}$; Proustite: Ag_3AsS_3 ; Rammelsbergite: NiAs ₂ ; Realgar: As_4S_4 ; Scorodite: $Fe^{3+}_2AsO_4 \cdot 2H_2O$; Selligmanite: $CuPbAsS_3$; Tennantite: $Cu_{12}As_4S_{13}$; Zincian tennantite/tetrahedrite: $(Cu_{9,80}Ag_{0,05}Au_{0,03})(Zn_{1,88}Fe_{0,14})(As_{2,78}Sb_{1,29})S_{13,01}$; Zincolivinite: $CuZn(AsO_4)(OH)$	
Empirical formula of specific As-bearing ore minerals: Agardite-(Nd) [48]: $[Nd_{0,19}La_{0,14}Y_{0,12}Pr_{0,05}Gd_{0,02}Ce_{0,02}Sm_{0,02}Dy_{0,02}Zr_{0,02}Er_{0,02}Ee_{0,58}Ca_{0,39}La_{0,44}Zr_{0,44})_{\Sigma 5,93}(AsO_4)_3(OH)_{5,38} \cdot 2,64H_2O$; Attikaite [43, 44]: $Ca_{2,94}Cu^{2+}_{1,93}Al_{1,97}Mg_{0,04}Fe^{2+}_{0,02}[(As_{3,74}S_{0,16}P_{0,12})_{\Sigma 4,02}O_{16,08}](OH)_{3,87} \cdot 2,05H_2O$; Kamarizaitite [45, 46]: $Ca_{0,03}Fe^{3+}_{2,86}(AsO_4)_{1,96}(SO_4)_{0,10}(OH)_{2,74} \cdot 3,27H_2O$; Tennantite [58]: $(Cu_{0,91}Ag_{0,01})(Zn_{1,75}Fe_{0,18})(As_{3,97}Sb_{0,06}Te_{0,03})S_{13,09}$; Zincolivinite [42]: $Cu_{0,94}Zn_{1,03}Fe_{0,02}[(AsO_4)_{0,98}(PO_4)_{0,02}](OH)_{0,98}(H_2O)_{0,10}$	
^a According to the literature [58] the empirical formula of As-bearing tetrahedrite (As: 3.06 wt%) has been calculated to be $(Cu_{9,64}Ag_{0,23})(Zn_{1,89}Fe_{0,08})(As_{0,68}Sb_{3,43})S_{13,04}$. This mineral obviously belongs to the tennantite-tetrahedrite series: $(Cu,Ag,Fe,Zn)_{12}As_3S_{13} - (Cu,Fe,Ag,Zn)_{12}Sb_4S_{13}$	
^b As hosted in rounded fragments of goethite [69]	
^c As associated with Al-oxyhydroxides [69]	
^d As associated with Fe–Cr–Ti-bearing phases [75, 76]	

mineralization, in contrast to western Chalkidiki where there is no apparent As mineralization but severe contamination occurs due to the rise of geothermal fluids. As in the environment of Kassandra mines is probably not widely distributed in the environment due to natural immobilization mechanisms such as the formation of insoluble Fe-arsenate phases (scorodite). The natural scavenging of As into Fe(III)-oxy-hydroxy-sulfate phases, as happens in the case of mine water [29], can be another explanation of relatively low As pollution in Kassandra mines and eastern Chalkidiki.

2.2 Arsenic in Lavrion Pb–Zn–Ag Abandoned Mine (Attica)

The carbonate-hosted massive sulfide Pb–Zn–Ag ores of Lavrion abandoned mine (Fig. 3 and Table 1), which is mainly related to the detachment fault resulting from the separation and superposition of the Cycladic “Blueschist” and the “Basal” units, accommodates several As-bearing minerals [30, 31]. The first documented attendance reported the existence of bulk As elevated concentration in the ores of Lavrion, which was published in the beginning of twentieth century [12] referring to specific As value of 0.3 wt% in Sounion (Attica) ore and up to 1.71 wt% in neighboring Legraina (Sounion, Attica).

Mineralogical investigations thoroughly both determined the sulfide mineral assemblages (Table 3), generating and hosting in the entire massive sulfide Pb–Zn–Ag ores of Lavrion [30, 31] and focused on the polymetallic Plaka ore system, but especially on a late Pb–As–Sb–Cu–Ag-rich banded vein [31, 32]. In addition, relevant investigations focusing on an adjacent ore at Kamariza area [31, 33], and on other neighboring mines situated in the district of Lavrion [31] were also carried out. All of the above studies [31] confirmed the presence of arsenopyrite [30, 32, 33], occurring as euhedral rhomb-shaped to subhedral grains that usually interlock with euhedral to subhedral pyrite (hosting As with mean value of 0.64 wt%) and sphalerite [30], or as idiomorphic crystals up to 200 μm in length [32]. Microprobe analyses indicate that pyrite grains can host an average of 0.64 wt% As [30]. In addition, the existence of several primary sulfarsenides [31], such as gersdorffite (associated with sulfides and fluorite; [30]) hosting av. 49.82 wt% As [33] and realgar (mainly related to calcite and base metal sulfides; [30]), as well as arsenides, such as löllingite (As mean values: 70.55 wt% [30]; 69.46 wt% [32]) and rammelsbergite [34] were also reported. Moreover, the existence of proustite (As: 13.8–14.9 wt%) always together with pyrargyrite and usually associated with pearcite-arsenopolybasite (As: 5.3–7.5 wt%), enargite (As: 19.4 wt% [30]; 17.13 wt% [33]) was proved [30]. Especially native arsenic (As: 91.1–97.2 wt% [30]; 95.58 wt% [32]) was observed as dendritic inclusions in galena crystals forming botryoidal crusts up to 5 cm wide on open cracks of carbonate minerals and spatially associated with silver sulfosalts in the investigated ores [30, 32]. Finally, fahlore (tennantite-tetrahedrite series) with a relatively high As content (As in fahlore/freibergite: 3.5–8.9 wt% and in fahlore/tetrahedrite: 3.6–8.5 wt%, respectively) is an abundant sulfosalts in the mines

[30]. Ag-Bi-tetrahedrite/tennantite aggregates in the Plaka deposit were measured to contain between 8.76 and 17.56 wt% As amount [32], whereas tetrahedrite/tennantite group minerals, accommodated in Kamariza deposit, were probed to host significant (0.88–19.45 wt%) arsenic concentration [33]. According to electron microprobe analyses [32], other secondary non As-minerals were also found to accommodate, in their structure, remarkable As concentrations, such as bourmonite (As: 0.76 wt%), Ag-tetrahedrite (As: 1.75 wt%), heteromorphite (As: 1.28 wt%), falkmanite (As: 0.57 wt%), veenite (As: 1.22 wt%), miargyrite (As: 1.12 wt%), and pyrrargyrite (As: 0.64 wt%).

For the first time in the literature, extremely rare secondary As-mineral species (Table 2) named as agardite-(Nd), attikaite, georgiadesite, hilarionite, kamarizaite, nealite, and zincolivenite were discovered in the Lavrion mines (Greece). In particular, a Pb-arsenate chloride, named georgiadesite (Tables 2 and 3), was discovered by Lacroix and Schulten at the beginning of twentieth century, in the Lavrion mines formed by action of seawater on Pb-bearing phases at Vrissaki point slags [35, 36]. A later chemical and crystallographic study described the georgiadesite as monoclinic with no twinning relationship [37]. More recently, a structural study [38] of this As-bearing lead mineral from the type locality showed that arsenic occurs as As^{3+} and not as As^{5+} , revealing its revised chemical formula as $\text{Pb}_4(\text{As}^{3+}\text{O}_3)\text{Cl}_4(\text{OH})$, approved by IMA/CNMMN (Table 2). A similar worldwide discovery was the detection of another bright orange, transparent lead chloride arsenite (As^{3+}) mineral in the ancient slags of Lavrion mines, named as nealite (Tables 2 and 3) from Dunn and Rouse [39], with As content measured up to 17.30 wt% in the studied crystal (always twinned with the twofold twin axis in $\{001\}$) [39]. Furthermore, nealite crystal formula was determined as $\text{Pb}_4\text{Fe}(\text{AsO}_3)_2\text{Cl}_4 \cdot 2\text{H}_2\text{O}$, and also the As atoms were observed to form AsO_3 pyramids [40]. XRD studies on nealite crystal, from type locality, were additionally elaborated [41]. Nealite is the first mineral found to contain ferrous iron atom [39] coordinated with oxygen and chlorine atoms simultaneously [40]. Nevertheless, another totally new mineral analog of olivenite and of adamite, observed as green or greenish blue translucent crystals with vitreous luster, with streaks and conchoidal fracture, and finally named as zincolivenite (Tables 2 and 3) was found for the first time in Kamariza mining area, Lavrion [42]. Zincolivenite has been found in association with adamite (Voudouris P, personal communication) (see Table 3 and Fig. 2) and with arseniosiderite (Table 3), as well [42]. Besides, new As-minerals named attikaite and kamarizaite (see Tables 2 and 3) were discovered for the first time in Kamariza deposit (Lavrion) in 2007 [43, 44] and in 2009 the latter mineral [45, 46], respectively. Attikaite was observed as light blue to greenish blue color crystals, with a pale black streak, to form spheroidal segregations consisting of thin flexible orthorhombic crystals [43, 44], whereas kamarizaite yellow to beige crystals, with light yellow streak, occur as fine-grained monomineralic aggregates composed of platy crystals and submicron kidney-shaped segregations [45, 46] as well. Attikaite was measured to contain 45.45 wt% As_2O_5 , and has been found together with other As-bearing minerals in Kamariza (i.e., arsenocrandalite and arsenogoyazite [44]; see Table 3). On the other hand, kamarizaite was also measured to contain 39.89 wt% As_2O_5 and has found in association with scorodite in the dump of the Kamariza mine ([45, 46]; see Table 3). Recently, at Hilarion mine (Kamariza

deposit, Lavrion) were also found two more As-mineral named hilarionite [47] and agardite-(Nd) [48, 49] (see Tables 2 and 3), respectively. In particular, agardite-(Nd) was observed as transparent, light bluish green, with white streak, and luster vitreous in crystals and silky in aggregates [48]. Hexagonal crystals of agardite-(Nd) have been found associated with zincolivenite in the locality [48] and were measured to contain 33.65 wt% As_2O_5 . Additionally, in Kamariza and/or Hilarion mines (Lavrion) annabergite, austinite, duftite, beudantite, and conichalcite were also found (Voudouris P, personal communication).

Herein, it is constructive to note that other As-bearing phases are also formed in the Lavrion coastal area, due to seawater reaction with metals remaining in cavities of the dumped old metallurgical slags. According to IMA/CNMNC these new phases cannot be referred to as new minerals due to anthropogenic impact that possibly affects the mineralization. Such materials are also new Pb–chlorite–arsenite phases ($Pb_5(As^{3+}O_3)Cl_7$ and $Pb_2(As^{3+}O_2OH)Cl_2$) that were collected from historic black metallurgical slags of Punta Zeza area south of Lavrion [50, 51].

2.3 Arsenic in Kirki Pb–Zn Abandoned Mines (Thrace)

The environmental impact of the past mining activities neighboring with the Eirini local river (e.g., at the abandoned Kirki mining area including the hydrothermal Pb–Zn Aghios Philippos deposits at the northern part of Kirki) resulted in the exposure mainly to the rain and to the drainage water, of mining wastes together with the residues of the mining concentrates, due to their late disclosure, as they still remain displayed at plant's location (e.g., cracked tailing ponds, open pits). In the related Pagoni Rachi deposit located south of the Pb–Zn Aghios Philippos deposits, there was no mining activity in the past, and therefore no mining wastes. Thus, the existing mining wastes comprise a potential source of toxic and heavy metals (e.g., As), which through their transportation by rain, drainage waters, and also by Eirini local river (discharges into Aegean sea at a distance of 23 km, on the east coast of Alexandroupolis town) could be finally dispersed into the surrounding area [52] and subsequently could originate the hypothetical contamination of the hydrologic system of the entire investigated area. In the case of the potential As source in abandoned Kirki mines, several studies [52–56] were carried out. Results of these works reveal that the As concentration in the investigated remaining solid materials of the tailing ponds is extreme highly enriched (up to 944 ppm), whereas chemical analyses of the piles of concentrates as well as in the soil and the surface sediments around the flotation plant remarked that As enrichment is up to 5,243 and 1,732 ppm, respectively [52, 54]. Nevertheless, the chemical analyses of the detected As-bearing secondary minerals (beudantite, bukovskyite, scorodite; see Table 3) that form, together with other several secondary minerals, thin layers covering the floor of the highly acidic pit lake, confirmed the presence of highly As concentration (497–1,582 ppm) and the highly acidic and oxidative conditions [53, 55, 56], as well. Potential results of this highly acidic pit lake formation

could be the forthcoming release and the subsequent load of high concentrations of As to the environment. A recent unpublished diploma thesis [57] applied the hydrological model SWAT (Soil and Water Assessment Tool) at the Eirini stream watershed, located nearby the Kirki abandoned mixed sulfide mine (Evros, Thrace, Greece) that situated upstream in the river basin, in order to monitor the flow-rate and the water quality.

Arsenic-bearing mineralization (Table 3) in hydrothermal Pb–Zn Aghios Philippos deposit (north of Kirki flotation plant), and in Pagoni Rachi polymetallic deposit (south of the Pb–Zn Aghios Philippos deposit), both hosted at the abandoned Kirki mining area (see Fig. 3 and Table 1), between Sapes and Esymi (Thrace, Greece), has been described by several authors [58–64], respectively. Aghios Philippos is developed in the periphery of the Pagoni Rachi prospect.

The mineral kirkiite (see Tables 2 and 3), worldwide, was firstly discovered in Kirki mining areas (Greece) by Mořlo et al. [59] to exist in the hydrothermal polymetallic Pb–Zn deposit of Aghios Philippos [59]. Recently, a published article [65] referring to the kirkiite from the type locality, describes in details a highly pseudosymmetric structure, overloaded with heavy atoms and prone to multiple twinning. This study also found that the structure contains split As position, and two additional sites that could accommodate both As and Bi atoms. Moreover, the kirkiite empirical formula was presented once again ($\text{Pb}_{10}\text{Bi}_{2.16}\text{As}_{3.84}\text{S}_{19}$) slightly different with that of $\text{Pb}_{10.08}\text{Bi}_{2.55}\text{Sb}_{0.13}\text{As}_{2.91}\text{S}_{19}$ [59]. Also, concerning the As-mineralization in Pb–Zn Aghios Philippos deposit, evidences about the presence of minor primary As-sulfide minerals such as arsenopyrite, together with the sulfosalt Cu^{2+} -bearing pearceite (As content: 6.91–7.50 wt%; [58]) rich in Cu (up to 16 wt%; [58]) associated with Pb^{4+} -bearing tennantite (As content: 21.88 wt%; [58]) rich in Pb (up to 2.3 wt%; [58]), and related to an unrecognized phase (As content: 21.09–22.95 wt%; [58]) with similarities to watanabeite, as well as to Pb^{4+} -bearing enargite (As content: 21.13 wt%; [58]). Besides jordanite (and/or Bi-jordanite; [60]), luzonite and selligmanite (see Table 3) were demonstrated in the past [58, 60–64]. On the other hand, the authors [58] using EPMA microprobe, alternatively, detected almost similar to the previous paragenesis the occurrence of As-minerals in the Pagoni Rachi deposit (Kirki mining area; see Table 3), such as As-bearing tetrahedrite with As content 3.06 wt%, tennantite with As content 20.16 wt% and a solid solution between tennantite-tetrahedrite classified as zincian tennantite/tetrahedrite due to its high Zn content up to 8.0 wt% (As: 13.51 wt%) respectively.

2.4 Arsenic in the Perama Hill Au–Ag Active Mine (Thrace)

In the Perama Hill high-intermediate sulfidation epithermal Au–Ag deposit, located on the northeastern part of Petrota graben, nearby to the Kirki mining area (Thrace, Greece, see Fig. 3 and Table 1), arsenic-bearing mineralization [66–68] consists of enargite, luzonite, and tennantite (see Table 3). Tennantite is distinguished by means of microprobe investigation [67]. Thus, crystals of Bi,Zn-rich tennantite

(As: 18.08 wt%) have been found to intergrow with pyrite crystals, together with bismuthinite and lillianite homologues, whereas Fe-rich tennantite crystals seem to be associated with enargite crystals as well. Furthermore, Zn-rich tennantite crystals measured to contain up to 20.38 wt% As. Enargite (As: 18.15–21.88 wt %) seems to have a close association with tellurides whereas, together with its polymorph luzonite both coexist also with bismuthinite and Fe-rich tennantite. Nevertheless, the early-stage high sulfidation pyrite-enargite-bearing ores, proving by the coexistence of early pyrite together with and/or replaced by enargite surrounding by late tennantite, have been mentioned [68] to be crosscutting by the late-stage barite-tennantite-galena veins in the Perama Au–Ag deposit. The late-stage veins also include tellurides, and not only the earlier enargite ores. The potential effect of As-containing mineral phases in Perama Hill active mines on the groundwater has not been clarified yet and future research is needed. Actually concerning the local aquatic systems there are no previous papers focusing on As (and not only on minerals, ores, etc.).

2.5 Arsenic in Ni-Laterite Active Mines (Central and Northwestern Greece)

Investigation of As distribution in Ni-laterite deposits in active mining areas from Greece (Aghios Ioannis mines at Kokkino area, Larymna, Fthiotida, Central Greece; Aghios Ioannis area, central Evia; Kastoria, western Macedonia) was recently performed [69, 70], (see Fig. 3 and Table 1). In particular, the study of As, existing in individual Greek Ni-laterite deposits, indicates the elevated high content of the element especially in laterite samples derived from the lowermost part of the Aghios Ioannis bauxitic laterite deposit, Larymna (up to 2,600 ppm with an average of 573.3 ppm, in bulk), whereas the amount either in laterites from Aghios Ioannis (central Evia) or in laterites from Kastoria region is quite low (As in laterites from Aghios Ioannis, Evia: 2–3 ppm and As in deposit from Kastoria: 3–14 ppm, both in bulk). This dissimilarity in As concentration revealed the wide variation of the element's content in the laterite deposits [69]. This could be probably due to the different sources of the Greek deposits and/or of different spots into the same deposit (i.e., parent ophiolite complexes, local conditions of re-deposition, and involvement of the organic matter [70]) that supply the Ni-laterite deposits with As. Besides, SEM-EDS analyses of the investigated samples revealed that As in the studied laterite deposits is mostly associated with goethite (Fe-oxyhydroxide with As_2O_3 : 0.75–1.2 wt%, see Table 3) [69, 70]. Regardless of the high As concentration in samples from different laterite deposits and/or of different spots into the same deposit (e.g., Aghios Ioannis exploitable deposits, Larymna, central Greece), the mean average value of As in Greek laterites has been measured and it seems to be rather low (<10 ppm). Also the great variation in As hosted in Greek laterite deposits is in line with the

measuring As existing in the metallurgical product (ferro-nickel alloy) of the smelting plant located in Larymna, central Greece [69]. Thus, and also taking into account the assumption of the As-adsorption by goethite [70], the possible impact of the As on the ferronickel smelting in the metallurgical industry, as well as in the environment and in the human health seems to be controlled [69, 70].

2.6 Arsenic in Lachanas Sb-W Abandoned Mine (Thessaloniki)

The Sb and Sb-W ore deposits, related to Ternary volcanic intrusions, situated in Lachanas area (Pilaf-Tepe and Tasch-Kapou location sites) at the NNE of Thessaloniki city, have been examined in the past [71, 72]. Studies of these ores detected the presence of arsenopyrite together with major Sb and W minerals (antimonite and wolframite) coexisting with other minerals (quartz, pyrite, sericite, chlorite calcite, dolomite), as well as with some other Sb-sulfides (bournonite, boulangerite, and jamesonite). It should be noted that As from Lachanas area was measured in bulk [72] and found to vary from 100 ppm up to 1,800 ppm, whereas chemical analyses of Sb and Sb-W ore deposits [71] recorded very high As contents (0.03 wt% in mixed Sb-W ore), and up to 0.18 wt% (in Sb ore).

2.7 Arsenic in Bauxite Active Mines (Central Greece)

Parnassos-Ghiona allochthonous karst-type bauxite deposits are hosted within carbonate formations and divided into three bauxite horizons (from bottom to top: B1, B2 and B3) separated by limestones. The B3 horizon, locally and occasionally, underlies from a thin layer of As-rich coal (mean value of 18 ppm approximately, please see the relevant paragraph; [73]). Measurements of the As concentration of selected nontypical and nonindustrial black-gray Fe-rich bauxite sample, deriving beneath the contact between the coal and the B3 horizon, and situating in the Peralakkos mine [73] which is located in the Parnassos-Ghiona active mining areas (central Greece; see Fig. 3 and Table 1), were recently reported [69, 74]. These studies demonstrate the enrichment of As content in the black-gray Fe-rich bauxite sample (up to 300 ppm, in bulk; [74]), whereas the extremely highly elevated As concentration in yellow-gray bauxite samples is also reported (up to 890 ppm, in bulk; [69]). Black-gray Fe-rich bauxite sample consists mainly of pyrite (FeS_2) and also Al-oxyhydroxide (diaspore: AlOOH). Minor hematite (Fe_2O_3) and/or goethite (FeOOH) are also observed. Additionally, SEM-EDS analyses provide the information that the As is hosted in areas dominated by Al-oxyhydroxides (As_2O_3 : 1.39 wt%; [69]) of the bauxite samples (especially the “yellow-colored type”) and thus, the authors conclude that As is mostly associated with Al-oxyhydroxides (diaspore

and/or boehmite: AlOOH polymorphs) in bauxite (see Table 3; [69]). Moreover, they maintain that As enrichment of black–gray Fe-rich bauxite sample, from distinct sites beneath the As-rich thin coal layer in the B3 horizon, is probably related to the organic matter of the coal, assuming that the amount of the As accommodated in the bauxite can be influenced by the existence of this organic layer [69, 74]. However, according to very recent studies based on advanced analytical, microscopic and spectroscopic characterization techniques [75, 76], As in Greek bauxites, sampled from active mines of Parnassos-Ghiona area, may not be related to Al-oxyhydroxides (and also to S-phases) but to Fe–Cr–Ti-phases into relevant pisoliths.

3 Other Occurrences of As Ore Minerals in Greece

Ore occurrences in the Greek mainland, as well as in Greek islands, of remarkable concentrations of As, tightly associated with As-bearing ore minerals (e.g., arsenopyrite: FeAsS) and/or arsenic sulfides/sulfosalts (e.g., realgar: AsS in Agria, Volos, Pelion Mt.–unpublished data) have been thoroughly reported by several authors [12, 71, 72, 77–86] (see Fig. 3 as well as Tables 1 and 4).

A very recent study [77] on gold-bearing sulfide mineralization at Asimotrypes area, Pangeon Mt. (Serres-Kavala, Macedonia, Greece) revealed that Au-bearing sulfide precipitation (at $T \approx 270^\circ\text{C}$; $P = 1,800\text{--}2,000$ bars) formed an Au-bearing hypogene mineralization that consists of arsenopyrite (As: 41.7–43 wt%) together with traces of arsenian-pyrite (As: 0.01–3.8 wt%) and Cu₂As-sulfosalt (tennantite: Cu₁₂As₄S₁₃) dispersed into the Au-ore body, originating an As-ore occurrence (mean average As amount of unoxidized auriferous samples of 25,000 ppm; maximum As value of 496,250 ppm), as well (see Fig. 2, Table 4). Arsenopyrite was found to dominate minor chalcopyrite, galena, and sphalerite in the mineralized bodies. This hydrothermal alteration, associated with the auriferous bodies and veins, occurs within amphibolites facies rocks of the Southern Rhodope core complex. This is attributable to the leaching of the Paleozoic marine metasedimentary (marble) core complex, and interlayered mafic metavolcanic (amphibolites) and Miocene granitic rocks through fluid/rock interaction [77]. Nearby the Mount Pangeon in a neighboring region of Serres at Agistro area, Macedonia (unpublished data; see Fig. 3 as well as Tables 1 and 4) auriferous veins of arsenopyrite together with pyrite and pyrrotite are also occurring.

Massive sulfide ore associated with Greek ophiolite complexes occurring in the Othrys Mt. to Pindos Mt., consisting mainly of pyrite, chalcopyrite, and less amount of sphalerite and bornite, were found to accommodate relative high contents of As and Au [79]. In particular, elevated arsenic concentration was found at different sulfide ore samples from the Pindos ophiolite complex (Ioannina-Grevena, Epirus-western Macedonia; see Fig. 3 and Table 1). These samples were taken from the Perivoli region (SE slope of Smolikas Mt.), and in particular from a “Cyprus-type” sulfide ore occurrence situated at Kondros Hill area (mineral assemblages: pyrite, chalcopyrite, sphalerite and bornite) which shows an increased arsenic content up to

Table 4 Occurrences of As-minerals in Greece (non-mining areas)

Locality	As-minerals	References
Asimotrypes area, Pangeon Mt., Serres-Kavala, Macedonia	Arsenopyrite, As-pyrite, tennantite	[77]
Agistro area, Serres, Macedonia	Arsenopyrite ^a	–
Trilofon area, Veria, Macedonia	Cobaltite	[78]
Pindos ophiolite complex, Pindos Mt.	As-pyrite	[79]
Paliouri area, Karditsa, Western Thessaly	Arsenopyrite	[80]
Agia area, Ossa/Kissavos Mt., Eastern Thessaly	Arsenopyrite, Scorodite ^b	[81–84]
Agria area, Volos, Pelion Mt., Eastern Thessaly	Arsenopyrite, Realgar ^c	[81]
Panormos Bay, Tinos Island	Niccolite/Nickelite, Luzonite, Gersdorffite, Laggisite	[87]
Apigania Bay, Tinos Island	Arsenopyrite, Xanthoconite, Proustite, Rammelsbergite, Laggisite, Polybasite, Native As ^d	[88]
Keramos area, Chios Island	(–) ^e	[84]

^aUnpublished data

^bReported only by Chatzidiakos et al. [84] in the area of Bourboulithra (Melivoia, Agia, Ossa/Kissavos Mt., Eastern Thessaly)

^cUnpublished data of a study [81] though presented a map did not mention the As-hosted phase)

^dReported as native As nanoparticles into pyrite crystals [88]

^eThere is no indication for As-hosted phase [84]

150 ppm (in bulk), and also from a “Fe–Cu–Ni–Co” sulfide ore occurrence situated at Tsoumes area (mineral assemblages: pyrrhotite, pyrite, pentlandite, chalcopyrite, and magnetite) with its As concentration varying between 20 and 27 ppm (in bulk), respectively. Additionally, chemical analysis of samples derived from the “Cyprus-type” sulfide ore occurrence at the Aspropotamos region (east of Perivoli region, SE slope of Smolikas Mt.) indicates a decreased As content from 15 to 25 ppm (in bulk) in regarding to the Neropriona area’s samples (consist mainly of disseminated pyrite and chalcopyrite) and moreover to 22 ppm (in bulk) concerning the Aspropotamos area’s quartz veins samples comprise mainly of disseminated pyrite, chalcopyrite, and pyrrhotite, as well. On the other hand, “Cyprus-type” sulfide ore samples from the Othrys ophiolite complex (Aghioi Theodoroi and Limogardi areas, Fthiotida, central Greece; see Fig. 3 and Table 1) revealed a significant low content of As (20 ppm, in bulk). Furthermore, advanced microbeam technique (SIMS) adequately illustrates the quantitative chemical composition of As in selected minerals from the sulfide ore occurrences from Pindos ophiolite complex [79]. The SIMS analyses confirmed the relative high As contents in coarse- and fine-grained As-bearing pyrite associated with bornite + covellite + siegenite assemblage. Thus, the variation of As concentration in the coarse-grained pyrite is between 110 and 3,080 ppm av. 1,290 ppm), in the fine-grained pyrite is between 170 and 12,900 ppm av. 1,610 ppm), and in very fine intergrowth with bornite is

between 130 and 2,710 ppm av. 1,180 ppm), respectively. Similarly, the elevated amount of As in selected coarse- and fine-grained As-bearing pyrite is also associated with chalcopyrite (As variation in coarse-grains: 72–1,552 ppm with an average value of 817 ppm; As variation in fine-grained: 205–311 ppm with an average value of 275 ppm) and with sphalerite (As variation in very fine intergrowths with sphalerite: 272–915 ppm with an average value of 585 ppm). Finally, pyrite associated with bornite was measured to have significant As content in coarse-grained crystals (As: 39–198 ppm; av. 105 ppm), in fine-grained crystals (As: 84–378 ppm; av. 225 ppm) as well as in very fine intergrowths with bornite (As: 373–1,279 ppm; av. 790 ppm), respectively. Conclusively, coarse- and fine-grained pyrite associated with chalcopyrite, bornite, and with assemblages of bornite, covellite, and siegenite seems to incorporate significant amount of As in micro-scale, assuming that the presence of arsenian pyrite (Table 4) is present in the massive sulfide ores occur in Pindos ophiolite complex [79].

As-bearing sulfides existing in Ophiolite-hosted ore deposit are thoroughly described [78] also at the area between Trilofon and Fitia villages, Eastern part of Vermion Mt. (NW of the city of Veria). In particular, the presence of cobaltite (theoretical formula: CoAsS) was identified. Special emphasis was given to its chemical composition ($\text{Co}_{0.84}\text{Ni}_{0.11}\text{Fe}_{0.05}\text{As}_{0.98}\text{S}_{1.02}$). Microprobe analyses from the cobaltite euhedral small crystals intergrowing within pyrrhotite demonstrated that As was varying between 44.40 and 45.93 wt%. The ore occurs in an area of ophiolites and flysch and situated within diabases and serpentinites forming lenses, bands, and disseminations. The mineralogical paragenesis of the ore is cobaltite, pyrrhotite, chalcopyrite, pyrite, and sphalerite (crystallization order). The authors concluded that cobaltite was crystallized at 500–600°C.

Additionally, copper ore deposit studied [80] in the area Paliouri area, near Karditsa (Western Thessaly) consists mainly of pyrite, sphalerite, and chalcopyrite as well as of gangue minerals (e.g., quartz and calcite), although the existence of euhedral and elongated crystals of arsenopyrite together with pyrite crystals was also proven. The entire area that Cu-ore occurs consists of basic and ultrabasic igneous rocks (e.g., serpentinites, spilites).

It is already well known that mineralogical and geochemical investigations in the region of Eastern Thessaly were undertaken far away in the past [12], reporting As mineralization in ore occurrences with no mining activity. A brief report of these occurrences in Eastern Thessaly [81] succinctly describes the ternary hydrothermal sulfides of As related to granitic intrusions in the area of Melivoia village, Agia, Ossa/Kissavos Mt. as well as in the area of Agria village, Volos, Pelion Mt. (see Fig. 3), concerning that the As hosting mineral is arsenopyrite. This As-sulfide mineral is accommodated within the metamorphic basic ophiolitic rocks (amphibolites, prasinites) as well as within the metamorphic rocks of sedimentary origin (mica-chlorite schists, quartz-chlorite-mica schists) [82, 83]. Arsenopyrite (FeAsS) together with galena (PbS), chalcopyrite (CuFeS_2), pyrite (FeS_2), sphalerite ($(\text{Zn,Fe})\text{S}$), and stibnite (Sb_2S_3) used to form sulfide mineralization paragenesis in the entire investigated area [81]. Crystals of scorodite ($\text{FeAsO}_4 \cdot 2\text{H}_2\text{O}$) with length of 50 μm were also found in rocks from Bourboulithra area (Melivoia) by

Chatzidiakos et al. [84]. Relevant work implied that the As and the Sb mineralization are both related to each other [82]. Moreover, the authors [82–84] suggested that the extended occurrence of arsenopyrite in the area lying between Melivoia, Velika, Skiti, and Ano Polydendri (cultivated region of Agia, Eastern Thessaly) is probably the natural source of As contamination either in the groundwaters or in the soils. The relevant studies revealed that the Agia's groundwaters have relatively elevated As concentration (mean value of 12 ppb; maximum value of 125 ppb), as well as Agia's soils are characterized by relatively increased concentration (As: 5–242 ppm) with much higher mean average (As: 13 ppm) in comparison with that of the average of the global soil composition of (As: 2–20 ppm) mentioned by Yan-Chu [85] and lately re-noted by Hughes et al. [86], respectively. Decisively, Chatzidiakos et al. [84] predicted the trivalent oxidation state of the As in the groundwaters and implied that the As^{3+} natural pollution reflects mainly the influence of arsenopyrite mineralization and, thus, is due to the dissolution of FeAsS . Nevertheless, they assumed a direct combination of the As natural pollution with some anthropogenic inputs in the cultivated area of Agia (Eastern Thessaly) [82]. Additionally, this natural groundwater As contamination is also well reflected by the existence of hydrothermally altered zones in the investigated area.

Besides, recent studies [87, 88] on Tinos island, Greece, thoroughly represent an abundant ore mineralization due to the presence of epithermal ore systems in Panormos [87] hosting in Mesozoic marbles and Apigania Bay [88] hosting in Mesozoic marbles and schists, as well. Bulk chemical analysis of the hosting rocks, complementary, affirmed the high As composition in the island (marbles, schists of blueschists belt and milky quartz veins were found to contain 66, 67 and 41 ppm As in bulk, respectively). Both ore occurrences are characterized by numerous ore and gangue minerals associated with arsenic. The Panormos Bay ore system, among others (precious metals, ore and gangue minerals), also was identified arsenide minerals (e.g., niccolite or nickelite: NiAs), sulfosalts (e.g., luzonite: Cu_3AsS_4), Ni, As-sulfides [e.g., gersdorffite (NiAsS)], and other such as laggisite ($\text{Co}_{0.8}\text{Ni}_{0.2}\text{As}$), whereas the Apigania Bay mineralization exhibit some differences. The latter As-enriched epithermal mineralization consists mainly of arsenopyrite and minor of As-sulfides/sulfosalts, such as xanthoconite (Ag_3AsS_3), proustite (Ag_3AsS_3), rammelsbergite ($(\text{Ni},\text{Co},\text{Fe})\text{As}_2$), laggisite ($\text{Co}_{0.8}\text{Ni}_{0.2}\text{As}$), and/or As-bearing polybasite ($[(\text{Ag},\text{Cu})_6(\text{Sb},\text{As})_2\text{S}_7][\text{Ag}_9\text{CuS}_4]$). Also, pyrite crystals measured contain up to 2.24 wt% As, assuming that this is due to the existence of native As nanoparticles into it, while specks or laths of proustite and xanthoconite are intergrown with pyrite and sphalerite crystals [88]. Finally, electron microprobe analyses in selective grains and characteristic crystals from Tinos island confirmed the abundant existence of As in sulfides and sulfosalts, resulting that pyrite, arsenopyrite, xanthoconite, proustite, rammelsbergite, and laggisite are rich in As (1.85, 44.85, 15.02, 14.99, 68.28, and 55.03 wt%, respectively).

On the other hand, preliminary studies of the oxidation state of As in groundwaters from the island of Chios (Keramos area, NW part of Chios, Eastern Aegean sea, Greece) suggested, on the basis of theoretical calculations, that the dominant species of As are trivalent and the concentration of As increases up to

6.13 ppb. A relevant geochemical study [89] examining the possible influence of geology on As concentration in groundwater, stream water, and stream sediments in Keramos gulf of Lesvos Island (NE Aegean sea, Greece), assumed that the measurement of the elevated As concentration cannot be attributed to the geothermal activity of the investigated area, but ascribed to the presence of the adjacent ophiolitic ultramafic formations, which possibly accommodate As-bearing minerals. The study concluded that these formations are apparently the predominant factor of the corresponding As geochemical behavior.

4 Arsenic in Areas with Geothermal Fluids and Volcanic Activity

Arsenic in groundwaters and soils, influenced by geothermal activity (possibly mixed with geothermal fluids in deep horizons) due to faults, is intensively observed in northern Greece (see Fig. 3 and Table 1; [90–98]), and in particular at greater Thessaloniki (including Axios river and western Chalkidiki). This highly populated area has very limited water resources, and subsequently As-contaminated groundwaters have minimized the water supply potential for people and animals. In groundwaters, derived from specific wells of greater area of Thessaloniki and the Axios river delta, rather elevated As concentrations were measured (4–130 ppb), attributed to the possible effect of pH on As mobilization, as positive correlation of As with the pH values was also estimated [93]. On the other hand, elevated As concentrations were also recorded near Volvi Lake [92]. However, according to Kouras et al. [95] and Voutsas et al. [96] the As contamination of groundwaters is really severe in western Chalkidiki near Nea Triglia area. In this area As concentrations were recorded to be up to 1,840 ppb with EU permission level for potable water to be 10 ppb. Arsenic seems to be correlated with U [94] as well as with B [96]. The sources of As, released to the surface by geothermal fluids (33–42°C) circulating through faults, may be related to igneous rocks underlying thick sedimentary formations. This assumption is also supported by the geochemical fact that As was also correlated with K, Mn, and Fe, indicating geogenic origin and the presence of hydrothermal conditions resulted in enhancements of their mobility [95]. A study of hydrothermal waters from springs and boreholes with an average As concentration of 36 and 70 ppb, respectively, that are enriched in several constituents (e.g., H₂S, K, B, NO₂, Mn) was also carried out for Anthemous basin (between western Chalkidiki and Thessaloniki) [91]. This study provides also a representative model of As enrichment of waters from springs and boreholes, attributable to the local hydrothermal fluids circulation, influenced by the presence of a specific geological basement (e.g., existence of granodiorite that probable is leached by water circulation through fracture zones) and by hydrothermal conditions (e.g., $T = 23\text{--}28^\circ\text{C}$, pH: 6.2–7.3, Eh from –0.21 to –0.88 mV, TDS up to 5,850 ppm, H₂S: 60–70 vol.%, etc.), causing the further enrichment of

groundwater in As and other metals. Thus, hydrothermal fluids enhanced the groundwater in As, which then deposits As-rich metalliferous sediments (av. 147 ppm in As) and rich in As travertine (av. 235 ppm in As) due to its discharge through WNW–ESE faults in the western Chalkidiki peninsula [91]. In a very recent study by Winkel et al. [98], alkaline groundwaters in western Chalkidiki containing up to 3,760 $\mu\text{g/L}$ As, were found to be associated with arsenate (As^{5+})-rich (As: up to 913 mg/Kg) travertine according to Synchrotron radiation spectroscopic study (micro-XRF and -XAS). Thus, the influence of the reported geothermal activity results in the natural pollution of the underground water and consequently of the soils of the investigated areas.

Herein, it is noteworthy to report a rare example of As-mineralization as a consequence of the influence of hydrothermal fluids in the caves of Aghia Paraskevi (SW of Kassandra peninsula, western Chalkidiki). Orpiment (As_2S_3) crystals, with specific amount of As between 60.7 and 61.32 wt%, are formed very close to the surface of thermal Na–Cl type spring waters ($T = 35.0\text{--}39.2^\circ\text{C}$, pH: 6.35–7.00 and TDS: 35.964–43.521 mg L^{-1}) in these active sulfuric acid caves, due to the hydrothermal influence as a result of the mixing of seawater with the meteoric origin of geothermal waters of the cave [99].

The enrichment of As in sediments situated in areas of volcanic activity in South Aegean Active Volcanic Arc (SAAVA, also known as Hellenic Volcanic Arc) (Fig. 3 and Table 1), is suspended as a possible influence of hydrothermal fluids. In particular, measurements of As concentrations in surface siliceous (As: 10.1–27.0 ppm) and in carbonate sediments (2.4–27 ppm) derived from Methana Island [100] reveal an average of 20.45 ppm and of 6.67 ppm, which are both rather elevated compared to the As concentration of the upper continental crust – UCC [101], respectively (see Fig. 4). Furthermore, the geochemical investigation elaborated on submarine hydrothermal fields of Milos Island (south Aegean Hellenic Volcanic Arc) significantly showed that the corresponding sediment cores, derived from Voudia Bay (average of 9 ppm in As content), Palaeochori (average of 57 ppm in As content) as well as from Rivari (average of 108 ppm in As content), accommodate a relative high As amount [102, 103], contrast to UCC As content (Fig. 4). A very recent study [104] just discovered poorly crystalline orpiment (As_2O_3), in the bottom of the sea at Palaeochori and Spathi Bays (off the southeast coast of Milos Island), yielded by the abundant hydrothermal venting of acidic and highly sulfidic fluids occurring in this shallow-sea environment. These fluids are characterized by an extremely high As concentration, up to 300 times higher than of the seawater, and indeed far exceed to the mid-ocean ridge (MOR) and back-arc basin (BAB) fluids As content, respectively. They suggest that unique orpiment phase is derived by the mixing of the overlying seawater with these hydrothermal fluids moving from the leachate metamorphic basement – due to water–rock interaction – upwards, through an abundant vein system, towards to the surface of the bottom of the sea in critical boiled conditions. They also believe that the source of the extremely elevated amount of As is the combination of the leaching phenomena of the greenschist facies metamorphic basement due to the water–rock interaction, and of the directly partition of the As into the vapor phase (under critical conditions) in this local hydrothermal system.

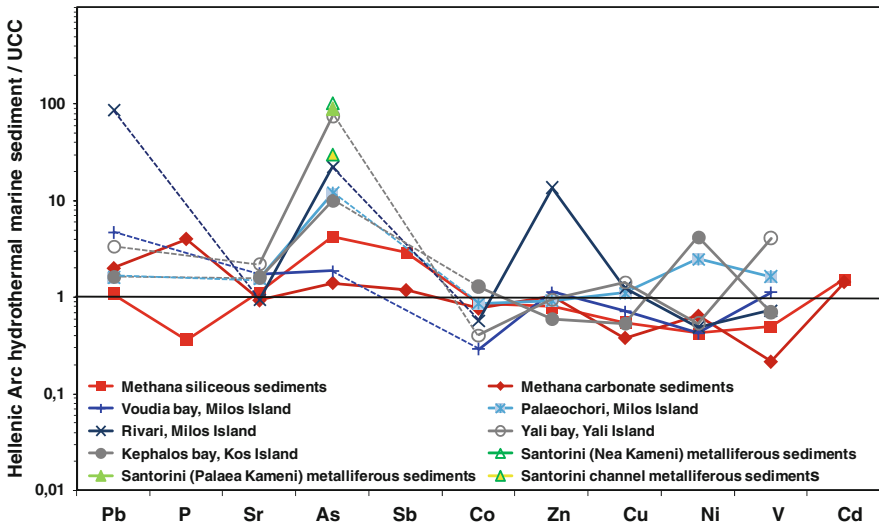
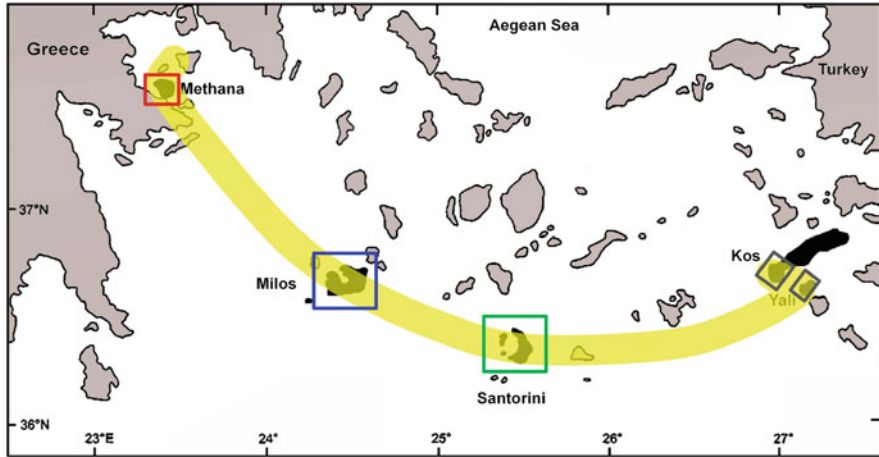


Fig. 4 *Upper image*: simplified map indicating the Methana (NE Peloponnesse), Milos, Santorini, Yali and Kos volcanic centers, acting as significant As sources in the Hellenic Volcanic Arc. *Lower image*: Upper Continental Crust (UCC)-normalized (according to Rudnick and Gao [101]) spider diagram of trace elements in marine hydrothermal precipitates showing an extreme As geochemical positive anomaly in the whole Hellenic Volcanic Arc. Average values of Methana siliceous sediments [100]: red thick line and solid square; Average values of Methana carbonate sediments [100]: darker red-brown thick line and solid lozenges; Milos Island sediment [102, 103]: blue thick line and plus symbol correspond to Voudia Bay samples, light blue thick line and asterisk in lighter blue background correspond to Palaeochori, dark blue thick line and cross correspond to Rivari, respectively; Yali Island (Yali Bay) sediments [103, 105]: gray thick line and open circle; Kos Island (Kephalos Bay) sediments [101, 103] gray thick line and closed circle; Average values of Santorini caldera metalliferous marine sediments [106]: green thick line and open triangle correspond to Nea Kameni islet, light green thick line and closed triangle correspond to Palaea Kameni islet, yellow thick line and green triangles with yellow filling color correspond to Santorini “channel” situated between Palaea and Nea Kameni islets

Another intense As enrichment phenomenon was alternatively found in sediments from Yali Bay, Yali Island (average of 356 ppm in As content) and from Kephalos Bay at Kos Island sediments (average of 48 ppm in As content), respectively [103, 105]. On the other hand, chemical analyses conducted in selected areas of Santorini Island, and especially measuring the As concentration in metalliferous sediments from Nea Kameni (As: av. 493 ppm), Palaea Kameni (As: av. 425 ppm) and from the area of the channel (As: av. 145 ppm) located between the latter two small islets, exposed again the hydrothermal enrichment of As, together with Sb. Moreover, this investigation described the impact of the formation of freshly precipitating Fe-oxides resulting the scavenge of the hydrothermal As into the sediments [106]. Therefore, all of the above studies indicate an extreme As enrichment in the hydrothermally influenced sediments, compared to UCC (Fig. 4), either associated with a relative elevated Sb concentration (e.g., in the case of Methana sediments [100]) or related to Fe–Mn rich layers (e.g., in the case of Santorini [106] and Milos [102, 103] sediment cores). These findings suggest a relatively recent hydrothermal activity, as a result of the volcanic activity in the Hellenic Volcanic Arc. Finally, in a recent investigation, peculiar As-sulfides of possible biogenic origin were also discovered in the floor of the submarine crater of Kolumbo volcano located north of Santorini [16–18].

5 Arsenic in Coals

Lignites, as the most common type of coals in Greece, are mainly situated at the three lignite-bearing main coal deposits (e.g., [107–109], see Fig. 3 and Table 1) in Ptolemais and Florina (Florina-Ptolemais-Servia main basin in western Macedonia, NW Greece), in Megalopolis (Megalopolis basin in Peloponnese, southern Greece) as well as in Drama lignite deposit (Drama basin in eastern Macedonia, NE Greece). Similar to the above, smaller coal deposits such as Domenico lignite deposit [110] in Ellassona lignite basin (Larissa district, Northern Thessaly), lignite-bearing strata [107, 111] in Ioannina basin (Ioannina, Epirus), and Plakia lignite deposit [111] in Plakia basin (Crete Island) have also been geochemically examined in the past. Moreover, the As content of all of these coal deposits has been measured, concerning that the mentioned deposits in Greece could be potential sources of this hazardous element.

Recently, a new occurrence of a nonindustrial thin layer of coal, at the Peralakkos mine located in the Parnassos-Ghiona bauxite mining area, overlying bauxite horizon B3 (please see relevant paragraph and Fig. 3 as well as Table 1) has discovered and a relevant article [73] demonstrates that accommodate an average of 18 ppm of As content, approximately.

Geochemical investigation of Lava xylite/lignite deposit (a sub-basin at the Servia basin – southeast of Kozani, northern Greece – situated in the southern part of the elongated intermontane Florina-Ptolemais-Servia main basin) has revealed [107, 112] that As can be considered as a highly enriched element. Estimation of arsenic in air-dried lignite samples reveals an average value at

9.32 ppm with maximum at 27.83 ppm [112]. It is mentioned that part of the As may be organically bound, while the rest probably occurs as a solid solution or as As-purite. Similar study [107] calculated the As concentration either to air-dried lignites or to lignite ashes (heated at 1,000°C) derived from Kozani (Lava and Anatoliko), Ptolemais (Kardia), and Florina (Anargyri and Achlada) lignite sub-basins. The results concluded with the As enrichment in all of the investigated samples (Kozani: av. 58.45 ppm for air-dried lignites and av. 293.9 ppm for lignite ashes; Ptolemais: av. 22.2 ppm for air-dried lignites and av. 104 ppm for lignite ashes; Florina: av. 10.7 ppm for air-dried lignites and av. 48.6 ppm for lignite ashes), respectively. The entire coal deposit from the Florina-Ptolemais-Servia main basin, which is divided into several lignite-bearing sub-basins, is belonging to the Ptolemais-Amynteon Lignite Center (P-ALC) in Northern Greece.

On the other hand, other opencast mines at Domenico lignite deposits, Ellassona basin, Larissa, Thessaly [110], as well as at Lofoi lignite-bearing deposit, Florina lignite-bearing basin [113] were also examined for their trace elements composition in the lignite ashes (lignitic samples that prior heated at 850°C). The results showed the As concentration at the lignite ashes, compared to that of the earth crust's average of 1.8 ppm [114], is strongly enriched. The As mean average content is 46.5 ppm with a maximum value of 104 ppm corresponding to Florina basin's lignitic samples, whereas the composition of As at the lignitic samples from Ellassona basin is up to 150 ppm (mean average at 32.06 ppm). This is ascribed to the existence of olivinite and granitic rocks regarding the Florina lignite-bearing deposit, and it is strongly believed that these silicic and mafic-ultramafic surrounding rocks in the area actively contributed to the formation of the deposit. Correspondingly, the As enrichment occurs at the samples from Ellassona lignite basin is attributed to the geothermal activity that had affected the area during the past, confirming the presence of travertine in the overburden sediments. Nevertheless, strong positive correlation between Mo and As is observed at both Florina and Ellassona lignite samples [110, 113] that can be explained due to the existence of sulfide minerals, as well as an intermediate to strong positive correlation of Cr and As is also notable concerning the Florina lignite samples [113].

Lignites from the Ptolemais Basin have similarities to those of Drama basin with regard to their deposition under similar geologic conditions [112]. The Drama basin consists mainly of peat and lignite and minor of clay, sands, and muds. The lignite deposit can be divided into three lignite seams A, B, and C (from the bottom to the top). Seam A can also separated into three sub-seams A3, A2, and A1 (from the bottom to the top), respectively [108, 115, 116]. In accordance with a previous study [107] reporting a range of As concentration at air-dried lignites (sampling site near Pangeon Mt.: 34–124 ppm; sampling at the main lignite deposit: 13.2–90.3 ppm) as well as at heated (1,000°C) lignite ashes (sampling site near Pangeon Mt.: 856–1,131 ppm; sampling at the Dipotama lignite deposit: 50.9–1,675.0 ppm), a newly detailed geochemical study [116] also analyzed several composited samples (air-dried lignites and lignite ashes heated at 1,000°C) from the Drama lignite basin. The latter study showed that As is highly enriched to the air-dried lignites (av. 62 ppm) as to their corresponding heated lignite ashes

av. 185 ppm), compared to the crustal abundances and also to the surrounding rocks (<2 ppm at metamorphic rocks; up to 2.7 ppm at igneous rocks), as well. It is noteworthy that As concentration exhibits a vertical variation between different sampling sites at different seams of the lignite basin (i.e., As content of air-dried lignites of seam C is approximately 25 ppm and remarkable increasing up to 149.0 ppm for the seam A3 samples; also, As average content of heated lignite ashes varies from 78.45 ppm (for seam C samples) up to 399.5 ppm for seam A3 samples, respectively). Analogous works related to the main Drama lignite [115], and to the Philippi peatland [117] have been evaluated, as well. These latter studies affirmed the highly As enrichment to the air-dried lignites from Drama main lignite deposit (up to 138 ppm; [115]), as well as to the air-dried lignites derived from the nearby Philippi peatland (82.27–259.80 ppm; [117]). Conclusively, arsenic in the Drama lignite deposit has an increasing trend from the surrounding rocks to the air-dried lignites up to the heated (1,000°C) ashes. Additionally, authors [115] suggested that arsenic from the surrounding crystalline rocks is initially mobilized and transferred by the surface water, and whereupon is deposited in the peat swamp and subsequently incorporated in the lignite. Finally, they indicated that As does not emit to the atmosphere due to the existence of high amounts of Fe, Ca-oxides, which trap most of this hazardous element at the final lignite's residue (fly ash) during combustion.

Moreover, lignite-bearing strata have been observed in the northern part of the intermontane Ioannina basin, Epirus [111], consisting mainly of a deeper lignite formation (comprising of one solid layer) and a shallower interval (splitting into 3–4 thin layers). Relevant to the previous results statement [111] was carried out through the geochemical and mineralogical investigation of selected samples derived from this lignite-bearing deposit in point of the arsenic content of it. The study noted that As may be associated inorganically with pyrite (probably due to the absence of phosphate minerals in the lignite deposit), organically with clays or even with carbonates, as well. In general, the vertical variation of As (from 1.93 to 46.40 ppm) is strongly remarkable, and obviously is highly enriched in the shallower interval, compared to its almost depleted concentration at the deeper interval in the lignite-bearing strata of Ioannina basin. Relevant work [107] calculated the high As concentration to the air-dried lignite samples av. 46.6 ppm) and to the heated (1,000°C) ashes av. 165 ppm), as well.

Nevertheless, analogous geochemical investigation [118] at the lignite samples from Plakia deposit located at the Plakia lignite basin (Crete Island) showed an enrichment of the As concentration (16.7–47.7 ppm) comparing to that of the world's coals [119]. The authors mentioned that there is positive correlation between the As, Mo, U, and the S in the lignite samples, as well as among the S-bearing minerals and the total concentration of these chalcophile elements in the lignite, indicating directly that the As, Mo, and U, most probable, are associated with sulfur-bearing minerals.

Additionally, geochemical investigation of derived lignite samples from Megalopolis lignite basin in Peloponnese [107], southern Greece (Megalopolis Lignite Center – MLC) indicated that they also incorporate As. Arsenic concentrations

were detected in air-dried lignites av. 11.8 ppm), as well as in 1,000°C heated lignitic ashes av. 24.95 ppm).

It is well known that the combustion of the coal (e.g., lignite) produces the fly ash (i.e., coal's residue), and also that the concentration of the elements of the fly ash and their potential leachability are closely related to the coal's composition burned in the power plants and the relevant technological processes. Thus, as coal (lignite and/or xylite) from the main mining districts (i.e., Ptolemais-Amynteon Lignite Center (P-ALC) in northern Greece and Megalopolis Lignite Center (MLC) in the Peloponnese) is consumed for the electric power production, several tonnes of fly ash are produced annually. Thus, it was strongly recommended to examine the potential transfer of As source from the parent coal deposit to the residue and finally possibly to the environment, as well. Except the above investigations of heated lignite samples at 850°C [110, 113], several other published articles [120, 121] have been examined primarily the lignite industrial residue (fly ash) from the power stations of Greece (Megalopolis A, Amynteon, Agios Dimitrios, Ptolemais, and Kardias) concerning the potential passing of major and trace elements from the coal to the environment, through the exposing fly ash to the groundwater, during the subsequent landfilling of it. All of the relevant works measured the As amount that passes from the coal to the fly ash (20.5–38.8 ppm, [120, 121]) and also have calculated the As content at the fly ashes' leachates. They concluded that the As cannot easily be released from the fly ash, due to the low mobility of the element at the investigated leaching samples. Thus, As content in the fly ash of lignites has a relative low potential hazard for the environment [120, 121].

6 Potential Arsenic Sources in Metamorphic Rocks

The nature of As in metamorphic rocks of Greece differs to that of other geological sources, due to different hosting minerals. Arsenic in metamorphic rocks prefers to incorporate in several As-bearing Mn-silicates and not in sulfide minerals. These As sources are mainly located in Eocene blueschist belt of the Attico-Cycladic Crystalline Complex of the Hellenides, Aegean sea, Greece (see Fig. 3 and Table 1) and especially at Mili area, near Karystos (southern Evia) [122], at the areas of Akra Bouri and Mili [123] as well as at Andros Island in the areas of Vasilikon Mt. and Vourkoti [124], of Apikia [122] and of Apikia, Petalon, Rdisa, and Vitali [123].

In particular, on the Island of Andros, piemontite-spessartine and piemontite quartzites are the ferromanganoan metasediments that markedly accommodate As quantities [123]. These metamorphic – As enriched – rocks are derived from Mn-nodule-bearing sediments consisting of a mixture of terrigenous illitic clays with biogenic radiolarian ooze. They usually form layers of significant lateral extension intercalated within piemontite-free muscovite-chlorite quartzites and schists with scattering oxide-rich lenses. Mineralogical investigation [122, 124] not only showed the presence of quartz, piemontite, spessartine, braunite, Mg-chlorite, hematite, phengite, phlogopite, and rutile but also proved the

existence of As-bearing ardennite as accessory mineral, together with other accessories (Na-amphibolite, clinopyroxene, albite, apatite, and tourmaline), but in different quantities (mainly < 2 vol.%, and rarely between 2 and 20 vol.%). In contrast to Andros assemblages, the mineral composition of southern Evvia is quartz, piemontite, sursassite, braunite, Mg-chlorite, hematite, rutile, and titanite in coexistence with the essential accessory mineral of As-bearing ardennite [122], too. Trace element analysis of Fe,Mn-metasediments, from Andros island, confirmed the general enrichment of As (mean average: 434 ppm). It should be noted that the maximum content of As measured at 2,500 ppm. This strong enrichment was attributed [123, 124] to the allochemical processes during diagenesis and/or early high-*P* – low-*T* metamorphism (>11 kbar and 360–420°C) under highly oxidizing conditions. These processes resulted in the decomposition of the oxyhydroxides from the Mn nodules and micronodules, releasing the relative trace elements (such as As) and therefore effected to the As mobilization from the sedimentary column, which obviously taken up by hydrous pore fluids, accumulated in newly formed mineral assemblages that can accommodate selectively these elements and conclusively the subsequent concentration of the arsenic in the Mn-silicate minerals, such as ardennite. More recent work [123] examined As⁵⁺-V⁵⁺-bearing silicate ardennites from southern Evvia (Akra Bouri and Mili, near Karystos) and Andros Island (Apikia, Petalon, Rdisa, Vitali area), revealing that the Andros' ardennites are commonly Ca–Mn³⁺–As⁵⁺-rich silicate minerals. Furthermore, Pasero et al. [123] suggested that the As⁵⁺ incorporates in isolated T4 tetrahedron (Andros Island), whereas As⁵⁺ occupies sites at T4 tetrahedron together with V⁵⁺ (Akra Bouri, Southern Evvia) as well as with Si⁴⁺ (Mili, Southern Evvia). They recommended that Si⁴⁺-(As, V, P)⁵⁺ substitution in T4 is maintained by variations in the overall hydrogen content. Conversely, As⁵⁺ (or V⁵⁺ plus some Si⁴⁺) predominates in the less rigidly bounded and slightly larger T4 tetrahedron in most ardennites.

Finally, according to very recent research [125] unique As-bearing rock-forming minerals also occur in metamorphic rocks of Varnavas area (NE Attica) and Syros Island (Cyclades).

7 Arsenic in Phosphate Deposits

Neogene phosphate deposits have been well described [126] as notable As hosting rocks in Greece. Phosphate rocks, containing elevated amount of As, occur in several locations in Greece (see Fig. 3). In particular, phosphates of marine origin appearing as a thick-bedded, whitish to yellowish-brown phosphatic limestone outcrop, formed at an outer shelf-upper slope environment (Palliki peninsula, southwestern part of Kefalonia Island). Their arsenic content is varying between 5.0 and 15.0 ppm. Phosphates formed at a hemipelagic environment, occur in the northern part of the Karteros basin (Prassas Hill, Heraklion, Crete Island), embedding into a yellowish-brown sandstone beds. Chemical analysis of Cretan

phosphates revealed the highest value of As (up to 35.6 ppm) comparing to the rest of Greek phosphate deposits. On the other hand, phosphates developed in a lacustrine environment are present in Komnina area and in Vegora lignite quarry (Florina-Ptolemais lignite basin, western Macedonia) as well as in Drymos area (Sarantaporo-Elassona basin). Similar to the marine origin, but not as high amount as the Cretan deposit has, the latter phosphates exhibit a detectable As amount (Komnina deposit: 7.6 ppm; Vegora deposit: 10–15 ppm; Drymos deposit: 1.0–6.8 ppm). In all of the presented cases, As is mainly attributed to the existence of the organic matter of the hosting deposits [126].

8 Arsenic in Desert (Saharan) Dust and “Red Rain”

Huge quantities of mineral dust are transported every year from the arid desert regions of northern Africa over the Mediterranean areas (3.9×10^6 t year⁻¹). Sahara desert is responsible for the global emission of 50% of the total mass of mineral aerosols to the atmosphere. Aeolian transport of Saharan dust influences significantly the rain acidity and furthermore the climate to the Mediterranean, causing among others, intense “red (or mud) rain” and even “red snow” episodes. During these episodes geological material from Sahara is deposited to the aquatic, terrestrial, and urban environment [127–129] (see also Fig. 3). This material, transported from N. Africa to Greece, hosts both inorganic nutrients (e.g., K, Ca, Mg, Fe) and contaminants, including metals (e.g., Pb, Cr, Cu, Ni) and metalloids (mainly As). Arsenic in the dust particles is not detectable by conventional point analyses techniques such as SEM-EDS. However, recent Synchrotron-based reports revealed that As, together with other very hazardous elements such as Pb, are concentrated in specific phases of Saharan dust from “red rain” precipitated over Athens, Greece [130, 131]. It has been mentioned that the mean annual atmospheric mass fluxes are severe in south Greece, and particularly in Crete Island, reaching the value of 21 g m⁻², one of the highest in Mediterranean [132]. In the case of western Mediterranean, it has been estimated that the atmospheric input of As is 95–132 t year⁻¹ [133]. There is no specific indication for eastern Mediterranean in the literature, up to now, but it is presumed that there is a permanent supply of significant quantities of As in Greece due to annual Saharan dust deposition.

9 Conclusion

Geological sources of arsenic in the environment of Greece include As-containing ores in active and abandoned mining areas, geothermal/hydrothermal waters, lignites in exploited and unexploited deposits, As-minerals in various rock types such as metamorphic rocks, and mineral dust originating in Sahara desert. These sources, as well as various anthropogenic As fluxes, may create distinct areas of

contaminated groundwater, soils and marine environments. The most important and persisting source of As exposure to the Greek populace appears to be the geothermal and hydrothermal fluids arising from faults as well as the volcanic activity which, in turn, affect underground, surface, and marine aquatic environments. On the other hand, past mining in Greece does not affect significantly the aquatic systems, compared to the permanent supply of As in geothermal and volcanic areas. The only exception might be the Lavrion past mining area, although further research is needed to confirm this statement. The methodological approach presented in this chapter may represent a useful example for similar analyses with regard to the other areas of the world affected by As pollution.

Acknowledgements We would like to kindly thank Prof. Thomas J. Walsh, MD (Professor of Medicine in Microbiology and Immunology, Weill Cornell Medical College, USA) for critical reading and fruitful comments on the manuscript. We also thank Assist. Prof. Panagiotis Voudouris (Faculty of Geology & Geoenvironment, University of Athens, Greece) for critical discussion and comments concerning As-minerals in Lavrion historical mines and Perama Hill epithermal Au–Ag deposit (Thrace).

References

1. Henke KR, Hutchison A (2009) Arsenic chemistry. In: Henke KR (ed) Arsenic environmental chemistry, health threats and waste treatment. Wiley, UK
2. Ravenscroft P, Brammer H, Richards K (2009) Arsenic pollution: a global synthesis. RGS-IBG Book Series. Wiley, UK
3. Nriagu JO, Bhattacharya P, Mukherjee AB, Bundschuh J, Zevenhoven R, Loeppert RH (2007) Arsenic in soil and groundwater: an overview. In: Bhattacharya P et al (eds) Arsenic in soil and groundwater environment: biogeochemical interactions, health effects and remediation, vol 9, 1st edn. Elsevier, New York
4. Salminen R (ed), Batista MJ, Bidovec M, Demetriades A, De Vivo B, De Vos W, Duris M, Gilucis A, Gregorauskiene V, Halamic J, Heitzmann P, Lima A, Jordan G, Klaver G, Klein P, Lis J, Locutura J, Marsina K, Mazreku A, O'Connor PJ, Olsson SÅ, Ottesen RT, Petersell V, Plant JA, Reeder S, Salpeteur I, Sandström H, Siewers U, Steenfelt A, Tarvainen T (2005) Geochemical atlas of Europe. Part 1: background information, methodology and maps. Espoo Geological Survey of Finland, p 526. <http://weppi.gtk.fi/publ/foregsatlas/>
5. Nordstrom DK (2002) Worldwide occurrences of arsenic in ground water. *Science* 296:1–2
6. Godelitsas A, Nastos P, Mertzimekis TJ, Toli K, Simon R, Steininger R, Göttlicher J (2011) A microscopic and synchrotron-based characterization of urban particulate matter (PM₁₀-PM_{2.5} and PM_{2.5}) from Athens atmosphere, Greece. *Nuc Instrum Meth Phys Res B* 269:3077–3081
7. Caley ER (1949) On the prehistoric use of arsenical copper in the Aegean region. *Hesperia Suppl* 8:60–63, <http://www.jstor.org/stable/1353882>
8. Fitton JL (1989) *Esse Quam Videri*: a reconsideration of the Kythnos hoard of early cycladic tools. *Am J Archaeol* 93(1):31–39, <http://www.jstor.org/stable/505397>
9. Mangou H, Ioannou PV (1999) On the chemical composition of prehistoric Greek copper-based artefacts from mainland Greece. *Annual Br Sch Athens* 94:81–100, <http://www.jstor.org/stable/30103453>
10. Caley ER, Richards JFC (1956) *Theophrastus – on stones*. The Ohio State University, Columbus, p 238
11. Eichholz DE (1965) *Theophrastus “De lapidibus”*. Clarendon, Oxford, p 141

12. Zenghelis CD (1903) Ores and minerals – useful for Greece – statistical notes. Hestia Printing Office, Athens, p 15, In French
13. Ktenas K (1923) Elements of mineralogy – minerals of Greece, 2nd edn. Athens, Greece (In Greek)
14. Tsakonas A (1932) Statistics of the mining industry of Greece during the year of 1931. Ministry of Finance, Hellenic Republic, National Printing Office, p 60 (In Greek)
15. Tsakonas A (1948) Statistics of the mining industry of Greece during the year of 1947. Ministry of Finance, Hellenic Republic, National Printing Office, p 64 (In Greek)
16. Nomikou P, Kiliyas SP, Carey S, Godelitsas A, Croff Bell K, Polymenakou PN, Gamaletsos P, Betzelou K (2012) New geological, mineralogical and microbiological data of the Kolumbo shallow submarine volcano, NE of Santorini Caldera, Greece. The Deep-Sea and Sub-Seafloor Frontiers Conference – DS³F, Sitges (Barcelona), 11–14 March 2012, Spain (Abstract)
17. Nomikou P, Kiliyas SP, Godelitsas A, Sakellariou D, Argyraki A, Stathopoulou E, Betzelou K, Carey S, Cartner K, Croff Bell K, Roman C, Ballard B (2012) Evidence of the Kolumbo magmatic system from the study of erupted products and hydrothermal activity. Unrest at Santorini Caldera, Santorini Meeting, 27–28 March 2012, Santorini, Greece (Abstract)
18. Kiliyas SP, Nomikou P, Papanikolaou D, Polymenakou PN, Godelitsas A, Argyraki A, Carey S, Gamaletsos P, Mertzimekis TJ, Stathopoulou E, Goettlicher J, Steininger R, Betzelou K, Livanos I, Christakis C, Croff Bell K, Scoullou M (2013) New insights into hydrothermal vent processes in the unique shallow-submarine arc-volcano Kolumbo, Santorini (submitted to Scientific Report)
19. Kalogeropoulos SI, Kiliyas SP, Bitzios DC, Nicolaou M, Both RA (1989) Genesis of the olympias carbonate-hosted Pb-Zn(Au, Ag) sulfide ore deposit, Eastern Chalkidiki peninsula, Northern Greece. *Econ Geol* 84:1210–1234
20. Nebel ML, Hutchinson RW, Zartman RE (1991) Metamorphism and polygenesis of the Madem Lakkos polymetallic sulfide deposit, Chalkidiki, Greece. *Econ Geol* 86:81–105
21. Kiliyas SP, Kalogeropoulos SI (1988) Physicochemical conditions during ore formation of the Olympias Pb-Zn(Au, Ag) massive sulfide ore deposit, Chalkidiki Peninsula, N. Greece. Abstract in *Proc Geol Soc. Greece Cong*, 4th May 1988. Athens, Greece, p 64
22. Cabri LJ, Chryssoulis SL (1990) Genesis of the Olympias carbonate-hosted Pb-Zn(Au, Ag) sulfide ore deposit, eastern Chalkidiki peninsula, northern Greece – a discussion. *Econ Geol* 85:651–652
23. Hahn A, Naden J, Treloar PJ, Kiliyas SP, Rankin AH, Forward P (2012) A new time frame for the mineralization in the Kassandra mine district, N Greece: deposit formation during metamorphic core complex exhumation. *European Mineralogical Conference EMC2012* 1:742
24. Nikolaou M (1969) Recent research on the composition of the Kassandra mines orebodies. *Proc Acad Athens* 44:82–93 (In Greek with English abstract)
25. Eliopoulos DG, Economou-Eliopoulos M (1991) Platinum-group elements and gold contents in the Skouries porphyry copper deposits, Chalkidiki peninsula, Northern Greece. *Econ Geol* 86:740–749
26. Economou-Eliopoulos M, Eliopoulos D (1993) Platinum, palladium and gold content in the porphyry-Cu systems of the Vertiskos formation, Serbomacedonian Massif. *Bull Geol Soc Greece XXVIII*(2):393–405
27. Kelepertzis E, Argyraki A, Daftsis E, Ballas D (2010) Quality characteristics of surface waters at Asprolakkas river basin, N.E. Chalkidiki, Greece. *Bull Geol Soc Greece XLIII* (4):1737–1746
28. Argyraki A, Plakaki A, Godelitsas A (2007) Characterization of garden soil pollution within a mining village environment. *Bull Geol Soc Greece XXXVII*(3):1331–1342
29. Godelitsas A, Göttlicher J, Foustoukos D, Sanakis I, Chrissafis K, Kehagias T, Zorba T, Paraskevopoulos KM (2009) Arsenate-bearing natural schwertmannite-type phase in acid mine drainage (AMD) precipitates from N. Greece. *Geochim Cosmochim Acta* 73:A443

30. Skarpelis N (2007) The Lavrion deposit (SE Attica, Greece): Geology, mineralogy and minor elements chemistry. *Neuer Jb Miner Abh* 183(3):227–249
31. Bonsall TA, Spry PG, Voudouris PC, Tombros S, Seymour KS, Melfos V (2011) The Geochemistry of carbonate-replacement Pb-Zn-Ag mineralization in the Lavrion District, Attica, Greece: fluid inclusion, stable isotope, and rare earth element studies. *Econ Geol* 106:619–651
32. Voudouris P, Melfos V, Spry PG, Bonsall TA, Tarkian M, Economou-Eliopoulos M (2008) Mineralogical and fluid inclusion constraints on the evolution of the Plaka intrusion-related ore system, Lavrion, Greece. *Mineral Petrol* 93:79–110
33. Voudouris P, Melfos V, Spry PG, Bonsall TA, Tarkian M, Solomos C (2008) Carbonate-replacement Pb-Zn-Ag ± Au mineralization in the Kamariza area, Lavrion, Greece: mineralogy and thermochemical conditions of formation. *Miner Petrol* 94:85–104
34. Marinos GP, Petrascheck WE (1956) Laurium. *Geological and Geophysical Research* 4/1. Institute for Geology and Subsurface Research, p. 247 (In Greek)
35. Lacroix A, Schulten A (1907) Sur une nouvelle espèce minérale, provenant des scories plombées athéniennes du Laurium. *C R Acad Sci Paris* 145:783–785 (In French)
36. Lacroix A, Schulten A (1908) Note sur des minéraux plombifères des scories athéniennes du Laurium. *Bull Soc fr Minéral* 31:79–90 (In French)
37. Rouse RC, Dunn PJ (1983) New data on georgiadesite. *Mineral Mag* 47:219–220
38. Pasero M, Vacchiano D (2000) Crystal structure and revision of the chemical formula of georgiadesite, $Pb_4(AsO_3)Cl_4(OH)$. *Mineral Mag* 64(5):879–884
39. Dunn PJ, Rouse RC (1980) Nealite a new mineral from Laurion, Greece. *Mineral Rec* 11:299–301
40. Pertlik F, Schnorrer G (1993) A re-appraisal of the chemical formula of Nealite, $Pb_4Fe(AsO_3)2Cl_4 \cdot 2H_2O$, on the basis of a crystal structure determination. *Miner Petrol* 48:193–200
41. Giuseppetti G, Mazzi F, Tadini C (1993) The crystal structure of nealite: $Pb_4Fe(AsO_3)2Cl_4 \cdot 2H_2O$. *Neues Jb Miner Monatshefte* 6:278–288
42. Chukanov NV, Pushcharovsky DY, Zubkova NV, Pekov IV, Pasero M, Merlino S, Möckel S, Rabadanov MK, Belakovskiy DI (2007) Zincolivenite $CuZn(AsO_4)(OH)$: a new adamite-group mineral with ordered distribution of Cu and Zn. *Doklady Earth Sci* 415A(6):841–845
43. Chukanov NV, Pekov IV, Zadov AE (2007) Attikaite, $Ca_3Cu_2Al_2(AsO_4)_4(OH)_4 \cdot 2H_2O$, a new mineral species. *Zapiski RMO, Proc Russ Mineral Soc* 136(2):17–24 (In Russian with English abstract)
44. Chukanov NV, Pekov IV, Zadov AE (2007) Attikaite, $Ca_3Cu_2Al_2(AsO_4)_4(OH)_4 \cdot 2H_2O$, a new mineral species. *Geol Ore Deposit* 49(8):720–726
45. Chukanov NV, Pekov IV, Möckel S, Mukhanova AA, Belakovskiy DI, Levitskaya LA, Bekenova GK (2009) Kamarizaitite, $Fe_3^{3+}(AsO_4)_2(OH)_3 \cdot 3H_2O$, a new mineral species, arsenate analogue of tenticite. *Zapiski RMO, Proc Russ Mineral Soc* 138(3):100–108 (In Russian; English abstract)
46. Chukanov NV, Pekov IV, Möckel S, Mukhanova AA, Belakovskiy DI, Levitskaya LA, Bekenova GK (2010) Kamarizaitite, $Fe_3^{3+}(AsO_4)_2(OH)_3 \cdot 3H_2O$, a new mineral species, arsenate analogue of tenticite. *Geol Ore Deposit* 52(7):599–605
47. Pekov IV, Chukanov NV, Yapaskurt VO, Rusakov VS, Belakovskiy DI, Turchkova AG, Voudouris P, Katerinopoulos A, Magganas A (2012) Hilarionite, IMA 2011-089. *CNMNC Newsletter No. 12, February 2012*, page 154. *Mineral Mag* 76:151–155
48. Pekov IV, Chukanov NV, Zadov AE, Voudouris P, Magganas A, Katerinopoulos A (2011) Agardite-(Nd), $NdCu_6(AsO_4)_3(OH)_6 \cdot 3H_2O$, from the Hilarion mine, Lavrion, Greece: mineral description and chemical relations with other members of the agardite-zálesiite solid-solution system. *J Geosci* 56:249–255
49. Pekov IV, Chukanov NV, Zadov AE, Voudouris P, Magganas A, Katerinopoulos A (2011) Agardite-(Nd), IMA 2010-056. *CNMNC Newsletter No. 7, February 2011*, page 30. *Mineral Mag* 75:27–31

50. Siidra OI, Krivovichev SV, Chucanov NV, Pekov IV, Magganas A, Katerinopoulos A, Voudouris P (2011) The crystal structure of $Pb_5(AsO_3^{3+}OH_3)Cl_7$ from the historic slags of Lavrion, Greece – a novel PB(II) chloride arsenite. *Mineral Mag* 75(2):337–345
51. Siidra OI, Chucanov NV, Pekov IV, Krivovichev SV, Magganas A, Katerinopoulos A, Voudouris P (2012) $Pb_2(AsO_2OH)Cl_2$, a new phase from the Lavrion ancient slags, Greece: occurrence and characterization. *Mineral Mag* 76(3):597–602
52. Arikas K, Watzl V, Goetz D (2004) The environmental pollution from mining activities in Kirki, Alexandroupolis area. *Bull Geol Soc Greece XXXVI*:140–149 (In Greek with English abstract)
53. Triantafyllidis S (2006) Environmental risk assessment of mining and processing activities and rehabilitation proposals in Evros and Rhodope prefectures (Thrace, NE Greece). PhD Thesis. University of Athens, Athens, Greece, p 307. (In Greek – unpublished)
54. Arikas K (2007) Mineralogical and geochemical study of the Kirki mining wastes, Evros region, Greece – determination of the environmental impact by toxic and heavy metals. *Bull Geol Soc Greece* 40(3):1343–1353
55. Triantafyllidis S, Skarpelis N (2006) Mineral formation in an acid pit lake from a high-sulfidation ore deposit: Kirki, NE Greece from a high-sulfidation ore deposit: Kirki, NE Greece. *J Geochem Explor* 88:68–71
56. Triantafyllidis S, Skarpelis N (2010) Geochemical investigation and modeling of an acid pit lake from a high sulfidation ore deposit: Kirki, NE Greece. *Bull Geol Soc Greece XLIII* (5):2417–2424
57. Zacharia C (2010) Description of pollutants dispersion from mining activities using modern software tools. Diploma Thesis, National Technical University of Athens, Athens, Greece, p 121. (In Greek with English abstract – unpublished)
58. Voudouris P, Papavassiliou C, Melfos V (2005) Silver mineralogy of St Philippos deposit (NE Greece) and its relationship to a Te-bearing porphyry-Cu-Mo mineralization. In: Cook N, Bonev I (eds), Au-Ag-Te-Se deposits. *Geochem Mineral Petrol* 43:155–160
59. Moëlo Y, Oudin E, Makovicky E, Karup-Møller S, Pillard F, Bornuat M, Evangelou E (1985) La kirkiite, $Pb_{10}Bi_3As_3S_{19}$, une nouvelle espèce minérale homologue de la jordanite. *Bull Mineral* 108:667–677 (In French with English abstract)
60. Dimou E (1987) Mineralogical composition of Kirki ore deposit (Aghios Philippos ore deposit). Impacts to the ore enrichment. In report of the institute of geology and mineral exploration – I.G.M.E., p 55 (Internal Report – unpublished data)
61. Michael C, Konstantinides D, Ashworth K, Perdikatsis V, Demetriades A (1989) The Kirki vein polymetallic mineralization. *Geol Rhodopica* 1:366–373
62. Michailidis K, Filippidis A, Vavelidis M, Evangelou E (1989) Chemical composition of some ore minerals from the St. Philippos (Kirki) polymetallic deposits. *Geol Rhodopica* 1:389–395
63. Vavelidis M, Filippidis A, Michailidis K, Evangelou E (1989) The polymetallic ore mineralization of the Kirki area, Alexandroupolis district, Northern Greece. *Geol Rhodopica* 1:350–365
64. Skarpelis N (1999) The Aghios Philippos ore deposit, Kirki (Western Thrace). A base-metal part of a high-sulfidation epithermal system. *Bull Geol Soc Greece XXXIII*:51–60
65. Makovicky E, Balić-Žunić T, Karanović L, Poleti D (2006) The crystal structure of Kirkiite, $Pb_{10}Bi_3As_3S_{19}$. *Can Mineral* 44:177–188
66. Lescuyer JL, Bailly L, Cassard D, Lips ALW, Piantone P, McAlister M (2003) Sediment-hosted gold in south-eastern Europe: the epithermal deposit of Perama, Thrace, Greece. In: Eliopoulos DG et al (eds) *Mineral exploration and sustainable development*. Millpress, Rotterdam, pp 499–502
67. Voudouris P, Papavassiliou C, Alfieris D, Falalakis G (2007) Gold-silver tellurides and bismuth sulfosalts in the high-intermediate sulfidation Perama Hill deposit, western Thrace (NE Greece). *Geol Surv Finl* 53:77–84
68. Voudouris P, Spry PG, Melfos V, Alfieris D (2007) Tellurides and bismuth sulfosalts in gold occurrences of Greece: mineralogical and genetic considerations. *Geol Surv Finl* 53:85–94

69. Eliopoulos DG, Economou-Eliopoulos M (2010) Arsenic distribution in laterite deposits of the Balkan Peninsula. *Proceedings of the XIX CBGA Congress, Thessaloniki, Greece* 100:325–332
70. Eliopoulos DG, Economou-Eliopoulos M, Apostolikas A, Golightly JP (2012) Geochemical features of nickel-laterite deposits from the Balkan peninsula and Gordes, Turkey: the genetic and environmental significance of arsenic. *Ore Geol Rev* 48:413–427
71. Paraskevopoulos GM (1958) Genesis of tungsten and antimony ore deposits in the Lahana area, Central Macedonia. *Ann Geol Pays Hell* 9:227–241 (In Greek with German abs)
72. Kelepertsis A (1980) The mineralogical-geochemical features of the antimony ore deposits in Central Macedonia and their genesis problem. *Proc Acad Athens* 55:156–168 (In Greek with English abstract)
73. Kalaitzidis S, Siavalas G, Skarpelis N, Araujo CV, Christanis K (2010) Late Cretaceous coal overlying karstic bauxite deposits in the Parnassus-Ghiona unit, central Greece: coal characteristics and depositional environment. *Int J Coal Geol* 81:211–226
74. Laskou M, Economou-Eliopoulos M (2007) The role of microorganisms on the mineralogical and geochemical characteristics of the Parnassos-Ghiona bauxite deposits, Greece. *J Geochem Explor* 93:67–77
75. Godelitsas A, Gamaletsos P, Mertzimekis TJ, Göttlicher J, Steininger R, Bárdossy G (2012) Distribution and speciation of contaminants in bauxite and red mud from Ajka alumina plant, Hungary. ANKA Synchrotron Facility (KIT) Annual Report 2012 (in press)
76. Gamaletsos P et al (2013) New insights into the mineralogy and geochemistry of Greek karst bauxites (in preparation)
77. Eliopoulos DG, Kiliass SP (2011) Marble-hosted submicroscopic gold mineralization at Asimotrypes area, Mount Pangeon, Southern Rhodope core complex, Greece. *Econ Geol* 106:751–780
78. Skounakis S, Sovatzoglou-Skounakis E (1983) Cobaltite from the Trifon sulphide mineralization occurrences (Veria, Greece). *Chem Erde-Geochem* 42:63–68
79. Economou-Eliopoulos M, Eliopoulos D, Chryssoulis S (2008) A comparison of high-Au massive sulfide ores hosted in ophiolite complexes of the Balkan Peninsula with modern analogues: genetic significance. *Ore Geol Rev* 33:81–100
80. Skounakis S (1973) The origin of the copper ore deposit of Paliouri area (District of Karditsa). *Ann Geol Pays Hell* 25:317–327 (In Greek with English abstract)
81. Migiros G (1998) The mineral wealth of Thessaly (Central Greece). Geotectonic setting – resource development. *Miner Wealth* 108:15–26 (In Greek with English abstract)
82. Skordas K, Kelepertsis A (2005) Soil contamination by toxic metals in the cultivated region of Agia, Thessaly, Greece. Identification of sources of contamination. *Environ Geol* 48:615–624
83. Kelepertsis A, Alexakis D, Skordas K (2006) Arsenic, antimony and other toxic elements in the drinking water of Eastern Thessaly in Greece and its possible effects on human health. *Environ Geol* 50:76–84
84. Chatzidiakos E, Fanouraki M, Kelepertsis A, Argyraki A, Alexakis D (2009) Speciation and mobility of Arsenic and Antimony in groundwater at Melivoia, East Thessaly and Keramos area NW Chios, Greece. In: *Proceedings of the 8th international hydrogeological congress of Greece, Athens, vol 1* pp 219–228
85. Yan-Chu H (1994) Arsenic distribution in soils. In: Nriagu JO (ed) *Arsenic in the environment, Part I: Cycling and characterization*. Wiley, Hoboken, pp 17–47
86. Hughes MF, Beck BD, Chen Y, Lewis AS, Thomas DJ (2011) Arsenic exposure and toxicology: a historic perspective. *Toxicol Sci* 123(2):305–332
87. Tombros S, Seymour KST, Williams-Jones AE, Spry PG (2007) The genesis of epithermal Au-Ag-Te mineralization, Panormos Bay, Tinos Island, Cyclades, Greece. *Econ Geol* 102 (7):1269–1294

88. Tombros SF, Seymour KST, Williams-Jones AE, Spry PG (2008) Later stages of evolution of an epithermal system: Au-Ag mineralizations at Apigania Bay, Tinos Island, Cyclades, Hellas, Greece. *Miner Petrol* 94:175–194
89. Aloupi M, Angelidis MO, Gavriil AM, Koulousaris M, Varnavas SP (2009) Influence of geology on arsenic concentrations in ground and surface water in central Lesvos, Greece. *Environ Monit Assess* 151:383–396
90. Mitrakas M (2001) A survey of arsenic levels in tap underground and thermal mineral waters of Greece. *Fresenius Environ Bull* 10:717–721
91. Nimfopoulos MK, Hadjispyrou SA, Polya DA, Michailidis K, Trontsios G (2002) Geochemical conditions and environmental pollution from hydrothermal waters of the Anthemous Basin, Thessaloniki District, N. Greece. In: *Proceedings 6th Congress Geographical Society of Greece*, pp 428–436
92. Fytianos K, Christoforidis C (2004) Nitrate arsenic and chloride pollution of drinking water in Northern Greece. Elaboration by applying GIS. *Environ Monit Assess* 93:55–67
93. Katsoyiannis IA, Katsoyiannis AA (2006) Arsenic and other metal contamination of ground waters in the industrial area of Thessaloniki, Northern Greece. *Environ Monit Assess* 151:383–396
94. Katsoyiannis IA, Hug SJ, Ammann A, Zikoudi A, Hatziliontos C (2007) Arsenic speciation and uranium concentrations in drinking water supply wells in Northern Greece: correlations with redox indicative parameters and implications for groundwater treatment. *Sci Total Environ* 383:128–140
95. Kouras A, Katsoyiannis I, Voutsas D (2007) Distribution of arsenic in groundwater in the area of Chalkidiki, Northern Greece. *J Hazard Mater* 147:890–899
96. Voutsas D, Dotsika E, Kouras A, Poutoukis D, Kouimtzis T (2009) Study on distribution and origin of boron in groundwater in the sea of Chalkidiki, Northern Greece by employing chemical and isotopic tracers. *J Hazard Mater* 172:1264–1272
97. Cassentini B, Hug SJ, Nikolaidis NP (2011) Arsenic accumulation in irrigated agricultural soils in Northern Greece. *Sci Total Environ* 409:4802–4810
98. Winkel LHE, Casentini B, Bardelli F, Voegelin A, Nikolaidis NP, Charlet L (2013) Speciation of As in Greek travertines: co-precipitation of arsenate with calcite. *Geochim Cosmochim Acta* 106:99–110
99. Lazaridis G, Melfos V, Papadopoulou L (2011) The first cave occurrence of orpiment (As_2S_3) from the sulfuric acid caves of Aghia Paraskevi (Kassandra Peninsula, N. Greece). *Int J Speleol* 40(2):133–139
100. Huebner A, Rahder E, Rahnera S, Halbach P, Varnavas SP (2004) Geochemistry of hydrothermally influenced sediments off Methana (western Hellenic volcanic arc). *Chem Erde-Geochem* 64:75–94
101. Rudnick R, Gao S (2003) Composition of the continental crust. In: *The Crust* HD. Holland HD, Turekian KK (eds) *Treatise on geochemistry*, vol. 3. Elsevier – Pergamon, Oxford, pp 1–64
102. Cronan DS, Varnavas SP (2001) Metalliferous sediments off Milos, Hellenic volcanic Arc. *Explor Min Geol* 8:289–297
103. Varnavas SP, Cronan DS (2005) Submarine hydrothermal activity off Santorini and Milos Central Hellenic volcanic arc: a synthesis. *Chem Geol* 224:40–54
104. Price RE, Savov I, Planer-Friedrich B, Bühring SI (2013) Processes influencing extreme As enrichment in shallow-sea hydrothermal fluids of Milos Island, Greece. *Chem Geol*, in press. <http://dx.doi.org/10.1016/j.chemgeo.2012.06.007>
105. Varnavas SP, Cronan DS (1991) Hydrothermal metallogenic processes off the islands of Nisiros and Kos in the Hellenic volcanic arc. *Mar Geol* 99:109–133
106. Varnavas SP, Cronan DS (1988) Arsenic, antimony and bismuth in sediments and waters from Santorini hydrothermal field, Greece. *Chem Geol* 67:295–305
107. Foscolos AE, Goodarzi F, Koukouzas CN, Hatziyiannis G (1989) Reconnaissance study of mineral matter and trace elements in Greek lignites. *Chem Geol* 76:107–130

108. Koukouzas C, Koukouzas N (1995) Coals of Greece: distribution, quality and reserves. In: Whateley MKG, Spears DA (eds) *European coal geology*, vol. 82. Geol Soc Spec Publ, pp 171–180
109. Papanicolaou C, Kotis T, Foscolos A, Goodarzi F (2004) Coals of Greece: a review of properties, uses and future perspectives. *Int J Coal Geol* 58:147–169
110. Pentari D, Foscolos AE, Perdikatsis V (2004) Trace element contents in the Domeniko lignite deposit, Elassona basin, central Greece. *Int J Coal Geol* 58:261–268
111. Gentzis T, Goodarzi F, Foscolos AE (1997) Geochemistry and mineralogy of Greek lignites from the Ioannina Basin. *Energy Source* 19:111–128
112. Georgakopoulos A (2001) Trace elements in the Lava xylite/lignite deposit, Servia basin, northern Greece. *Energy Source* 23:143–156
113. Pentari D, Foscolos AE, Perdikatsis V (2008) Trace elements in the lignite-bearing area of Lofoi, Florina basin, Western Greek Macedonia, Greece. *Energy Source* 30:316–324
114. Mason B, Moore CB (1982) *Principles of geochemistry*. Wiley, NY
115. Foscolos AE, Goodarzi F, Koukouzas C, Hatziyiannis G (1998) Assessment of environmental impact of coal exploration and exploitation in the Drama basin, northeastern Greek – Macedonia. *Energy Source* 20(9):795–820
116. Filippidis A, Georgakopoulos A, Kassoli-Fourmaraki A, Misaelides P, Yiakkoupis P, Broussoulis J (1996) Trace element contents in composited samples of three lignite seams from the central part of the Drama lignite deposit, Macedonia, Greece. *Int J Coal Geol* 29:219–234
117. Christanis K, Georgakopoulos A, Fernández-Turiel JL, Bouzinos A (1998) Geological factors influencing the concentration of trace elements in the Philippi peatland, eastern Macedonia, Greece. *Int J Coal Geol* 36:295–313
118. Gentzis T, Goodarzi F, Koukouzas CN, Foscolos AE (1996) Petrology, mineralogy, and geochemistry of lignites from Crete, Greece. *Int J Coal Geol* 30:131–150
119. Clarke L, Sloss L (1992) Trace elements: emissions from coal combustion and gasification. *Int Energy Agency Rep CR/49*, London, p 111
120. Georgakopoulos A, Filippidis A, Kassoli-Fourmaraki A, Fernandez-Turiel JL, Llorens JF, Mousty F (2002) Leachability of major and trace elements of fly ash from Ptolemais power station, northern Greece. *Energy Source* 24:103–113
121. Georgakopoulos A, Filippidis A, Kassoli-Fourmaraki A, Iordanidis A, Fernandez-Turiel JL, Llorens JF, Gimeno D (2002) Environmentally important elements in fly ashes and their leachates of the power stations of Greece. *Energy Source* 24:83–91
122. Reinecke T (1986) Phase relationships of sursassite and other Mn-silicates in highly oxidized low-grade, high-pressure metamorphic rocks from Evvia and Andros Islands, Greece. *Contrib Miner Petr* 94:110–126
123. Pasero M, Reinecke T, Fransolet AM (1994) Crystal structure refinements and compositional control of Mn–Mg–Ca ardennites from the Belgian Ardennes, Greece, and the Western Alps. *Neuer Jb Miner Abh* 166(2):137–167
124. Reinecke T, Okrusch M, Richter P (1985) Geochemistry of ferromanganoan metasediments from the island of Andros, Cycladic blueschist belt, Greece. *Chem Geol* 53:249–278
125. Godelitsas A et al (2012) As and Sb minerals in metamorphic rocks of Attico-Cycladic complex: a review and new data (in preparation)
126. Stamatakis MG (2004) Phosphate deposits of Neogene age in Greece. *Mineralogy, geochemistry and genetic implications*. *Chem Erde-Geochem* 64:329–357
127. Avila A, Queralt-Mitjans I, Alarcón M (1997) Mineralogical composition of African dust delivered by red rains over northeastern Spain. *J Geophys Res* 102(D18):21977–21996
128. Loÿe-Pilot MD, Martin JM, Morelli J (1986) Influence of Saharan dust on the rain acidity and atmospheric input to the Mediterranean. *Nature* 321:427–428
129. Papastefanou C, Manolopoulou M, Stoulos S, Ioannidou A, Gerasopoulos E (2001) Coloured rain dust from Sahara Desert is still radioactive. *J Environ Radioactiv* 55:109–112

130. Godelitsas A, Toli K, Simon R (2009) Elemental distribution in Saharan dust from red rain precipitated over Athens, Greece. ANKA Synchrotron Facility (KIT) Annual Report 2009
131. Godelitsas A, Nastos P, Mertzimekis TJ, Toli K, Simon R, Steininger R, Göttlicher J (2010) Characterization of Saharan dust and urban particulate matter (PM_{2.5} and PM₁₀) from Athens atmosphere, Greece. ANKA Synchrotron Facility (KIT) Annual Report 2009/2010
132. Statham PJ, Hart V (2005) Dissolved iron in the Cretan Sea (eastern Mediterranean). *Limnol Oceanogr* 50(4):1142–1148
133. Elbaz-Poulichet F, Guieu C, Morley NH (2001) A reassessment of trace metal budgets in the western Mediterranean sea. *Mar Pollut Bull* 42(8):623–627
134. Dunn PJ, Rouse RC (1985) Freedite and thorikosite from Långban, Sweden, and Laurion, Greece: two new species related to the synthetic bismuth oxyhalides. *Am Mineral* 70:845–848
135. Downs RT (2006) The RRUFF Project: an integrated study of the chemistry, crystallography, Raman and infrared spectroscopy of minerals. Program and Abstracts of the 19th General Meeting of the International Mineralogical Association in Kobe, Japan. O03-13. http://rruff.info/about/about_general.php
136. Rakovan J (2007) Words to the wise – more than 4,000 to be expected. *Rocks Miner* 82(5):423–424
137. Tarvainen T, Reeder S, Albanese S (2005) Database management and map production. In: Salminen R et al. (ed) *Geochemical atlas of Europe. Part 1: background information, methodology and maps*. Espoo, Geological Survey of Finland, p 526, 36 figures, 362 maps. <http://weppi.gtk.fi/publ/foregsatlas/>

Groundwater Contamination Studies by Environmental Isotopes: A review

Barbara Nisi, Brunella Raco, and Elissavet Dotsika

Abstract Water demand for urban, industrial, and agricultural purposes is a major concern in developed and third world countries. A careful evaluation for an appropriate and sustainable use of water resources is a priority. Geochemical processes can lead to measurable variations of the aquatic environment, which can be studied through the analysis of the dissolved solutes. Even if this review is not meant to be exhaustive, it is intended to give a view on the importance of environmental isotopes in the context of groundwater quality assessments. This is done by briefly recalling some basic notions for each described system, followed by relevant applications and reports about some significant case studies. This review includes well-established isotopic systematics, such as those of O and H in water, C in dissolved inorganic carbon (DIC), S and O in sulfates, and N and O in nitrates and those of boron and Sr, which in the last lustrums have found large application in the field of water geochemistry. This chapter ends with some examples related to nontraditional isotopes, i.e., Fe, Cr, and Cu, in order to highlight the potential of the environmental isotopes to trace sources, fate, and behavior of different solutes and metals in surface water and groundwater.

Keywords Environmental isotopes, Groundwater, Isotopic fractionation, Land management, Untraditional isotopes

B. Nisi (✉) and B. Raco

CNR-IGG Institute of Geosciences and Earth Resources, Via Moruzzi, 1, 56124 Pisa, Italy
e-mail: b.nisi@igg.cnr.it

E. Dotsika

Stable Isotope Unit, Institute of Materials Science, National Centre for Scientific Research “Demokritos”, 153 10 Agia Paraskevi, Athens, Greece

Contents

1	Introduction	117
2	Hydrogen and Oxygen Stable Isotopes	119
2.1	Background Principles	119
2.2	Groundwater Origin, Recharge, and Mixing Processes	120
3	Carbon Stable Isotopes	123
3.1	Background Principles	123
3.2	Applications to Environmental Geochemistry Studies	124
4	Sulfur Stable Isotopes	126
4.1	Background Principles	126
4.2	Application Studies to Groundwater and Surface Waters	128
5	Nitrogen Stable Isotopes	130
5.1	Background Principles	130
5.2	Applications to Groundwater and Surface Water Studies	131
6	Boron and Strontium Isotopes	133
6.1	Background Principles	133
6.2	Isotope Applications in Hydrology	135
7	Untraditional Isotopes: The Metal (Fe, Cr, and Cu) Stable Isotopes	136
7.1	Iron Isotopes	136
7.2	Chromium Isotopes	138
7.3	Copper Isotopes	139
8	Conclusions	140
	References	141

Abbreviations

AMD	Acid Mine Drainage
CCS	Carbon Capture and Storage
CDT	Canyon Diablo Troilite
CIMWL	Central Italy Meteoric Water Line
DIC	Dissolved Inorganic Carbon
GMWL	Global Meteoric Water Line
IAEA	International Atomic Energy Agency
IRMM	Institute for Reference Materials and Measurements
MMWL	Mediterranean Meteoric Water Line
NIST	National Institute of Standards and Technology
SLAP	Standard Light Antarctic Precipitation
SMOW	Standard Mean Ocean Water
SRM	Standard Reference Materials
VPDB	Vienna Pee Dee Belemnite
VSMOW	Vienna Standard Mean Ocean Water

1 Introduction

Deterioration of water quality has received considerable attention over the last few decades in response to the increasingly severe contamination of surface water and shallow groundwater by anthropogenic contaminants [1, 2]. Groundwater is an important alternative source of water supply for those cities located in arid to semiarid climates. New awareness of the potential danger to water supplies posed by the use of agricultural chemicals and urban industrial development has also focused attention on the nature of rainfall–runoff and recharge processes and the mobility of various solutes in shallow systems [3]. A proper assessment of groundwater quality requires the quantification of the total recharge and the composition of the various sources involved. These quantitative assessments enable to identify the origin and the fate of chemical compounds and also develop management practices to preserve water quality and devise remediation plans for sites that are already polluted.

Natural waters are complex chemical solutions. They always contain a number of dissolved species, suspended materials, and organic substances. Stable, radiogenic, and radioactive isotopes of elements or compounds present in the aqueous medium are outstanding sources of information on the processes occurring in the hydrosphere [4]. The most widely used isotopes in hydrogeochemistry are the stable isotopes of oxygen, hydrogen, carbon, sulfur, and nitrogen and the cosmogenic radioisotopes such as tritium and carbon-14. Other investigations on the stable and radioactive isotopes of helium, strontium, and others are also frequently applied. However, in the recent years, nontraditional stable isotopes of metals (e.g., Li, Mg, Fe, Cu, Zn) have been successfully studied in different geological materials, as more precise and powerful instrumentations and improved analytical capabilities have been introduced. Similarly, investigations on mass-independent isotope geochemistry, the use of clumped isotope geochemistry, and measurements of position-specific isotope effects in organic compounds will be providing new insights in the comprehension of the geochemical processes that affect the exogenous and endogenous cycles of the elements, opening new frontiers in the field of isotope geochemistry.

Environmental isotope studies of natural waters are concerned with the principles governing the distribution of the stable and radioactive isotopes in the hydrosphere. Such studies are aimed to estimate the factors that determine these principles and to interpret hydrodynamical and hydrogeochemical processes involved on the basis of the isotope composition of the various elements in solution. Currently, environmental isotopes routinely contribute to such investigations, complementing geochemistry and hydrogeology. For instance, the stable isotopic composition of water is modified by meteoric process, and so the recharge waters in a particular environment will acquire a characteristic isotopic signature. This signature then serves as a natural tracer. Isotope tracers have been extremely useful in providing new insights into hydrologic processes because they integrate small-

$\begin{matrix} 2 \\ 1 \end{matrix} \text{H}$ Hydrogen-2 2.014101	$\begin{matrix} 13 \\ 6 \end{matrix} \text{C}$ Carbon-13 13.00335	$\begin{matrix} 15 \\ 7 \end{matrix} \text{N}$ Nitrogen-15 15.00010	$\begin{matrix} 18 \\ 8 \end{matrix} \text{O}$ Oxygen-18 17.99916	$\begin{matrix} 34 \\ 16 \end{matrix} \text{S}$ Sulphur-34 33.96786
$\begin{matrix} 1 \\ 1 \end{matrix} \text{H}$ Hydrogen-1 1.007825	$\begin{matrix} 12 \\ 6 \end{matrix} \text{C}$ Carbon-12 12.00000	$\begin{matrix} 14 \\ 7 \end{matrix} \text{N}$ Nitrogen-14 14.00307	$\begin{matrix} 16 \\ 8 \end{matrix} \text{O}$ Oxygen-16 15.99491	$\begin{matrix} 32 \\ 16 \end{matrix} \text{S}$ Sulphur-32 31.97207

Fig. 1 Differences in the chemical properties of the isotopes H, C, N, O, and S

scale variability to give an effective indication of the processes occurring at catchment-scale.

The environmental isotopes represent one of the most useful tools in geochemistry to investigate groundwater quality, geochemical evolution, recharge processes, rock–water interaction, and the origin of salinity and contaminant processes.

The main purpose of this chapter is to provide an overview of recent advances in the use of naturally occurring stable isotopes including radiogenic isotopes (e.g., Sr), which are important hydrological tracers for recognizing natural and anthropogenic processes in aquifer systems.

It is a matter of fact that the isotopic systematics of specific ratios or single isotopic abundances are well known, whereas other isotopes are considered not too exhaustively discussed as no many data are still available. Eventually, new isotopic pairs have recently been applied to the context of environmental geochemistry and can be considered as new frontiers in this important discipline.

The structure of this chapter reflects the composite framework described above. This chapter firstly reviews well-established isotopic applications (oxygen and hydrogen in H_2O , carbon in dissolved inorganic carbon (DIC), nitrogen and oxygen in nitrates, and sulfur and oxygen in sulfates, whose reference isotopes are reported in Fig. 1). Then, some hints about recently applied isotopic ratios ($^{87}\text{Sr}/^{86}\text{Sr}$ and $^{11}\text{B}/^{10}\text{B}$) are described. The last part of the chapter deals with new isotopic ratios (iron, chromium, and copper), whose studies are still to be defined as they deserve to be more deeply investigated. For the sake of brevity, radiometric age dating of water with ^3H , ^{14}C , ^{81}Kr , and ^{36}Cl has been omitted in this chapter, being rather marginal to the context. The reader may refer to the following papers, which are specifically addressed to the topics related to water dating: e.g., Morgenstern et al. [5] and Stewart et al. [6] (tritium), Schiff et al. [7] and Mayorga et al. [8]

(carbon), Lange and Hebert [9] and Visser et al. [10] (krypton), and Palau et al. [11] and Khaska et al. [12] (chlorine).

2 Hydrogen and Oxygen Stable Isotopes

2.1 Background Principles

Both hydrogen and oxygen consist of a number of isotopes, whose variations in natural waters are the basis for applying the isotope methodology in hydrology. Hydrogen, whose major stable isotope is ^1H , occurs in the hydrosphere at a mass abundance of 99.985% and is accompanied by 0.015% of the heavy isotope, ^2H or *deuterium*. The chemical element oxygen has three stable isotopes, ^{16}O , ^{17}O , and ^{18}O , with abundances of 99.76, 0.035, and 0.2%, respectively [4]. Stable environmental isotopes are measured as the ratio of the two most abundant isotopes, for instance, $^2\text{H}/^1\text{H}$ or $^{18}\text{O}/^{16}\text{O}$ (the rare isotope at numerator and the more abundant at denominator), and are referred to international reference standards by using the typical δ notation defined as follows:

$$\delta = \frac{R_{\text{sample}}}{R_{\text{standard}}} - 1 \quad (1)$$

where R is the abundance ratio of the isotopic species (i.e., $^2\text{H}/^1\text{H}$ or $^{18}\text{O}/^{16}\text{O}$). Since δ is usually a small number, the “delta” is given in ‰ (per mil, equivalent to 10^{-3}). The δ notation for $^2\text{H}/^1\text{H}$ and $^{18}\text{O}/^{16}\text{O}$ can be expressed as $^2\delta$ or $\delta^2\text{H}$ and $^{18}\delta$ or $\delta^{18}\text{O}$, respectively. The accepted standard for the isotopes in water is VSMOW (Vienna Standard Mean Ocean Water), which is close to the original standard of SMOW (hypothetical water catalogued by the former National Bureau of Standards), as defined by Craig [13]. Abundance ratios for $^2\text{H}/^1\text{H}_{\text{VSMOW}}$ and $^{18}\text{O}/^{16}\text{O}_{\text{VSMOW}}$ are $155.75 \pm 0.05 \times 10^{-6}$ [14–16] and $2,005.20 \pm 0.45 \times 10^{-6}$ [17], respectively. These abundances are the values reported for the reference standard VSMOW, defining the value of $\delta=0\text{‰}$ on the VSMOW scale. For waters which have depleted $\delta^2\text{H}$ and $\delta^{18}\text{O}$ values with respect to that of ocean water, a second water standard was distributed by the International Atomic Energy Agency (IAEA): Standard Light Antarctic Precipitation (SLAP). This value with respect to VSMOW was evaluated on the basis of an interlaboratory comparison by IAEA, defined as $\delta^2\text{H} = -428.0\text{‰ VSMOW}$ and $\delta^{18}\text{O}_{\text{SLAP}} = -55.50\text{‰ VSMOW}$ [18].

The isotopes of hydrogen and oxygen, being components of water molecules, are indicators of all the processes of natural water movement, which have occurred during the history of existence of the Earth. According to Rozanski et al. [4] in the hydrologic cycle, the variability ranges of $^2\text{H}/^1\text{H}$ and $^{18}\text{O}/^{16}\text{O}$ are between -450 and $+100\text{‰}$ and from -50 to $+50\text{‰}$, respectively. In general, the $^2\text{H}/^1\text{H}$ or $^{18}\text{O}/^{16}\text{O}$ ratios mainly vary due to phase changes from vapor to liquid or ice and vice versa.

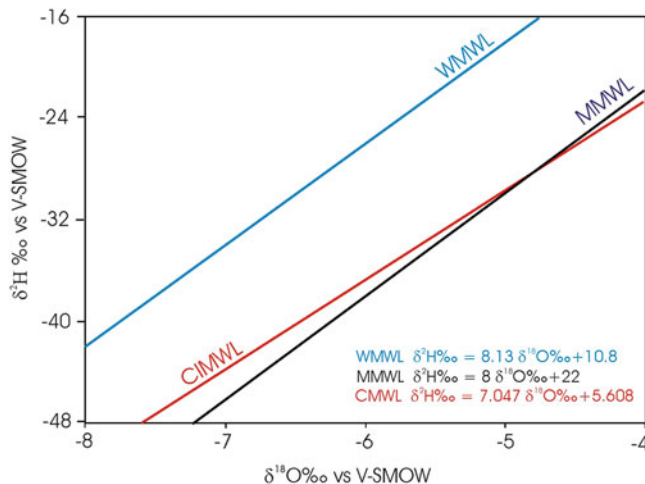


Fig. 2 Binary diagram of the isotopic ratios of hydrogen vs. oxygen. Mediterranean Meteoric Water Line (MMWL) [20], World Meteoric Water Line (WMWL) [21], and Central Italy Meteoric Water Line (CIMWL) [22]. From Sappa et al. [23], modified

The ratios of hydrogen and oxygen isotopes are linearly correlated, and the trend of variations characterizes the Global Meteoric Water Line (GMWL) where $\delta^2\text{H} = 8\delta^{18}\text{O} + 10$ [19]. Later on, Gat and Carmi [20] suggested for the Mediterranean Meteoric Water Line (MMWL) the relationship $\delta^2\text{H} = 8\delta^{18}\text{O} + 15$ between $\delta^2\text{H}$ and $\delta^{18}\text{O}$. In the classical $\delta^2\text{H}$ vs. $\delta^{18}\text{O}$ binary diagram, the reference meteoric lines, e.g., GMWL and MMWL, are commonly drawn with those of local and/or regional interest (Fig. 2). For the most part, the positive intercept in this regression originates from the difference in isotopic fractionation effects of water-vapor equilibrium and of vapor diffusion in air (e.g., review of [24]). Deviations from a line with slope of 8 and zero intercept indicate an excess (or depletion) of deuterium defined by Dansgaard [25] as $d\text{-excess} = \delta^2\text{H} - 8\delta^{18}\text{O}$. It has mainly been correlated with the environmental conditions existing in the source area of the water vapor [20, 26]. The degree of excess (or depletion) is phenomenologically related to geographic parameters such as latitude, altitude, and distance from the coast and to the fraction precipitated from a vapor mass content (e.g., [27–31]) (Fig. 3).

2.2 Groundwater Origin, Recharge, and Mixing Processes

One of the most typical applications in isotope hydrology is the identification of recharge areas of underground aquifers by comparing the isotopic signatures of precipitation and with those of groundwaters collected from springs and/or wells.

Spatial variability of the $\delta^2\text{H}$ or $\delta^{18}\text{O}$ values in precipitation reflects the combination of source-region labeling, rainout, and recycling effects that affect air masses

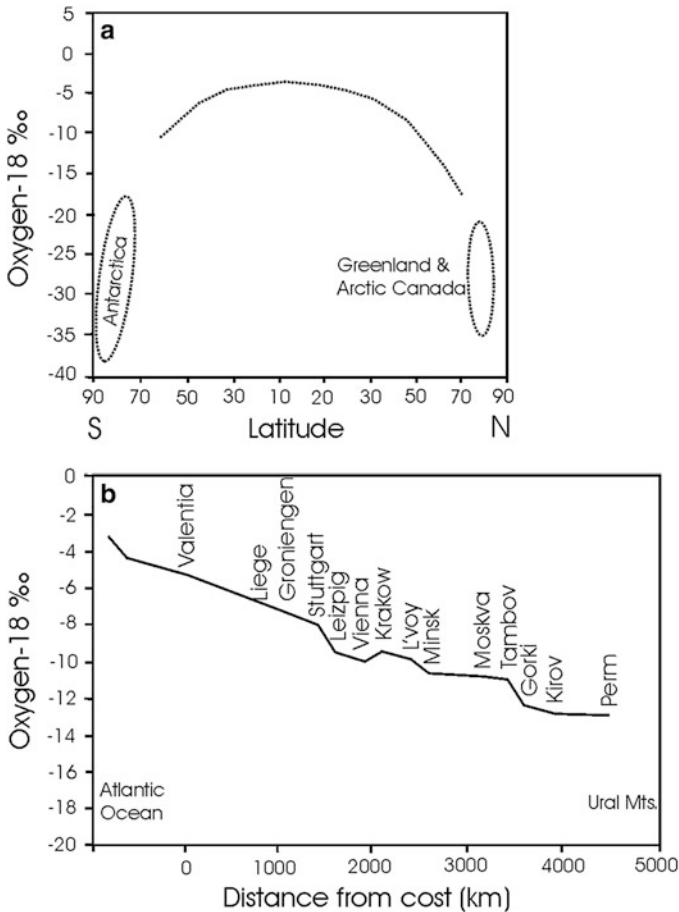


Fig. 3 Distribution of $\delta^{18}\text{O}$ values correlated with latitude (a) and distance from the coast (b)

bringing vapor to different geographic regions. The isotopic compositions of precipitation have been mapped at several scales: global distribution (e.g., [32]), regional scale (e.g., [22]), and detailed scales (e.g., [33]). Minissale and Vaselli [34] and references therein proposed an alternative method based on indirect measurements using karst springs as natural pluviometers in Italy. They recalculated the average elevations of their recharge areas by shifting the original altitude values of spring waters along the 0.2‰ m^{-1} line, proposed by Longinelli and Selmo [22], as representative of the mean isotopic altitude gradient ($\Delta\delta^{18}\text{O}$) for the Italian meteoric precipitations.

The determination of the origin of groundwater as well as the manner and the rate of recharge and discharge is of major importance for its management especially in waterless areas [35, 36]. The development of tracer techniques using stable isotopes enables approaches to groundwater movement in many regions [37–45]. The case

study of the Souss Basin, which is one of the most important basins in Southern High Atlas Mountains (Morocco), describes the typical problem of water in arid areas. According to Bouragba et al. [46], hydrogen and oxygen isotopic signatures reveal a rapid infiltration before evaporation of meteoric waters. The depletion in groundwater stable isotopes shows a recharge under different conditions. During wet periods, the precipitation altitude was indeed higher than that observed in different meteorological conditions [46].

The $\delta^{18}\text{O}$ and $\delta^2\text{H}$ values from shallow groundwater systems reflect those of the local average precipitation although they can be modified at some extent by selective recharge and fractionation processes, which may alter the pristine $\delta^{18}\text{O}$ and $\delta^2\text{H}$ values before the water reaches the saturated zone. The recent study by Liu and Yamanaka [47] has dealt with the quantitative contribution of different sources feeding the groundwater recharge applying an isotopic ($\delta^{18}\text{O}$ and δD) and hydrochemical approach to facilitate an integrated management of ground and surface water resources. This investigation was carried out in the area of Ashikaga (central Japan) that hosts the largest plain of Japan, which is traversed by the Watarase River. Sampling included meteoric waters, which were collected monthly for one year, 12 groundwaters from domestic wells, and 4 river samples. The isotopic signatures allowed to distinguish the different origins of the waters. The isotopic composition of pluvial water varied temporally in response to several factors (temperature effect and amount effect), with remarkably differences between the warm (April to September) and the cool (October to March) periods. It is considered that precipitation in the warm period is a more effective recharge source than that in the cool period. The 1-year observation of the isotopic signature of precipitation was not however assumed as representative of the local precipitation. On the contrary, river water and groundwater samples clearly showed weak variation, and their δ values were significantly distinct with respect to those of precipitation, suggesting considerably long residence times (at least >1 year). In addition, the close relationship observed between the mean δ values of river water and the mean elevation of the catchment reflected the altitude effect. In more detail, the low δ values of the river water corresponded to high elevation of its recharge zone. The isotopic composition of the groundwater samples ranked them between pluvial and river waters. This was also indicating (i) evaporation from shallow wells, (ii) contribution of the aquifer to the river recharge, and (iii) mixing processes of waters with different origins, e.g., direct infiltration, river seepage, and mountain block recharge.

Salinization of water resources is one of the most widespread processes that deteriorates water quality. Salinization is due to the inflow of saline dense water during heavy withdrawals of freshwater from coastal aquifers and/or mobilization of saline formation waters by overexploitation of inland aquifer systems. The combined use of oxygen and hydrogen isotopes is presently able to identify different salinization pathways. For instance, recently by a temporal monitoring of superficial waters, Petrini et al. [48] have examined the issues related to salinization and water quality in the drainage system of Ravenna coastal plain that extends for about 1,500 km² bordered to the east by the northern Adriatic Sea

coastline (Italy). In this study, the combined use of oxygen and hydrogen demonstrated to be a useful tool in the management of water resources, allowing the water sources, recharge processes, and the risk of saltwater intrusion or pollution to be investigated. In particular, the oxygen and hydrogen isotopic composition of rainwater was used to construct a local meteoric water line defining a correlation given by $\delta^2\text{H} = (7.00 \pm 0.17) \times \delta^{18}\text{O}$ (5.80 ± 1.3). In addition, they showed that waters from the coastal system range in composition from -8.53 to -0.69‰ and from -60.10 to -5.44‰ for $\delta^{18}\text{O}$ and $\delta^2\text{H}$, respectively, reflecting the variable contribution of a marine component.

3 Carbon Stable Isotopes

3.1 Background Principles

The chemical element carbon has two stable isotopes, ^{12}C and ^{13}C , and their abundances are of about 98.9 and 1.1%, respectively. Ratios of these isotopes are reported in ‰ relative to the Vienna Pee Dee Belemnite (VPDB) standard. The $^{13}\text{C}/^{12}\text{C}$ ratio of the VPDB standard is 0.011796 [49] and is expressed as $\delta^{13}\text{C}$, similarly to Eq. (1) for hydrogen and oxygen isotopes.

Carbon isotope analyses are useful when studying aquatic and hydrogeological systems in contact with CO_2 . Examples of such applications include investigations in carbon cycle and flux (e.g., [50–53]), chemical weathering (e.g., [54]), degassing from thermal and cold springs (e.g., [55, 56]), volcanic–hydrothermal systems (e.g., [57, 58]), and, as a relatively new field, geochemical trapping in CO_2 injection (carbon capture and storage (CCS)) projects (e.g., [59–61]).

Measurements of concentration and $\delta^{13}\text{C}$ values of DIC, which is referred to the following equation [62]:

$$\delta^{13}\text{C}_{\text{DIC}} = \delta^{13}\text{C}_{(\text{CO}_{2(\text{aq})} + \text{HCO}_3^- + \text{CO}_3^{2-})} \quad (2)$$

are routinely used in studies of carbon geochemistry and biogeochemistry of natural waters. Part of the carbon cycle is shown in Fig. 4. The primary reactions that generate DIC are weathering of carbonate and silicate minerals produced from (i) acid rain or other strong acids, (ii) carbonic acid formed by the dissolution of biogenic soil CO_2 as rainwater infiltrates, and (iii) dissolution of deep CO_2 (typically in active tectonic areas). The DIC pool can be influenced by contributions from groundwater, tributary streams, biogenic uptake and release of CO_2 , and CO_2 invasion from or evasion to the atmosphere. These processes influence both DIC concentrations and $\delta^{13}\text{C}_{\text{DIC}}$ values. Changes in the carbon isotopic ratios result from isotope fractionation processes accompanying the transformation of carbon or from mixing of carbon from different sources. The $\delta^{13}\text{C}_{\text{DIC}}$ values in catchment waters are generally in the range of -5 to -25‰ [63]. $\delta^{13}\text{C}$ values together with

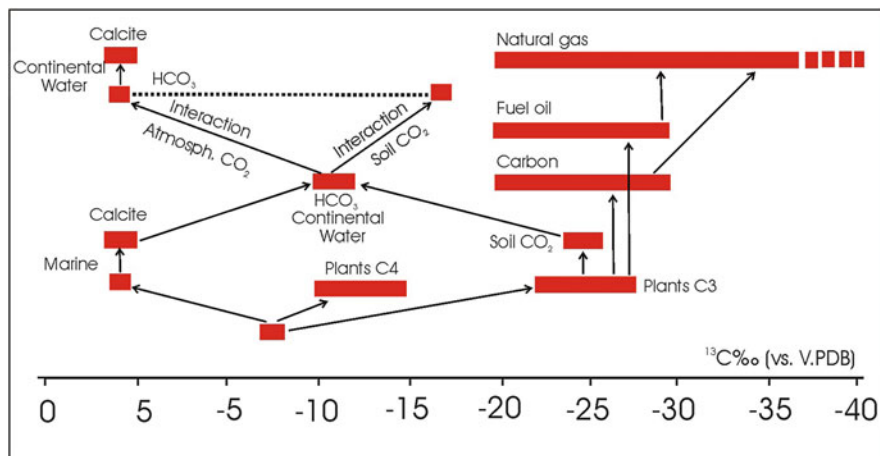


Fig. 4 Conceptual model showing the main processes that control the sources of dissolved inorganic carbon (DIC)

major ion chemistry and/or other isotope tracers (e.g., $\delta^{34}\text{S}$, $^{87}\text{Sr}/^{86}\text{Sr}$) can be used to evaluate proportions of DIC [64] and to estimate sources, sinks, and fluxes of carbon (e.g., [65, 66]).

3.2 Applications to Environmental Geochemistry Studies

Numerous authors have analyzed and used carbon isotopes as indicators of biogeochemical reactions taking places within catchment and river basins (e.g., [54, 67, 68]). Large rivers play an important role in controlling the $\delta^{13}\text{C}_{\text{DIC}}$ values by biological recycling of carbon and equilibration with atmospheric CO_2 . These studies have shown that upstream reaches and tributaries are cause for the primary pool of DIC supplied to the main stem of large rivers controlling the carbon isotope compositions further downstream (e.g., [69, 70]). Several attempts were made to evaluate the effects of these processes. Atekwana and Krishnamurthy [67] studied the seasonal concentrations and $\delta^{13}\text{C}$ of DIC in the river–tributary system in Kalamazoo, southwest Michigan (USA). They reported that the riverine DIC concentrations decreased (from 48.9 to 45.9 and from 60.4 to 48.6 mg C/L for river and tributaries, respectively), while $\delta^{13}\text{C}_{\text{DIC}}$ values increased (from -9.9 to -8.7 and from -11.4 to -9.7 ‰ for river and tributaries, respectively) in summertime due to photosynthesis. On the other hand, DIC concentrations incremented (from 51.9 to 53.4 and from 52.2 to 66.8 mg C/L for river and tributaries, respectively) and $\delta^{13}\text{C}_{\text{DIC}}$ values decreased (from -9.9 to -10.2 and from -9.3 to -12.8 ‰ for rivers and tributaries, respectively) during the late fall as photosynthesis declined and in-stream decay and respiration increased. These authors suggested that the difference in absolute values of concentrations and those of

$\delta^{13}\text{C}_{\text{DIC}}$ between the main river and its tributaries was derivable by shorter residence times of water in the tributaries when compared to those of the main course.

DIC concentrations and $\delta^{13}\text{C}_{\text{DIC}}$ values are also useful tracers of the DIC sources and the evolutionary history of DIC in contaminated streams. Atekwana and Fonyuy [71] and Ali and Atekwana [72] measured the $\delta^{13}\text{C}_{\text{DIC}}$ values to assess the extent of H^+ production from acid mine drainage (AMD) pollution of stream waters on inorganic carbon processing and $\delta^{13}\text{C}_{\text{DIC}}$ over spatial and temporal scales. Ali and Atekwana [72] investigated at the Federal Tailings Pile in the St. Joe State Park in southeastern Missouri (USA) the acidification and neutralization effects on the carbonate evolution in a shallow aquifer affected by a metal sulfide-rich and carbonate-rich tailing pile. Their isotopic modeling suggested that in the vadose zone, HCO_3^- dehydration produced degassing of $\text{CO}_{2(\text{g})}$ from pore water and groundwater with $\delta^{13}\text{C}_{\text{DIC}}$ of -3.1 to -6.8% .

Changes in the pH values resulting from AMD pollution and the chemical evolution of AMD in streams affect the speciation of DIC. Most importantly, the decrease in stream of pH due to AMD-produced H^+ drove DIC speciation to carbonic acid (H_2CO_3), which subsequently dissociated to $\text{CO}_{2(\text{aq})}$. The degassing of CO_2 from streams should be accompanied by enrichment in $\delta^{13}\text{C}_{\text{DIC}}$ due to preferential loss of ^{12}C with respect to ^{13}C [73]. Atekwana and Fonyuy [71] demonstrated that $\delta^{13}\text{C}_{\text{DIC}}$ enriched by $<3.0\%$ when CO_2 loss was proton enhanced and isotopic fractionation was mostly controlled by diffusion. The $\delta^{13}\text{C}_{\text{DIC}}$ value enriched by $>3.0\%$ when CO_2 loss was neutralization induced and CO_2 loss was accompanied by partial exchange of carbon between DIC and atmospheric CO_2 . Atekwana and Fonyuy [71] concluded that DIC loss and $\delta^{13}\text{C}_{\text{DIC}}$ enrichment in AMD-contaminated streams were depending on (i) the amount and rate of production of proton formed by metal hydrolysis, (ii) mechanism of CO_2 loss, and (iii) buffering capacity of the streams.

Monitoring stable carbon isotopes and subsequent determination of isotope mass balance is a method to evaluate the fate of CO_2 and distribution of DIC in deep aquifers. Recently, this approach was applied to several studies related to the subsurface storage of CO_2 (CCS), e.g., geochemical trapping in CO_2 injection projects (e.g., [59, 60]). Nisi et al. [61] investigated the isotopic carbon of dissolved CO_2 and DIC related to surface and spring waters and dissolved gases in the area of Hontomín–Huermece (Burgos, Spain) to verify whether CO_2 leakages, induced by the injection of CO_2 , might have been able to affect the quality of the waters in the local shallow hydrological circuits. In fact, the isotopic and chemical equilibrium of the C-bearing inorganic species can be used to trace CO_2 leakage if the injected CO_2 would have an isotopic carbon ratio that differs with respect to that already present [74]. Industrial CO_2 to be injected in a pilot site is indeed usually derived by refinery gas processing, and the $\delta^{13}\text{C}_{\text{CO}_2}$ values are rather negative, e.g., from -36 [61] to -28% VPDB as that used in the Ketzin pilot site [75]. Nisi et al. [61] reported that the baseline of $\delta^{13}\text{C}_{\text{DIC}}$ of the Hontomín–Huermece shallow aquifer had a value -10% VPDB and that the $\delta^{13}\text{C}_{\text{CO}_2}$ values measured in the Hontomín–Huermece waters are clustering around -20% VPDB, i.e., more positive than those of the injected CO_2 at Ketzin and likely similar to that expected to be injected

in the Spanish site. Nisi et al. [61] applied a theoretical model representing the DIC and $\delta^{13}\text{C}_{\text{DIC}}$ evolution of infiltrating water through carbonate terrains where a CO_2 source was active, according to two different ways: (i) addition of soil CO_2 deriving from oxidation of organic matter and root respiration (biogenic) and (ii) addition of deeply derived CO_2 and in equilibrium with calcite. This model predicted that the injection of CO_2 with a carbon isotopic value of -30‰ VPDB should decrease $\delta^{13}\text{C}_{\text{DIC}}$ to more negative values than those measured. By simulating the addition of 100 steps of 0.01 mol of CO_2 ($\delta^{13}\text{C}_{\text{CO}_2} = -30\text{‰}$ VPDB and $\delta^{13}\text{C}_{\text{DIC}} = -10\text{‰}$ VPDB) and considering the maximum (0.008 mol/kg), minimum (0.0033 mol/kg), and mean (0.0052 mol/kg) DIC values of the Hontomín–Huermececes waters, the resulting $\delta^{13}\text{C}_{\text{DIC}}$ and DIC values would indeed be -28.6‰ and 0.12 mol/kg, -29.4‰ and 0.11 mol/kg, and -29.1‰ and 0.11 mol/kg, respectively.

4 Sulfur Stable Isotopes

4.1 Background Principles

Sulfur has four stable isotopes: ^{32}S (95.02%), ^{33}S (0.75%), ^{34}S (4.21%), and ^{36}S (0.02%) [76]. Like ^{18}O , ^2H , and ^{13}C , sulfur isotopes are expressed with the delta notation defined by Eq. (1). Stable isotope compositions are reported as $\delta^{34}\text{S}$, ratios of $^{34}\text{S}/^{32}\text{S}$ in ‰ relative to the standard CDT (FeS phase of the Canyon Diablo Troilite meteorite) for which the value 0.0450 was assigned. Figure 5 shows the ranges of $\delta^{34}\text{S}$ values found in nature for a number of different forms of sulfur.

Sulfur species can be sampled from water as sulfate (SO_4^{2-}) or sulfide (H_2S or HS^-) for measuring $\delta^{34}\text{S}$ and, for sulfate, $\delta^{18}\text{O}$. Oxygen-18 in sulfate is referred to the VSMOW reference standard. Bacterial reduction of SO_4 is one of primary sources to explain the sulfur isotopic variability observed in natural aquatic systems. Sulfate-reducing bacteria utilize dissolved sulfate as an electron acceptor during the oxidation of organic matter, producing H_2S gas that has a $\delta^{34}\text{S}$ value of -25‰ , i.e., lower than that of the sulfate source [64]. On the other hand, not significantly fractionation of sulfur isotopes is expected for the following processes, such as (i) isotopic exchange between SO_4^{2-} and HS^- or H_2S in low-temperature environments, (ii) weathering of sulfate minerals and sulfide, and (iii) adsorption–desorption interactions with organic matter [78, 79].

The main use of sulfur isotopes has been aimed to understand the formation of polymetallic sulfide ore deposits, which can be originated in either sedimentary or igneous environments. $\delta^{34}\text{S}$ values exceeding $+20\text{‰}$ are found in association with evaporitic rocks and limestone deposits [63]. Sulfur associated with diagenetic environments generally reflects the composition of biogenic sulfide produced by bacterial reduction of marine sulfate and generally shows negative $\delta^{34}\text{S}$ values (from -30 to $+5\text{‰}$, [80, 81]). On the other hand, sulfur associated with crystalline rocks derived from the mantle is isotopically similar to that of the reference

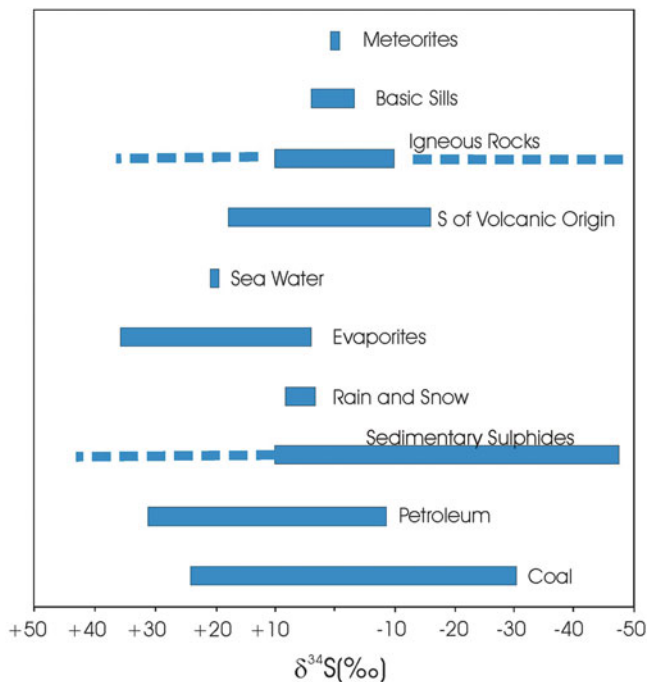


Fig. 5 Sulfur isotope distribution in nature. From Thode [77], modified

standard, whose $\delta^{34}\text{S}$ values are from 0 to +5‰. Nevertheless, volcanic rocks are occasionally characterized by $\delta^{34}\text{S}$ values up to +20‰, suggesting recycling processes of oceanic sulfate at subduction zones.

In environmental geochemistry studies, the evaluation of sulfate sources and cycling has been coupled with the analysis of the oxygen isotopic composition of sulfate. Sulfur and oxygen isotopic compositions of dissolved sulfate ($\delta^{34}\text{S}_{\text{-SO}_4}$ and $\delta^{18}\text{O}_{\text{-SO}_4}$, respectively) have been used to clarify sources and transformation processes of sulfur in aquatic systems associated with anthropogenic activities. These isotopes can provide meaningful information about various potential sources of sulfate in the watershed (e.g., dissolution of sulfate-bearing evaporitic minerals, such as gypsum and anhydrite, mineralization of organic matter, oxidation of sulfide minerals, infiltration from anthropogenic sources, atmospheric deposition) (e.g., [82, 83]). In recent years, the use of stable sulfur isotopes has been expanded to address diverse surface water and groundwater issues, e.g., cycling of sulfur in agricultural watersheds, origin of salinity in coastal aquifers, groundwater contamination by landfill leachate plumes, and acid mine drainage (e.g., [84–87]).

4.2 Application Studies to Groundwater and Surface Waters

Groundwater salinization in coastal regions is frequently observed in confined aquifers as well as in unconfined aquifers. In the case of unconfined aquifers close to coastal regions, water salinization is, as previously mentioned, usually induced by seawater intrusion relative to a decline in the piezometric level, which is commonly associated with excessive pumping (overexploitation) of groundwater. In the case of coastal confined aquifers, the groundwater system is generally isolated from seawater by confining bed of clay-rich sediments, which were mostly deposited in the latest transgressions. Yamanaka and Kumagai [88] used a combination of $\delta^{34}\text{S}_{\text{-SO}_4}$ values (ranging from +1.2 to +79.5‰) and chemical compositions of brackish groundwater to examine the provenance of salinity in a confined aquifer system in the SW Nobi Plain (central Japan). They highlighted that water chemistry was explained by sulfate reduction in combination with the mixing of two types of seawater: (i) present seawater and (ii) SO_4 -free seawater, with the fresh recharge water. In particular, the $\delta^{34}\text{S}_{\text{-SO}_4}$ values showed that present and fossil seawaters were responsible at most of 10.7 and 9.4% of the brackish groundwater volume, respectively.

Deterioration of the quality of groundwater in urban areas has become a major environmental concern worldwide. In this respect, researchers have applied $\delta^{34}\text{S}_{\text{-SO}_4}$ and $\delta^{18}\text{O}_{\text{-SO}_4}$ since they have a distinctive isotopic composition to identify pollution sources. Cortecchi et al. [89] investigated the $\delta^{34}\text{S}_{\text{-SO}_4}$ isotopic signature of the Arno river (northern Tuscany, Italy) and its main tributaries in order to constrain the areal distribution of the anthropogenic contribution across a heavily industrialized and densely urbanized territory, where the human load increases downwards from the Apennine ridge to the Tyrrhenian sea coast. These authors observed that the $\delta^{34}\text{S}_{\text{-SO}_4}$ values from natural inputs were ranging approximately between -15 and $+4\%$, likely related to the oxidation of pyrite disseminated in bedrocks, and $\delta^{34}\text{S}_{\text{-SO}_4}$ values between $+15$ and $+23\%$, as a result of dissolution processes of evaporitic rocks. Conversely, the sulfur isotopic signature associated with anthropogenic sources (possibly in the chemical forms of Na_2SO_4 and FeSO_4) was characterized by $\delta^{34}\text{S}_{\text{-SO}_4}$ values varying between 1 and 8‰.

Urban groundwater contamination problems are becoming increasingly recognized in all Asian megacities ([90] and reference therein). In the Taipei (Taiwan) urban area, one of the most densely populated areas in the world, the investigation of the hydrogeochemical groundwater characteristics and the causes of pollution are subjects of prime importance for water resource preservation in the Pacific island. Hosono et al. [90] explored the $\delta^{34}\text{S}_{\text{-SO}_4}$ and $\delta^{18}\text{O}_{\text{-SO}_4}$ isotope variability with the aim of understanding the subsurface nature and environmental status of such area. Importantly, they isotopically recognized possible sources, which were affecting the Taipei groundwater system. Within the analyzed data, the sulfate isotopic compositions of waters reacted with chemical fertilizers showed that the $\delta^{34}\text{S}_{\text{-SO}_4}$ and $\delta^{18}\text{O}_{\text{-SO}_4}$ values were ranging from -5.0 to $+14.4\%$ and from $+13.1$ to $+25.7\%$, respectively. Dissolved sulfate derived by chemical detergents had

$\delta^{34}\text{S}_{\text{-SO}_4}$ and $\delta^{18}\text{O}_{\text{-SO}_4}$ values from -3.7 to $+24.4\%$ and from $+11.6$ to $+20.6\%$, respectively. Eventually, the isotopic compositions of industrially processed high concentration sulfuric acid were characterized by $\delta^{34}\text{S}_{\text{-SO}_4} = 1.2\%$ and $\delta^{18}\text{O}_{\text{-SO}_4} = 9.5$.

Recently, the isotopic signature of dissolved sulfate was used to provide valuable information about the nature of water inputs to the sewage flow. The dynamics of various hydrologic processes that commonly occur within the sewer system, such as groundwater infiltration, rainwater percolation, or release from retention basins, can readily be described by using water isotope ratios. Houhou et al. [86] applied a combined water and sulfate dual isotope approach ($\delta^{34}\text{S}_{\text{-SO}_4}$ and $\delta^{18}\text{O}_{\text{-SO}_4}$) to examine the contribution of different water sources to flow within an urban sewer system. Houhou et al. [86] found that sulfate originating from urine was also detected as a tracer of human waste impacts, since $\delta^{18}\text{O}_{\text{-SO}_4}$ of urine is isotopically distinct from other sulfate sources (values around 4.5% for $\delta^{34}\text{S}_{\text{-SO}_4}$ and between 5.9 and 7.5% for $\delta^{18}\text{O}_{\text{-SO}_4}$). Inorganic sulfate indeed represents the main end product of sulfur metabolism in the human body, although other forms such as ester sulfate represent a $9\text{--}15\%$ fraction of the urinary sulfate ([86] and references therein). In the last years, intensive investigations of the stable isotopic composition of sulfate from groundwater, surface waters, and acidic mine drainage were performed due to the dominant role of sulfur as a component of AMD. Isotopic ($\delta^{34}\text{S}_{\text{-SO}_4}$ and $\delta^{18}\text{O}_{\text{-SO}_4}$) compositions can be used to clarify sources and transformation processes of sulfur in aquatic systems associated with coal mining ([87] and references therein). It is well assessed that the exposure of pyrite and other metal sulfides to weathering under atmospheric conditions produces sulfuric acid, with subsequent mobilization of other toxic substances (metals, metalloids) into groundwater and surface water (e.g., [91] and references therein). The Great Falls–Lewistown Coal Field in central Montana contains over 400 abandoned underground coal mines, many of which are discharging acidic waters with serious environmental consequences [84]. In this respect, Gammons et al. [84] examined the spatial and temporal changes in the chemistry of the mine waters and used the stable isotopes to address the sources of water and dissolved sulfate in the abandoned coal mines, as well as the surrounding sedimentary aquifers. They reported that most sulfates in these waters were derived by oxidation of pyrite in the coal with $\delta^{34}\text{S}_{\text{-SO}_4}$ and $\delta^{18}\text{O}_{\text{-SO}_4}$ values ranging from -16.1 to -9.3% and from -12.5 to -9.1% , respectively, while pyrite samples in coal from drill cuttings produced $\delta^{34}\text{S}$ values from -27.2 to -19.6% . Bacterial sulfate reduction is known to cause extreme fractionation of S isotopes ([84] and references therein). The fact that the mine waters and pyrite samples in this study are strongly depleted in ^{34}S suggests that bacterial sulfate reduction played an important role in the formation of the high-S coals. Gammons et al. [84] concluded that sulfate in the AMD waters was isotopically distinct from that in the underlying aquifer, and that mine drainage may have leaked into the aquifer.

5 Nitrogen Stable Isotopes

5.1 Background Principles

There are two naturally occurring stable isotopes of nitrogen, ^{14}N and ^{15}N . The majority of N in the atmosphere is consisting of ^{14}N (99.6337%), whereas the remainder is ^{15}N (0.3663%) [92]. Stable isotope ratios are expressed with the delta notation defined by Eq. (1) as $\delta^{15}\text{N}$: $^{15}\text{N}/^{14}\text{N}$ ratios in ‰ relative to the atmospheric air (AIR-NBS). The dominant source of nitrogen in most natural ecosystems is the atmosphere ($\delta^{15}\text{N} = 0\text{‰}$). Most terrestrial materials have $\delta^{15}\text{N}$ values between -20 and $+30\text{‰}$. As a consequence, plants fixing N_2 from the atmosphere have $\delta^{15}\text{N}$ values of about -5 to $+2\text{‰}$ [93]. Typical available soil N has $\delta^{15}\text{N}$ values from 0 to $+8\text{‰}$, although the $\delta^{15}\text{N}$ interval for refractory soil N may be larger [94–96]. Rock sources of N are generally considered negligible contributors to groundwater and surface water, but they can be important in some environments [97]. The use of isotopes to trace nitrogen reactions in hydrology gained further attention when it became possible to routinely measure the ^{18}O contents of nitrate [98]. The combination of $\delta^{15}\text{N}$ and $\delta^{18}\text{O}$ (whose values are reported relative to VSMOW) now provides a tool that enables us to distinguish between nitrates of different origins, to recognize denitrification processes, and to discuss the N-budget in the soil–water system (e.g., [94, 96, 99–107]). $\delta^{15}\text{N}$ values of NO_3 from various sources and sinks are reported in Fig. 6. Nitrate (NO_3) concentrations in public water supplies have risen above acceptable levels in many areas of the world, largely as a result of overuse of fertilizers and contamination by human and animal waste. Identifying

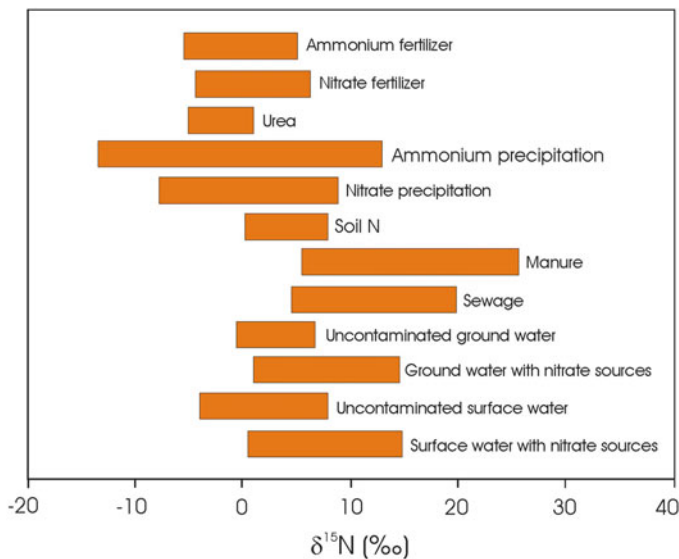


Fig. 6 $\delta^{15}\text{N}$ values of NO_3 from various sources and sinks. Fields are from Xue et al. [96]

the dominant source or sources of nitrate and other solutes to surface water and groundwater systems is critical for making effective contaminant management decisions. Overuse of fertilizers results in high concentrations of nitrates, able to modify the isotopic composition of N-NO₃ in superficial water and groundwater. Nitrates from synthetic fertilizers have $\delta^{15}\text{N}$ values varying from -6 to $+6\text{‰}$ AIR [94, 96]), while those of $\delta^{18}\text{O}$ are $22\pm 3\text{‰}$ VSMOW [98], because they are produced from atmospheric nitrogen ($\delta^{15}\text{N} = 0\text{‰}$) and oxygen ($\delta^{18}\text{O} = 23.5\text{‰}$). Nitrate derived from manure and sewage is isotopically distinct from that of fertilizers in both $\delta^{15}\text{N}$ (from $+5$ to 25‰ , [64, 94, 96]) and $\delta^{18}\text{O}$ ($<15\text{‰}$, [94]). Nitrate from wet and dry atmospheric deposition has a wide range of $\delta^{15}\text{N}$ values of approximately -10 to $+15\text{‰}$ and can also be originated from human activities, such as agriculture, vehicle exhaust, and power plant emissions [108]. In general, biologically mediated reactions (e.g., assimilation, nitrification, and denitrification) strongly control nitrogen dynamics in the soil and can influence and/or affect nitrogen dynamics in water. For instance, in the stepwise conversion of NO₃⁻ to N₂, nitrogen isotopes are fractionated: the lighter isotope (¹⁴N) is preferentially partitioned in the products, while the heavier one (¹⁵N) becomes concentrated in the residual reactants [109]. Several studies have employed both $\delta^{15}\text{N}$ and $\delta^{18}\text{O}$ of nitrate in the estimation of denitrification in the water system. They reported that a linear relationship, indicating an enrichment of ¹⁵N relative to ¹⁸O by a factor between 1.3:1, 1.5:1, and 2.1:1, gives strong clues for denitrification processes [110–113].

5.2 Applications to Groundwater and Surface Water Studies

Nitrate contamination of surface water and groundwater is an environmental problem in many regions of the world. High nitrate concentrations in drinking water are also believed to be a health hazard. At global scale, groundwater is a critical resource for both drinking water and other applications, such as agricultural irrigation. A prerequisite for controlling and managing nitrate pollution is to identify sources of nitrate. Contamination of aquifers from nitrate and other solutes is a significant concern, and therefore, the use of nitrate isotopes to understand contaminant sources and nitrate cycling in groundwater has become much more common. Karst aquifers are particularly vulnerable to nitrate contamination from anthropogenic sources due to the rapid movement of water in their conduit networks. Many studies have shown that stable isotope techniques are useful for evaluating sources of nitrogen because certain sources of nitrate have characteristic or distinctive isotopic compositions (e.g., [96] and references therein). Li et al. [114] used nitrate isotopes combined with chemical compositions to identify the primary sources of contamination and characterize the processes affecting nitrate in the karstic groundwater system of the Zunyi area (SW China) during summer and winter. The wide range of $\delta^{15}\text{N}_{\text{-NO}_3}$ values (from -1.8 to $+22.7\text{‰}$) and the intercorrelations between NO₃ and K observed in this study suggested that there

were at least three major sources contributing to the nitrate pollution of the groundwater in Zunyi, which included organic manure and synthetic fertilizer, and urban sewage effluents, while there was no direct evidence to show that denitrification occurred in the aquifer evaluated. However, Einsiedl and Mayer [115] reported that denitrification could have occurred in the porous rock matrix of a karst aquifer in southern Germany.

Generally speaking, elevated concentrations by nitrate in groundwater and surface water were most often measured in regions of intensive agriculture and principally attributed to the impacts of organic and chemical fertilizer inputs. In this respect, Savard et al. [116] analyzed the isotope ratios of the potential nitrate sources and measured the isotope and concentrations of nitrate in groundwater and surface water samples collected during eight campaigns distributed over the 2003–2004 and 2004–2005 seasonal cycles to constrain a conceptual apportionment model quantifying the relative seasonal N contributions in an area of intense potato production in the Wilmot River basin (PEI, Canada). In the Wilton region, the potential sources of nitrogen included urea fertilizer (H_2NCONH_2), whose $\delta^{15}\text{N}$ values were ranging from -1.9 to $+1.1\text{‰}$, whereas the wet atmospheric load varied between -11.8 and $+11.4\text{‰}$ and $+22.8$ and $+83.2\text{‰}$ for $\delta^{15}\text{N}$ and $\delta^{18}\text{O}$ values, respectively [116]. According to Savard et al. [116], elevated nitrate levels were coupled with agricultural activities and appeared to be most closely associated with extensive use of fertilizers for row crop production, rather than with other potential sources such as atmospheric load.

In agricultural regions, fertilizers and irrigation are the primary factors that contribute to increase world crop production. The use of fertilizers accounts for approximately 50% of the yield increase and greater irrigation for another substantial part [117]. In this respect, China is the world's greatest producer and consumer of fertilizers using about 31% of the total amount of fertilizers used worldwide [118]. Zhang et al. [119], by using a dual isotopic analysis of NO_3 , conducted a study in the North China Plain with the aim to identify nitrate pollution in both surface water and groundwater in irrigated agricultural regions. Zhang et al. [119] showed that the main sources of nitrate were nitrification of fertilizer and sewage in surface water, whereas groundwater sources during the dry season were mineralization of soil organic N and sewage. When fertilizers were applied, nitrate was transported by precipitation through the soil layers to the groundwater in the wet season. Savard et al. [116] and Zhang et al. [119] concluded that strategies to attenuate contamination by nitrate in waters of temperate climate row-cropping regions must consider nitrogen cycling by soil organic matter including the crucial role of crop residues throughout both the growing and nongrowing seasons. In particular, they suggested that plowing and its associated stimulation of mineralization and nitrification and the application of manures and its nitrogen loading should be timed to optimize crop uptake and minimize leaching losses.

Identification of nitrate sources is important in preserving water quality and achieving sustainability of the water resources. However, the occurrence of multiple inputs and/or the presence of overlapping point and nonpoint sources makes this task complicated. For instance, sewage and manure end members have overlapping

$\delta^{15}\text{N}_{\text{-NO}_3}$ and $\delta^{18}\text{O}_{\text{-NO}_3}$ values, and their differentiation on this basis is critical. In a recent review, Fenech et al. [103] showed that chemical markers (such as pharmaceuticals and food additives) with nitrate isotopes are suitable to differentiate sewage and manure sources of nitrate contamination. It is worthwhile to mention that a number of potential chemical markers are consumed by both humans and livestock, e.g., antimicrobial agents such as some tetracyclines and sulfonamides ([103] and references therein). Some examples of pharmaceuticals, which are used for the treatment of humans, animals, or both, are given in Fenech et al. [103], indicating these substances as suitable indicators of human and animal sources.

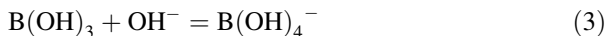
6 Boron and Strontium Isotopes

6.1 Background Principles

Boron is a ubiquitous minor or trace constituent in all natural surface and subsurface aquatic systems. It is mainly derived from the interaction of fluids with the crust ($\sim 10\text{--}13 \text{ mg kg}^{-1} \text{ B}$) [120] and/or mixing between fluids from different reservoirs and weathering of rocks and soils characterized by B-bearing minerals, whose the highest concentrations are recorded in waters leaching B-bearing salt deposits [121]. In coastal areas, rain containing sea salt from ocean spray provides another natural B source, but such inputs decline with distance from the coast [122]. The boron budget of surface and subsurface aquatic systems can considerably be affected by discharge of anthropogenic boron-laden waters. Elevated B levels in surface waters most commonly occur in industrial and urban areas. Among the many possible sources of anthropogenic B, domestic and some industrial wastewater effluents, herbicides and insecticides, glass manufacturing wastes, antifreeze, landfill and coal mine leachates, fly ash, petroleum products, slag, sewage sludge, manure, and compost ([123] and references therein) are those which mainly affect the natural waters. In hydrological investigations, the B isotope ratios often provide the fingerprint needed to identify the origin of B dissolved in natural waters, because it enables distinguishing B from natural sources from that due to anthropogenic sources ([124, 125] and references therein).

Boron has two naturally occurring stable isotopes, ^{11}B and ^{10}B . The isotopic composition of boron is expressed as a ratio of the two naturally occurring stable isotopes ^{11}B (80.1%) and ^{10}B (19.9%). The delta notation is similar to that expressed in Eq. (1), i.e., $\delta^{11}\text{B} = [(^{11}\text{B}/^{10}\text{B})_{\text{sample}} / (^{11}\text{B}/^{10}\text{B})_{\text{standard}} - 1] \times 1,000$, where the standard is the NBS boric acid 951, whose $^{11}\text{B}/^{10}\text{B}$ is 4.04362 ± 0.00137 [126].

Boron isotope fractionations are almost entirely controlled by the partitioning between the two dominant dissolved species $\text{B}(\text{OH})_3$, trigonal and planar, and $\text{B}(\text{OH})_4^-$, tetrahedral, through the reaction:



The relative abundances of the boron-dissolved species are pH dependent.

The large relative mass difference between the two stable boron isotopes leads to a wide range of isotope variations in nature with diagnostic signatures of crustal, meteoric, and marine B sources. The $\delta^{11}\text{B}$ approximate ranges of the main B reservoirs are +4 to +58‰ for marine B, -31 to +26‰ for nonmarine B, -17 to -2‰ for igneous B, and -34 to +22‰ for metamorphic B ([127] and references therein). Natural waters (such as seawater, river water, rainwater, groundwater, saline formation water, brines, and geothermal fluids) encompass a range in $\delta^{11}\text{B}$ from -16 to +60‰ ([128] and references therein).

Strontium is classified as a trace element, and in aquatic environment, it occurs as a divalent cation that readily substitutes for Ca^{2+} in carbonates, sulfates, feldspars, and other Ca-bearing rock-forming minerals (e.g., plagioclase, apatite, calcium carbonate, especially aragonite). These include the primary mineralogy of the sediments, secondary weathering products, and cement. Strontium has four naturally occurring isotopes, ^{88}Sr , ^{87}Sr , ^{86}Sr , and ^{84}Sr , all of which are stable. The isotopic abundances of strontium isotopes are variable because of the formation of radiogenic ^{87}Sr by the decay of naturally occurring ^{87}Rb . For the Rb–Sr isotope system, the mechanism of interest for the decay is represented by the following equation:



Over time, the amount of the daughter (radiogenic) isotope in a system increases and the amount of the parent (radioactive) isotope decreases as it decays away. If the rate of radioactive decay is known, we can use the increase in the amount of radiogenic isotopes to measure time. In practice, this is commonly done by measuring the concentration of the radiogenic isotope relative to a non-radiogenic isotope of the same element, e.g., ^{87}Sr is referenced to ^{86}Sr and the $^{87}\text{Sr}/^{86}\text{Sr}$ ratio (e.g., [129]) is measured. Although the minerals in igneous and metamorphic rocks may have identical Sr isotope ratios at the time of formation, the decay of ^{87}Rb (which has a half-life of 4.88×10^{10} , [129]) to ^{87}Sr leads, over time, to differences in $^{87}\text{Sr}/^{86}\text{Sr}$.

In freshwater systems, the residence times of waters are sufficiently short (days to 10^{2-3} years) compared to the half-life of ^{87}Rb ; thus, the radioactive decay of ^{87}Rb can be considered negligible. The application of Sr isotope ratios as a natural tracer in water–rock interaction studies and in assessing mixing relationships is now well established (e.g., [130–133]). $^{87}\text{Sr}/^{86}\text{Sr}$ ratio is diagnostic of Sr sources and, by analogy, Ca sources. The Sr isotopic signature can usefully be utilized as hydrology tracer since Sr derived from any mineral through weathering reactions maintains in solution the same $^{87}\text{Sr}/^{86}\text{Sr}$ ratio of the original mineral, i.e., no fractionation processes take place, differently to the stable isotopic systematics previously described. Strontium isotopic fractionation is negligible even when this element

is removed from water by either mineral precipitation or cation exchange process (e.g., [134]). A prerequisite for the use of Sr isotopes as tracer for groundwater pollution is a sufficient variability in the signature of the $^{87}\text{Sr}/^{86}\text{Sr}$ ratios among the different end members. Such variations have been observed between natural groundwater and human inputs (e.g., [135–137]).

6.2 Isotope Applications in Hydrology

As previously stated, seawater intrusion has for long been recognized as a serious threat to the groundwater quality in coastal aquifers. The increasing use of groundwater has in many places, especially in arid and semiarid regions, caused kilometer-scale intrusions resulting in severe groundwater quality problems (e.g., [138] and references therein). In this respect, traditional tracers such as chloride yield limited information on hydrochemical evolutionary trends because evapo-concentration effects can mask the indicators of groundwater flow paths. It is in these hydrogeological settings that trace element isotopes become particularly useful. Boron isotopes become much more powerful tools when combined with other isotope systematics such as Sr (e.g., [127, 139, 140]). Recently, Meredith et al. [141] have applied B and Sr concentrations and their isotopic compositions to the alluvial Darling River (a catchment about 650,000 km²) groundwater system (water samples were collected from 19 wells), which is located in inland Australia in order to provide (i) information on the hydrology of the system, (ii) evaluation of the groundwater recharge, and, finally, (iii) identification of water–sediment interaction processes leading to the hydrochemical evolution of saline groundwaters in the catchment. In this study, the trace element isotopes have showed a complex hydrogeochemical process in the same aquifer system. The $\delta^{11}\text{B}$ values were all higher than seawater and close to some of the highest $\delta^{11}\text{B}$ values ever reported in the literature for a groundwater system (from +44.4 to +53.9‰), while the $^{87}\text{Sr}/^{86}\text{Sr}$ ratios ranged from 0.708 to 0.713. The measurement of the trace element isotopes permitted to delineate the groundwater end members that included (i) shallow dilute waters from wells proximal to the channel (Darling River), (ii) saline groundwaters from wells located far away from the channel (Darling River), and (iii) deep saline groundwaters. By interpreting the geochemical and isotopic data, it was found that groundwaters influenced by river recharge were controlled by water–sediment reactions that varied substantially within the unsaturated zone. Groundwater–surface water exchange from fresh bank storage formed dilute groundwaters where B and Sr were related to clay mineral reactions.

Several studies have demonstrated the use of $^{87}\text{Sr}/^{86}\text{Sr}$ ratio and B isotopes in tracing anthropogenic inputs in groundwater and originated from industrial and household effluents, wastewater, and fertilizers [123, 133, 142–144]. For instance, Petelet-Giraud et al. [145] conducted a study in the Dommel catchment (1,800 km² large), which is a riverine system located in northern Belgium (380 km²) and in the southern part of the Netherlands, with the aim to investigate Sr and B isotopes as

potential tracers to discriminate the natural versus anthropogenic sources of the dissolved load and to identify various pollution sources such as agriculture, industrial activity, and wastewater treatment plants. Hasenmueller and Criss [123] showed that municipal drinking water used for lawn irrigation contributes substantial nonpoint loads of B and other chemicals (S species, Li, and Cu) to surface water and shallow groundwater in the St. Louis (Missouri, USA) area.

Jiang [146] investigated the effects of human activities (agriculture and sewage effluents) on the Sr isotope geochemistry in the Nandong Underground River System, which is located in a typical karst area dominated by agriculture in SE Yunnan Province (China). This study showed that agricultural fertilizers and sewage effluents significantly modified the natural $^{87}\text{Sr}/^{86}\text{Sr}$ ratio signature of groundwater that was otherwise dominated by water–rock interaction. Three major sources of Sr were distinguished on the basis of $^{87}\text{Sr}/^{86}\text{Sr}$ ratios and Sr concentrations. Two sources of Sr were the Triassic calcite- and dolomite-rich aquifers, where waters were characterized by low Sr concentrations (0.1–0.2 mg/L) and low $^{87}\text{Sr}/^{86}\text{Sr}$ ratios (0.7075–0.7080 and 0.7080–0.7100, respectively); the third input was anthropogenic and related to Sr sourced by agricultural fertilizers and sewage effluents with waters affecting the $^{87}\text{Sr}/^{86}\text{Sr}$ ratios (0.7080–0.8352 for agricultural fertilizers and 0.7080–0.7200 for sewage effluents, respectively), with higher Sr concentrations (0.24–0.51 mg/L).

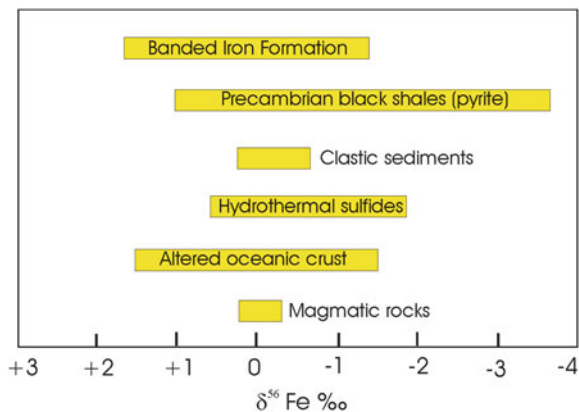
7 Untraditional Isotopes: The Metal (Fe, Cr, and Cu) Stable Isotopes

The differences in the relative, mass-dependent abundances of stable isotopes have the potential to elucidate sources and fate of contaminants in the biosphere. In this section, the potential uses of nontraditional stable isotope systems to trace sources, fate, and behavior of metals in the environment are presented. In particular, a basic review of isotopic fractionation mechanisms as well as summaries for three contaminants (Fe, Cr, and Cu) and their isotope systematics, fractionation processes, and environmental applications is here provided.

7.1 Iron Isotopes

Iron is an essential nutrient and is the third most abundant element that participates in a wide range of biotically and abiotically controlled redox processes in different geochemical environments. Iron solubility is highly dependent on its redox state. In oxygenated aquatic systems, concentrations of dissolved Fe are generally low due to the low solubility of its oxidized forms, which tend to form nanoparticle aggregates and colloids of oxy-hydroxides, thus precipitating [147, 148]. Iron has

Fig. 7 Iron isotope distribution in nature. Fields are from Hoefs [151]



four naturally occurring stable isotopes, ^{54}Fe (5.84%), ^{56}Fe (91.76%), ^{57}Fe (2.12%), and ^{58}Fe (0.28%), and the natural, mass-dependent isotope variations of Fe in rocks record a span in the range of $\sim 4\text{‰}$ for the $^{56}\text{Fe}/^{54}\text{Fe}$ ratio [149]. Iron isotope data in the literature have been reported with the standard δ notation, and the $\delta^{56}\text{Fe}$ ($^{56}\text{Fe}/^{54}\text{Fe}$) and $\delta^{57}\text{Fe}$ ($^{57}\text{Fe}/^{54}\text{Fe}$) values are most commonly used as defined by Eq. (1). The choice of the reference reservoir for calculating δ values is quite variable among different laboratories. Most authors are used to report the Fe isotope data as relative to terrestrial igneous rocks or to the IRMM-014 (Institute for Reference Materials and Measurements) standard [149]. Therefore, interlaboratory comparisons are obtained by normalizing the Fe isotope ratios to IRMM-014, this standard rapidly becoming the most accepted interlaboratory standard. According to Dauphas and Rouxel [150], Fe isotopic systematics can be considered a valuable tool to study the Fe biogeochemical cycle and can potentially be used to trace its transport in aqueous systems. Figure 7 shows the ranges of $\delta^{56}\text{Fe}$ values found in nature for a number of different forms of iron.

Iron stable isotope fractionations during aqueous and biological processes include redox reactions [152, 153], adsorption and mineral dissolution [154, 155], precipitation [156, 157], and dissimilatory Fe reduction, where Fe(III) oxides act as electron acceptors for anaerobic respiration [158–160]. Beard and Johnson [149] and references therein reported that in general microbiological reduction of Fe^{3+} forms a much larger quantity of iron with distinct $\delta^{56}\text{Fe}$ values than those produced by abiological processes. The bulk continental crust has $\delta^{56}\text{Fe}$ values close to zero [149]. Hydrothermal fluids at mid-ocean ridges and river waters have $\delta^{56}\text{Fe}$ values between 0 and -1‰ [161–163]. In modern aqueous environments, such as the oceans, dissolved Fe contents are low (upper oceans <1 nM, [164]) and their isotopic compositions are sensitive indicators of Fe sources and pathways. Johnson and Beard [165] indicated that iron isotopes are exceptional indicators of Fe redox cycling, particularly in low-temperature environments where isotopic fractionations are relatively large and where significant pools of Fe^{2+} and Fe^{3+} may coexist. In a recent study, Castorina et al. [166] observed significant variations for the Fe

isotopes measured in Fe-rich groundwaters in aquifers from the Low Friuli Plain coastland (northern Adriatic Sea, Italy), an area impacted by strong industrialization, including past and present metallurgic activities and steel production related to manufacturing of low-alloyed steel. In this study, Fe contents ranged from 0.48 to 9.99 mg/L and from 2.50 to 43.8 mg/L in low-salinity and brackish waters, respectively. The $\delta^{56}\text{Fe}$ value was varying over a wide range: from -5.29 to $+0.87\text{‰}$ in low-salinity waters and between -2.34 and $+2.15\text{‰}$ in brackish waters. The isotopically lighter compositions were interpreted as reflecting isotopic fractionation during repeated cycling of Fe precipitation. Castorina et al. [166] concluded that the positive $\delta^{56}\text{Fe}$ values might be indicative of either a higher solubility of oxy-hydroxides, which during diagenesis preferentially incorporated the isotopically heavier fraction of Fe, or leaching processes of the foundry landfill disposal, which characterizes the site. Recent in-depth reviews on Fe isotope geochemistry may be found in Johnson and Beard [165] and Bullen [167].

7.2 Chromium Isotopes

Chromium is a trace element abundantly occurring in ultramafic and mafic rock minerals and represents an important contaminant in surface water and groundwater although its mobility and environmental impact are strongly depending on its valence state and redox transformations. Chromium is present in two oxidation states, Cr(III), as cation Cr^{3+} , and Cr(VI), as oxyanion (CrO_4^{2-} , HCrO_4^- , and HCr_2O_7^-), which have different chemical behaviors: Cr^{3+} is the dominant form in most minerals and in water under reducing conditions, whereas Cr(VI) is stable under oxidizing conditions and highly toxic leading to health problems such as lung cancer and dermatitis (e.g., [168]). Chromium is a common anthropogenic contaminant in surface waters and the potential toxicity of Cr(VI), and its fairly common occurrence as a point-source contaminant has spurred research into the ability of Cr stable isotopes to provide information on Cr sources, transport mechanisms, and fates in the environment. Chromium has four stable isotopes with the following abundances: ^{50}Cr (4.35%), ^{52}Cr (83.79%), ^{53}Cr (9.50%), and ^{54}Cr (2.36%) [169]. Variations of the isotope ratios are expressed using the delta notation according to Eq. (1), the $\delta^{53}\text{Cr}$ value being relative to the $^{53}\text{Cr}/^{52}\text{Cr}$ ratio referred to that of the NIST SRM 797 (National Institute of Standards and Technology Standard Reference Materials) standard. The measured range of $^{53}\text{Cr}/^{52}\text{Cr}$ in natural materials is presently -6‰ , essentially reflecting the range measured for naturally occurring Cr(VI) in groundwater [170]. Equilibrium fractionations between Cr(VI) and Cr(III) were estimated by Schauble [171], who predicted Cr isotope fractionations of $>1\text{‰}$ between Cr species with different oxidation states. Ellis et al. [172], Sikora et al. [173], Berna et al. [174], Zink et al. [175], Dossing et al. [176], Basu and Johnson [177], Han et al. [178], Jamieson-Hanes et al. [179], and Kitchen et al. [180] studied the fractionation of Cr isotopes in a series of Cr(VI) reduction experiments. The results showed a general trend of

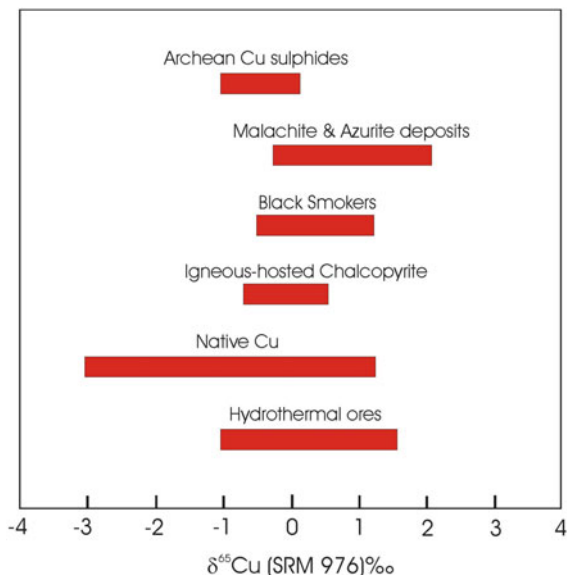
accumulating heavier Cr isotopes in the unreacted Cr(VI) species and an accumulation of the lighter ones in the produced Cr(III), whereas Cr(III) did not undergo rapid isotopic exchange during Cr(III) oxidation runs [175]. These properties make Cr isotope investigations suitable to detect and quantify redox changes in different geochemical reservoirs. In this respect, the tracking of Cr(VI) reduction is especially powerful when dealing with subsoil Cr(VI) contamination and related remediation actions. Recent in-depth reviews on Cr isotope geochemistry may be found in Villalobos-Aragón et al. [181], Bonnand et al. [182], Wanner and Sonnenthal [183], and Frei et al. [184].

7.3 Copper Isotopes

Copper is present in the Earth's crust at mg kg^{-1} level [185] and enters natural water and soil reservoirs from rock weathering and anthropogenic contamination sources. The major Cu-bearing minerals are sulfides (e.g., chalcopyrite, bornite, chalcocite), and, under oxidizing conditions, secondary copper minerals in the form of oxides and carbonates host this chalcophile element. Copper is a nutrient element, although toxic for all aquatic photosynthetic microorganisms when elevated concentrations occur (e.g., [186, 187]), due to its ability to either readily accept or donate single electrons as it changes oxidation states. Copper occurs in two oxidation states, Cu^+ and Cu^{2+} , and rarely in the form of native copper. Copper may form a great variety of complexes with very different coordination numbers such as square, trigonal, and tetragonal complexes. These properties are ideal prerequisites for relatively large isotope fractionations. Copper has two stable isotopes ^{63}Cu (69.1%) and ^{65}Cu (30.9%). As with light stable isotope systems, variations in transition-metal isotope ratios can be described using the δ notation in ‰. The $\delta^{65}\text{Cu}$ values are calculated as reported in Eq. (1) and the reference $^{65}\text{Cu}/^{63}\text{Cu}$ ratio is the NIST SRM 976 (0.4456, [188]). Figure 8 shows the ranges of $\delta^{65}\text{Cu}$ values found in nature for a number of different forms of copper.

Experimental investigations have demonstrated that redox reactions between Cu (I) and Cu(II) species are the principal process that fractionates Cu isotopes in natural systems [189]. As a consequence, copper isotope ratios may be used to interpret useful details of natural redox processes. The measured range of $^{65}\text{Cu}/^{63}\text{Cu}$ in natural materials is approximately 9‰ for solid samples ($\delta^{65}\text{Cu} = -3.0$ to $+5.7$ ‰) and 3‰ for water samples ($\delta^{65}\text{Cu} = -0.7$ to $+1.4$ ‰) ([167] and references therein). Recent studies, related to the Cu isotope variations in a variety of stream waters draining historical mining districts located in the USA and Europe, have shown that the $\delta^{65}\text{Cu}$ values were varying from -0.7 to $+1.4$ ‰, pointing out that Cu mineral weathering did not deliver a single averaged isotope composition to drainage water [190]. At large scale, Cu isotopes can provide important insights about the nature of the parameters which control the fractionation processes. In this respect, Vance et al. [191] studied the $^{65}\text{Cu}/^{63}\text{Cu}$ ratios in estuarine waters and particulates, riverine, and open ocean waters. They reported that in estuarine samples the $\delta^{65}\text{Cu}$ values of dissolved Cu were between 0.8 and

Fig. 8 Copper isotope distribution in nature. Fields are from Ehrlich et al. [189]



1.5‰, i.e., greater than that of Cu associated with particulate material. Moreover, dissolved Cu in rivers had $\delta^{65}\text{Cu}$ values ranging from 0.02 to 1.45‰, most of them being heavier than those measured in crustal rocks (+0.16‰). Vance et al. [191] concluded that the isotopic contrast reflects the different partitioning of the weathered pool of Cu between an isotopically light fraction adsorbed onto suspended particles and an isotopically heavy dissolved fraction dominated by Cu bound to strong organic complexes.

8 Conclusions

The use of stable and (subordinately) radiogenic isotopes in hydrologic systems is playing an important role to address water resource sustainability issues worldwide. The possibility to evaluate and quantify effects and modalities of isotopic fractionation affecting the light elements such as oxygen, hydrogen, carbon, sulfur, nitrogen, and boron provides outstanding opportunities to identify sources and to trace transformation processes. Stable isotope applications are nowadays well-established approaches in hydrogeochemistry, and some of them are routinely analyzed to contribute to the understanding of the hydrological circuits as well as the presence of anthropogenic contamination/pollution. Environmental isotope geochemistry is a fast-growing discipline as new additional isotopic systems are set up and applied to different geological and urban, industrial, and agricultural areas. In this review, we have provided some examples of their application to highlight the potential of traditional and nontraditional stable isotope systems to

trace sources, fate, and behavior of different solutes and metals in surface water and groundwater. In these studies, stable isotopes have demonstrated to be a powerful tool in order to analyze situations that cannot be faced with conventional techniques. However, at a large scale, the isotopic signatures can significantly change and often not enough data are provided to determine the original source, as their determination is time-consuming and costly. On the other hand, new techniques, particularly for what regards oxygen and hydrogen isotopes, are presently able to provide a large number of determinations in a short time. Nevertheless, we acknowledge that the best approach in environmental studies is to combine as many tracers as possible, which should include and integrate chemical and isotopic data. This combination constitutes an important requisite for hydrogeochemical researches in general, and for the main focus of this book in particular, regarding study of the main threats to the quality of groundwater.

Acknowledgments We would like to kindly thank Andrea Scozzari for critical reading and fruitful comments on the manuscript. Many thanks are due to the reviewer for his insightful and constructive suggestions that significantly improved an early version of the manuscript.

References

1. UN-Water (2011) Annual Reporter 2011. October 2012
2. World Health Organization (WHO) (1992) Our planet, our health. Report of WHO Commission on health and environment. World Health Organization, Geneva
3. Appelo CAJ, Postma D (1993) Geochemistry, groundwater and pollution. A. A. Balkema, Rotterdam, p 536
4. Rozanski K, Froehlich K, Mook WG (2001) UNESCO/IAEA series. Mook WG (eds) Environmental isotopes in the hydrological cycle principles and applications, International Hydrological No 39, vol 3. UNESCO, Paris
5. Morgenstern U, Stewart MK, Stenger R (2010) Dating of streamwater using tritium in a post nuclear bomb pulse world: Continuous variation of mean transit time with streamflow. *Hydrol Earth Syst Sci* 14:2289–2301
6. Stewart MK, Morgenstern U, McDonnell JJ (2010) Truncation of stream residence time: How the use of stable isotopes has skewed our concept of streamwater age and origin. *Hydrolog Process* 24:1646–1659
7. Schiff SL, Aravena R, Trumbore SE, Dillon PJ (1990) Dissolved organic carbon cycling in forested watersheds: a carbon isotope approach. *Water Resour Res* 26:2949–2957
8. Mayorga E, Aufdenkampe AK, Masiello CA (2005) Young organic matter as a source of carbon dioxide outgassing from Amazonian rivers. *Nature* 436(7050):538–541
9. Lange T, Hebert D (2001) A new site for ^{85}Kr measurements on groundwater samples. *Radiat Phys Chem* 61:679–680
10. Visser A, Broers HP, Purtschert R, Sültenfuß J, De Jonge M (2013) Groundwater age distributions at a public drinking water supply well field derived from multiple age tracers (^{85}Kr , $^3\text{H}/^3\text{He}$, and ^{39}Ar). *Water Resour Res* 49(11):7778–7796
11. Palau J, Marchesi M, Chambon JCC, Aravena R, Canals T, Binning PJ, Bjerg PL, Otero N, Soler A (2014) Multi-isotope (carbon and chlorine) analysis for fingerprinting and site

- characterization at a fractured bedrock aquifer contaminated by chlorinated ethenes. *Sci Total Environ* 475:61–70
12. Khaska M, Le Gal La Salle C, Lancelot J, Team, A.S.T.E.R, Mohamad A, Verdoux P, Noret A, Simler R (2013) Origin of groundwater salinity (current seawater vs. saline deep water) in a coastal karst aquifer based on Sr and Cl isotopes. Case study of the La Clape massif (southern France). *Appl Geochem* 37:212–227
 13. Craig H (1961) Standards for reporting concentrations of deuterium and oxygen-18 in natural waters. *Science* 133:1833–1834
 14. De Wit JC, Van der Straaten CM, Mook WG (1980) Determination of the absolute D/H ratio of VSMOW and SLAP. *Geostandard Newslett* 4:33–36
 15. Hagemann R, Nief G, Roth E (1970) Absolute isotopic scale for deuterium analysis of natural waters. Absolute D/H ratio for SMOW. *Tellus* 22:712–715
 16. Tse RS, Wong SC, Yuen CP (1980) Determination of deuterium/hydrogen ratios in natural waters by Fourier transform nuclear magnetic resonance spectrometry. *Anal Chem* 52:2445
 17. Baertschi P (1976) Absolute ^{18}O content of standard mean ocean water. *Earth Planet Sci Lett* 31:341–344
 18. Gonfiantini R (1978) Standards for stable isotope measurements in natural compounds. *Nature* 271:534–536
 19. Craig H (1961) Isotopic variations in meteoric waters. *Science* 133:1702–1703
 20. Gat JR, Carmi H (1970) Evolution of the isotopic composition of atmospheric waters in the Mediterranean sea area. *J Geophys Res* 75:3039–3040
 21. Rozanski K, Araguas Araguas L, Gonfiantini R (1993) Isotopic patterns in modern global precipitation. In: Swart PK et al (eds) *Climate change in continental isotopic records*, vol 78, Geophysical monograph series. AGU, Washington DC, pp 1–36
 22. Longinelli A, Selmo E (2003) Isotopic composition of precipitation in Italy: a first overall map. *J Hydrol* 270:75–88
 23. Sappa G, Barbieri M, Ergul S, Ferranti F (2012) Hydrogeological conceptual model of groundwater from carbonate aquifers using environmental isotopes (^{18}O , ^2H) and chemical tracers: a case study in Southern Latium Region, Central Italy. *J Water Resource Protect* 4 (9):695–716. doi:[10.4236/jwarp.2012.49080](https://doi.org/10.4236/jwarp.2012.49080)
 24. Gat JR (1996) Oxygen and hydrogen isotopes in the hydrologic cycle. *Annu Rev Earth Planet Sci* 24:225–262
 25. Dansgaard W (1964) Stable isotopes in precipitation. *Tellus* 16:436–468
 26. Gat JR, Klein B, Kushnir Y, Roether W, Wernli H, Yam R, Shemesh A (2003) Isotope composition of air moisture over the Mediterranean sea: an index of the air–sea interaction pattern. *Tellus Ser B* 55:953–965
 27. Andreo B, Liñán C, Carrasco F, Jimenez de Cisneros C, Caballero F, Mudry J (2004) Influence of rainfall quantity on the isotopic composition (^{18}O and ^2H) of water in mountainous areas. Application for groundwater research in the Yunquera-Nieves karst aquifers (S Spain). *Appl Geochem* 19:561–574
 28. Argiriou AA, Lykoudis S (2006) Isotopic composition of precipitation in Greece. *J Hydrol* 327:486–495
 29. Celle-Jeanton H, Gonfiantini R, Travi Y, Sol B (2004) Oxygen-18 variations of rainwater during precipitation: application of the Rayleigh model to selected rainfalls in southern France. *J Hydrol* 289:165–177
 30. Celle-Jeanton H, Travi Y, Blavoux B (2001) Isotopic typology of the precipitation in the Western Mediterranean Region at three different time scales. *Geophys Res Lett* 28:1215–1218. doi:[10.1029/2000GL012407](https://doi.org/10.1029/2000GL012407)
 31. Vreča P, Krajcar Bronic I, Horvatincic N, Baresic J (2006) Isotopic characteristics of precipitation in Slovenia and Croatia: comparison of continental and maritime stations. *J Hydrol* 330:457–469
 32. Bowen GJ, Revenaugh J (2003) Interpolating the isotopic composition of modern meteoric precipitation. *Water Resour Res* 39(10):1299. doi:[10.1029/2003WR002086](https://doi.org/10.1029/2003WR002086)

33. Liotta M, Grassa F, D'Alessandro W, Favara R, Gagliano Candela E, Pisciotta A, Scaletta C (2013) Isotope composition of meteoric water in Sicily, Italy. *Appl Geochem* 34:199–206
34. Minissale A, Vaselli O (2011) Karst springs as “natural” pluviometers: constraints on the isotopic composition of rainfall in the Apennines of central Italy. *Appl Geochem* 26:838–852
35. Chen JS, Sun XX, Gu WZ, Tan HB, Rao WB, Dong HZ, Liu XY, Su ZG (2012) Isotopic and hydrochemical data to restrict the origin of the groundwater in the Badain Jaran Desert, Northern China. *Geochem Int* 50(5):455–465, © Pleiades Publishing, Ltd., 2012
36. Yin L, Hou G, Tao Z, Li Y (2010) Origin and recharge estimates of groundwater in the ordos plateau, People's Republic of China. *Environ Earth Sci* 60:1731–1738
37. Andersen SM, Meredith K, Timms W, Acworth RI (2008) Investigation of $\delta^{18}\text{O}$ and $\delta^2\text{H}$ in the Namoi River catchment – elucidating recharge sources and the extent of surface water/groundwater interaction. International Association of Hydrogeologists Congress XXXVI, Toyama, Japan. 26 October–1 November
38. Arslan H, Cemek B, Demir Y (2012) Determination of seawater intrusion via hydrochemicals and isotopes in Bafla Plain. *Turkey Water Resour Manage* 26:3907–3922. doi:[10.1007/s11269-012-0112-3](https://doi.org/10.1007/s11269-012-0112-3)
39. Lorenzen G, Sprenger C, Baudron P, Gupta D, Pekdeger A (2011) Origin and dynamics of groundwater salinity in the alluvial plains of western Delhi and adjacent territories of Haryana State, India. *Hydrolog Process* 26:2333–2345
40. Praasma T, Novakowski K, Kyser K, Hall K (2009) Using stable isotopes and hydraulic head data to investigate groundwater recharge and discharge in a fractured rock aquifer. *J Hydrol* 366:35–45
41. Qin D, Zhao Z, Han L, Qian Y, Ou L, Wu Z, Wang M (2012) Determination of groundwater recharge regime and flowpath in the Lower Heihe River basin in an arid area of Northwest China by using environmental tracers: implications for vegetation degradation in the Ejina Oasis. *Appl Geochem* 27:1133–1145
42. Somay MA, Gemici Ü (2009) Assessment of the salinization process at the coastal area with hydrogeochemical tools and geographical information systems (GIS): Selçuk Plain, Izmir, Turkey. *Water Air Soil Pollut* 201:55–74
43. Song X, Liu X, Xia J, Yu J, Tang C (2006) A study of interaction between surface water and groundwater using environmental isotope in Huaisha River basin. *Sci China D Earth Sci* 49(12):1299–1310
44. Wang Y, Jiao JJ (2012) Origin of groundwater salinity and hydrogeochemical processes in the confined Quaternary aquifer of the Pearl River Delta, China. *J Hydrol* 438–439:112–124
45. Yang L, Song X, Zhang Y, Han D, Zhang B, Long D (2012) Characterizing interactions between surface water and groundwater in the Jialu River basin using major ion chemistry and stable isotopes. *Hydrol Earth Syst Sci Discuss* 9:5955–5981
46. Bouragba L, Jacques Mudry J, Bouchaou L, Hsissou Y, Tagma T (2011) Characterization of groundwater in the Souss upstream basin: Hydrochemical and environmental isotopes approaches. *Afr J Environ Sci Technol* 5(4):307–315, April 2011
47. Liu Y, Yamanaka T (2012) Tracing groundwater recharge sources in a mountain-plain transitional area using stable isotopes and hydrochemistry. *J Hydrol* 464–465:116–126
48. Petrini R, Pennisi M, Vittorini A, Cidu R, Vianello G, Aviani U (2014) Geochemistry and stable isotope composition of surface waters from the Ravenna plain (Italy): Implications for the management of water resources in agricultural lands. *Environ Earth Sci* 71(12):5099–5111
49. Coplen TB, Hopple JA, Böhlke JK, Peiser HS, Rieder SE, Krouse HR, Rosman KJR, Ding T, Vocke RD Jr, Révész KM, Lamberty A, Taylor P, Bièvre PD (2002) Compilation of minimum and maximum isotope ratios of selected materials and reagents. *Water Resour Investig Rep* 01–4222:98
50. Chiodini G, Frondini F, Kerrick DM, Rogie J, Parello F, Peruzzi L, Zanzari AR (1999) Quantification of deep CO_2 fluxes from Central Italy. Examples of carbon balance for regional aquifers and of soil diffuse degassing. *Chem Geol* 159:205–222

51. Elío J, Nisi B, Ortega MF, Mazadiego LF, Vaselli O, Grandia F (2013) CO₂ soil flux baseline at the CO₂ injection pilot plant of Hontomin (Burgos, Spain). *Int J Greenhouse Gas Contr* 18:224–236
52. Minissale A (2004) Origin, transport and discharge of CO₂ in central Italy. *Earth Sci Rev* 66:89–141
53. Schulte P, van Geldern R, Freitag H, Karim A, Négrel P, Petelet-Giraud E, Probst A, Probst J-L, Telmer K, Veizer J, Barth JAC (2011) Applications of stable water and carbon isotopes in watershed research: weathering, carbon cycling, and water balances. *Earth Sci Rev* 109 (1–2):20–31
54. Skidmore M, Sharp M, Tranter M (2004) Kinetic isotopic fractionation during carbonate dissolution in laboratory experiments: implications for detection of microbial CO₂ signatures using $\delta^{13}\text{C}\text{-DIC}$. *Geochim Cosmochim Acta* 68(21):4309–4317
55. Chiodini G, Caliro S, Cardellini C, Avino R, Granieri D, Schmidt A (2008) Carbon isotopic composition of soil CO₂ efflux, a powerful method to discriminate different sources feeding soil CO₂ degassing in volcanic-hydrothermal areas. *Earth Planet Sci Lett* 274(3–4):372–379
56. Chiodini G, Frondini F, Cardellini C, Parello F, Peruzzi L (2000) Rate of diffuse carbon dioxide earth degassing estimated from carbon balance of regional aquifers: the case of Central Apennine (Italy). *J Geophys Res* 105:8423–8434
57. Frondini F, Caliro S, Cardellini C, Chiodini G, Morgantini N (2009) Carbon dioxide degassing and thermal energy release in the Monte Amiata volcanic-geothermal area (Italy). *Appl Geochem* 24:860–875
58. Tassi F, Vaselli O, Cuccoli F, Buccianti A, Nisi B, Lognoli E, Montegrossi G (2009) A geochemical multi-methodological approach in hazard assessment of CO₂-rich gas emissions at Mt. Amiata volcano (Tuscany, central Italy). *Water Air Pollut Focus* 9:117–127
59. Becker V, Myrtilinen A, Blum P, van Geldern R, Barth JAC (2011) Predicting $\delta^{13}\text{C}_{\text{DIC}}$ dynamics in CCS: a scheme based on a review of inorganic carbon chemistry under elevated pressures and temperatures. *Int J Greenhouse Gas Contr* 5(5):1250–1258
60. Myrtilinen A, Becker V, Nowak M, Zimmer M, Pilz P, Barth J (2012) Analyses of pre-injection reservoir data for stable carbon isotope trend predictions in CO₂ monitoring: preparing for CO₂ injection. *Environ Earth Sci* 67:473. doi:10.1007/s12665-012-1710-3
61. Nisi B, Vaselli O, Delgado HA, Tassi F (2013) Dissolved Nitrates in the groundwater of the Cecina Plain (Tuscany, Central-Western Italy): Clues from the isotopic signature of NO₃. *Appl Geochem* 34:38–52
62. Zhang J, Quay PD, Wilbur DO (1995) Carbon isotope fractionation during gas-water exchange and dissolution of CO₂. *Geochim Cosmochim Acta* 59(1):107–114
63. Kendall C, Doctor DH, Young MB (2014) Environmental isotope applications in hydrologic studies. In: Holland H, Turekian K (eds) *Treatise on geochemistry*, 2nd Ed, vol 7. Elsevier, Amsterdam, p 273–327
64. Clark ID, Fritz P (1997) *Environmental Isotopes in Hydrogeology*. CRC, New York, p 328
65. Aravena R, Schiff SL, Trumbore SE, Dillon PJ, Elgood R (1992) Evaluating dissolved inorganic carbon cycling in a forested lake watershed using carbon isotopes. *Radiocarbon* 34(3):636–645
66. Taylor CB, Fox VJ (1996) An isotopic study of dissolved inorganic carbon in the catchment of the Waimakariri River and deep ground water of the North Canterbury Plains, New Zealand. *J Hydrol* 186:161–190
67. Atekwana EA, Krishnamurthy RV (1998) Seasonal variations of dissolved inorganic carbon and $\text{d}13\text{C}$ of surface waters: Application of a modified gas evolution technique. *J Hydrol* 205:26–278
68. Kendall C, McDonnell JJ, Gu W (2001) A look inside “black box” hydrograph separation models: a study at the Hydrohill catchment. *Hydrolog Process* 15:1877–1902
69. Hélié J-F, Hillaire-Marcel C, Rondeau B (2002) Seasonal changes in the sources and fluxes of dissolved inorganic carbon through the St. Lawrence River—Isotopic and chemical constraint. *Chem Geol* 186:117–138

70. Yang C, Telmer K, Veizer J (1996) Chemical dynamics of the St-Lawrence riverine system: $\delta\text{DH}_2\text{O}$, $\delta\text{18OH}_2\text{O}$, δ13CDIC , δ34S sulfate, and dissolved $87\text{Sr}/86\text{Sr}$. *Geochim Cosmochim Acta* 60(5):851–866
71. Atekwana EA, Fonyuy EW (2009) Dissolved inorganic carbon concentrations and stable carbon isotope ratios in streams polluted by variable amounts of acid mine drainage. *J Hydrol* 372:136–148
72. Ali HN, Atekwana EA (2011) The effect of sulfuric acid neutralization on carbonate and stable carbon isotope evolution of shallow groundwater. *Chem Geol* 284:217–228
73. Telmer K, Veizer J (1999) Carbon fluxes, $p\text{CO}_2$, and substrate weathering in a large northern river basin, Canada: carbon isotope perspectives. *Chem Geol* 159:61–86
74. Raistrick M, Mayer B, Shevalier M, Perez RJ, Hutcheon I, Perkins E, Gunter B (2006) Using chemical and isotopic data to quantify ionic trapping of injected carbon dioxide in oil field brines. *Environ Sci Technol* 40:6744–6749
75. Myrntinen A, Becker V, van Geldern R, Würdemann H, Morozova D, Zimmer M, Taubald H, Blum P, Barth JAC (2010) Carbon and oxygen isotope indications for CO_2 behaviour after injection: first results from the Ketzin site (Germany). *Int J Greenhouse Gas Control* 4:1000–1006
76. MacNamara J, Thode HG (1950) Comparison of the isotopic composition of terrestrial and meteoritic sulfur. *Phys Rev* 78:307–308
77. Thode HG (1991) Sulphur isotopes in nature and the environment: an overview. In: Krouse HR, Grinenko VA (eds) *Stable isotopes: natural and anthropogenic sulphur in the environment*. Wiley, Chichester, New York, Brisbane, Toronto, Singapore
78. Holser WT, Kaplan IR (1966) Isotope geochemistry of sedimentary sulfates. *Chem Geol* 1:93–135
79. Szaran J, Niezgodna H, Halas S (1998) New determination of oxygen and sulphur isotope fractionation between gypsum and dissolved sulphate. *RMZ Mater Geoenviron* 45:180–182
80. Migdisov AA, Ronov AB, Grinenko VA (1983) The sulphur cycle in the lithosphere. In: Ivanov MV, Freney JR (eds) *The global biogeochemical sulphur cycle*, SCOPE 19. Wiley, Chichester, pp 25–95
81. Strauss H (1997) The isotopic composition of sedimentary sulfur through time. *Palaeogeogr Palaeoclimatol Palaeoecol* 132:97–118
82. Krouse HR, Mayer B (2000) Sulphur and oxygen isotopes in sulphate. In: Cook P, Herzceg A (eds) *Environmental tracers in subsurface hydrology*. Kluwer Academic Publishers, Norwell, pp 195–231
83. Rock L, Mayer B (2009) Identifying the influence of geology, land use, and anthropogenic activities on riverine sulfate on a watershed scale by combining hydrometric, chemical and isotopic approaches. *Chem Geol* 262:121–130
84. Gammons CH, Duaiame TE, Parker SR, Poulson SR, Kennelly P (2010) Geochemistry and stable isotope investigation of acid mine drainage associated with abandoned coal mines in central Montana, USA. *Chem Geol* 269:100–112
85. Hinckley ES, Kendall C, Loague K (2008) Not all water becomes wine: Sulfur inputs as an opportune tracer of hydrochemical losses from vineyards. *Water Resour Res* 44:W00401. doi:[10.1029/2007WR006672](https://doi.org/10.1029/2007WR006672)
86. Houhou J, Lartiges BS, France-Lanord C et al (2010) Isotopic tracing of clear water sources in an urban sewer: a combined water and dissolved sulfate stable isotope approach. *Water Res* 44:256–266
87. Shin W-J, Ryu J-S, Mayer B, Lee K-S, Lee S-W (2014) Natural and anthropogenic sources and processes affecting water chemistry in two South Korean streams. *Sci Total Environ* 485–486:270–280
88. Yamanaka M, Kumagai Y (2006) Sulfur isotope constraint on the provenance of salinity in a confined aquifer system of the southwestern Nobi Plain, central Japan. *J Hydrol* 325:35–55

89. Cortecchi G, Dinelli E, Bencini A, Adorni Braccesi A, La Ruffa G (2002) Natural and anthropogenic SO₄ sources in the Arno river catchment, Northern Tuscany, Italy: a chemical and isotopic reconnaissance. *Appl Geochem* 17:79–92
90. Hosono T, Wangb C-H, Umezawa Y, Nakano T, Onodera S-I NT, Yoshimizu C, Tayasu I, Taniguchi M (2011) Multiple isotope (H, O, N, S and Sr) approach elucidates complex pollution causes in the shallow groundwaters of the Taipei urban area. *J Hydrol* 397:23–36
91. Blowes DW, Ptacek CJ, Jambor JL, Weisener CG (2003) The geochemistry of acid mine drainage. In: Lollar BS (ed) Holland HD, Turekian KK executive (eds) *Treatise on geochemistry*, vol 9. Elsevier, Amsterdam, pp 149–204, p 612. ISBN 0-08-043751-6
92. Junk G, Svec HV (1958) The absolute abundance of the nitrogen isotopes in the atmosphere and compressed gas from various sources. *Geochim Cosmochim Acta* 14:234–243
93. Fry B (1991) Stable isotope diagrams of freshwater food webs. *Ecology* 72:2293–2297
94. Kendall C (1998) Tracing nitrogen sources and cycling in catchments. In: Kendall C, McDonnell JJ (eds) *Isotope-tracers in catchment hydrology*. Elsevier, Amsterdam (The Netherlands)
95. Kendall C, Elliott EM, Wankel SD (2007) Tracing anthropogenic inputs of nitrogen to ecosystems. In: Michener RH, Lajtha K (eds) *Stable isotopes in ecology and environmental science*, 2nd edn. Blackwell, Oxford, pp 375–449
96. Xue D, Botte J, Baets BD, Accoe F, Nestler A, Taylor P, Cleemput OV, Berglund M, Boeckx P (2009) Present limitations and future prospects of stable isotope methods for nitrate source identification in surface- and groundwater. *Water Res* 43:1159–1170
97. Holloway JM, Dahlgren RA (2002) Nitrogen in rock: occurrences and biogeochemical implications. *Global Biogeochem Cycles* 16(4):1118. doi:[10.1029/2002GB001862](https://doi.org/10.1029/2002GB001862)
98. Amberger A, Schmidt H-L (1987) Natürliche Isotopengehalte von Nitrat als Indikatoren für dessen Herkunft. *Geochim Cosmochim Acta* 51:2699–2705
99. Kendall C, Aravena R (2000) Nitrate isotopes in groundwater systems. In: Cook P, Herczeg AL (eds) *Environmental tracers in subsurface hydrology*. Kluwer Academic Publishers, Dordrecht, pp 261–297
100. Panno SV, Hackley KC, Hwang HH, Kelly WR (2001) Determination of the sources of nitrate contamination in karst springs using isotopic and chemical indicator. *Chem Geol* 179:113–128
101. Burns DA, Kendall C (2002) Analysis of delta N-15 and delta O-18 to differentiate NO₃⁻ sources in runoff at two watersheds in the Catskill Mountains of New York. *Water Resour Res* 38(5):1–14
102. Campbell DH, Kendall C, Chang CCY, Silva SR, Tonnessen KA (2002) Pathways for nitrate release from an alpine watershed: determination using δ¹⁵N and δ¹⁸O. *Water Resour Res* 38(5):1–11
103. Fenech C, Rock L, Nolan K, Tobin J, Morrisey A (2012) The Potential for a suite of isotope and chemical markers to differentiate sources of nitrate contamination: a review. *Water Res.* 46, 2023–2041
104. Fukada T, Hiscock KM, Dennis PF (2004) A dual-isotope approach to the nitrogen hydrochemistry of an urban aquifer. *Appl Geochem* 19:709–719
105. Kwang-Sik L, Yeon-Sik B, Dongho L, Yongje K, Kangjoo K (2008) Tracing the sources of nitrate in the Han River watershed in Korea, using δ¹⁵N–NO₃ and δ¹⁸O–NO₃ values. *Sci Total Environ* 395:117–124
106. Nisi B, Vaselli O, Tassi F, de Elío J, Delgado HA, Mazadiego LF, Ortega M (2013) Hydrogeochemistry of surface and underground waters in the Hontomin-Huermeces area (Burgos, Spain). *Int J Greenhouse Gas Contr* 14:151–168
107. Nisi B, Vaselli O, Bucciati A, Silva SR (2005) Sources of nitrate in the Arno River Waters: constraints δ¹⁵N and δ¹⁸O. *GeoActa* 4:13–24
108. Elliott EM, Kendall C, Boyer EW (2009) Dual nitrate isotopes in dry deposition: utility for partitioning NO_x source contributions to landscape nitrogen deposition. *J Geophys Res G Biogeosci* 114(4):G04020. doi:[10.1029/2008JG000889](https://doi.org/10.1029/2008JG000889)

109. Mariotti A, Landreau A, Simon B (1988) N isotope biogeochemistry and natural denitrification process in groundwater: application to the chalk aquifer of northern France. *Geochim Cosmochim Acta* 52:1869–1878
110. Aravena R, Robertson WD (1998) Use of multiple isotope tracers to evaluate denitrification in ground water: study of nitrate from a large-flux septic system plume. *Ground Water* 36:975–982
111. Chen DJJ, MacQuarrie KTB (2005) Correlation of $\delta^{15}\text{N}$ and $\delta^{18}\text{O}$ in NO_3^- sources during denitrification in groundwater. *J Environ Eng Sci* 4:221–226
112. Fukada T, Hiscock KM, Dennis PF, Grischek T (2003) A dual isotope approach to identify denitrification in ground water at a river bank infiltration site. *Water Res* 37:3070–3078
113. Mengis M, Schiff SL, Harris M, English MC, Aravena R, Elgood RJ, Maclean A (1999) Multiple geochemical and isotopic approaches for assessing ground water NO_3^- elimination in a riparian zone. *Ground Water* 37:448–457
114. Li SL, Liu CQ, Lang YC, Zhao ZQ, Zhou ZH (2010) Tracing the sources of nitrate in karstic groundwater in Zunyi, Southwest China: a combined nitrogen isotope and water chemistry approach. *Environ Earth Sci* 60:1415–1423
115. Einsiedl F, Mayer B (2006) Hydrodynamic and microbial processes controlling nitrate in a fissured-porous karst aquifer of the Franconian Alb, Southern Germany. *Environ Sci Technol* 40(21):6697–6702
116. Savard MM, Somers G, Smirnoff A, Paradis D, Bochove E, Liao S (2010) Nitrate isotopes unveil distinct seasonal N-sources and the critical role of crop residues in groundwater contamination. *J Hydrol* 381:134–141
117. Nellemann C, MacDevette M, Manders T, Eickhout B, Svihus B, Prins AG, Kaltenborn BP (eds) (2009) The environmental food crisis – The environment’s role in averting future food crises. A UNEP rapid response assessment. United Nations Environment Programme, GRID-Arendal, Birkeland Trykkeri AS, Norway, ISBN: 978-82-7701-054-0
118. Su XS, Wang H, Zhang YL (2013) Health risk assessment of nitrate contamination in groundwater: a case study of an agricultural area in Northeast China. *Water Resour Manage* 27:3025–3034
119. Zhang Y, Li F, Zhang Q, Li J, Liu Q (2014) Tracing nitrate pollution sources and transformation in surface- and ground-waters using environmental isotopes. *Sci Total Environ* 490:213–222
120. Leeman WP, Sisson VP (1996) Geochemistry of boron and its implications for crustal and mantle processes. In: Grew ES, Anovitz LM (eds) *Boron: mineralogy, petrology and geochemistry, reviews of mineralogy*, vol 33. Mineralogical Society of America, Washington, pp 645–707
121. Christ CL, Boron HH (1978) In: Wedepohl KH (ed) *Elements H(1) to Al(13)*, vol II/1. Springer, Berlin, pp 5-A-1–5-O-10
122. Jahiruddin M, Smart R, Wade AJ, Neal C, Cresser MS (1998) Factors regulating the distribution of boron in water in the River Dee catchment in north east Scotland. *Sci Total Environ* 210/211:53–62
123. Hasenmueller EA, Criss RE (2013) Multiple sources of boron in urban surface waters and groundwaters. *Sci Total Environ* 447:235–247
124. Pennisi M, Bianchini G, Muti A, Kloppmann W, Gonfiantini R (2006) Behaviour of boron and strontium isotopes in groundwater–aquifer interactions in the Cornia Plain (Tuscany, Italy). *Appl Geochem* 21:1169–1183
125. Vengosh A, Heumann KG, Juraske S, Kasher R (1994) Boron isotope applications for tracing sources of contamination in groundwater. *Environ Sci Technol* 28:1968–1974
126. Catanzaro EJ, Champion CE, Garner EL, Malinenko G, Sappenfield KM, Shields KM (1970) Boric acid: isotopic and assay standard reference materials. US National Bureau of Standards, Special Publication, Washington, D.C. 260–17, p 70

127. Pennisi M, Gonfiantini R, Grassi S, Squarci P (2006) The utilization of boron and strontium isotopes for the assessment of boron contamination of the Cecina River alluvial aquifer (central-western Tuscany, Italy). *Appl Geochem* 21:643–655
128. Barth SR (2000) Geochemical and boron, oxygen and hydrogen isotopic constraints on the origin of salinity in groundwaters from the crystalline basement of the Alpine Foreland. *Appl Geochem* 15:937–952
129. Faure G (1986) *Principles of isotope geology*. Wiley, New York, p 589
130. Négrel P, Casanova J, Aranyossy JF (2001) Strontium isotope systematics used to decipher the origin of groundwaters sampled from granitoids: the Vienne Case (France). *Chem Geol* 177:287–308
131. Négrel P, Petelet-Giraud E (2005) Strontium isotopes as tracers of groundwater-induced floods: the Somma case study (France). *J Hydrol* 305:99–119
132. Nisi B, Buccianti A, Vaselli O, Perini G, Tassi F, Minissale A, Montegrossi G (2008) Hydrogeochemistry and strontium isotopes in the Arno River Basin (Tuscany, Italy): Constraints on natural controls by statistical modelling. *J Hydrol* 360:166–183
133. Widory D, Kloppmann W, Chery L, Bonnin J, Rochdi H, Guinamant JL (2004) Nitrate in groundwater: an isotopic multi-tracer approach. *J Contam Hydrol* 72:165–188
134. Bullen TD, Krabbenhoft DP, Kendall C (1996) Kinetic and mineralogic controls on the evolution of groundwater chemistry and $^{87}\text{Sr}/^{86}\text{Sr}$ in a sandy silicate aquifer, northern Wisconsin, USA. *Geochim Cosmochim Acta* 60:1807–1821
135. Horan MF, Bohlke JM (1996) Isotopic composition of strontium in agriculture ground waters, Locust Grove Maryland. American Geophysical Union Spring Meeting, p S-102
136. Négrel P (1999) Geochemical study of a granitic area—The Margeride Mountains, France: chemical element behaviour and $^{87}\text{Sr}/^{86}\text{Sr}$ constraints. *Aquat Geochem* 5:125–165
137. Négrel P, Deschamps P (1996) Natural and anthropogenic budgets of a small watershed in the Massif Central (France): chemical and strontium isotopic characterization of water and sediments. *Aquat Geochem* 2:1–27
138. Jørgensen NO, Andersen MS, Engesgaard P (2008) Investigation of a dynamic seawater intrusion event using strontium isotopes ($^{87}\text{Sr}/^{86}\text{Sr}$). *J Hydrol* 348:257–269
139. Bouchaou L, Michelot JL, Vengosh A, Hsissou Y, Qurtobi M, Gaye CB, Bullen TD, Zuppi GM (2008) Application of multiple isotopic and geochemical tracers for investigation of recharge, salinization, and residence time of water in the Souss–Massa aquifer, southwest of Morocco. *J Hydrol* 352:267–287
140. Dotsika E, Poutoukis D, Kloppmann W, Guerrot C, Voutsas D, Kouimtzis TH (2010) The use of O, H, B, Sr and S isotopes for tracing the origin of dissolved boron in groundwater in Central Macedonia, Greece. *Appl Geochem* 25:1783–1796
141. Meredith K, Moriguti T, Tomascak P, Hollins S, Nakamura E (2013) The lithium, boron and strontium isotopic systematics of groundwaters from an arid aquifer system: Implications for recharge and weathering processes. *Geochim Cosmochim Acta* 112:20–31
142. Cary L, Casanova J, Gaaloul N, Guerrot C (2013) Combining boron isotopes and carbamazepine to trace sewage in salinized groundwater: A case study in Cap Bon, Tunisia. *Appl Geochem* 34:126–139
143. Han G, Liu C (2006) Strontium isotope and major ion chemistry of the rainwaters from Guiyang, Guizhou Province. *China Sci Total Environ* 364:165–174
144. Soler A, Canals A, Goldstein S, Otero N, Antich N, Spangenberg J (2002) Sulfur and strontium isotope composition of the Llobregat river (NE Spain): tracers of natural and anthropogenic chemicals in stream waters. *Water Air Soil Pollut* 136:207–224
145. Petelet-Giraud E, Klaver G, Négrel P (2009) Natural versus anthropogenic sources in the surface- and groundwater dissolved load of the Dommel river (Meuse basin): constraints by boron and strontium isotopes and gadolinium anomaly. *J Hydrol* 369:336–349
146. Jiang Y (2011) Strontium isotope geochemistry of groundwater affected by human activities in Nandong underground river system, China. *Appl Geochem* 26:371–379

147. Johnson KS, Gordon RM, Coale KH (1997) What controls dissolved iron concentrations in the world ocean? *Mar Chem* 57:137–161
148. Pham AN, Rose AL, Feitz AJ, Waite TD (2006) Kinetics of Fe(III) precipitation in aqueous solutions at pH 6.0–9.5 and 25 °C. *Geochim Cosmochim Acta* 70:640–650
149. Beard BL, Johnson CM (2004) Fe isotope variations in the modern and ancient earth and other planetary bodies. *Rev Mineral Geochem* 55:319–357
150. Dauphas N, Rouxel O (2006) Mass spectrometry and natural variations of iron isotopes. *Mass Spectrom Rev* 25:515–550
151. Hoefs J (2009) *Stable isotope geochemistry*. Springer, Berlin/Heidelberg
152. Skulan JL, Beard BL, Johnson CM (2002) Kinetic and equilibrium Fe isotope fractionation between aqueous Fe(III) and hematite. *Geochim Cosmochim Acta* 66:2995–3015
153. Welch SA, Beard BL, Johnson CM, Braterman PS (2003) Kinetic and equilibrium Fe isotope fractionation between aqueous Fe(II) and Fe(III). *Geochim Cosmochim Acta* 67(4231):4250
154. Brantley SL, Liermann LJ, Gynn RL, Anbar A, Icopini GA, Barling J (2004) Fe isotopic fractionation during mineral dissolution with and without bacteria. *Geochim Cosmochim Acta* 68:3189–3204
155. Teutsch N, von Gutten U, Porcelli D, Cirpka OA, Halliday AN (2005) Adsorption as a cause for iron isotope fractionation in reduced groundwater. *Geochim Cosmochim Acta* 69:4175–4185
156. Butler IB, Archer C, Vance D, Oldroyd A, Rickard D (2005) Fe isotope fractionation on FeS formation in ambient aqueous solution. *Earth Planet Sci Lett* 236:430–442
157. Wiesli RA, Beard BL, Johnson CM (2004) Experimental determination of Fe isotope fractionation between aqueous Fe(II), siderite and “green rust” in abiotic systems. *Chem Geol* 211:343–362
158. Crosby HA, Roden EE, Johnson CM, Beard BL (2007) The mechanisms of iron isotope fractionation produced during dissimilatory Fe(III) reduction by *Shewanella putrefaciens* and *Geobacter sulfurreducens*. *Geobiology* 5:169–189
159. Icopini GA, Anbar AD, Ruebush SS, Tien M, Brantley SL (2004) Iron isotope fractionation during microbial reduction of iron: the importance of adsorption. *Geology* 32:205–208
160. Johnson CM, Roden EE, Welch SA, Beard BL (2005) Experimental constraints on Fe isotope fractionation during magnetite and Fe carbonate formation coupled to dissimilatory hydrous ferric oxide reduction. *Geochim Cosmochim Acta* 69:963–993
161. Fantle MS, DePaolo DJ (2004) Iron isotopic fractionation during continental weathering. *Earth Planet Sci Lett* 228(3–4):547–562
162. Bergquist BA, Boyle EA (2006) Iron isotopes in the Amazon River system: weathering and transport signatures. *Earth Planet Sci Lett* 248(1–2):54–68
163. Severmann S, German CR, Edmonds HN, Beard BL, Johnson CM (2003) The modification of hydrothermal Fe-isotopic signature during plume-processing. *Geochim Cosmochim Acta* 67:A424
164. Wu J, Boyle E, Sunda W, Wen L-S (2001) Soluble and colloidal iron in the Oligotrophic North Atlantic and North Pacific. *Science* 293:847–849
165. Johnson CM, Beard BL (2006) Fe isotopes: an emerging technique for understanding modern and ancient biogeochemical cycles. *GSA Today* 16(11):1–10
166. Castorina F, Petrini R, Galic A, Slejko FF, Aviani U, Pezzetta E, Cavazzini G (2013) The fate of iron in waters from a coastal environment impacted by metallurgical industry in Northern Italy: hydrochemistry and Fe-isotopes. *Appl Geochem* 34:222–230
167. Bullen TD (2014) Metal stable isotopes in weathering and hydrology. In: Holland H, Turekian K (eds) *Treatise on Geochemistry*, 2nd edn, vol 7. Elsevier, Amsterdam, p 329–359
168. Kotas J, Stasicka Z (2000) Chromium occurrence in the environment and methods of its speciation. *Environ Pollut* 107:263–283
169. Rosman JR, Taylor PD (1998) Isotopic compositions of the elements (technical report): commission on atomic weights and isotopic abundances. *Pure Appl Chem* 70:217–235
170. Izbicki JA, Ball JW, Bullen TD, Sutley SJ (2008) Chromium, chromium isotopes and selected trace elements, western Mojave Desert, USA. *Appl Geochem* 23:1325–1352
171. Schauble EA (2004) Applying stable isotope fractionation theory to new systems. In: Johnson CM, Beard BL, Albarede F (eds) *Geochemistry of non-traditional stable isotopes*. Reviews

- in mineralogy and geochemistry, vol 55. Mineralogical Society of America and Geochemical Society, Washington, DC, pp 65–111
172. Ellis AS, Johnson TM, Bullen TD (2002) Chromium isotopes and the fate of hexavalent chromium in the environment. *Science* 295:2060–2062
 173. Sikora ER, Johnson TM, Bullen TD (2008) Microbial mass-dependent fractionation of chromium isotopes. *Geochim Cosmochim Acta* 72:3631–3641
 174. Berna EC, Johnson TM, Makdisi RS, Basui A (2010) Cr stable isotopes as indicators of Cr (VI) reduction in groundwater: a detailed time-series study of a point-source plume. *Environ Sci Tech* 44:1043–1048
 175. Zink S, Schoenberg R, Staubwasser M (2010) Isotopic fractionation and reaction kinetics between Cr(III) and Cr(VI) in aqueous media. *Geochim Cosmochim Acta* 74:5729–5745
 176. Dossing LN, Dideriksen K, Stipp SLS, Frei R (2011) Reduction of hexavalent chromium by ferrous iron: a process of chromium isotope fractionation and its relevance to natural environments. *Chem Geol* 285:157–166
 177. Basu A, Johnson TM (2012) Determination of hexavalent chromium reduction using Cr stable isotopes: isotopic fractionation factors for permeable reactive barrier materials. *Environ Sci Tech* 46:5353–5360
 178. Han R, Qin L, Brown ST, Christensen JN, Beller HR (2012) Differential isotopic fractionation during Cr(VI) reduction by an aquifer-derived bacterium under aerobic versus denitrifying conditions. *Appl Environ Microbiol* 78:2462–2464
 179. Jamieson-Hanes JH, Gibson BD, Lindsay MJB, Kim Y, Ptacek CJ, Blowes DW (2012) Chromium isotope fractionation during reduction of Cr(VI) under saturated flow conditions. *Environ Sci Tech* 46:6783–6789
 180. Kitchen JW, Johnson TM, Bullen TD, Zhu J, Raddatz A (2012) Chromium isotope fractionation factors for reduction of Cr(VI) by aqueous Fe(II) and organic molecules. *Geochim Cosmochim Acta* 89:190–201
 181. Villalobos-Aragón A, Ellis AS, Armienta MA, Morton-Bermea O, Johnson TM (2012) Geochemistry and Cr stable isotopes of Cr-contaminated groundwater in León valley, Guanajuato, México. *Appl Geochem* 27:1783–1794
 182. Bonnand P, James RH, Parkinson IJ, Connelly DP, Fairchild IJ (2013) The chromium isotopic composition of seawater and marine carbonates. *Earth Planet Sci Lett* 382:10–20
 183. Wanner C, Sonnenthal EL (2013) Assessing the control on the effective kinetic Cr isotope fractionation factor: A reactive transport modeling approach. *Chem Geol* 337–338:88–98
 184. Frei R, Poiré D, Frei KM (2014) Weathering on land and transport of chromium to the ocean in a subtropical region (Misiones, NW Argentina): a chromium stable isotope perspective. *Chem Geol* 381:110–124
 185. Wedepohl KH (1995) The composition of the continental crust. *Geochim Cosmochim Acta* 59:217–239
 186. Bruins MR, Kapil S, Oehme FW (2000) Microbial resistance to metals in the environment. *Ecotoxicol Environ Saf* 45:198–207
 187. Ercal N, Gurer-Orhan H, Aykin-Burns N (2001) Toxic metals and oxidative stress part I: mechanisms involved in metal induced oxidative damage. *Curr Top Med Chem* 1:529–539
 188. Shields WR, Goldich SS, Garner EL, Murphy TJ (1965) Natural variations in the abundance ratio and the atomic weight of copper. *J Geophys Res* 70:479–491
 189. Ehrlich S, Butler I, Halicz L, Rickard D, Oldroyd A, Matthews A (2004) Experimental study of the copper isotope fractionation between aqueous Cu(II) and covellite, CuS. *Chem Geol* 209:259–269
 190. Borrok DM, Nimick DA, Wanty RB, Ridley WI (2008) Isotopic variations of dissolved copper and zinc in stream waters affected by historical mining. *Geochim Cosmochim Acta* 72:329–344
 191. Vance D, Archer C, Bermin J, Perkins J, Statham PJ, Lohan MC, Ellwood MJ, Mills RA (2008) The copper isotope geochemistry of rivers and the oceans. *Earth Planet Sci Lett* 274:204–213

The Importance of Reduced-Scale Experiments for the Characterization of Porous Media

S. Straface and E. Rizzo

Abstract In order to reduce threats to the quality of groundwater resources, prevention and control are the most important activities to carry out. In general, these activities require the ability to model the flow and solute transport phenomena in the aquifer. Thus, it is essential to collect information about potential contamination sources, boundary conditions, hydrological forcing, and the magnitudes and spatial distributions of the hydrodynamic and hydrodispersive parameters of the porous media. Measurements of such parameters, available only at a finite number of locations, are often obtained by means of different techniques and can be representative of various measurement scales.

The use of available data, necessarily distributed on different scales, for characterizing porous media at a defined scale is a key question of great interest. With the aim to investigate on the hydraulic conductivity scale effect on a homogeneous porous medium, several experiments were carried out at the Hydrogeosite Laboratory (Marsico Nuovo, Italy). This laboratory is a large scale model sized $10 \times 7 \times 3 \text{ m}^3$, filled with a homogeneous medium made up of quartz-rich sand. The results are described by separating the two important scale-ambits under consideration, obtaining two scale power laws. Moreover, the scale effect of the hydraulic conductivity has been detected by considering the water flow type (uniform or radial) into the porous medium. However, the results, either considering the only scale law or multi-scale laws, confirm what was proved by several authors for heterogeneous porous media, that is the trend of hydraulic conductivity to reach a higher limit when the measurement scale increases and, in our opinion, regardless of the heterogeneity of the porous medium. Finally, a hydrogeophysical

S. Straface (✉)

Dipartimento Difesa Suolo, Università della Calabria, Rende, Italy

CNR-IMAA, Marsico Nuovo, Italy

e-mail: Salvatore.straface@unical.it

E. Rizzo

CNR-IMAA, Marsico Nuovo, Italy

approach is described in this chapter, in order to show how a passive geophysical method as self-potential can estimate the hydraulic conductivity. It is an important step when large site should be characterized and few direct borehole data are available. These aspects are important because the hydraulic conductivity estimation is the first step for the characterization of a site.

Keywords Characterization, Experiments, Groundwater, Hydrogeophysics, Scale effect

Contents

1	Introduction	152
2	Materials and Methods	154
2.1	Hydraulic Measurements	154
3	Experiments and Results	158
3.1	Hydraulic Tests	159
4	Results and Discussion	165
5	Hydrogeophysical Approach	167
6	Conclusions	171
	References	173

Abbreviations

PET Polyethylene terephthalate
 SP Self potential

1 Introduction

Any substance that is placed or injected in the ground has the potential to affect groundwater quality. Land management practices can create diffuse or point sources of groundwater contamination, or alter natural groundwater recharge and flow paths, and some management activities can pose a risk that aquifers with good water quality will be polluted by water leakage from aquifers of poor water quality. This seriously threatens the quality of groundwater supply, especially in areas where the water table is high, i.e. situated near the earth surface.

In various branches of physics, data are usually transferred from a given scale to a different scale by means of different methods of upscaling (or downscaling). Regarding the issues related to the groundwater, reviews of deterministic and stochastic approaches addressing the hydraulic conductivity scaling problem for real aquifers have been offered by Renard and de Marsily [1] and recently by Sanchez-Vila et al. [2].

Since subsoil is heterogeneous and complex and data are generally scarce, the analysis of the processes of hydrological system at different scales is often fronted by means of a stochastic approach. Generally, the macroscopic properties measured at various points inside the hydrogeologic unit, more or less homogeneous, are usually considered as a sample from a statistically homogeneous, spatially correlated random field. Stochastic theories assume that all the functions (included correlation scale and variance) which are suitable for describing these random variables can be obtained from data available through direct geostatistical analysis (e.g., [3] and citation here included) or inverse models [4–6].

The hypothesis that the hydrogeologic units are statistically homogeneous, and so can be described through the unique integral scale of flow and transport parameters, was discussed in recent years on the basis of: (1) hydraulic conductivity varies at every measure-scale; (2) dispersivity changes at every scale selected for the event of contamination; (3) the integral scale varies at every sampling-domain dimension; (4) hydraulic conductivity, porosity, and dispersivity vary when the spatial resolution changes ([7], and their citations). This suggests that statistical homogeneity may not be an effective characteristic of the hydrogeologic medium properties, but a consequence of the investigation scale and the inference method [8].

Moreover, it is always more evident that the hydrogeologic properties of the porous and fractured media [9], as many other geologic and geophysical variables, may be statistically nonhomogeneous. Some aspects of this statistical nonhomogeneity are reproduced by various fractal models, such as fractional Gaussian noise the corresponding approximations by laws of power [10, 11], or the multifractals [12]. It is particularly interesting to observe that multiscale variability of several flow and transport parameters, in different geologic structures, at various sites and scales, is consistent with a fractal description of the logarithm of the hydraulic conductivity [13, 14].

Many of the above said scale dependences are captured upon the assumption that the logarithm of the hydraulic conductivity may be represented by introducing a hierarchy of statistically homogeneous random variables, characterized by mutually uncorrelated spatial variations, each of them is associated with a unique variance [15].

Then, this chapter briefly recalls some theoretical aspects, which are the basis of hydraulic conductivity measurement methods, defining for each of them the number of required measurements, that are fundamental statistical parameters characterizing the correspondent data set in terms of representative linear volumes and dimensions. Successively the scale law is defined for each of the measured values of the group of K measurements. The results obtained at the different scales and different typologies of water flow induced within the porous medium during the experiments are reported. Moreover, consequent to different values of K , due to different observation scales, a hydrogeophysical approach is introduced in order to highlight a new indirect method, which can strongly contribute to the assessment of K for a large scale approach.

2 Materials and Methods

2.1 Hydraulic Measurements

Modeling of flow and transport in porous media requires information about the spatial distributions of properties such as hydraulic conductivity. Measurements of such parameters, available only at a finite number of locations, are often obtained by means of different techniques and can be representative of various measurement scales. In this work, different techniques have been applied in order to estimate the magnitude of hydraulic conductivity at many different scales. Afterwards, we resume briefly the theory of such techniques in the specific conditions of the experiments shown.

2.1.1 Oedometer Tests

Oedometer is an instrument which may be utilized for evaluating the value of the hydraulic conductivity for small soil volumes, being careful to rebuilt faithfully the conditions in site. Generally, test of laboratory by means of the oedometer is subdivided into the following phases: (1) sampling of the soil, (2) extraction of the sample by means of a cutting ring with a 10 cm diameter like that of the oedometer, (3) placement of the sample within the oedometer, (4) saturation of the sample, (5) application of the external pressures in order to rebuilt the condition in site, and (6) execution of the test.

Repeating the measurements for several times, an average flow rate Q is measured and applying the Darcy's law the hydraulic conductivity of each sample calculated. In order to make more reliable the hydraulic conductivity estimation, the test is repeated almost three times for each sample and its average is calculated.

2.1.2 Falling Head Permeameter Tests

Falling head permeameter tests is a classical laboratory measurement of hydraulic conductivity. It is formed with a proctor type permeability cell, two porous cell plates and filter-papers used during the permeability tests. During the test, the hydraulic head at the up-gradient end and the discharge through the sample are measured at every fixed time. By means of these measurements it is possible to know how the head changes with respect to the time and then calculate the hydraulic conductivity of the sample. In fact, introducing the Darcy's law into the continuity equation and integrating it, it is possible to obtain a relationship for calculating the porous medium hydraulic conductivity [35]:

$$K = \frac{aL}{A(t - t_0)} \ln\left(\frac{h}{h_0}\right), \quad (1)$$

with h and h_0 are, respectively, the head at the time t and at the time of starting up t_0 , a is the section of the pressure gauges, A and L respectively the sample section and its height.

2.1.3 Slug Tests

In general, the slug test consists of measuring the recovery of head in a well after a quasi-instantaneous change in head due to the introducing of a solid object or equivalent volume of water into the well producing an abrupt increase in water level [16]. Following this sudden change, the water level in the well returns to static conditions as water moves out of the well in response to the gradient imposed by the sudden change in head. The variation of hydraulic head with time can be used to estimate the hydraulic conductivity of the formation through comparisons with theoretical models of test responses.

For this kind of tests, the aquifer-well screen geometry is very important and assumes a key role in the data analysis. Specifically, an unconfined formation with wells screened across the water table is considered in this study.

The vast majority of slug tests performed in unconfined formations in wells screened across the water table with the Bouwer and Rice [36] method is analyzed. This method, however, was developed for the analysis of tests performed in wells where water table is above the top of the screen, so the empirical coefficients used in the Bower and Rice method were developed for slug tests where the effective screen does not change. Previously, Boast and Kirkham [17] proposed a mathematical model for the analysis of slug tests in wells screened across water table, for wells with aspect ratios, i.e. the ratio between the length (b) and the effective radius (r_w) of the well screen, between 1 and 100. Dagan [18] proposed a more efficient approximated semi-analytical approach to evaluate the solution, but only for aspect ratios greater than 50:

$$\ln\left(\frac{H(t)(2b - H_0)}{H_0(2b - H(H(t)))}\right) = -\frac{2K_r b t}{\left(\frac{1}{P}\right)r_c^2}, \tag{2}$$

where $H(t)$ is the hydraulic head deviation from static condition, H_0 the measured value for the initial displacement determined immediately after test initiation, K_r the radial component of the hydraulic conductivity of the formation, t the total time since the start of the slug test, P a dimensionless flow parameter, and r_c is the effective radius of well casing. The form of the (2) indicates that a plot of the logarithm of the normalized head term on the left-hand side vs time will be linear.

Thus, the Dagan method for wells screened across the water table involves calculating the slope of a straight line fit to a plot of the response data using that value to estimate the radial component of hydraulic conductivity:

$$K_r = \frac{m r_c^2}{2bP}, \tag{3}$$

where m is the slope of the logarithm of the normalized term vs time. If the aspect ratio is lower than 50, as in our case, the tabulated values of shape factors calculated by means of the Boast and Kirkham [17] model can be used and converted to P -values through the following equation:

$$P = \frac{864 \left(\frac{r_c}{b}\right)^2}{2 \left(\frac{H(t)}{b}\right) \left[1 - \left(\frac{H(t)}{2b}\right)\right] C_{BK}}, \quad (4)$$

where C_{BK} is a shape factor for specific $H(t)$, b and r_c values.

2.1.4 Short Pumping Tests

The short pumping test is an experimental method based on the exact solution of the unsteady, radial groundwater flow equation able to derive hydraulic conductivity and specific storage coefficient using only the first derivative with respect to time of the early induced drawdown [19]. In fact, when analyzing the behavior of the third derivative of the drawdown with respect to logarithmic time, it is easy to note that it vanishes when the first derivative attains its peak value (Fig. 2 in [19]). Since the third log-derivative is zero if and only if the argument of the Theis well function is equal to unity, this condition can be used easily to estimate the transmissivity and the storage coefficient, knowing the time at which the first derivative reaches its peak (t'), and so overcoming the problem of actually computing the third log-derivative, which is very unstable [37]. So, if the time t' is known, K can be obtained using the Theis solution by means of the following expression:

$$K = \frac{QW_1}{4\pi r^2 B w(t')}, \quad (5)$$

where Q is the pumping flow rate, W_1 is the well function value for $u = 1$ (i.e. 0.2194), r is the distance of the borehole from the pumping well, B is the saturated thickness, and $w(t')$ is the drawdown at the peak time.

The peak time ($r^2 S/4 t$) is directly proportional to the square distance of the borehole from the pumping well and the storage coefficient and inversely to the transmissivity. Generally, it occurs at a time very close to the pumping startup; for this reason, this experiment type is named short pumping test.

2.1.5 Pumping Tests

Traditionally, aquifer properties are determined by collecting drawdown time data of the aquifer induced by pumping, and then matching the data with analytical solutions, which assume homogeneity of the aquifer.

The “Theis solution” (1935) is one of the commonly used analytical solutions in aquifer tests. It is derived from the equation of unsteady radial, horizontal, ground-water flow in a confined aquifer with constant K and S_S . Although the Theis solution is strictly applicable only to such idealized flow and aquifer conditions, it has been widely used in the field to estimate aquifer properties given drawdown time data from an observation well during an aquifer test.

In our case, pumping tests will be carried out in the Hydrogeosite large model, so in an unconfined aquifer. The condition of the unconfined aquifer led to the use of the Neuman-type Curve method (1975) that supplies the permeability K and of the specific yield S_y of the porous medium for a homogeneous and anisotropic unconfined aquifer with delayed drainage. According to this theory, the drawdown time adimensional curve is an S-shaped curve, made up of a very steep first length corresponding to the initial instants, a flatter second length at the intermediate times and again a steep length until the quasi-steady state condition is reached. This curve trend differs from the Theis solution for confined aquifers in the presence of the intermediate length that interrupts the monotonic trend of the curve. This different behavior is essentially due to the delayed drainage of the amount of stored water in the unsaturated zone. The S-shaped curve may be more or less (monotonic) evident depending on the unsaturated thickness or penetration degree of the pumping well [20].

In fact, when the unsaturated thickness is very thin with respect to the saturated zone, the quantity of stored water in the unsaturated zone is small and therefore the delayed drainage is negligible. The monotonic behavior could be explained with the Tartakovsky and Neuman [21] theory, in which the effect of unsaturated flow on drawdown is captured fully by the dimensionless parameter $K_D = kb$ in which k is a constitutive exponent having the dimension of inverse length and b is the initial saturated thickness. According to this solution, unsaturated flow is seen to have significant impact on dimensionless log–log time-drawdown behavior when K_D is less than 1 (the aquifer has large retention capacity and/or small initial saturated thickness). The impact of unsaturated flow diminishes as K_D increases, becoming small or insignificant at K_D greater than 10 (small retention capacity and/or large saturated thickness). At these large K_D values, this solution practically coincides with that of Neuman [38]. When K_D is small, unsaturated flow causes dimensionless drawdown to increase at early and intermediate dimensionless times and to decrease at late time, the impact being least pronounced at early time and most pronounced at intermediate time. The overall effect is to eliminate S-shaped inflections, rendering the dimensionless log–log time-drawdown curve more monotonic.

Moreover, the effect of the vertical flow of the unsaturated zone on the draw-down in a borehole decreases with an increase of the degree of penetration of the well and of the borehole. The reason is that as the pumping well penetrates the saturated zone more fully vertical flux components, which dominate drainage from the unsaturated zone, diminish. On the other hand, the effect of unsaturated flow is most pronounced at the water table, more so closer to the pumping well than farther from it, and least near the aquifer bottom. This is so because the average is less sensitive than are point drawdowns to vertical fluxes and hence to drainage from above the water table.

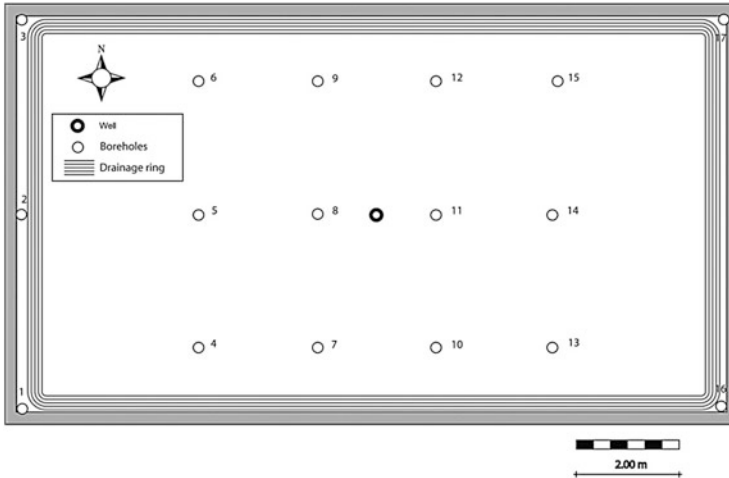


Fig. 1 A sketch of the large scale model hydrogeosite. The *numbered circles* represent the piezometers, while the *bold circle* represents the pumping well

As a consequence of these conditions drawdown-time data are aligned on the Late Theis-type Curve in the Neuman Type Curve, and according to this, Theis solution as a confined aquifer is applied.

3 Experiments and Results

In 2006, at the Geophysics Laboratory of the CNR-IMAA-Pole of Marsico Nuovo (Italy), a large scale facility was created $10 \times 7 \times 3 \text{ m}^3$ in size and filled with a homogeneous quartz-rich sand (95% SiO_2), with a high percentage (86.4%) of grains between 0.063 and 0.125 mm and a medium-high permeability [20].

From a hydraulic point of view, 17 observation boreholes, a pumping well and a drainage ring around its edge were emplaced (Fig. 1). Both boreholes and pumping well are completely penetrating and completed with corrugated drainpipes in PET (polyethylene terephthalate) and covered with geo-textile to stop the sand entering. The drainage ring, connected to two inlet/outlet tanks, allows the head boundary conditions to be obtained (fixed or variable with time) or no flow condition depending on the configurations required during the experiment. The pumping well is equipped with an external peristaltic-type pump, while the 17 boreholes are fitted with pressure-sensing transducers that enable continuous, high precision monitoring of the variations in the hydraulic head as well as in the drawdown due to pumping.

The following describes the various tests carried out at different scales in Hydrogeosite. The order in which the tests are described is not a function of the volume of support, but of the temporal order with which they were made.

Table 1 Hydraulic conductivity values (10^{-7} m/s) obtained by means of oedometer tests on soil sample extracted in the hydrogeosite

Location	K_I	K_{II}	K_{III}	Mean
4	4.87	2.54	n.a.	3.70
6	1.31	1.43	1.89	1.54
8	5.07	3.41	2.64	3.71
12	4.67	3.52	3.07	3.75
13	2.23	2.41	n.a.	2.32
14	n.a.	3.04	3.38	3.21
Well	2.94	3.71	n.a.	3.33
Mean				3.08
SD				0.84

3.1 Hydraulic Tests

3.1.1 Oedometer Tests

At first, we show measurements of hydraulic conductivity realized by means of the oedometer tests. Close to piezometers in the Hydrogeosite and until a depth of about 10 cm, 15 soil samples were extracted and, in order to preserve soil moisture, a plastic film was wrapped up around each of them. Since the soil was allocated in the oedometer, a mean uniform steady state flow was established imposing a difference of hydraulic pressure between the bottom and the top. This was at the atmospheric pressure because the valve was open. Through a buret the water volume of the sample was measured at fixed intervals of time Δt and repeated for about 10 times for each experiment, in order to calculate an average flow rate Q . So, by means of Darcy's law the hydraulic conductivity of each sample was calculated. With the aim to make more reliable the hydraulic conductivity estimation, the experiment was repeated three times for each sample and the average value was calculated.

In this case, due to the mean uniform flow that occurs in the oedometer, the support volume is about 236 cm^3 and the characteristic length is the distance between the bottom and the top of the oedometer, i.e. 3 cm. As we can see in Table 1, arithmetic mean of the hydraulic conductivities is 3.08×10^{-7} m/s while the standard deviation is 8.42×10^{-8} .

3.1.2 Falling Head Permeameter Tests

As done for the oedometer test, also for the falling head permeameter an undisturbed soil samples were extracted from the Hydrogeosite, but in this case only three soil cores were sampled in different locations of the Hydrogeosite. The used falling head permeameter had a proctor type permeability cell 11.68 cm high and with an area of 81.39 cm^2 . The cell plate had bores of 2 mm of diameter within a grid with 1 cm spacing. The filter-paper used during the permeability tests was of type N. 40.

Table 2 Hydraulic conductivity values (10^{-6} m/s) obtained by means of falling head permeameter tests on soil sample extracted in the hydrogeosite

Location	K_I	K_{II}	K_{III}	K_{IV}	K_V	K_{VI}	K_{VII}	Mean
1	5.16	5.94	56.5	5.30	–	–	–	5.51
2	2.78	2.48	2.25	2.15	2.03	2.36	2.10	2.31
3	0.82	1.06	0.96	0.93	1.04	0.95	0.91	0.95
Mean								2.92
SD								2.34

Before beginning the tests, the soil sample was left to saturate for about 12 h. During the test, the hydraulic head at the up-gradient end and the discharge through the sample were measured with a sampling rate of 20 s. By means of these measurements and by using the equation of the Darcy law, we have calculated the hydraulic conductivity of the sample. So, in this case a mean uniform flow occurs in the permeameter, and the support volume can be evaluated to about 951 cm^3 and the characteristic length is the permeameter high, i.e. 11.68 cm. Analyzing the data, an arithmetic mean of the hydraulic conductivities of 2.92×10^{-6} m/s was obtained with a standard deviation of 2.34×10^{-6} for K (Table 2).

3.1.3 Pumping Tests

The experiments were preceded by a preliminary study phase by means of a “numerical laboratory” or rather a mathematical model capable of simulating the behavior of the physical model and therefore of calculating the optimum pumping flow, the boundary conditions, the length of the transitory in the pumping and recovery phase, as well as the response of the physical model in terms of hydraulic head.

Once the preliminary study phase was concluded, the facility was filled from the bottom to avoid the formation of air bubbles and using the drainage ring a (initial) hydraulic head was fixed at 2.80 m above the bottom of the facility. With this boundary conditions three classical pumping tests were carried out and drawdowns were monitored in the Hydrogeosite boreholes. The flow pumped from the well was fixed and monitored using an electromagnetic flow meter with a digital converter. The pumping lasted the time necessary to reach steady state condition in each pumping test. The condition of the unconfined aquifer led to the use of the Neuman type-Curve (1975) that supplies the hydraulic conductivity K and the specific yield S_y of the porous medium for a homogeneous and anisotropic unconfined aquifer with an infinite extension and fully penetrating well and with delayed drainage. According to Tartakovsky and Neuman [21], applying the Neuman-type curve to the drawdown-time data, these points fall on the Theis-type curve (Fig. 2) because of the small unsaturated thickness, the fully penetrating pumping well and the large retention capacity of the sand.

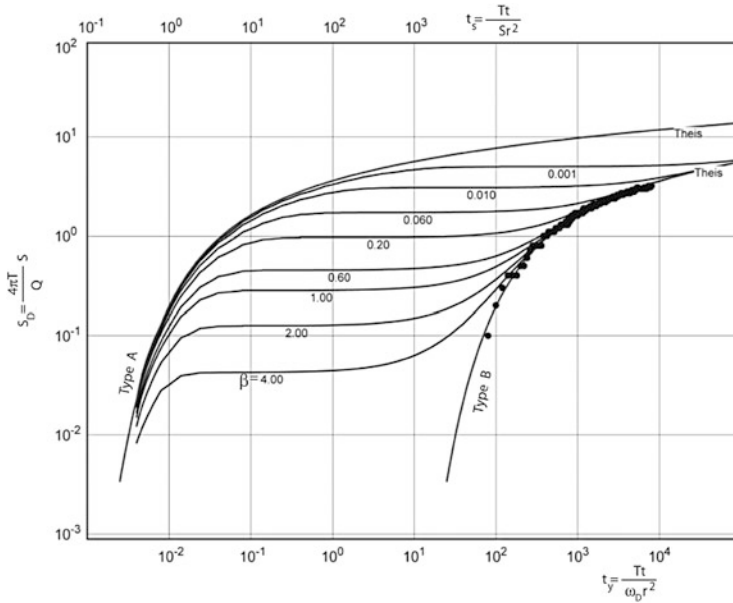


Fig. 2 Analysis of the drawdown for borehole 14 using the Neuman Type-Curve. The same behavior was obtained for all the other drawdown-time curves for all the other monitored boreholes for each pumping test

Table 3 Hydraulic conductivity values (10^{-5} m/s) obtained by means of classical pumping tests in the hydrogeosite

Location	K_I	K_{II}	K_{III}	Mean
4	3.82	4.93	4.42	4.39
5	3.41	n.a.	4.34	3.88
6	n.a.	4.11	4.45	4.28
7	n.a.	4.96	4.15	4.55
8	3.41	4.61	4.28	4.10
9	3.41	5.44	4.23	4.36
10	3.41	4.56	4.23	4.07
11	2.71	4.64	4.13	3.83
12	n.a.	5.07	4.29	6.48
13	n.a.	5.49	4.11	4.80
14	3.40	n.a.	4.19	3.80
15	n.a.	4.89	n.a.	4.89
Mean				4.26
SD				0.38

Analyzing the pumping tests and all boreholes data, following results were obtained: arithmetic mean of the hydraulic conductivities is 4.30×10^{-5} m/s with a standard deviation of 3.78×10^{-6} for K (Table 3).

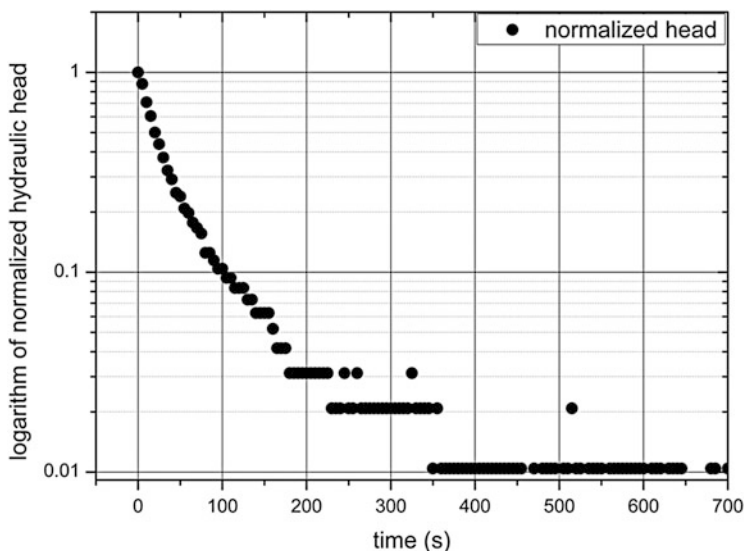


Fig. 3 Slug test: plot of normalized hydraulic head vs time

Table 4 Hydraulic conductivity values (10^{-5} m/s) obtained by means of slug tests in the boreholes of the hydrogeosite large model

Location	K_I	K_{II}	Mean
4	2.14	1.97	2.06
7	3.49	3.87	3.68
8	3.35	2.59	2.97
9	3.80	2.97	3.39
12	2.52	2.70	2.61
13	2.70	2.78	2.74
14	2.29	2.12	2.20
15	2.97	2.94	2.96
Mean			2.83
SD			0.55

3.1.4 Slug Tests

In order to characterize the porous medium eight slug tests were carried out in the boreholes of the large model and head changes through time were measured. The Dagan method for wells screened across the water table (1) has been used to estimate the hydraulic conductivity of the sand (Fig. 3). Using shape factors calculated by means of the Boast and Kirkham model (3) the calculated arithmetic mean of the hydraulic conductivities is 2.83×10^{-5} m/s with a standard deviation of 5.50×10^{-6} for K (Table 4).

For the aim of this study it is important to determine the support volume of slug test. Various are the methods proposed in literature for the calculus of support volume, or the influence radius, but all of them are empirical and more or less

complex. The method, here selected, is that suggested by Butler [16] and proposed by Barker and Black [22]:

$$R_{\max} = \frac{r_w}{\sqrt{a}},$$

where the slug test influence radius is indicated with R_{\max} , the well radius with r_w and the storage coefficient with a which may be calculated by means of the following equation proposed by Cooper and Jacob [23]:

$$a = \frac{r_w^2 S_s B}{r_c^2},$$

having indicated with S_s the specific storage coefficient, B the saturated thickness of the pool, and r_c the inner diameter of the well or piezometer in which the slug test was realized. Utilizing the average storage coefficient obtained by means of pumping tests ($S_s = 6.31 \times 10^{-3}$), a saturated thickness of 2.60 m and a borehole radius of 0.06 m, the influence radius is of near 0.45 m and, consequently, the support volume is about 0.412 m³.

3.1.5 Short Pumping Test

In the Hydrogeosite, a short pumping test was carried out after several classical pumping tests in order to estimate hydraulic conductivity with the early-time drawdown [19].

Analyzing drawdown in early-time in monitored boreholes and using the (5) it was possible to calculate hydraulic conductivity values. As it can be seen in Fig. 4, in borehole 4, far from the pumping well 3.6 m, the maximum is reached after 817 s and at this time the drawdown is equal to 0.0217 m. With these values of t' and $w(t')$, a value of $K = 2.88 \times 10^{-5}$ m/s is obtained. The same analysis was applied to the drawdown data from borehole 5, also around 3 m from the pumping well, where the maximum is reached after 508 s and at this time the drawdown is equal to 0.0166 m. With these values of t' and $w(t')$, the hydraulic conductivity K is equal to 3.76×10^{-5} m/s. With this data, the arithmetic mean of the hydraulic conductivities is 3.32×10^{-5} m/s, while a standard deviation of 6.21×10^{-6} for K was obtained (Table 5).

Regarding the support volume of this experimental test, analyzing the drawdown rate curve, we can estimate the influence volume of the porous medium at the peak time. Oliver [24] provided a formula for this estimate, which is valid for a small permeability variation from an average value:

$$r = \left(\frac{\bar{k}t}{n\mu c_t} \right), \quad (6)$$

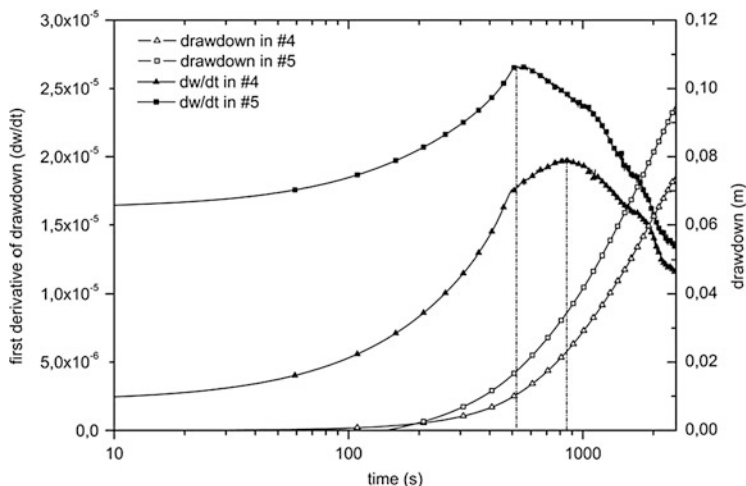


Fig. 4 Experimental pumping test in the hydrogeosite facility. Logarithmic plot of the draw-down (w) and the first derivative (dw/dt) versus time, for the boreholes 4 and 5

Table 5 Hydraulic conductivity values (10^{-5} m/s) obtained by means of short pumping test in the hydrogeosite large model

Location	K
4	2.88
5	3.76
Mean	3.32
SD	0.62

Table 6 Summary of measurements method applied on the uniform sand of the hydrogeosite large scale model and their major characteristics

Experimental test	Volume (m^3)	Length (m)	Flow type
Oedometer	2.36×10^{-5}	3×10^{-2}	1D mean uniform
Falling head permeameter	9.51×10^{-4}	1.17×10^{-1}	1D mean uniform
Slug	4.12×10^{-1}	4.49×10^{-1}	Radial (divergent)
Short pumping	$0.42 \times 10^{+1}$	$0.14 \times 10^{+1}$	Radial (convergent)
Pumping	$2.69 \times 10^{+1}$	$0.35 \times 10^{+1}$	Radial (convergent)

where r is the radial distance between the pumping well and the boundary of influence volume (i.e., support volume) (m), k is the average intrinsic permeability (mm), t is the time (h), n is the porosity (non-dimensional), μ is the dynamic viscosity (Pa s), and c_t is the total compressibility (Pa^{-1}).

Equation (6) was applied to the short pumping test data to estimate the support volume. In this case an influenced volume of about $4.2 m^3$ and, consequently, an influence radius of about 1.4 m was obtained.

Afterwards a summary of the tests carried out in the large scale laboratory model with some characteristic aspects of them are reported in Table 6.

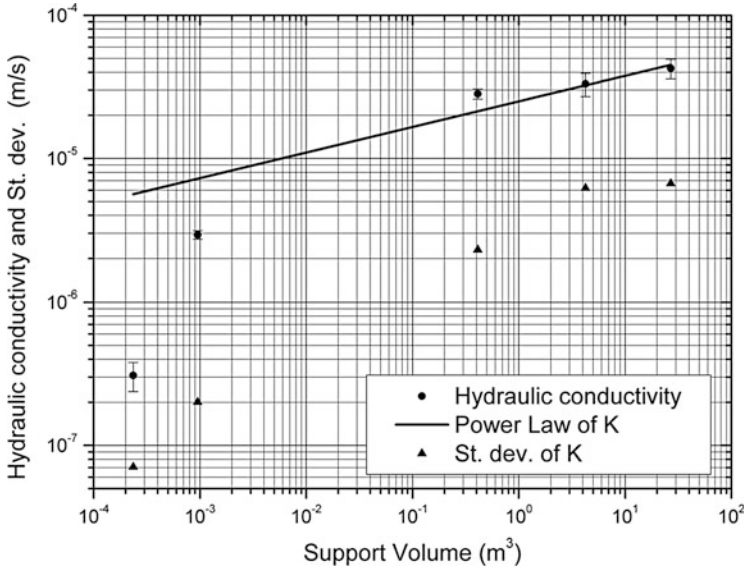


Fig. 5 Behavior of the hydraulic conductivity mean and its standard deviation with respect to support volume for each experimental test realized with a homogeneous quartz-rich sand in the hydrogeosite laboratory. The *straight line* represents the power law (7) in log–log axes obtained by means of a nonlinear least square method

4 Results and Discussion

For each experimental test, hydraulic conductivity was estimated in order to know its value at various scales. In fact, although the pool was filled with a unique sand type, a homogeneous quartz-rich sand (95% of SiO₂) equipped with a granulometry with a high percentage (86.4%) of grains between 0.063 and 0.125 mm, the pores distribution is chaotic and so a heterogeneity behavior, although small, is assumed. According to this assumption, hydraulic conductivity estimates show an evident scale effect even if the porous medium could be considered homogeneous respect to real aquifers. As we can see in Table 1 mean hydraulic conductivity grows with support volume as the standard deviation of *K*.

Now, it is necessary to analyze thoroughly the behavior of the hydraulic conductivity as support volume, or characteristic length, of the experimental test grows. Firstly, we have fitted these scattered points with different functions by means of a nonlinear least square method obtaining the best fitting ($R^2 = 0.90$) with a power law (Fig. 5). The following equation describes the scale dependence of hydraulic conductivity as a function of the support volume:

$$K = 2.503 \times 10^{-5} V^{0.179}. \tag{7}$$

By observing Fig. 5 it is possible to see a different scaling behavior for the small scale and large scale: (1) the first two values of hydraulic conductivity, relative to oedometer and falling head tests, respectively, were obtained with a uniform mean gradient flow condition, (2) the next three points represent hydraulic conductivities obtained in the Hydrogeosite by means of slug, short pumping and classical pumping tests in which a radial flow condition was established, (3) although the scale law, expressed by (7), shows a good determination coefficient, it is scarcely influenced by the low-scale values, whereas it is influenced strongly by the greater values and (4) it is evident that hydraulic conductivity obeys at two kinds of scaling law depending on the fluid flow type or on the experimental test scale (i.e., column scale or large model (Hydrogeosite) scale) [7]. Afterwards we interpolated the results of the characterization at different scales with two power laws, in the following way:

- For the first two hydraulic conductivity values representing both the uniform mean gradient flow and column tests, a coefficient of determination R^2 of 0.998 and the following relation:

$$K = 0.223 V^{1.614}. \quad (8)$$

- For the hydraulic conductivities estimated in the Hydrogeosite by means of slug, short pumping and classical pumping tests in which a radial flow founds, the following equation with R^2 equals to 0.931:

$$K = 3.00 \times 10^{-5} V^{0.101}. \quad (9)$$

Combining the fitted power laws for the two dependence scale hypotheses (i.e. fluid flow type and experimental scale) we have obtained the two plots showed in Fig. 6. These results are consistent with the findings of Fallico et al. [25, 26] obtained on the same porous medium but with a different apparatus for the small-scale experiments and using only three measurement scales.

In order to understand the reason of the scale effect and in particular to discriminate if this effect is due to the fluid flow type or to the experimental test scale another experiment was carried out. In this experiment the large scale laboratory model was used as a permeameter. Imposing in the drainage ring a little hydraulic head gradient between up-gradient and down-gradient ends a uniform flow was established in the pool. During the test, the discharge through the pool was measured at different times and hydraulic conductivity was estimated using the Darcy's law. Assuming as cross section area an average of that up-gradient and down-gradient ends the hydraulic conductivity is:

$$K = \frac{QL}{\Delta H B \bar{H}},$$

where Q is the discharge, L and B are, respectively, longitudinal and transversal length of the pool and \bar{H} is the mean hydraulic head. For this case, a hydraulic

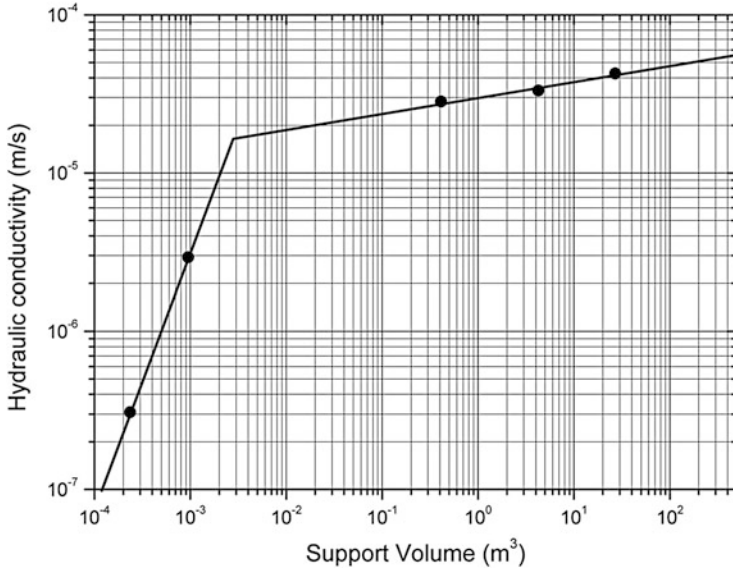


Fig. 6 Hydraulic conductivity versus support volume with two power laws: the first part is fitted with a power law valid for uniform gradient flow (8) and the second part for radial flow (9)

conductivity estimate of 5.86×10^{-5} m/s was obtained. The value of the hydraulic conductivity estimated for the large permeameter is well fitted by means of the large scale power law and this means that the scaling law of the hydraulic conductivity to many small scales (of the order of 10^{-3}) is different from that at larger scales (field scale) (Fig. 7).

5 Hydrogeophysical Approach

The characterization of a heterogeneous aquifer involves a wide spectrum of high resolution direct measurements of the characteristic parameters, as the pumping tests and the relative measurements of the drawdown induced. These estimation approaches are intrusive and the hydrological system is perturbed by the presence of perforations and the measurements are performed in a limited number of points due to high costs. On the contrary the geophysics is nonintrusive and obtain a great deal of information by low cost approach.

In the last few decades, hydrologists have increasingly begun to use geophysical information to estimate groundwater flow parameters [20, 39, 40, 41]. The correlation between self-potential signals and groundwater flow is supported by several authors in the past, which defined a detectable electrical field in the subsurface. At

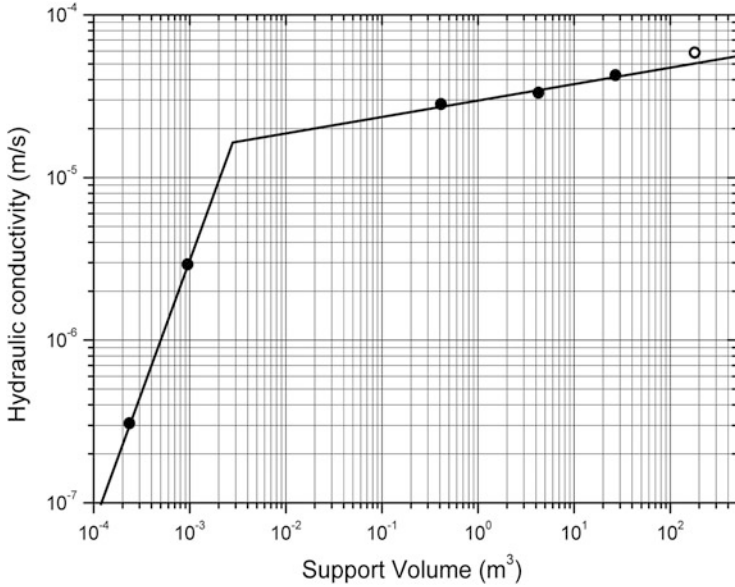


Fig. 7 Hydraulic conductivity (*black dots*) vs. support volume with the two power laws: the first part is fitted with a power law valid for uniform gradient flow and the second part for radial flow. *Circle* is the value of hydraulic conductivity for the large permeameter test

present, the electrokinetic theory [42, 43] is the main physical principle, which describes the link between the water flow in a porous medium and the generation of an electrical field. The self-potential (SP) method is a passive geoelectrical technique that consists of measuring, by means of a pair of non-polarizable electrodes inserted into the ground surface, the potential differences due to the presence of an electric field produced by natural sources distributed in the subsoil, generated by various phenomena (hydraulic, chemical, thermal). The output can be in the form of long profiles and/or maps.

In the last few years, various algorithms have been developed to determine the distribution of sources responsible for the self-potential anomalies recorded at the ground surface. Recently, several researchers have been developing interpretation schemes that could be applied to the natural electrical field recorded during pumping tests [44, 39, 45, 46]. This approach benefits from two advantages: the use of inexpensive sensors and the non-intrusive nature of the self-potential measurements.

When we assume the porous medium as homogeneous in the electrical sense, the governing equation of the electrical flow under steady state conditions is:

$$\nabla^2 \varphi = -C' \nabla^2 h. \quad (10)$$

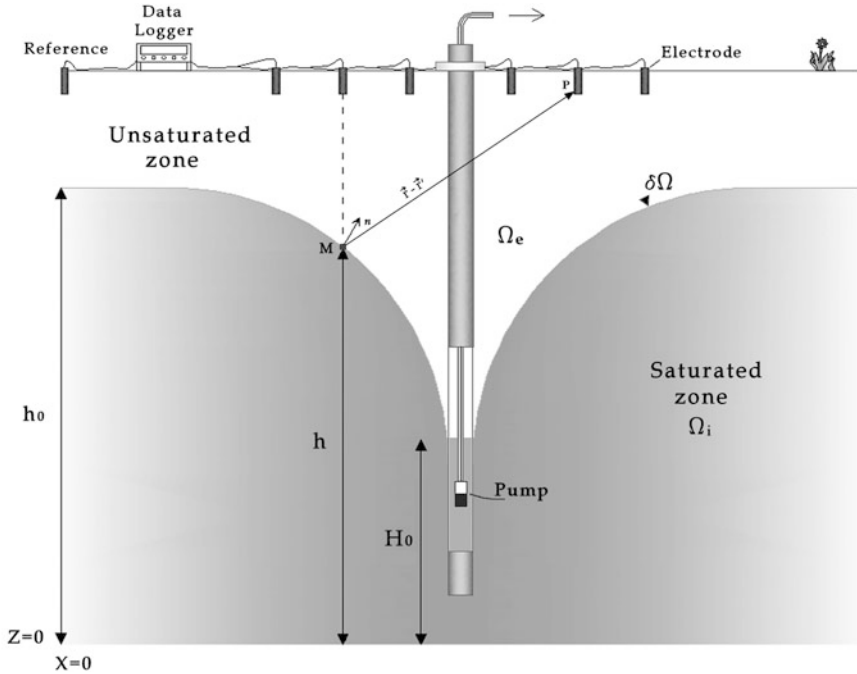


Fig. 8 Cross section of the depression cone of the water table in the vicinity of a pumping well in steady state conditions and monitoring of the self-potential signals [46]

During a pumping test, the hydraulic head $h(r)$ at distance r from the pumping well (Fig. 8) in a homogeneous unconfined aquifer and with the Dupuit’s assumption is:

$$h(r) = \left[h_0^2 + \frac{Q}{\pi K} \ln\left(\frac{r}{R}\right) \right]^{1/2}, \tag{11}$$

where Q is the volumetric pumping rate, h_0 is the hydraulic head where the influence of the pumping is negligible and R is the influence radius.

Combining the (10) and (11) and applying the Green’s theorem we obtain:

$$\varphi(r) = \left(\frac{C'Q^2}{4\pi^2K^2} \right) \int_R^r \frac{dr'}{r'^2 h^2(r')}. \tag{12}$$

By solving (12) numerically, it is possible to use it as the forward model in the inversion of the self-potential signals registered at different distances r from the pumping well, for hydraulic conductivity.

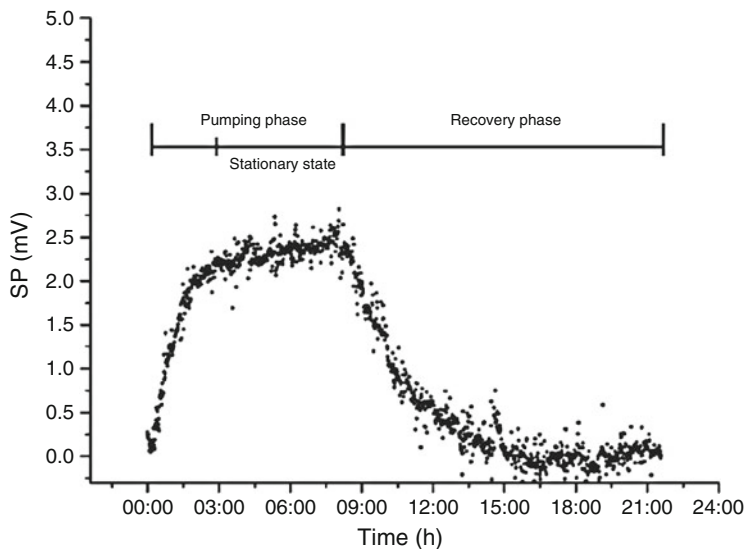


Fig. 9 Self-potential values acquired in a channel during the pumping test [46]

In 2006, at the Hydrogeosite Laboratory of the CNR-IMAA-Pole of Marsico Nuovo (PZ), in the same period of the hydraulic test described before, during a pumping test we acquired several self-potential values by 63 non-polarizable Petiau electrodes (SDEC, Francia) installed on the surface of the model, along seven parallel lines 1 m apart, each with nine electrodes placed 1 m apart. Self-potential values are measured by means of a multichannel system realized ad hoc and made up of a Keithley Instruments datalogger on which each non-polarizable electrode was connected to the reference electrode placed in the area least influenced by the variation of the hydraulic head. The flow rate pumped from the well was fixed at 0.085 L/s, according to what had been calculated with the mathematical model, and monitored using an electromagnetic flowmeter with digital converter. The pumping lasted about 8 h, while the subsequent recovery phase lasted about 12 h. Figure 9 shows the SP curve acquired with time in a channel (ch. 43) during the pumping test, after a correction of the drift effect due to negligible phenomena (i.e., electrode drift). The drift correction was achieved by use of a detrending statistic tool which involved fitting a polynomial function to pre-pumping data (usually it was linear) and then subtracting it from all the data. As can be easily seen, the different hydraulic phases of the experiment are distinctly evidenced by the SP electrical signal: the steady state condition is reached after about 3 h from the start of the pumping (increasing trend of the SP signal), and after about 8 h the pump has been shut down and the recovery phase begins (the SP signal goes in the initial conditions).

In order to estimate the hydraulic conductivity of the porous medium filling the Hydrogeosite, by means of the pumping test, the self-potential signals measured in pseudo-steady state condition were used. When assuming the homogeneity of the

porous medium, the electrical potential depends only on the distance r from the pumping well. So, the self-potential signals generated by the groundwater flow can be used to estimate the hydraulic conductivity of an unconfined aquifer, by inverting (12). Different methodology should be applied to estimate the hydraulic conductivity. Rizzo et al. [39] describe an analytical method to solve the (12) by means of a power law relationship:

$$\varphi(r) = Ar^{-1}. \quad (13)$$

Then, it becomes possible to estimate the mean hydraulic conductivity of an unconfined aquifer, by calculating the value of A from a best fitting of the electrical potential data in terms of the distance from the pumping well.

Another way was proposed by Straface et al. [46] to invert hydraulic conductivity by a nonlinear least square method. This method is based on the minimization of the following cost function:

$$F = (\varphi(r) - \hat{\varphi}(r))^T S_P^{-1} (\varphi(r) - \hat{\varphi}(r)). \quad (14)$$

The two methodologies estimate the hydraulic conductivity K obtaining: 5.8×10^{-6} m/s by Rizzo et al. [39] and 1.52×10^{-5} m/s by Straface et al. [46]. The two estimation are not so different, but the latter approach is closer to the hydraulic conductivity value obtained by means of the Neuman type-curve method (4.26×10^{-5} m/s).

6 Conclusions

Several authors suggest that hydraulic conductivity tends to increase with the support volume at subregional scale [27, 28]. In particular, a similar phenomenon was described by Schulze et al. (1999) for a variety of consolidated and unconsolidated media.

Previous figures reveal that the measured hydraulic conductivity increases with the scale of measurement: the increase is too uniform and too large to be a coincidence. The increase also cannot be attributed to systematic differences or inaccuracy among the different measurements techniques [7].

Generally, the porous medium heterogeneity is charged with the hydraulic conductivity scale effect [27–31]. In this case, the porous medium has a small heterogeneity; nevertheless, the scale effect is very evident at the experimental scales utilized, because the pore distribution inside the porous medium is likely to be not completely uniform.

On the other hand, there are many uncertainties about the specific mechanisms through which the influence of the heterogeneity on the aquifer parameters takes place, particularly on the hydraulic conductivity. Certainly as the involved-volume

of the porous-medium is increasing, also the possibility of variations in the characteristics of the medium increases (i.e., the heterogeneity increases), with possible changes of dimensions of the solid grains and consequently of the vacuum, as well as possible changes of density, formation of discontinuities like fractures, or changes in the granulometric structure of the medium. However, with decreasing volumes the porous medium does not tend necessarily to the homogeneity; in fact, also for limited scale ranges the detected parameter increases when the scale is increased. So, the mechanism through which the heterogeneity acts must be examined more opportunely.

The dimension of the pores and their continuity are certainly the most evident peculiarity. It is clear that the dimensions of the pores may influence the conductivity value so that the higher are the values of the first, the greater are the values of the second; analogously, since the continuity of the little channels increases also the conductivity increases, or vice-versa, and if there is no continuity there is no flow.

However, either for the flow or the transport phenomena, the dimensions of the pores present a greater influence in locally reduced ambit, while the continuity and the accessibility of the little channels influence more within parts of porous medium larger [32–34]. Therefore it is possible to retain that in the considered smallest volumes of the porous media, like the ones corresponding to the measured samples in the laboratory, the scale effect is due to in large part the first of the above said factors, i.e. the variability of dimension of the pores; while in the larger volumes, like those involved in the measurement of k usually used in field, the second of the above said factors, i.e. the continuity of the little channels and the degree of the interconnection of the net which they shape strongly influences the scale effect for the detected parameter.

Such a circumstance justifies the subdivision of the total amplitude of the sample of values of the detected parameter in two parts: the first referred to low-scale values and the second referred to greater scale values. As already underlined, the scale laws corresponding to the considered single parts are in this way more significant than the only law describing the phenomenon in examination for all the dash which consists of the first and the second dash above considered. It follows that if at the same time measurements of K are taken in account at the very different (small and large) scales, instead of researching an only scale law it is convenient to partialize the set of the available values so a law is determined at every scale dash; these can describe more correctly and reliably the phenomenon under observation in the respective ambits, as a combination of several physical behaviors of the system.

Anyway, these results, either considering the unique scale law (7) or multi-scale laws, i.e. (8) and (9), confirm what was proved by Clauser [28] for numerous types of soils, that is the trend of hydraulic conductivity to reach a higher limit when the measurement scale increases and, in our opinion, regardless of the heterogeneity of the porous medium.

Groundwater is a key element of the water cycle and is the largest available resource of fresh water. The knowledge of hydrodynamic and hydrodispersive parameters is fundamental in order to model the flow and contaminant transport in the aquifers and to prevent and control groundwater resources against the threats by uncontrolled industrial, agricultural, and urban management practices.

References

1. Renard P, de Marsily G (1997) Calculating equivalent permeability: a review. *Adv Water Res* 20(5–6):253–278
2. Sanchez-Vila X, Guadagnini A, Carrera J (2006) Representative hydraulic conductivities in saturated groundwater flow. *Rev Geophys* 44:RG3002. doi:[10.1029/2005RG000169](https://doi.org/10.1029/2005RG000169)
3. Rubin Y (2003) *Applied stochastic hydrogeology*. Oxford University Press, Oxford. ISBN 019513804X, 9780195138047
4. Zhu J, Yeh T-CJ (2006) Analysis of hydraulic tomography using temporal moments of drawdown recovery data. *Water Resour Res* 42:W02403. doi:[10.1029/2005WR004309](https://doi.org/10.1029/2005WR004309)
5. Hernandez F, Neuman SP, Guadagnini A, Carrera J (2006) Inverse stochastic moment analysis of steady state flow in randomly heterogeneous media. *Water Resour Res* 42:5. doi:[10.1029/2005WR004449](https://doi.org/10.1029/2005WR004449)
6. Neuman SP, Blattstein A, Riva M, Tartakovsky DM, Guadagnini A, Ptak T (2007) Type curve interpretation of late-time pumping test data in randomly heterogeneous aquifers. *Water Resour Res* 43(10):W10421. doi:[10.1029/2007WR005871](https://doi.org/10.1029/2007WR005871)
7. Neuman SP, di Federico V (2003) Multifaceted nature of hydrogeologic scaling and its interpretation. *Rev Geophys* 41(3):1014. doi:[10.1029/2003RG000130](https://doi.org/10.1029/2003RG000130)
8. Neuman SP, Riva M, Guadagnini A (2008) On the geostatistical characterization of hierarchical media. *Water Resour Res* 44(2):W02403. doi:[10.1029/2007WR006228](https://doi.org/10.1029/2007WR006228)
9. Molz FJ, Rajaram H, Lu S (2004) Stochastic fractal-based models of heterogeneity in subsurface hydrology: origins, applications, limitations, and future research questions. *Rev Geophys* 42:RG1002. doi:[10.1029/2003RG000126](https://doi.org/10.1029/2003RG000126)
10. Glimm W, Lindquist B, Pereira F, Zhang Q (1993) A theory of macrodispersion for the scale-up problem. *Transp Porous Media* 13(1):97–122
11. Dagan G (1994) Significance of heterogeneity of evolving scales to transport in porous formations. *Water Resour Res* 30(12):3327–3336
12. Liu HH, Molz FJ (1997) Multifractal analysis of hydraulic conductivity distributions. *Water Resour Res* 33(11):2483–2488
13. Neuman SP (1994) Generalized scaling of permeabilities: validation and effect of support scale. *Geophys Res Lett* 21:349–352
14. di Federico V, Neuman SP (1997) Scaling of random fields by means of truncated power variograms and associated spectra. *Water Resour Res* 33(5):1075–1085
15. Neuman SP (2003) Relationship between juxtaposed, overlapping and fractal representations of multimodal spatial variability. *Water Resour Res* 9(8):1205–1352. doi:[10.1029/2002WR001755](https://doi.org/10.1029/2002WR001755)
16. Butler JJ (1998) *The design, performance, and analysis of slug tests*. Lewis Publisher CRC Press, University of Kansas, New York. ISBN 1566702305
17. Boast W, Kirkham D (1971) Auger hole, seepage theory. *Soil Sci Soc Am Proc* 35(3):365
18. Dagan G (1978) A note on packer, slug, and recovery tests in unconfined aquifers. *Water Resour Res* 14(5):929
19. Straface S (2009) Estimation of transmissivity and storage coefficient by means of a derivative method using the early-time drawdown. *Hydrogeol J* 17(7):1679–1687
20. Straface S, Rizzo E, Chidichimo F (2010) Estimation of hydraulic conductivity and water table map in a large scale laboratory model by means of the self-potential method. *J Geophys Res* 115(B06105):1–16. doi:[10.1029/2009JB007053](https://doi.org/10.1029/2009JB007053)
21. Tartakovsky GD, Neuman SP (2006) Three-dimensional saturated-unsaturated flow with axial symmetry to a partially penetrating well in a compressible unconfined aquifer. *Water Resour Res* 43:W01410. doi:[10.1029/2006WR005153](https://doi.org/10.1029/2006WR005153)
22. Barker JA, Black JH (1983) Slug tests in fissured aquifers. *Water Resour Res* 19(6):1558
23. Cooper HH, Jacob CE (1946) A generalized graphical method for evaluating formation constants and summarizing well-field history. *Eos Trans Am Geophys Union* 27(4):526
24. Oliver DS (1990) The averaging process in permeability estimation from well-test data. *SPE Form Eval* pp 319–324

25. Fallico C, De Bartolo S, Troisi S, Veltri M (2010) Scaling analysis of hydraulic conductivity and porosity on a sandy medium of an unconfined aquifer reproduced in the laboratory. *Geoderma* 160:3–12
26. Fallico C, Vita MC, De Bartolo S, Straface S (2012) Scaling effect of the hydraulic conductivity in a confined aquifer. *Soil Sci.* doi:[10.1097/SS.0b013e31824f179c](https://doi.org/10.1097/SS.0b013e31824f179c)
27. Schulze-Makuch D, Cherkauer DS (1998) Variations in hydraulic conductivity with scale of measurement during aquifer tests in heterogeneous, porous carbonate rocks. *Hydrogeol J* 6:204–215
28. Clauser C (1992) Permeability of crystalline rocks. *EOS, Trans Am Geophys Union* 73:233–238
29. Carrera J (1993) An overview of uncertainties in modeling groundwater solute transport. *J Contam Hydrol* 13(1–4):23–48
30. Guimerà, Vives L, Carrera J (1995) A discussion of scale effects on hydraulic conductivity at a granitic site, el berrocal, Spain. *Geophys Res Lett* 22:1449–1452
31. Schulze-Makuch D, Carlson DA, Cherkauer DS, Malik P (1999) Scale dependency of hydraulic conductivity in heterogeneous media. *Ground Water* 37:904–919
32. Bartoli F, Genevois-Gomendy V, Royer JJ, Niquet S, Vivier H, Grayson R (2005) A multiscale study of silty soil structure. *Eur J Soil Sci* 56:207–223
33. Bird NRA, Perrier E (2010) Multiscale percolation properties of fractal pore network. *Geoderma* 160:105–110
34. Ewing RP, Hu Q, Liu C (2010) Scale dependence of intragranular porosity, tortuosity, and diffusivity. *Water Resour Res* 46:W06513. doi:[10.1029/2009WR008183](https://doi.org/10.1029/2009WR008183)
35. de Marsily G (1986) *Quantitative hydrogeology: groundwater hydrology for engineers*. Academic, Orlando. ISBN 0-12-208915-4
36. Bouwer H, Rice RC (1976) A slug test determining hydraulic conductivity of unconfined aquifers with completely or partially penetrating wells. *Water Resour Res* 12(3):423
37. Bourdet D (2002) *Well test analysis: the use of advanced interpretation models*. Elsevier Science NV, Amsterdam. ISBN 0-444-5D968-2
38. Neuman SP (1975) Analysis of pumping test data from anisotropic unconfined aquifers considering delayed gravity response. *Water Resour Res* 11(2):329–342
39. Rizzo E, Suski B, Revil A, Straface S, Troisi S (2004) Self-potential signals associated with pumping-tests experiments. *J Geophys Res* 109(B10203). doi:[10.1029/2004JB003049](https://doi.org/10.1029/2004JB003049)
40. Cassiani G, Böhm G, Vesnaver A, Nicolich R (1998) A geostatistical framework for incorporating seismic tomography auxiliary data into hydraulic conductivity estimation. *J Hydrol* 206:58–74
41. Cassiani G, Medina MA (1997) Incorporating auxiliary geophysical data into ground-water flow parameter estimation. *Ground Water* 35:79–91
42. Bernabé Y (1998) Streaming potential in heterogeneous networks. *J Geophys Res* 103:20827–20841
43. Lorne B, Perrier F, Avouac JP (1999) Streaming potential measurements: 1. Properties of the electrical double layer from crushed rock samples. *J Geophys Res* 104:17857–17877
44. Revil A, Naudet V, Nouzaret J, Pessel M (2003) Principles of electrography applied to self-potential electrokinetic sources and hydrogeological applications. *Water Resour Res* 39(5):1114. doi:[10.1029/2001WR000916](https://doi.org/10.1029/2001WR000916)
45. Titov K, Revil A, Konasovsky P, Straface S, Troisi S (2005) Numerical modeling of self-potential signals associated with a pumping test experiment. *Geophys J Int* 162:641–650
46. Straface S, Fallico C, Troisi S, Rizzo E, Revil A (2007) An inverse procedure to estimate transmissivity from heads and self-potential signals. *Ground Water* 45(4):420–428

Mathematical Models as Tools for Prevention and Risk Estimates of Groundwater Pollution: Contributions and Challenges

Bouabid El Mansouri, Malika Kili, Jamal Chao, Ahmed Fekri, and Abdelaziz Mridekh

Abstract In many parts of the world, groundwater is the only resource available to meet the vital needs of the population, especially in dry areas. The availability and quality of such resources are highly threatened now by climate change and numerous pollution factors.

Numerical models of flow and transport in saturated porous media are of major significance in the realization of simulations of management scenarios and in the evaluation of potential risks of pollution. The main constraint to the development and implementation of these models is the quantification of the parameters of flow and transport phenomena. In fact, these parameters fully control the results of the simulations. To overcome these limitations, field experiments are essential in order to minimize the errors associated with the results of these simulations.

This chapter presents some applications on different Moroccan sites, which are vulnerable to pollution, allowing the risk assessment related with the threats to the local groundwater resources and showing the major role of these tools for the preservation of the quality of groundwater resources.

Keywords DRASTIC method, GIS, Groundwater pollution, Mathematical models, Morocco, Protection of catchment sites, Risk prevention

B. El Mansouri (✉), M. Kili, and J. Chao
Laboratory of Geosciences of natural resources, Ibn Tofail University, Maamora Campus,
BP 133, 14000 Kenitra, Morocco
e-mail: b_elmansouri@yahoo.fr

A. Fekri
University Hassan II of Mohammedia, Mohammedia, Morocco

A. Mridekh
Department of Geology, Moulay Ismail University, Mekens, Morocco

Contents

1	General Concepts of the Mathematical Models	176
2	Convection-Diffusion Modeling	177
3	Numerical Models as Tools for Groundwater Protection	179
3.1	Prediction of the Pollution from a Landfill	179
3.2	Dimensioning the Protected Perimeter of Catchment Site	179
3.3	Contributions of GIS Technology for Transport Numerical Models: Modeling Approach in Vulnerability Framework	185
4	Conclusion	190
	References	190

Abbreviations

DRASTIC	Depth to water, net Recharge, Aquifer media, Soil media, Topography, Impact of vadose zone media, and hydraulic Conductivity of the aquifer
GIS	Geographic information systems

1 General Concepts of the Mathematical Models

A model is a conceptualization of reality. It is an image of reality that we create, an incomplete and partial image that includes features and attributes of the reality in which we are interested in particular, or that we have the chance (or opportunity) to know [1]. A mathematical model is a set of concepts of interest formalized in the form of mathematical expressions. The mathematical model is translated to a numerical model that can solve equations representing the phenomena within the limits of our interest. In the field of groundwater modeling, models are classified in three main categories: deterministic models, black boxes, and stochastic/statistic models [1].

The hydrodynamic and transport deterministic models are based on physical laws that are more or less complex and approaching reality. Konikow and Bredehoeft [2] point out that the forecasts, which are usually outside the range of observed conditions, typically are limited by uncertainties due to the sparse and inaccurate data, poor definition of stress acting on the system, and errors in system conceptualization. Even though forecasts of future events using models may be imprecise, they do represent the best available information at a given time that can be used in decision making. Simulation models can be used as learning tools to identify additional data needed in order to better define and understand groundwater systems. These models have the capacity to test and quantify the consequences of various errors and uncertainties in the information needed to determine the cause-effect relationship and related models-based forecast [3]. In the process of forecasting, this model capability may be the most important aspect in order to define the uncertainties of the forecasting, allowing water

managers to evaluate the significance of their decisions. Also, this process may allow the evaluation of unexpected consequences of such decisions.

2 Convection-Diffusion Modeling

Solute transport models have become an indispensable tool for assessing environmental risks to groundwater resources, remediation engineering, or the engineering of underground repositories of municipal and nuclear wastes. This development was essentially driven by a growing interest in groundwater quality and the evolution of computer technology, making transport simulations widely available to researchers, engineers, and consultants. However, although numerical models of solute transport have undergone a significant improvement over the last decades, the claims made from the users have also increased. While users initially intended to simply have a rough idea, for example, of the potential threat of a contamination source on a drinking water well using homogenous parameters for their solute transport model, the failure of many of these models has led the modeling community to recognize that solute transport models need to be able to account for the complexity of parameters found in field problems.

The complexity of solute transport in subsurface systems is based on a multiplicity of processes: the occurrence of a variety of chemical, physicochemical, and biochemical mechanisms often varying spatially, the temporal variability of the flow field, and the heterogeneity of hydraulic conductivity. Unfortunately, complete knowledge of all these parameters will never be available and, hence, solute transport models need to be able to quantify the uncertainty associated with the model predictions. One possibility to achieve this is the use of a stochastic approach where, due to the lack of detailed knowledge about the aquifer properties, multiple and equally plausible representations are generated and analyzed.

A further issue when using solute transport models is the problem of scales [4]. Numerical models are usually discretized into model grid blocks, which are almost always much larger than the scale of heterogeneity of the corresponding parameter and/or the measurement support scale. The process of transforming the detailed description of parameters in a grid constructed scale to a coarser grid, with less detailed description for the purpose of numerical modeling, is referred to as upscaling [5].

Upscaling methods have been developed to overcome this problem although principally focusing on flow. Less research has been done on the upscaling of solute transport. The problem of scales for solute transport was first recognized by the apparent scale dependence of dispersivity, raising the question whether the classical advection-dispersion equation is capable of correctly simulating solute transport for strongly heterogeneous aquifers using coarse model grid blocks in comparison to the small-scale variability of aquifer properties. In fact, more recent research on solute transport upscaling has demonstrated that, when moving from a highly discretized model to a coarsely discretized one, we need to account additionally for mass transfer between model grid blocks and, hence either a mass transfer

process has to be added to the advection-dispersion equation or even a different solute transport equation, e.g., continuous time random walk and fractional advection-dispersion equation, has to be used [4].

The convection-diffusion models are commonly used to perform studies of the assessment impact on the environment. These models describe the evolution of the concentration of conservative or degradable solutes in the aquifer. Material can react with other substances that are present in groundwater. Concentrations of transported substances are also subject to diffusion which coefficients can be determined either by direct measures or by using a numerical model. The transport equation in most general form can be written as follows:

$$S \frac{\partial H}{\partial t} + \text{div}(b\omega_c V) = q \quad (1)$$

$$\omega_c V = -K \nabla H \quad (2)$$

$$\frac{\partial C}{\partial t} = -\frac{V}{R} \text{grad}C + \text{div}\left(\frac{D}{R} \text{grad}C\right) - \lambda C + \frac{q}{bR\omega_c} C + \frac{S}{bR\omega_c} \quad (3)$$

where S is the storage coefficient (confined aquifer) or effective porosity (phreatic aquifer) (dimensionless); H is the piezometric head (L); t represents the time; b is the thickness of saturated flow (L); ω_c is the cinematic porosity; V is the average linear velocity (LT^{-1}); q is the source/sink term (LT^{-1}); K is the permeability tensor (LT^{-1}); C is the solute concentration (ML^{-3}); λ is the degradation rate of pollutant (T^{-1}); R is the retardation factor; and D is the dispersion coefficient (L^2T^{-1}). In isotropic medium, the dispersion coefficient can be expressed as follows [6]:

$$D_{xx} = \alpha_L \frac{V_x^2}{V} + \alpha_T \frac{V_y^2}{V} + D_m; \quad D_{yy} = \alpha_L \frac{V_y^2}{V} + \alpha_T \frac{V_x^2}{V} + D_m \quad (4)$$

where D_{xx} and D_{yy} represent the dispersion along the main axes of isotropy; α_L and α_T are respectively the longitudinal and transversal dispersivities; V_x and V_y are the velocity in main axes of flow; V is the velocity module; and D_m is the molecular diffusion.

However, in simple case studies the use of analytical solutions is much more interesting. These solutions have a direct application and keep the modeler away from efforts of the various phases of the numerical modeling. A minimal amount of data is needed since all sectors of a parameter are assigned the same value. The solution given for a saturated homogeneous porous medium [7] in De Marsily [8] is

$$\frac{C}{C_0} = \frac{1}{2} \text{erfc}\left(\frac{L - v_x t}{\sqrt{4D_x t}}\right) + \frac{1}{2} \exp\left(\frac{v_x L}{\sqrt{D_x}}\right) \text{erfc}\left(\frac{L + v_x t}{\sqrt{4D_x t}}\right) \quad (5)$$

Others analytical formulae are given for various situations (2D, 3D, heterogeneous porous medium, etc.)

3 Numerical Models as Tools for Groundwater Protection

3.1 Prediction of the Pollution from a Landfill

Landfills are sites that accommodate daily amounts of solid waste from urban and industrial areas. In many cases, such receiving locations of these discharges are not properly developed. Indeed, these discharges produce liquid of leachate that may seep into the porous medium and contaminate the groundwater.

In situations where landfills are located in relatively permeable materials such as sand, gravel, or fractured rock, leachate migration may cause contamination over an area many times larger than the area occupied by the landfills. The infiltration of water through the landfill will continue to produce leachate for many decades. Transport by groundwater flow in the material will cause contamination of great part of the zone [9].

To predict the effect of any pollution from a landfill of a major urban area in the East of Morocco (agglomeration of the city of Oujda), we performed a hydrodynamic model calibrated in steady and transient states. Then, we implemented a transport model supported by MT3D/GMS. The simulations have mainly shown areas that would be affected by the pollution over time (Fig. 1c). This result represents a guide to stakeholders for the implementation of barriers to protect the drinking water supply, which should delimit the polluted area.

3.2 Dimensioning the Protected Perimeter of Catchment Site

The perimeters of the catchment protection are geographical areas established around the wells dedicated to drinking water supply in order to ensure the preservation of the resource. The objective is to minimize the risk of punctual and accidental pollution of these wells resources.

This protection has three levels established from hydrogeological studies:

- Immediate protection perimeter: all activities in this perimeter are prohibited except those related to the exploitation and maintenance of the well. Its purpose is to prevent the deterioration of structures and prevent the release of pollutants close to the catchment.
- Closed protection perimeter: wider area (typically a few acres) for which any activity that is likely to cause pollution is prohibited or subject to special procedures (construction, deposits, discharges. . .). Its objective is to prevent the migration of pollutants into the catchment.

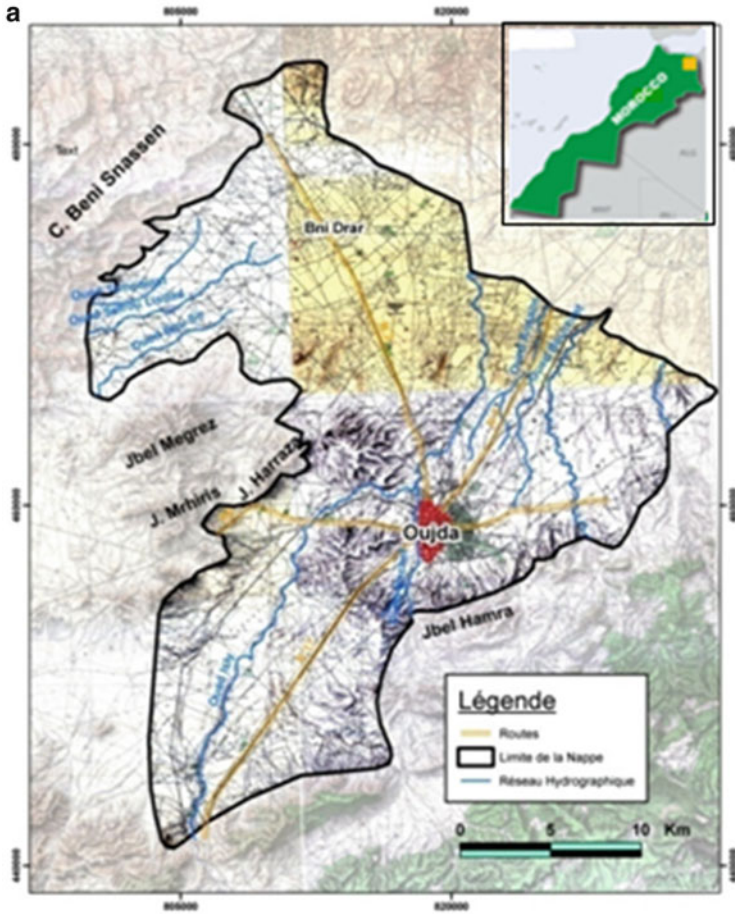


Fig. 1 (continued)

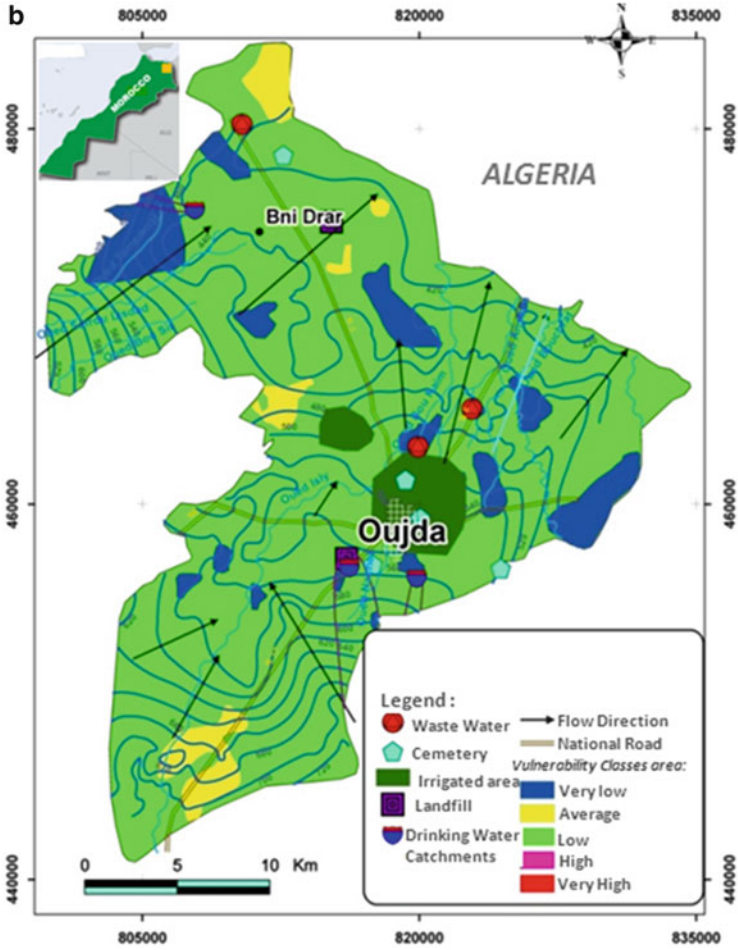


Fig. 1 (continued)

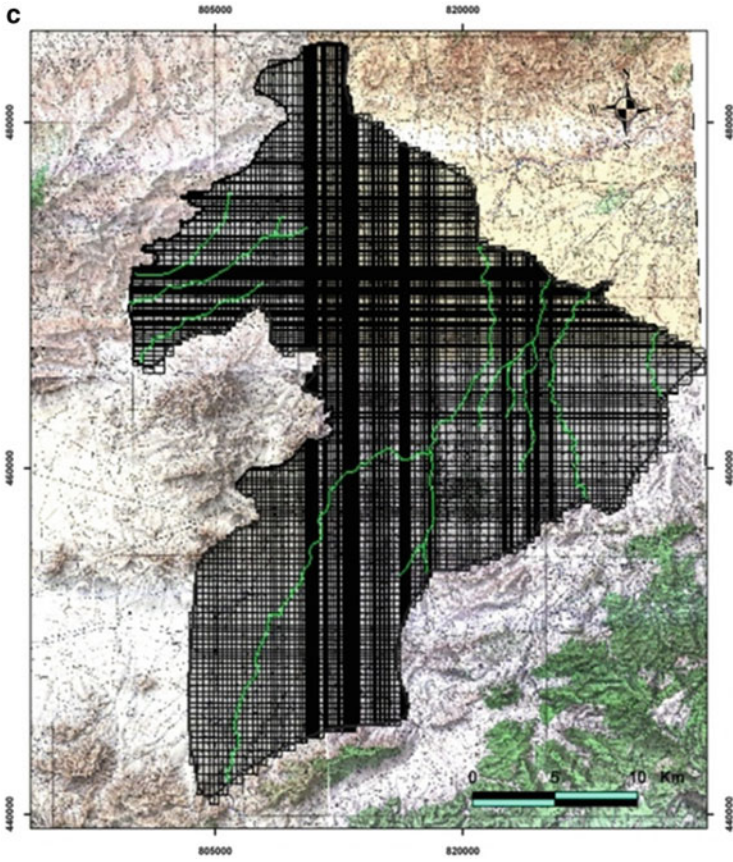


Fig. 1 (continued)

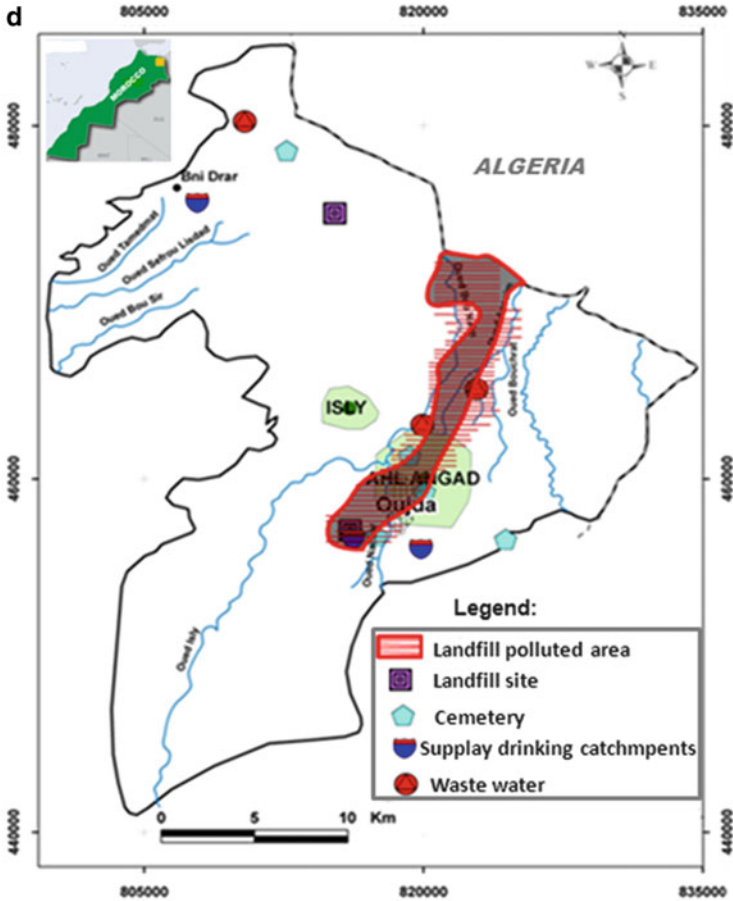


Fig. 1 Transport modeling of landfill leachate in Angad aquifer (Eastern Morocco). (a) Location and studied area; (b) environmental hydrogeology of the studied area; (c) finite difference grid of the studied area; (d) shape of the area affected by the landfill leachate

- Remote protection perimeter: this scope is optional and is created if certain activities are likely to cause significant pollution. This sector is usually the feeding area of the catchment point or even the entire watershed.

The design of these protection perimeters is based on several analytical calculation methods [10,11]. Such methods are based on simplifying assumptions as the homogeneity of the hydrogeological environment.

Numerical models can also be used for the design of these protection areas. These methods have the advantage of taking into account the complexity of the aquifer environment such as heterogeneity, anisotropy, and complex boundary. To this end, we have developed a numerical code that is based on the convection-diffusion equation to calculate a 50-day isochrone from around the catchment site

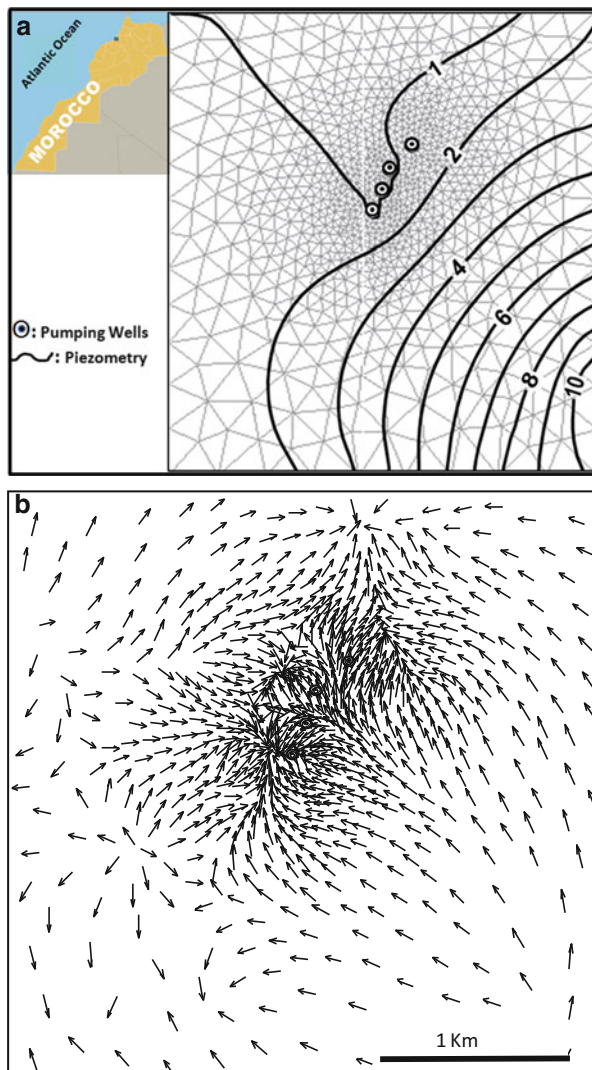


Fig. 2 Numerical modeling of the catchment site. (a) Finite element mesh in Sidi Taibi site. (b) Calculus of flow direction in the environment of pumping wells

of Sidi Taibi in Maamora aquifer (NW Morocco). The space between catchments and the isochrone is considered as close protection perimeter. The same method is applied to Ahmed Taleb catchment site located in the North of Kenitra (Fig. 2). These wells produce an annual volume of 8 mm^3 and represent the main resource of water supply for Kenitra population and partially contribute to the water supply for Rabat. On the field, the 50-day isochrone means that any pollution occurring outside of this isochrone cannot reach the pumping well after a period of 50 days

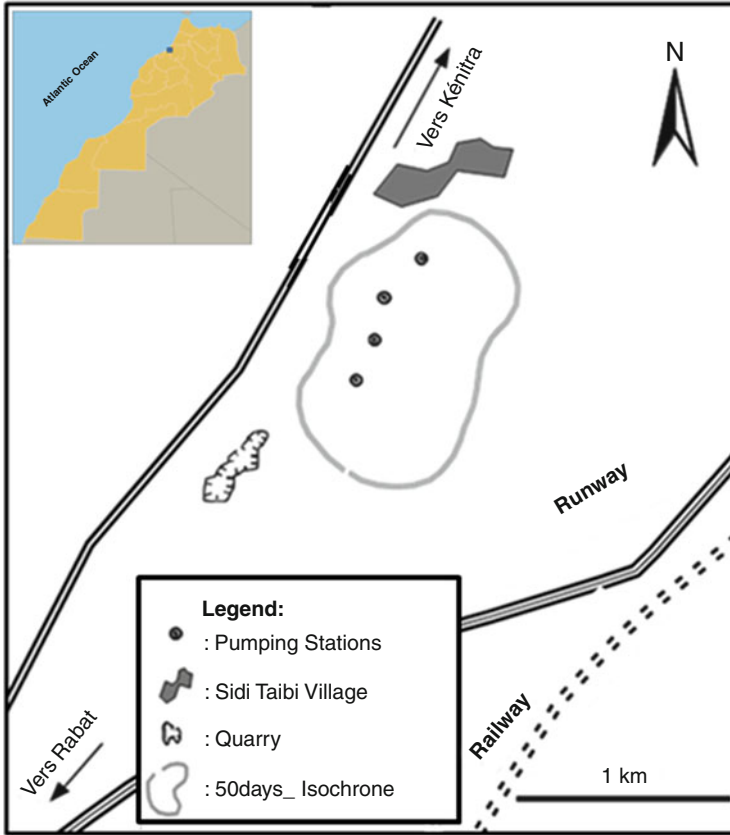


Fig. 3 Design of the protecting perimeter of the catchment site by numerical model in Ahmed Taieb (north of Kenitra City, Maamora aquifer)

(Fig. 2b, c). This period would allow policy makers to act according to the nature and severity of the generated pollution to mitigate its impact. Whereas, if the pollution occurs inside the perimeter, it reaches the wells within less than 50 days (Fig. 3).

3.3 Contributions of GIS Technology for Transport Numerical Models: Modeling Approach in Vulnerability Framework

The engineering of natural resources such as hydrogeological systems requires the usage of a large amount of data of various types: geological, hydrogeological, environmental, and socioeconomic. A major effort is usually spent in the organization of these data. Recently, geographic information systems (GIS) have become very

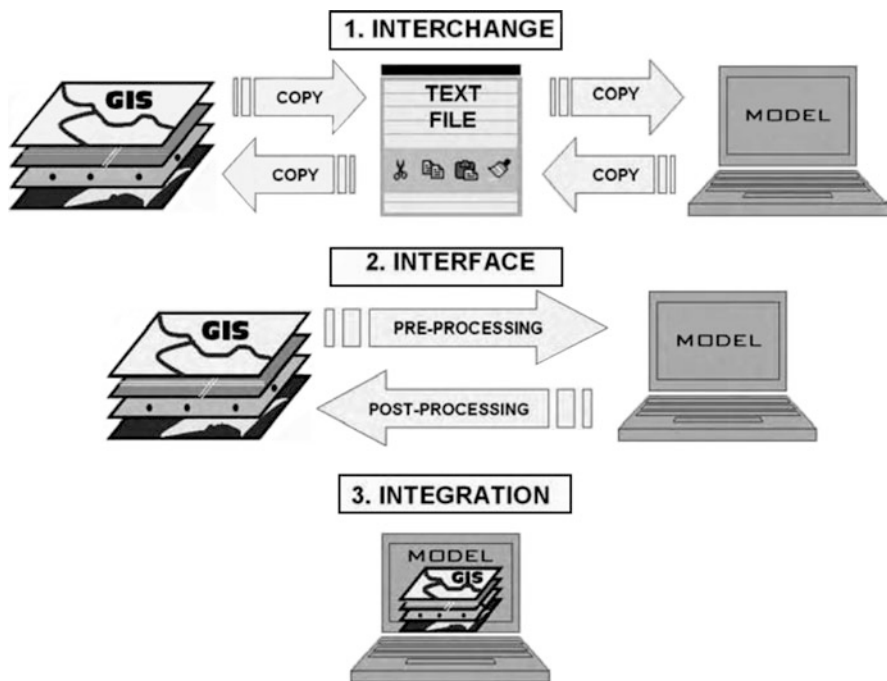


Fig. 4 Relationship GIS and the calculation models [12]

user-friendly tools for data processing and organizing. A geographic information system is an information system of hardware, software, and processes designed to facilitate the collection, management, manipulation, analysis, modeling, and display of spatially referenced data to solve complex problems of development and management. This tool usually contains several kinds of geographical objects that are organized into themes that often appear as layers. Each layer contains objects of the same type (limits of groundwater, rivers, roads, recharge areas, urban areas, wells, areas of potential pollution, etc.). Each object consists of a shape (geometry of the object) and a description, also called semantics.

Nowadays, GIS is being used in concert with applications such as modeling, maintenance management, capital planning, and customer service (Fig. 4). These developments make GIS an excellent tool for management in all water aspects, especially water resources and their environments [13]. Experts believe that in the near future, most water industry professionals will be using GIS in the same way they are now using word processor or spreadsheet [12].

In the aspect of groundwater resources protection, groundwater vulnerability maps are designed to show areas of greatest potential for groundwater contamination on the basis of hydrogeologic and anthropogenic factors.

These types of maps are developed by using GIS to combine data layers such as land use, soil types, and piezometry. Usually, groundwater vulnerability is determined

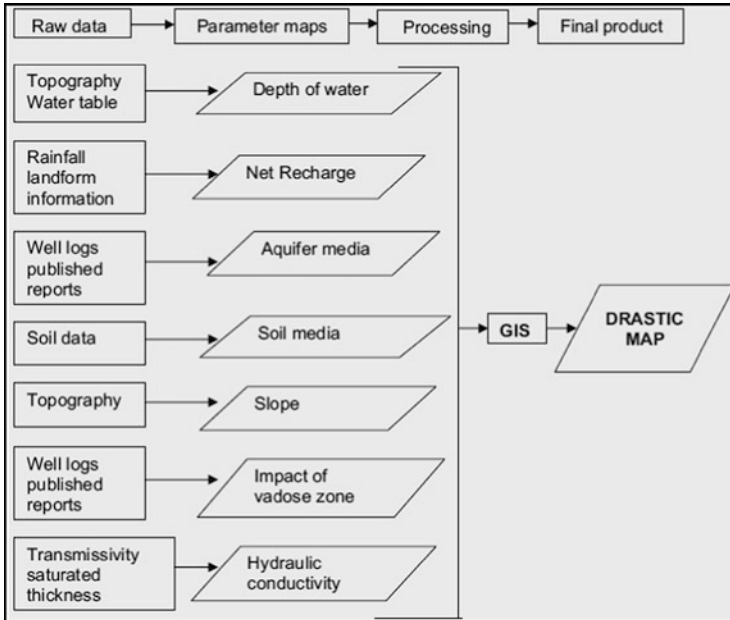


Fig. 5 Flow chart of methodology for groundwater vulnerability analysis using DRASTIC model in GIS [14]

by assigning rating points to each data layer, and then by the sum of these points we get the vulnerability map.

The most widely used groundwater vulnerability mapping method is DRASTIC, standing for the seven factors considered in the method: Depth to water, net Recharge, Aquifer media, Soil media, Topography, Impact of vadose zone media, and hydraulic Conductivity of the aquifer [15] (Fig. 5). The DRASTIC method has been used to develop groundwater vulnerability maps in many parts of the world [16–19]. Other methods have been developed such as SINTACS and GOD.

Each of the hydrogeologic factors is assigned a rating from one to ten based on a range of values. The ratings are then multiplied by a relative weight ranging from one to five. The most significant factors have a weight of five; the least significant have a weight of one.

The equation for determining the DRASTIC index is [20]:

$$D_r D_w + R_r R_w + A_r A_w + S_r S_w + T_r T_w + I_r I_w + C_r C_w = \text{DRASTIC Index}$$

where $D, R, A, S, T, I,$ and C represent the seven hydrogeologic factors, r designates the rating, and w is the weight. The smallest possible DRASTIC index rating is 23 and the largest is 226. The resulting DRASTIC index represents a relative measure of groundwater vulnerability. The higher the DRASTIC index, the greater is the vulnerability of the aquifer to contamination. A site with a low DRASTIC index is not free from

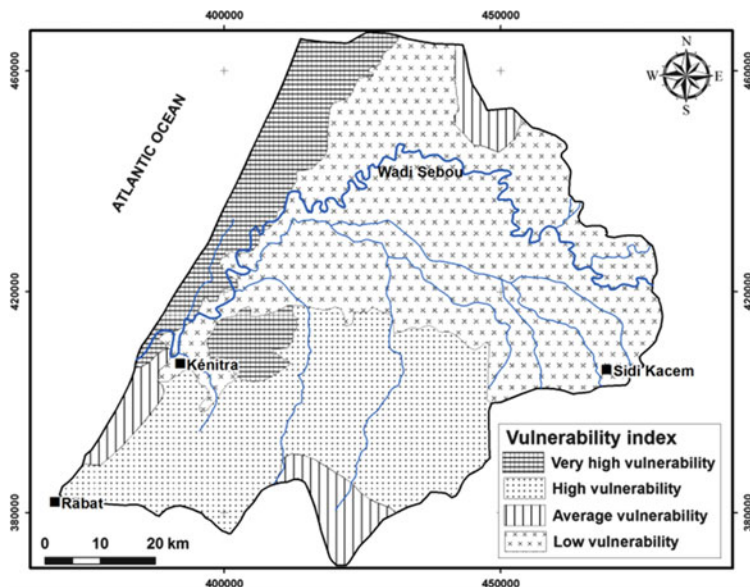


Fig. 6 Optimizing grid in transport model by vulnerability zones evaluated by GIS methods: Mnasra vulnerability map (DRASTIC method)

groundwater contamination, but it is less susceptible to contamination compared with the sites with higher DRASTIC indices.

The Sebou basin is located in the NW Morocco. It is one of the largest Basins of the country. This is the only basin in Morocco, with a surplus water balance. The annual volume of renewable water resources is about $7,000 \text{ mm}^3$ [21].

The basin includes several urban centers and several agricultural and industrial activities which exploit the groundwater basin. Its groundwater resources are located in the aquifers of Maâmora-Gharb. These aquifers are spread over a surface of $7,500 \text{ km}^2$ and sometimes occur in a multilayer system.

With the objective of protecting these groundwater resources from pollution potential factors, we, at first stage, mapped their vulnerability by the DRASTIC method. This established map shows that the most vulnerable area is the coastal zone of the basin called Mnasra. This area is dominated by an unconfined aquifer with excellent hydrogeological parameters and it is highly sought by catchment sites that guarantee supply drinking water; Ahmed Taleb in the North of Kenitra with an annual volume of 5 mm^3 and Sidi Taibi in the South with 3 mm^3 .

Besides, this coastal area is subject to significant pressure to satisfy the demand for irrigation. In fact, thanks to the groundwater resources available in Mnasra zone, this area is experiencing an intense agricultural activity which represents a potential source of pollution due to the excessive use of fertilizers [22].

The establishment of the vulnerability map showed that the coastal zone area Mnasra is the most vulnerable (Fig. 6). This information is very important to

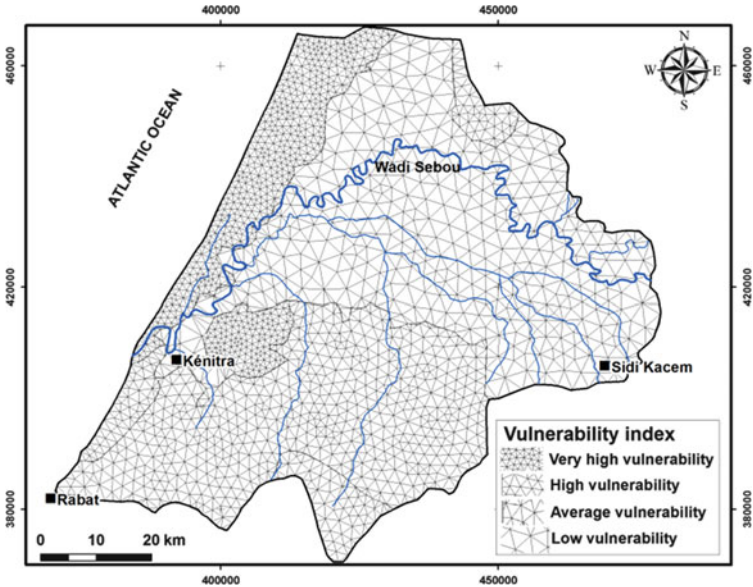


Fig. 7 Optimizing grid in transport model by vulnerability zones evaluated by GIS methods – transport model grid: mesh optimization by vulnerability zones

announce measures for groundwater resources protection. For this purpose, numerical modeling is a tool for the realization of simulations to predict the potential pollution.

The development of a numerical model simulation for the Gharb-Maâmora aquifer system is necessary for the assessment of pollution risk of the drinking water catchments. The vulnerability map (Fig. 6) may play a role in optimizing the mesh (domain discretization). Indeed, the least vulnerable areas could be covered by a less dense mesh, while the most vulnerable areas would be covered by high-density mesh, since the area is sensitive to pollution and a very good resolution of the calculation is recommended in this zone. So, the vulnerability map is an optimization tool for numerical computation (Fig. 7).

The vulnerability evaluation of aquifer domain before the transport modeling phase enables the optimizing of this phase. Indeed, the areas of the aquifer that are not vulnerable or are less vulnerable may be covered by a low density mesh where the equation will be resolved. However, vulnerable areas may contain a fine mesh (high density) in order to perform accurate calculations by increasing the number of the nodes. The model could have its meshes optimized, which has an impact on the time and errors calculation.

4 Conclusion

The groundwater resources are vital for a significant proportion of the human population of the globe. Degradation factors of the quality of these resources are numerous and increasing.

Groundwater is inherently susceptible to contamination from anthropogenic activities and the remediation is very difficult and expensive. Prevention of contamination is, hence, critical in effective groundwater management.

Numerical tools such as models and information systems can provide invaluable assistance on the realization of simulations and scenario changes in the quality of these resources. These tools can also enable to resize perimeters of the catchments protection where water is intended for human consumption. These tools can also represent elements for decision support on potentially polluting projects.

Factors threatening the quality of groundwater resources are natural and human. The mathematical and numerical models have substantial contributions to the evaluation and control of these threats. However, their uses and concepts largely depend on assumptions about the field and the expertise of the modeler to find a deal between the complex state of the field and the simplifying assumptions which sometimes mar the scenarios produced by these models.

References

1. Cunge J (1988) Modèles mathématiques en hydraulique et en hydrologie. *Traité construction*, vol C-180. Techniques de l'ingénieur, pp 1-18
2. Konikow LF, Bredehoeft JD (1992) Groundwater models cannot be validated. *Adv Water Resour* 75-83
3. Todd DK, Mays LW (2005) *Groundwater hydrology*, 3rd edn. Wiley
4. Salamon P (2006) On modeling contaminant transport in complex porous media using random walk particle tracking. PhD Thesis, Instituto de Ingenieria del agua y medio Ambiente
5. Farag Botros FE (2007) On upscaling groundwater flow and transport parameters in porous and fractured media. PhD. University of Nevada, Reno
6. Zheng B (2002) <http://www2.nau.edu/~doetqp-p/courses/env303a/lec36/lec36.htm>
7. Ogata A (1970) Theory of dispersion in granular media. US Geological Survey Professional Paper 411-I34
8. De Marsily G (1986) *Quantitative hydrogeology: groundwater hydrology for engineers*. Academic
9. Freeze AR, Cherry JA (1979) *Groundwater*. Prentice Hall, Englewood Cliffs
10. Bear J, Jacob M (1965) On the movement of water bodies injected into aquifers. *J Hydrol* 3:37-57
11. Grubb S (1993) Analytical model for estimation of steady state captures zones of pumping wells in confined and unconfined aquifers. *Ground Water* 31(1):27-32
12. Shamsi UM (2005) GIS applications for water, wastewater, and stormwater systems. Taylor & Francis, New York, 413 p
13. Lynn EJ (2009) *Geographic information systems in water resources engineering*. CRC Press. Taylor & Francis Group, New York
14. Rahman A (2008) A GIS based DRASTIC model for assessing groundwater vulnerability in shallow aquifer in Aligarh, India. *Appl Geogr* 28:32-53

15. Aller L, Bennett T, Lehr JH, Petty RJ, Hackett G (1987) DRASTIC: a standardized system for evaluating ground water pollution potential using hydrogeological settings. EPA Report 600-2-87/035. Robert S. Kerr Environmental Research Laboratory, Office of Research and Development, U.S. EPA, Ada, Oklahoma, 455 pp
16. Koterba MT, Banks WSL, Shedlock RJ (1993) Pesticides in shallow groundwater in the Delmarva Peninsula. *J Environ Qual* 22:500–518
17. Barbash JE, Resek EA (1996) Pesticides in ground water—distribution, trends, and governing factors. Ann Arbor, Chelsea, 588 pp
18. Environmental Protection Agency (1993) A review of methods for assessing aquifer sensitivity and ground water vulnerability to pesticide contamination. U.S. Environmental Protection Agency, EPA/813/R-93/002, 147 pp
19. Rupert MG (1999) Improvements to the DRASTIC ground-water vulnerability mapping method. USGS, Fact Sheet FS-066-99
20. Osborn NI, Eckenstein E, Koon KQ (1998) Oklahoma water resources board. Technical report, 98-5
21. ABHS (2011) Etude d'actualisation du Plan Directeur d'Aménagement Intégré des Ressources en Eau du bassin hydraulique de Sebou (PDAIRE). Note de Synthèse
22. El Mansouri B (1999) Développement d'outils et concepts pour la gestion des eaux souterraines. PhD, Université Ibn Tofail, Kénitra, Maroc

Groundwater Monitoring and Control by Using Electromagnetic Sensing Techniques

M. Bavusi, V. Lapenna, A. Loperte, E. Gueguen, G. De Martino, I. Adurno, I. Catapano, and F. Soldovieri

Abstract Groundwater resources, which are exposed to overexploitation and pollution at regional and local levels, may take benefit from fast, nonintrusive, and inexpensive monitoring methods based on electromagnetic techniques. In fact, the available technologies can help to improve management and protection of the aquifers. This chapter deals with the role of electromagnetic sensing techniques in water monitoring with a specific focus to pollution surveys in groundwater bodies. Being sensitive to the presence of water in the subsoil and its electrical conductivity, which in turn depends on the ionic content, the electromagnetic sensing techniques are useful tools for groundwater identification and soil quality assessment. In fact, these sensing techniques offer advantages such as quickness, nonintrusivity, and the possibility of investigating large areas at reasonable costs. However, the appropriate use of these techniques implies an adequate knowledge of their working principles as well as of their on field application procedures, which mainly depend on the survey aim and the geological and logistic conditions of the site. This chapter also discusses the uncertainty in the interpretation of results, which is due to the fact that the electromagnetic sensing techniques are based on indirect inspections. Several strategies can be exploited to reduce ambiguity of results, such as the integration of different electromagnetic techniques and the comparison between field data and those provided by laboratory experiments. These issues are herein addressed through practical examples concerning two study cases, one referred to a site located in Serbia-Herzegovina and one located in Italy. In particular, we illustrate the physical concepts, the operative aspects, the data processing, and the integration of results concerning the following measurement

M. Bavusi, V. Lapenna, A. Loperte, E. Gueguen, G. De Martino, and I. Adurno
Istituto di Metodologie per l'Analisi Ambientale, Consiglio Nazionale delle Ricerche,
C.da S. Loja, 85050 Tito Scalo (Pz), Italy

I. Catapano and F. Soldovieri (✉)
Istituto per il Rilevamento Elettromagnetico dell'Ambiente, Consiglio Nazionale delle
Ricerche, Via Diocleziano 328, 80124, Napoli, Italy
e-mail: soldovieri.f@irea.cnr.it

techniques: electrical resistivity tomography (ERT), ground-penetrating radar (GPR), time-domain-induced polarization (time domain IP), and self-potential method (SP). The two study cases concerns an industrial site and a large waste dump structure. These sites represent specific examples of soil monitoring and have been selected in order to evaluate the performance of the proposed techniques. For each site, we provide a description of the survey results accounting for geological evidences, logistic constraints, and physical limitation of the used techniques. Finally, we highlight the advantages offered by a cooperative use of different techniques and suggest strategies to overcome intrinsic limitations of each one of the considered survey methods.

Keywords Electromagnetic sensing techniques, Water monitoring, Electrical resistivity tomography, Ground-penetrating radar, Induced polarization, Self-potential

Contents

1	Introduction	194
2	The Electromagnetic Sensing Techniques: Theoretical Overview	197
2.1	Electrical Resistivity Tomography	197
2.2	The Ground-Penetrating Radar	200
2.3	Time-Domain-Induced Polarization	203
2.4	Self-Potential Method	206
3	Case Studies	209
3.1	The Kablova Industrial Site	209
3.2	The Montegrosso-Pallareta Waste Dump Complex	213
3.3	Understand the Uncertainties, Overcome the Limitations	219
	References	221

Abbreviations

ABK	Asphalt and backfill stratum
BRK	Bedrock
ERT	Electrical resistivity tomography
GPR	Ground-penetrating radar
IP	Induced polarization
MSW	Municipal solid waste
MWT	Microwave tomography
SAD	Saturated alluvial deposits
SP	Self-potential method

1 Introduction

Over the past 50 years, the world's population has doubled and agricultural as well as industrial productions have dramatically increased. This population growth associated with the climate changes has put water resources under an ever-increasing strain [1].

The water resources group (<http://www.2030wrg.org>) estimates that in just 20 years, global demand for water will be 40% higher than it is today and more than 50% higher in the most rapidly developing countries.

Moreover, anthropic activities such as agriculture, industry, and waste management will increase the impact on the fresh groundwater resources produced by contaminants such as, for instance, nitrates, chlorinated hydrocarbons and heavy metals.

The presence of nitrates is related to their agricultural use and produces a widespread groundwater pollution. A measurable effect of this pollution is the general growth of water electrical conductivity, which can be considered a measure of groundwater salinity and then of water quality [2].

On the other hand, chlorinated hydrocarbons and heavy metals arising from old landfills, contaminated industrial sites and industrial activities, petrochemical activities as well as military sites are concerned with localized critical situations [2].

Therefore, groundwater resources are affected by two main kinds of threat: overexploitation and pollution.

In order to successfully tackle these problems, it is necessary to improve not only the water production and management but also the water monitoring.

A fast, less expensive and effective tool is needed with the aim to monitor water quality in large areas with reasonable costs.

Geophysical techniques can represent an effective monitoring tool in order to implement protocols for rapid estimation of water resources and water quality. Among these, electromagnetic sensing techniques offer the possibility of a fast groundwater monitoring at reasonable costs due to their noninvasivity and survey quickness.

The electromagnetic techniques exploit signals measured in passive and active modalities, which make available information about the electromagnetic features of ground structure provided that they are properly processed. In this frame, it is worth remarking that water content strongly influences the electromagnetic response of the subsoil. More in detail, the suitability of electromagnetic sensing techniques in the groundwater monitoring is supported by the following factors [3]:

- the electromagnetic and electrical properties of the rocks are strongly controlled by the presence of groundwater;
- the groundwater distribution is controlled by geological features such as lithology, porosity and permeability, which are factors that can be mapped;
- the chemical composition of the groundwater affects its electromagnetic properties.

Then, electromagnetic sensing techniques are able to:

- detect the presence or absence of groundwater in the surveyed areas, for instance, the same rock can exhibit resistivity values very different if it is saturated or dry;
- estimate the amount of exploitable water by mapping shallow and buried geological features in order to define the aquifer;
- indicate the presence of possible pollutants.

In particular, the input of a pollutant in the subsoil always produces detectable modifications in the electric, magnetic, and electromagnetic parameters. For instance, electrolytic substances decrease the resistivity of the water [4]. Other substances, such as hydrocarbon, can modify the resistivity in unexpected ways, depending on the presence of bacterial activity [5]. Moreover, geological features, such as permeability boundaries, lithologic changes, and porosity variations, control the entity and diffusion of the pollutant [6].

Electromagnetic techniques mainly used in the groundwater prospection are the electrical resistivity tomography (ERT), the time-domain-induced polarization (IP), and the self-potential method (SP). Shallow prospection can be conveniently faced by using the ground-penetrating radar (GPR).

Moreover, the points detailed below should be taken into account to carry out a proper groundwater monitoring and diagnostics by electromagnetic sensing techniques [3].

- Proper design of the fieldwork including the techniques suitable for the problem under investigation.
- Choice of a suitable geometry for each electromagnetic sensing technique. As a matter of fact, each technique is sensitive to a particular property of the underground and needs one or more specific survey geometry. In the last decade, technological development provided increasingly sensitive sensors that have improved performances in terms of accuracy and resolution and offer the possibility to effectively implement 3D survey geometries.
- Management of robust processing and inversion routines. Electromagnetic sensing techniques depend strongly on an “interpretation” component, which has to be reduced at minimum by using data processing, integration, and fusion algorithms able to provide results in an automatic way.
- Improvement of the ability to reduce the interpretation ambiguity of the results. To pursue this aim, one can integrate heterogeneous data, i.e., the electromagnetic sensing techniques can be cooperatively exploited in order to minimize the uncertainties. In this respect, it is worth taking into account that each technique provides data needed to be processed by specific algorithms. Moreover, the output of each technique can be plotted as map, section, or data volume so that a proper graphical rendering is needed in order to correctly present all the results.

Despite significant technological improvement have been performed, currently several limitations affect the potentiality offered by the electromagnetic sensing techniques, especially with regard to the interpretative models. As a matter of fact, the physical-chemical and biological phenomena arising in the case of groundwater pollution are not yet fully understood. For instance, the role of bacterial activity in the modification of electromagnetic parameters during the pollutant degradation process is still not clear. Therefore, the associated electromagnetic signals cannot be linked to their source.

However, the electromagnetic sensing techniques have all the features to be a preliminary screening tool for the characterization of contaminated or at-risk sites. They provide, in the form of maps and sections, important information about the presence and position of a pollutant plume and can represent a constraint useful

to plan further direct measurement campaigns based on sampling collection and laboratory analysis.

This chapter deals with four electromagnetic sensing techniques: ERT, GPR, IP and SP. After their theoretical bases description, we illustrate their application, data processing and interpretation to highlight their strengths and weaknesses in the framework of real electromagnetic surveys. In particular, two cases of local groundwater contamination are taken into account: the first one regards an industrial site and precisely the shallow characterization by means of ERT and GPR surveys of the ground surrounding a phenol tank located in the Kablova industrial site (Serbia-Herzegovina). The second one concerns the application of ERT, IP, and SP method as tools for deep characterization of the Montegrosso-Pallareta waste dump structure (Italy).

2 The Electromagnetic Sensing Techniques: Theoretical Overview

This paragraph describes the working principles and the operative modalities of the electromagnetic sensing techniques applied in the study cases described later and it is devoted to highlight their imaging capabilities as well as their physical and applicative limits. This is useful to determine the electromagnetic sensing technique most suitable for each study case at hand and provide guidelines for a combined use of different techniques in order to reduce their proper drawbacks and unavoidable uncertainties.

2.1 *Electrical Resistivity Tomography*

The electrical resistivity tomography (ERT) is an active electromagnetic sensing techniques which, in its theoretical measurement configuration, is based on the injection of an electrical current (I [mA]) in the subsoil by means of a pair of electrodes (A and B) and the subsequent measurement by using another pair of electrodes (M and N) of the electrical potential (ΔV [mV]) [7, 8]. In order to reduce electrode polarization effects, which could affect the accuracy of the measure, the injected current is modulated as a low-frequency square or sinusoidal wave. There are several possible electrode arrangements and Fig. 1 depicts the most used ones, which are the Wenner, Schlumberger, and dipole-dipole arrays.

Whatever the used array, the ERT is based on the measure of the ground electrical potential while the current is injected. In this circumstance, it is possible to calculate the apparent resistivity (ρ_a):

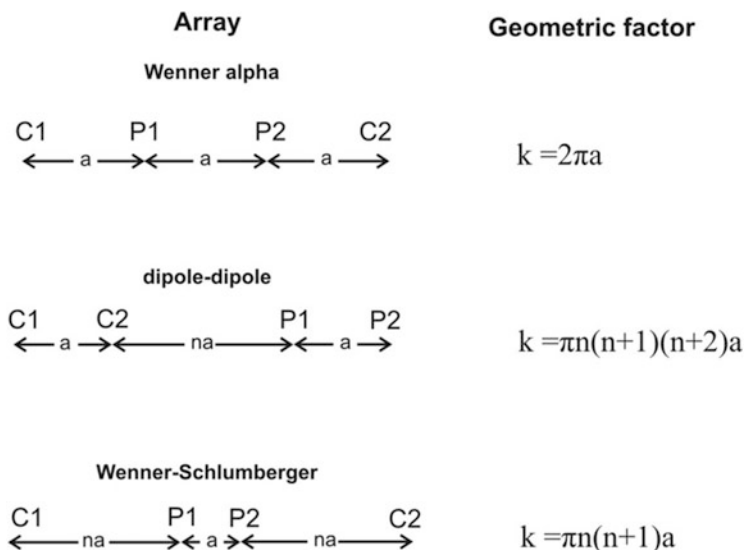


Fig. 1 Schematic representation of the usually deployed linear arrays of electrodes, with their geometrical characteristics. C1–C2: current electrodes; P1–P2: potential electrodes; a : electrode spacing; k : geometric factor; n : ratio of the distance between the C1–P1 electrodes and the C1–C2 dipole spacing

$$\rho_a = k(\Delta V/I) \quad (1)$$

where ρ_a is expressed in Ωm and k is a geometrical factor depending on the adopted array configuration (see Fig. 1 for the value of the geometrical factor). Subsoil position of the measurement point depends on the position of the electrodes at the surface and on the used array configuration [7]. In addition, investigation depth and spatial resolution depend on the deployed electrode spacing: large spacing allows good depth of exploration while, small spacing provides a good spatial resolution. As a consequence, the optimal electrode spacing is achieved as a trade-off of these two conflicting requirements.

In general, the choice of the array configuration depends on the site features as well as on depth, size, and composition of the target as well as on the desired signal/noise ratio. Details about array configurations and their sensitivity functions are reported in [8].

Modern georesistivimeters have multielectrode systems able to acquire a large number of data by automatically switching quadrupoles for each array, which is composed of a consistent number of electrodes properly fitted on the ground.

The result of such an acquisition is a distribution of data describing the apparent resistivity lying on the vertical plane passing through the acquisition profile. A data inversion procedure is needed in order to determine a subsurface model whose response is consistent with the measured data [8]. Model parameters are linked to the model response by using finite difference [9, 10] or finite-element methods [11]

Table 1 Resistivity value of natural materials

Material	Resistivity (Ωm)
Air	Infinite
Pyrite	3×10^{-1}
Galena	2×10^{-3}
Quartz	4×10^{10} – 2×10^{14}
Calcite	1×10^{12} – 1×10^{13}
Rock salt	30 – 1×10^{13}
Mica	9×10^{12} – 1×10^{14}
Granite	100 – 1×10^6
Gabbro	1×10^3 – 1×10^6
Basalt	10 – 1×10^7
Limestones	50 – 1×10^7
Sandstones	1 – 1×10^8
Shales	20 – 2×10^3
Dolomite	100 – $10,000$
Sand	1 – $1,000$
Clay	1 – 100
Ground water	0.5 – 300
Seawater	0.2

and the initial model is iteratively optimized until the difference between the model response and the observed data is minimized.

The model obtained by the inversion process is a representation of the subsoil in terms of electrical resistivity. Final process, which is the interpretation in geological terms of the resistivity section, requires the knowledge of the relationship between electrical resistivity and geological materials.

Since the rocks are mainly formed by silicates, which are nonconducting materials, their electrical resistivity mainly depends on the electrical resistivity of the water porosity as well as on the degree of saturation and it follows the Archie's law [12]:

$$\rho = a\varphi^{-b}f^{-c}\rho_w \quad (2)$$

where φ is the porosity, f is the saturation degree, ρ_w is the water resistivity, and a , b , and c are empirical parameters.

Table 1 reports the electrical resistivity of the most diffuse material of the Earth crust.

Table 1 brings three important implications:

- the ERT is very sensitive to the presence of water and its ionic content;
- depending on their water content, several materials can exhibit the same electrical resistivity or the same material can have different resistivity values;
- the a priori geologic knowledge of an area is essential in order to correctly interpret an ERT result in terms of lithology and hydrogeology.

ERT is able to localize a contaminant in a geologic system. In fact, it is demonstrated that it is sufficient to add 25 ppm of ionic substance in the water aquifer to increase the conductivity of 1 mS/m [13] and that hydrocarbon biodegradation processes produce anomalous conductive zones [5].

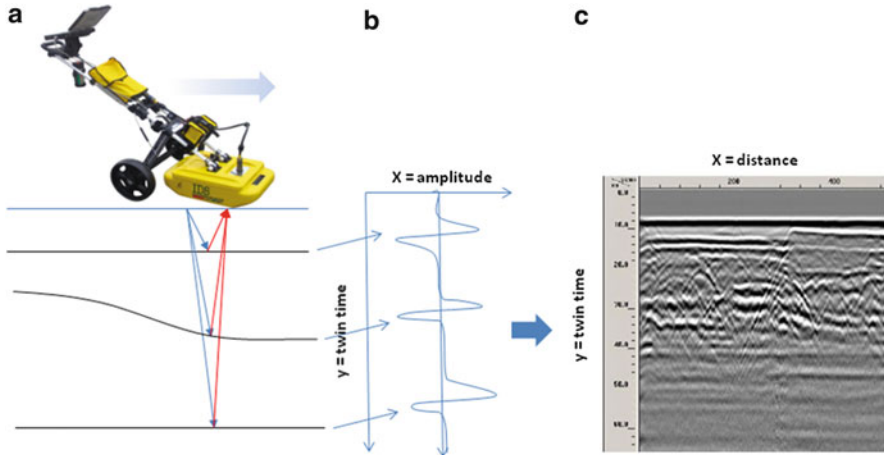


Fig. 2 Schematic representation of the GPR working principle: a) or B-scan GPR image and signal propagation; b) single gathered trace or A-scan; c) raw-data radargram.

These features make ERT a tool able to estimate the parameters needed to formulate transportation models of pollutants [14]. For these reasons, ERT can be very useful to detect possible losses of contaminant liquid from storage sites.

2.2 The Ground-Penetrating Radar

The ground-penetrating radar (GPR) is an active electromagnetic technique whose working principle is that of a common radar system. In particular, a transmitting antenna radiates an electromagnetic wave, usually a microwave pulsed signal whose spectrum belongs to the range from 10 MHz to some GHz, and a receiving antenna gathers the backscattered signal engendered by hidden targets, i.e., anomalies arising into the electromagnetic features of the surveyed medium (Fig. 2).

In this respect, it is worth noting that at microwaves, large part of the materials are nonmagnetic. As a consequence, the most important electromagnetic parameter is the relative permittivity, which can be a complex quantity in the case of dispersive media [15].

The usually adopted GPR measurement configuration is the *common offset single fold* (see Fig. 2a), in which the transmitting and receiving antennas are placed at a certain distance into a single fold, which is moved along one or more lines at the air-medium interface. At each position, the transmitting antenna radiates a wavelet, which, interacting with the target, gives rise to a backscattered field that is collected by the receiving antenna. The signal measured at each position of the antenna system is named A-scan and its peaks identify the interfaces between different materials (see Fig. 2b).

Table 2 Relative dielectric permittivity of geologic materials measured at 100 MHz

Material	Relative dielectric permittivity (ϵ_r)
Air	1
Dry sand	3–5
Dry silt	3–30
Ice	3–4
Asphalt	3–5
Volcanic ash/pumice	4–7
Limestone	4–8
Granite	4–6
Permafrost	4–5
Coal	4–5
Shale	5–15
Clay	5–40
Concrete	6
Saturated silt	10–40
Dry sandy coastal land	10
Average organic-rich surface soil	12
Marsh or forested land	12
Organic-rich agricultural land	15
Saturated sand	20–30
Freshwater	80
Seawater	81–88

The time instant at which each peak occurs is called round trip travel time and it is the time employed by the wave to reach the target and come back to the antenna. Hence, once the round trip travel t_r is known, the depth d_r of the target, i.e., the distance occurring among the electromagnetic anomaly and the antenna system, can be calculated as:

$$d_r = \frac{vt_r}{2} \quad (3)$$

where the number 2 at denominator is needed in order to consider just one way travel path and v denotes the velocity of electromagnetic signal into the probed medium. Such a velocity depends on the *relative dielectric permittivity* (ϵ_r) of the surveyed medium:

$$v = \frac{c}{\sqrt{\epsilon_r}} \quad (4)$$

c being the speed of light in vacuum, which can be approximated to 0.3 m/ns. The *relative dielectric permittivity* can be estimated by using direct or indirect methods [15, 16] and its values for several materials encountered in geological surveys are given in Table 2.

In addition, it is worth remarking that the amplitude of each peak is directly proportional to the *reflection coefficient* R , which can be expressed both in terms of wave velocities v_1 and v_2 inside two different media

$$R = \frac{(v_1 - v_2)}{(v_1 + v_2)} \quad (5)$$

and as a function of their relative dielectric permittivities ϵ_1 and ϵ_2

$$R = \frac{(\sqrt{\epsilon_1} - \sqrt{\epsilon_2})}{(\sqrt{\epsilon_1} + \sqrt{\epsilon_2})} \quad (6)$$

From Eqs. (5) and (6), one can immediately observe that the larger is the contrast of electromagnetic properties, the greater is the amplitude of the reflected wave.

A set of A-scans gathered along a measurement line is referred as raw-data radargram and it is often plotted in greyscale as Fig. 2c shows, where white and black colors identify positive and negative peaks, respectively.

The radargram is a space-time image providing a coded representation of the target, which does not correspond to its geometrical shape. As a matter of fact, since the travel time changes when the antenna system is moved along the measurement line, a punctual reflector appears as a hyperbolic pattern, whose vertex and eccentricity depend on the position of the targets and their size. In addition, objects having more complex shapes will result in more complex patterns.

To properly plan a GPR survey, it is crucial to account for the depth penetration and the spatial resolution.

As far as the penetration depth is concerned, it is worth remarking that several attenuation phenomena may decrease the amplitude of the electromagnetic signal along its path from the transmitting antenna to the target and from this latter to the receiving antennas. In particular, the main attenuation phenomena are:

- *scattering*: objects, whose size is approximately equal to the probing wavelength, spread energy in all the spatial directions producing “clutter noise” in the radar data;
- *absorption*: the electromagnetic energy is converted into heat;
- *geometric attenuation*: the electromagnetic energy is distributed over spherical wavefronts and decays at a rate proportional to $1/r^2$ where r is the distance of the wavefront from the antenna;
- *electromagnetic attenuation*: it is a complex function of the electromagnetic properties of the investigated medium and the frequency of the signal.

The combination of all these phenomena limits the investigation depth reachable by GPR as compared to other geophysical methods.

The other key feature is the spatial resolution, which is recognized as range (or depth) resolution and lateral (or angular) resolution. These represent the minimum distances along vertical and horizontal directions, respectively, which must occur between two targets in order to make them distinguishable one to the other one.

Depth penetration and spatial resolution strongly depend on the central frequency of the probing signal and then on the adopted antenna system. In particular, the use of a high-frequency probing signal provides a great spatial resolution but a poor penetration depth. Conversely, low-frequency signals allow to increase the penetration depth but limit the achievable spatial resolution [17, 18]. For this reason, the GPR revealed a precious multi-scale tool. It can be successfully applied in archeological prospections [16, 19–21], polluted area characterization [22], diagnostics of dams [23] and bridges [24], reinforced concrete [25, 26], and historical building diagnostics [27, 28].

In this respect, it is important to properly select the antenna central frequency suitable for the problem at hand by balancing the opposite requirements of spatial resolution and investigation depth.

Furthermore, it is important to emphasize that spatial resolution is not constant, but it decreases with increasing depth [15]. Accordingly, electrically small objects can be detectable if they are shallow but can be missed if they are at great distance from the measurement surface.

To properly interpret GPR data, a key aspect is the choice of the data processing strategy, that is a sequence of operations performed in order to focus punctual reflections, restore correct objects geometry from complex radargrams, eliminate noise and unwanted reflections, and convert the vertical time axis into a depth axis by performing the velocity analysis.

Strong skills and experience in data processing are required in order to produce reliable images. These aspects limit the use of GPR to expert users and introduce elements of subjectivity in the interpretation of the survey results.

In the last years, novel processing approaches based on the solution of an inverse scattering problem have been developed and assessed in several applicative contexts [24–28]. These approaches, commonly referred as microwave tomography (MWT), are based on the use of approximate models of the electromagnetic scattering phenomena [29, 30] and offer the advantage to provide automatically reliable GPR images, which can be easily interpreted by non-expert users.

To conclude this section it is worth pointing out that GPR can be a very fast method for mapping pollution in shallow context. In fact, pollutant acts by changing the electric permittivity and conductivity of subsoil. A change in the electrical permittivity produces changes in the reflection of the electromagnetic waves that can be easily detected. A change in the conductivity produce a change in the amplitude of the electromagnetic waves. Generally, ionic contaminants produce absorptive zones recognizable in the radargram.

2.3 Time-Domain-Induced Polarization

Time-domain-induced polarization (time-domain IP) measurements can be carried out by using the same instrumentations and array configurations of the ERT, with

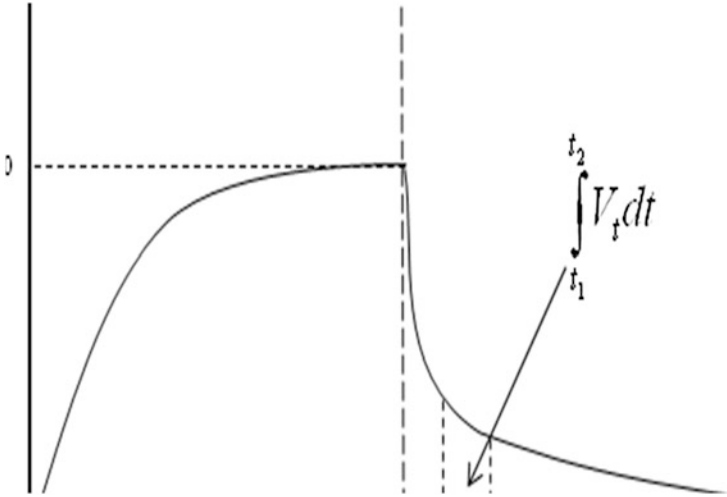


Fig. 3 Charge and discharge curve of the electric potential during an IP measurement

the difference that the measurement of the electrical potential (V) is immediately performed just after that the current injection (I) is turned off.

In this way, the measurement is concerned with the transitory describing the exponential decay of the electrical potential according to the discharge curve as that shown in Fig. 3.

Chargeability (M), which is the searched parameter, is provided by the following integral relation:

$$M = \frac{100}{V_0(t_2 - t_1)} \int_{t_1}^{t_2} V_t dt \quad (7)$$

where V_0 is the initial voltage (at t_1), V_t the time behavior of the voltage, and t_1 and t_2 are the times between which the integration is performed. In particular, t_1 is taken a few milliseconds after the current has been switched off in order to avoid opening extra current; t_2 is considered some hundreds of milliseconds after t_1 so to have an integration time sufficiently long to describe the phenomenon while avoiding to integrate on the time interval where the signal/noise ratio is lower.

According to Eq. (7), the chargeability M is expressed in seconds (or better ms). Usually, commercial instrumentations that use the Newmont standard method (M 331) allow us to express chargeability indifferently in mV/V or ms since the integration time of the discharge curve is 1 s [31].

Induced polarization can be interpreted by means of two phenomena as it is shown in Fig. 4 [32].

Electrode polarization: it is well known that a metal in an electrolytic solution can generate an electrical potential (Nernst potential) in the thin liquid layers immediately in contact with the metal. The application of an electrical current

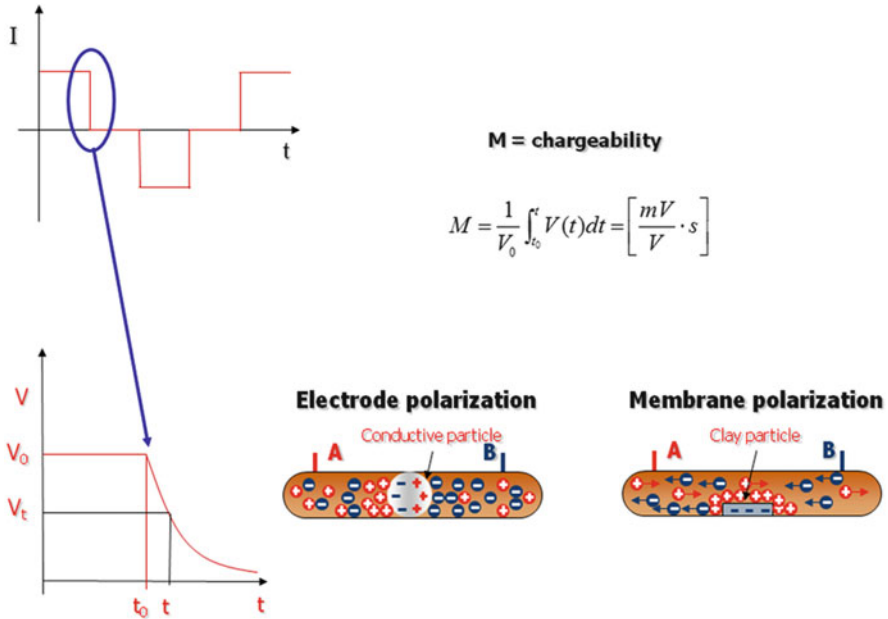


Fig. 4 Mechanisms involved in the polarization phenomenon: electrode polarization and membrane polarization

to the system perturbs the charge balance that assumes a new configuration. The interruption of the exciting current leads to a return at the previous “equilibrium” situation of equilibrium after a small and finite time.

Membrane or clay polarization: bottlenecks in a pore can lead to an unbalance of charges in the presence of an electrical current (Fig. 4). In fact, the surface of minerals, which is negatively charged, attracts cations by the fluid up to a thickness of about 100 μm. A bottleneck below this limit can produce an accumulation of cations in the presence of an electrical current, and, consequently, an unbalance in the charge distribution. When the current is turned off, charges return at their normal configuration after a small time. The same phenomenon can be explained if the bottleneck is due to a clay particle that is negatively charged.

Time-domain IP measurements require special electrodes and shielded cables. On the other hand, several authors explored the possibility to carry out measurements by using steel electrodes and cables normally used for ERT measurements. In this case, several precautions are required:

- measurements have to be carried out in the presence of low noise and a good electrode contact with the ground is required [33];
- in order to limit the charge-up effect, a pair of electrodes can be used as potential dipole, provided that a certain time interval has been elapsed after they have been used as current electrodes [34];
- if possible, the charge-up correction has to be carried out [35, 36].

Time-domain IP data have to be inverted in order to achieve the true model in terms of chargeability. The process is made by inverting conductivity data by considering that in a non-polarizing medium, it can be written:

$$\sigma'_i = \sigma_i(1 - m_i) \quad (8)$$

where σ'_i is the apparent conductivity of a non-polarizing medium and σ_i and m_i are the conductivity and chargeability of a polarizing medium, respectively.

The inversion can be designed in order to invert at the same time σ' , i.e., σ_i , and calculate m_i at the end of the process.

Time-domain IP has been originally conceived in order to detect mineral bodies [32], but now is currently used in order to monitor the quality of water [37], for detecting dissolved pollutants in the groundwater [38], for environmental monitoring [34–36]. The main drawback in environmental field is the lack of a model able to explain macroscopic evidences of IP [39]. This lack complicates the interpretation of IP data.

Anyway, the methodology can be successfully used in order to characterize waste dumps and surrounding areas and it provides information complementary to the ERT [40, 41].

2.4 Self-Potential Method

Self-potential (SP) method is based on the measurement of the electrical potential occurring between two points of the Earth surface without injecting any current. This passive method dates back to 1830, when Robert Fox used a pair of copper electrodes connected to a galvanometer in order to detect a copper sulfide deposit. In the 1920, the SP method was considered a standard technique for detecting massive metallic ores [32]. Nowadays the technique, which is unchanged in its general working principle, can be carried out by using high-impedance multimeters and unpolarizable electrodes that make it quick and cheap.

Self-potential arises in the presence of buried ore bodies [42, 43], quartz dicks, groundwater flow, biochemical reactions and vegetable biological processes. Table 3 summarizes main natural sources of electrical self-potential and the corresponding polarity and magnitude of the emitted signal.

Different mechanisms are responsible of the SP occurrence [44] and are listed in the following subsections.

2.4.1 Diffusion or Membrane Potential

Diffusion or membrane potential is generated in the presence of ionic species with different concentrations and mobilities. In fact, if the mobility of ions and cations, which migrate according to the concentration gradient, changes a charge

Table 3 SP anomalies and related sources

Source	SP signal
Sulfide ore bodies (pyrite, chalcopyrite, pyrrotite, sphalerite, galena), graphite, magnetite, copper, manganese	Negative, tens of mV
Quartz veins, pegmatites	Positive, tens of mV
Flow of fluids, geochemical reactions	$-100 \leq \text{mV} \leq +100$
Bioelectricity (plants and trees)	Negative, ≤ 300 mV
Flow of groundwater	Positive or negative, hundreds of mV
Topographic gradient	Negative, > 2 V

distribution occurs and a difference of potential of some tens of mV can be produced. At the equilibrium, the diffusion potential is:

$$E_d = -\frac{RT(I_a - I_c)}{nF(I_a - I_c)} \ln(C_1/C_2) \quad (9)$$

where I_a and I_c are the mobility of ions and cations, respectively, n is the ion valence, R the universal constant of gas, T the absolute temperature, F the Faraday constant (i.e., the charge of an Avogadro's number of electrons; $F = 96.48530929$ C/mol ± 0.0289456 C/mol), and C_1 and C_2 are the concentrations of the ionic quantities.

In the presence of a geologic boundary between clay and another non-clayey sediment, the mobility of anions is prevented into the clay (i.e., $I_a = 0$). In this case, the difference of potential is expressed by the Nernst equation:

$$E_N = -\frac{RT}{nF} \ln(C_1/C_2) \quad (10)$$

describing the *Nernst potential or clay potential* occurring at the boundary between clays and other non-clayey sediments.

2.4.2 Streaming Potential

Known also as z-potential or electrokinetic potential, it is due to the flowing of a fluid into a porous medium driven by a pressure gradient [44–46].

The Helmholtz-Smoluchowski equation describes the streaming potential ΔV of a fluid moving in a porous medium under a pressure gradient ΔP :

$$\Delta V = (\varepsilon\zeta/\mu\sigma)\Delta P \quad (11)$$

where ε is the dielectric constant of the fluid, ζ is the zeta-potential that is related to the double electrical layer formed by ions close to a grain boundary, and σ and μ are the electrical conductivity and viscosity of the fluid, respectively.

In areas with heavy rainfall, porous rock and steep topography, the streaming potentials can reach values up to 3 mV [44].

From the application point of view, it is useful to consider the streaming potential as a direct function of the hydraulic gradient between two points of the Earth surface following the first-order approximation of the Fournier equation [47, 48]:

$$\phi - \phi_0 = C'(h - h_0) \quad (12)$$

where ϕ and h are the potential and the hydraulic head at measurement station, respectively, and ϕ_0 and h_0 are the potential and the hydraulic head at reference station. C' is the electrokinetic coupling coefficient expressed in mV/m [48].

2.4.3 Mineral Potential

Mineral potential is associated to the presence of mineralized ore bodies following the geo-battery model of Sato and Mooney [42]. Following these authors, a sulfide ore body located across the water table can generate redox reactions and, consequently, a difference of potential measurable as SP signal at the surface. Anyway, this model results enough incomplete since it doesn't explain strong SP signals, which have been measured up to 800 mV, the sign of the anomaly, which is always negative near the ore body, and the fact that the geo-battery is always charged up. Moreover, the model doesn't explain anomalies due to ore bodies completely up or below the water table or water table fluctuations [44].

2.4.4 Bioelectrical Potential

Bioelectrical potential is generated in correspondence of the tree roots, which can operate an ion selection by sucking water. Their effect is measurable in hundreds of mV.

Sensitivity of the SP method to a great number of sources and the absence of models able to explain them represent the main obstacle to the interpretation of an SP signal. However the method is versatile and quick in order to identify water flux in complex aquifer [46] and in landslides [49] as well as in order to detect leakage in dams and embankments [44, 50, 51].

Since the membrane potential is very sensitive to the temperature, the SP method is applied successfully in the hydrothermal and volcanic areas [51–53]. Moreover, recently, the SP method has been applied to polluted areas and waste dumps where, further that the streaming potential component producing a negative signal [45, 49], it has been highlighted an electrochemical potential producing a positive anomaly directed as the groundwater flux [48]. Residual potential obtained by subtracting the streaming potential component is in agreement with the redox potential directly measured in hole [48]. The leachate containing organic matter produces redox reactions reducing different chemical species as a function of the distance of

the pollutant [54]. Strong anomalies detected directly into the waste dumps can represent leachate accumulations [41].

3 Case Studies

This paragraph provides examples concerning the use of the above described electromagnetic sensing techniques. The first case study concerns the Kablova industrial site located in Jagodina (Serbia-Herzegovina) where the goal of the survey was the estimation of water tightness of a tank of phenols. The required high spatial resolution and low investigation depth suggested to exploit high-resolution ERT and GPR. The second example concerns the verification of the tightness of the Montegrosso-Pallareta large waste dump structure located in Potenza (Italy). Logistics and geological complexities of the area as well as the large size of the waste dump structure imposed the use of large-spacing (20 m) ERT, time domain IP, and SP method.

3.1 *The Kablova Industrial Site*

The following example illustrates as the ERT and GPR have been used in order to check the presence of phenols into the ground and groundwater of the Kablova industrial site in Jagodina (Serbia-Herzegovina).

The Kablova Holding is a leading manufacturer of electrical and telecommunication cables in the world, which was in the past an example of industrialization appreciated throughout the world. Unfortunately, its waste management process has suffered rapid deterioration in recent decades due to changing market and to the Balkan war. In particular, a storage tank of phenols, abandoned since the 1980s, has become a matter of concern for possible losses and subsequent infiltration of its content into the subsoil.

As far as the ERT survey is concerned, four ERT profiles have been carried out close to the phenol pool in order to check the presence of phenols in the soil and groundwater (Fig. 5).

For all profiles, Wenner-Schlumberger array has been used and electrode spacing of 1–5 m has been used for the first three and the last tomography, respectively.

The three smaller profiles were made close to three of four sides of the “lake of phenols” so as to intercept any possible loss into the ground. Unfortunately, it was not possible to acquire a profile along the southern side, due to the very dense vegetation and the presence of hazardous waste. But this did not affect the validity of the survey because the flow lines of the groundwater flow are reasonably oriented from north towards the river.

Results of these three sections are depicted in Fig. 6.



Fig. 5 Location of the Kablova factory waste disposal area embedding the “phenol pool.” The location of ERT surveys (T1, T2, and T3) and expected groundwater flow are indicated. Copyright 2013 Digital Globe, 2013 Google (modified)

Their resistivity ranges between 14 and 1000 Ωm , while the investigated depth is about 8 m. The highest resistivity values (from 90 to 1000 Ωm) can be associated to the pavement, which is made by asphalt and backfill (abk). In addition, the same resistivity values characterize some areas that could represent a deep bedrock (brk).

The lowest resistivity values (14–90 Ωm) can be attributed to the presence of saturated alluvial deposits (sad).

In correspondence of the phenol pool no variations in the resistivity of the saturated alluvial deposits were observed, indicating that no significant loss occurs from the tank. Indeed phenols are characterized by very high resistivity values ($6 \times 10^4 \Omega\text{m}$), which certainly would have affected the electrical resistivity of the investigated subsoil.

This evidence is confirmed by the tomography T4, showing the resistivity of the subsurface until a depth of about 40 m (Fig. 7).

Due to its lower spatial resolution, this tomography cannot detect the asphalt and backfill stratum (abk). However, the saturated alluvial deposits are well defined even if their resistivity appears slightly higher than the ones in the previous surveys. Within the bedrock resistive nuclei (rn) are visible. Their resistivity is about 500–600 (Ωm) and they can be interpreted as resistive paleo-canals.

This evidence allowed to exclude the presence of significant losses from the phenol tank into the groundwater and then into the nearby canal.

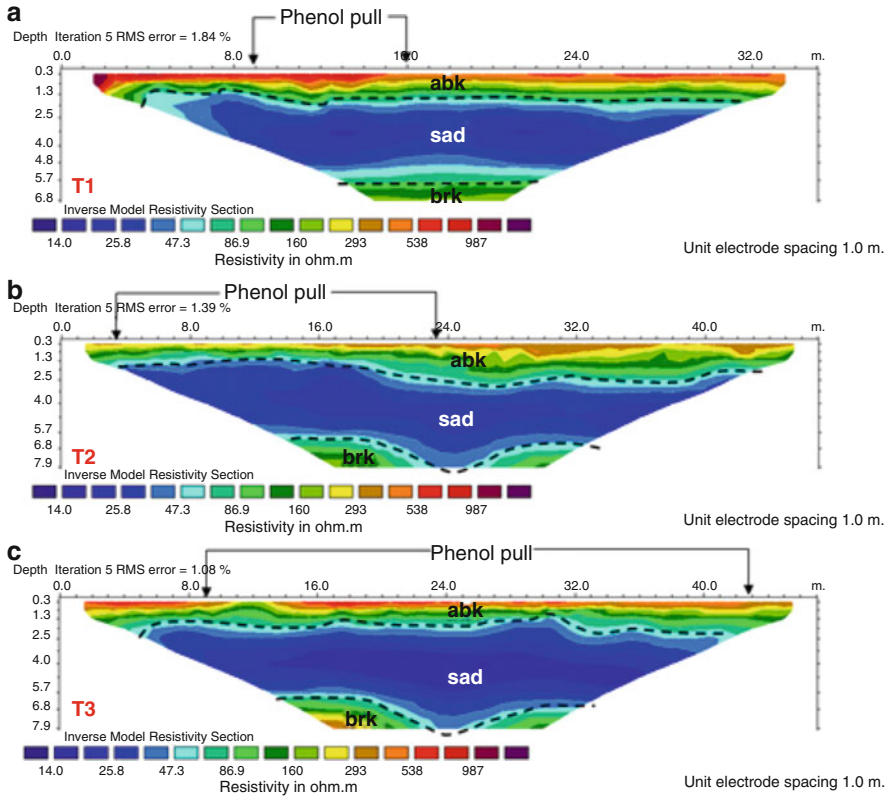


Fig. 6 ERT inversion results corresponding to the data gathered in the area of Fig. 5 a) T1 survey; b) T2 surveys; c) T3 survey. *abk* asphalt and backfill, *sad* saturated alluvial deposits, *brk* bedrock

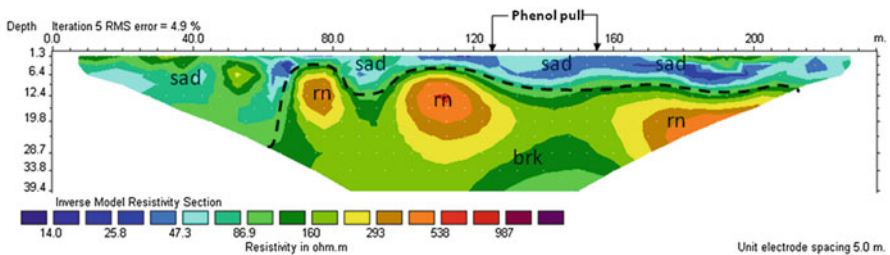


Fig. 7 ERT inversion result for T4 survey carried out in the area of Fig. 5. *sad* saturated alluvial deposits, *brk* bedrock, *rn* resistive nucleus

Anyway, in order to have an independent method able to confirm this evidence, a GPR survey has been also carried out. In particular, four radargrams have been gathered on the same survey lines of Fig. 5 by using an acquisition module GSSI SIR 3000 equipped with a 400 MHz antenna and having survey cart and encoder. The system was parameterized with a time window of 80 ns and 32 scans/m, 512 samples/scan, and 16 bits/sample.

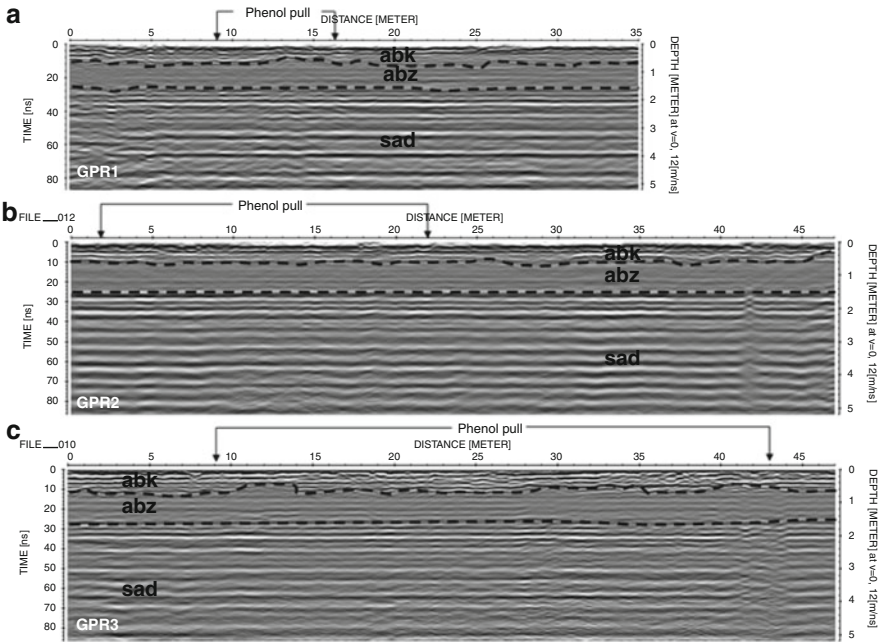


Fig. 8 Radargrams carried out in the area of Fig. 5 a) GPR1; b) GPR2; c) GPR3 *abk* asphalt and backfill, *abz* absorptive zone, *sad* saturated alluvial deposits

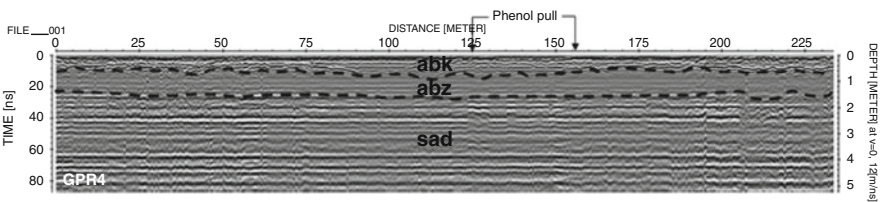


Fig. 9 Radargram GPR4 carried out in the area of Fig. 5. *abk* asphalt and backfill, *abz* absorptive zone, *sad* saturated alluvial deposits

The data processing has involved the following steps: *zero time correction*, *remove header gain*, *automatic gain control*, *resampling*, *fk-filtering*, and *migration* (by using a wave average velocity of 0.12 m/ns based on hyperbole adaptation analysis).

With reference to Fig. 8, which depicts the first three radargrams (GPR1, GPR2, and GPR3) and shows the subsoil up to 5 m depth, one can detect three layers that from top to bottom can be identified as:

- a shallow layer (up to 8 ns or 0.6 m reflective layer) showing a continuous series of reflectors that become locally chaotic and can be related to asphalt and backfill (*abk*).
- an intermediate absorptive layer (16 ns or 0.6 m to 22 ns or 1.80 m) that can be correlated with a layer in place of saturated silt and clay (*abz*).

- a deep layer (more than 22 ns or 1.80 m) with a series of well-marked and continuous horizontal reflectors that can be interpreted as coarse sediments saturated alluvial deposits (sad).

In agreement with the corresponding ERT profiles (Fig. 6), radargrams do not show any alteration or modification in the section corresponding to the position of the “lake of phenols.”

Figure 9 depicts the radargram GPR4 carried out in correspondence of the ERT T4 of Fig. 7 and also in this case the radargram results in agreement with corresponding ERT data and the other radargrams.

These results confirm the interpretation based on the ERT data.

3.2 The Montegrosso-Pallareta Waste Dump Complex

From a geophysical point of view, a waste dump is basically a very conductive body composed of waste and leachate contained into a basin, which is confined by very electrically resistive plastic liner.

Because of the liquids contained in the waste and due to chemical and biochemical reactions with infiltrated rainwater, a landfill produces a certain amount of leachate. Leachate is a liquid containing dissolved and suspended material. In particular, dissolved material includes organic matter (alcohols, acids, aldehydes, short chain sugars, etc.), inorganic macro components (common cations and anions including sulfate, chloride, iron, aluminum, zinc, and ammonia), heavy metals (Pb, Ni, Cu, Hg), and xenobiotic organic compounds such as halogenated organics (PCBs, dioxins, etc.) [55].

The only barrier to the leakage of this slurry is a waterproof structure consisting in layers of clay or bentonite and HDPE sheets placed at the bottom, where a drainage system allows to periodically pull out the leachate. HDPE liners must have high tensile strength, flexibility, elongation without failure and must be resistant to the UV rays, temperature changes, and chemical attack. Of course, these features can deteriorate with time so that old waste dumps may disperse leachate into the ground and groundwater. Therefore, there is the necessity of diagnostic tools able to detect the HDPE liner failure and the consequent leachate contamination of groundwater.

From a practical point of view, geological complexities and logistic difficulties have to be considered, in order to gather reliable geophysical data.

In the following example the electromagnetic sensing techniques have been applied in order to monitor the Montegrosso-Pallareta dump and in particular the release of contaminant liquids due to the failure of plastic liners and clayey layers.

The Montegrosso-Pallareta waste dump complex consists of six industrial (sludge) and municipal solid waste (MSW) reservoirs with irregular shape filled from 1989 to 2001 (Fig. 10).

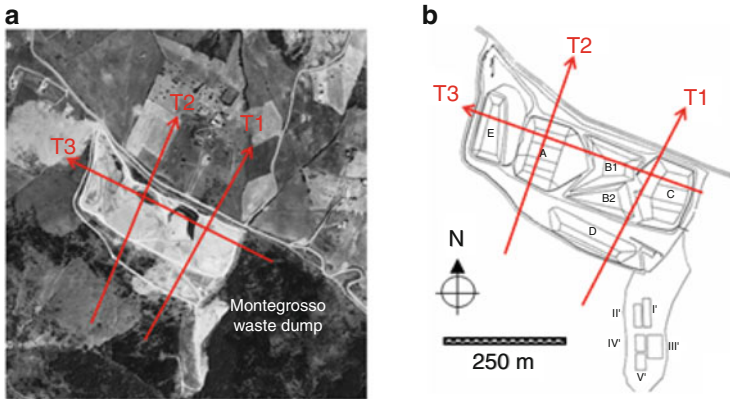


Fig. 10 Montegrosso-Pallareta waste disposal complex (Basilicata Region, Italy). (a) Aerial image; (b) Scheme of reservoirs and location of ERT T1, T2, and T3 surveys

Table 4 Filling time and kind of refusal stored in the Montegrosso-Pallareta waste dump complex between 1989 and 2000

Basin	Start filling	End Filling	Volume (mc)	MSW tons	Sludge tons	Total tons
A	January 1990	March 1993	100,000	76,000	15,200	91,200
B1	October 1996	June 1998	80,000	41,400	8,000	49,400
B2	October 1995	September 1996	20,000	23,500	4,800	28,300
B2	July 1999	August 2000	20,000	30,800	0	30,800
C	April 1993	September 1995	96,000	58,000	11,600	69,600
D	May 1989	December 1989	10,000	16,000	0	16,000
E	September 2000	May 2001	90,000	20,500	0	20,500

It occupies an area of 150,000 m² on the top of Mount Montegrosso. Table 4 summarizes stored waste and industrial sludge volumes and filling periods for each basin.

From the geological point of view, the landfill is located on the Argille Varicolori formation, a sequence consisting of clays, quartz sandstones, and calcarenites intensely folded and fractured by tectonic processes [56].

As a matter of fact, the Argille Varicolori formations are known to have extremely low electrical resistivity values (<10 Ωm) in the presence of water [49, 57]. This aspect must be taken into account during the data interpretation because low-resistive zones could be interpreted as losses of contaminant with the risk of false positives.

Figure 11 depicts the results of tomographic inversion carried out starting from three dipole-dipole datasets, acquired by using a georesistivimeter IRIS Syscal R1 and a multielectrode 20 m spaced cable, along the profiles of Fig. 10.

Table 5 summarizes the features of the three surveys.

After the inversion process, performed by using Res2DInv (Geotomo Software), the investigated depth resulted in 105 m and the estimated resistivity ranged from 1 to 180 Ωm.

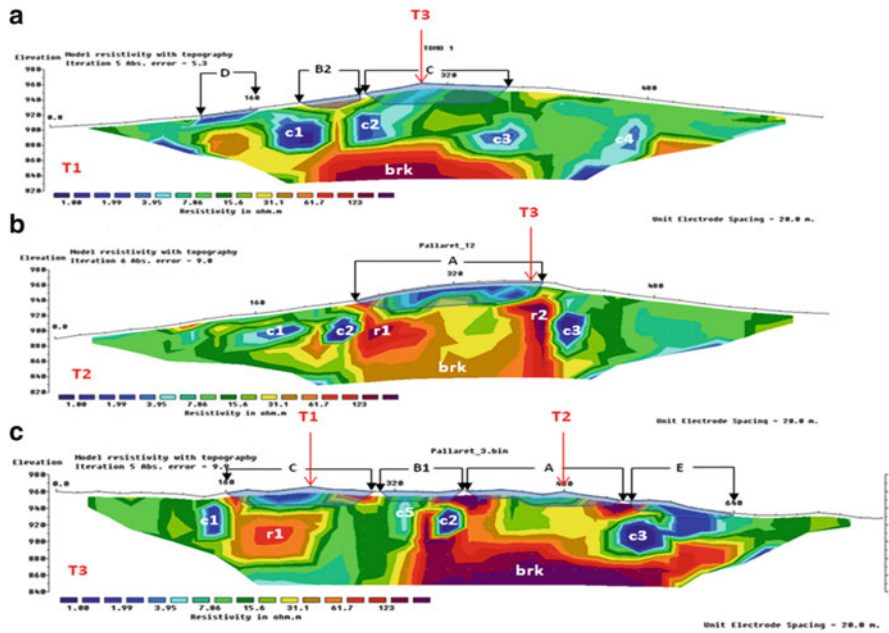


Fig. 11 ERT inversion results of the surveys carried out at Montegrosso-Pallareta waste disposal complex (Basilicata Region, Italy): a) T1 survey; b) T2 survey, 3) T3 survey.

Table 5 Geometrical features of the ERT profiles of Fig. 5

Profile	Electrode spacing (m)	Electrode number	Length (m)
T1	20	32	620
T2	20	32	620
T3	20	40	780

As a first approximation, the lowest values (1–15 Ωm) can be attributed to clay saturated soils, waste, and leachate. The intermediate ones (15–100 Ωm) can be attributed to wet clay soil. The highest resistivity values (larger than 100 Ωm) can be associated to limestone, over-consolidated clays, and HDPE liners. Using this rough rule, we try to provide a preliminary interpretation of tomographic sections.

Figure 11a shows the tomography T1 carried out across the basins D, B2, and C.

Basins C and D appear conductive while B2 is characterized by high resistivity values. Tomography shows four conductive nuclei (c1, c2, c3, and c4) that can be interpreted both like clay soils and contaminant. At the end, a resistive body (labeled brk in Fig. 11) located at 80 m in depth can be interpreted as the bedrock constituted by over-consolidated (thus, dry) clays.

Figure 11b depicts the ERT T2 carried out across the basin A, approximately parallel to the profile T1. The waste basin appears conductive (1–10 Ωm), whereas several conductive nuclei (c1, c2, c3, and c4) are detected. They can be related, except for the nucleus c4, to the same ones detected in the ERT T1. The bedrock

(brk) appears less resistive compared to the one in the ERT T1, while two resistive features (r1 and r2) appear below the two ends of the basin.

Figure 11c shows the ERT T3 crossing through the basins C, B1, A, and E. All the basins appear conductive with resistive nuclei at the extremes of the investigated area. Some conductive nuclei (c1, c2, and c3) and a resistive nucleus (r1) are detected. Finally, a resistive bedrock (brk) is detected at 80 m of depth.

With the exception of the basin B2, which appears resistive, all other basins result to be conductive, as it was expected. This evidence can be explained by taking into account that whatever cross section is considered basins have trapezoidal shape. Then, when the basin is sectioned near a boundary, as well as in the case of the ERT1 cutting the basin B2, the thickness of waste is low and the spatial resolution of the method can be insufficient to detect the waste in this zone. This hypothesis is supported by the fact that basin A is better defined in section T2, where the basin is cut in the middle, than in the T3, where it is sectioned on northern edge where the thickness of waste is very modest. This is the same for the basin C that is better defined in the tomography T3, which intersects it in the half, than in the section T1, that passes through its western margin.

With reference to the section T3, the basin B1 is not very well defined, but it is possible to observe a conductive vertical element (c5), which may be associated with a possible loss of leachate.

In the following, we summarize what it has been observed.

- Basins are better characterized when they are cut in the point of maximum thickness, which generally coincides with the center. The 20 m electrode spatial offset may cause a poor spatial resolution in case of reduced thickness of refuse.
- The ERT detected a series of conductive nuclei (c1–c5) that can be related to the clay minerals but also to contaminants.
- Basin edges appear resistive. This aspect, particularly visible in the section T3, can be due to the effect of the HDPE liner borders on the dipole-dipole array used.
- The bedrock below the basin A in the section T2 appears less resistive than in sections T1 and T2.
- The conductive body c5 could be a leachate loss.

ERT results suggest to perform core drills in the chemically conductive nuclei (c1, c2, c3, c4, and c5) in order to analyze material samples. Then, in complex geological context as the one in this example, the ERT is not able to discriminate, with full sureness, the contaminated areas from the naturally conductive ones. Anyway, ERT allows to identify the areas where other kind of indirect surveys and sampling and chemical analysis have to be carried out. So, in geologically complex circumstances, the technique ERT must be considered as a preliminary diagnostic tool useful to drive the exploitation of other more specific methods.

In attempt to understand if conductive zones were caused by clay minerals or leachate contamination, the IP data have been gathered by exploiting the array used for the ERT. The inverted IP sections are shown in Fig. 12.

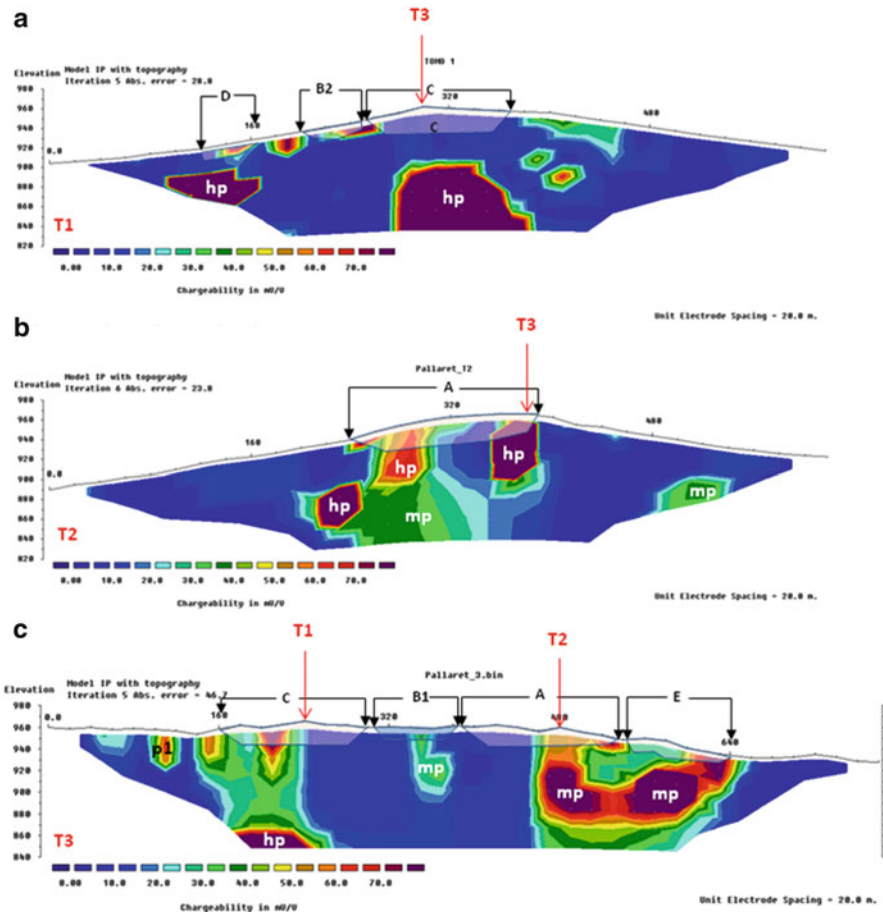


Fig. 12 Time-domain IP results for the surveys carried out at Montegrosso-Pallareta waste disposal complex (Basilicata Region, Italy) a) T1 survey; b) T2 survey; c) T3 survey.

With reference to Fig. 12, one can observe that the chargeability values range from 0 to 75 mV/V. The lowest values (0–20 mV/V) can be associated to membrane polarization due to clay minerals present in the Argille Varicolori formation.

Middle values (20–50 mV/V) have been detected mainly close and beneath the basins. In fact, they could be representative of leachate plumes leaked from the landfill. In fact, leachate is rich in metals under the form of solution and suspended [40]. Suspended fraction can produce strong polarization values [40] in function of size metal grains [58].

Finally, the highest values (>50 mV/V) can be associated to the basins (HP) or to deep bodies. The highest values present into the basins are due to the metal cumuli as demonstrated by Angoran and others (1974) [59] and to leachate diffusion into surrounding permeable materials [60, 61]. The highest values located

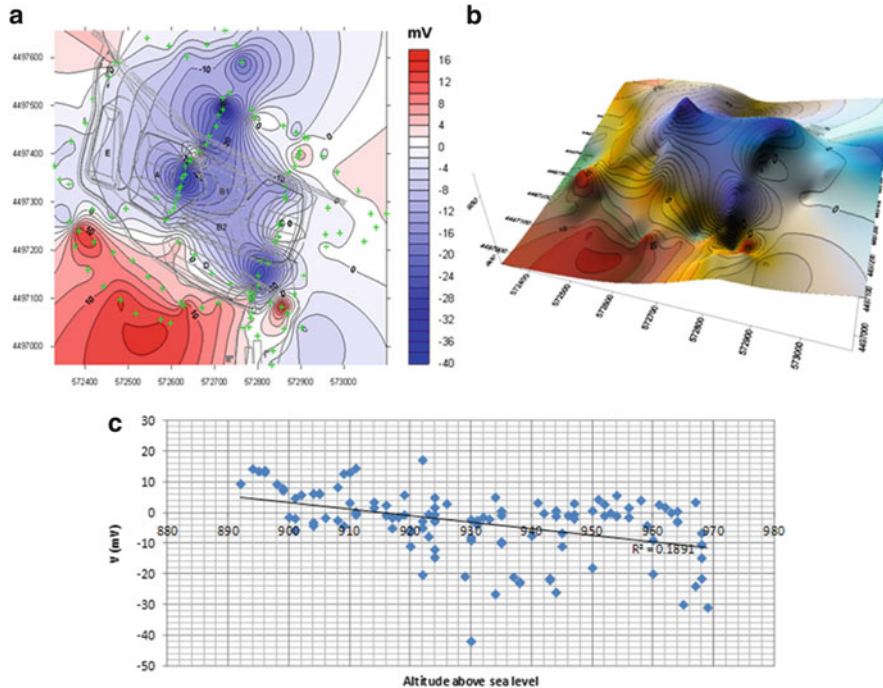


Fig. 13 Self-potential measurement at Montegrosso-Pallareta waste dump complex. (a) Self-potential pattern built by using 115 self-potential measurements; (b) plot describing the distribution of self-potential on the topography; (c) scatterplot of self-potential versus altitude

in depth are localized at the boundaries separating very conductive bodies from the resistive ones.

By comparing IP results with ERT results of Fig. 11, we make the following observations:

- Conductive nuclei c1, c2, c3, c4, and c5 exhibit low chargeability values compatible with a membrane polarization and thus they have to be considered uncontaminated clay nuclei.
- The strong chargeability at the basin boundaries could be due to the HDPE liner producing high resistive nuclei in the ERT results.
- The bedrock below the basin A in the section T2 shows middle values of chargeability (mp), which may be due to a leachate contamination. In fact in the corresponding ERT section, the bedrock appears less resistive than in the other sections.

Then, it is possible to exclude conductive low-polarizing nuclei as a candidate for leachate cumuli and to establish an alert situation below the basin (A) where middle values of chargeability are associated to a general reduction of resistivity involving the bedrock too.

ERT and IP surveys provided deep information about the waste dumps and soil, but no information about water flux and possible leachate transportation. Then, an SP survey has been carried out in attempt to highlight possible signals related to leachate contamination. Figure 13a and b depicts the SP pattern obtained by a Kriging interpolation of 115 values of self-potential referred to a unique base station.

The SP signal ranges between -42 and 17.2 mV, with a prevalence of negative values of the electrical potential localized within the perimeter of the plant and in the external northwestern portion. On the contrary, positive values occupy an outdoor area located in the southwestern portion of the map.

This distribution of values can be explained by accounting for a combination of mechanisms related to the streaming potential [62–64] and redox reactions [44, 48]. In fact, because of the high natural and artificial altitude gradients, it is reasonable to expect negative values in the top area linked to a stream of water downwards [46] (Fig. 13b).

Anyway the contribution of topographical gradient in terms of streaming potential is not prevalent as the scatterplot of Fig. 13c shows.

Therefore, the contribution related to the redox reactions that occur in the basins can justify, albeit in a qualitative way, the minimum value just in correspondence of these basins, particularly the basin A. The spontaneous potential outside of the basins shows zero values near the southwestern edge of the complex and becomes positive towards SW. On the contrary, northeastern side shows negative values that could be the combined effect of pollutant and streaming potential.

3.3 Understand the Uncertainties, Overcome the Limitations

This chapter has dealt with the description of four electromagnetic sensing techniques, which are ERT, GPR, IP, and SP, and their potentialities in the frame of groundwater quality monitoring.

We described physical concepts and acquisition modalities in order to highlight the uncertainties and limitations of each technique. In fact, the choice of the methods to be applied is strongly influenced by site conditions and type of the target to be characterized [65]. For instance, although there are some attempt in order to apply GPR in shallow waste dump for HDP liner integrity detection [66, 67], this technique was not suitable to the Montegrosso-Pallareta site, due to the clayey nature of the ground, which is absorptive and requires a depth of investigation beyond the capability of the GPR technique.

Once the suitable techniques have been selected, they have to be customized in order to fit the physical features of the target and have to be capable of detecting it. The survey design is the phase where each technique is set in terms of geometry (orientation and length of profiles, 2D or 3D survey), electrode spacing or electromagnetic frequencies and number of measures.

For instance, the electrode spacing and electrode number are two important parameters that influence the answer of the ERT method since they act on the available spatial resolution and the investigation depth. Their effect is well visible in the case of Kablova site by comparing the tomographies ERT1, ERT2, and ERT3 with ERT4. The used electrode spacing played a different role in the case of Montegrosso-Pallareta complex, where the basin thickness resulted lower than the used electrode spatial offset as, in the margin of the waste dumps, basins appeared resistive.

Another important choice is the orientation of the survey lines. It has to be fixed according to the geological, topographical, and hydrogeological conditions of the site. For instance, in the Kablova site, the orientation of the ERT and GPR profiles has been chosen by accounting for the inferred groundwater flux and the logistic conditions. Accordingly, the missing ERT on the south side of the phenol pool was not determinant in the data interpretation.

Moreover, sometimes there are uncertainties related to the physical limits of the used configuration. For instance, in Montegrosso-Pallareta site, the resistive nuclei at basin margins have been interpreted as a change in the properties of the electrode array (i.e., in the k coefficient) due to the HDPE liners.

Sometimes, the incomplete knowledge of the physics at the basis of the investigated phenomenon, such as in the case of the IP and SP techniques, can represent an obstacle. In order to overcome this drawback and reduce the interpretation ambiguities affecting the results of each sensing techniques, the international scientific production in recent years has shown a growing interest in the integrated approach, particularly in Environmental Geophysics, field where physical-chemical and biochemical processes related to pollutant presence have not yet been well understood [47, 48].

In particular, it can be convenient to combine two or more techniques in order to get more accurate and less ambiguous results.

For instance, the combination of ERT and GPR in the Kablova site allowed to determine with more accuracy and confidence the absence of phenols into the ground and groundwater. Moreover, the combination of ERT and IP allowed to distinguish clay nuclei (characterized by low membrane polarization values) from leachate cumuli (showing very high redox polarization values).

Moreover, the characterization of a target according to different physical parameters may be useful to highlight several aspects of the investigated site. In this sense, the use of SP in Montegrosso-Pallareta site allowed to have a spatial map of the possible pollutant reflecting the shallow water transport of contaminants. On the other hand, the results provided by the ERT and IP surveys highlight pollution phenomena at greater depths.

The use of electromagnetic techniques requires knowledge of geological, geophysical, and field experience [65]. In other words, it is important to provide an interpretation of the achieved results that accounts for a priori geological and hydrogeological information. For instance, the presence of clayey formations in the Montegrosso-Pallareta site is the key aspect to understand the contribution of membrane polarization, streaming potential and redox potential in the composition

of the SP signal. In particular, the low contribution of the streaming potential (which in turn is roughly depending on the altitude) inferred by the scatterplot of Fig. 13 is in agreement with limited permeability of clays present in the area.

Sometimes, electromagnetic surveys can detect unexpected situations such as in the case of hydrocarbons contaminated soils that can provide an unexpected lowering of resistivity [5]. These situations reveal that physical-chemical and biological mechanisms occurring in the polluted areas are not yet completely understood. On the other hand, electric and electromagnetic data suggested that contaminant plumes conductivity is depending on the ionic species concentration, which in turn is driven by the groundwater flow [48, 68]. To corroborate this hypothesis, laboratory experiments reproducing on field conditions seem to be a promising tool to improve the knowledge of certain physical mechanisms.

We can conclude that at the present time electromagnetic sensing techniques can be useful tools in order to have a preliminary screening of a possible polluted area. Their proper and rigorous application, taking into account logistic constraints and geological knowledge of the site, allows to detect polluted areas, trace contaminant distribution and infer processes occurring in the surveyed area. Although most phenomena at the bases of gathered signals are not yet well understood, electromagnetic techniques can be very useful in defining direct sampling points and remediation strategies.

Acknowledgments Surveys and results at Kablova site (Serbia-Herzegovina) has been carried out and funded in the Framework Program Agreement Balkans, Line 2.3 P.R.I.M.A.—“Integrated Project: environmental monitoring in areas of high criticality, technical assistance for the formulation of plans and programs for the protection, preservation and improvement of natural resources in polluted sites—subproject CAB Jagodina”.

Moreover, the authors would like to thank the ACTA S.p.A operator of the Montegrosso-Pallareta landfill complex for its support in the implementation of geophysical surveys.

This work is dedicated to the memory of our dear friend and colleague Ivana Adurno whose smile continues to shine in our hearts.

References

1. European Environment Agency (2010) The European environment. State and outlook 2010, Water resources: quantity and flows. Publications Office of the European Union, Copenhagen
2. Agency EE (1999) Groundwater quality and quantity in Europe. Office for Official Publications of the European Communities, Copenhagen
3. Meju M (2002) Environmental geophysics: conceptual models, challenges, and the way forward. *Leading Edge* 21(5):460–464
4. Naudet V, Revil A, Rizzo E, Bottero JY, Begassat P (2004) Groundwater redox conditions and conductivity in a contaminant plume from geoelectrical investigations. *Hydrol Earth Syst Sci* 8(1):8–22
5. Atekwana EA, Sauck WA, Werkema DD Jr (2000) Investigations of geoelectrical signatures at a hydrocarbon contaminated site. *J Appl Geophy* 44:167–180
6. Reynolds JM (1995) An introduction to applied and environmental geophysics. Wiley, Chichester

7. Edwards LS (1977) A modified pseudosection for resistivity and IP. *Geophysics* 42(5): 1020–1036
8. Loke MH (2002) Tutorial: 2-D and 3-D electrical imaging surveys, Copyright 1996–2002, <http://personales.upv.es/jpadin/coursenotes.pdf>
9. Dey A, Morrison HF (1979) Resistivity modelling for arbitrary shaped two-dimensional structures. *Geophys Prospect* 27:1020–1036
10. Dey A, Morrison HF (1979) Resistivity modeling for arbitrarily shaped three-dimensional shaped structures. *Geophysics* 44:753–780
11. Silvester PP, Ferrari RL (1990) Finite elements for electrical engineers, 2nd edn. Cambridge University Press, Cambridge
12. Archie GE (1942) The electrical resistivity log as an aid in determining some reservoir characteristics. *Petroleum Tran AIME* 146:54–62
13. Benson AK (1995) Applications of ground penetrating radar in assessing some geological hazards: examples of groundwater contamination, faults, cavities. *J Appl Geophy* 33:177–193
14. Aristodemou E, Thomas-Betts A (2000) DC resistivity and induced polarization investigation at waste disposal and its environments. *J Appl Geophy* 44:275–302
15. Daniels DJ (2002) Ground penetrating radar. IET, Stevenage Herts
16. Conyers LB, Goodman D (1997) Ground-penetrating radar: an introduction for archaeologists. AltaMira, Walnut Creek
17. Doolittle JA, Collins ME (1995) Use of soil information to determine application of groundpenetrating radar. *J Appl Geophy* 33:101–108
18. Noon DA, Stickley GF, Longstaff D (1998) A frequency-independent characterisation of GPR penetration and resolution performance. *J Appl Geophy* 40:127–137
19. Heritage E (2008) Geophysical surveys in archaeological field evaluation. English Heritage Publishing, Swindon
20. Bavusi M, Giocoli A, Rizzo E, Lapenna V (2009) Geophysical characterisation of Carlo's V Castle (Crotona, Italy). *J Appl Geophy* 67:386–401
21. Loperte A, Satriani A, Bavusi M, Lapenna V, Del Lungo S, Sabelli R, Gizzi FT (2011) Geophysical prospecting in archaeology: investigations in Santa Venera, south suburb of Poseidonia-Paestum, Campania, southern Italy. *J Geophys Eng* 8:S23. doi:10.1088/1742-2132/8/3/S03
22. Chianese D, D'Emilio M, Bavusi M, Lapenna V, Macchiato M (2006) Magnetic and ground probing radar measurements for soil pollution mapping in the industrial area of Val Basento (Basilicata Region, Southern Italy): a case study. *Environ Geol* 49:389–404
23. Loperte A, Bavusi M, Cerverizzo G, Lapenna V, Soldovieri F (2011). Ground penetrating radar in dam monitoring: the test case of Acerenza (Southern Italy). *Intern J Geophys* 2011: 9 Article ID 654194
24. Bavusi M, Soldovieri F, Di Napoli R, Loperte A, Di Cesare A, Ponzo FC, Lapenna C (2011) Ground penetrating radar and microwave tomography 3D applications for the deck evaluation of the Musmeci bridge in Potenza, Italy. *J Geophys Eng* 8:S33–S46, Special issue: “Non-invasive sensing techniques and geophysical methods for cultural heritage and Civil Infrastructures Monitoring”
25. Soldovieri F, Solimene R, Lo Monte L, Bavusi M, Loperte A (2010) Sparse reconstruction from GPR data with applications to rebar detection. *IEEE Trans Inst Meas* 60(3):1070–1079
26. Bavusi M, Bernini R, Lapenna V, Loperte A, Soldovieri F, Ponzo FC, Di Cesare A, Ditommaso R (2012) Electromagnetic sensing techniques for non-destructive diagnosis of civil engineering structures, earthquake-resistant structures – design, assessment and rehabilitation. In: Moustafa A (ed) *InTech*. ISBN: 978-953-51-0123-9, <http://www.intechopen.com/books/earthquake-resistant-structures-design-assessment-and-rehabilitation/electromagnetic-sensing-techniques-for-civil-engineering-structures-non-destructive-diagnostics>
27. Bavusi M, Soldovieri F, Piscitelli S, Loperte A, Vallianatos F, Soupios P (2010) Ground-penetrating radar and microwave tomography to evaluate the crack and joint geometry in

- historical buildings: some examples from Chania, Crete, Greece. *Near Surface Geophys* 8:377–387
28. Bavusi M, Di Napoli R, Soldovieri F (2010) Microwave tomographic approach for masonry investigation: some real results. *Adv Geosci* 24:83–88
 29. Leone G, Soldovieri F (2003) Analysis of the distorted Born approximation for subsurface reconstruction: truncation and uncertainties effect. *IEEE Trans Geosci Remote Sens* 41(1): 66–74
 30. Soldovieri F, Orlando L (2009) Novel tomographic based approach and processing strategies for multi-frequency antennas GPR measurements using multi-frequency antennas. *J Cultural Heritage* 10:e83–e92
 31. Sammis CG, Henyey TL (1987) Geophysics field measurements, part B, vol 24. Academic, Orlando
 32. Reynolds JM (1997) An introduction to applied and environmental geophysics. Wiley, Chichester
 33. Leroux V, Dahlin T (2003) Site conditions requiring extra precaution for induced polarization measurements. In: Proceedings of the 9th meeting environmental and engineering geophysics, Prague, 31 August–4 September 2003, O-052
 34. Leroux V, Dahlin T (2001) IP imaging field tests in southern Sweden. In: Proceedings of the EEGS'01, Birmingham, 2–6 September 2001, ENVM08
 35. Leroux V, Dahlin T (2002) Induced polarisation at waste site in southern Sweden. In: Proceedings of the 8th meeting environmental and engineering geophysics, Aveiro, 8–12 September 2002
 36. Dahlin T, Leroux V, Nissen J (2002) Measuring techniques in induced polarisation imaging. *J Appl Geophys* 50:279–298
 37. Buselli G, Lu K (2001) Groundwater contamination monitoring with multichannel electrical and electromagnetic methods. *J Appl Geophys* 48:11–23
 38. Yuval, Oldenburg DW (1996) DC resistivity and IP methods in acid mine drainage problems: results from the Copper Cliff mine tailings impoundments. *J Appl Geophys* 34(n.3):187–198
 39. Slater LD, Lesmes D (2002) IP interpretation in environmental investigations. *Geophysics* 67:77–88. doi:[10.1190/1.1451353](https://doi.org/10.1190/1.1451353)
 40. Abu-Zeid N, Bianchini G, Santarato G, Vaccaro C (2004) Geochemical characterisation and geophysical mapping of Landfill leachates: the Marozzo canal case study (NE Italy). *Environ Geol* 45:439–447. doi:[10.1007/s00254-003-0895-x](https://doi.org/10.1007/s00254-003-0895-x)
 41. Bavusi M, Rizzo E, Lapenna V (2006) Electromagnetic methods to characterize the Savoia di Lucania waste dump (Southern Italy). *Environ Geol* 51:301–308. doi:[10.1007/s00254-006-0327-9](https://doi.org/10.1007/s00254-006-0327-9)
 42. Sato M, Mooney HM (1960) The electrochemical mechanism of sulfide self-potentials. *Geophysics* 25:226–249
 43. Bernt Lile O (1996) Self potential anomaly over a sulfide conductor tested for use as a current source. *J Appl Geophys* 36:97–104
 44. Nyquist JE, Corry CE (2002) Self-potential: the ugly duckling of environmental geophysics. *Leading Edge* 21(5):446–451
 45. Vichabian Y, Morgan FD (2002) Self potentials in cave detection. *Leading Edge* 21:871–886
 46. Schiavone D, Quarto R (1984) Self potential prospecting in the study of water movements. *Geoexploration* 22:47–58
 47. Revil A, Naudet V, Nouazaret J, Pessel M (2003) Principles of electrography applied to self potential electrokinetic sources and hydrogeological application. *Water Resour Res* 39:1114. doi:[10/109/2001 WR000916](https://doi.org/10/109/2001 WR000916)
 48. Naudet V, Revil A, Rizzo E, Bottero JY, Bégassat P (2004) Groundwater redox conditions and conductivity in a contaminant plume from geoelectrical investigations. *Hydrol Earth Syst Sci* 8(1):8–22. doi:[10.5194/hess-8-8-2004](https://doi.org/10.5194/hess-8-8-2004)

49. Perrone A, Iannuzzi A, Lapenna V, Lorenzo P, Piscitelli S, Rizzo E, Sdao F (2004) High-resolution electrical imaging of the Varco d'Izzo earthflow (southern Italy). *J Appl Geophys* 56:17–29
50. Bogoslovsky VA, Ogilvy AA (1970) Natural potential anomalies as a quantitative index of seepage from water reservoir. *Geophys Prospect* 18(2):261–268
51. Butler DK, Llopis JL (1990) assessment of anomalous seepage conditions. In: *Geotechnical an environmental geophysics*, pp 153–174, eISBN: 978-1-56080-278-5; Print ISBN: 978-0-931830-99-0
52. Hashimoto T, Mogi T, Yasunori N, Ogawa Y, Ujihara N, Oikawa M, Saito M, Nurhasan MS, Wakabayashi T, Yoshimura R, Hurst AW, Utsugi M, Tanaka Y (2004) Self-potential studies in volcanic areas -Rishiri, Kusatsu-Shirane, and White Island. *Geophysics* 12(2):97–113
53. Nishino T, Kainuma N, Matsuyama K, Muraoka A (2000) Self-potential survey in Hachijojima. In: *Proceedings of the world geothermal congress, Kyushu–Tohoku, 28 May–10 June 2000*
54. Christensen TH, Bjerg PL, Banwart SA, Jakobsen R, Heron G, Albrechtsen HJ (2000) Characterization of redox conditions in groundwater contaminant plumes. *J Contam Hydrol* 45:165–241
55. Kjeldsen P, Barlaz MA, Rooker PA, Baun A, Ledin A, Christensen TH (2002) Present and long-term composition of MSW Landfill Leachate: a review. *Critical Rev Environ Sci Tech* 32(4):297–336
56. Selli R (1962) Il Paleogene nel quadro della geologia dell'Italia meridionale. *Mem Soc Geol Ital* 3:737–790
57. Lapenna V, Lorenzo P, Perrone A, Piscitelli S, Sdao F, Rizzo E (2003) High-resolution geoelectrical tomographies in the study of the Giarrossa landslide (Potenza, Basilicata). *Bull Eng Geol Environ* 62(3):259–268
58. Schön JH (1996) *Physical properties of rocks—fundamentals and principles of petrophysics*. Pergamon, Oxford, 583 pp
59. Angoran YE, Fitterman DV, Marshall DJ (1974) Induced polarization: a geophysical method for locating cultural metallic refuse. *Science* 184:1287–1288
60. Iliceto V, Santarato G, Merola R, Ardizzoni F, Finotti F (1994) La polarizzazione indotta nella localizzazione di discariche di rifiuti solidi urbani. *Ingegneria sanitaria ambientale*. Genn.Apr.j:63–72
61. Aristodemu E, Thomas-Betts A (2000) DC resistivity and induced polarization investigations at a waste disposal site and its environments. *J Appl Geophys* 44:275–302
62. Fournier C (1989) Spontaneous potentials and resistivity surveys applied to hydrogeology in a volcanic area: case history of the Chaîne des Puys (Puy-de-Dôme, France). *Geophys Prosp* 1:647–668
63. Birch FS (1998) Imaging the water table by filtering self-potential profiles. *Ground Water* 36:779–782
64. Revil A, Hermitte D, Voltz M, Moussa R, Lacas JG, Bourrié G, Trolard F (2002) Self-potential signals associated with variations of the hydraulic head during an infiltration experiment. *Geophys Res Lett* 29. doi:10.1029/2001 GL014294
65. Hrabar S (1998) Environmental geophysics: what is needed to be successful. *Leading Edge* 17(6):813–839
66. Splajt T, LE Ferrier F (2003) Application of ground penetrating radar in mapping and monitoring landfill sites. *Environ Geol* 44:963–967
67. Dahlin T, Jeppsson H (1995) Geophysical investigations of a waste deposit in southern Sweden. In: Bell RS (ed) *Proceedings of the 8th EEGS symposium on the application of geophysics to engineering and environmental problems, April 23–26, 1995, Orlando*. pp 97–105
68. Karlik G, Ali Kaya M (2001) Investigation of groundwater contamination using electric and electromagnetic methods at an open waste-disposal site: a case study from Isparta, Turkey. *Environ Geol* 40(6):725–731

Pollution Detection by Electromagnetic Induction and Electrical Resistivity Methods: An Introductory Note with Case Studies

Yuri Manstein and Andrea Scozzari

Abstract This chapter introduces the combined usage of electromagnetic induction and electrical resistivity methods for the assessment of soil pollution at shallow depths, with a particular focus on situations of potential contamination of groundwater. After a brief introduction of the electrical resistivity tomography (ERT) and the electromagnetic induction (EMI) techniques, three case studies are presented, dealing with potential threats to groundwater resources, in which the synergic usage of ERT and EMI permitted effective investigations about the contamination status and possible threats.

Keywords Electrical resistivity tomography, Electromagnetic induction, Geophysical surveys

Contents

1	Introduction	226
2	In Situ Methods	227
2.1	Electrical Resistivity Tomography	228
2.2	Electromagnetic Induction Methods	229
2.3	Data Output and Representation	231

Y. Manstein (✉)

Trofimuk Institute of Petroleum Geology and Geophysics, Siberian Branch of Russian Academy of Science, Bld. 3, Koptyuga Street, 630090 Novosibirsk, Russia
e-mail: MansteinYA@ipgg.sbras.ru

A. Scozzari

CNR Institute of Information Science and Technologies (CNR-ISTI), Via Moruzzi 1, 56124 Pisa, Italy
e-mail: a.scozzari@isti.cnr.it

3	Case Studies	231
3.1	Case 1: Belovo	231
3.2	Case 2: Petroleum Contamination	232
3.3	Case 3: Pesticide Contamination	233
4	Conclusions	236
	References	236

Abbreviations

EM	Electromagnetic
EMI	Electromagnetic induction
EMI-F	Electromagnetic induction frequency domain
ERT	Electrical resistivity tomography
GPS	Global positioning system
TEM	Time domain electromagnetic
VES	Vertical electrical sounding

1 Introduction

It is well known that specific electrical resistivity of water (or specific electrical conductivity) depends on its mineralisation, on the presence of suspended particles and of eventual organic compounds. This permits to study the concentration of eventual polluting agents in the water by direct or indirect measurements of specific electrical resistivity.

Shallow earth electromagnetic (EM) survey methods (EM profiling, mapping and sounding) and electrical resistivity tomography (ERT) have increased significantly in the past decades. The pollution of groundwater and surface water can be detected and studied by these methods, by observing the changes of specific electrical resistivity associated with the presence of pollution. The measurement unit of the specific electrical resistivity is Ωm . Its reciprocal value, i.e. the specific electrical conductivity, is measured in S/m (siemens per metre) or mho/m. The electrical conductivity of water is commonly expressed in mS/cm or $\mu\text{S/cm}$.

It is well known that the specific electrical resistivity of the ground depends also on its lithological composition [1]. As a result, pollution of groundwater is usually detectable by measurements of the electrical resistivity of the ground, which is permeated by water, taking into account its lithological characteristics.

The main features characterising the shallow depth earth (i.e. “soil” or “ground”) are:

- Lithological porous skeleton with water of various salinity
- Various particle size distribution (i.e. clay, sand, gravel, rocks) and water content
- Altered levels possibly interbedded to no altered ones
- Pieces of (armoured) concrete, bricks, wood and waste (artificial ground)

- Voids: tunnels, karst, pipes, low-density (excavated) areas, etc.
- Local targets: buried objects and archaeological targets

The main features characterising the bedrock are:

- Presence of flat or inclined stratification
- Discontinuities due to faults, fractures (at large or small scale) or cavities (i.e. karst pits), eventually filled with water and/or clay and sand

The combination of lithological knowledge, hydrological and hydrogeological information and chemical analyses of water (at least the principal anions and cations contributing to its electrical conductivity) is a fundamental aspect for the definition of the observed scenario and its interpretation.

Groundwater is always present in every kind of soil. The presence of water affects the specific electrical resistivity of the soil. The specific resistivity of fresh water is varying between 40 and 150 Ωm , according to the natural mineralisation and temperature. Soluble (ionic) pollutants can change the resistivity drastically, by decreasing the resistivity to the a few Ωm and even lower than 1 Ωm in case of high concentration of sulphates [2]; for example, in a sandy soil, the addition of 25 ppm of ionic species to the groundwater increases ground conductivity by approximately 1 mS/m [3]. In the case of oil and organic pollution, resistivity can be increased by tens of Ωm . Organic contaminants are generally characterised by a high dielectric constant and very low conductivity, thus contributing to increase the ground resistivity, although with a much lower incidence with respect to an equivalent percentage of ionic contaminant. This is mainly due to the fact that most organics are not found in emulsion with water and the stratified pattern alters significantly only the electrical properties of a thin layer, making organics in water still detectable by resistivity measurements but at a lesser degree than ionic compounds.

In general, the contamination of water can be studied by in situ measurements of specific electrical resistivity of the ground by using non-invasive near-surface geophysical methods. The methods and instruments necessary to perform such a study must be sensitive enough, especially in case of organic contamination, to permit a sufficiently low detection threshold for the practical usage.

2 In Situ Methods

The electrical conductivity measurement of groundwater samples, squeezed from soil samples, is a very important reference for in situ surveys. Conductivity measurements in the laboratory are typically performed at a controlled reference temperature, which is usually set at 25°C. The mere measurement of the conductivity of water samples extracted from samples of the investigated soil is a fundamental support to the interpretation of data collected by the non-invasive geophysical campaigns [4].

2.1 Electrical Resistivity Tomography

The electrical resistivity tomography (ERT) method is based on what is considered the oldest geophysical technique: the four-electrode electrical resistivity measurement, so-called electrical resistivity method, developed by Schlumberger brothers in the beginning of the twentieth century [5]. The aim of this section is to illustrate practical arrangements for the execution of geoelectrical measurements according to the ERT technique, while more basic information can be found in the chapter by Bavusi et al. inside this book.

Figure 1 shows a hypothetic electrode arrangement and a simplified representation of the investigated layers. Electrodes A and B (often called *current electrodes*) are connected to a transmitter, which generates a known direct electric current I , while electrodes M and N (*potential electrodes*) are connected to a receiver, which measures the voltage U across the MN pair of electrodes. In order to get information about the soil at different depths, the measurement is repeated ($A'B'$, $A''B''$, etc.) by increasing the depth of the current penetration by broadening the A to B distance (Fig. 1). The apparent electrical resistivity ρ_a can be calculated as

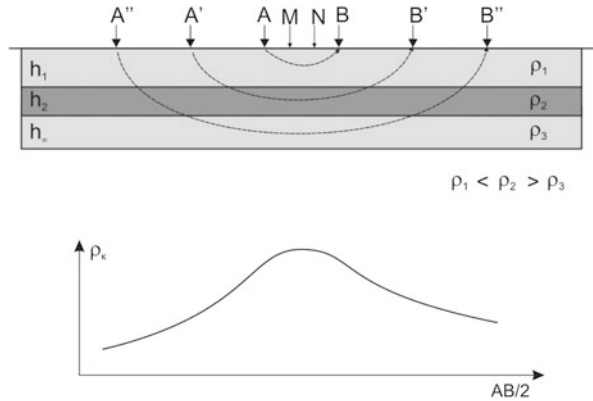
$$\rho_a = K \cdot (U/I)$$

where $K = \frac{2\pi}{\frac{1}{|AM|} + \frac{1}{|BM|} + \frac{1}{|AN|} + \frac{1}{|BN|}}$ is a geometric factor [1] and the square brackets contain distances in meters

At the bottom of Fig. 1, there is the plot of ρ_a vs. $AB/2$, which is known as the *sounding curve* of the VES (vertical electrical sounding). Another embodiment of electrical resistivity method is the electrical profiling. In this case the same arrangement of AMNB electrodes is rigidly shifted along the measurement line. The result in this case is in the form of a diagram (*profiling curve*) of ρ_a vs. the measurement position along the line [6].

During the 1980s new devices for the application of electrical resistivity methods took place. Such devices can connect many (usually 12–50) electrodes, which are typically placed with a regular spacing along the measurement line, for most of the practical arrangements. The layout of an ERT device on the field, thus, consists in a multielectrode configuration where the role of each electrode is determined by an automatic switch. In fact, using an internal automatic switchboard, an electrical resistivity tomography (ERT) device can make hundreds of measurements along one line within few minutes. ERT surveys involve the acquisition of the numerous combinations of four-electrode resistivity measurements that are possible between multiple arrays of electrodes. The configurations may use two surface electrode arrays, one surface and one downhole array (surface to borehole), two downhole electrode arrays (cross-borehole), or even two boreholes and one surface array. This type of survey, referred to as tomography, generates a high-resolution image of the planar surface containing the electrode array [7]. Such data can be also used to build 2D geoelectrical cross sections. With a number of parallel 2D cross sections and/or surface distribution of electrodes, a sort of 3D visualisation can be built. The

Fig. 1 Simplified representation of the investigated layers with hypothetical electrode arrangements. The bottom picture represents a generic sounding curve



electrical resistivity methods are developing for about one century. The measurement speed increased by hundreds of times and the capability of 2D and 3D data representation, aided by fast data inversion systems, permit to build a complete description of subsurface electrical conductivity distribution and visualise the resulting patterns in few hours. However, the further increase of data acquisition speed is limited by the nature of the mechanisms underlying the electrical current flow in geological media, which require proper settling times in order to perform each measurement session correctly.

2.2 Electromagnetic Induction Methods

Electromagnetic methods have a special place in the arsenal of geophysical tools available for environmental investigations in general and groundwater contamination study in particular. They owe their status to a number of factors. First, electromagnetic methods are directly influenced by the electrical properties of the pore fluids. Second, electromagnetic methods are sensitive to changes in geological layers and allow them to be used for geological mapping, which is a very appreciable feature for environmental tasks. Third, there is a wide range of electromagnetic equipment available in the market, in terms of methodology of investigation and different degrees of performance. The equipment is generally user-friendly and operational costs are relatively low. Fourth, electromagnetic survey techniques are non-invasive [8].

There have been a number of notable publications and reviews about electromagnetic methods for general and environmental studies within the past 50 years. The focus and applications of these methods shifted from traditional mineral deposit prospecting to groundwater and, more recently, to more general environmental studies. The interested reader could be addressed to a two-volume set edited by Misac N. Nabighian [9, 10] on applied electromagnetic methods, which covers theory, field methods and data interpretation of the active source electromagnetic

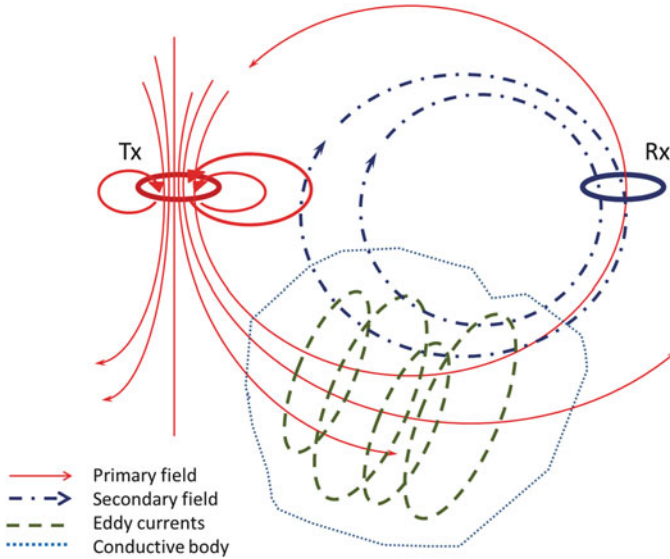


Fig. 2 Simplified sketch of the electromagnetic mechanisms underlying the electromagnetic induction methods

techniques, such as the one discussed here. Several chapters concerning environmental problems are found in Volume 1 [9]. Volume 2 [10] gives more practical results than can be directly applied to environmental studies.

The electromagnetic induction methods (EMI) are based on the physical phenomena of induction. The principles of the method are illustrated by the sketch shown in Fig. 2. Since the soil is electrically conductive (at different degrees, as discussed in the previous section), it is always possible to induce an electromagnetic (secondary) field in it, by placing the electromagnetic transmitter (Tx) of the primary electromagnetic field near the ground. The primary field induces an Eddy current, which in turn produces the secondary field. Then, the secondary field can be measured by an electric and/or magnetic receiver (Rx) at the surface. The sounding factors in EMI methods are (1) the spacing between transmitter and receiver, (2) the duration of signal recording after the cut-off of the transmitting signal (time domain), and (3) the transmitting signal frequency (frequency domain). Deeper discussion of these aspects can be found in Balkov et al. [11].

EMI devices characterised by various configurations of transmitter(s) and receiver(s), working in time domain (TEM) or in frequency domain (EMI-F) modes, are forming a large array of devices that are produced worldwide and are intended to explore the Earth from the first metres to the deep mantle [12]. In particular, the EMI-F devices for near-surface exploration are widely used for environmental studies and water pollution exploration. Some examples of successful TEM application for water pollution exploration are also known [3].

2.3 Data Output and Representation

The methodology of near-surface ERT and EM induction surveys includes linear and areal exploration approaches. The first approach gives vertical cross sections (ERT and EM sounding) and linear diagrams (EM profiling). Instead, the areal exploration results can be presented as maps and 3D pictures. An EM shallow depth instrument usually can be used by one operator, while an ERT crew should include three to five persons. Survey speed can reach up to 10 km of linear survey per day. It is very important to bind the measurement points (stations) to the map of the area explored, because precise geo-referencing is a necessary requirement for a proper interpretation of the results.

3 Case Studies

This section presents an overview of case studies in which an electrical resistivity survey was used for groundwater contamination study and assessment, by combination of EMI and ERT techniques.

3.1 Case 1: Belovo

The acid drainage from an abandoned zinc factory is leaking to a nearby swamp, producing a remarkable environmental problem. The drainage consists of a mixture of copper, silver and other water-soluble sulphates. The polluted area was studied first by EMI mapping. The obtained map of the polluted area is shown in Fig. 3. An electrical resistivity tomography made along the red dotted line (see Fig. 4) gives the cross section shown in Fig. 4. Field works were performed in the winter time and took a total time of 3 h. The observable pattern in Fig. 4 suggests a particular interpretation of this cross section, i.e. not only the swamp contains highly mineralised water characterised by low resistivity, but contamination also reaches a groundwater layer below the swamp bottom.

By combination of the information provided by EMI mapping and by ERT profiling, an evaluation of the contaminated volume of water can be done. In fact, the area of contamination can be assessed by EMI mapping, while a cross section with an indication of the contaminated water depth is given by the ERT measurement. The concentrations of the various metals dissolved in water, determined by analytical measurements, enable also the further calculation of the volumetric contribution of each metal.

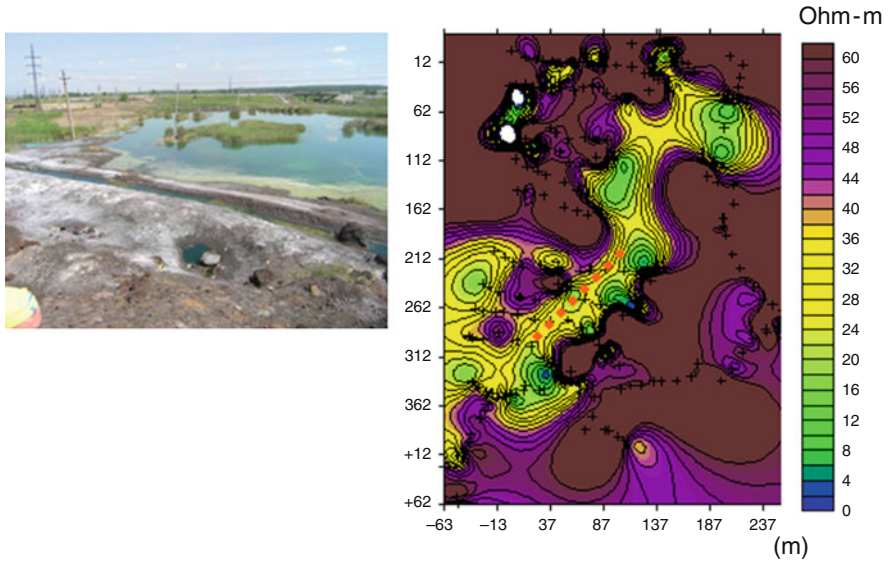


Fig. 3 Map of the polluted area made by the electromagnetic induction method (Belovo site). The left picture shows a view of the site

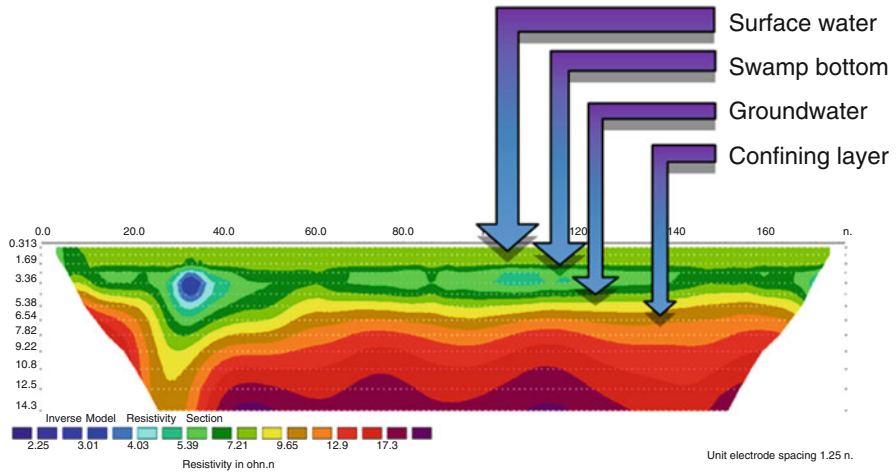


Fig. 4 ERT cross section made along the dotted line shown in Fig. 3 (Belovo site)

3.2 Case 2: Petroleum Contamination

The land along an oil pipeline can be monitored periodically by using EMI devices, in order to check possible minor leakages of oil. The result of one of such studies is presented in Fig. 5. Data representation is in the form of a cross section of

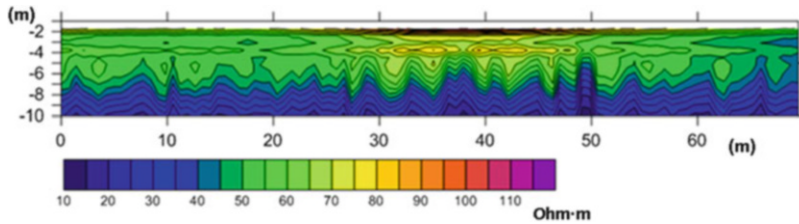


Fig. 5 Cross section of a resistivity measurement obtained with an EMI multifrequency instrument

pseudoresistivity, obtained by an EMI multifrequency instrument after reconstruction algorithms [11, 13].

Regular measurement surveys are performed by the security department of the pipeline service company, which is using the instrument since more than 5 years at the time of writing this chapter, mainly for surveillance purposes, such as the detection of leakages and of illegal connections to the pipe.

By observing Fig. 5, it is apparent how the natural horizontal layering of the cross section is disturbed by a resistive anomaly approximately 20 m long (see the pattern between 27th and 47th m, about 4 m deep). The excavation work done in the area following this survey showed an actual soil contamination with oil. Duration of the field work for the line shown has been approximately 3 min, proving the high effectiveness of this technique.

3.3 Case 3: Pesticide Contamination

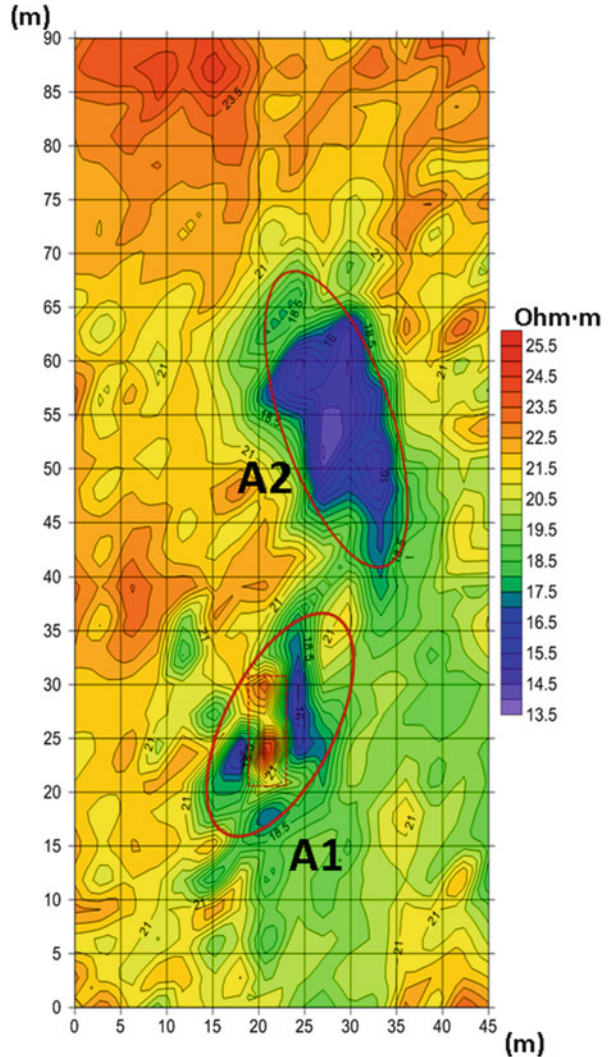
This experience regards a contaminated site, where in the late 1980s a quantity of expired pesticides were buried in a 5 m-deep pit, covered by loamy soil and a concrete covering over a portion about 4×10 m. The total weight of the buried pesticides was about 5 t and the total size of the investigated area was 90×45 m.

The area of the pit was firstly studied by EMI mapping with a 3×3 m grid, followed by ERT and EMI with a thinner grid in specific portions. Field activities took one working day.

The map of electrical resistivity is shown in Fig. 6. The red dotted rectangle shows the location of the concrete covering of the pit. Average resistivity outside of the pit is $18\text{--}22 \Omega\text{m}$. Two areas of decreased resistivity can be noted: the first one is around the pit (A1) and the second one about 10 m to the north (A2). The anomalous areas are shown with red ovals.

After individuation of the areas containing detectable anomalies, a detailed study was performed by EMI mapping with a thinner grid (1×1 m) and by parallel ERT lines. A 3D representation of data, which permits an easy identification of anomalies, is shown in Fig. 7. The subpanels of Fig. 7 show the 3D results from three different viewpoints.

Fig. 6 Map of electrical resistivity (pesticide contamination study)



Two soil samples were taken inside the A1 and A2 areas, respectively. Laboratory analysis showed that the content of pesticides was 1,000 times higher than regulatory limits at A1 and an additional ten times higher than regulatory limits at the A2 area.

One geoelectrical cross section across both A1 and A2 areas shows that deeper than the anomalous volumes there is a more resistive layer, the upper boundary of which is shown as a red line in Fig. 8. Most probably it is a layer with less content of clay consisting in a more sandy soil, compared to the upper layer. In case of infiltration down to this presumably more permeable layer, the overall contamination can easily go further the confined volumes.

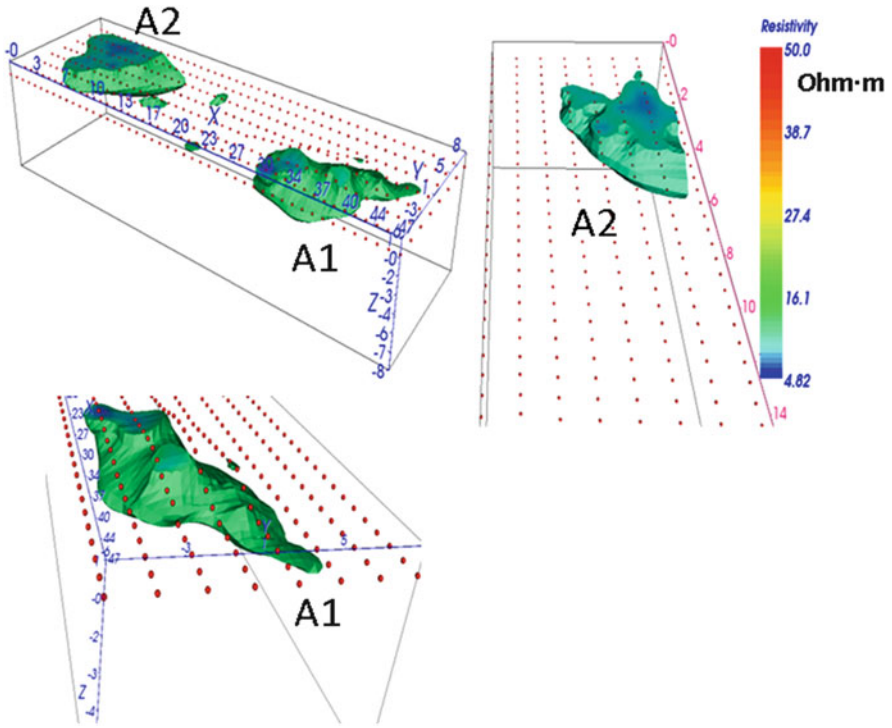


Fig. 7 3D representation of EMI data (pesticide contamination study)

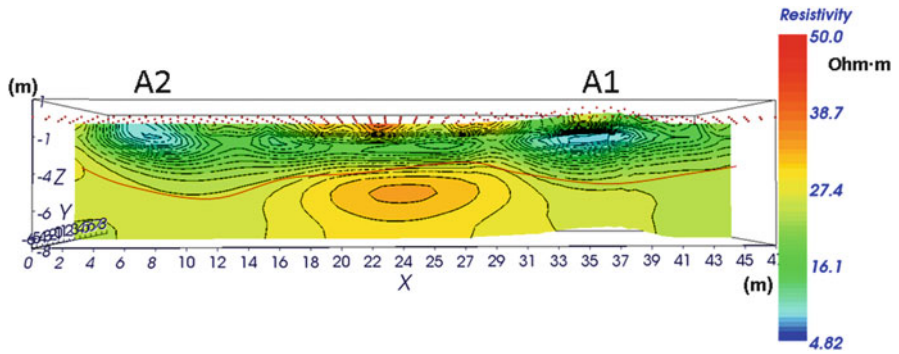


Fig. 8 ERT cross section across A1 and A2 areas (pesticide contamination study)

4 Conclusions

Electromagnetic induction and electrical resistivity surveys are very fast and effective techniques for soil and water contamination studies and are also useful tools for the assessment of environmental risks, particularly concerning the threats to groundwater resources.

The current state of the art of ERT and EMI measurement techniques, with the aid of adequate data analysis and interpretation tools, reached a sufficient degree of maturity for a cost-effective pollution risk management.

Nowadays, the most important action finalised to improve the effectiveness of such investigation techniques is the dissemination of best practice cases between water protection bodies, administrations and other stakeholders, focused on the management of risks about the pollution of water and environmental risks in general. This chapter aims at giving a useful contribution also to those who are not necessarily familiar with geophysical methods, but who may be directly or indirectly users of the geophysical techniques discussed, in the framework of groundwater contamination studies.

References

1. Roy A, Apparao A (1971) Depth of investigation in direct current methods. *Geophys Prospect* 36:943–959
2. Bortnikova SB, Manstein YA et al (2011) Acid mine drainage migration of belovo zinc plant (South Siberia, Russia): a multidisciplinary study. *Water Security in the Mediterranean Region. NATO Science for Peace and Security Series C: Environmental Security*, pp 191–208
3. Wightman WE, Jalinoos F, Sirls P, Hanna K (2003) Application of geophysical methods to highway related problems. Federal Highway Administration, Central Federal Lands Highway Division, Lakewood, CO, Publication No. FHWA-IF-04-021
4. Pozdnyakov AI, Pozdnyakova LA, Pozdnyakova AD (1996) Stationary electrical fields in soils. KMK Scientific Press, Moscow (In Russian)
5. Schlumberger C, Schlumberger M (1932) Depth of exploration attainable by potential methods of electrical exploration. *Geophys Prospect* 97:127–133
6. Manstein AK (2004) Near surface geophysics. Novosibirsk State University Publishing, Novosibirsk (in Russian)
7. Zonge K, Wynn J, Urquhart S (2013) Resistivity, induced polarization, and complex resistivity. In: Butler DK (ed) *Near surface geophysics. SEG*, pp 265–266
8. Fitterman D V, Labson VF (2013) Electromagnetic induction methods for environmental problems. In: Butler DK (ed) *SEG investigations in geophysics series; no. 13. SEG*, pp 301–302
9. Nabighian MN (1988) *Electromagnetic methods in applied geophysics, vol 1. SEG*
10. Nabighian MN (1991) *Electromagnetic methods in applied geophysics, vol 2. SEG*
11. Balkov EV, Epov MI, Manstein AK, Manstein YA (2006) Electromagnetic induction frequency sounding: estimation of penetration depth. *Extended abstracts book of Near Surface 2006 conference, vol 4*

12. Manstein Yu, Manstein A, Santarato G et al (2003) 2003 EGU conference. Multi-frequency electromagnetic sounding tool ems. prototype 3. comparison with commercial devices. Abstracts book, EGU conference
13. Balkov EV, Epov MI, Manstein AK, and Manstein YA (2004) Elements of calibration and data interpretation of EMI sounding device EMS. Extended abstracts book of Near Surface 2004 conference (EAGE), vol 4

The Combination of Geoelectrical Measurements and Hydro-Geochemical Studies for the Evaluation of Groundwater Pollution in Mining Tailings Areas

Svetlana Bortnikova, Nataliya Yurkevich, Elisaveta Bessonova,
Yury Karin, and Olga Saeva

Abstract Sulfide-bearing mill wastes of the Salair Ore Processing Plant situated in the Kemerovo region (Russia) were investigated in the time period 1999–2011. Multipurpose studies of the Talmovskie mining tailings allowed the determination of the composition of the wastes, the acid mine drainages, and the affected groundwater. Geophysical sounding techniques (frequency sounding and electrical tomography) were used to trace the geoelectric zoning of the wastes, expressed as a consistent change of the electrical resistivity specific electrical resistance (SER) from zone to zone. Layers with low resistivity indicate areas with pore spaces filled by highly mineralized solutions. These layers extend to depths of 4–5 m, indicating the penetration of toxicants into the groundwater horizon. The pollution of groundwater was confirmed by chemical analysis, according to which the concentrations of Zn, Pb, and Cd in water samples from the wells are two to three orders of magnitude higher than the maximum permissible concentration (MPC). The authors provide an attempt to identify the correlation and quantitative relationships between SER and the total amount of various metal species present in the wastes and water extracts. The proposed approach permitted to estimate the amount of accumulated tailings, in order to predict changes in the total concentrations of Mn, Al, Fe, Cu, Zn, Cd, and Pb in waste and water extracts to a depth of 30 m.

Keywords Acid mine drainage, Geoelectrical zoning, Groundwater pollution, Metals, Sulfide-bearing wastes

S. Bortnikova (✉), N. Yurkevich, Y. Karin, and O. Saeva
Trofimuk Institute of Petroleum Geology and Geophysics, Siberian Branch of
Russian Academy of Science (SB RAS), Novosibirsk, Russia
e-mail: BortnikovaSB@ipgg.nsc.ru

E. Bessonova
Sobolev Institute of Geology and Mineralogy, Siberian Branch of Russian Academy
of Science (SB RAS), Novosibirsk, Russia

Contents

1	Introduction	240
2	Study Object	241
3	Methodology	243
4	Results and Discussion	244
4.1	Mineral Composition of Wastes	244
4.2	Geochemistry of the Tailings	245
4.3	Geophysical Data	250
4.4	Pore- and Groundwater Composition	252
5	Conclusions	255
	References	255

Abbreviations

EFS	Electromagnetic frequency sounding
ET	Electrical tomography
ICP-MS	Mass spectrometry with inductively coupled plasma
MPC	Maximum permissible concentration
SB RAS	Siberian branch of Russian academy of sciences
SEM	Scanning electron microscope
SER	Specific electrical resistance
SER _{fs}	Specific electric resistivity of the wastes according to frequency sounding
SER _p	Specific electrical resistance measured by direct conductometry in the pastes
SOPP	Salair ore processing plant
XRD	X-ray diffraction analysis
XRF SR	X-ray fluorescence with synchrotron radiation

1 Introduction

Mining activity entails the accumulation of sulfide-bearing mill wastes with high concentrations of ore and impurity elements. Hundreds of thousands of tons of waste and mined ores with Fe, Cu, Zn, Cd, and impurities (As, Sb) lower than the industry level have been dumped in tailings and discharged spontaneously in river beds for decades. Oxidation of the sulfide minerals results in the formation of acidic solutions with high concentrations of SO_4^{2-} , Cu, Zn, Fe, As, Sb, and other soluble species. These elements migrate out of tailing dumps with drainage streams, are discharged into rivers, seep into groundwater, and are carried for tens of kilometers by wind [1–5]. Examples of such aggressive waste deposits and clinkers are the clinkers of the Belovo zinc processing plant, the cyanidation cakes of the Berikul and Komsomolsk ore-bearing plants (Kemerovo region), and the tailings of the Karabash copper smelting plant [6, 7]. As a consequence, zones of geochemical anomalies have formed in the vicinity of stored wastes. These areas are characterized by extremely high concentrations of Fe, Cu, Zn, Cd, Pb, As, and Sb

in surface and groundwaters, soils, snow and air compared with the background and with the MPC levels [8–12].

The main monitoring methods of mine tailings and polluted groundwaters consist in geochemical analyses, which include a series of activities, i.e. sample preparation, field and laboratory measurements of physical parameters, element and mineral composition, thermodynamic modeling for the species calculation, and interpretation of the actual data. Traditional geochemical approaches require significant investments of time and money and often do not allow the selection of optimum sampling sites. Vertical electrical sounding allows outlining the mine tailing dump location, detecting the depth of the waste and the penetration area of highly mineralized fluids into groundwater, calculating the resources of valuable components in technogenic deposits and, with the appropriate technology, assessing the feasibility of re-extraction [13–15]. It is also true that site-specific chemical characterisation is in any case necessary in order to calibrate the electromagnetic sounding results. In this context, geoelectric measurements are primarily used to address the choice of sampling points. So, the combination of the geochemical and geophysical techniques can be seen in terms of optimization of the direct chemical measurements.

The specific features of the studied wastes are the multicomponent composition and heterogeneity of the tailings. Because the geoelectrical properties of wastes are determined by their mineral composition, moisture content, porosity, particle size, and pore water mineralization [16], the investigation of mine tailings using geophysical methods is a complex task.

The aim of this work is to estimate the groundwater pollution caused by mining activity using a complex geochemical and geophysical methodology, tested on the wastes of the Salair Ore Processing Plant (SOPP, Kemerovo region, Russia). The authors used electric prospecting to define areas with the lowest resistivities (ρ) at depths of 0–40 m. These conductive zones were sampled for the waste and pore water composition in a range of depths 0–3 m. Groundwaters within the vicinity of the tailings were also collected. The physical properties, resistivity, and chemical composition of the waste samples, the element concentrations and their species in the pore and groundwaters were measured. The constraint equations were calculated to define the relationships among the resistivity, particle size, humidity, and chemical (elemental) composition of the sampled solids and solutions. These equations allowed the estimation of groundwater pollution. On the base of complex geochemical and geophysical investigations, we determined the penetration of highly mineralized solutions into groundwater.

2 Study Object

The Talmovskie tailings impoundment is located in the town of Salair, in the Kemerovo region of southwestern Siberia (Fig. 1). The Salair mine has been working since the 1930s, and gold- and silver-bearing barite-polymetallic sulfide

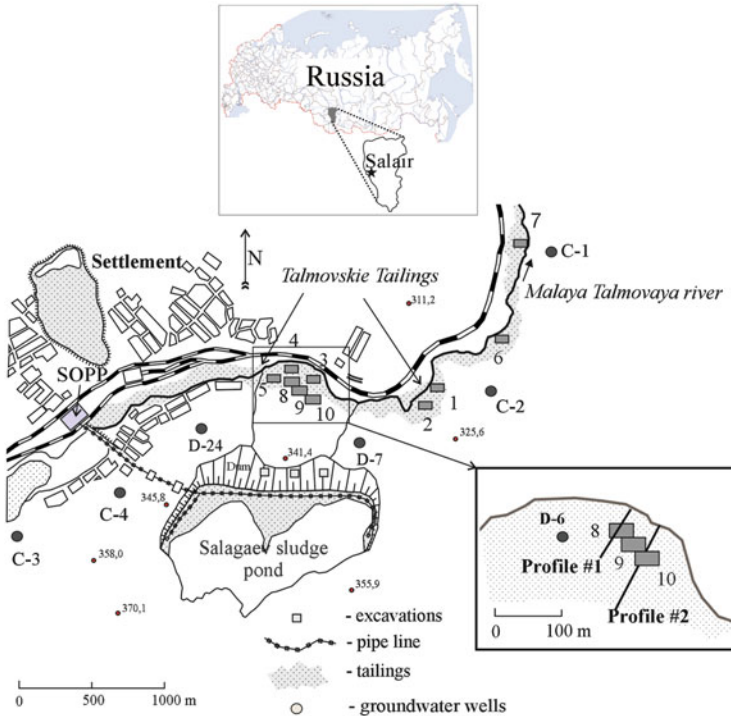


Fig. 1 Schematic map of the study area with the geophysical profiles

ore bodies have been exploited. The sulfides are located within the subvolcanic series of dacite porphyries among Lower Cambrian limestones. The geological structure, mineralogy, and geochemical characteristics have been studied previously by numerous Siberian geologists. The Talmovskie tailings dump is the first tailing dump of the Salair Ore Processing Plant. Ore recovery was first performed at a gold-extracting plant, where quartz-barite ores from open pits in the oxidation zone were processed. Sulfide-bearing mill wastes were stored in the dammed stream of the Small Talmovaya River in 1932–1942 as a belt with a width of 30 m and a length of 8 km (Fig. 1). The thickness of the tailings does not exceed 3 m. Approximately 1 million tons of wastes have been accumulated in the channel of the Malaya Talmovaya river in close proximity to the town of Salair during the last 10 years. The stored waste is bulked by soil on the surface. The storage is dried during the summer and covered by water during floods. The M. Talmovaya River flows on the surface of the tailings impoundment. The described conditions support the intensive transformation of the sulfide-bearing wastes due to oxidation by atmospheric and water oxygen, and there is intensive removal of the dissolved metals in the river network and groundwaters [7]. Pyrite is the most common (75–90% of the total sulfide) of the sulfide minerals in the wastes. Less common are sphalerite (8–19%), galena (2–14%), and single grains of chalcopyrite [6].

3 Methodology

The methods include sampling, analyses of the bulk chemicals and the elemental and mineral composition, determination of the petro-physical properties, geophysical sounding of the wastes, statistical methods of data processing, calculations of the numerical relationships between resistivity and chemical composition, solution of the inverse problem (i.e., estimation of the chemical composition of the waste down to a depth of 40 m by combining the geophysical survey with geochemical measurements), and prediction of the groundwater pollution.

All works were performed in the following order:

- Electrical tomography and electromagnetic frequency sounding [16] for the construction of the storage sections on the two co-directional profiles (Fig. 1) and for revealing the geoelectric zoning in the subsurface environment. The length of profile no. 1 for electromagnetic frequency sounding is 45 m and the maximum probing depth is 8 m; the length of profile no. 2 for electro-tomography is 150 m, the distance between the electrodes is 5 m. The electro-tomographic method (profile no. 2) allowed us to reveal the geoelectric zoning in the subsurface environment at a depth from 0 to 30 m. Electromagnetic frequency sounding (profile no. 1) was used to clarify the geoelectric structure of the wastes in the upper 8 m.
- Sampling of pits in areas with the lowest resistivities to a depth of 1.6 m. Detailed sampling of the area included the collection of surface and subsurface material and pore water within the tailings, which was conducted in 2004–2011. The samples were collected, and measurements were made, in order to reveal the geochemical behavior of the elements during storage and, in particular, to determine the relative mobility of the metals (Zn, Cu, Pb, Cd, and Fe) under storage conditions. The study location and sample sites are shown in Fig. 1. Tailings were excavated in order to reveal vertical sections of the waste and were sampled in detail. Excavations were made using a shovel to dig through the tailings, in order to get a detailed record of layering in the different parts of the impoundment. Each pit extended to the bottom of the tailings. Samples were collected from each distinctive layer that was visually consistent for a thickness of more than 10 cm. The collected samples were placed in polyethylene bags. The stratigraphy of the tailings was constructed from exposures in the pits and was used to study the vertical zoning.
- Preparation of the pastes and pore waters; pH, Eh, and conductivity measurements; and transportation to the laboratory.

The pastes were prepared by mixing the sampled wastes and distilled water (1:2 by volume). We used distilled water (pH 5.6) to simulate the interaction between atmospheric precipitation and sulfide wastes with the AMD formation. The pH and Eh values of the pastes allow us to predict the acid production potential of the wastes and correct the selection of sampling points for further chemical analysis.

Pore water was squeezed from the samples for only the moist silty layers at each site. These samples were subjected to a pressure of 100 Pa using a sampling press, and the released water was filtered through 0.45- μm Millipore filters. A fraction of each water sample was immediately acidified in the laboratory to $\text{pH} < 2$ with concentrated HNO_3 acid to analyze the cation and trace element concentrations. The pH values were measured in the field using the “Anion 410B” instrument (Infraspac-Analyt Company). Solid samples were dried and later used for the water extraction tests in the laboratory and the elemental analyses.

- X-ray fluorescence with synchrotron radiation (XRF SR) was used to determine elemental composition (Si, Ti, Al, Fe, Mn, Ca, Mg, K, Na, Ba, Cu, Zn, Cd, Pb, As, Sb) at the VEPP-3 station at the Institute of Nuclear Physics SB RAS, Novosibirsk [17].
- Preparation of the aqueous extracts at a water:waste ratio of 8:1 (by mass). Measuring pH and Eh by potentiometry and conductivity by conductometry. Determination of the anion (Cl^- , HCO_3^- , SO_4^{2-}) concentrations using the titrimetric and turbidimetric methods and determination of the concentrations of the elements Ca, Mg, K, Na, Al, Mn, Fe, Cu, Zn, Cd, Ni, Co, Pb, As, and Sb by mass spectrometry with inductively coupled plasma (ICP-MS) in the water samples.
- The element and mineral compositions of the wastes were analyzed using a Jeol JSM-638OLA scanning electron microscope (SEM) and by X-ray diffraction analysis (XRD).
- Determination of the resistivity, particle size distribution, density, porosity, and moisture content in the solid samples.

The accuracy and precision of these methods were estimated to be 10–15% or better.

4 Results and Discussion

4.1 Mineral Composition of Wastes

4.1.1 Initial Minerals

The mineralogy of the investigated samples from the Talmovskie tailings is determined by the Salair ore composition and secondary alteration of the initial sulfides. The sulfide content reaches 5–7%, and the primary mineral is pyrite. The sulfides of Pb, Zn, and Cu are represented by small monomineral grains of galena (2–14%), sphalerite (8–19%), and trace amounts of chalcopyrite, tennantite, and tetrahedrite. Secondary rims on the surfaces of the sulfide grains mask the characteristic features of sulfides and prevent a more accurate estimation of the amount of a mineral. The remainder of the mass includes debris from host rocks

of different compositions (quartzites, limestones, and quartz-sericite schists) and mineral grains (quartz, calcite, dolomite, barite, and muscovite).

4.1.2 Secondary Minerals

Amorphous Fe-hydroxides cover grains of pyrite, sphalerite, and chalcopyrite in the form of incrustations, rims, and films. As a rule, the amount of hydroxide increases in micro-layers containing a high percentage of sulfides and a medium coarse-grained texture, which allows the penetration of oxygen.

Amorphous silica was recorded by X-ray methods in efflorescences on the surface of the tailings. Gypsum is the most abundant secondary mineral, and it often cements a tailing bulk mass. Two different morphological forms of gypsum are observed. The first form is well-crystallized grains of “dovetail” with a size up to 1 mm. The second form is fine-grained semi-transparent gray aggregates, which can be identified by the X-ray method. Jarosite forms thin, loose rims, and porous reddish aggregates on oxidized sulfide grains. Rozenite was discovered on the tailings’ surface as intergrowth with other secondary sulfates. Anglesite forms rims and incrustation. An investigation with the help of a scanning microscope shows phosphorous and chlorine in the composition of these rims; consequently, we can conclude the occurrence of pyromorphite, i.e. chlorophosphanet of lead $Pb_5Cl(PO_4)_3$. Sulfates of Zn form efflorescences on the tailing surface and on pit walls. The amount of secondary minerals gives evidence of an active process of oxidation and the alteration of the tailings.

4.2 Geochemistry of the Tailings

4.2.1 Bulk Chemical Composition of the Tailings

The statistical summary of the chemical composition of the tailing samples presented in Table 1 shows that the bulk composition varies over a wide range. Thereinafter the average (mean) value is symbolized by μ , the standard deviation by s , and the number of analyses by n . The major component is silica ($\mu = 53$ wt% of SiO_2 , $s = 11\%$). The next most abundant elements are Ba ($\mu = 21.22$ wt% of $BaSO_4$, $s = 10.3$) and Al ($\mu = 10.63$ wt% of Al_2O_3 , $s = 3.0$).

The concentrations of these components are consistent with the mineral composition of the barite-polymetallic ore bodies observed with the debris of the host rocks.

The contents of valuable components and their amounts are presented in Table 2 along with their concentrations in the ores, which were processed at the Salair plant until recent times. At the beginning of the deposit’s exploitation, the contents of nonferrous and precious metals in ores were several times higher than at present. Correspondingly, losses during the processing of ores were much

Table 1 Bulk chemical composition of the tailings (wt% of dry matter) ($n = 22$)

	SiO ₂	TiO ₂	Al ₂ O ₃	Fe ₂ O ₃	MnO	MgO	CaO	Na ₂ O	K ₂ O	P ₂ O ₅	Ba	H ₂ O
μ	53.0	0.39	10.63	5.31	0.14	1.61	3.01	0.90	0.87	0.19	12.48	5.84
Min	27.35	0.19	4.59	2.50	0.035	0.71	0.79	dl	0.13	0.12	0.43	2.35
Max	66.78	0.95	15.66	11.04	0.25	2.76	6.79	2.63	1.88	0.32	18.35	10.88
s	10.53	0.27	3.0	2.12	0.06	0.65	1.84	0.71	0.57	0.05	6.09	2.34

Table 2 Total concentration of metals in tailings

	Zn	Pb	Cu	Cd	Fe
μ	1.05	3,100	870	45	3.6
Min	0.115	65	160	5	2.2
Max	2.4	7,990	3,420	240	7.6
s	0.51	2,290	620	34	1.6
Salair ore ^a					
Primary	2.30	3,200	800	10	3.2
Oxidized	0.32	4,300	670	6	3.8

Zn in wt%, other metals in ppm ($n = 60$)

^aArchive data

higher in absolute magnitude than at present, resulting in considerable concentrations of useful components in the tailings, sometimes exceeding even their contents in the ores.

The differences in the metal concentrations throughout the tailing impoundments are not large (Table 2), but we detected a significant difference in the concentration range along vertical cross-sections. In the comparatively “young” part of the impoundment (cross-section nos. 7 and 1, Fig. 1), the max/min is 6–8 times (the highest range was measured for Cd); in the “oldest” parts (cross-section nos. 3 and 5, Fig. 1), the ratio reaches 180 (Table 3). This sharp increase of the ratio is an evidence of a more active metal redistribution in the old parts of the impoundments compared with the newer sections, which is found even after 70 years of age.

In the cross-section no. 7, which is located in the least altered (newest) part of the impoundment, the total metals are distributed quite uniformly. The distinctive feature of this particular cross-section structure is the presence of the concentrated layer SP-7/2 at a depth of 15–25 cm (Fig. 2). The layer consists of clay minerals and retains water migrated from the surface. As a result, the geochemical barrier described as “hardpan” [20] formed here. The hardpan is composed of secondary minerals and phases formed in the pore space and of cemented initial minerals. The water-soluble phases of the metals were precipitated on this layer, and the percentages of water-soluble Zn, Cu, and Cd are as high as 25% of their total concentrations (Table 4). In addition, clay minerals caused protonization. This process was identified during water extraction from samples of this layer (Fig. 2). After 15 min, the pH value of the extracted water decreased to 2.59, implying an acid media during the secondary mineral formation.

The second hardpan (less-pronounced) is located in cross-section no. 7 at a groundwater level of ~180–210 cm (layers SP-7/8a and 7/9). In this level,

Table 3 Concentration of metals in particular cross-sections of the tailings

	Zn (%)	Pb (%)	Cu (ppm)	Cd (ppm)
Vertical section no. 7 (<i>n</i> = 14)				
μ	1.4	0.11	620	41
Min	0.36	0.016	220	9.4
Max	2.4	0.45	1,200	78
<i>s</i>	0.55	0.11	250	20
max/min	6.7	28	5.5	8.3
Vertical section no. 1 (<i>n</i> = 15)				
μ	1.1	0.46	900	51
Min	0.54	0.21	340	20
Max	1.7	0.79	1,300	69
<i>s</i>	0.35	0.20	300	15
max/min	3.1	3.7	3.8	3.4
Vertical section no. 3 (<i>n</i> = 10)				
μ	1.1	0.56	1,500	58
min	0.60	0.27	470	22
max	1.4	0.80	3,040	240
<i>s</i>	0.30	0.17	730	64
max/min	2.3	3.0	6.5	11
Vertical section no. 5 (<i>n</i> = 18)				
μ	1.2	0.20	930	43
min	0.058	0.065	42	1.3
max	1.96	0.41	3,400	240
<i>s</i>	0.52	0.12	730	30
max/min	34	64	81	180

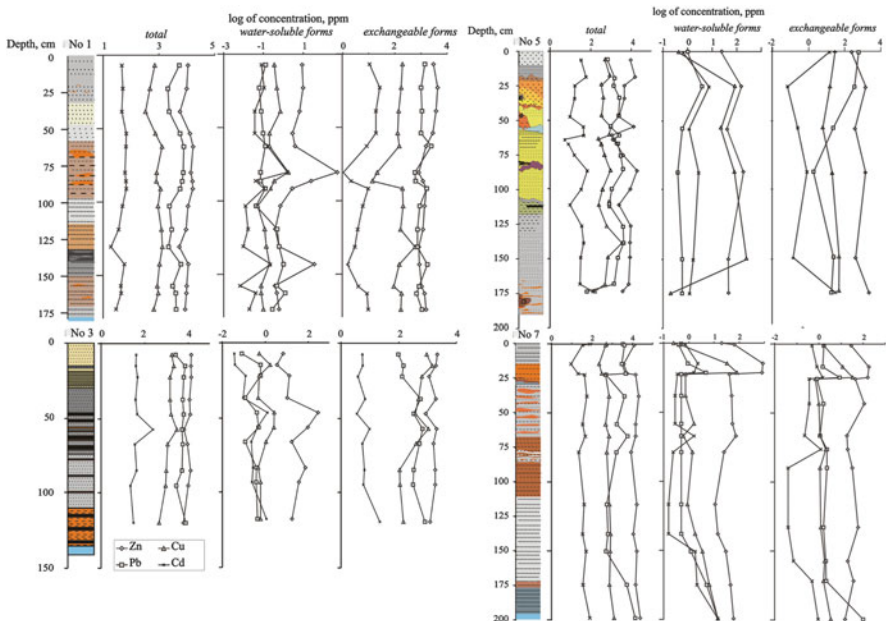


Fig. 2 Vertical sections showing layering patterns and total concentrations of water-soluble and exchangeable elements in the tailings

Table 4 Percentage of water-soluble metals in layers of vertical sections

Sample	Depth (cm)	% of water-soluble species				pH
		Zn	Pb	Cu	Cd	
Vertical section no. 7						
SP-7/1	1	0.54	0.031	0.1	2.2	6.68
SP-7/2	15	24	0.092	15	24	2.86
SP-7/2a	22	15	0.32	27	8	2.80
SP-7/3	23	0.29	0.31	0.16	0.86	6.85
SP-7/4	39	0.25	0.038	0.11	0.52	6.35
SP-7/4a	60	0.39	0.089	0.35	0.85	6.39
SP-7/5	69	0.53	0.026	0.086	3.5	6.48
SP-7/5a	81	0.30	0.093	0.26	1.1	6.17
SP-7/6	120	0.069	0.28	0.12	0.40	6.18
SP-7/7	142	0.13	0.25	0.21	0.47	6.34
SP-7/8	155	0.19	0.75	0.45	3.6	6.15
SP-7/8a	180	0.32	0.3	0.88	5.8	5.77
SP-7/9	205	3.7	0.58	4.50	2.8	4.86

Table 5 Percentage of water-soluble metals in layers of vertical sections

Sample	Depth (cm)	% of water-soluble species				pH
		Zn	Pb	Cu	Cd	
Vertical section no. 1						
SP-1/1	7	0.080	0.0024	0.049	0.17	8.07
SP-1/2	23	0.097	0.0028	0.096	0.20	8.06
SP-1/3	39	0.11	0.0032	0.21	0.075	8.05
SP-1/4	54	0.022	0.0017	0.026	0.052	8.14
SP-1/5a	63	0.023	0.0016	0.015	0.24	8.13
SP-1/5b	81	3.7	0.00094	0.21	2.6	5.47
SP-1/5B	87	0.15	0.0010	0.042	0.060	7.19
SP-1/5r	92	0.017	0.0022	0.020	0.15	8.07
SP-1/6a	104	0.0064	0.0018	0.0053	0.025	7.98
SP-1/6b	120	0.0042	0.017	0.0092	0.046	8.21
SP-1/6B	132	0.011	0.027	0.010	0.048	7.92
SP-1/7	144	0.31	0.016	0.019	0.40	7.65
SP-1/8a	159	0.0038	0.015	0.0084	0.014	8.26
SP-1/8b	164	0.0047	0.030	0.00785	0.089	8.16
SP-1/9	175	0.0069	0.0066	0.015	0.065	8.25

water-soluble metals increase (as do the concentration and the percentage), and the pH value of water extraction decreases in comparison with the upstream layers. This pattern means that with water ingression in these hardpans (seasonal rains, snow melting, and raising of the groundwater level), cationic exchange leads to the rapid acidification of water. As a result, water-soluble and weakly sorbed metal species may be released in the solutions.

In the vertical section no. 1, the distribution of metals is similar to that in cross-section no. 7, which is proved by the high correlation coefficients among the metals (Table 5). Two geochemical barriers were found in this cross-section

Table 6 Percentage of water-soluble metals in layers of vertical sections

Sample	Depth (cm)	% of water-soluble species				
		Zn	Pb	Cu	Cd	pH
Vertical section no. 3						
SP-3/1	7.5	0.05	0.009	0.03	0.08	8.68
SP-3/2	15	0.03	0.024	0.08	0.10	8.37
SP-3/3	22.5	0.10	0.028	0.04	0.26	7.85
SP-3/4	37.5	0.09	0.006	0.03	0.24	7.92
SP-3/5a	47.5	2.36	0.020	0.16	2.78	5.75
SP-3/5b	57.5	1.52	0.027	0.08	0.18	6.87
SP-3/6	85	0.06	0.021	0.05	0.63	8.32
SP-3/6b	95	0.37	0.038	0.07	1.07	7.50
SP-3/7a	120	0.30	0.016	0.13	3.75	7.76

and are marked by a sharp increase of water-soluble species. The first barrier is located at a depth of ~60 cm and the second at ~130 cm (Fig. 2, Table 5). The upper barrier accumulated a higher quantity of secondary minerals than the lower barrier. In contrast to the cross-section no. 7, the percentage of water-soluble species here is less than 3.7% for Zn and 2.6% for Cd. It is possible that mobile species had leached from the tailings to this part of the impoundment and that the measured concentrations of water-soluble phases represent the remainders.

Cross-section no. 3 is represented by dry material with an insignificant quantity of ocher lenses in the middle part (layers 3/5 and 3/6). The metals are distributed irregularly, with concentrations increasing downward, except Pb, which decreases up to the last layer (Table 6). In this cross-section, we find three concentrated layers, although the concentration of exchangeable metals here is not high compared with the layer from cross-section nos. 7 and 1. Obviously, in this cross-section, sorb barriers, which are able to accumulate high amounts of migrated metals, are absent. Additionally, the redistribution of secondary minerals takes place along the whole of the section in more or less suitable layers, but a significant accumulation of secondary minerals does not occur (Fig. 2).

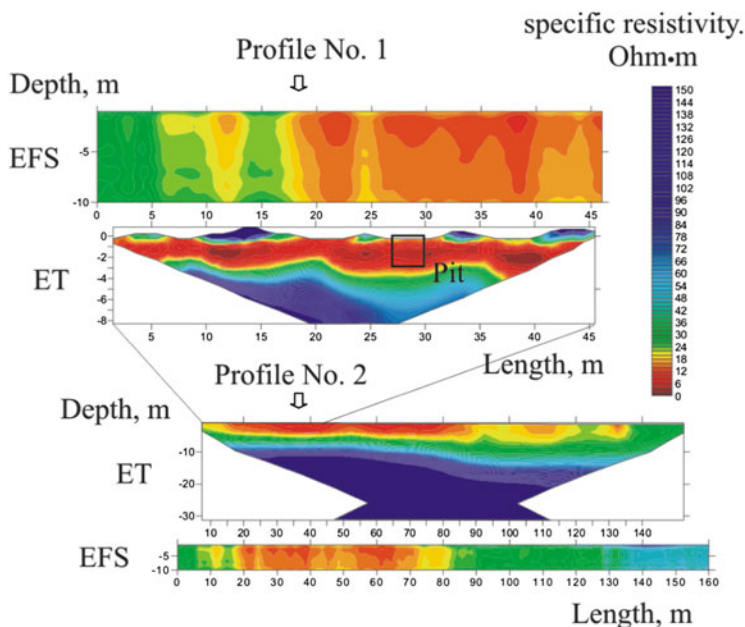
Vertical section no. 5 is located in the oldest part of the tailing impoundments, where the first wastes of the Salair ore processing were stored. In this part of the tailings, substance oxidation is manifested most clearly in the abundance of red ochre.

Trace elements Cu and Cd are distributed irregularly, with a max/min ratio = 180 and 81, respectively; for Pb and Zn, these ratios are 64 and 34, respectively (Fig. 2, Table 7). These ratio values can serve as a mark of the degree of redistribution of each element along the vertical direction. We can also observe the reverse order between the mobility of these metals (Cd > Cu > Pb > Zn) and their content in the tailings (Zn > Pb > Cu > Cd). Correlation between metals is absent in this vertical section, except for Pb–Cu.

A high amount of secondary metals form precipitates on the concentrated barriers (hardpans), especially Cu and Cd (more than 40% for Cd, Table 6).

Table 7 Percentage of water-soluble metals in layers of vertical sections

Depth (cm)	% of water-soluble species					
	Zn	Pb	Cu	Cd	pH	
Vertical section no. 3						
SP-5/1	1	0.18	0.012	0.051	1.5	7.89
SP-5/3	26	2.9	0.308	19	39	5.45
SP-5/7	56	0.33	0.014	2.5	2.5	6.87
SP-5/8	88	8.6	0.0014	19	42	4.58
SP-5/16	150	0.54	0.022	30	4.3	7.86
SP-5/18	175	0.96	0.88	0.080	0.86	8.64

**Fig. 3** Vertical zoning of the Talmovskie Mine Tailings according to the data of the electromagnetic frequency sounding (EFS) and electrical tomography (ET)

4.3 Geophysical Data

Geophysical methods have been applied in order to further clarify the structure of the waste to a depth of 7 m and find evidence of infiltration drainage to groundwater. The section on profile no. 1 is characterized by a range of resistivities of 1–150 Ohm m. The upper part of the section (0–5 m vertically) is represented by the most conductive rocks with resistivities 1–20 Ohm m (Fig. 3). This layer is apparently confined within the highly mineralized wastes of the Salair Ore Processing Plant in the range 2–3.5 m. High-impedance (70–150 Ohm m) heaps

Table 8 Specific electric resistivity of the wastes according to frequency sounding (SER_{fs}) and parameters of the pastes and aqueous extracts (average values for pits nos. 8–10)

Depth (cm)	SER_{fs} (Ohm m)	Humidity (%)	Parameters of the pastes			Σ (Al, Mn, Fe, Cu, Zn, Cd, Pb, Sb) in aqueous extracts (mg/L)
			SER_p (Ohm m)	Eh (mV)	pH	
2	16	8	13	646	3.1	30
25	9.0	7	8.0	693	3.0	110
45	10	8	4.8	738	2.8	110
70	4.8	3	4.3	729	2.9	80
120	4.0	29	3.4	719	3.1	370
160	4.0	32	3.2	642	3.7	760

located at elevations of 10–18, 32–35, and 40–45 m on the profile represent bulk soil. Deeper (3.5–5 m vertically), there is a layer with a resistivity from 25 up to 35 Ohm m belonging to the waterproof horizon. At the bottom of the section, at 5–8 m in depth, the resistivities vary from 40 to 150 Ohm m, which is typical for low-conductive bedrock.

The section on profile no. 2 is characterized by resistivities varying within a range of 1–150 Ohm m. There is an upper layer (0–3 m vertically) with highly conductive waste followed by the waterproof horizon and the bedrock, which is deeper than 10 m. Three pits of 1.6 m depth were excavated and tested. Their location is 28 m from the beginning of the profiles in the area of the highly conductive material (Fig. 3).

The waste material is heterogeneous, has a bright red and brown color, and smells of sulfuric acid. The upper layers are composed of coarse sand with a predominantly quartz, barite and pyrite mineral composition. After a depth of 30 cm, the waste matter is represented by red and bright red coarse-grained sands, and the main mineral phases are barite and pyrite. The lower horizon is composed of dense gray-brown watered material with a particle size of 1.1 mm, and the mineral composition is dominated by quartz, plagioclase, potassium feldspar, and pyrite.

The pH values of the field-prepared pastes vary within the range of 2.8–3.6, and the redox potential ranges from 640 to 740 mV, which indicates oxidation of the waste material. The specific electrical resistance measured by direct conductometry in the pastes (SER_p) varies within the range 3.2–13 Ohm m and correlates well with the results of the SER_{fs} obtained by frequency sounding (Table 8, Fig. 4).

The plots of pH and resistivity values vs. depth are substantially specular reflections with respect to the distribution of Eh: horizons with the lowest pH values are characterized by a high redox potential and low resistance (high conductivity, Fig. 4). The pH values increase and the Eh and resistivity decrease with depth due to the flow of the slightly alkaline groundwater in the pit after a depth of 1.2 m. The total Cu, Zn, Cd, and Pb concentrations in the aqueous extracts and the humidity of the wastes in the lowest horizon increase (760 mg/L and 32 %, respectively, Table 8), which indicates intense leaching.

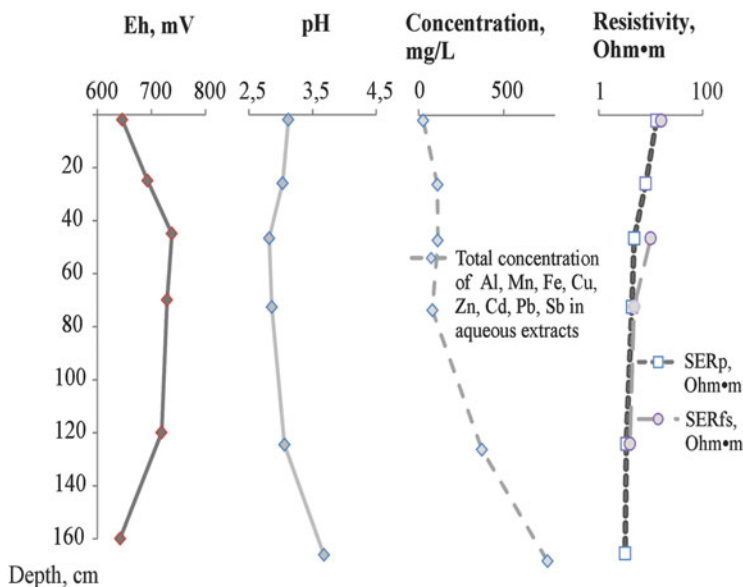


Fig. 4 Eh, pH of the pastes, total concentration of the elements in aqueous extracts, specific electric resistivity of the pastes (SER_p), measured in-situ by conductometry, and in the wastes according to frequency sounding (SER_{fs})

The lowest resistivities are also in the lowest water-bearing horizons with the highest concentrations of SO_4^{2-} , Cu^{2+} , Zn^{2+} , Cd^{2+} in the aqueous extracts. Intensive leaching reduces the metal content in the solids and increases concentrations in the solutions (Table 9). The percentage of the water-soluble species of Cu, Zn, and Cd in the lower horizon is much higher than in the upper layers, reaching 14% for Zn, 5.7% for Cd, and 3.5% for Cu in % of the total content of all species. The low mobility of lead in the acid sulfate-bearing solutions is associated with the formation of the insoluble anglesite PbSO_4 . Obviously, flooding of the tailings by groundwater and intense leaching of the metals occurs at a depth greater than ~160 cm.

4.4 Pore- and Groundwater Composition

The pore waters coexisting with the solids have a highly variable composition (major components and trace elements), which is determined by the local physico-chemical conditions in the different areas and layers (Table 10). The pore solutions are weakly acidic (pH 5–6). Ca^{2+} and Mg^{2+} dominate in the cation composition, SO_4^{2-} prevails among the anions, and concentration of sulfate-ions reaches 4,500 mg/L. The increased acidity and sulfate of the solutions indicate the active oxidation processes of sulfides in the waste and the dissolution of secondary sulfate

Table 9 Composition of the wastes, aqueous extracts, and percentage of the soluble species (average values for pits nos. 8–10)

Depth (cm)	Content of the elements in the wastes (ppm)			
	Cu	Zn	Cd	Pb
2	980	5,000	13	3,600
25	320	6,000	14	4,800
45	1,500	19,000	52	8,800
70	1,300	41,000	120	14,000
120	220	2,500	14	150
160	290	4,800	39	220

Depth (cm)	Aqueous extracts (mg/L)					pH
	Cu	Zn	Cd	Pb	SO ₄ ²⁻	
2	0.89	14	0.07	0.06	570	2.5
25	2.4	66	0.13	0.12	530	2.8
45	1.5	104	0.26	0.65	500	2.8
70	1.3	58	0.13	3.3	420	2.1
120	6.9	311	0.78	0.05	1,000	2.4
160	10	660	2.2	0.04	1,200	3.0

Depth (cm)	% of water-soluble species			
	Cu	Zn	Cd	Pb
2	0.09	0.28	0.55	0.001
25	0.74	1.09	0.96	0.002
45	0.10	0.54	0.49	0.007
70	0.10	0.14	0.11	0.02
120	3.15	12	5.53	0.03
160	3.53	14	5.73	0.02

Table 10 Major ion composition in pore waters of the Talmovskie tailings (mg/L)

Component	P-1	P-2	P-3	P-4	P-6
pH	5.98	5.09	6.44	5.54	6.36
Ca ²⁺ +Mg ²⁺	570	1,500	1,000	540	570
Na ⁺	53	28	52	55	26
K ⁺	36	8.0	11	18	20
HCO ₃ ²⁻	Not detected	Not detected	130	Not detected	120
SO ₄ ²⁻	1,600	4,500	3,400	2,800	1,800
Cl ⁻	78	29	27	28	33
F ⁻	360	10	24	6.0	6.0
NO ₃ ⁻	140	Not detected	Not detected	Not detected	58

minerals, such as jarosite KFe₃(SO₄)₂(OH)₆, orthoserpierit Cu₃(SO₄)₂(OH)₂·2H₂O, and magnesiocopiapite MgFe₄(SO₄)₆(OH)₂·20H₂O.

The variations of Zn in the pore water are notably broad; its concentrations are mostly high, reaching 1,000 mg/L (Table 11). It is necessary to take into account the peculiarities of the pore water solutions, i.e., the low content of HCO₃⁻ and the high

Table 11 Concentrations of metals in pore water of the Talmovskie tailings (mg/L)

	Zn	Pb	Cu	Cd	Fe
P-1	16	8.5	2.3	0.05	0.5
P-1/9	203	0.046	1.0	1.0	0.27
P-2	1,000	5.7	0.35	3.5	140
P-2/13	128	0.022	0.7	0.35	0.11
P-2/14	142	0.085	0.8	0.81	0.25
P-3	177	4.4	1.0	4.1	1.1
P-4	750	18	1.2	1.6	100
P-6	0.02	1.0	0.02	0.01	1.3
P-6/10	29	0.007	0.21	0.52	0.08
P-6/15	0.54	0.13	0.36	0.0004	0.67
P-6/16	1.3	0.15	0.44	0.0014	0.44
P-6/18	0.8	0.24	0.5	0.0013	0.52

Table 12 Concentrations of elements in water samples from wells

	Concentration ($\mu\text{g/L}$)			
	Cu	Zn	Cd	Pb
D 6	64	98,000	410	15
D 7	125	10,000	5,900	1,000
D 24	8.7	8,800	5.3	3.0
C 1	4.0	7,300	1.4	0.7
C 2	6.7	5,900	1.3	190
C 3	5.5	5,200	0.61	0.7
C 4	110	3,900	0.34	0.5
MPC ^a	1,000	1,000	1.0	10
Average in river waters ^b	7.0	20	0.01	1.0

^aMaximum Permissible Concentration for Chemical Compounds in Water Reservoirs, accepted in Russia (HN 2.1.5.1315-03) [18]

^bAccording to Taylor and McLennan [19]

level of SO_4^{2-} . Therefore, instead of the formation of smithsonite ZnCO_3 on the surface of sphalerite ZnS , zinc remains in the solution. The lead concentrations are not high because of its easy coupling with sulfate and the consequential formation of PbSO_4 ; in some cases, however, concentration of lead may increase up to 10–17 mg/L. The concentrations of Cu, Cd, and Fe are lower than those for zinc, but in isolated samples, 100–140 mg/L of iron was detected (Table 11).

The chemical analyses of the groundwater samples from the wells located in close proximity to the Talmovskie tailings (Fig. 2) indicate high contents of Cu, Zn, Cd, and Pb in the groundwater (Table 12). The copper concentrations range from 4 to 125 $\mu\text{g/L}$, and the Cd and Pb concentrations range from 0.5 to 5,900 $\mu\text{g/L}$. The zinc concentrations are the highest compared with the other elements: up to 98 mg/L (sample D6, Table 12). It is important to note that the concentration of zinc in all the analyzed samples is higher than the MPC by 4–100 times. The Cd concentrations significantly exceed the MPC (up to 5,900 times) in five of the seven

samples. The concentration of Pb increases compared with the MPC by 3–1,000 times in three of the seven samples. The concentrations of all elements (except for copper in three samples) are significantly higher than the average content in river waters [19].

5 Conclusions

It should be emphasized that significant amounts of water-soluble forms were observed over the vertical sections. In the lowest layers, however, the concentration of water-soluble species decreased, obviously due to the removal of mobile forms by groundwater below the water table. The percentage of exchangeable species varies in a wide range along the vertical sections – from traces up to very high values, especially for Pb. All of these factors provide evidence of a high degree of oxidation and alteration of tailings in this part of the impoundment and consequently the redistribution, removal, and precipitation of secondary metal minerals and phases.

Electrical tomography and electromagnetic frequency sounding allowed the delineation of the tailings of the Salair Ore Processing Plant and the prediction of changes in the composition of waste with depth. The existence of secondary modified and oxidized zones of the waste material with a high proportion of water-soluble, mobile forms of elements, was estimated down to a depth of 7 m, based on data from the geophysical surveys and geochemical analyses. The authors made the first attempt to develop and test this approach, in order to quantify the resources of the valuable components in the tailings and to evaluate the environmental risks presented by underflooding of the stored wastes by seasonal streams and groundwaters.

As expected, the leaching of metals from the tailings stockpiled in the Talmovskie tailings and the migration of drainage solutions lead to a significant pollution of local groundwater, causing irreparable damage to the supply of clean drinking water at the regional level and, thus affecting the health of local residents.

Acknowledgments We are grateful to our honored editor Dr. Andrea Scozzari and operators of analytical devices Irina Nikolaeva, Yuri Kolmogorov, Nadezhda Palchic. This study was supported by grants RFBR No. 11-05-00742 and No. MK-3242-2011.5 of the Foundation of the Russian Federation President.

References

1. Salomons W (1995) Environmental impact of metals derived from mining activities: processes, predictions, prevention. *J Geochem Expl* 52:5–23
2. Yakhontova LK, Zverev VP (2000) Fundamentals of the supergene mineralogy. Dal'nauka, Vladivostok

3. Dinelli E, Lucchini F, Fabbri M, Cortecchi G (2001) Metal distribution and environmental problems related to sulfide oxidation in the Libiola copper mine area (Ligurian Apennines Italy). *J Geochem Expl* 74:141–152
4. Lottermoser BG (2007) Mine wastes. Characterization, treatment, environmental impacts, 2nd edn. Springer, Berlin
5. Álvarez A, Valenzuela-García J, Meza-Figueroa D, de la O-Villanueva M, Ramírez-Hernández J, Almendariz-Tapia J, Pérez-Segura E (2011) Impact of mining activities on sediments in a semi-arid environment: San Pedro River, Sonora, Mexico. *Appl Geochem* 26(12):2101–2112
6. Bortnikova SB, Gas'kova OL, Ayriyants AA (2003) Technogenic lakes: substance accumulation, evolution, and influence on the environment. Pub. House of SB RAS, Dep. "Geo", Novosibirsk
7. Bortnikova SB, Gas'kova OL, Bessonova EP (2006) Geochemistry of technogenic systems. Acad. Pub. "Geo", Novosibirsk, 169 pp
8. Moore JW, Ramamoorthy S (1984) Heavy metals in natural waters. Springer, New York
9. Alekseenko VA (2000) Environmental geochemistry. Logos, Moscow, 627 pp
10. Panin MS (2002) Chemical ecology. Semipalatinsk State University Press, Semipalatinsk, 852 pp
11. Leybourne M, Goodfellow W (2010) Geochemistry of surface waters associated with an undisturbed Zn–Pb massive sulfide deposit: water–rock reactions, solute sources and the role of trace carbonate. *Chem Geol* 279(1–3):40–54
12. Teršič T, Gosar M, Šajn R (2009) Impact of mining activities on soils and sediments at the historical mining area in Podljubelj, NW Slovenia. *J Geochem Expl* 100(1):1–10
13. Poisson J, Chouteau M, Aubertin M, Campos D (2009) Geophysical experiments to image the shallow internal structure and the moisture distribution of a mine waste rock pile. *J Appl Geoph* 67:179–192
14. Martinez-Pagan P, Faz A, Acosta JA, Carmona DM, Martinez-Martinez S (2011) A multi-disciplinary study for mining landscape reclamation: a study case on two tailing ponds in the Region of Murcia (SE Spain). *Phys Chem Earth* 36:1331–1344
15. Banerjee KS, Sharma SP, Sarangi AK, Sengupta D (2011) Delineation of subsurface structures using resistivity, VLF and radiometric measurement around a U-tailings pond and its hydrogeological implication. *Phys Chem Earth* 36:1345–1352
16. Manstein AK (2002) Near-surface geophysics. Pub. House of Novosib. State Univ, Novosibirsk
17. Baryshev VB, Kolmogorov YP, Kulipanov GN, Scrinisky AN (1986) Synchrotron X-ray fluorescent analysis. *J Anal Chem* 41:389
18. HN 2.1.5.1315-03 (2003) Maximum permissible concentration (MPC) of chemical substances in the water of drinking and cultural-domestic water objects, Intr. 15/06/2003, Russian Ministry of Health, Moscow, p 6
19. Taylor SR, McLennan SM (1985) Continental crust: its composition and evolution. Blackwell, Oxford
20. Blowes DW, Reardon E, Jambor JL, Cherry JA (1991) The formation and potential importance of cemented layers in inactive sulfide mine tailings. *Geochim Cosmochim Acta* 55:965–978

Microfluidic Optical Methods: A Review

Genni Testa, Gianluca Persichetti, and Romeo Bernini

Abstract This chapter reviews the state-of-the-art microfluidic optical methods for water monitoring and analysis. Microfluidics permits to reduce the system dimension, increasing its analytical speed and sensitivity. It also permits to achieve an unprecedented economy of scale, by dramatically increasing production throughput and reducing individual costs. The different linear optical phenomena (e.g., refractive index variations, absorption) and non-linear phenomena (e.g., fluorescence, phosphorescence, Raman scattering) are analysed and discussed in this chapter; in fact, the choice of a particular optical method depends on the analyte and the sensitivity required. Authors show that the strong integration between optics and microfluidics permits to reduce the measurement time, the cost and the portability of the sensing system, opening unprecedented possibilities in the context of water quality monitoring.

Keywords Colorimetric method, Fluorescence spectroscopy, Micro-total-analysis systems, Microfluidic, Microfluid injection analysis system, Raman spectroscopy

Contents

1	Introduction	258
2	Refractive Index Methods	260
3	Colorimetric Methods	262
4	Fluorescence	266
4.1	Flow Cytometers and Counting Particles	268
4.2	Biosensors	270
5	Surface-Enhanced Raman Scattering	273
	References	274

G. Testa, G. Persichetti, and R. Bernini (✉)
Istituto per il Rilevamento Elettromagnetico dell’Ambiente (CNR-IREA), Via Diocleziano
328, 80124, Napoli, Italy
e-mail: bernini.r@irea.cnr.it

Abbreviations

AWACSS	Automated Water Analyser Computer Supported System
CFU	Colony-forming unit
LED	Light-emitting diode
LIF	Laser-induced fluorescence
LOC	Lab-on-chip
LOD	Limit of detection
MG	Malachite green method
MZI	Mach–Zehnder interferometer
μ FIA	Microfluid injection analysis system
μ TAS	Micro-total-analysis systems
OLED	Organic light-emitting diode
OWLS	Optical waveguide lightmode spectroscopy
PDMS	Polydimethylsiloxane
PE	Polyethylene
PEDD	Paired emitter–detector diode
PI	Propidium iodide
PMMA	Poly(methylmethacrylate)
RI	Refractive index
RIFS	Reflectometric interference spectroscopy
SAM	Self-assembled monolayer
SERS	Surface-enhanced Raman scattering
SPR	Surface plasmon resonance
SPW	Surface plasma wave
TIRF	Total internal reflection fluorescence
UV	Ultraviolet

1 Introduction

In the last years, a great effort has been devoted to the development of the so-called LOC or μ TAS [1, 2], devices that are self-sustaining and can perform assays and report results without external cues.

Targeted applications of such μ TAS range from chemical–biological agent detection to clinical diagnostic and environmental monitoring. In order to carry out a complete assay, these systems require the integration of a wide variety of functional components on a microchip [3, 4]. The success of these devices relies on the ability to control and analyse small sample volumes using complex integrated microfluidic devices.

Microfluidics deals with the behaviour and the process of fluids on a microscopic (or smaller) scale [5]. By processing samples on the nanolitre (10^{-9} l) or even picolitre (10^{-12} l) scale, microfluidics has the potential to revolutionize chemical analysis in the same manner that integrated circuits have revolutionized computers

and electronics. The reduced dimension permits to increase speed and sensitivity while at the same time achieving an unprecedented economy of scale, dramatically increasing throughput and reducing cost.

However, it is important to underline that, unlike microelectronics, in microfluidics the fundamental physics changes very rapidly as the size is decreased. At a micron scale, fluids can exhibit dramatically different performances from that in macroscale leading to inherently unique dynamics [5]. Due to the large surface-area-to-volume ratio boundary driven effects, especially surface tension forces, play a dominant role. Additionally, typically viscous energy dissipation is dominant and inertial effects are negligible. This results in a turbulence-free flow, so layers containing different analytes can move along together, mixing only by diffusion. The laminar flow at a microscale not only significantly reduces the amount of reagent required thereby decreasing the cost-per-test but also help establish rapid response times and efficient chemical separation. As an example, electrophoresis is 100 times faster when the system size is ten times smaller. Furthermore, it allows combining various functions (mixing, reaction, analysis) on the same chip in an automated manner or with little human intervention.

Microfluidic systems are made up of an intricate network of microchannels and microdevices (pumps, valves, filters, etc.) that can be made from a variety of materials, including glass, silicon or polymer [6]. However, the economic benefits of polymer often make it the most attractive choice.

Microscale engineering also makes it possible to integrate chemistry with mechanics, electronics and optics and to integrate several analytical systems into very small areas. Where required, these can interface with conventional-sized peripherals for data interpretation and transmission.

Several transduction methods like electrical, electrochemical, optical, piezoelectric and thermal can be integrated with microfluidic devices [7]. However, in the choice of the detection method for microfluidic devices, it must be taken into account that in microscale sensing system, the reduced analysis volumes mean a decrease of the number of analytes available for detection, making it more difficult to detect them. From this point, optical measurements permit to obtain very high sensitivity, down to single-molecule detection also with a tiny amount of sample; furthermore optical devices can be integrated with microfluidic ones [8].

This chapter reviews the state-of-the-art microfluidic optical methods for water monitoring and analysis. The different linear optical phenomena (e.g., refractive index variations, absorption) and non-linear phenomena (e.g., fluorescence, phosphorescence, Raman scattering) are analysed and discussed. The choice of a particular optical method depends on the analyte and the sensitivity required. We show that the strong integration between optics and microfluidics permits to reduce the time, the cost and the portability of the sensing system.

2 Refractive Index Methods

In this approach the sensing mechanism is based on variations of the refractive index close to the sensor surface. RI is a physical quantity defined by the speed of light through a substance, relative to the speed of light in the vacuum. The main advantage of these methods is that they are label free. The RI has been proposed as a generic quality indicator for drinking water quality [9]. In fact, any substance, when dissolved in water, will change the refractive index of the water matrix. Typically, the refractive index variation is proportional to both concentration and refractive index of the substance. Virtually all relevant substances have refractive indices that are clearly higher than water.

This approach permits to measure a sum parameter (RI) to which theoretically all substances contribute. It is very interesting for a fast and low-cost continuous monitoring, either in-line or online, of the quality and safety of water in their distribution networks. For example, it could be used as an early warning of a change in water quality, which can be followed up by more detailed analysis, for example, in order to determine whether the change is potentially hazardous.

This approach was firstly proposed by Ramsden [9] that used OWLS to measure RI variation. In this case an integrated optical grating coupler is incorporated in an optical waveguide in which the light can propagate, generating an evanescent field. The range of this field extends slightly above the waveguides (approximately 100 nm), allowing it to probe the composition of a water sample flowing over the sensor. By measuring the phase velocities of a selected guided mode it is possible to evaluate the RI variation within a thin layer adjacent to the waveguide surface. Experiments performed with tap water and river water showed that the measured response was predominantly due to the adsorption of dissolved and suspended matter (macromolecules and particles) at the surface of the waveguide. In order to increase the sensitivity, a new sensor platform has been recently proposed and tested [10]. The sensor is based on an integrated optical version of the MZI. The interferometric approach permits to measure a minimal change in refractive index in the order of magnitude of 10^{-7} RI that correspond to the detection limits of concentration of parts per million (ppm) levels for any chemical contaminant.

However, in some application the identification and the quantitative analysis of the individual components in water are necessary. In this case, a non-specific RI sensor can be transformed into a specific sensor by immobilizing on its surface a recognition element that, when interacting with the analyte of interest, change the RI on sensor surface.

OWLS technology has been applied to microbiology, including the detection of *Salmonella typhimurium* in water (detection limit of 1×10^7 CFU/ml [11]). The sensor surface was functionalized with a specific antibody thus making the sensor specific for the detection of human pathogens. Using a similar approach, Cooper et al. [12] developed a rapid and sensitive detection method for *Legionella pneumophila* contamination in a water sample in less than 25 min with an LOD of 1.3×10^4 CFU/ml. OWLS has been also applied for pesticide detection [13]; the

transducer is incorporated in a microprocessor-controlled flow system allowing complete automation of incubation, regeneration and data acquisition. The experimental results performed with herbicides from the s-triazine group, like terbutryn and atrazine, have shown a detection limit of 15 nM for terbutryn.

RIFS is another optical technique that has been applied to microfluidic monitoring of water samples. The sensing principle is based on white light interference in thin transparent films. A light beam passing the interface between two media of different refractive index is partly reflected. As the reflected beams travel different optical paths, a phase difference is introduced. These reflected partial beams superimpose resulting in an interference spectrum that is detected using a diode array spectrometer. The target analyte interacts with the sensor surface that causes a change in the optical thickness of the layer $n \times d$ due to the change of the physical layer thickness d and the refractive index n within this layer. A change in the optical thickness results in a modulation of the interference spectrum that allows observing the binding behaviour of the target analyte.

A prototype atrazine sensor based on RIFS was investigated by Brecht et al. [14]. The device was tested using real groundwater samples spiked with 0.1, 0.25, 0.5, 1, 2.5, 5 and 10 ppb of atrazine, and a limit of detection of about 0.25 ppb was obtained.

Another widely used approach is the SPR. In SPR sensors, a SPW is excited by a light wave and the effect of this interaction with the sensing layer is measured. A surface plasma wave or a surface plasmon polariton is an electromagnetic wave which propagates along the boundary between a dielectric and a metal [15]. Owing to the fact that the vast majority of the field of an SPW is concentrated in the dielectric, the propagation constant of the SPW is extremely sensitive to changes in the refractive index of the dielectric. SPR-based sensors have been used as platform that, in conjunction with appropriate recognition elements, can be tailored for detection of chemical and biological contaminants like organic chemicals (pesticides, herbicides, etc.), inorganic chemicals (heavy metals), microbial pathogens and toxins.

Several SPR instruments that integrate optics, microfluidics, electronics and biosensor technology have been developed in the last years.

Using a simple SPR instrument, which is not equipped with either regulated flow system or temperature controller, Gobi et al. developed an SPR immunosensor for dichlorophenoxyacetic acid (2,4-D) detection [16]. Dichlorophenoxyacetic acid is one of the most widely used herbicides for control of broadleaf weeds in agriculture, forestry and right-of-way applications. The proposed system has been shown to be capable of detecting concentrations of 2,4-D in buffer as low as 0.5 ng/ml (ppb) with a response time of 20 min, and the 2,4-D detection is possible in the concentration range from 0.5 ng/ml to 1 µg/ml (ppm).

Similarly, using a portable surface plasmon resonance optical biosensor device, Mauriz et al. were able to determine organic pollutants, such as organochlorine (DDT), organophosphate (chlorpyrifos) and carbamate (carbaryl) compounds, in natural water samples within the range proposed by the European legislation [17]. The covalent immobilization of the analyte derivative through an alkanethiol SAM allowed the reusability of the sensor surface during more than 250 regeneration

cycles. The analysis time for a complete assay cycle, including regeneration, was 24 min. The size and electronic configuration of the device allow its portability and utilization on real contaminated locations. In addition, this sensor has also the capability of a wireless transmission of data from real contaminated locations to a central laboratory.

3 Colorimetric Methods

Light absorption spectroscopic approach for water quality monitoring is very widely applied due to the high selectivity, accuracy and sensitivity. This method is based on the measurement of the amount of light absorbed at a specific wavelength by a substance. However, since most of the water pollutants do not naturally absorb in the UV–visible range, most spectrophotometric methods are based on the use of UV–visible chromophore, and for this reason they are called colorimetric methods.

The basic principle of the light absorption spectroscopy is described by the Lambert–Beer law which permits to determine the concentration of an analyte by measuring the light intensity attenuation according to the following:

$$I = I_0 e^{-\epsilon cl} \quad (1)$$

where I is the intensity of the light emerging from the cuvette containing the analytes, I_0 is the intensity of the incident light, ϵ is the absorptivity coefficient (that depends on the chemical species), l is the pathlength through the sample and c is the concentration of absorbing species. From Eq. (1) it is evident that long optical pathlengths are advantageous in order to increase light absorption and detect chemical species at very low concentration.

Colorimetric method typically relies on the use of reagents that, in the presence of the analyte, give rise to the formation of a dye. As the formed dye concentration is linearly proportional to the analyte one, by measuring the optical absorption at a dye's specific wavelength, it is possible to measure the concentration of the analyte. This method is widely and successfully applied due to the high stability and selectivity of the involved chemical reactions. A variety of colorimetric assay chemistries exist; the Griess assay, for example, is the most commonly used for nitrite analysis [18–21]. The azo dye formed during the reaction of sulfanilamide hydrochloride and *N*-(1-naphthyl)ethylenediamine dihydrochloride with nitrite is characterized by optical absorption at $\lambda = 543$ nm. Another example is the Berthelot assay, in which an indophenol dye with optical absorption at $\lambda = 632$ nm is produced when reacting with ammonia.

Basically, a colorimeter instrument is composed of a white light source (LED, tungsten halogen lamp, etc.), a cuvette containing the solution to test and a light detector (photodiode, photomultipliers, etc.). Commercially available benchtop colorimeter instruments for water analysis have limited deployment capabilities

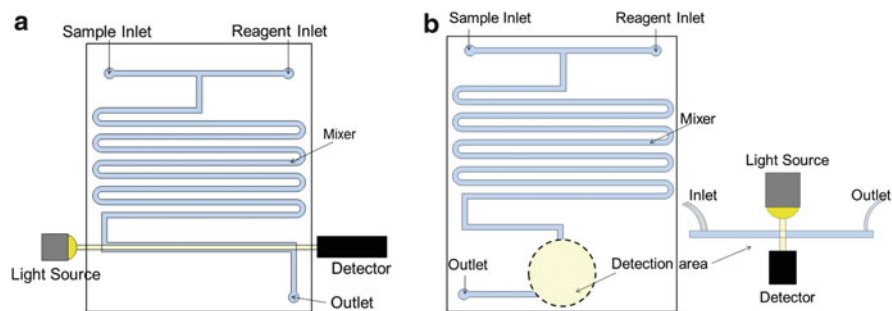


Fig. 1 (a) Planar light source and detector configuration and (b) perpendicular configuration

and scenarios; their large physical size (e.g., 40–50 cm long and 10–15 cm diameter) limits the portability of the system avoiding the field deployability; moreover, the excessive reagent usage (ml per sample) and the high power consumption make these instruments very expensive.

For water monitoring, in order to be more easily performed outside the laboratory, instruments which could be mass produced, cheaper and easily used would need to be developed. The uses of microfluidic technologies have the potential to address these needs, including the problem of reagent consumption, as well as the size and power challenge associated with macro-sized benchtop colorimeter instruments.

Various microfluidic colorimeter instruments have been developed and tested for use in water quality monitoring. Usually, they are μ FIA systems, meaning sample and reagent are pumped into and out of the fluid handling system with a continuous piping network.

Essentially, the microfluidic system is composed of a net of fluidic microchannels for reagents and sample delivering, where the reagent mixing system is usually a long serpentine (Fig. 1a, b). For the optical detection system, two main configurations are used, based on the orientation between the optical source and the detector. In the planar design (Fig. 1a) the light propagates along the sample microchannel before reaching the light detector. This configuration presents the strong advantage to increase the optical path length and hence the limits of detection [18–20]. A perpendicular light and detector arrangement (Fig. 1b) has been also successfully developed [21, 22]; in this case however the optical pathlength is limited to hundreds of microns, in this way reducing the LOD.

Several fabrication techniques and materials are used to fabricate microfluidic chips: deep etching silicon or glass substrates, micromilling, hot embossing and laser ablation of plastic substrates and elastomer moulds built using a soft lithography process. Each of these fabrication processes presents some advantages and disadvantages and, for this reason, in developing microfluidic colorimeters, the fabrication method is chosen based on the type of application and desired performance.

First attempts to develop miniaturized colorimetric devices have focused on the realization of the microfluidic channel network for handling the fluids to be sampled and have been realized in glass or silicon using photolithographic method.

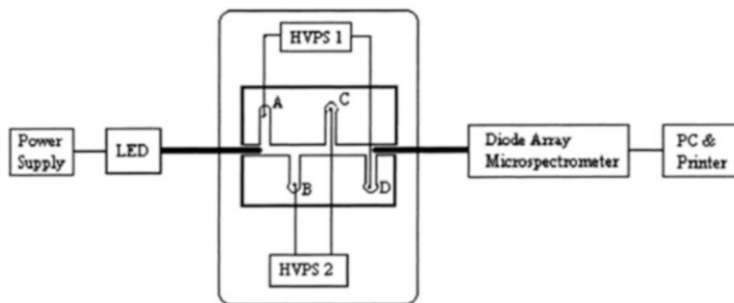


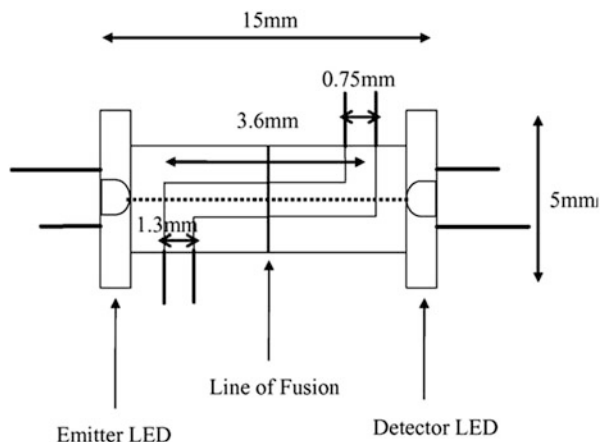
Fig. 2 A schematic of the micro-flow injection manifold for the determination of nitrite proposed by Greenway et al. Reprinted with permission from [20]

One of the first works on the realization of miniaturized system for colorimetric measurements has been performed by Greenway et al. [20] and implemented the Griess reaction on a glass microfluidic device. The device was a micro-flow injection analysis system based on electro-osmotic flow and with an off-chip optical system (LED and the spectrophotometer coupled with optical fibres) for colorimetric measurements (Fig. 2). Glass microfluidic channels (with size of few hundred of microns) for mixing reagents and delivering the sample have been realized by a glass wet etching process. With this system, an LOD of 0.2 mol/l was achieved using a pathlength of few mm, demonstrating the potential of a portable system to be used in the field of water quality monitoring.

Daykin and Haswell [23] demonstrated another of the early examples of μ FIA system for analysing orthophosphate in water. The system has been realized on glass substrates by lithographic method; also in this case the optical system comprises fibre optics coupled to an LED photodiode system. The detection of orthophosphate was obtained along a pathlength of just 7 mm, with an LOD of 0.7 μ g/l and by using the molybdenum blue spectrophotometric method. With this system the authors demonstrated the possibility to realize a reliable manifold for orthophosphate analysis on small scale, claiming the distinct advantages to have reduced reagent usage (total system volume approximately 0.5–1, sample volume approximately 50 nl) and an increased speed of analysis (3 min).

In the work of Daridon et al. [24], an example of a more sophisticated microfluidic system that has been proposed in order to get a better control over the rate of a Berthelot reaction, through the optimization of the reaction parameters, is shown. In fact, when slow kinetic reactions are involved (as it is in the case of Berthelot reaction), small sample volumes could be unrepresentative; this problem has been overcome by a careful design of the mixing and reaction channels and by adapting the flow rates for ensuring efficient mixing by diffusion. The device consists of a silicon chip between two glass plates and uses a pathlength of 400 μ m. Also in this case the optical system comprises optical fibre connected to the source and the detector.

Fig. 3 Schematic of the integrated PEDD flow analysis device. Reprinted with permission from [28]

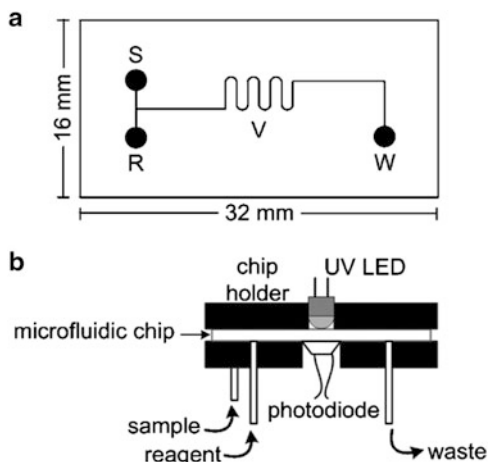


The control of the mixing degree in microchannels is of essential importance in the field of chemical analysis and in particular of the colorimetric-based analysis. In order to obtain efficient mixing at the microscale, different strategies based on the integration of both active and passive mixing elements can be used [25, 26]. In the work of del Mar Baeza et al., a hybrid glass–silicon microfluidic device has been developed for μ FIA of nitrite that exploits multicommutation concept to enhance the mixing process [27]. Moreover, the optical measurements were made using an LED as optical source and a photodiode as a detector that were both fully integrated with the microfluidic system on the same chip, leading to an appreciable reduction of cost and size.

The integration of the detection system is one of the most relevant aspects to be addressed in the development of compact and robust analytical microsystems. With this aim, more recently, in the work presented by O'Toole et al. [28, 29], a novel PEDD optical detection method, with a miniaturized light-emitting-diode-based detector (Fig. 3), is proposed and optimized in order to be fully integrated with the microfluidic part. A PEDD consists of two LEDs arranged in various configurations; one LED is used as light source and the other is used as detector for the transmitted light. The optical flow cell was fabricated through the conjoined LEDs along the light path, in this way achieving the full integration between the microfluidic and optical part. The proposed device has been tested successfully for the colorimetric determination of phosphate in water based on MG method [29], achieving an LOD of $\sim 2 \mu\text{M}$.

In order to further reduce the cost and the complexity of the involved processes, in the last years more affordable fabrication methods and materials have been used for the realization of these instruments. Common plastic materials include PMMA, PE and silicones (PDMS). The dimensions of the channels in the devices cover a large span of depths (and widths) from 10 to 100 μm [18, 21, 22, 30–32]. Moreover, polymers exhibit several useful properties such as optical transparency, machinability and mouldability and a wide range of surface properties [33].

Fig. 4 (a) Microfluidic chip layout with sample (*S*) and reagent (*R*) inlets, a serpentine reaction channel and viewing (*V*) area and waste (*W*) outlet; (b) cross-sectional view of the microfluidic chip holder and detection components. Reprinted with permission from [34]



In the work of McGraw et al. [34] a device for the colorimetric detection of phosphate in natural waters has been realized with integrated PMMA-based microfluidic chip. The device comprises colorimetric detection, wireless communication, power supply and microfluidic system towards a compact and portable system for in situ usage. Instead of a microcuvette with separated inlets and mixer [35], a passive serpentine micromixer milled in the PMMA has been used for sample delivering and reacting, thus reducing the overall size of the chip. The length and width of serpentine have been chosen to cover the entire active area of a photodiode detector (Fig. 4).

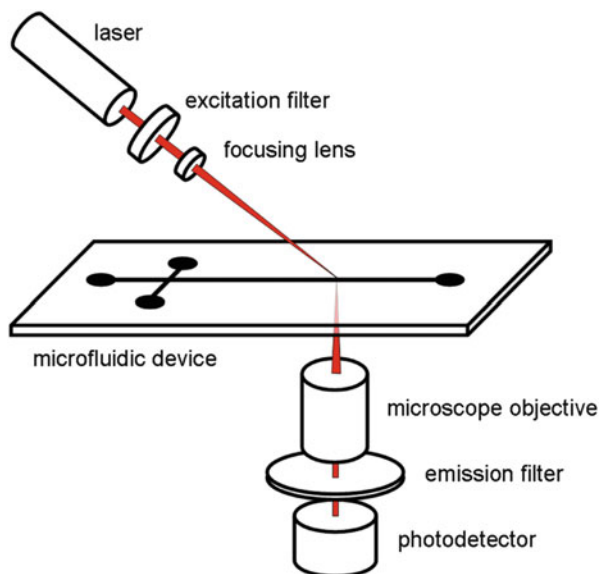
More recently, Sieben et al. [18] have proposed a novel platform based on tinted PMMA for the colorimetric detection of nitrite. The device integrates both the fluid processing and the optical detection on the same chip, towards a low-cost and portable sensitive environmental nitrite sensor, which enables us to achieve an LOD of 14 nM on an absorbance pathlength of 25 mm.

4 Fluorescence

Fluorescence is recognized as one of the most applied detection method in microfluidic devices due to its high sensitivity and selectivity. This technique is based on the fluorescence phenomenon which occurs for some molecules or substances, if suitably excited. After an optical excitation, the molecules relax into the lowermost vibrational level of their electronic state. From this excited level a decay occurs: this decay is said radiative if photons are emitted or non radiative if there is no photon emission. When radiative transition involves states with same spin orientation, this phenomenon is named as fluorescence.

A schematic fluorescence measurement arrangement is depicted in Fig. 5. In microfluidic device a typical setup is composed of an optical source, an excitation

Fig. 5 Common setup used in microfluidic device for fluorescence detection



filter used to filter out any unwanted chromatic component in the excitation light, a focusing system to focus the light into the microfluidic channel or the sensitive part of the device, an emission filter to detect only in the wavelength range of interest and an optical system to collect the fluorescence (often a microscope objective). Several excitation sources are available. Lamp-based excitation systems represent a flexible option in terms of the wavelength choice but not always adequate in terms of intensity.

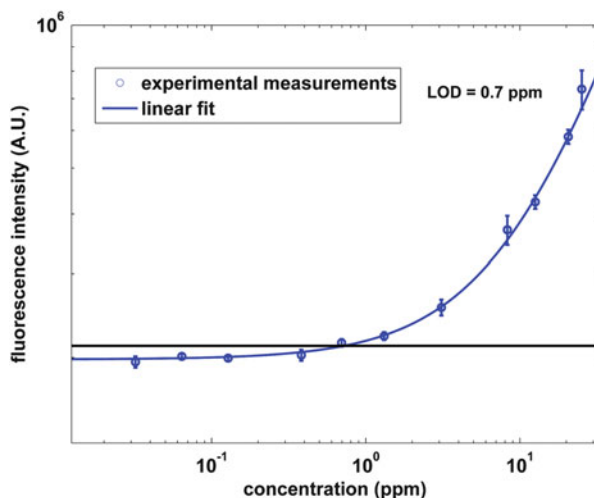
Laser remains one of the most widely used optical source in microfluidic optical devices. The related detection technique, known as LIF, is very attractive because of its compatibility with typical chip dimensions.

The low divergence and the coherence properties of a laser source allow easiness in beam focusing on microchannels, leading to very small detection volumes and achieving a considerable irradiation amount [36–38].

LEDs have been successfully integrated as light source and OLEDs also seem to be a promising optical source. OLEDs, in some specific geometry configurations, could be a more effective choice with respect to LED, because of their flat film-like shape. This allows an easy integration into microfluidic devices and in bringing them into close proximity of the channel or of the device-sensitive element.

As fluorescence-based detection methods allow to achieve very low LOD, a very large number of microfluidic arrangements or devices exploiting in some way the fluorescence phenomenon have been proposed to detect pollutants or dangerous chemical species in water [39, 40]. In particular, the use of UV sources allows to excite the fluorescence of a very wide range of organic pollutants, for instance, bacterial cells [41] or hydrocarbons [42]. An example of calibration curve for

Fig. 6 Fluorescence detection of toluene in water solution (unpublished)



hydrocarbon detection in water sample by UV-excited (266 nm) fluorescence is shown in Fig. 6.

Not all analytes or pollutants interesting in monitoring of water resources exhibit the so-called primary fluorescence (or autofluorescence). As it will be shown, different procedures are used to turn non-fluorescent or weakly fluorescent sample molecules into highly luminescent products. Labelling the analyte with some fluorescent dye is a common procedure to detect analytes that do not exhibit autofluorescence. In this case the fluorescence achieved is called secondary (or induced). A very effective method is represented by immunofluorescence, in which the fluorochrome couples with antibodies. These antibodies can be designed very specifically for certain biological targets so that they lead to an extremely selective labelling result. In the following, some examples of microfluidic devices exploiting fluorescence detection will be shown.

4.1 Flow Cytometers and Counting Particles

Flow cytometry is a technique largely used for particle counting and analysis, providing for instance rapid quantification of bacteria and algae. In this technique, a cell or particle suspension is injected, under laminar condition, and hydrodynamically focused, through a sensing region where it is exposed to a monochromatic focused light beam. The particles under analysis are usually pre-stained for identification. Thus each type of particle emits a fluorescence signal that is collected by means of a detector. The signal intensity provides information on the size and morphology of the detected bacteria.

Commercial flow cytometers are available for accurate analysis of cells or particles. These devices require a large number of electronic, fluidic and optical

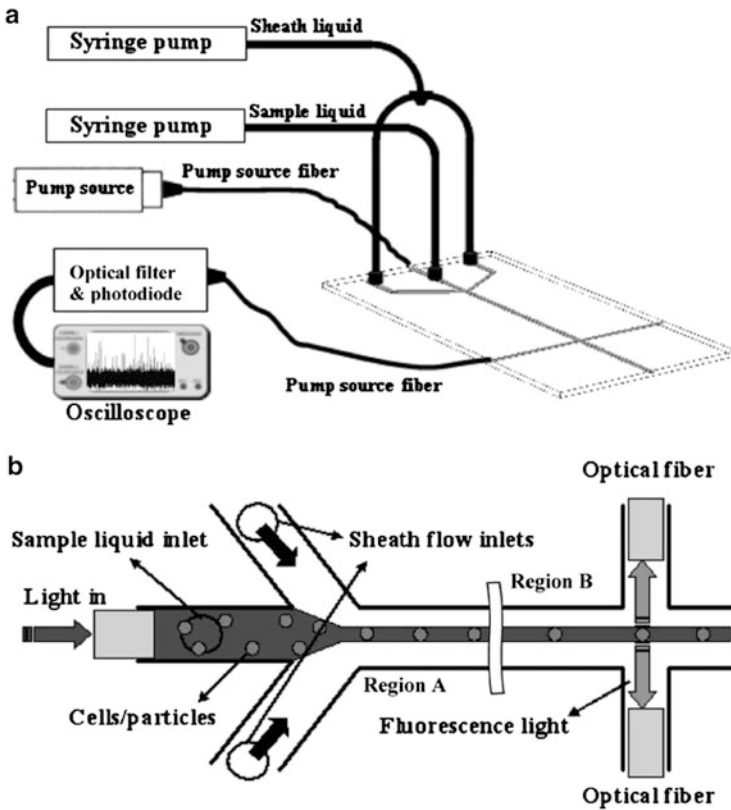


Fig. 7 A schematic layout of a typical microfluidic flow cytometer (a). Top view (b). Adapted with permission from [45]

components resulting in a cumbersome instrument. In addition commercial flow cytometers are complex, fragile and expensive instruments.

Recently, flow cytometers have been successfully tailored for microfluidic devices [43, 44] allowing a fast detection and an easy portability of the device (Fig. 7).

Cytometers and counting particles method based on fluorescence have been used, for instance, to count *Escherichia coli* bacteria [46, 47]. In particular in the work of Inatomi et al. [47] a simultaneous detection of live and dead (or injured) cells has been achieved by staining *E. coli* bacteria with two different fluorescent dyes.

It is known that the viability of bacterial populations can be determined by staining a sample with a combination of various fluorescent dyes [48–50]. Inatomi and co-workers used PI which is generally excluded by intact plasma membrane; hence an uptake of PI was considered as indicator of dead or injured cells.

Labelling cells seems to be not a mandatory process to accomplish inflow cytometry because cells of many organisms exhibit autofluorescence [51].

Primary fluorescence can be generated by a range of metabolites and structural components including flavins, lipofuscins, nicotinamide-adenine dinucleotide and nicotinamide-adenine dinucleotide phosphate. Lu et al. [40] demonstrate the quantification of the number of bacterial cells based on the autofluorescence from the cell lysate of three pathogenic bacteria (*Listeria monocytogenes* F4244, *Salmonella* Enteritidis PT1 and *E. coli* O157:H7 EDL 933) on a microfluidic chip. They tested the microfluidic device performing both off-chip (by means of sonication and centrifugation) and on-chip lysis by means of entrapment and electrical lysis of bacterial cells straight into the device. In the experiment, a plug of around 150 pL containing lysate from 240 to 4,100 cells was injected into a microfluidic channel with downstream laser-induced fluorescence detection under electrophoresis conditions.

They demonstrate a rapid quantification of the number of bacterial cells without labelling. Autofluorescence intensity increased with the number of cells almost linearly and the LOD was determined to be around 200–400 cells for all three bacteria.

4.2 Biosensors

Biosensors are a very big family of sensors that use a biochemical recognition element immobilized in a transducer to detect the specimen of interest. Their potential for environmental applications has been widely reviewed in different publications [52–56].

Several biological receptors have been exploited, for instance, enzymes, cells, antibodies, subcellular organelles, tissue slices, several plant glycoproteins (that act like antibodies) and, lately, bio-mimics.

Different signal transduction mechanisms are possible, but in the following we will focus our attention on fluorescence detection only. Biosensors exhibit several advantages, as they can be arranged in portable devices performing real-time measurements and in addition they often are fast and cost-effective. Microfluidic biosensors have been applied to the area of environmental monitoring for a wide range of analytes. In the following some examples applied for water pollutant detection will be described.

DNAzymes are DNA-based biocatalysts able to perform chemical transformations [57, 58]. Liu and Lu were the first to employ DNAzymes to obtain functional nanomaterials that are sensitive to chemical stimuli [59]. Employing a Pb²⁺-specific DNAzyme, a sensor for lead detection has been proposed [60].

The device was tested considering lead ion concentration from 0.1 to 200 μM. A linear range of 0.1–100 μM Pb²⁺ and an LOD of 11 nM were obtained.

The key aspect of their sensor was the combination of a lead-specific DNAzyme with a device containing a network of microfluidic channels. The sensor consists of an enzyme strand and a substrate DNA. In the presence of target metal ions (Pb²⁺) the substrate cleaves into two fragments. The 5' end of the substrate DNA is labelled with a fluorophore (FAM), whereas its 3' end is labelled with a quencher (Dabcyl) which is able to quench the fluorescence of FAM in the substrate DNA

because of its closeness. A nanocapillary array membrane connects the source channel with the receiving channel. This membrane is used to control fluid flows and to deliver a small volume of sample in a well-determined detection window where the DNAzyme is interrogated using LIF detection. When the lead sample reaches the DNAzyme sensor, the substrate DNA is cleaved; consequently fluorophore fragments are released increasing the FAM fluorescence signal which is not any more quenched by the Dabcyl.

Another interesting biological receptor used in microfluidic sensors consists in employing unicellular micro-organisms.

Arsenic, often present in groundwater, has been detected by using a microfluidic fluorescent biosensor exploiting *E. coli* DH5 α pProbe-gfp(tagless)-arsR-ABS bacteria [61]. This specific strain was engineered to produce green fluorescent protein (GFP) in response to arsenite [62]. Bacteria were loaded against a microfabricated filter present in the microfluidic channel where the solution flows. The fluorescence-detected signal showed a clear response to concentrations of 50 $\mu\text{g/l}$ of arsenite.

The use of unicellular micro-organisms in evaluating the presence of pollutants in water is not limited to bacteria. Algae also have been used because a large number of pollutants are capable of affecting photosystem activity and therefore photosynthesis inhibition is an effective indicator of toxic effects.

Fluorescence detection is considered as a sensitive method to measure algal photosynthesis inhibition [63].

A portable and integrated sensor based on organic optoelectronic components has been recently realized for algal fluorescence measurements [64]. The integrated microfluidic chip has been optimized to measure whole cell fluorescence for unicellular organisms, like algae and cyanobacteria. The device has been tested using green algae *Chlamydomonas reinhardtii* (CC-125). In these organisms, light energy absorbed by chlorophyll complex molecules in PSII is first used for photosynthesis, while the excess energy is dissipated as heat or re-emitted as fluorescence at longer wavelengths in the red/far red range of the spectrum.

The optical source was a blue organic light-emitting diode which excited algae in order to produce fluorescence intensity related to photosynthetic activity and therefore dependent on pollutant concentration. As detector, an organic photodetector was fabricated using new semiconducting polymers with alternating thieno-[3,4-*b*]-thiophene and benzodithiophene [65] exhibiting a high external quantum efficiency of more than 60 % in the wavelength region of interest.

Herbicide fluorescence measurements performed on Diuron showed high detection sensitivity for concentrations of this herbicide as low as 7.5 nM. Those measurements have been obtained detecting the fluorescence variation of a 1×10^6 cell/ml green algal culture exposed to the contaminated solution.

Among biosensor devices, immunosensors deserve a particular mention as they allow easy arrangement in microarrays leading to multi-analyte determination. In this case the recognition elements are based on the highly specific binding properties of antibodies with antigens.

Immunosensors combined with fluorescence detection allow high detection sensitivity; in particular, TIRF has proved to meet the requirements in environmental trace

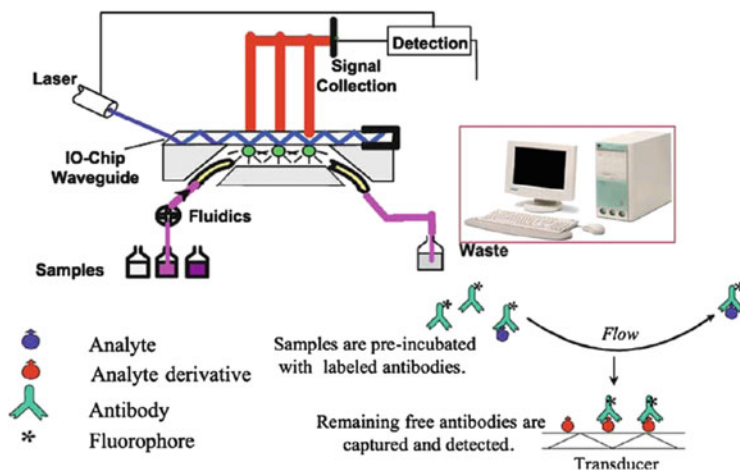


Fig. 8 Setup for TIRF sensing: evanescent field excites fluorophores interacting with immobilized analyte derivatives. The fluorescence light is collected by optical fibres and then is filtered and detected by photodetectors. Reprinted with permission from [66]

analytics [66]. In TIRF sensors, when the condition for total internal reflection takes place, an evanescent field occurs at the interface between two dielectric media. This field decays exponentially into the media of lower refractive index. The excitation light is guided into an optical waveguide and a portion of this radiation will produce an evanescent field able to excite the fluorescence and consequently to interact with the analytes.

In order to avoid non-specific binding, a bulk polymer layer is present at the interface between waveguide and fluidics. This layer is also the basis for immobilized derivatives of analytes to be detected in the sample solution.

By using modern spotting techniques, it is possible to arrange different areas with different immobilized analyte derivatives and therefore, multiple analyte detection is easily accomplished.

Antibodies and sample solution containing different analytes in various concentrations can be mixed by means of a flow injection setup. When labelled antibodies diffuse to the surface of the transducer, they are able to interact with the immobilized analyte derivatives, providing a readout signal which can be guided to the detector, for instance, by means of optical fibres. A schematic working principle is shown in Fig. 8.

High concentration of a specific analyte blocks the related antibody and therefore the corresponding signal will be very low. On the contrary, when the analyte concentration is low, a large number of antibodies are available and then captured, generating a high signal. The corresponding calibration curves will follow a sigmoidal behaviour if the signal is plotted over the concentration in a semi-logarithmic scale.

Two noteworthy examples of microfluidic multi-analyte immunosensor based on TIRF are the River Analyser (RIANA) [67] and the Automated Water Analyser Computer Supported System (AWACSS) [68].

In RIANA system, a laser beam emitting at $\lambda = 633$ nm has been coupled to a glass slide via a bevelled end face and guided through the length of the transducer. Antibodies labelled with Cy5.5 allowed simultaneous detection of estrone, isotopuron and atrazine at the surface by means of a multiplexed binding inhibition assay. The analyte derivative has been immobilized on aminodextran surfaces. Optical fibres and photodiodes have been used to collect the fluorescence signal originated in each evanescent spot. Estrone, isotopuron and atrazine are detected with LOD of 0.08, 0.05 and 0.16 $\mu\text{g/l}$, respectively, taking 15 min for a single run. In a further development of the device [69] four different analytes (atrazine, bisphenol A, estrone and isotopuron) were detected simultaneously in 12 min with an LOD below 0.020 $\mu\text{g/l}$ for all the analytes.

The AWACSS sensor consists of a fibre-pigtailed chip with 32 evanescent field-sensing regions. In this system, laser light is coupled into an optical transducer with chemically modified surface containing a Y-junction splitter structure that generates four parallel waveguides. Analyte-specific antibodies labelled with fluorescent markers (Cy5.5 or Alexa Fluor 680) are incubated with the analyte samples for a short time. Then the solution flows over the transducer, the surface-bound labelled antibodies are excited in the evanescent field and the fluorescence is collected by means of 32 optical fibres and detected using the same number of photodiodes. AWACSS detected simultaneously six different analytes (atrazine, isotopuron, bisphenol A, estrone, propanil and sulfamethizole) with a detection limit for each of them below 0.02 $\mu\text{g/l}$ [70]. Two prototypes of the AWACSS system were designed and constructed and over 20 antibodies and their corresponding analyte derivatives for surface modification were developed.

5 Surface-Enhanced Raman Scattering

Raman spectroscopy is a well-known analytical method able to provide rich information about molecular structure and composition. This technique is based on the Raman effect, an inelastic light scattering between molecules or solids and photons, involving rotational or vibrational transitions. In the Raman process a photon is absorbed to a virtual level; subsequently when the molecule relaxes towards a different rotational or vibrational level a photon is emitted. As this transition involves specific rotational or vibrational levels, those emissions will provide a sort of spectral fingerprint by which the molecule can be identified.

Even though this is a powerful spectroscopic technique, because of its extremely small cross section (typically 10^{-30} to 10^{-25} $\text{cm}^2/\text{molecule}$), Raman scattering process is not suitable to be employed in ultra-sensitive detection method under normal conditions. One of the solutions to overcome this issue is represented by the SERS.

The discovery of SERS [71–73] has allowed enhancing the Raman cross section of a molecule and provided a label-free analytical technique for characterizing molecular structure information. In order to increase Raman signal, SERS takes advantage of the optical properties of nanostructured metal surfaces. By means of incorporation of metallic nanostructures, SERS allows enhancement factors up to 14 orders of magnitude [74] providing sensitivities comparable with fluorescence detection. So far the largest enhancement factor of the Raman signal has been achieved by applying gold, silver and copper nanostructures of 10–100 nm size. The signal improvement is attributed to a strong amplification of the electromagnetic fields near the plasmon resonances of metal substrates [75] and to spatially local effects, which are commonly referred to as chemical enhancement [76–80]. The fast development in the application of SERS has contributed also to progress in microfluidic devices allowing detection of various biological and environmental analytes. The main element in combining SERS with microfluidic devices has been the employment of particular microchannel expressly designed to mix metal nanocolloids with analytes and at the same time able to provide flow rate control. In the last years, Choo's group has demonstrated several successful application of microfluidic devices with SERS detection to the trace analysis of water pollutants.

A specifically shaped microfluidic channel PDMS chip has been applied by Choo's group in combination with SERS detection to the trace analysis of cyanide, which is one of the most hazardous toxic pollutants in groundwaters [81]. In this work, streams of silver colloid and cyanide sample solutions were efficiently mixed in an alligator teeth-shaped channel.

In order to neutralize the cyanide anions, polyamine spermine tetrachloride was used as the agent and this solution was mixed with silver colloids in the alligator teeth-shaped microfluidic channel. As a result, the cyanide anions were effectively adsorbed on silver nanoparticles. Performing measurements using a Raman microscope system, the LOD for cyanide solution was determined to be in the 0.5–1.0 ppb range.

In another work [82] the same group performed a quantitative analysis of methyl parathion pesticides employing a microfluidic device similar to the one previously described. The detection limit found in this case has been 0.1 ppm.

Malachite green, an industrial dye, was successfully detected designing a zigzag-shaped channel to enhance mixing for the detection [83]. Malachite green molecules were more effectively adsorbed onto the silver nanoparticles along the zigzag-shaped microchannel allowing an LOD below 1–2 ppb.

References

1. Manz A, Graber N, Widmer M (1990) Miniaturized total chemical analysis systems: a novel concept for chemical sensing. *Sens Actuators B* 1:244–248
2. Dittrich PS, Manz A (2006) Lab on a chip: microfluidics in drug discovery. *Nat Rev Drug Discov* 5:210–218

3. van den Berg A, Lammerink TSJ (1998) Micro total analysis systems: micro-fluidic aspects, integration concept and applications. In: *Microsystem technology in chemistry and life science*. Springer, Berlin, pp 21–49
4. Mark D, Haeberle S, Roth G, von Stetten F, Zengerle R (2010) Microfluidic lab-on-a-chip platforms: requirements, characteristics and applications. *Chem Soc Rev* 39:1153–1182
5. Squires TM, Quake SR (2005) Microfluidics: fluid physics at the nanoliter scale. *Rev Mod Phys* 77:977–1026
6. Herold KE, Rasooly A (2009) Lab on a chip technology. In: *Fabrication and microfluidics*, vol 1. Caister Academic, Norfolk
7. Jang A, Zou Z, Lee KK, Ahn CH, Bishop PL (2011) State-of-the-art lab chip sensors for environmental water monitoring. *Meas Sci Technol* 22:032001
8. Mogensen KB, Kutter JP (2009) Optical detection in microfluidic systems. *Electrophoresis* 30: S92–S100
9. Ramsden JJ (1999) A sum parameter sensor for water quality. *Wat Res* 33:1147–1150
10. Tangena BH, Janssen PJCM, Tiesjema G, van den Brandhof EJ, Klein Koerkamp M, Verhoef JW, Filippi A, van Delft W (2010) A novel approach for early warning of drinking water contamination events. In: *Proceedings of the 4th international conference on water contamination emergencies: monitoring, understanding, acting*, October 2010
11. Kim N, Park I-S, Kim W-Y (2007) Salmonella detection with a direct-binding optical grating coupler immunosensor. *Sens Actuators B Chem* 121:606–615
12. Cooper IR, Meikle ST, Standen G, Hanlon GW, Santin M (2009) The rapid and specific real-time detection of *Legionella pneumophila* in water samples using optical waveguide lightmode spectroscopy. *J Microbiol Methods* 78:40–44
13. Bier FF, Schmidt RD (1994) Real time analysis of competitive binding using grating coupler immunosensors for pesticide detection. *Biosens Bioelectron* 9:125–130
14. Brecht A, Piehler J, Lang G, Gauglitz G (1995) A direct optical immunosensor for atrazine detection. *Anal Chim Acta* 311:289–299
15. Dostálek J, Homola J (2006) SPR biosensors for environmental monitoring. *Springer Ser Chem Sens Biosens* 4:191–206
16. Gobi KV, Tanaka H, Shoyamac Y, Miura N (2005) Highly sensitive regenerable immunosensor for label-free detection of 2,4-dichlorophenoxyacetic acid at ppb levels by using surface plasmon resonance imaging. *Sens Actuators B* 111–112:562–571
17. Mauriz E, Calle A, Montoya A, Lechuga LM (2006) Determination of environmental organic pollutants with a portable optical immunosensor. *Talanta* 69:359–364
18. Sieben VJ, Floquet CFA, Ogilvie IRG, Mowlem MC, Morgan H (2010) Microfluidic colourimetric chemical analysis system: application to nitrite detection. *Anal Methods* 2:484–491
19. da Rocha ZM, Martinez-Cisneros CS, Seabra AC, Valdés F, Gongora-Rubio MR, Alonso-Chamarro J (2012) Compact and autonomous multiwavelength microanalyzer for in-line and in situ colorimetric determinations. *Lab Chip* 12:109–117
20. Greenway GM, Haswell SJ, Petsul PH (1999) Characterisation of a micro-total analytical system for the determination of nitrite with spectrophotometric detection. *Anal Chim Acta* 387:1–10
21. Rainelli A, Stratz R, Schweizer K, Hauser PC (2003) Miniature flow-injection analysis manifold created by micromilling. *Talanta* 61:659–665
22. Cleary J, Slater C, McGraw C, Diamond D (2008) An autonomous microfluidic sensor for phosphate: on-site analysis of treated wastewater. *IEEE Sens J* 8:508–519
23. Daykin RNC, Haswell SJ (1995) Development of a micro flow injection manifold for the determination of orthophosphate. *Anal Chim Acta* 313:155–159
24. Daridon A, Sequeria M, Pennarum-Thomas G, Dirac H, Krog JP, Gravesen P, Lichtenberg J, Diamond D, Verpoorte E, de Rooij NF (2001) Chemical sensing using an integrated microfluidic system based on the Berthelot reaction. *Sens Actuator B* 76:235–243

25. Ehrfeld W, Golbig K, Hessel V, Löwe H, Richter T (1999) Characterization of mixing in micromixers by a test reaction: single mixing units and mixer arrays. *Ind Eng Chem Res* 38:1075–1082
26. Liu RH, Stremmer MA, Sharp KV, Olsen MG, Santiago JG, Adrian RJ, Aref H, Beebe DJ (2000) Passive mixing in a three-dimensional serpentine microchannel. *J Microelectromech Syst* 9:190–197
27. del Mar Baeza M, Ibanez-Garcia N, Baucells J, Bartrolí J, Alonso J (2006) Microflow injection system based on a multicommutation technique for nitrite determination in wastewaters. *Analyst* 131:1109–1115
28. O'Toole M, Lau KT, Diamon D (2005) Photometric detection in flow analysis systems using integrated PEDDs. *Talanta* 66:1340–1344
29. O'Toole M, Lau KT, Shepherd R, Slater C, Diamon D (2007) Determination of phosphate using a highly sensitive paired emitter–detector diode photometric flow detector. *Anal Chim Acta* 597:290–294
30. Rodrigues ERGO, Lapa RAS (2009) Development of micro-flow devices by direct-milling on poly(methyl methacrylate) substrates with integrated optical detection. *Microchim Acta* 166:189–195
31. Cleary J, Slater C, Diamond D (2007) Field-deployable microfluidic sensor for phosphate in natural waters. In: *IEEE sensors conference, Atlanta, 28–31 October 2007*, pp 1001–1004
32. Koch CR, Ingle JD, Remcho VT (2008) Miniaturizing the whole device: micrototal-analysis system for in-situ colorimetric water quality monitoring. In: *Twelfth international conference on miniaturized systems for chemistry and life sciences, San Diego, 12–16 October 2008*, pp 1900–1903
33. Sollier E, Murray C, Maoddi P, Di Carlo D (2011) Rapid proto-typing polymers for microfluidic devices and high pressure injections. *Lab Chip* 11:3752–3765
34. McGraw CM, Stitzel SE, Cleary J, Slater C, Diamond D (2007) Autonomous microfluidic system for phosphate detection. *Talanta* 71:1180–1185
35. Bowden M, Diamond D (2003) The determination of phosphorus in a microfluidic manifold demonstrating long-term reagent lifetime and chemical stability utilising a colorimetric method. *Sens Actuator B* 90:170–174
36. Auroux PA, Iossifidis D, Reyes DR, Manz A (2002) Micro total analysis systems. 2. Analytical standard operations and applications. *Anal Chem* 74:2637–2652
37. Fu JL, Fang Q, Zhang T, Jin XH, Fang ZL (2006) Laser-induced fluorescence detection system for microfluidic chips based on an orthogonal optical arrangement. *Anal Chem* 78:3827–3834
38. Johnson ME, Landers JP (2004) Fundamentals and practice for ultrasensitive laser-induced fluorescence detection in microanalytical system. *Electrophoresis* 25:3513–3527
39. Persichetti G, Testa G, Bernini R (2013) High sensitivity UV fluorescence spectroscopy based on an optofluidic jet waveguide. *Opt Express* 20:24219–24230
40. Bao N, Jagadeesan B, Bhunia AK, Yao Y, Lu C (2008) Quantification of bacterial cells based on autofluorescence on a microfluidic platform. *J Chromatogr A* 1181:153–158
41. Leblanc L, Dufour E (2002) Monitoring the identity of bacteria using their intrinsic fluorescence. *FEMS Microbiol Lett* 211:147–153
42. Patra D (2003) Applications and new developments in fluorescence spectroscopic techniques for the analysis of polycyclic aromatic hydrocarbons. *Appl Spectrosc Rev* 38:155–185
43. Chung TD, Kim HC (2007) Recent advances in miniaturized microfluidic flow cytometry for clinical use. *Electrophoresis* 28:4511–4520
44. Liu P, Meagher RJ, Light YK, Yilmaz S, Chakraborty R, Arkin AP, Hazen TC, Singh AK (2011) Microfluidic fluorescence in situ hybridization and flow cytometry (μ FlowFISH). *Lab Chip* 11:2673–2679
45. Bernini R, De Nuccio E, Brescia F, Minardo A, Zeni L, Sarro PM, Palumbo R, Scarfi MR (2006) Development and characterization of an integrated silicon micro flow cytometer. *Anal Bioanal Chem* 386:1267–1272

46. Jha AK, Tripathi A, Bose A (2011) A microfluidic device for bacteria detection in aqueous samples. *Environ Technol* 32:1661–1667
47. Inatomi KI, Izuo SI, Lee SS (2006) Application of a microfluidic device for counting of bacteria. *Lett Appl Microbiol* 43:296–300
48. Jepras RI, Carter J, Pearson SC, Paul EF, Wilkinson MJ (1995) Development of a robust flow cytometric assay for determining numbers of viable bacteria. *Appl Environ Microbiol* 61:2696–2701
49. Lebaron P, Parthuisot N, Catala P (1998) Comparison of blue nucleic acid dyes for flow cytometric enumeration of bacteria in aquatic systems. *Appl Environ Microbiol* 72:87–95
50. Parthuisot N, Catala P, Lebaron P, Clermont D, Bizet C (2003) A sensitive and rapid method to determine the viability of freeze-dried bacterial cells. *Lett Appl Microbiol* 36:412–417
51. Billinton N, Knight AW (2001) Seeing the wood through the trees: a review of techniques for distinguishing green fluorescent protein from endogenous autofluorescence. *Anal Biochem* 291:175–197
52. Marco MP, Barceló D (1996) Environmental application of analytical biosensors. *Meas Sci Technol* 7:1547–1562
53. Rogers KR (1998) Biosensor technology for environmental measurement. In: Meyers RA (ed) *Encyclopedia of environmental analysis and remediation*. Wiley, New York
54. Mallat E, Barceló D, Barzen C, Gauglitz G, Abuknesha R (2001) Immunosensors for pesticide determination in natural waters. *Trends Anal Chem* 20:124–132
55. Rodriguez-Mozaz S, Lopez de Alda MJ, Marco MP, Barceló D (2005) Biosensors for environmental monitoring: a global perspective. *Talanta* 65:291–297
56. Rodriguez-Mozaz S, Marco M-P, Lopez de Alda MJ, Barceló D (2004) Biosensors for environmental applications: future development trends. *Pure Appl Chem* 76:723–752
57. Breaker RR, Joyce GF (1994) A DNA enzyme that cleaves RNA. *Chem Biol* 1:223–229
58. Breaker RR (1997) DNA enzymes. *Nat Biotechnol* 15:427–431
59. Liu J, Lu Y (2003) A colorimetric lead biosensor using DNzyme directed assembly of gold nanoparticles. *J Am Chem Soc* 125:6642–6643
60. Chang IH, Tulock JJ, Liu J, Kim WS, Cannon DM Jr, Lu Y, Bohn PW, Sweedler JV, Croperk DM (2005) Miniaturized lead sensor based on lead-specific DNzyme in a nanocapillary interconnected microfluidic device. *Environ Sci Technol* 39:3756–3761
61. Theytaz J, Braschler T, van Lintel H, Renaud P, Diesel E, Merulla D, van der Meer J (2009) Biochip with *E. coli* bacteria for detection of arsenic in drinking water. *Procedia Chem* 1:1003–1006
62. Stocker J, Balluch D, Gsell M, Harms H, Feliciano J, Daunert S, Malik KA, van der Meer JR (2003) Development of a set of simple bacterial biosensors for quantitative and rapid measurements of arsenite and arsenate in potable water. *Environ Sci Technol* 37:4743–4750
63. Juneau P, El Berdey A, Popovic R (2002) PAM fluorometry in the determination of the sensitivity of *Chlorella vulgaris*, *Selenastrum capricornutum*, and *Chlamydomonas reinhardtii* to copper. *Arch Environ Contam Toxicol* 42:155–164
64. Lefevre F, Chalifour A, Yu L, Chodavarapu V, Juneau P, Izquierdo R (2012) Algal fluorescence sensor integrated into a microfluidic chip for water pollutant detection. *Lab Chip* 12:787–793
65. Liang Y, Yu L (2010) A new class of semiconducting polymers for bulk heterojunction solar cells with exceptionally high performance. *Acc Chem Res* 43:1227–1236
66. Gauglitz G, Proll G (2008) Total internal reflection fluorescence sensing – quality assurance and application to water analysis. In: Resch-Genger U (ed) *Standardization and quality assurance in fluorescence measurements I*, vol 5, Springer series on fluorescence. Springer-Verlag Berlin, Heidelberg, pp 415–428
67. Rodriguez-Mozaz S, Reder S, Lopez de Alda M, Gauglitz G, Barcelo D (2004) Simultaneous multi-analyte determination of estrone, isoproturon and atrazine in natural waters by the RIVER ANALyser (RIANA), an optical immunosensor. *Biosens Bioelectron* 19:633–640
68. Tschmelak J, Proll G, Riedt J, Kaiser J, Kraemmer P, Barzaga L, Wilkinson JS, Hua P, Hole JP, Nudd R, Jackson M, Abuknesha R, Barceló D, Rodriguez-Mozaz S, Lopez de Alda MJ, Sacher F,

- Stien J, Slobodnik J, Oswald P, Kozmenko H, Korenkova E, Tothova L, Krascenits Z, Gauglitz G (2005) Automated water analyser computer supported system (AWACSS). Part I: project objectives, basic technology, immunoassay development, software design and networking. *Biosens Bioelectron* 20:1499–1508
69. Tschmelak J, Proll G, Gauglitz G (2004) Verification of performance with the automated direct optical TIRF immunosensor (river analyser) in single and multi-analyte assays with real water samples. *Biosens Bioelectron* 20:743–752
70. Tschmelak J, Proll G, Riedt J, Kaiser J, Kraemmer P, Barzaga L, Wilkinson JS, Hua P, Hole JP, Nudd R, Jackson M, Abuknesha R, Barceló D, Rodriguez-Mozaz S, Lopez de Alda MJ, Sacher F, Stien J, Slobodnik J, Oswald P, Kozmenko H, Korenkova E, Tothova L, Krascenits Z, Gauglitz G (2005) Automated water analyser computer supported system (AWACSS). Part II: intelligent, remote-controlled, cost-effective, on-line, water-monitoring measurement system. *Biosens Bioelectron* 20:1509–1519
71. Fleischmann M, Hendra PJ, McQuillan AJ (1974) Raman spectra of pyridine adsorbed at a silver electrode. *Chem Phys Lett* 26:163–166
72. Jeanmaire DL, Van Duyne RP (1977) Surface Raman spectroelectrochemistry: part I. Heterocyclic, aromatic, and aliphatic amines adsorbed on the anodized silver electrode. *J Electroanal Chem Interfacial Electrochem* 84:1–20
73. Grant AM, Creighton JA (1977) Anomalous intense Raman spectra of pyridine at a silver electrode. *J Am Chem Soc* 99:5215–5217
74. Kneipp K, Kneipp H, Itzkan I, Dasari RR, Michael MS (2002) Ultrasensitive chemical analysis by Raman spectroscopy. *J Phys Condens Matter* 14:R597–R624
75. Stiles PL, Dieringer JA, Shah NC, Van Duyne RP (2008) Surface-enhanced Raman spectroscopy. *Annu Rev Anal Chem* 1:601–626
76. Persson BNJ (1981) On the theory of surface-enhanced Raman scattering. *Chem Phys Lett* 82:561–565
77. Lombardi JR, Birke RL, Lu T, Xu J (1986) Charge-transfer theory of surface enhanced Raman spectroscopy: Herzberg–Teller contributions. *J Chem Phys* 84:4174–4180
78. Zhao L, Jensen L, Schatz GC (2006) Pyridine-Ag₂₀ cluster: a model system for studying surface-enhanced Raman scattering. *J Am Chem Soc* 128:2911–2919
79. Saikin SK, Olivares-Amaya R, Rappoport D, Stopa M, Aspuru-Guzik A (2009) On the chemical bonding effects in the Raman response: benzenethiol adsorbed on silver clusters. *Phys Chem Chem Phys* 11:9401–9411
80. Alexson DA, Badescu SC, Glembocki OJ, Prokes SM, Rendell RW (2009) Metal-adsorbate hybridized electronic states and their impact on surface enhanced Raman scattering. *Chem Phys Lett* 477:144–149
81. Yea K, Lee S, Kyong JB, Choo J, Lee EK, Joo S-W, Lee S (2005) Ultra-sensitive trace analysis of cyanide water pollutant in a PDMS microfluidic channel using surface-enhanced Raman spectroscopy. *Analyst* 130:1009–1011
82. Lee D, Lee S, Seong GH, Choo J, Lee EK, Gweon DG, Lee S (2006) Quantitative analysis of methyl parathion pesticides in a polydimethylsiloxane microfluidic channel using confocal surface-enhanced Raman spectroscopy. *Appl Spectrosc* 60:373–377
83. Lee S, Choi J, Chen L, Park B, Kyong JB, Seong GH, Choo J, Lee Y, Shin KH, Lee EK, Joo SW, Lee KH (2007) Fast and sensitive trace analysis of malachite green using a surface-enhanced Raman microfluidic sensor. *Anal Chim Acta* 590:139–144

Non-conventional Electrochemical and Optical Sensor Systems

Corrado Di Natale, Francesca Dini, and Andrea Scozzari

Abstract Electroanalytical methods are a common tool for the assessment of chemical peculiarities of aqueous solutions. Also, the analysis of water based on optical sensors is a mature field of research, which already led to industrial applications and standard laboratory practices. Nevertheless, scientific literature is still offering new sensor techniques and innovative measurement approaches in both fields. In particular, for fast characterisation of liquids and change detection applications in a continuous monitoring context, the technology of taste sensors based on electrochemical techniques is still witnessing a growing interest. Such devices are often defined as “electronic tongues” or “e-tongues”. In addition, emerging inexpensive and portable devices with optical-sensing capabilities can be used for monitoring applications with a novel approach. This chapter gives an overview of recent techniques developed in both fields and presents several potential applications and case studies that deal with the context of water quality assessment. A brief introduction about the basics of each measurement technology, even if not exhaustive, is also provided.

Keywords Computer screen photo-assisted technique, Drinking water, Electrochemistry, Electronic tongue, Optical sensors

C. Di Natale and F. Dini
Department of Electronic Engineering, University of Rome Tor Vergata, Rome, Italy
e-mail: dinatale@uniroma2.it

A. Scozzari (✉)
CNR Institute of Information Science and Technologies (CNR-ISTI), Via Moruzzi 1, 56124
Pisa, Italy
e-mail: a.scozzari@isti.cnr.it

Contents

1	Introduction	280
2	E-Tongue Based on Potentiometric Arrays	282
2.1	Fundamentals of Potentiometry	282
2.2	A Common Application in the Context of Water Quality: Characterisation of Mineral Waters	285
3	E-Tongue Based on Voltammetry	287
3.1	Fundamentals of Voltammetry	288
3.2	Sensors Used for Water Applications	291
3.3	Signal Processing	293
3.4	A View on Commonly Presented Applications in the Context of Water Quality ..	296
4	Optical Detection	300
4.1	Principles of Chemical Detection in Optics	300
4.2	The Computer Screen Photo-Assisted Technique	303
4.3	CSPT Measurements	304
4.4	Case Study: The Detection of Natural Cr(VI) with a CSPT Setup	306
5	Conclusions	308
	References	309

Abbreviations

CSPT	Computer screen photo-assisted technique
HPCA	Hierarchical PCA
ISE	Ion-selective electrode
LAPV	Large amplitude pulse voltammetry
MLAPS	Multiple light-addressable potentiometric sensor
PCA	Principal components analysis
REF	Reference electrode
ST	Slantnet transform
WE	Working electrode

1 Introduction

Monitoring technologies take an essential role in the implementation of innovative and integrated techniques for the sustainable management of groundwater resources. As a general idea, the information coming from traditional field instrumentation, typically providing the main physical/chemical parameters of water, is inadequate to fully assess the quality of water destined to human consumption. On the other hand, a complete laboratory analytical measurement is expensive and does not provide continuous control over the resource.

There is an expanding interest in multi-sensor systems for the assessment of general attributes of a process under monitoring, which are applicable to various environmental contexts. Such devices are generally based on the technology of taste sensors developed in the research framework of biomimetic systems. Acceleration in the advancement of this field has been done during the last 2 decades. In fact,

there are now fairly mature, low-cost and attractive technologies that can produce overall quality indicators of a natural resource in a non-conventional manner.

This chapter gives an overview of non-conventional electrochemical and optical measurement approaches, which have been proposed in the literature in the framework of multi-sensor systems for wet-chemical applications. Systems based on these principles are often referred to as “electronic tongues” or “e-tongues” [1–4]. As a general idea, the combination of non-specific and even overlapping sensor responses (which are often very informative) can address the issue of extracting aggregate chemical information, useful to characterise the liquid under measurement. Electronic tongues can actually be used as taste sensors, but, more generally, they can be applied to a broader context where the human taste is not necessarily involved.

A high number of e-tongues have been described in the literature, based on different measurement techniques, such as potentiometry with ion-selective electrodes (ISE), lipid/polymer membranes, SH-SAW (shear horizontal surface acoustic wave) devices, spectrophotometry and voltammetry. Among this diversity of measurement techniques, most of the proposed approaches are based on electrochemical methods.

Behind the somewhat misleading terms “electronic tongue” and “taste sensor”, one finds some kind of array of sensors. The sensor array in these systems produces signals, which are not necessarily selective to any particular species in the measured sample, but a signal pattern (often a large dataset) is generated, which can be related to some chemical/physical features of the sample. In this particular framework, electrochemical methods are probably among the oldest measurement techniques and also comprise a very wide range of analytical possibilities, enriched by relatively recent developments in signal processing, sensors manufacturing and front-end electronic systems [5].

For what regards electrochemical techniques, potentiometry is the fundamental principle of e-tongues based on arrays of ISE. The proposed devices are essentially based on the cross-selectivity between electrodes that are made sensitive to different ion species [2, 4]. Further explanation about this class of devices is given in Sect. 2 of this chapter.

Another class of electrochemical techniques used in the context of e-tongues is represented by voltammetry. Voltammetry is a group of electroanalytical methods in which information about the analyte is derived from the measurement of a current flowing in a polarised working electrode, as a function of an imposed potential between such electrode and a reference [2, 5]. Further explanation about this class of devices is given in Sect. 3 of this chapter.

Deep theoretical explanations about the working principles of potentiometry and voltammetry can be found in Bard and Faulkner [6] and Janata [7].

Among the relatively wide literature available, applications of these techniques to water classification and change detection purposes can be found in Di Natale et al. [8], Winquist et al. [9], Legin et al. [10], Paolesse et al. [11], Ciosek et al. [12], Lvova et al. [13], Scozzari [14] and Scozzari et al. [15]. It must be noted that even the combination between potentiometry and voltammetry has been proposed in the literature with promising results. As an example, in Men et al. [16], the authors combine a multiple light-addressable potentiometric sensor (MLAPS)

with stripping voltammetry, in order to improve the detection capability of heavy metals in wastewater or seawater.

Finally, this chapter introduces non-conventional optical sensor systems, having the capability to provide overall information about the quality of water, in the perspective of low-cost monitoring systems easy to deploy and use. Recent findings demonstrated the analytical capabilities of a regular computer screen with a web camera for detecting and recognising different molecules with an inexpensive (and eventually disposable) optical-sensing interface. This technique can also potentially enable common devices like mobile phones to act as a particular kind of water quality sensors. This class of devices will be discussed in Sect. 4.

2 E-Tongue Based on Potentiometric Arrays

2.1 Fundamentals of Potentiometry

In potentiometry, the potential of an electrochemical cell is measured in static conditions. The advantage of this approach is that since no current flows the composition of the solution remains unaltered.

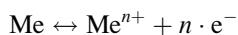
The electrochemical cell is in principle formed by two semi-cells each containing an electrode immersed in an ionic solution. Typically one of the two cells is a reference cell where a standard solution maintains the immersed electrode to a constant potential. The other cell is the working cell where the working electrode is in contact with the solution to be measured. The electrical continuity between the two cells is maintained by a salt bridge containing an inert electrolyte (e.g. KCl) and terminated by porous glasses. A schematic picture of a standard electrochemical cell is shown in Fig. 1.

The potential of the electrochemical cell is given by

$$E_{\text{CELL}} = E_{\text{C}} - E_{\text{REF}}$$

where E_{C} and E_{REF} are the reduction potentials of the reactions occurring at both electrodes. These potentials are a function of the ionic species in equilibrium with the electrode. The relationship is given by the Nernst equation.

The Nernst equation can be demonstrated in different conditions. For instance in the case of a metal electrode aimed at measuring the concentration of ions of the same metal (the so-called electrode of the first kind) the electrode potential can be derived from a simple thermodynamical approach. Let us consider the following reaction occurring at the metal surface where atoms of the metal flow in ionic form into the solution leaving an excess of electrons in the solid and ions from the solution recombine with the electrode electrons:



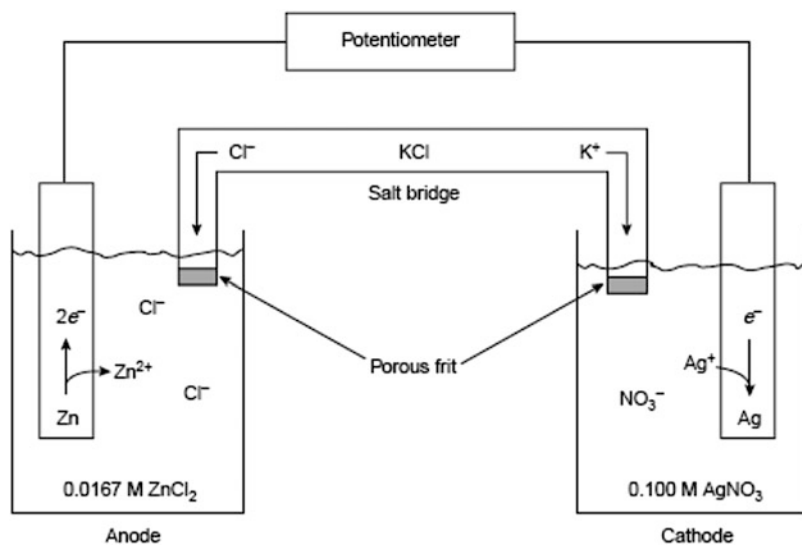


Fig. 1 Schematic view of a general electrochemical cell for potentiometric analysis

The free energies of reagent and products are

$$G_{\text{Me}} = G_{0,\text{Me}} + RT \cdot \ln(a_{\text{Me}}); \quad G_{\text{Me}^{n+}} = G_{0,\text{Me}^{n+}} + RT \cdot \ln(a_{\text{Me}^{n+}})$$

Noteworthy, the concentration of the species is replaced by a quantity called activity. The activity takes into account the screening effects of polar and charged molecules in solution. The activity is proportional to the concentration ($a = \gamma \cdot C$), where in many practical applications γ is very close to one.

The change of free energy is equal to the electric work necessary for the reaction

$$\begin{aligned} -L &= -Q \cdot V = G_{\text{Me}^{n+}} - G_{0,\text{Me}} = (G_{0,\text{Me}^{n+}} - G_{0,\text{Me}}) + RT \cdot \ln \frac{a_{\text{Me}^{n+}}}{a_{\text{Me}}} \\ &= G_0 + RT \cdot \ln \frac{a_{\text{Me}^{n+}}}{a_{\text{Me}}} \end{aligned}$$

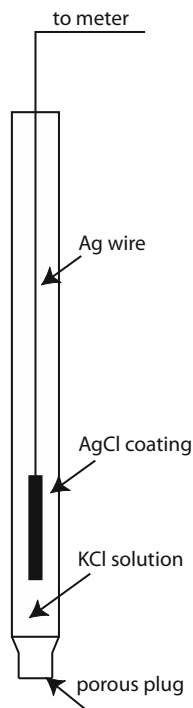
where Q is the involved charge and V is the electrode potential with respect to the solution. A convenient way to calculate the charge is the Faraday constant that is defined as the charge of a mole of electrons ($1 \text{ F} = 96,485 \text{ C/mol}$).

For sensor applications, the ionic species in the solution is the analyte of interest, and $a_{\text{Me}^{n+}}$ is the object of the measure. Considering that the activity of a pure solid, such as a metal, is equal to one, the electrode potential is given by

$$V = -\frac{G_0}{nF} - \frac{RT}{nF} \cdot \ln(a_{\text{Me}^{n+}})$$

For practical reasons, the natural logarithm is replaced by the logarithm in base 10 and then the Nernst equation is written as

Fig. 2 Simple drawing of an Ag/AgCl reference electrode. One of the semi-cells and the salt bridge of Fig. 1 are contained in this element



$$V = V_0 - K \cdot \log(a_{\text{Me}^{n+}})$$

where $K \sim 59$ mV/decade is the Nernst constant.

In order to measure the potential V , a reference electrode whose potential is a stable reference independent of the analyte and the composition of the solution is necessary. This is provided by reference electrodes, such as the Ag/AgCl electrode. This is a silver electrode coated by a layer of AgCl and immersed in a solution of KCl. The electrode potential can be modulated by adjusting the KCl solution. Figure 2 shows a standard Ag/AgCl electrode; the KCl solution provides also the saline bridge and the glass enclosure is terminated by a porous frit. A reference electrode based on Ag/AgCl can also be prepared with screen-printed technology giving rise to a miniaturised element that can be conveniently used in small and robust sensor systems [17].

The potentiometric measurement requires the use of an amplifier with a virtually infinite input resistance. These conditions cannot be met in practice, but for the scope a number of amplifiers with very large input resistance are available. Particularly suitable to the scope is the so-called instrumentation amplifier. This is a particular amplifier provided by a differential input, suitable for making differential voltage measurements. The input stages of these devices must exhibit low current losses and high impedance, as it is a typical requirement for electrometric applications.

The input current, which is the leakage current flowing into the electrochemical cell, is typically of the order of femtoamperes.

Electrodes sensitive to a wide variety of ionic compounds are currently available. However, the selectivity of these sensors is not absolute. Selectivity is a great concern in practical applications, where the exact composition of the sample is not known a priori, and then the target analyte can be in a mixture with a large number of interfering compounds.

The selectivity of an ISE is described by the Nikolsky equation, where the sensitivity to the primary ion is compared with the sensitivity to the interferents:

$$V = V_0 - 2.303 \cdot \frac{RT}{nF} \cdot \log \left[a_A + \sum_i K_{A,i} \cdot a_i^{n_A/n_i} \right]$$

where a_A is the activity of the primary ion, namely, the species for which the dominant sensitivity is found. The effect of the i -th interferent is weighted by the coefficient $K_{A,i}$ that is the selectivity coefficient, namely, the ratio of sensitivity to the i -th species with respect to the primary ion; a_i is the activity of the i -th interferent and n_A and n_i are the charge numbers of the primary ion and the interferent, respectively.

In a multi-ion environment the behaviour of the electrode potential is no longer explained by the Nikolsij equation and the estimation of the concentration of ions becomes uncertain.

In these conditions, it is advantageous to release the concept of selective sensors and to approach the concept of sensor array [18]. This is an experimental procedure based on an array of partially selective sensors coupled with a multivariate analysis algorithm. This procedure stems from the so-called electronic noses, namely, arrays of gas sensors mimicking the behaviour of olfaction [19]. In the 1990s, this concept has been transferred also to sensors operated in solution, giving rise to the so-called electronic tongue. Potentiometric electronic tongues have been developed using different materials such as lipidic membranes [20], chalcogenide glasses [21], metals [13], polymers [22] and porphyrins [11], among others.

2.2 A Common Application in the Context of Water Quality: Characterisation of Mineral Waters

As an example of application we report here the usage of a large array of 29 sensors for the characterisation of mineral waters [10]. Materials of the sensors were chalcogenide glass and PVC membranes, specifically designed in order to have an enhanced cross-selectivity. They were complemented by conventional ISE such as pH glass electrode, sodium- and chloride-selective sensors. All measurements were performed versus a conventional Ag/AgCl reference electrode.

The measurements have been made with 6 Italian bottled mineral waters (Levissima, Fiuggi, Sangemini, Oliveto, San Pellegrino and Ferrarelle) and the

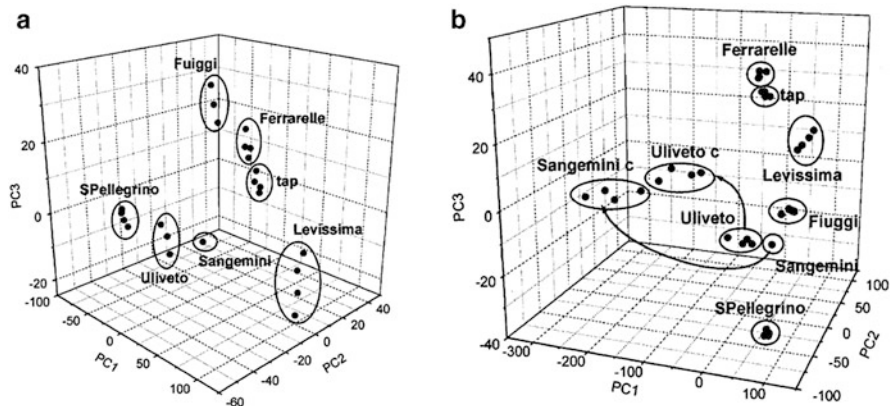


Fig. 3 (a) PCA scores plot of mineral and tap waters. (b) PCA scores plot of the same samples of (a), but completed with two mineral waters added with an amount of organic material; the deviation, occurring along PC1, suggests the high sensitivity of the whole array to organic compounds dissolved in water [10]

tap water from Rome water supply. All waters were bought over the counter. Some of the waters were sparkling ones. The excess of CO_2 was removed by an intensive long stirring before the measurements. Discrimination of the different kinds of mineral waters using the electronic tongue is shown as a principal components analysis (PCA) score plot in Fig. 3.

All the samples can be easily distinguished with the help of the whole array of 29 sensors, but a smaller sub-array, including 5 sensors, appeared to be enough for reliable classification, which is shown in Fig. 3a.

At the second stage pieces of strawberry (4 g of fruit per 1 L) were introduced into the bottles of two different mineral waters (Sangemini and Ulliveto) and kept for 4 days. This experiment was carried out as an illustration of the ability of the device to detect some chemical and/or biological disturbance in the analysed sample. Results are shown in Fig. 3b. The samples of the mineral water to be contaminated were chosen randomly as well as the pollutant itself; thus, it was possible to conclude that any contaminated water can be distinguished from any pure one belonging to this test set, by using the electronic tongue. This is true at least for the variety of waters studied, but, taking into account that the chosen water samples represent a wide range of possible combinations, the results are likely to be universal.

Besides qualitative recognition of the mineral waters, the quantitative analysis of the content of their components has been experimented by the potentiometric electronic tongue. The concentration of some species, e.g. some ions, can be determined conventionally using ISE, such as pH, fluoride-, chloride-, sodium- and potassium-selective electrodes, etc. Using the electronic tongue approach all these ions can be measured simultaneously with a multicomponent approach [8]. Moreover, it is also possible to determine the components for which no highly

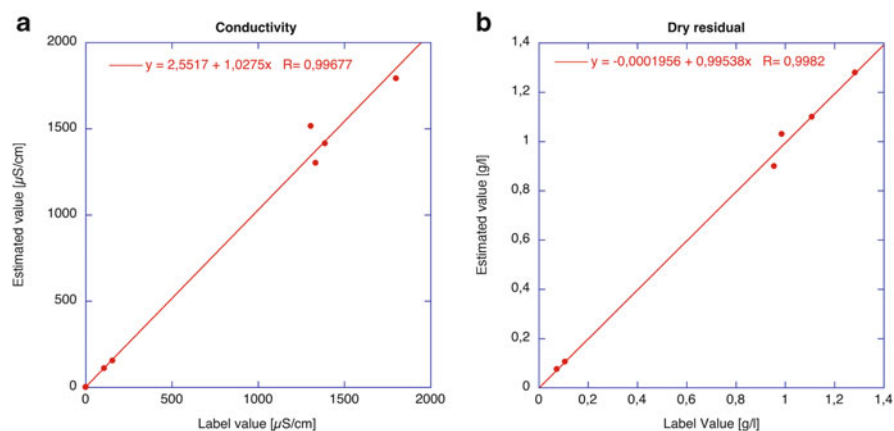


Fig. 4 Scatter plots showing the estimation of conductivity (a) and dry residuals (b) from the electronic tongue data

selective electrodes are known, e.g. HCO_3^- . We have also tried to estimate some characteristics of the mineral waters that usually cannot be measured by ion-selective chemical sensors: conductivity, dry residual and SiO_2 content. The results of quantitative determination of these parameters are summarised in the scatter plots of Fig. 4. All the parameters can be measured with reasonable precision. Thus, using the potentiometric electronic tongue, it is possible to determine a set of values necessary for the standard characterisation of the drinkable water quality in a single measurement.

3 E-Tongue Based on Voltammetry

During the late 1990s, voltammetry has been proposed as a possible tool for the characterisation of liquids with a non-conventional chemometric approach [9, 23, 24]. Actually, it is a mature sensor technique, which fundamentals come from the early twentieth century, and has been accepted as a standard technique in the mid of the century.

Information about the controlled potential microelectrode techniques is given here at an introductory level, to allow the reader to have an adequate understanding of the methods presented in this chapter. Deep theoretical texts about the fundamentals of electrochemical methods, and specifically about voltammetry, can be found in the cited literature.

The next subsections will illustrate the working principles of e-tongues based on voltammetry and their specific methodological approach.

3.1 *Fundamentals of Voltammetry*

Nernst's intuition about the feasibility of some electrochemical analogy of the light spectral analysis methods found its first tangible embodiment in the conception of the polarographic technique [25, 26] presented by Jaroslav Heyrovsky at the meeting of the Faraday Society, held in November 1923. Heyrovsky has shown that a "polarised drop of a mercury capillary cathode represents a reversible state of equilibrium", in order to achieve a truly reproducible measurement by the current–voltage diagrams obtained in polarisation experiments.

The first textbooks and data about polarographic methods have been produced across the World War II period, being substantially recognised as a standard technique in the mid of the century, when polarographic data were presented as laboratory standard datasets, such as the one presented by Semerano and Griggio [27].

The first potentiostat presented by Hickling during 1942 was a substantial step forward in the exploitation of the analytical possibilities offered by polarographic methods and voltammetry in general [28]. Hickling already perceived that "a device whereby the potential of a working electrode can be fixed at any desired arbitrary value would seem to have many valuable applications in the exploration of electrolytic processes". It was the beginning of the controlled potential microelectrode techniques.

Technological advances in the 1960s–1970s led to the commercial development of laboratory devices based on voltammetry, and a variety of standard methods have been rapidly proposed in the literature and rated as affordable by the science community.

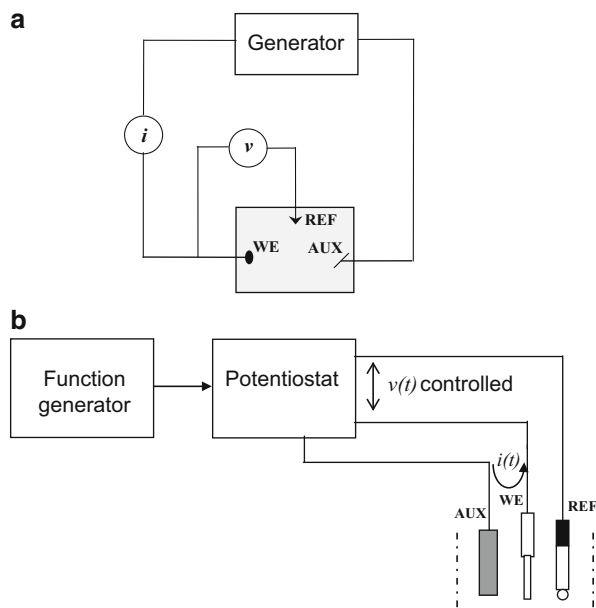
Nowadays, with the aid of a suitable signal processing methodology, voltammetry represents an interesting option for the continuous monitoring of a process, thanks to its very low analytical limits and to the large amount of data that it is possible to obtain, particularly with "pulse polarography" experiments.

In voltammetry, the information about the analyte is obtained by measuring the current flowing through a polarised working electrode (WE), given an imposed voltage between WE and a reference electrode (REF). That is, the WE potential (calculated with respect to REF) is forced to follow a predetermined program or waveshape, and the current i is measured as a function of the applied potential or as a function of time. The electronic device that implements such concept is called "potentiostat" [2, 5, 15, 28].

In the most common 3-electrode implementations, the potentiostat is a device which injects current into an auxiliary electrode (AUX), closing the current loop via a working electrode (WE), in order to impose a known difference of potential between WE and a reference electrode (REF). Such voltage has to be measured with a high impedance differential amplifier, to make negligible the current going through REF. Figure 5a, b shows a generic cell configuration and a simplified schematic diagram of an experimental system for voltammetry, respectively.

The voltage imposed across WE and REF is supposed to be determined by a function generator placed at the input of the potentiostat. The experimental observation

Fig. 5 (a) Generic three-electrode cell configuration; (b) simplified schematic diagram of an experimental system



that is obtained from each measurement session is the response of the potentiostat-cell system to the excitation signal (voltage) used, that is, the loop current $i(t)$.

Thus, the electrochemical behaviour of a system can be determined by imposing known varying potentials between WE and REF and recording either the current–voltage curve (voltammogram) or its current-time version (chronoamperogram), which are obtained in each experiment.

Among the wide literature that is available to probe further into this class of techniques, the fundamentals about electrochemical methods, and specifically about square-wave voltammetry, can be found in Bard and Faulkner [6], Korthum [29] and Mirceski et al. [30].

The different activation overpotential levels, diffusion coefficients and mass-transfer limits that are exhibited by each species in a solution generate a different contribution to the complex voltammogram obtained; the shape of such contribution depends also on the waveform of the excitation signal.

There is a wide range of possible implementations of measurement methods based on voltammetry, according to the type and material of the working electrodes (i.e. solid metal microelectrodes, dropping mercury, planar rotating discs, carbon electrodes, etc.) and according to the particular electrochemical experiment that implies a different program imposed by the generator (i.e. the excitation signal).

It is known that a very informative electrochemical signature of a liquid sample can be obtained by applying a series of square-shaped pulses having different amplitudes as $v(t)$ and recording the obtained current versus time curve, i.e. $i(t)$. More specifically, the usage of pulse voltammetry has been presented in different contexts [9, 15, 31] as an efficient sensor technique for classification and

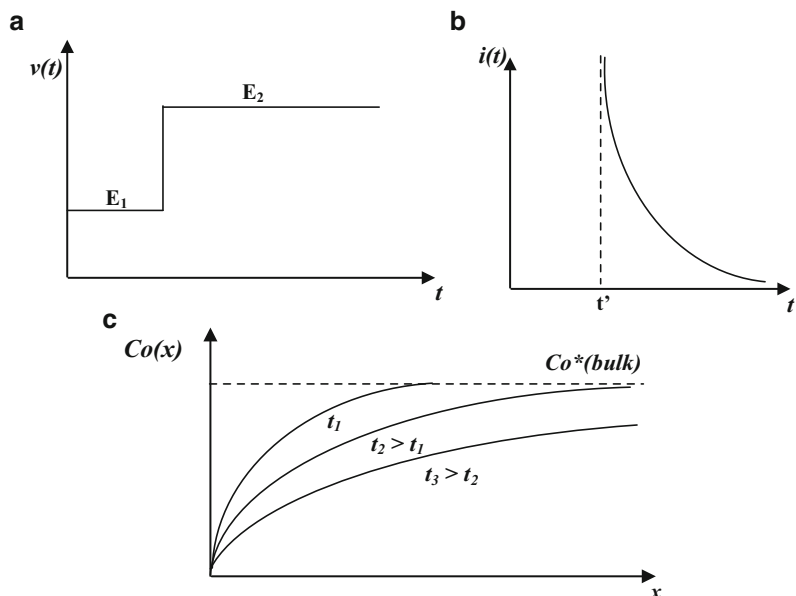


Fig. 6 (a) Excitation signal waveform for the basic step experiment; (b) $i(t)$ for the step experiment; (c) concentration profiles at various times

characterisation purposes. In particular, the cited literature proposes excitation signals consisting in a series of rectangular pulses modulated by ramps, both in offset and in amplitude, depending on the peculiarities of the specific methods.

When the applied wavelshape is a step signal, such as the one shown in Fig. 6a, the obtained response depends on the levels of the applied potential. Under the hypothesis that there is only one dissolved species and that it is electrochemically inactive at potential E_1 but reduced at potential E_2 , a typical response of the experimental system would be the one shown in Fig. 6b. In fact, the electroactive species eliminated (reduced) at the WE produces a concentration gradient in the proximity of such electrode, such as the one shown in Fig. 6c.

Moreover, it is known [6, 29] that the flux (thus the current) is proportional to the concentration gradient; thus, the decay of $i(t)$ is basically due to the fact that the flux causes the depletion volume to thicken. The slope of the concentration profile $Co(x)$ from the WE surface declines while the current flows; thus, the depletion volume gets higher, producing the described decay of $i(t)$. An example of the concentration profile behaviour versus time is shown in Fig. 6c, where Co^* is the bulk concentration of the electroactive species considered.

An example of application is represented by the large amplitude pulse voltammetry (LAPV) technique [3, 9, 15, 31] that applies a series of square pulses modulated by a ramp signal; this approach is equivalent to making a sequence of step experiments involving different species in a progressive manner, according to their excitation overpotential.

Both the ability to classify samples and the ability to detect changes in a solution under measurement have been investigated in the recent literature regarding voltammetry for water quality assessment. Some developments during the last decade [15, 31–33] gave particular attention to the signal processing chain, in the framework of pattern recognition techniques for automatic monitoring systems. In the works cited, emphasis has been given to the assessment of water quality and to food processing applications. The next sections will focus on water quality applications.

3.2 *Sensors Used for Water Applications*

Most experimental setups described in this class of devices make use a potentiostat (see Sect. 3.1), which drives one or more working electrodes made of solid metal, and are aimed at developing low-cost distributed devices. Such devices are expected to have low maintenance requirements and some capability to withstand harsh environments. Figures 7 and 8 show an experimental device mounted on the water tap [31] and a laboratory device with electrodes placed in a measurement cell [34], respectively.

In the most common fashion, the presented prototypes rely on multiple working electrodes selected by relay switches, typically with a reference electrode (e.g. Ag/AgCl) and an AUX (or counter-electrode) often consisting in a steel plate, having the responsibility to inject the current driven by the potentiostat into the electrochemical cell. An array of working electrodes made by solid metal (e.g. gold, iridium, platinum, palladium, rhenium and rhodium) are generally found in the literature [2, 9, 15, 31]. Such hardware configuration (with 2–6 working electrodes) is commonly combined with the measurement scheme of pulse voltammetry.

Other configurations are reported, e.g. screen-printed WE and REF electrodes made by various materials, such as a Pd/Ag alloy and Au as described in Buehler et al. [35]. Also, applications based on stripping techniques have been presented, often in combination with specific materials for the wet surfaces of the working electrodes, such as thick-film graphite and screen-printed carbon electrodes, as illustrated in Brainina et al. [36]; such methods basically consist in the preliminary accumulation of the analyte on the WE (by applying an adequate potential) and the successive measurement by sweeping the potentiostat towards opposite potentials.

Figure 9 shows a simplified block diagram of an e-tongue setup based on pulse voltammetry. The experimental observation, which is obtained by each measurement session, is the response of the potentiostat-cell system to the excitation signal $v_e(t)$ imposed, in terms of loop current $i_{WE}(t)$. Under the hypothesis that all the current losses in the system can be neglected, $i_{WE}(t)$ is equal to the output current of the control amplifier (1).

The potential on the WE is tied to the analog ground by the I/V converter (3); the output of the differential electrometer (2) is connected to the negative input of the control amplifier (1) closing the feedback loop, ensuring that the voltage difference between the reference electrode REF and the selected WE is equal to the voltage set



Fig. 7 An experimental device mounted on the water tap

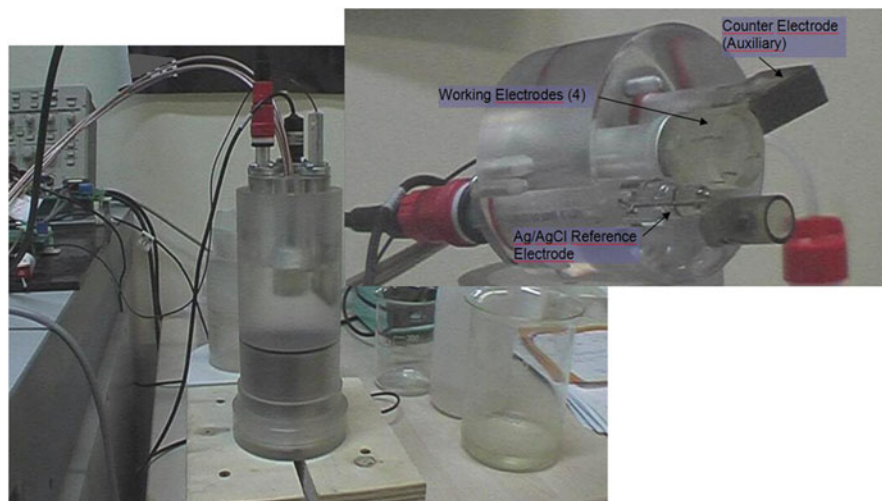


Fig. 8 A laboratory device with electrodes mounted in a measurement cell

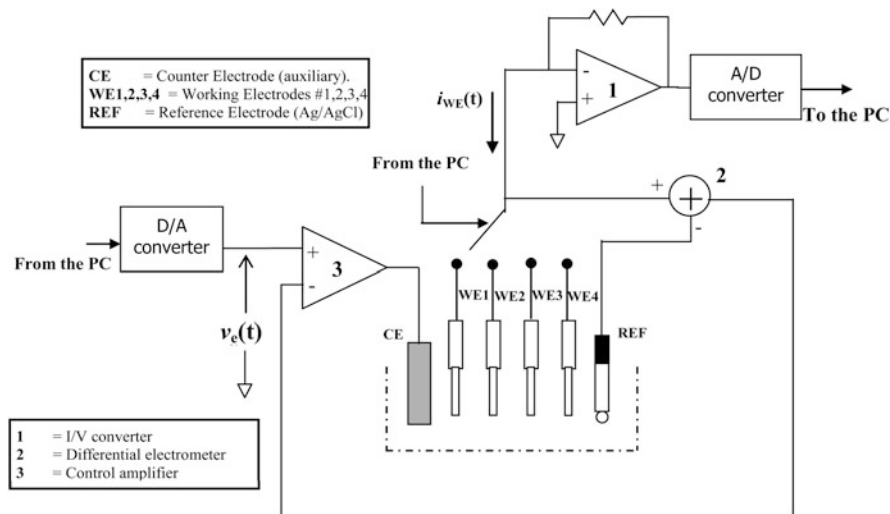


Fig. 9 Simplified block diagram of an e-tongue setup based on voltammetry

by the input signal $v_e(t)$. All of that is true until both the voltage assumed by the AUX CE and the current which flows through it lie in the output swing capability of (1).

Automatic measurements are often performed by controlling the potentiostat with a personal computer (PC) and an adequate software. In the example shown in Fig. 9, the PC controls the excitation waveform $v_e(t)$, acquires the resulting current $i_{WE}(t)$ and drives the switching sequence of the working electrodes during each measurement session.

As a practical example, Fig. 10 shows the shape of a LAPV excitation signal, as firstly described by Winquist et al. [9]. Figure 11 shows a typical set of recorded chronoamperograms for a system comprising 4 working electrodes.

3.3 Signal Processing

In most e-tongues based on voltammetry, samples of the current signal measured by the potentiostat are sequentially collected, making a kind of chronoamperometry rather than a traditional polarography. Each observation may be represented as a vector represented in a multidimensional space, where each component corresponds to a specific instant in the time domain.

For multi-electrode systems (i.e. multiple working electrodes), one session is formed by K sequences of M data points (i.e. time-domain samples), each one generated by the voltammetric scan involving each one of the K WEs.

In this class of non-standard chemometric approaches, the large multivariate space generated by the time series of the acquired current signal is used to characterise the

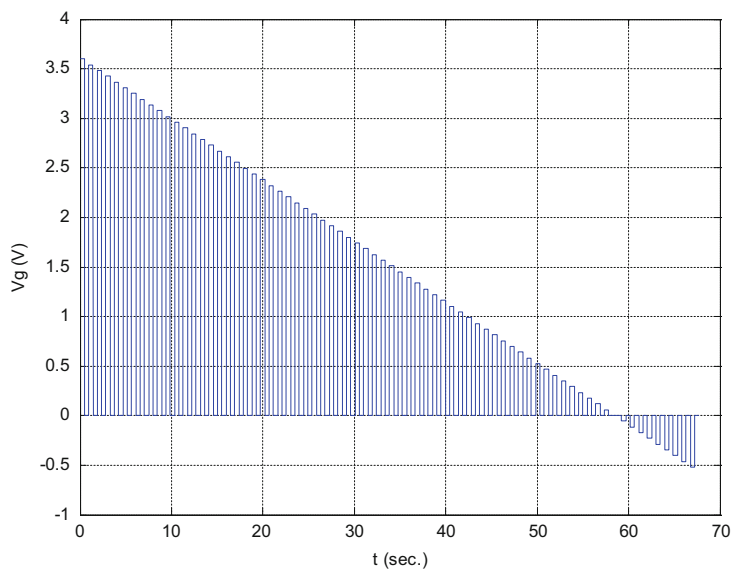


Fig. 10 LAPV excitation signal according to Winquist et al. [9]

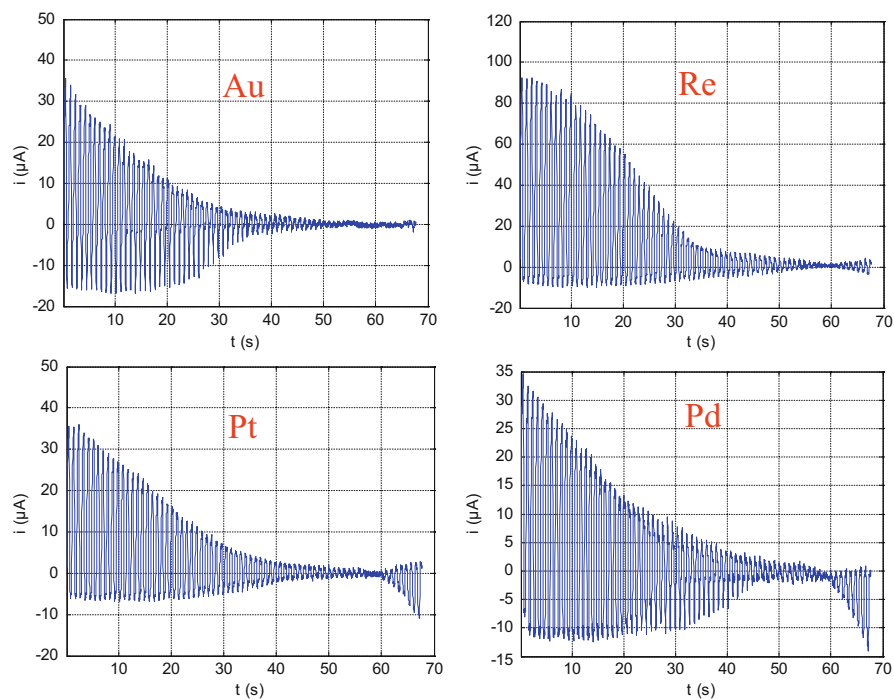


Fig. 11 Set of four voltammetric measurements made with distinct working electrodes on the same sample of bottled mineral water. The respective electrode material is specified by the text in red colour

fluid under measurement. Various signal processing techniques applied to such datasets have been proposed in the literature, all of them essentially oriented to the projection of the acquired data onto a representation sub-space, by reducing the dimensionality of the measurement space (the one hosting the observation vectors). Such dimensionality reduction is equivalent of saying that only the most relevant features are extracted from the acquired time series, leading to a set of vectors having smaller dimensionality than the original data, but still preserving most of the information; this is accomplished by selecting the most informative components in the observation space according to some metric that maximises the performance of the system (i.e. discrimination between classes, change detection capability). Among the wide literature available for an appropriate understanding of the basic concepts of feature selection, supervised/unsupervised classification and transformed-domain operations, good reference books can be found in the context of the analysis of remotely sensed data, where most of these techniques have been developed and applied. Two good reference books are given here as an adequate beginning [37, 38].

Some authors focused their investigations on the data compaction properties of transformed domains like DWT (discrete wavelet transform) and DCT (discrete cosine transform) [15, 39, 40], in order to enhance the discrimination capability in reduced-dimensionality sub-spaces. This is proposed as a preprocessing step, often in combination with PCA applied as a second step, as a feature extraction and visualisation tool. PCA alone and PCA-derived tools (e.g. HPCA—hierarchical PCA) have also been proposed as a feature extractor directly applied to the acquired datasets [41]. Feature selection by genetic algorithms applied to polarographic and stripping voltammetric datasets has also been successfully experimented [42]. More recently, the combination of the Slantnet transform (ST) with a neural network classifier has been proposed for the automatic authentication of water samples by using pulse voltammetry as a measurement technique [43]. All of the cited papers can represent a good starting point to analyse the different strategies that have been studied and proposed in this particular context.

As a general idea, feature selection represents a critical issue in multi-dimensional data processing, because it has the dual objective of delivering the most accurate information with a minimum amount of data while keeping the computational efficiency at the maximum; this justifies the effort to design suitable algorithms and optimise their performance. Selected features (i.e. transformed-domain coefficients, time-domain samples and/or their principal components) can be forwarded to three possible processing paths, corresponding to the following three activities:

- Automatic classification
- Change detection
- Data representation, based on a further reduction of dimensionality

All these three processing possibilities are explored in the literature, with particular attention given to supervised classification systems and the individuation of suitable representation sub-spaces, like the ones used to show the data examples presented in the next section.

3.4 A View on Commonly Presented Applications in the Context of Water Quality

The applications presented in most of the literature about voltammetric e-tongues are focused on the experimentation of the following capabilities:

- Discrimination between clusters in a supervised classification scheme
- Detection of changes in the chemical characteristics of water
- Characterisation and validation of samples

When dealing with the big amount of data coming from a high sampling rate pulsed voltammetry, the reduction of dimensionality of the acquired dataset is a crucial issue (see Sect. 3.3 and references therein). The extraction of suitable features enhances the discrimination of the observations between different classes, by projecting the observed vector onto a reduced-dimensionality space (feature space).

In this framework, three selected implementations are given as an example of the three capabilities cited above. All of them are focusing on water quality applications. The selected examples are given in order to provide an overview of possibilities offered by this measurement approach. In-depth information about the sensor systems used and details about the signal processing techniques used in each application example can be found in the cited literature.

3.4.1 Classification

The classification system proposed in this example is based on a supervised procedure that determines the basis of the feature space (i.e. the basis onto which the observed vectors are projected) by using a training set of suitable measurements. In practice, only part of the collected measurements (training set) is used to determine the combinations of components of the observed vectors that enhance the discrimination between a priori known classes, in order to adhere to a supervised classification scheme. In this specific case, the a priori classes are represented by different brands of bottled mineral water, and the feature vectors are extracted from the DCT version of the observed vectors. The system designed by means of such training set is then used in the subsequent measurements, which are thus used as a “test set”.

This example concerns 4 brands (classes) of Italian bottled mineral water, with an overall dataset formed by 40 measurements (10 per each class), allocated in 5 sessions distributed in 10 days (i.e. one session per day, not necessarily consecutive). Each session consisted in 8 measurements (2 per each brand/class) performed in random order, to check repeatability of the system and avoid eventual artefacts due to a repeated measurement sequence.

Data presented here have been obtained by LAPV measurements with 4 working electrodes made by solid metals (Au, Re, Pt, Pd). Figure 12 shows graphical results in terms of projection onto the representation sub-space of each of the measurements.

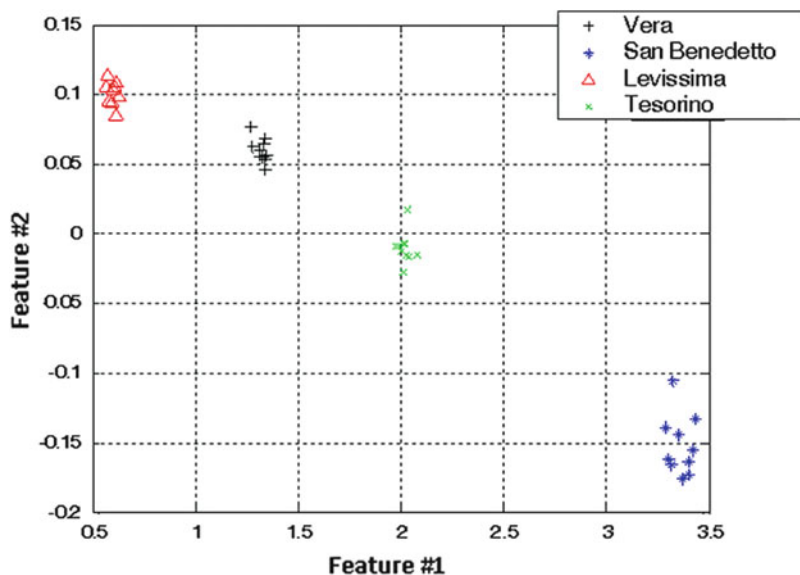


Fig. 12 Graphical representation of the measurements in the “classification” experiment, after projection onto a bi-dimensional representation space

The discrimination between the four different brands of mineral water appears to be obvious to the human observer and allows the successful usage of even the simplest threshold classifiers. In order to keep general and not give as assumed this particularly favourable situation, an automatic classifier based on an MLP-NN (multilayer perceptron-neural network) has been experimented on the feature set extracted from the collected data.

As concerns the MLP-NN, a one hidden layer with four neurons architecture has been chosen. The selected transfer function for the hidden layer neurons was a log-sigmoid one, while the output neuron had a linear transfer function. As expected, the network trained by the said 8 examples achieved 100% of classification accuracy on the full dataset, consisting into 40 measurements.

Details about this application example can be found in Scozzari et al. [34].

Such automatic classification capability, due to the high discrimination exhibited by this kind of systems, is the gateway to the change detection and sample validation applications that are of direct relevance to the water quality context.

3.4.2 Change Detection

The demonstration of the change detection capability of such systems relies on a field experiment, in which water samples are taken at the input and the output of a carbon filter pack, in order to detect how treated water is separated from raw water in the representation domain. This peculiarity gives the possibility to observe eventual changes in the behaviour of the filter, in terms of projections of the input/output

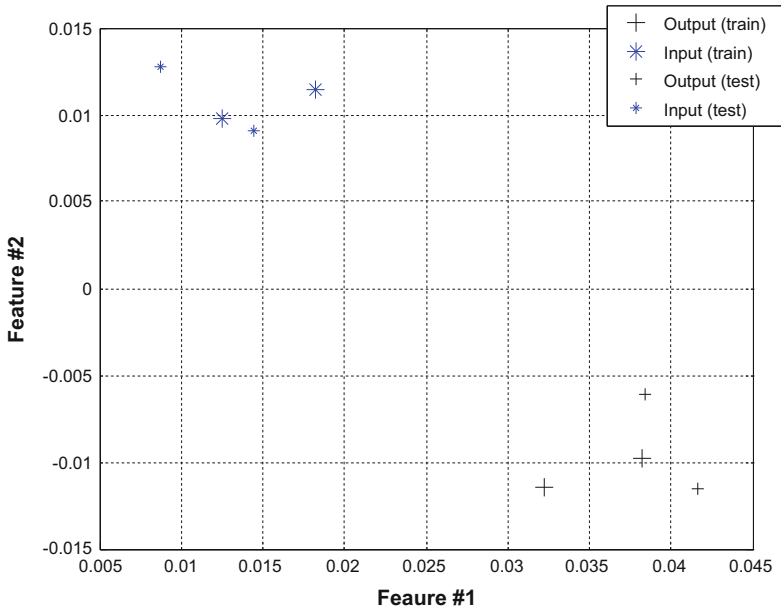


Fig. 13 Graphical representation of the measurements in the “change detection” experiment, after projection onto a bi-dimensional representation space

samples onto the representation domain. In this case study, four wells in the proximity of two different industrial areas have been considered, all exhibiting a slight pollution due to trichloroethylene and tetrachloroethylene from an unidentified source, probably a dismissed activity of industrial oil treatment [44].

Even though the pollution level was inside legal limits for drinkable water, a carbon filter pack has been installed. Water samples have been taken from one of the wells, at both the input and the output of the filter. The measurement procedure has been repeated twice for each sample and in reverse order, with the aim to exclude any artefacts linked with the measurement sequence. The separation between raw and filtered water is again apparent (Fig. 13), confirming the perspective capability to detect eventual changes in the performance of the water filter, in terms of positioning the projected clusters (both in relative and absolute position).

The first 4 observations (2 OUTs and 2 INs) are used as a training set. The second 4 observations (2 INs and 2 OUTs) are used as a test set, i.e. they are projected onto the bi-dimensional feature space determined by using the first training set of vectors.

3.4.3 Sample Characterisation

One effective way to assess the characterisation capability of non-specific sensor systems is to perform traditional chemical-analytical measurements over a wide range of water samples, comparing the results with the output of the multi-electrode

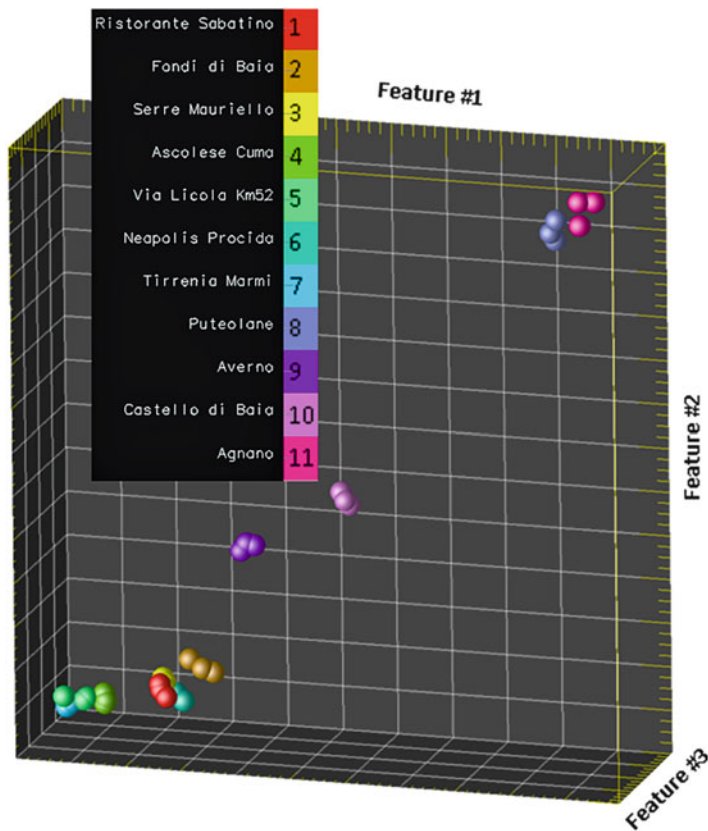


Fig. 14 Representation of 11 water classes in the e-tongue feature space for the “sample characterisation” experiment (three measurements per each class)

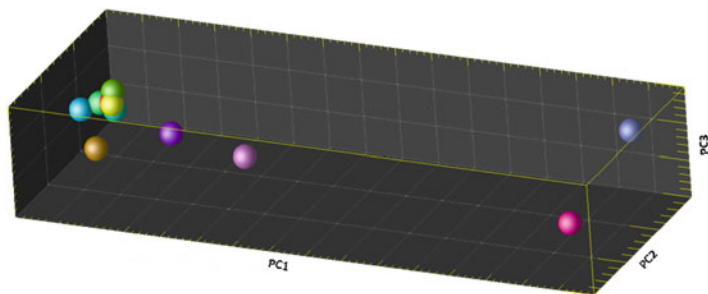


Fig. 15 Representation of the same 11 water classes shown in Fig. 14 in the domain spanned by the first three principal components of the analytical measurements. The two pictures share the same legend

device, i.e. the e-tongue. The example shown here comprises 11 classes of ground-water and surface water, all of them taken in the Campi Flegrei area of Naples, southern Italy [14].

The interesting aspect that makes this case study a kind of natural benchmark lies in the fact that different kinds of water with different chemical characteristics can be found in a small area of a few sq. km. Their different peculiarities well suit the concept of making a general characterisation of the water by giving an aggregate chemical information, as it is one of the major strength of an e-tongue system. According to the representation metric, similarity between samples is expected to be reflected by their distribution in the representation domain. A test of such characterisation capability is shown by comparing the e-tongue results with classical classification/clustering based on traditional chemical-analytical measurements.

Figure 14 shows a tridimensional representation of the distribution of the 11 classes according to the e-tongue (three measurements each class, in order to check the repeatability of the system). Figure 15 shows the PCA applied to the analytical chemical measurements, where 15 parameters were taken into consideration. The projection of the 15 measured parameters onto the first 3 principal components is shown in Fig. 15.

It must be remarked that e-tongue measurements were not made on site; thus, a loss of information about redox potentials, due to sample transportation and its interfacing with free air, is expected. Samples destined to the analytical chemical measurements have been collected and treated in the same way. As a consequence, the main discriminating factor for the e-tongue measurements comes to be the chemical composition of each sample, making the comparison with the principal components of the analytical measurements particularly interesting.

It appears immediately clear how the two thermal water samples (“Terme Puteolane” and “Agnano”, numbers 8 and 11) are strongly discriminated from the others in both the representations. In addition, the water samples grouped in the PCA representation (numbers 1..7) are also close to each other according to the e-tongue results, even with the sample number 2 exhibiting a slight separation from the remaining six. It is finally interesting to see that the “Averno” and “Castello di Baia” samples (9 and 10) are discriminated in both domains, staying in the middle between the two groups (1..7 and 8..11).

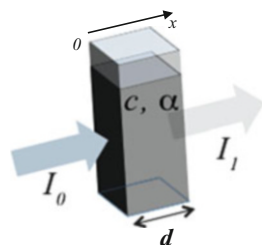
4 Optical Detection

4.1 Principles of Chemical Detection in Optics

In the most conventional arrangement of optical detection systems for liquid phase samples, the sample is irradiated with a monochromatic radiation and the extent of the interaction is evaluated from the attenuation of the original radiation or by observing the secondary radiation emitted by the sample.

The classical way to observe emission or absorption spectra is to disperse the radiation, which means separate the different wavelengths from each other.

Fig. 16 Simplified sketch for the explanation of the light transmission measurement concept



A triangular prism of transparent material or diffraction gratings can be used to this purpose. Absorbance is usually measured with spectrophotometers. In spectrophotometers, the light is dispersed and collimated into a beam of nearly parallel rays, so that only a narrow band of wavelengths passes through the sample at one time. A detector determines the intensity of the transmitted radiation.

A quantity that is commonly plotted to represent an absorption spectrum is the transmittance, $T(\lambda)$, defined as follows:

$$T(\lambda) = \frac{I(\lambda)}{I_0(\lambda)}$$

where $I(\lambda)$ is the spectral intensity after the light beam passes through the cell and $I_0(\lambda)$ is the incident spectral intensity. Complementarily, the absorbance is defined as follows:

$$A(\lambda) = -\log[T(\lambda)] = \log \frac{I_0(\lambda)}{I(\lambda)}$$

Absorption spectroscopy can be used to measure the concentration of a chemical species dispersed in the optical path between source and detector. Figure 16 shows the drawing of a cell containing an absorbing substance with concentration c , with a beam of light passing through it in the x direction. Considering a thin slab of unit area within the cell, lying between a generic abscissa x_0 and $x_0 + dx$, the volume of the slab is dx times the unit area, so the amount of absorbing substance in this portion of the cell equals $C \cdot dx$ times the unit area.

Let the intensity of light in the small range of wavelengths $d\lambda$ be denoted by $I(\lambda, x) d\lambda$. This intensity depends on x because of absorption phenomena that make the light extinguish while travelling through the cell. The amount of light absorbed in the slab per unit of time is proportional to the initial intensity of light and to the amount of absorbing substance, so that the change in I from one side of the thin slab to the other is given by

$$-dI = k(\lambda) \cdot I \cdot C \cdot dx$$

The proportionality factor k is a function of wavelength that does not depend on concentration. Roughly, spectrometric applications rely on the fact that $k(\lambda)$ is

different from zero only for wavelengths where the photon energy equals the energy difference between a significantly occupied molecular energy level and a higher level, giving rise to a kind of spectral signature of the involved substances.

Previous equation is a differential equation that can be solved for the intensity of light as a function of position. It is solved by a definite integration, letting $x = 0$ be the front of the cell and $x = d$ be the back of the cell. Assuming that the concentration is uniform, it yields

$$A(\lambda) = \varepsilon(\lambda) \cdot C \cdot d$$

This equation is known as Beer-Lambert law, where $\varepsilon(\lambda)$ is the absorptivity (also called the extinction coefficient). The absorptivity depends on the wavelength of light as well as on the absorbing substance and on the solvent. This relationship is well obeyed by many substances at low concentrations. Deviations occur at higher concentrations, corresponding to an extinction coefficient that is dependent on concentration. These deviations can be caused by specific chemical effects such as association of the molecules of the substance, which provides one way to study molecular association.

When an analyte does not exhibit a convenient spectroscopic optical response such as absorption or luminescence, sensing can be achieved by monitoring the optical response of an intermediate species or reagent whose response is modulated by the presence of the analyte. In fact, in a classical sensing scheme of optical sensors for liquid phase applications, a reagent has a specific reaction towards certain analytes by changing optical properties of the solution, such as absorbance, reflectance or fluorescence.

This indirect sensing technique requires the reagent to be immobilised, either in the liquid or in the solid phase, to facilitate interactions with the analyte. Reagent-based optical sensing is based mainly on solid-phase immobilisation matrices, where the reagent dye can be adsorbed, covalently or ionically attached or simply encapsulated in a solid matrix that is permeable to the analyte. If the immobilisation matrix has the capability of being coated on a substrate in liquid form, as is the case for sol-gel glasses or polymer coatings, a wide range of sensor configurations is enabled including, for example, fibre-optic, planar waveguide and array-based sensors. Indirect optical sensors are very well developed for pH sensing that is based on the change in optical absorption of organic pH indicators. They also allow for colourimetric detection of CO₂ by measuring the pH change in response to carbonic acid generated by the acidic CO₂ gas [45]. On the other hand, many analytes are detected with luminescent probes with the advantage that luminescence is intrinsically more sensitive than absorption as a sensing technique [46].

In those applications that need to study the distribution of the concentration of non-luminescent species over larger areas, the system to be analysed is exposed to a *paint* that responds to the respective parameter of interest. The term *paint* refers to a material that consists of a solvent, a polymeric support (sometimes referred to as a binder) and an indicator dye. This mixture can be painted or sprayed onto the surface of the object of interest or can be manufactured as a thin film that, after

solvent evaporation, is placed on the system to be studied. The indicator dye in the paint undergoes diffusional equilibration with its environment, and the analyte of interest thereby modulates either the fluorescence or the absorption features of the paint, which is then photographed or imaged.

4.2 The Computer Screen Photo-Assisted Technique

The computer screen photo-assisted technique (CSPT) is an optical-sensing interface firstly reported by Lundström and Filippini in 2003, which allows for the analytical investigation of visible absorption features of several kinds of samples [47]. It consists of easily available, cheap and widespread diffuse computer peripherals. The basic hardware is a standard computer screen that is used as a programmable polychromatic light source and a web camera used as a three bands detector.

Computer screens are capable of displaying confined areas of arbitrary shape, colour and intensity that can be two-dimensionally scanned on the screen with resolutions down to 200 μm resolution defined by the pixel pitch (distance between two contiguous cells of the same colour) [48, 49]. In CRT monitors an electron beam scans the inner surface of the screen, exciting a spot of phosphorescent coating emitting a burst of visible light that decays until it is reached again by the beam in the next scanning cycle. Colour CRT screens use three electron beams exciting blobs of three different screen coatings. In this case the phosphors are band-limited emitters of visible light corresponding to the perception of red, green and blue. The frequency at which the beams reach the same spot is about 85 Hz, and since it is faster than the eye's response it induces the perception of a steady intensity. On the contrary, in LCD screens each cell contains a liquid crystal between two crossed linear polarisers. If a voltage is applied to the cell, the liquid crystals rotate the direction of polarisation of the light allowing to regulate the intensity escaping from the second polariser. A large area white lamp illuminates the rear of the screen. Colour screens are produced by the repetition of groups of cells with red, green and blue filters. LCD screens produce a steady intensity and can refresh images at relatively low frequencies, typically 60 Hz. As far as CSPT measurements are concerned, the main differences between these two types of screens are the pulsed nature of the CRT displays and the linearly polarised light emitted from LCD screens [50].

The light emitted from a computer screen is not monochromatic, but it is the combination of three polychromatic primary sources. The spectral radiance of these primaries excites the human perception of red, green and blue colours. Any other colour can be generated by the linear combination of these primaries according to Jackson et al. [51]:

$$v_i(\lambda) = r_i \cdot R(\lambda) + g_i \cdot G(\lambda) + b_i \cdot B(\lambda)$$

where $R(\lambda)$, $G(\lambda)$ and $B(\lambda)$ are the spectral radiances of the primary colours, r_i , g_i and b_i are numbers within [0 1] that represent the particular modulation of the

primaries for a given desired colour, and λ , the wavelength, is limited to the visible range (390–800 nm). Conventional true colour systems have a resolution of 8 bits (0–255 values) for each colour channel, for a total of 2^{24} colours that can be displayed on the screen.

Digital colour cameras capture colour images of the real world by transmitting the image through a number of colour filters having different spectral transmittances and sampling the resulting coloured images by using electronic sensors.

4.3 CSPT Measurements

During a CSPT measurement, a colour sequence is displayed in a portion of the screen to illuminate the sample. The light emerging from the assay is simultaneously acquired by the camera operating at a capture rate usually of 1 frame/s. The result of such a measurement is a digital video file (AVI format) of the array under different illuminating colours. The video stream is then decomposed into individual frames and the information from selected regions of interest (ROIs) in the image is extracted. ROIs are marked with white circles in Fig. 17, and they are located both on the sensing spots and on background areas.

The digital values of each colour level (red, green and blue components) of the pixels contained in the ROI are averaged, yielding the intensity per colour channel of each screen colour. As a result, a distinctive spectral signature of the sample is obtained. Usually it is in the form of intensity versus illuminating colours curves, and it is often referred to as CSPT fingerprint (Fig. 18a). The CSPT measurement of the transmittance $T(\lambda)$ of any substance transforms this illuminating space into a measured space distinctive of the substance. The measured space contains both the spectral signature of the substances and that of the particular CSPT assembly where the measurement is performed. In order to highlight the substance signature, the measured space is subtracted by the measured space without substance, corresponding to the intensities measured in the background areas as shown in Fig. 18b.

Different substances transform the illuminating space in different measured spaces, and emerging light colours become aligned with the respective camera channels. In CSPT measurements, depending on the transmittance of the evaluated substance, the response to some illuminating colour combinations becomes clustered in the measured space, thus reducing the discrimination capability in terms of spectral diversity of the collected fingerprints. Under this point of view, longer colour sequences (i.e. enriched by a higher number of colour combinations) have better chances to always incorporate well-performing patterns.

Illuminating sequences homogeneously representing the illuminating space produce diverse distributions of measured values, suggesting the possibility to optimise such sequences for the spectral properties of any particular compound. However, it is also evident that certain substances will always be represented by a larger volume of the colour space. The larger the volume they occupy in the measured space, the better the chances to find an illuminating sequence that separates all the pertaining features, thus creating a distinctive fingerprint. In summary, for substance transmittances with

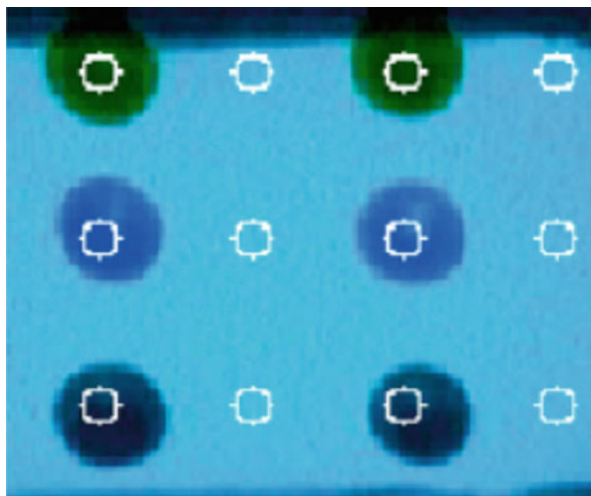


Fig. 17 Camera image of sensing layers under a *bluish illumination*. The regions of interest (ROIs) for each sensitive layer and the corresponding background are also shown

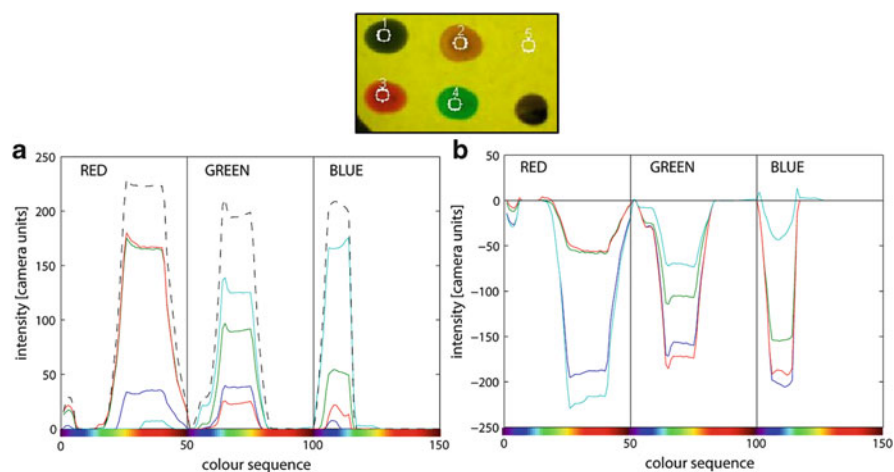


Fig. 18 (a) CSPT fingerprints of sensing layers reported in the *inset*, obtained by concatenating the intensity in the three camera channels for an illumination sequence made of 50 colour combinations. The *black dashed line* represents the reference light source or background (circle number 5 in the *inset*). (b) Difference between the same fingerprints and the background intensity. It allows to evaluate the absorption exhibited by each spot

their minima at the centre of the visible spectrum, CSPT is able to retain more spectral features than for substances absorbing at the borders of the spectrum. These better conditions for substances that affect green, yellow and orange light than for blue or red light can be intuitively associated to the restricted contribution of the later substances

on the signals of various channels. So, substances absorbing light in the far red (or blue) only affect the red (or blue) signal of the camera, whereas a green, yellow or orange absorbing substance gathers distinctive contributions from all the channels, thus enriching the information contained in the fingerprint and improving the discrimination capability [52].

Usually, most applications are well accomplished with a sequence of 50 colours that gradually change from blue to red. However, for selected indicators, a shorter and more targeted sequence can be defined, which allows for a continuous imaging of spectral features of the substance.

4.4 Case Study: The Detection of Natural Cr(VI) with a CSPT Setup

The potentiality of CSPT is illustrated in an application aimed at evaluating the concentration of Cr(VI) in natural springs [53]. Here the CSPT is used as a method to measure the colour changes in a colourimetric assay for Cr(VI). CSPT results are compared with those obtained by a standard UV–VIS spectrophotometer. Results show that CSPT is a valid alternative for colourimetric assay read-out. It is particularly important to consider that CSPT equipment used for different applications (such as computers and cameras) are temporarily turned into analytical devices without altering their primary function. On this basis, this result demonstrates the possibility to enable analytical capabilities to a personal level.

Hexavalent chromium is a toxic compound with teratogenic and carcinogenic effects on humans. Its presence in the environment is typically due to anthropogenic activities [54]. Nonetheless, recently natural occurring concentrations of Cr(VI) largely exceeding the limits for groundwater quality have been found worldwide [55, 56]. These anomalies originate from oxidative dissolution, probably driven by mixed-valence Mn oxides, of Cr(III)-bearing minerals contained in particular kinds of rocks called serpentinites and ultramafites, which constitute 1% approximately of the terrestrial landscape and are also found within densely inhabited areas of the Circum-Pacific and Mediterranean regions. As a consequence, the control of Cr(VI) becomes important even in the absence of human activities, displacing the monitoring of this substance from the output of relevant industrial plants to the common water distribution network, by the observation of water bodies prone to the pollution from Cr(VI) of natural origin. Besides more sophisticated techniques, an efficient detection of Cr(VI) is obtained by an analytical procedure based on the absorbance change, around 540 nm, consequent to the reaction of a sample of water with a specific reagent (diphenylcarbazide) under acid conditions.

Figure 19 shows the CSPT measurement arrangement. Figure 20 shows the fingerprints collected during the measurement campaign described in Santonico et al. [53]. The largest changes of differential intensities collected by the camera are observed in the green channel under green colour illumination. Nonetheless, PLS

Fig. 19 CSPT arrangement. The camera and the sample holder are fixed to the screen of a notebook where a window displays the illumination sequence. In the picture also the image captured by the camera is visible in another window. The software routine runs in MATLAB

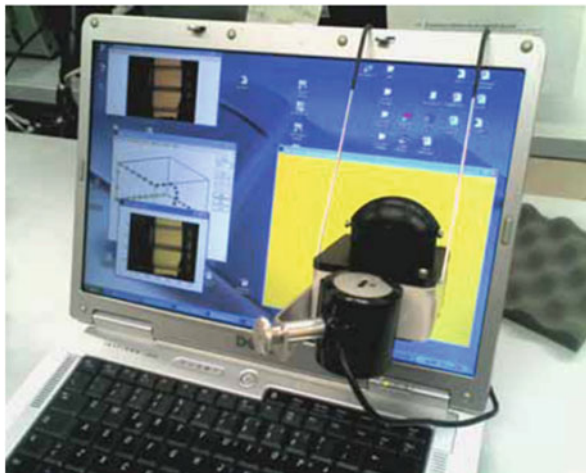
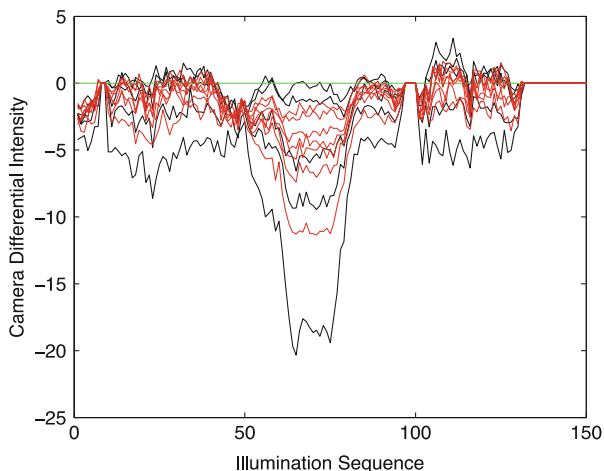


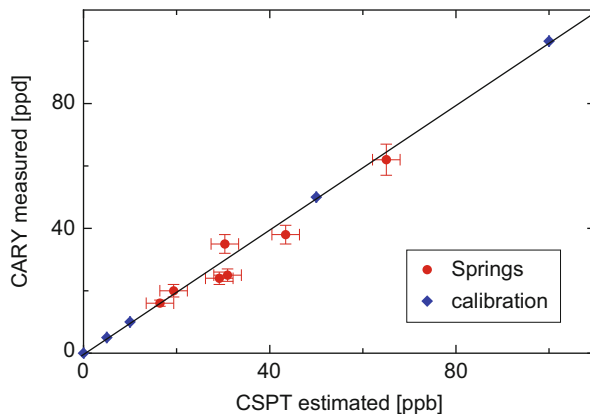
Fig. 20 Collected fingerprints related to calibration samples (*black lines*) and spring waters (*red lines*). Largest changes occur in the green camera channel under green light illumination



modelling was applied to whole fingerprints exploiting the PLS property of variable selection. The PLS model was built by using the calibration solutions.

The Cr(VI) concentrations in these solutions were considered as not affected by errors. PLS model was optimised by a leave-one-out cross-validation procedure, and the number of latent variables was chosen by minimising the root mean square error of validation. As a result, a model with four latent variables was defined; the root mean square of calibration (RMSEC) was 0.01 ppb and the root mean square of validation (RMSECV) was 2.9 ppb. The error of ± 2.9 ppb was then applied to the Cr(VI) estimations. Validated PLS model was applied to the fingerprints of spring waters; results were compared with those provided by commercially available instruments, such as a Cary spectrophotometer and a Hanna portable instrument. For these instruments the estimated errors mentioned in the previous section were

Fig. 21 Comparison of spectrophotometry and CSPT estimation of Cr(VI) concentration in spring water samples



applied. Figure 20 shows the collected fingerprints related to the calibration samples and the spring waters. Figure 21 shows the Cr(VI) in natural spring water estimated by the CSPT plotted versus the values measured with a Cary spectrophotometer; the calibration data are also plotted.

5 Conclusions

This chapter gives an overview of new technologies for the assessment and control of the quality of water resources, as an alternative to the classical chemical-analytical approaches. In particular, non-conventional electroanalytical devices such as e-tongues (or taste sensors) can be applied to the continuous monitoring of natural resources, with advantages in terms of availability, wide analytical coverage and low cost of the method.

Possible applications for this class of devices may include the usage of expert systems to trigger automatic samplers, alert human operators or perform other automatic actions when the observed data exhibit a significant change with respect to a given reference, e.g. moving outside known boundaries, which may represent an anomalous condition. Being non-specific to particular chemical species, e-tongue systems are good candidates to monitoring applications where the mere detection of an overall quality change (e.g. the presence of an unexpected pollutant) is the most required characteristic.

Another fairly mature, inexpensive and very attractive technology described in this chapter is the CSPT, taken as a promising example of non-conventional approach to water quality measurements based on optical sensor systems. In fact, the combined usage of a display (e.g. a computer screen) and a generic camera (e.g. a webcam) has been demonstrated as an effective platform for measuring optical properties of liquid samples. Such an approach is a natural candidate for ubiquitous analyses in the context of water quality monitoring and is complementary to the

electrochemical e-tongues, enriching the analytical possibilities offered by these non-conventional techniques.

References

1. Hauptmann P, Borngraeber R, Schroeder J, Auge J (2000) Artificial electronic tongue in comparison to the electronic nose—state of the art and trends. In: Proceedings of IEEE/EIA international frequency control symposium and exhibition, p 22–29
2. Krantz-Rulcker C, Stenberg M, Winquist F, Lundstrom I (2001) Electronic tongues for environmental monitoring based on sensor arrays and pattern recognition: a review. *Anal Chim Acta* 426(2):217–226
3. Lindquist M, Wide P (2001) Virtual water quality tests with an electronic tongue. In: Proceedings of IEEE IMTC, Budapest, Hungary, May 21–23, p 1320–1324
4. Vlasov Y, Legin A, Rudnitskaya A, Di Natale C, D'Amico A (2005) Nonspecific sensor arrays (“electronic tongue”) for chemical analysis of liquids: (IUPAC technical report). *Pure Appl Chem* 77:1965–1983
5. Scozzari A (2008) Electrochemical sensing methods: a brief review. In: Evangelista V et al. (eds) *Algal toxins: nature, occurrence, effect and detection*. NATO science for peace and security series A: chemistry and biology. Springer Science + Business Media B.V., p 335–351. doi:10.1007/978-1-4020-8480-5_16
6. Bard AJ, Faulkner LR (1980, 2000) (1st, 2nd edn) *Electrochemical methods, fundamentals and applications*. Wiley, New York
7. Janata J (1989, 2009) (1st, 2nd edn) *Principles of chemical sensors*. Springer, New York, 340 pp
8. Di Natale C, Macagnano A, Davide F, D'Amico A, Legin A, Vlasov Y, Rudnitskaya A, Selezenev B (1997) Multicomponent analysis on polluted waters by means of an electronic tongue. *Sens Actuator B Chem* 44:423–428
9. Winquist F, Wide P, Lundstrom I (1997) An electronic tongue based on voltammetry. *Anal Chim Acta* 357(1/2):21–31
10. Legin A, Rudnitskaya A, Vlasov Y, Di Natale C, Mazzone E, D'Amico A (1999) Application of electronic tongue for quantitative analysis of mineral water and wine. *Electroanalysis* 11:814–820
11. Paolesse R, Di Natale C, Burgio M, Martinelli E, Mazzone E, Palleschi G, D'Amico A (2003) Porphyrin-based array of cross-selective electrodes for analysis of liquid samples. *Sens Actuator B* 95:400–405
12. Ciosek P, Brzózka Z, Wróblewski W (2004) Classification of beverages using a reduced sensor array. *Sens Actuator B* 103:76–83
13. Lvova L, Martinelli E, Mazzone E, Pede A, Paolesse R, Di Natale C, D'Amico A (2006) Electronic tongue based on an array of metallic potentiometric sensors. *Talanta* 70:833–839
14. Scozzari A (2007) Application of an e-tongue to groundwater monitoring: a measurement perspective. In: Bullen TD, Wang Y (eds), *Twelfth symposium on water-rock interaction*. Taylor & Francis, Kunming (China), vol 2, p 1115–1118
15. Scozzari A, Acito N, Corsini G (2007) A novel method based on voltammetry for the qualitative analysis of water. *IEEE Trans Instrum Meas* 56(6). doi:10.1109/TIM.2007.903600
16. Men H, Zou S, Li Y, Wang Y, Ye X, Wang P (2005) A novel electronic tongue combined MLAPS with stripping voltammetry for environmental detection. *Sens Actuator B Chem* 110(2):350–357. doi:10.1016/j.snb.2005.02.032
17. Tymeszki L, Zwierkowska W, Koncki R (2004) Screen printed electrode for potentiometric measurements. *Anal Chim Acta* 526:3–11

18. Otto M, Thomas J (1985) Model studies on multiple channel analysis for free magnesium, calcium, sodium and potassium at physiological concentration levels with ion-selective electrode. *Anal Chem* 57:2647
19. Gardner JW, Bartlett PN (1994) A brief history of electronic noses. *Sens Actuator B* 18–19: 211–220
20. Hayashi H, Yamanaka M, Toko K, Yamafiji K (1990) Multichannel taste sensor using lipid membrane. *Sens Actuator B* 2:205–213
21. Di Natale C, Davide F, Brunink J, D'Amico A, Vlasov Y, Legin A, Rudnitskaya A (1996) Multicomponent analysis of heavy metal cations and inorganic anions in liquids by a non-selective chalcogenide glass sensor array. *Sens Actuator B* 34:539–542
22. Riul A, Malmegrim RR, Fonseca FJ, Mattoso LHC (2003) An artificial taste sensor based on conducting polymers. *Biosens Bioelectron* 18:1365–1369
23. Winquist F, Krantz-Rulcker C, Wide P, Lundstrom I (1999) Monitoring of freshness of milk by an electronic tongue on the basis of voltammetry. *Meas Sci Technol* 9(12):1937–1946. doi:10.1088/0957-0233/9/12/002
24. Winquist F, Lundstrom I, Wide P (1999) The combination of an electronic tongue and an electronic nose. *Sensors and Actuators B: Chemical*. In: Twelfth European conference on solid-state transducers—9th UK conference on sensors and their applications, Southampton, UK, vol 58, issue 1–3, p 512–517. doi:10.1016/S0925-4005(99)00155-0
25. Heyrovský J (1924) The processes at the mercury dropping cathode. Part I. The deposition of metals. *Trans Faraday Soc* 19:692–702. doi:10.1039/TF9241900692
26. Heyrovský J (1924) The processes at the mercury dropping cathode. Part II. The hydrogen overpotential. *Trans Faraday Soc* 19:785–788. doi:10.1039/TF9241900785
27. Semerano G, Griggio L (1957) Selected values of polarographic data. *Arti grafiche Panetto & Petrelli, Spoleto*, p 286
28. Hickling A (1942) Studies in electrode polarisation. Part IV.—the automatic control of the potential of a working electrode. *Trans Faraday Soc* 38:27–33
29. Korthum G (1965) *Treatise on electrochemistry*. University of Tubingen, Germany, 2nd ed. American Elsevier, New York
30. Mirceski V, Komorsky-Lovric S, Lovric M (2007) *Square-wave voltammetry*. ISBN 978-3-540-73739-1, Springer
31. Scozzari A, Wide P (2008) The process from a redundant and general sensor concept—towards an optimal sensor strategy for the assessment of drinking water quality. In: *IEEE instrumentation and measurement technology conference, proceedings*, p 836–841. doi:10.1109/IMTC.2008.4547153
32. Iliiev B, Lindquist M, Robertsson L, Wide P (2006) A fuzzy technique for food and water quality assessment with an electronic tongue. *Fuzzy Set Syst* 157(9):1155–1168
33. Pereira JMD, Postolache O, Girao PS (2007) A smart and portable solution for heavy metals concentration measurements. In: *Proceedings of the IEEE instrumentation and measurement technology conference*, p 2427–2430
34. Scozzari A, Acito N, Corsini G (2006) A supervised algorithm for water classification by voltammetric measurements. In: *Proceedings of the IEEE instrumentation and measurement technology conference*, p 725–728
35. Buehler MG, Kuhlman GM, Keymeulen D, Kounaves SP (2002) In: *Advanced electronic tongue concept, 2002 I.E. aerospace conference proceedings*, p 407–416
36. Brainina KZ, Kubysheva IV, Miroshnikova EG, Parshakov SI, Maksimov YG, Volkonsky AE (2001) Small-size sensors for the in-field stripping voltammetric analysis of water. *Field Anal Chem Tech* 5(6):260–271
37. Landgrebe DA (2003) *Signal theory methods in multispectral remote sensing*. Wiley, Hoboken, NJ
38. Richards JA (2012) *Remote sensing digital image analysis: an introduction*. Springer, Berlin, Heidelberg
39. Artursson T, Holmberg M (2002) Wavelet transform of electronic tongue data. *Sens Actuator B* 87:379–391

40. Scozzari A (2005) Signal analysis of voltammetric data series for water quality tests and classification. In: Proceedings of the IEEE instrumentation and measurement technology conference, p 89–92
41. Holmin S, Spångeus P, Krantz-Rülcker C, Winquist F (2001) Compression of electronic tongue data based on voltammetry—a comparative study. *Sens Actuator B Chem* 76(1–3): 455–464. doi:[10.1016/S0925-4005\(01\)00585-8](https://doi.org/10.1016/S0925-4005(01)00585-8)
42. Herrero A, Cruz OM (1999) Qualitative and quantitative aspects of the application of genetic algorithm-based variable selection in polarography and stripping voltammetry. *Anal Chim Acta* 378(1–3):245–259. doi:[10.1016/S0003-2670\(98\)00619-9](https://doi.org/10.1016/S0003-2670(98)00619-9)
43. Kundu PK, Chatterjee A, Panchariya PC (2011) Electronic tongue system for water sample authentication: a slantlet-transform-based approach. *IEEE Trans Instrum Meas* 60(6): 1959–1966. doi:[10.1109/TIM.2011.2115410](https://doi.org/10.1109/TIM.2011.2115410)
44. Scozzari A, Peruzzi P, Cioni R, Guidi M (2006) An innovative approach to urban water management based on taste sensors. EGU General Assembly, Wien
45. Segawa H, Ohnishi E, Arai Y, Yoshida K (2003) Sensitivity of fiber-optic carbon dioxide sensors utilizing indicator dye. *Sens Actuator B* 94:276–281
46. Paolesse R, Monti D, Dini F, Di Natale C (2011) Fluorescence based sensor arrays. *Top Curr Chem* 300:139–174
47. Filippini D, Svensson SPS, Lundström I (2003) Computer screen as a programmable light source for visible absorption characterization of (bio)chemical assays. *Chem Commun* 2:240–241
48. Filippini D, Alimelli A, Di Natale C, Paolesse R, D’Amico A, Lundstrom I (2006) Chemical sensing with familiar devices. *Angew Chem Int Ed* 45:3800–3803. doi:[10.1002/anie.200600050](https://doi.org/10.1002/anie.200600050)
49. Filippini D, Alimelli A, Di Natale C, Paolesse R, D’Amico A, Lundström I (2006) Chemical sensing with familiar devices. *Angew Chem* 118:3884–3887
50. Schubert EF, Kyu Kim J (2005) Solid-state light sources getting smart. *Science* 308:1274–1278
51. Jackson R, Mac Donald L, Freeman K (1994) Computer generated color. Wiley, New York
52. Filippini D, Lundström I (2006) Preferential color substances and optimized illuminations for computer screen photo-assisted classification. *Anal Chim Acta* 557:393–398
53. Santonico M, Scozzari A, Brozzo G, Marini L, D’Amico A, Filippini D, Lundstrom I, Di Natale C (2009) Detection of natural Xr(VI) with computer screen photo-assisted technology. *Proc Chem* 1:317–320
54. Nriagu J, Niebner E (eds) (1988) Chromium in the natural and human environments. Wiley, New York
55. Fantoni D, Brozzo G, Canepa M, Cipolli F, Marini L, Ottonello G, Vetusch Zoccolino M (2002) Natural hexavalent chromium in groundwaters interacting with ophiolitic rocks. *Environ Geol* 42:871–882
56. Oze C, Bird D, Fendorf S (2007) Genesis of hexavalent chromium from natural sources in soil and groundwater. *Proc Natl Acad Sci U S A* 104:6544–6549

Index

A

Absolute safety zone, 23
Acid mine drainage (AMD), 125, 239
Activity diagrams, 36
Africa, 19
Ag-tetrahedrite, 88
Analytical methods, 22
Angad aquifer (Eastern Morocco), 183
Anglesite, 71, 245, 252
Ankerite, 41
Annabergite, 89
Antibodies, 272
Antimonite, 58, 92
Antimony (Sb), 82, 83, 86, 92
Arsenic, 6, 53, 77
 metamorphic rocks, 103
 phosphate deposits, 104
 Saharan dust, 105
Arseniosiderite, 85, 86, 88
Arsenite, 88, 89, 271
Arsenopyrite (FeAsS), 36, 43, 58, 60, 63, 80–87, 90–96
Atrazine, 261, 273
Australia, 17
Automated Water Analyser Computer Supported System (AWACSS), 273

B

Bauxite active mines (Central Greece), 92
Belovo, 231, 240
Benzodithiophene, 271
Berikul, 240
Berthelot assay, 262, 264
Bioelectrical potential, 208

Biosensors, 270
Bismuthinite, 90
Bisphenol A, 273
Boron, isotopes, 133
Boulangerite, 82, 92
Bourmonite, 88
Bromide/chloride ratios, 35

C

Cadmium (Cd), 53, 55, 239
Carbaryl, 261
Carbon, C-14, 35
 stable isotopes, 123
Carbonates, 40
Carbon dioxide, atmospheric, 124
 capture and storage (CCS), 31, 32, 123
 geological storage, 31
 sequestration, 31
 supercritical, 38
Carbonic acid, 123, 125
Catchment sites, protection, 175, 179
Cerussite, 71
Chalcopyrite, 58, 82, 93–95, 139, 207, 242–245
Chalkidiki, 80
Change detection, 297
China, 18
Chlamydomonas reinhardtii, 271
Chlorite, 40
Chlorophosphanet, 245
Chlorpyrifos, 261
Chromium, 101, 115, 306
 isotopes, 138
Coals, arsenic, 100

Colorimetric methods, 257, 262
 Computer screen photo-assisted technique (CSPT), 279, 303
 Convection-diffusion modeling, 177
 Copper, 95, 115, 240
 isotopes, 139
 Cyanidation cakes, 240
 Cyanide, 274

D

Dawsonite, 41
 DDT, 261
 Detergents, 128
 Deuterium, 35, 119
 Dichlorophenoxyacetic acid (2,4-D), 261
 Diffusion potential (membrane potential), 206
 Dissolved inorganic carbon (DIC), 115, 118
 Diuron, 271
 DNAzymes, 270
 Dolomite, 41
 Downscaling, 152
 DRASTIC method, 175, 187
 Drinking water, 279
 safeguarding, 13
 Drinking Water Protected Areas (DWPAs), Europe, 15, 16

E

Electrical conductivity, 227
 Electrical field, pumping tests, 168
 Electrical resistivity tomography (ERT), 8, 193, 197, 225, 228
 Electrical tomography, 243
 Electrochemistry, 279
 Electromagnetic attenuation, 202
 Electromagnetic induction (EMI), 8, 225, 229
 Electromagnetic sensing, techniques, 193
 Electronic noses, 285
 Electronic tongues (e-tongues), 279, 281
 Enargite, 58, 84, 90, 91
 Enhanced oil recovery (EOR), 32
Escherichia coli, cytometry, 269
 Estrone, 273
 Europe, Directive 2000/60/EC, 15

F

Falkmanite, 88
 Falling head permeameter tests, 154, 159
 Feldspars, 40, 41, 46, 134, 251
 Fertilizers, 79, 128, 135, 188

 nitrates, 131, 132
 Flow cytometry, 268
 Fluorescence spectroscopy, 257, 266
 Freshwater, pollution, 1

G

Galena (PbS), 36–38, 43, 58, 87, 91, 93, 95, 242, 244
 Gas reservoirs, carbon dioxide storage, 44
 Gas–water–rock interaction, 31
 Geoelectrical zoning, 239
 Geographic information systems (GIS), 175, 185
 Geometric attenuation, 202
 Geometric methods, 20
 Geophysical surveys, 225
 Georgiadesite, 88
 Geothermal energy, 32, 97
 waters/fluids, 77, 79, 87, 98, 105, 134
 Gersdorffite, 87
 Global Meteoric Water Line (GMWL), 120
 Goethite, 92
 Gold, 58, 60, 65, 93, 241, 274, 291
 Greece, 6, 77
 Green fluorescent protein (GFP), 271
 Griess assay, 262, 264
 Ground-penetrating radar (GPR), 8, 193, 200
 Groundwater, 1, 227
 arsenic, 271
 atrazine, 261
 heavy metals, 239
 management, 1, 280
 mixing, 120
 monitoring, 31, 44, 57, 193
 origin, 120
 pollution, 175, 239
 protection directives, 13
 quality, 53
 recharge, 120
 urban, 128
 Gypsum, 245

H

HDPE sheets/liners, 213–220
 Heavy metals, 6, 33, 37, 43, 89, 195, 213, 261, 282
 Helmholtz–Smoluchowski equation, 207
 Heteromorphite, 88
 Hontomín–Huermececes waters, 125
 Hydraulic conductivity, 7, 22, 45, 151–171, 176, 187

- Hydrochemical characterization, 34
 Hydrodynamic trapping, 31, 33, 46
 Hydro-fracking, 32
 Hydrogen, 104, 117–123, 119, 140
 Hydrogeochemical modeling, 31
 Hydrogeochemistry, 31, 40
 Hydrogeological mapping, 22
 Hydrogeophysical approach, 167
 Hydrogeophysics, 151
 Hydrogeosite, 157, 159, 163
- I**
 Immunosensors, 271
 Industrial sludge, 213
 Ion-selective electrodes (ISE),
 Iron, 40, 115, 118, 213
 isotopes, 136
 Isoproturon, 273
 Isotopes, environmental, 115
 fractionation, 115
 untraditional, 115
- J**
 Jagodina (Serbia-Herzegovina), 209
 Jamesonite, 92
- K**
 Kablova industrial site, 209
 Kaolinite, 40
 Karabash, 240
 Kassandra mines (Olympias/Chalkidiki),
 arsenic, 81
 Kirki Pb–Zn abandoned mines (Thrace), 89
 Komsomolsk, 240
- L**
 Lab-on-chip, 258
 Lachanas Sb–W abandoned mine
 (Thessaloniki), 92
 Laggisite, 96
 Landfilling, 103
 Landfills, 8, 138, 179, 214
 heavy metals, 195
 leachate, 127, 133, 183, 213, 217
 pollution, prediction, 179
 Land management, 115, 152
 Lavrion Pb–Zn–Ag abandoned mine (Attica),
 87
 Lead (Pb), 36, 53–71, 80–90, 213, 239, 245,
 252, 254, 270
Legionella pneumophila, 260
- Lignites, 77, 80, 83
 arsenic, 100–105
 Lillianite, 90
 Lipid/polymer membranes, 281
Listeria monocytogenes, 270
- M**
 Maamora aquifer (NW Morocco), 184
 Madem Lakkos ores, 81
 Malachite green, 274
 Manure, 131–133
 Mathematical models, 175
 Maximum permissible concentration (MPC),
 239
 Membrane/clay polarization, 205
 Metalloids, 55
 Metals, 8, 98, 105, 115, 129, 136, 239
 heavy metals, 6, 33, 37, 43, 89, 195, 213,
 261, 282
 Metamorphic rocks, arsenic, 103
 Meteoric Water Line (MMWL), 120
 Miargyrite, 88
 Microelectronics, 259
 Microfluidics, 257
 fluorescence, 266
 Microfluid injection analysis, 257
 Micro-total-analysis systems (μ TAS), 257, 258
 Microwave tomography (MWT) 203
 Mineral potential, 208
 Mineral trapping, 31, 33, 41–46
 Mineral waters, characterisation, 285
 Montegrosso-Pallareta waste dump complex,
 213
 Morocco, 175
 Multidisciplinary approach, 13
 Multilayer perceptron-neural network
 (MLP-NN), 297
 Multisensor systems, 280
 Municipal solid waste (MSW) reservoirs, 213
- N**
N-(1-Naphthyl)ethylenediamine
 dihydrochloride, 262
 Nealite, 88
 Nickel, 92, 96
 Ni-laterite active mines (Central/NW Greece),
 91
 Nitrates, 115, 118, 130–132, 195
 Nitrification, 132
 Nitrite, 262–266
 Nitrogen, cycling, 132
 N-15, 131
 stable isotopes, 130

North German Basin, 35
 Numerical models, 23

O

Oedometer, 154, 159
 Ophiolite, 82, 93, 95
 Optical sensors, 279, 300
 Ores, 77, 87, 92, 105, 206
 Orpiment (As_2S_3), 36, 98
 Orthoclase, 40
 Orthophosphate, 264
 Oxygen, 88, 117, 119, 242, 245
 O-18, 35, 120

P

Parnassos-Ghiona bauxite mining area, 100
 Pearcite-arsenopolybasite, 87
 Perama Hill Au–Ag active mine (Thrace), 90
 Perfluorocarbon tracer gases (PFT), 44
 Pesticides, contamination, 8, 79, 233, 260
 Petroleum, contamination, 232
 Phase-diagrams, 36
 Phenol pool (Kablova), 210
 Pipelines, monitoring, 232
 Plausibility checks, 34
 Polarization, induced, 193
 Pore waters, 125, 195, 243, 252–254
 mineralization, 241
 Porosity, 21, 22, 38, 45, 153, 164, 178, 199,
 241, 244
 Potentiometry, 244, 281, 282
 Pressure
 freshwater aquifers, 32
 gradient, 207
 hydraulic, 159
 injection, 31, 44
 monitoring, 43
 saltwater migration, 38
 Propanil, 273
 Protection zones (PZs), 13, 24
 Ptolemais-Amynteon Lignite Center (P-ALC),
 101
 Public Drinking Water Source Areas
 (PDWSAs), 18
 Pumping tests, aquifer properties, 156, 160
 electrical field, 168
 Punta Zeza, 89
 Pyrargyrite, 88
 Pyrite (FeS_2), 60, 63, 65, 67, 81, 90, 95, 129,
 199, 242, 244, 251
 Pyromorphite, 245
 Pyrrhotite, 93

Q

Quartz, 40

R

Radar, ground-penetrating, 193
 Raman scattering/spectroscopy, 9, 257, 259,
 273
 Rammelsbergite, 87
 Realgar (As_4S_4), 36
 Red rain, 105
 Reflection coefficient, 202
 Reflectometric interference spectroscopy
 (RIFS), 261
 Refractive index methods, 260
 Relative dielectric permittivity, 201
 Remote protection perimeter, 183
 Reservoir protection zones (RPZs), 18
 Residual trapping, 46
 Risks, prevention, 175
 River Analyser (RIANA), 273
 Rozenite, 245
 Rubidium, 134

S

Safe Drinking Water Act (SDWA), 16
 Safeguard zones (SGZs), 16, 20
 Sahara desert, mineral dust, 77, 80, 105
 Salair Ore Processing Plant (SOPP, Kemerovo
 region, Russia), 241
 Salinization, 122, 128
 geogenic, 35
Salmonella typhimurium, 260
 Saltwater, 44
 displacement, 32
 intrusion, 31, 123
 migration, 38
 Sardinia (Italy), 53
 Saturation degree, 199
 Sb-W, 83, 86, 92
 Scale effect, 151
 Scheelite, 58
 Scorodite, 95
 Self-potential (SP), 8, 193, 206
 Short pumping test, 156, 163
 SH-SAW (shear horizontal surface acoustic
 wave) devices, 281
 Siderite, 40, 41, 46, 85
 Silver, 87, 231, 241, 274
 Slantnet transform (ST), 295
 Slug tests, 155, 162
 Smithsonite, 71
 Solution trapping, 31, 46

Source protection zones (SPZs), 16
Specific electrical resistance (SER), 239
Sphalerite, 58, 81, 242
Stability field-diagrams, 36
Stibnite, 95
Streaming potential, 207
Strontium, 117, 134
 isotopes, 133
Sulfamethizole, 273
Sulfanilamide hydrochloride, 262
Sulfarsenides, 87
Sulfates, 39, 63, 69, 115, 118, 126, 129, 134,
 227, 245, 252
 sulfate-reducing bacteria, 126
Sulfides, 58, 60, 65, 81, 87, 90, 98, 101, 126,
 240, 245
 sulfide-bearing wastes, 239
Sulfur, 102, 117, 126, 129
 stable isotopes, 126
Sulfuric acid, 98, 251
Surface-enhanced Raman scattering (SERS),
 273
Surface plasma wave, 261
Surface plasmon resonance (SPR), 261

T

Tailings, 245
Talmovskie tailings impoundment, 241
Terbutryn, 261
Tetrahedrite/tennantite, 88
Theis solution, 157
Thieno-[3,4-*b*]-thiophene, 271
Time-domain-induced polarization (time-
 domain IP), 8, 203

Total dissolved solids (TDS), 34
Total internal reflection fluorescence (TIRF),
 272
Trapping, mechanisms, 46
Tritium, 35, 61, 117, 118
Tuscany (Italy), 23

U

Urban groundwater contamination, 128
Urea, 132
USA, 16

V

Veenite, 88
Vienna Pee Dee Belemnite (VPDB), 123
Volcanoes, 77
 arsenic, 97
Voltammetry, e-tongue, 287

W

Water, analysis, 34
 monitoring, 193
 quality, 1
 resources, protection, 1
Water Framework Directive, EC, 54
Wellhead Protection Areas (WHPAs), 16

Z

Zinc (Zn), 8, 53, 55, 90, 213, 231, 239, 254